THE UNIVERSITY OF
WARWICK

University of Warwick institutional repository: http://go.warwick.ac.uk/wrap

A Thesis Submitted for the Degree of PhD at the University of Warwick

http://go.warwick.ac.uk/wrap/3123

This thesis is made available online and is protected by original copyright.

Please scroll down to view the document itself.

Please refer to the repository record for this item for information to help you to cite it. Our policy information is available from the repository home page.

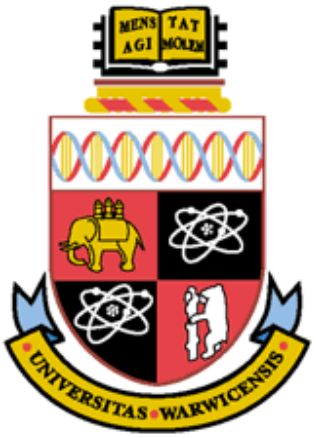

Traversing SPIV for the measurement of vortex rings under background rotation

Mark Brend

BEng

January 25, 2010

This report is submitted as partial fulfilment

of the requirements for the PhD Programme of the

School of Engineering

University of Warwick

2009

"The difficult is what takes a little time; the impossible is what takes a little longer."

Fridtjof Nansen

Contents

List of Tables

List of Figures

Acknowledgements

I would like to begin by thanking my supervisor, Prof. Peter J. Thomas for his continuing support, assistance and insight into geophysical vortex dynamics. I would further like to thank Dr Andrew Skeen (Etalon Research Ltd) for software services and tutelage in the art of PIV measurement and Peter Bryanston-Cross (University of Warwick, OEL) for loan of state of the art PIV equipment and processing software.

In addition thanks must go to the technical staff at the University of Warwick; in particular John Roe for inspired design work and Paul Hackett for highly skilled manufacture and construction of the large rotating facility. My colleagues have further been of great help and support, through difficult times; Dr Paul Dunkley, Dr Joe Naswara, Messrs Amit Kiran, David Hunter and Ms Sandy Gregorio. Finally thanks must go to Dr Amy Willetts for her continual support and advice concerning technical matters.

THE UNIVERSITY OF
WARWICK

AUTHOR: **Mark Brend** DEGREE: **PhD**

TITLE: **Traversing SPIV for the measurement of vortex rings under background rotation**

DATE OF DEPOSIT: .....

I agree that this thesis shall be available in accordance with the regulations governing the University of Warwick theses.

I agree that the summary of this thesis may be submitted for publication.

I **agree** that the thesis may be photocopied (single copies for study purposes only).

Theses with no restriction on photocopying will also be made available to the British Library for microfilming. The British Library may supply copies to individuals or libraries. subject to a statement from them that the copy is supplied for non-publishing purposes. All copies supplied by the British Library will carry the following statement:

> "Attention is drawn to the fact that the copyright of this thesis rests with its author. This copy of the thesis has been supplied on the condition that anyone who consults it is understood to recognise that its copyright rests with its author and that no quotation from the thesis and no information derived from it may be published without the author's written consent."

AUTHOR'S SIGNATURE: .....

USER'S DECLARATION

1. I undertake not to quote or make use of any information from this thesis without making acknowledgement to the author.
2. I further undertake to allow no-one else to use this thesis while it is in my care.

DATE SIGNATURE ADDRESS

.....

.....

.....

.....

.....

www.warwick.ac.uk

List of Publications

Journal papers

Brend, M.A., Thomas, P.J. (2009) "Decay of vortex rings in a rotating fluid". Phys. Fluids, 21, 044105.

Conference papers

Papers related to research material presented in this thesis

Oishi, Y., **Brend, M.A.**,, Thomas, P.J., Murai, Y., Takeda, Y. (2008) "Measurement of Oscillating Vortex Ring of Fundamental Mode Using Color PTV". To appear in the Proceedings of the 36th Visualization Symposium, organized by the Visualization Society of Japan, 22-23 July, Tokyo, Japan.

Brend, M.A., Thomas, P.J., Carpenter, P.W. (2006) "Experiments on Vortex-Ring Dynamics in a Rotating Fluid". Abstract published on p.111 in Book of Abstracts, Vol. 1, EUROMECH Fluid Mechanics Conference 6 (EFMC6), Royal Institute of Technology, Stockholm, Sweden 26-30 June.

Brend, M.A., Thomas, P.J. (2006) "Effects of Background Rotation on Vortex Rings". Paper presented at the annual half-day meeting on *The Dynamics of Rotating Fluids*, held at University College London, Department of Mathematics, 6 January 2006.

Brend, M.A., Thomas, P.J. Xiao, Z., Carpenter, P.W., Verzicco, R. (2005) "Experiments with a New, Unique Large-Scale Rig Investigating the Effects of Background Rotation on Vortex Rings in Water". In: Bulletin of the American Physical Society 50, No.9, p.165, Program of the 58th Annual Meeting of the Division of Fluid Dynamics, Chicago, Illinois, USA, 20-22 November 2005, ISSN 0003-0503.

Inaba, K., Kitaura, H., Murai, Y., Xiao, Z., Thomas, P.J., **Brend, M.**, Takeda, Y. (2005) "Analysis of a Vortex Ring in Rotating Field Using Multi-Dimensional UVP". In the: Book of Abstracts, 14th International Couette-Taylor Workshop, 5-7 September, Hokkaido University, Sapporo, Japan, pp. 99-100.

Thomas, P.J., Xiao, Z., **Brend, M.A.**, Carpenter, P.W. (2005) "The Influence of Background System Rotation on the Dynamics and the Stability of Vortex Rings", talk presented at the conference Recent Advances in Nonlinear Mechanics, 30 August - 1 September, University of Aberdeen, Aberdeen, Scotland.

Other papers

Gregorio, S.O., Thomas, P.J., **Brend, M.A.**, Ellingsen, I.H. Linden, P.F. (2008) "Oceanographic Coastal Currents over Bottom Slopes", talk presented at the EUROMECH, 7th European Fluid Mechanics Conference (EFMC7), University of Manchester, Manchester, UK, 14-18 September. Extended Abstract published on p. 125 in Book of Abstracts.

Gregorio, S.O., Thomas, P.J., **Brend, M.A.**, Ellingsen, I.H. Linden, P.F. (2008) "Effects of the Bottom Topography on Gravity-Driven Oceanographic Coastal Currents", talk presented at EUROMECH Colloquium 501 on 'Mixing of Coastal, Estuarine and Riverine Shallow Flows', Instituto di Idraulica e Infrastrutture Viarie, Università Politecnica delle Marche, Ancona, Italy.

Gregorio, S.O., Thomas, P.J., **Brend, M.A.**, Linden, P.F. (2008) "Large-

Scale and Small-Scale Laboratory Simulations of Gravity-Driven Coastal Currents". Ocean Sciences Meeting, Orlando, Florida, 2-7 March.

Presentations and seminars

Brend, M.A., Skeen, A. J., Thomas, P. J., Bryanston-Cross, P. (2009) Vortex rings and the effects of background rotation, University of Warwick Fluid Dynamics Research Centre seminar series.

Brend, M.A., Thomas, P. J. (2006) Effects of background rotation on vortex rings, The dynamics of rotating fluids meeting, University College London, Department of Mathematics.

Brend, M.A., Thomas, P. J. (2005) The effects of background rotation on vortex rings, Warwick Mathematics Institute 2005/2006 Turbulence Symposium: Workshop on Dynamical Systems, Fluid Dynamics and Turbulence, University of Warwick, Department of Mathematics.

Posters

Brend, M.A., Thomas, P. J., Carpenter, P.W. (2005) The effect of background rotation on Vortex rings, Poster presentation: Conference on Vortex Rings and Filaments in Classical and Quantum Systems, ICTP Trieste.

Abstract

This thesis describes the statistical measurement of vortex ring velocity fields. The measurements were conducted using high accuracy SPIV, with the measurement system traversing with the vortex ring. This incurred two sources of error: vibration led to the superposition of a fluctuating bias across the entire velocity frame; motion of the cameras over time gave rise to inaccuracies in the camera calibration, thus a registration error. Furthermore vortex rings' trajectories carried them away from the centre of the light sheet. The development, implementation and basic evaluation of the corrections to the velocity field to account for these problems (which showed an overall improvement) was a significant undertaking and constitutes a major portion of the work.

The vortex ring measurements were performed on the University of Warwick's recently commissioned unique, large scale, geophysical vortex facility. This enabled measurement of the vortex rings inside a rotating environment and the effects of Coriolis force upon discrete vortex structures to be investigated.

Through consideration of the mean velocity fields for non-rotating vortex rings and the properties derived thereof (trajectory, diameter, circulation, core diameter), several flow phenomena are discussed: the axial swirling flow seen by Naitoh *et al.* (2002) is shown to vary across a wide range of values and tentative support presented for the existence of differing classes of turbulent vortex rings (Dziedzic and Leutheusser, 2004).

Analysis of similar properties for vortex rings produced under background rotation, as well as reinterpretation of numerical results presented by Verzicco *et al.* (1996) (the single prior work on the subject), leads to a detailed description of the dynamics of the velocity field evolution. In addition, it is shown that non-dimensionalising time evolution curves of vortex ring trajectory and circulation cause data collapse across a range of generation conditions and rotation rates.

Keywords: Vortex rings, Stereoscopic particle image velocimetry, Self calibration, Background rotation

List of abbreviations

2C 3C	2 3 component
2D2C	2 dimension, 2 component
2D3C	2 dimension, 3 component
3D3C	3 dimension, 3 component
DC	Direct current
DLT	Direct linear transformation
HGS	Hollow glass spheres
IQR	Inter-quartile range
LFCPIV	Local field correction particle image velocimetry
LDA	LASER doppler anemometer
MSE	Mean squared error
ND:YAG	Neodymium-doped yttrium aluminium garnet
OEL	Optical engineering laboratory
px	Pixels
PID	Proportional/Integral/Derivative
PIV	Particle image velocimetry
PLV	Pulsed light velocimetry
PTV	Particle tracking velocimetry
RMS	Root mean square
SNR	Signal to noise ratio
SPIV	Stereoscopic particle image velocimetry
PPR	Pulses per revolution
RPM	Rotations per minute
TTL	Transistortransistor logic
USB	Universal serial bus
VMU	Vector map units
WIDIM	Window deformation iterative multigrid

CHAPTER 1

Introduction

Vortices are one of the basic dynamical structures governing fluid flows. Vortex rings represent one geometrically simple type of vortex that is often employed to study aspects of vortex dynamics due to its stability, ease of generation and inherent beauty. Rotating flows appear frequently in both nature and technological applications and are often associated with vortical flows. In such flows Coriolis force gives rise to phenomena absent from non-rotating flows and may greatly change the evolution of the flows measured.

In this work we perform stereoscopic particle image velocimetry (SPIV) measurements of vortex rings both with and without background rotation. We pay particular attention to the time evolution of vortex rings, which we measure by traversing the SPIV system at the same rate as the vortex ring. Measurement acquisition whilst traversing led to several artefacts manifesting themselves in both the velocity fields and the spatial calibration of the SPIV components. The techniques developed to overcome these issues are also presented, which are of interest to the PIV community, as they provide a robust means of applying corrections for the types of errors likely to occur in less-than ideal, non-laboratory conditions.

This work is centred around a newly commissioned experimental facility at the university of Warwick, specially designed for the study of vortex rings. The facility comprises a large octagonal water tank ($1m$ across, $2.5m$ high) mounted atop a sturdy rotating platform (c.f. section 4.2). This experimental platform is unique in terms of its size and to the author's knowledge, there are no comparable facilities elsewhere in the world capable of rotation. Due to the size of the facility, it is an extremely dangerous working environment, therefore after rotation has commenced, physical access is strictly limited. To overcome this, remote programmable motorised control of the rotating platform and drives mounted inside the rotating environment was enabled through the use of robotic motor controllers and actioned from the facility's control room.

The rotating tank described was designed specifically to measure the effects of background rotation on vortex ring dynamics, for which a single prior study exists (Verzicco *et al.*, 1996). To this end, vortex ring generation apparatus was mounted at the top of the facility, using a standard stepper motor controlled piston-cylinder arrangement. The vortex rings were generated in the water such that they propagated downwards toward the bottom of the tank. Vortex rings were produced both with the tank stationary and rotating, for which the tank was rotated for a sufficiently long time that the generator, the tank and water were all turning at the same rate (solid body rotation).

The work presented here consists of the integration of a state of the art SPIV system with the vortex generation facility, to enable high resolution measurement of the time evolution of the vortex ring velocity field. The PIV system and image analysis software was made available through an internal collaboration with Professor Peter Bryanston-Cross (University of Warwick Optical Engineering Laboratory).

The novel aspects of the work presented in this thesis may be broken into 7

sections:

1. The development of a traversing PIV system capable of following vortex rings under open loop control. This provides full field measurement of vortex ring evolution (chapter 4).

2. Complete automation of the instrumentation and experimental process, enabling long run-times without user intervention and so acquisition of statistically relevant numbers of samples, approximately 400 vortex rings were generated and followed per condition (chapter 4).

3. Traversing the SPIV system and following vortex rings gave rise to several, errors not normally present in PIV measurements. Processing techniques were developed to enable the analysis of the data acquired, correcting for uncertainty in vortex ring motion and also errors induced by the traversing system. These corrections are particularly useful for PIV measurements outside of non-idealised "laboratory" conditions (chapter 5).

4. Despite the major thrust of this work constituting a PIV study, some results are presented from an initial dye visualisation study (chapter 6). Results are presented concerning the maximum propagation distance of vortex rings under background rotation, the work in this chapter has recently been published and so closely follows Brend and Thomas (2009).

5. We provide the first simultaneous measurement of vortex ring evolution over time, measuring 3D vortex ring trajectory, circulation, vortex ring diameter, core diameter and vortex ring tilt (chapter 7). This is performed both for rotating and non-rotating vortex rings, and the statistical nature of the measurements allows for definitive isolation of trends within the data presented.

6. We further provide the first measurements of the spatio-temporal evolution of the velocity and vorticity fields. This is performed both for vortex rings with and without background rotation and from a statistical basis. This allows measurement across large times of the behaviour of the vortex ring (chapter 7).

7. Finally the results from the unique measurement system are discussed in relevance to previous vortex ring measurements. From this we provide a new outlook on vortex ring dynamics both with the effects of background rotation and without (chapter 8).

A comprehensive literature review is provided in sections 2 and 3, covering the major aspects of the PIV and vortex ring literature. This provides the context for the work, and the background knowledge necessary to gain an understanding of the developments to the SPIV technique.

CHAPTER 2

Particle Image Velocimetry

This chapter is concerned with a review of the particle image velocimetry (PIV) technique, necessitated by the developments to this technique presented in this work (chapter 5). Of particular relevance to the novel work presented are sections 2.3.4 and 2.4.2, as the principles outlined in these sections are used thoroughly in chapter 5. The remainder of this chapter aims to provide a succinct overview of the PIV technique to develop sufficient understanding that the reader unfamiliar with the PIV technique may follow sections 2.3.4 and 2.4.2 and also have an appreciation for the decisions made in the design of the experiments, chapter 4.

2.1 Introduction

Particle image velocimetry (PIV) is a technique for estimating flow velocities of fluids; due to its accuracy and relative ease of set up, it has become a standard tool implemented by the modern experimental fluid dynamicist. The first PIV measurements are accredited to Leese and Novak (1971), who made estimates of wind speed from satellite images of clouds. For more than a decade after this

PIV remained known as low seeding density laser speckle velocimetry until it was simultaneously reclassified by two independent groups Adrian (1984), Pickering and Halliwell (1984).

It is unsurprising that such a well established technique boasts a plethora of reviews on all aspects of the subject, including its historical development. As with many experimental techniques, technological advances have improved PIV greatly. For brevity, this work will only provide a basic overview of current methods and focus primarily on their applicability to liquid flows. For more information on the subject, the interested reader is directed toward any one of the excellent reviews available; Adrian (1991), Grant (1997), Raffel *et al.* (1998), Prasad (2000), Adrian (2005), Skeen (2006), Schröder and Willert (2008).

2.2 PIV acquisition

PIV infers fluid velocity by imaging markers, known as tracer or seeding particles. The markers are imaged at multiple points in time and from this the displacement of the seeding is measured. By knowing the time between images, one can simply calculate the velocity of each particle.

A PIV measurement is composed of two parts, the experimental setup and the subsequent image analysis, which computes the fluid velocity vector field. A typical PIV experimental setup consists of a camera mounted orthogonal to a measurement volume, the fluid within which is seeded with tracer particles. This is illustrated in figure 2.1. The measurement volume is imaged at times t_0 and $t_0 + \Delta t$, with each exposure lasting for time, δt. This is normally achieved by pulsing or externally modulating the source of illumination, most commonly a laser. The images of the particles are then analysed and velocity vectors computed.

Image analysis is normally performed in several stages, as illustrated in fig-

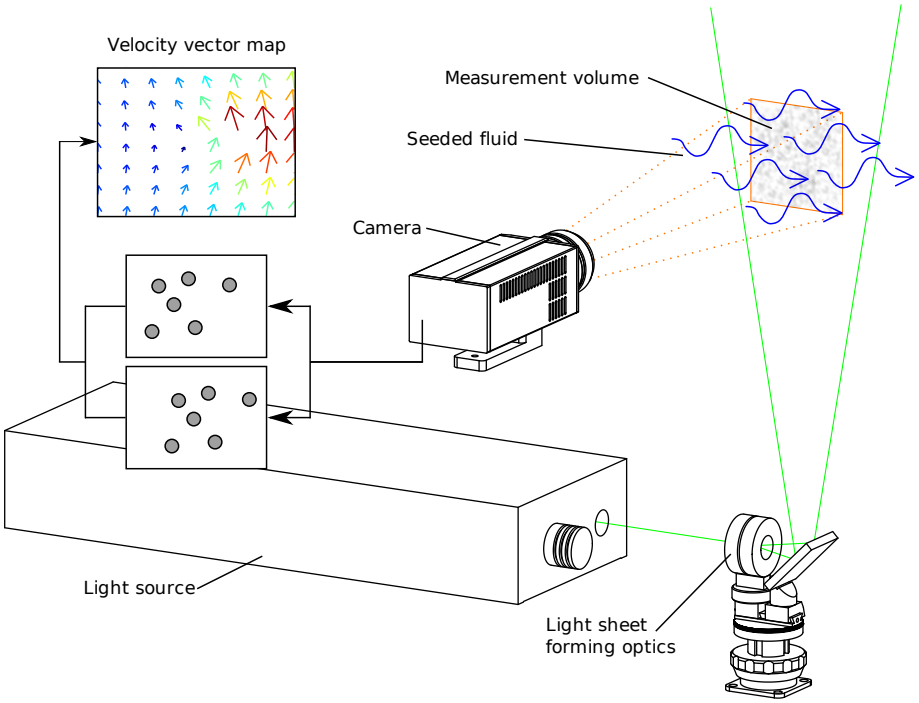

Figure 2.1: A typical PIV setup

ure 2.2. First the image is broken up into a number of sub-images, these are commonly called sub-windows or interrogation windows and it is these sub-images that are then analysed. The analysis consists of an image correlation which computes a correlation map. The position of the highest value in this correlation map indicates the most likely particle displacement for the correlated images.

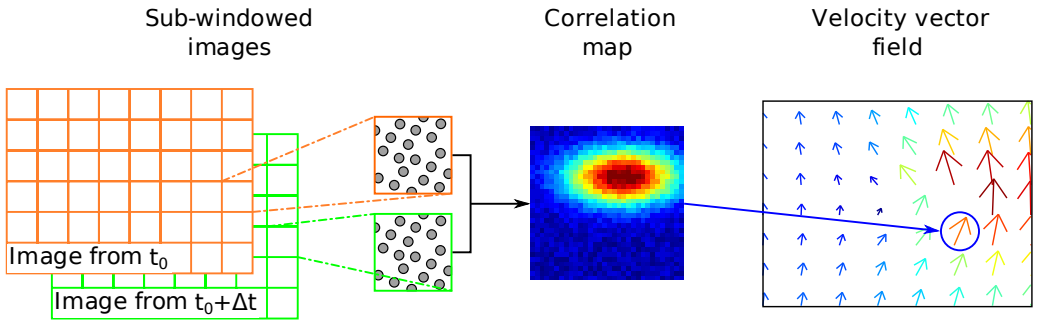

Figure 2.2: Typical PIV processing

2.2.1 Experimental setup

There are several important factors involved in the design of a PIV experiment. Consider first the relationship between camera framing and pulse encoding, several combinations are available, as illustrated in figure 2.3. One can record either a single frame or multiple frames, and each frame may be exposed once, twice or multiple times.

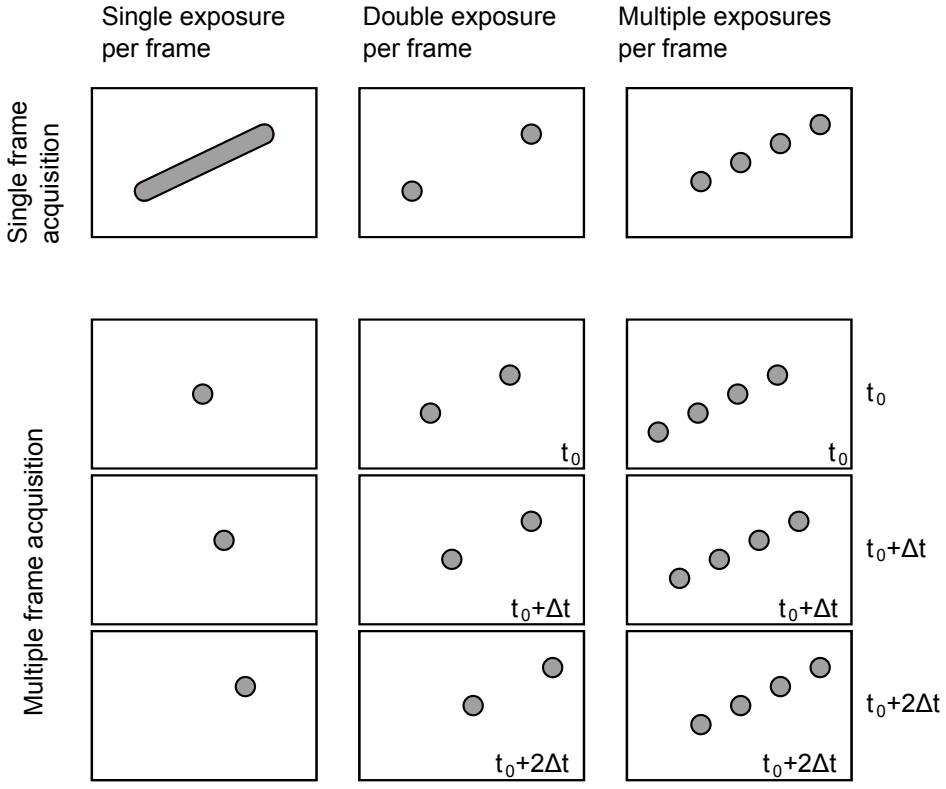

Figure 2.3: A comparison of pulse encoding methods, adapted from Adrian (1991)

Single frames containing a single exposure may be used to measure particle velocity. This requires that δt be relatively long, such that the acquired particle image forms a streak. This technique is referred to as particle streak velocimetry, but with the exception of 3 component (3C) measurements (Sinha and Kuhlman, 1992), the results are sufficiently high in error to render them worthy of only qualitative visualisation. The most significant error in streak velocimetry is the

inability to determine whether the measured streaks move out of the measurement volume. Particles leaving the measurement volume during the illumination time result in shorter streaks and an underestimate of velocity.

The major error arises from the ambiguity as to the cause of streak termination. It is impossible to determine if the streak ends because the exposure has been terminated or because the particle has left the measurement volume.

The remainder of pulse encoding methods can be divided into two distinct groups; cases where a single frame is exposed (these require auto-correlation analysis to generate velocity vectors) and cases where multiple frames are exposed (these require cross-correlation analysis).

The major problem with single frame exposure is that it contains an inherent directional ambiguity. Consider for example the double exposure, single frame case in figure 2.3. One cannot determine if the dot was in the left, or right-hand position first. Several work-arounds to this issue have been documented, examples include, but are not limited to; mechanical image shifting (Adrian, 1986), opto-electrical image shifting (Bertuccioli *et al.*, 1996), using pulses of different colour (Gogineni *et al.*, 1998) and more. Fixes such as these tend to introduce errors, are sensitive to precise alignment and greatly increase the complexity of experimental set up.

It has been shown that increasing the number of pulses recorded within each frame leads to an improvement in the signal to noise ratio (SNR) of the measurement (Keane and Adrian, 1991). This is because the number of particles within a given interrogation window is increased and there is a reduced likelihood of particles leaving the measurement volume. One has to ensure however that the pulse separations are long enough that the particle images don't overlap.

Cross-correlation of multiple frames (each containing a single exposure) does not suffer from the directional ambiguity associated with auto-correlation. Fur-

ther to this, a switch from auto-correlation to cross correlation provides a doubling of the signal to noise ratio (Keane and Adrian, 1992). Since the development of a digital camera sensor capable of imaging two frames in quick succession by Kodak in the mid-90's (Adrian, 2005), this has become the default method of acquisition.

2.2.2 Experimental parameters

When designing a PIV experiment, the most fundamental and perhaps most important parameter for consideration is the time between images exposures, Δt. The requirements of Δt are conflicting:

- Δt should be sufficiently short that the measurement is effectively instantaneous. As the calculation of velocity is performed using a finite difference gradient calculation, the error due to Taylor series truncation is minimised for small Δt (Boillot *et al.*, 1996).

- Δt should be long enough with respect to the exposure time, δt, that the particle images are not blurred. It is recommended that $\Delta t/\delta t > 20$ (Gray *et al.*, 1991), however in practice ratios are often substantially lower (Willert and Gharib, 1991).

- Δt should be short enough that few particles leave the measurement volume, thus reducing particle pairing. It is suggested that $|u_z|\Delta t/\Delta z_0 < {}^1/_4$ (Adrian, 1986).

- Δt should be sufficiently large that the measured particle displacements, $\Delta\mathbf{X}$, is significantly greater than measurement error. Measurement error is notoriously difficult to quantify in PIV studies; in practice, for a correctly set up PIV experiment, $\Delta\mathbf{X} >> 0.1px$ (Scarano, 2002).

A detailed analysis was made into selection of optimum Δt by Boillot *et al.* (1996). They concluded that:

$$\Delta t_{opt} = \sqrt{\frac{2cd_\tau}{M|\dot{\mathbf{u}}|}} \tag{2.1}$$

Here M is the lens magnification factor, c a dimensionless constant (typically $0.05 \leq c \leq 0.1$), d_τ is the diameter of a particle on the imaged on the camera's sensor and $\mathbf{u}$ is the fluid velocity. Unfortunately this analysis assumed that given pulses at times t and $t + \Delta t$, the velocity calculated would be for time t, which leads to truncation error $\mathscr{O}(\Delta t^2)$. Calculating the velocity at time $t + 1/2\Delta t$ instead however results in truncation error $\mathscr{O}(\Delta t^3)$ (Wereley and Meinhart, 2001; Meunier and Leweke, 2003).

From practical experience, Adrian (1986) recommends $M|\mathbf{u}|\Delta t/d_I \leq 1/4$, here d_I is the size of the interrogation window. It is in fact commonplace to decide the spatial resolution required and then adjust Δt until $M|\Delta\mathbf{X}| \leq 1/4 d_I$.

Another factor for consideration is the light sheet thickness, δz_0. For 2-component (2C) PIV, thick light sheets have a tendency to promote a low velocity bias. This is because particles with a high out of plane velocity component remain in the light sheet across Δt, thus reducing the velocity measurement. The maximum low velocity bias due to out of plane velocity has been quantified by Skeen (2006), and is detailed in equation (2.2).

$$\sigma_{OOP} \leq \frac{\sqrt{(\bar{\mathbf{u}}\Delta t)^2 - \Delta z_0^2}}{\bar{\mathbf{u}}\Delta t} \tag{2.2}$$

Very thin light sheets remove the problem of out of plane motion, as any out of plane motion carries tracer particles out of the measurement volume, this does however increase the error of velocity measurement. This error arises from reduced particle pairing, resulting in poor SNR in the correlation maps and in

turn, increased error. Alternatively, one can drastically reduce the error of out of plane motion by measuring it, using 3C techniques.

The measurement of the out of plane velocity component has the added benefit of removing perspective errors, as defined by Prasad (2000). These errors arise because any two light rays travelling from illuminated particles within the light sheet to the camera sensor will not be parallel. It was found that velocity errors of up to 10% could occur due to this.

Finally, the seeding density must be sufficiently large to provide high signal to noise ratio during correlation. Keane and Adrian (1992) state that the number of particles visible in an interrogation window N_I, must be greater than 10 for successful cross-correlation. For modern iterative algorithms (c.f. section 2.3.3 it is important for $N_I \gtrsim 10$ during initial passes, however PIV measurement may be successful, with N_I as low as 1 for final passes (Hart, 2000).

2.2.3 3 component velocimetry

3C pulsed light velocimetry measurements, such as PIV, may be made throughout a plane or a volume; these are referred to as 2D and 3D techniques respectively. Using this notation, a standard 2-component PIV system as described previously, would be termed a 2D2C measurement.

Perhaps the conceptually simplest method of generating 3C measurements is particle tracking velocimetry (PTV), which is normally performed as a 3D measurement. For this, multiple cameras are arranged such that each camera measurement has a different view of the measurement volume. Particle images are then matched between each camera, a 3D estimation of particle position may be made for all particles appearing in more than one camera image, this is due to the different perspective of the scene. The particle images are then matched against those acquired from subsequent exposures, thus providing a

particle displacement measurement.

This leads to two major drawbacks; firstly, the seeding density for effective volumetric PTV must be very low, so the view of any particle will not be obstructed by others in any camera. Resulting vector volumes from the technique contain at the most $\mathcal{O}(10^3)$ vectors (Maas *et al.*, 1993; Walpot *et al.*, 2006). Secondly, velocity measurements are spatially distributed with the particles, i.e. the resulting vectors lie on an unstructured grid. As shown by Sinha and Kuhlman (1992) this leads to significant errors in the calculation of velocity derived properties requiring spatial integrals or derivatives, for example vorticity.

The most common method of determining out of plane velocity is in a similar fashion to 3C-PTV, using multiple cameras, each with a different view of the measurement volume. This said there have been a number of single camera techniques developed and tested; Raffel *et al.* (1995) set up a system where three overlapping light sheets were staggered in the out of plane direction. Cross correlation was performed using very large interrogation windows, and the out of plane component measured from strength of the correlation signal. As the out of plane velocity increases, more particle pairs leave the light sheet and reduce the signal strength of the correlation.

Colour has also been used to provide depth information in single camera systems. Ido *et al.* (2003) illuminated a region with a liquid crystal projector, allowing accurate variation of hue with depth. If relatively large, spherical seeding particles are used, PTV algorithms may be used to measure the in plane displacement and the out of plane displacement may be estimated by looking at the change in hue of the particle image. Similarly, several authors have used multiple, discrete, differently coloured light sheets (Cenedese and Paglialunga, 1989; Brücker, 1996; Jaw *et al.*, 2003).

Many recent developments have been made in the field of tomographic PIV,

which produces 3D3C vector fields using a PIV style correlation. First a tomographic reconstruction technique is used to build a 3D representation of the scene from acquisitions made by a number of cameras; Elsinga *et al.* (2006) recommends a minimum of four. Two reconstructed scenes may then be cross correlated using the PIV algorithms extended for the extra dimension, resulting in a 3D correlation map which directly yields a 3C velocity vector.

Despite the abundance of techniques available for making 3C pulsed light velocimetry (PLV) measurements, the majority are made by a 2D3C technique called stereoscopic PIV. Two cameras are arranged such that each has a different view of the measurement volume, which is defined by a light sheet thick enough to retain particles across Δt (Prasad, 2000). The particle images from each camera are correlated independently, as in a 2C PIV setup, and through knowledge of the cameras' viewing orientation; these 2C vector fields can be combined to provide a full 3C measurement.

2.2.4 Seeding

The flow markers or seeding particles used to track the fluid flow in PLV techniques have two requirements placed upon them; to provide particle images suitable for correlation and to accurately represent the fluids motion. On the basis of the latter requirement, Westerweel (1997) suggests "ideal" seeding should; follow the fluid's motion exactly, not influence the fluid properties or flow and not interact with one another. These contradictory requirements are summarised succinctly by Adrian and Yao (1985) and Melling (1997), large particles improve light scattering, small particles follow the flow more faithfully.

In order to generate images that will provide high quality correlations, the seeding should provide large particle images that do not overlap (Prasad *et al.*, 1992). The upper limit of particle size is determined by the required window size,

c.f. section 2.2.2, whereas sub-pixel vector resolution is lost for particle images below $2px$ (Nogueira *et al.*, 2001). The images should also have high contrast with respect to the background, without being saturated.

Tables of seeding particle properties have occurred frequently in the literature, a detailed summary of these are provided by Skeen (2006). Rough estimates of suitable seeding particle diameters are provided by Adrian and Yao (1985); $d_p \simeq 5\mu m$ for air and $d_p \simeq 10\mu m$ for water.

2.2.4.1 Flow following

The assumption most often made during PIV experiment set up is that the flow markers follow the flow. Reality is better depicted by figure 2.4. The particle velocity is calculated from the particle's displacement, $\mathbf{\Delta X}$, as measured using the PIV correlation procedure. This vector is not necessarily equal to the particle motion, $\mathbf{u_p}$, which in turn is not necessarily equal to the fluid velocity $\mathbf{u_f}$.

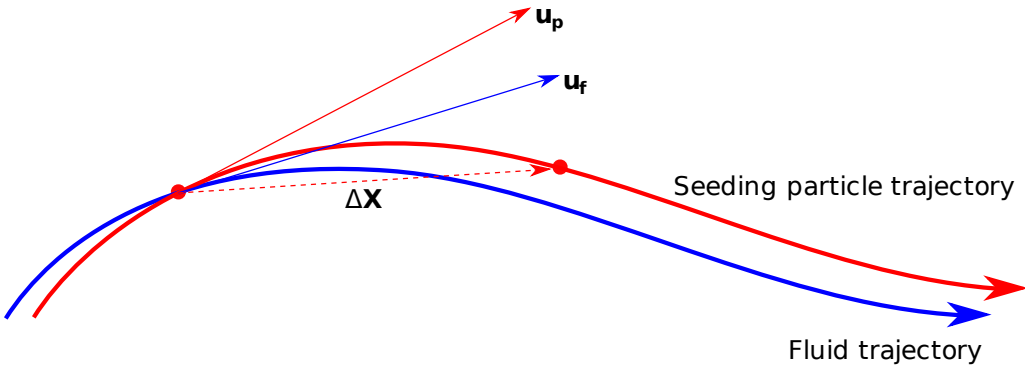

Figure 2.4: Illustration of the disparity between particle and fluid trajectories, adapted from Westerweel (1997)

For low particulate Reynolds numbers, $Re_p = \tilde{u} d_p \rho_f / \mu_f < 1$, where $\tilde{u} = |\mathbf{u_p} - \mathbf{v}|$, μ_f is the kinematic viscosity of the fluid and ρ_f the density of the fluid, particulate motion may be modelled by assuming Stokes drag. The effects of particle inertia are ignored and a model for particle motion is given in equa-

tion (2.3), which may be used to provide an estimate for the error in particle flow following (Grant, 1997).

$$\tilde{u} = \frac{d_p^2 \rho_p \dot{u}_p}{18\mu_f} \tag{2.3}$$

The use of equation (2.3) to predict the particle slip velocity does however introduce systematic errors in certain cases. Examples include Saffman lift, which occurs in strong shear (Saffman, 1965) and the centripetal forces arising from swirling flow (Grant, 1997). The Saffman lift, F_s is detailed in equation (2.4). Here ν_f is the dynamic viscosity of the fluid.

$$F_s = 81.2\mu_f \tilde{u} d_p^2 \sqrt{|\nabla \mathbf{u}|}/\sqrt{\nu_f} \tag{2.4}$$

Estimates of the effect of swirling flow can be made by assuming an axisymmetric two-dimensional flow and again Stokes drag. Considering the flow to have swirling and radial components u_θ and u_r, results in the equations of motion presented in equation (2.5) (Grant, 1997). Equations (2.5a) and (2.5b) provide combined Coriolis, centrifugal effect forcing on a particle within the swirling flow. Equation (2.5c) provides the relaxation time, τ_p of the particle, which gives the flow following capability of the particle.

$$\frac{du_{rp}}{dt} = \frac{u_{\theta p}^2}{r} + \frac{1}{\tau_p}(u_{rf} - u_{rp}) \tag{2.5a}$$

$$\frac{du_{\theta p}}{dt} = -2\frac{u_{\theta p} u_{rp}}{r} + \frac{1}{\tau_p}(u_{\theta f} - u_{\theta p}) \tag{2.5b}$$

$$\tau_p = \frac{\rho_p d_p^2}{18\mu} \tag{2.5c}$$

2.2.4.2 Flow alteration

The effect of tracer particles on their surroundings may be estimated using measurements that do not require fluid flow tracers, such as hot-wire anemometry. Measurements of this phenomena have also been made using laser Doppler anemometry (LDA) systems which rely on particle size filtering (Kulick *et al.*, 1994). Such experiments have shown that seeding particles are capable of modulating the turbulence intensity levels of fluid flows (Levy and Lockwood, 1981; Hetsroni, 1989; Gore and Crowe, 1991; Kulick *et al.*, 1994; Fessler and Eaton, 1999).

The majority of the work has been performed in air and the generally accepted trend is that relatively small particles, $\mathscr{O}(10\mu m)$, act to attenuate turbulence, whereas larger particles, $\mathscr{O}(500\mu m)$, act to enhance the turbulence. This effect is however dependant on the turbulent time and length scales of the flow and it is strongly dependent on seeding density and Stokes number. A reasonable claim is that turbulence modulation is reduced for lower seeding densities and lower Stokes numbers, beyond this accounts are conflicting.

Stokes number is a non-dimensional ratio between the responsiveness of a particle to fluid acceleration and the frequency of changes of the fluid, it is given in equation (2.6). Here τ_p is the particle relaxation time, as given in equation (2.5c) and τ_f is some time scale related to the flow speed. In the case of flow over a backward facing step, $\tau_f = 5H/U_0$ (Fessler and Eaton, 1999), H is step height, U_0 the centreline velocity.

$$St = \frac{\tau_p}{\tau_f} \tag{2.6}$$

In terms of PIV measurements, flow alteration should be a minimal problem, provided small particles are used.

2.2.4.3 Particle interactions

As pointed out by Adrian (1984), at the seeding densities required to generate the speckle patterns necessary for laser speckle velocimetry (the predecessor to PIV, where extremely high seeding densities were used), particle interactions are likely. For the lower seeding density case of PIV however, particle separations are typically $\mathscr{O}(10^3 d_p)$ (Melling, 1997) thus we can assume particle interactions a rarity.

2.2.4.4 Particle images

The diameter d_τ, of a particle as it appears on the camera's image plane may be calculated from equation (2.7a). For very small particles the method of light scattering changes, and a bright Airy disk appears around the particle (Adrian and Yao, 1985). The diameter of this disk, d_A is estimated in equation (2.7b). It can be seen that for very small particles, the disk will be larger than the particle image itself (Adrian and Yao, 1985). Here M is the magnification of the lens, $f^\sharp$ is the focal length of the lens divided by the aperture, commonly referred to as f-number and λ the wavelength of incident light.

$$d_\tau = \sqrt{M^2 d_p^2 + d_A^2} \tag{2.7a}$$

$$d_A = 2.44(M+1)\lambda f^\sharp \tag{2.7b}$$

Adrian (1991) provides detailed information pertinent to the calculation of the particle image's intensity. In summary, he shows that mean particle image intensity per unit area, $\epsilon \propto (d_p/\lambda)^n$. In the case of small seeding particles, $\mathscr{O}(1\mu m)$, $n = 3$, and for larger particles, $\mathscr{O}(10\mu m)$ or bigger, $n = 2$. Of interest is that for larger particles, the particle image intensity does not increase with

size, as both mean particle intensity and particle area increase with d_p^2.

2.3 PIV data processing

2.3.1 Correlation

Particle image displacements are calculated using a correlation technique, this provides a statistical measure of similarity between two signals. Modern PIV measurements are made using a single exposure on multiple frames, cross correlation is then used to analyse images, which are adjacent in time. This is formulated in equation (2.8) (Willert and Gharib, 1991; Keane and Adrian, 1992).

$$c(u,v) = A_{ij} \star B_{ij} = \sum_{x,y} A_{ij}(x,y) B_{ij}(x+u, y+v) \tag{2.8}$$

The correlation map, c provides the degree of similarity between the two interrogation windows, A_{ij}, B_{ij} as a function of their spatial offset, u, v this is illustrated figure 2.5. The interrogation windows, A_{ij}, B_{ij} are sub-images of the acquired images A and B. The value of each element within the correlation map array is equal to the product of overlayed image intensities, summed, an example cross correlation map is shown in 2.6a. The maximum in the correlation map reveals the spatial offset which maximises the similarity between the two images and in turn provides the best estimate of particle displacement.

For cases where it is not possible to split exposures across frames, a single frame is exposed multiple times. This is then analysed using auto correlation, which is a special case of cross correlation, $A_{ij} \star A_{ij}$ i.e. the cross correlation of image A_{ij} with itself. An example correlation map is shown in figure 2.6b, where an image containing two exposures has been auto correlated.

Figure 2.6b exhibits three peaks, the highest is the self correlation peak, at

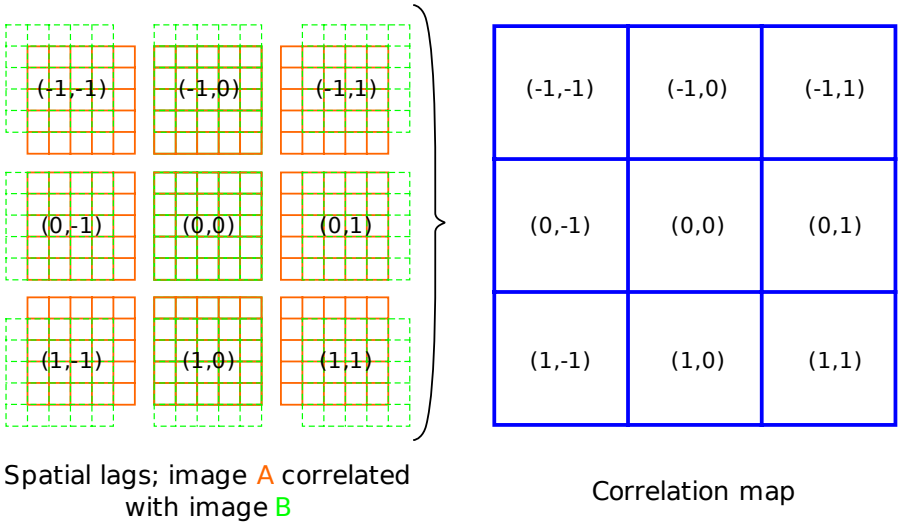

Figure 2.5: An illustration of the 9 image offsets involved in generating a 3×3 correlation map

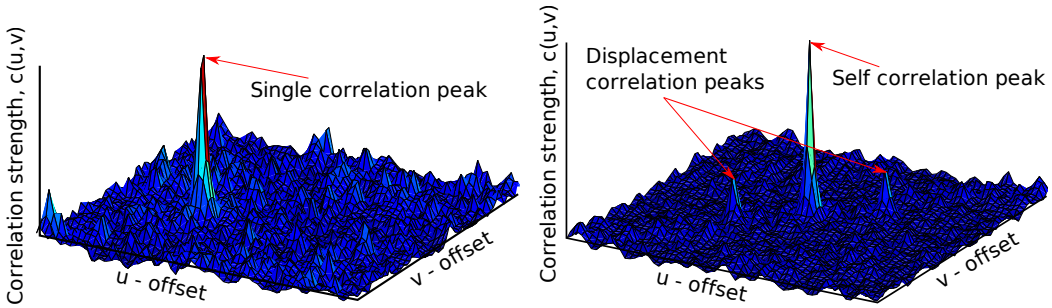

(a) Cross correlation (b) Autocorrelation

Figure 2.6: Comparison between correlation maps

offset $(0 \quad 0)$. The offset due to particle displacement is then represented by the two smaller, but still distinct peaks, the pair of peaks arise because of the directional ambiguity associated with auto correlation. Figure 2.6a gives the cross correlation analogue of figure 2.6b, a single peak is present, significantly improved SNR.

The direct computation of a correlation map is commonly performed using a convolution, which is a computationally expensive process, requiring $\mathcal{O}(K^2L^2)$ calculations (Roth and Katz, 2001). An alternative to this is phase correlation

which is performed as a single multiplication in the frequency domain, shown in equation (2.9). This reduces computational load to $\mathscr{O}(KL\log_2(KL))$ (Leese and Novak, 1971), and in the majority of PIV measurements provides a good approximation to cross correlation. Phase correlation has a tendency to worsen the effects of peak-locking (c.f. section 2.3.2) and is also unsuitable in cases such as LFCPIV where a windowing function is applied to the interrogation windows (c.f. section 2.3.3).

$$c(u,v) = \mathscr{F}^{-1}(\mathscr{F}^{*}(A_{ij})\mathscr{F}(B_{ij})) \tag{2.9}$$

Normalised cross correlation, detailed in equation (2.10) may be used instead of the standard cross correlation algorithm when increased accuracy is required (Nogueira *et al.*, 2001). Hu *et al.* (1998) show that it removes bias due to variable image intensity amongst other things from the produced correlation map. The normalised cross correlation may also be calculated in the frequency domain, however the computation of the denominator of equation (2.10) is non-trivial (Huang *et al.*, 1997). Therefore in cases where normalised cross correlation is advantageous, it is normally computed directly. Algorithms to compute normalised phase correlation are available, the interested reader is directed to Ronneberger *et al.* (1998).

$$\gamma(u,v) = \frac{\sum_{x,y}[A_{ij}(x,y) - \bar{A_{ij}}][B_{ij}(x+u,y+v) - \bar{B_{ij}}]}{\sqrt{\sum_{x,y}[A_{ij}(x,y) - \bar{A_{ij}}]^2[B_{ij}(x+u,y+v) - \bar{B_{ij}}]^2}} \tag{2.10}$$

Irrespective of the type of correlation used, the parameter effecting the errors in correlation most strongly is the size of the interrogation window chosen (Westerweel, 1997). For large window sizes spatial integration is over a large area, this

means more particle images, larger measurable displacements, hence increased SNR and reduced random error (Adrian, 1991). In the case where the fluid velocity has a strong gradient, large window sizes suffer poor particle matching across the domain, therefore some compromise is necessary.

The spatial resolution of the computed vector field may be enhanced by overlapping interrogation windows, common overlap schemes are 50% and 75% (Scarano *et al.*, 2005). An overlap of 50% quadruples the number of vectors calculated, 75% increases it by 16 times. An increased overlap improves the spatial resolution of the measurement, whilst maintaining good signal to noise ratio through large N_I. As the interrogation windows are overlapping however, the particle images in adjacent windows contribute to the velocities measured by convolving both windows. This implies an increased degree of spatial smoothing. It is for this reason that multi-grid methods have become popular (c.f. section 2.3.3).

2.3.2 Sub-pixel peak detection

The simplest improvement to be made in vector field calculation is in the location of the correlation peak. By employing a fitting method, the maxima may be interpolated to sub-pixel accuracy. The most frequently reported peak interpolation schemes are centroid, parabolic and Gaussian. Assuming particle images of $> 2px$, these methods should find the correlation to within $0.1px$ (Nogueira *et al.*, 2001). Further to this, iterative matching schemes based on Whittaker's method of signal reconstruction are sometimes employed, providing accuracy as high as $1/64px$ (Lourenco and Krothapalli, 1995).

A common issue associated with sub-pixel peak detection is so called peak-locking. This is where vectors' values suffer a tendency toward integer values - a fact that can be quickly identified by looking at a histogram of vector values. This arises for a number of reasons, including particles lying on interrogation window

borders. Nogueira *et al.* (2001) show that by performing direct normalised correlation, these errors may be minimised.

2.3.3 Multi-grid methods

Recall that for regions of high fluid gradient, small interrogation windows achieve better SNR than their larger counterparts. However in areas without high gradient, larger window sizes result in a higher SNR and are also able to measure larger particle displacements. Multi-grid or super-resolution methods aim to tackle this problem by simultaneously providing the benefits of both large and small interrogation windows.

A precursor to such methods was the "multi-step cross correlation with a discrete window offset" (Westerweel *et al.*, 1997). Here an initial cross correlation pass is performed, the result of which is used to shift the interrogation windows, one with respect to the other, as illustrated in figure 2.7.

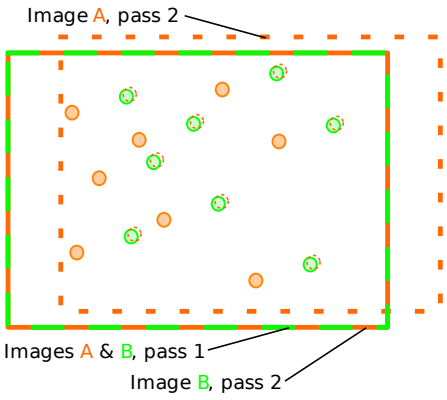

Figure 2.7: An illustration of window shifting

An advancement on this is an equal and opposite shift of both windows with respect to one another, resulting in a second order accurate approximation of velocity, as illustrated in figure 2.8 (Wereley and Meinhart, 2001; Meunier and Leweke, 2003). Furthermore by applying a fractional offset instead of discrete,

peak-locking errors are further reduced (Scarano, 2002). In order to perform fractional offsets, it is required that images be interpolated: bilinear, multidimensional polynomial and Whittaker's method (used in conjunction with either a Hamming or Blackman window) are popular choices (Scarano, 2002).

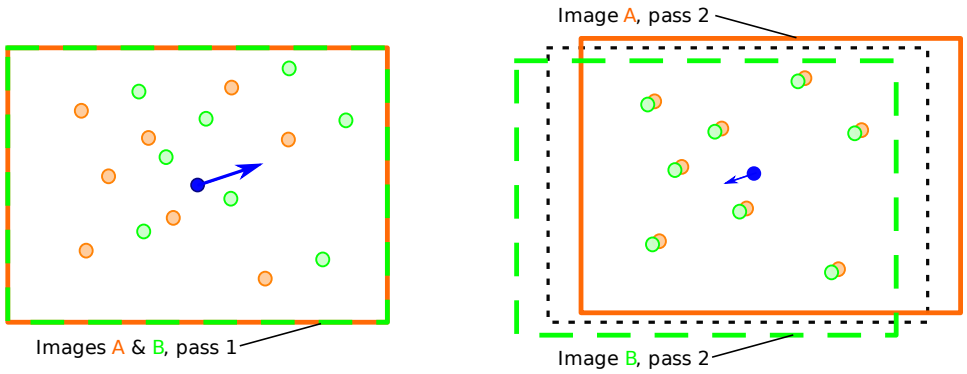

Figure 2.8: Second order accurate PIV through window offsetting

An extension of the fractional window offset is the multi-grid method. Here an initial window size is chosen, and one or more correlations performed, as in the standard fractional offset method. The window size is then decreased and the velocity field interpolated. This interpolated field is then used to offset the reduced size interrogation windows and the whole process is repeated with progressive window refinement until a suitably small window size is arrived at (Scarano and Riethmuller, 2000). This method is very robust and benefits from excellent all-round performance even in the presence of reasonable velocity gradients.

In situations where interrogation windows are larger than velocity gradients even multi-grid methods fail to accurately describe the flow field. In these cases, advanced deformable gridding techniques are required, this is where interrogation windows are manipulated according to some arbitrary 2D homography prescribed by the flow field, illustrated in figure 2.9.

Grid deformation was suggested by Huang *et al.* (1993) and Jambunathan *et al.* (1995), high frequency artefacts within the velocity field prevented reli-

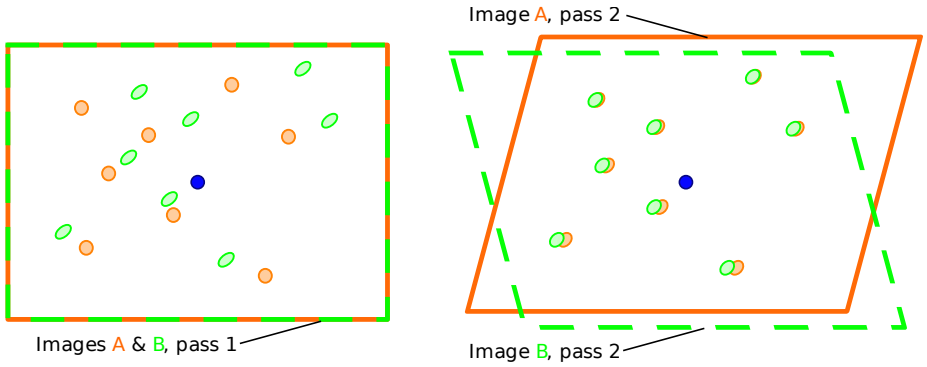

Figure 2.9: An illustration of window deformation methods

able implementation. Nogueira *et al.* (1999) used a windowing function to suppress the effects of the high frequency noise, although this had the undesirable side-effect of reduced SNR, as part of the signal was discarded in the weighting process. Despite this, the proposed "local field correction PIV" (LFCPIV) provided a major advancement, enabling the stable resolution of high gradients and inhomogeneities in the flow field.

Further advancement on this has been made by Scarano and Riethmuller (2000), who describes the WIDIM technique, which also provides a method capable of deforming interrogation windows based on the surrounding flow field. The WIDIM technique however includes progressive window refinement, providing high accuracy, dense vector maps even in the presence of shear.

2.3.4 Vector field post-processing

The PIV correlation process often results in spurious vectors due to noise in the correlation map. These are often obvious to the eye, due to their "unphysical deviation" from the surrounding fluid (Westerweel, 1994), as illustrated in figure 2.10, which contains unfiltered vectors from a poor correlation. The challenge of vector field post-processing is to separate valid and erroneous vectors, thereby allowing the latter to be discarded and optionally replaced.

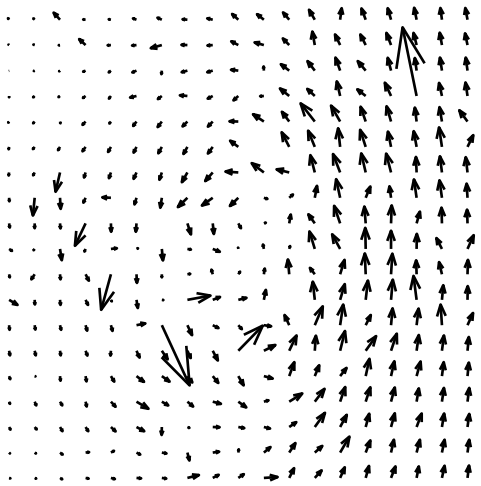

Figure 2.10: An example vector field, requiring post-processing

2.3.4.1 Vector filtering

Perhaps the most basic form of post-processing is the global filter. This is applied by placing size constraints on the vector components, the constraints having been selected based on a knowledge of the fluid flow. Any vector with a component outside of the allowed range is either discarded or marked as spurious. The effect of this is apparent from figure 2.11a, where red arrows highlight vectors marked as spurious by the global filter. In this vector field, it was known that the maximum possible fluid displacement in image coordinates was $\pm 10px$. In the case of vortical flows, such as this one it is often convenient to filter on vector magnitude, $|\mathbf{X}|$, however for flows with a large component in one direction, it is often more convenient to filter on each component of the velocity in turn.

It is well known that noisy correlation maps promote spurious particle displacement measurements. Keane and Adrian (1990) suggested the relative heights of the first and second correlation peaks as a measure of the quality of the correlation map, Q. In applying this filter, the user must specify a threshold for Q, and any vectors whose quality ratio falls below this threshold are marked as

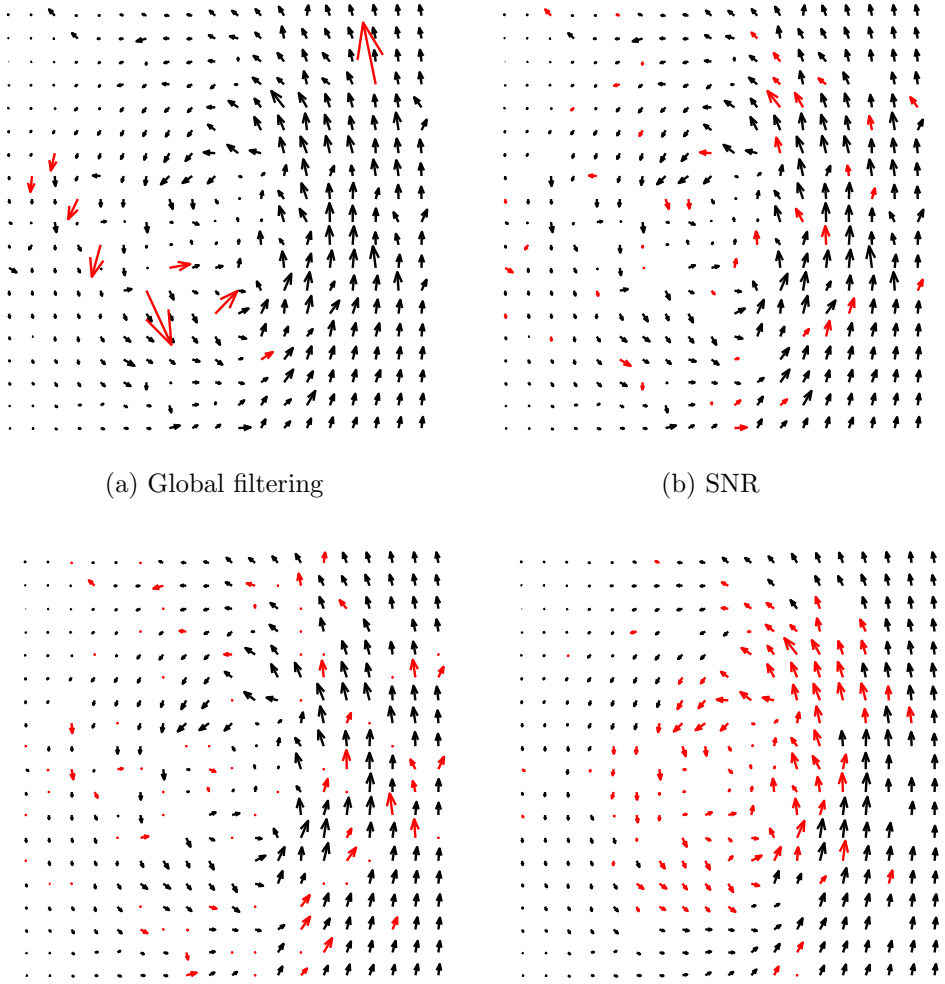

(a) Global filtering

(b) SNR

(c) Local filtering - lax

(d) Local filtering - strict

Figure 2.11: A demonstration of various post-processing operations

spurious. To aid in the understand of this, consider figure 2.12. The correlation map shown in 2.12a was produced from high quality particle images, contrast this to 2.12b, where the general quality of the images is lower.

This type of SNR filtering presents a method of removing vectors where the vector computation probably failed. Its effect may be seen by considering figure 2.11b and it is quite noticeable that many vectors removed appear to be valid, illustrating a major drawback in the SNR filter - its reliability.

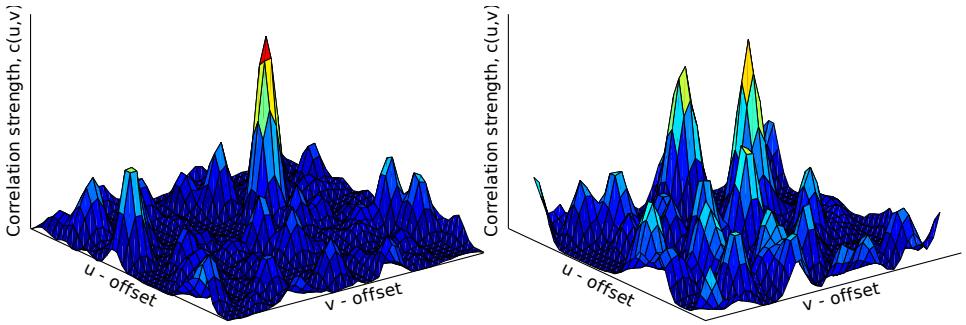

(a) Single peak (b) Double peak

Figure 2.12: Examples of the variable quality of correlation maps

Perhaps the most powerful tool available for spurious vector removal is the neighbourhood based or local filtering. In this case, each vector in the field is compared to its neighbours and if it is found to deviate too highly, in either magnitude or direction, it is marked as spurious. This is based on the idea that successful PIV requires relatively low velocity gradients, meaning that vectors should never deviate from their neighbours particularly wildly.

Westerweel (1994) proposed a method for local filtering, centring around the calculation of a residual displacement, r. Strictly speaking a residual gives the deviation of a measurement from the true value, however for a PIV measurement, the actual particle displacement is not known, therefore one must make an estimation of it. For a measured particle displacement $\mathbf{X_0}$, and an estimator to the real displacement $\hat{\mathbf{X}}_\mathbf{i}$, the residual is calculated as in equation (2.11).

$$r = |\mathbf{X_0} - \hat{\mathbf{X}}_\mathbf{i}| \tag{2.11}$$

Several methods of calculating $\hat{\mathbf{X}}_\mathbf{i}$ were presented by Westerweel (1994). The most sensible were the local mean and the local median, both of which operate on a small neighbourhood of vectors in the vicinity of the vector for validation, typically either a 3×3, 8-connected or a 5×5, 24-connected neighbourhood is

chosen, as illustrated in figure 2.13. In either case, the vector to be analysed is not included in the calculation of the estimator.

The principle behind the outlier detection, is that a valid vector is likely to lie close to the value of the real displacement and hence result in a small residual. A spurious vector however, is unlikely to lie close to the real displacement and so will result in a larger residual. On this basis, vectors greater than the residual by more than the approximate error in calculation of $\hat{\mathbf{X}}_\mathbf{i}$ are removed. It is typical to suggest that the removal occur for residuals greater than the product of some user defined constant and the standard deviation of the neighbourhood, equation (2.12). The purpose of the constant k is to allow adjust how strict the vector removal is, this is illustrated in figures 2.11c and 2.11d, which show the severity of relaxed and strict local filtering respectively.

$$r_{valid} < k\sigma_{\mathbf{X_i}} \tag{2.12}$$

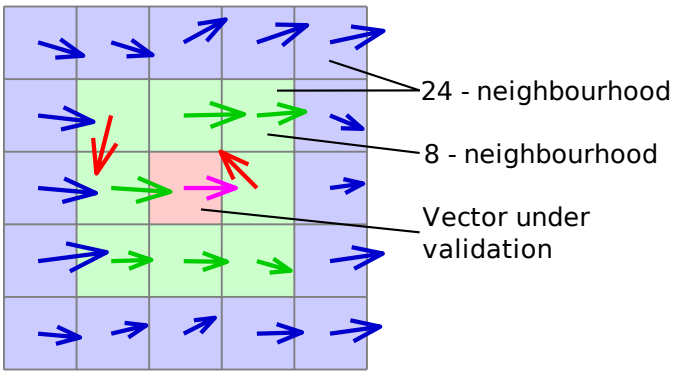

Figure 2.13: Illustration of vector neighbourhoods

As pointed out by Westerweel (1994), the median provides a substantially more robust estimator, this is because in the calculation of the mean, all variables receive an equal weighting. Thus a vector component of significantly different value will skew the resulting estimator, the non-linearity of median calculation

prevents this.

An improvement to this method was proposed by Nogueira *et al.* (1997), it was suggested that the validation of the vectors occur in order of local coherence, the measure of which is given in equation (2.13). This form was chosen to minimise computational cost. The subscript 0 indicates the vector to be validated, the subscript i indicates any one of the other N members of the neighbourhood. The aim of this approach is to reduce the number of erroneous vectors present when calculating the values for the local estimators throughout the field.

$$Q_c = \frac{\sum_{i=1}^{N} |\mathbf{X_0} - \mathbf{X_i}|}{\sum_{i=1}^{N} |\mathbf{X_i}|} \tag{2.13}$$

Significant improvement to the performance of the local field analysis was suggested by Westerweel and Scarano (2005). It was correctly pointed out that the basic median filtering put forward in equation (2.12) tends to suffer in situations where local coherence varies throughout the field. This is because a suitable value for the user selected constant k in an area of laminar flow will be quite different to that required in an area of highly turbulent flow. The modification proposed is to normalise the calculated residual, as shown in equation (2.14). The normalisation is performed with respect to the median of the residuals for each of the M vectors within the neighbourhood, each residual being given by, $\widehat{r_i} = |\mathbf{X_i} - \hat{\mathbf{X}}_\mathbf{i}|$.

$$r = \frac{|\mathbf{X_0} - \hat{\mathbf{X}}_\mathbf{i}|}{\widehat{r_i}} \tag{2.14}$$

2.3.4.2 Vector replacement

After erroneous vectors have been removed from the field, replacements may be made. Interpolation is probably the most commonly used method of vector replacement, this is where the vector's value is calculated from a combination of

its neighbours. Nogueira *et al.* (1997) suggested that when interpolating data, a polynomial surface fit using a 5×5, 24-connected area be employed. Interpolation should be used sparingly, as it misrepresents the measurements made of the flow. Single vector replacements, however are unlikely to be problematic, especially when window overlapping is used in the correlation stage.

A less problematic method of vector replacement is to consider the second, third or even fourth highest peak in the correlation map to potentially be valid. There is no limit to how many correlation peaks may assessed for their suitability, however it is rare that the fourth peak ever results in a suitable vector. When performing the replacement, it is typical to test the new vector's validity with a local filter, such as in equation (2.12).

After replacing or removing vectors from the field, it is necessary to perform another post-processing pass. This is because changes to a vector effect the value of the displacement estimator of those around it. Because of this, where a replacement is made with a vector calculated from a lesser correlation peak, it is marked as *unknown*, so as to not unfairly influence its surrounding vectors, until it has been suitably validated.

Finally it is worth noting that the performance of each of these operations on their own is significantly worse than their combined performance. Outlined below is a brief guide to high performance PIV post-processing; vectors are marked as either *unknown*, which indicates they are likely to be spurious or *invalid*, which means they are immediately removed.

1. Apply global filter during correlation, restricting vector peak search to valid areas of the correlation map.

2. Mark vectors below a certain quality Q as *unknown*. Suitable values vary significantly with image quality, typically $1.3 \simeq Q \simeq 1.8$.

3. Perform a local filter, preferably calculating the residual using the median of neighbours. The data is checked in order of local coherence, the highest being checked first. Vectors marked as *unknown* are also tested and if it is found that their disparity from their neighbours is suitable, they are unmarked. In the calculation of displacement estimators, neighbours marked as *unknown* or *invalid* are excluded. Any vectors whose residual is found to exceed the critical value are marked *invalid*. Values for the strictness of the filtering are typically $1 \leq k \leq 2$.

4. Any vectors marked as *invalid* or *unknown* are removed, alternative correlation peaks are used to replace the missing vectors, provided their residual is less than some critical value, as defined in equation (2.12). Typical values are $1.5 \leq k \leq 3$

5. If changes were made to the vector field, return to stage 3 for another local filtering pass, otherwise continue to stage 6.

6. Remove small clusters of n vectors, typically groups are removed on 8-connectivity where $n < 10$.

7. Perform any optional vector map smoothing passes.

2.4 Stereoscopic PIV

Stereoscopic PIV or SPIV is a straightforward extension to the standard 2C case. Two cameras are used to simultaneously record different views of the illuminated scene. In order to calculate the 3C velocity field, the two sets of particle images are correlated as per the standard 2C case. The cameras' relative positions to some origin in the measurement volume are used to combine these two 2C vector fields into a single 3C measurement. The relationship between the cameras and

the "world" is described using a calibration model, and this also enables the calculation of the 3C vectors.

2.4.1 Hardware configurations

SPIV systems fall into one of two hardware configurations, translational (Soloff *et al.*, 1997) or rotational (Zang and Prasad, 1997). In both cases, the two cameras are oriented such that they provide a different perspective of tracer particle motion, as illustrated in figure 2.14. In a translational system, the cameras are normally displaced such that both imaging planes are coplanar, figure 2.14a. In rotational systems, the most typical setup is one where the two cameras are rotated in opposite directions about a single axis, figure 2.14b. In both cases it is common to maintain as much symmetry as possible between the two camera setups, for example keeping $\theta_1 \sim \theta_2$, $S_1 \sim S_2$, $D_1 \sim D_2$ (where the superscript denotes the camera number) as well as using the same cameras and optics.

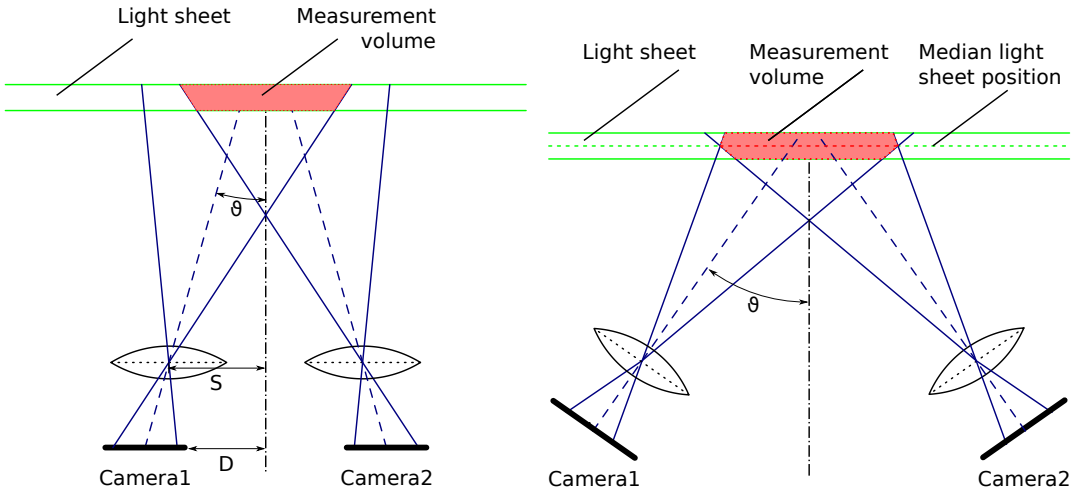

(a) Translational (b) Rotational

Figure 2.14: Translational and rotational stereoscopic arrangements, adapted from (Prasad, 2000)

The translation system was first described by Jacquot and Rastogi (1981);

examples of implementations include Sinha and Kuhlman (1992) and Soloff *et al.* (1997). The primary advantage of the translational method is that the image, object and lens planes all remain parallel. This means that particle images remain in focus without the requirement for aperture reduction.

In the most simplistic setup, $\theta_1 = \theta_2 = 0$, however this leads to a very small area commonly viewed by both cameras. As 2C information is required from two independent points of view to produce 3C vectors, the intersection of the two camera views defines the extent of the measured field. Therefore, as shown by figure 2.14a, the resulting 3C vector field will be small. A more problematic issue with the translation method arises from lens distortion, which causes a reduction in accuracy as θ increases, up to some limit, beyond which measurements are not possible (Soloff *et al.*, 1997; Prasad and Adrian, 1993).

In the case of the basic rotational system, as shown in figure 2.14b, the image and lens planes for each camera, are a-parallel to the corresponding image, lens planes from the other camera. In this orientation lens distortion does not limit the permissible θ. It is however plain to see that the distance between the plane and object plane depends upon the position within image. This means that the level of focus on the image plain will vary, as illustrated by figure 2.15a. Depending on θ, it may be possible to remove the blurring by reducing the lens aperture (thereby increasing the depth of field), alternatively by enforcing the Scheimpflug condition, the effect may be removed fully, as shown in figure 2.15b.

The Scheimpflug condition was suggested as a solution to this problem by Hinsch (1995), Prasad and Jensen (1995). The Scheimpflug condition is achieved by angling the lens plane with respect to the image plane, such that the planes intersect at a point on the object plane. This is illustrated in figure 2.16. It was first tested by Zang and Prasad (1997) and today forms an integral part of SPIV measurements.

(a) Without Scheimpflug adaptor (b) With Scheimpflug adaptor

Figure 2.15: Comparison between images taken with and without Scheimpflug adaptor, images from LaVision (2006).

It is also worth of noting that in liquid flow measurement, a refractive index step must at some point be breached. In the standard 2C case, this has a degrading effect on the images acquired, manifesting itself in the form of a non-linear radial distortion. This can be immediately appreciated by considering Snell's law, equation (2.15), and is illustrated in figure 2.17a.

$$\frac{\sin\phi_1}{\sin\phi_2} = \frac{v_1}{v_2} = \frac{n_2}{n_1} \tag{2.15}$$

It is plain that light arriving orthogonal to the refractive index step will continue on its original course, as in the case of the ray travelling along the optical axis in figure 2.17a, labelled A. Consider however a ray intersecting the edge of the camera sensor, for example the ray labelled C, at the point of refractive index change the ray is deflected, in the case of figure 2.17a $n_2 > n_1$, this results in a deflection toward the optical axis. The effect of this across the image, is a "pin-cushion" type radial distortion. This rarely causes problems for 2C PIV, as a radial distortion, centred about the optical axis is present in all camera lenses.

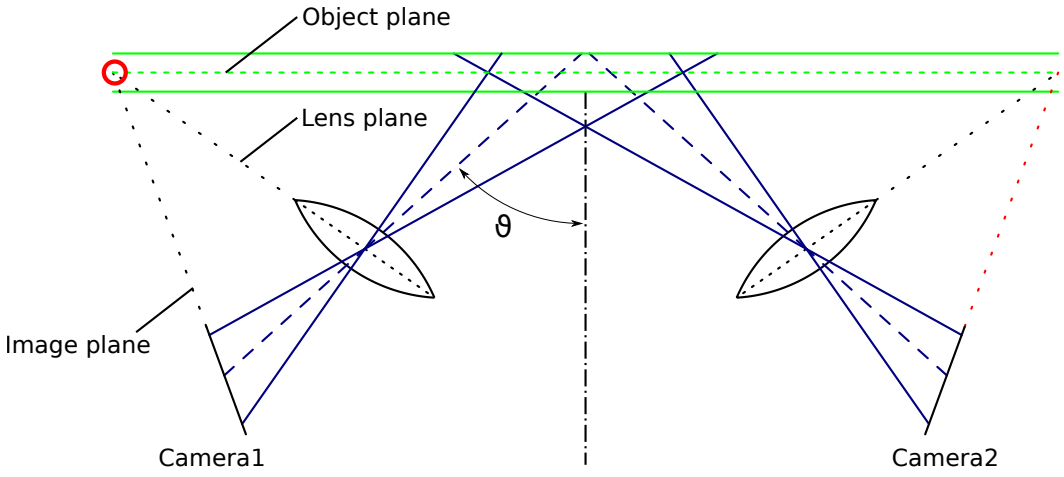

Figure 2.16: Illustration of the Scheimpflug condition, adapted from Prasad (2000)

Because of this it is commonplace to perform an adjustment for radial distortion as part of the camera calibration procedure.

In the case of a rotational stereoscopic setup however, the image distortion introduced by the refractive index step presents a significantly larger problem. In this case, as illustrated in figure 2.17b, the ray lying on the optical axis, B is not orthogonal to the refractive index step and so is deflected. Furthermore because the deflection of the rays intersecting the sensor is not symmetric about the optical axis, rays A and D are deflected differently. The deflection pattern of rays is instead symmetric about the ray that is orthogonal to the optical axis, C. These problems can be removed, almost entirely, by ensuring that viewing is parallel to the refractive index step. For stereo systems, this can be achieved by mounting a prism containing refractive index matching fluid at the refractive index step. The prism should have a surface normal to the optical axis of the camera (Prasad and Jensen, 1995; Dazin *et al.*, 2006a).

Should SPIV measurements be made without using a refractive index matching prism, non-uniform and differing distortions will be applied to images from each camera. This effect can be removed using advanced calibration techniques,

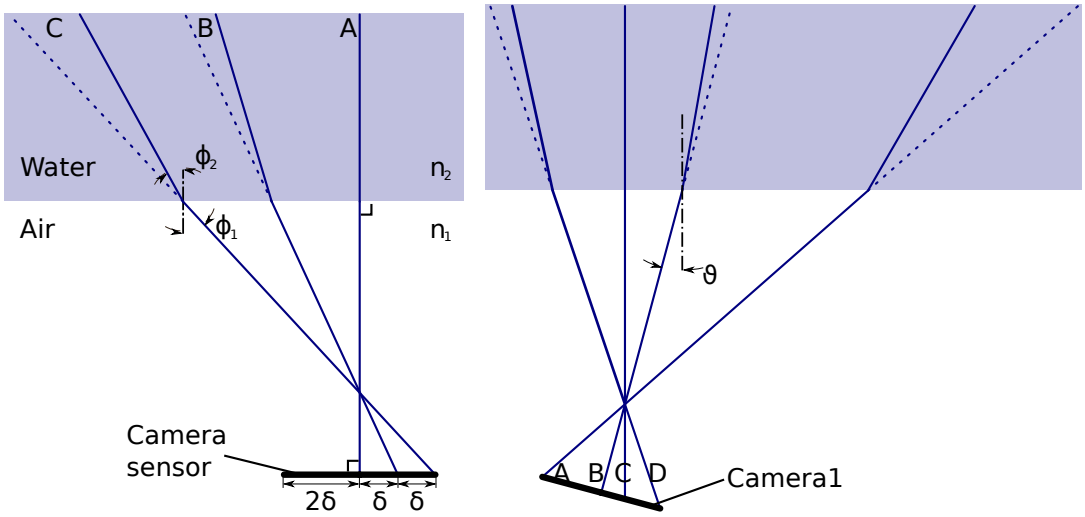

(a) Image and lens planes parallel to refractive index step

(b) Image and lens planes aparallel to refractive index step

Figure 2.17: Ray trace indicating light path onto a camera sensor, across a refractive index step

however in many situations it is advantageous to calibrate using models that assume radial distortion to be symmetric about the optical axis. If SPIV is attempted in this case a registration error will be present. In cases of a small angle between optical axis and refractive index step, θ, the error due to refraction issues will be negligible. For the large angles commonly associated with SPIV however, this error will be very large indeed and will impart a significant bias on the computed result.

A significant effect of employing a rotational SPIV setup (irrespective of whether the Scheimpflug condition is implemented) is the non-linear image stretching that occurs, as illustrated in figure 2.18. It is clear to see that this stretching has the undesirable effect that back-projected world coordinates from cameras 1 and 2 lie in different locations.

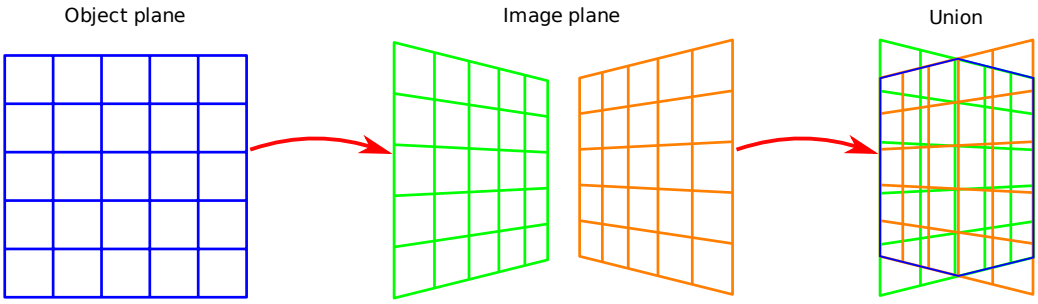

Figure 2.18: Field distortion caused by camera rotation

2.4.2 Camera calibration

The SPIV measurements of out of plane velocities relies on a knowledge of the relative locations of the two cameras used. As shown by Willert (1997), the accuracy of the computation of the combined vector field is extremely sensitive to errors in the definition of the relative camera positions. This manifests itself in two ways: firstly, errors in the angle between the cameras lead to an incorrect ratio between in plane and out of plane velocities; secondly, errors in the relative positions of the cameras results in the 2C velocity fields not matching up, (the significance of this error strongly depends on the strength of the velocity gradient). In the case of vortical flows, it can lead to disastrously erroneous third component data, as illustrated in figures 2.19 and 2.20.

The flow depicted is a single vortex with no out of plane, u_z component. Figures 2.19a and 2.20a show the relative alignment of the 2C velocity fields from the two cameras. Figures 2.19b and 2.20b show vector maps of the reconstructed 3C vector field, u_z is shown by background colours.

One can clearly see that where the correct calibration is used, the vortex contours overlap and the resulting 3C vector field shows no out of plane motion, figure 2.19. In the case of a poorly constructed calibration, the vortex contours are shifted with respect to one another and the combined 3C vector map is

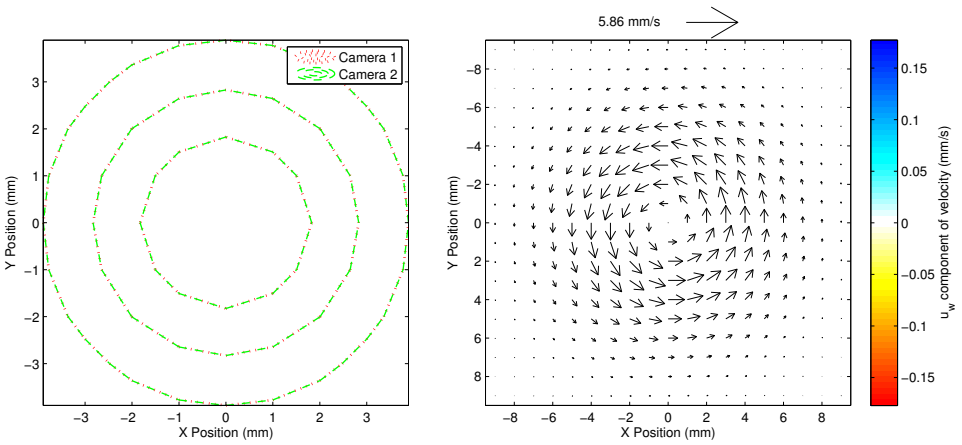

(a) Vorticity contours (b) 3C velocity vector field

Figure 2.19: A velocity field, warped with a correct calibration

influenced, 2.20. It is worth noting, that the in plane velocities are effected very little, the major change is to the out of plane velocity, u_z.

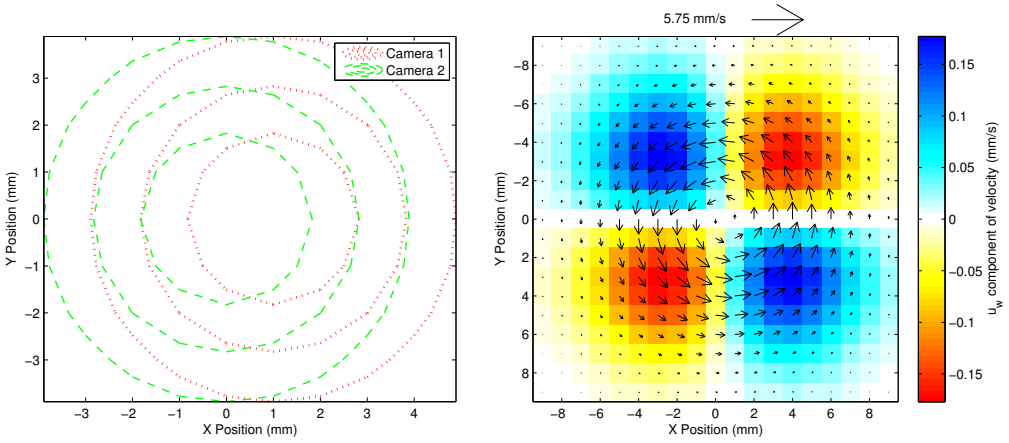

(a) Vorticity contours (b) 3C velocity vector field

Figure 2.20: A velocity field, warped with an incorrect calibration

Early SPIV systems used geometric measurement of camera positions to define their relative positions (Prasad and Adrian, 1993), this however provides insufficient resolution or flexibility and machine vision techniques performing camera calibration swiftly became the norm. Modern techniques expect calibration res-

olution better than $0.01px$ (Heikkilä and Silvén, 1997).

Camera calibration is used to determine a transform between some coordinate system located on the camera sensor and some imaged coordinate system, commonly called the world coordinate system. Points in the world coordinate system, are described with respect to a user defined world origin, by a position vector, $\mathbf{X}$. The purpose of the camera calibration is to provide a mathematical function, such that an acquired image may be back-projected onto the world coordinate system. The inverse calibration provides a method of forward projection from world coordinates, onto image coordinates.

2.4.2.1 Projection systems

To calculate a camera calibration, an object of known geometry is positioned within the measurement volume and imaged. By finding points in the image, $\mathbf{x_i}$ corresponding to known points on the target object, $\mathbf{X_i}$, a mapping function, $f(x)$ may be found such that $\mathbf{x_i} = f(\mathbf{X_i})$. As measurements of both $\mathbf{x_i}$ and $\mathbf{X_i}$ will contain some error, many point correspondences are required, enabling a solution to be fitted, thus reducing the error.

The model used to calculate the mapping function between world and image coordinates is either geometric or generalised (Coudert and Schon, 2001). In the geometric projection case, geometric optics are assumed and a ray-trace is modelled, requiring several equations to be solved. For generalised projection, the world coordinates are related to image coordinates through an arbitrary mapping function. For this, 2D cubic polynomials are common (Soloff *et al.*, 1997), however 2D quadratic polynomials and bicubic splines have also been investigated (Lawson and Wu, 1997).

The geometric model is normally considered preferable as it requires 22 parameters to be fitted for the stereoscopic case, whereas a generalised 3^{rd} order

polynomial requires 80. It has been shown repeatedly that the basic geometric model with judicious correction for distortion performs well Tsai (1987); Heikkilä and Silvén (1997); Willert (2006), implying that the extra parameters fitted as part of a generalised model are unnecessary, and can result in an over-fit where the mapping function is fitted to noise (Wieneke, 2005). This said, generalised calibrations far surpass geometric in the case of arbitrary distortions, such as viewing through multiple refractive index steps, or where the assumption of geometric optics fails.

Both models require that the world coordinate system coincide with the light sheet; if the calibration target is slightly misaligned, registration errors will be incurred. If a geometric model is used, a process known as "self-calibration" (c.f. section 2.4.2.4) may be used to remove these errors.

2.4.2.2 The pinhole model

A simple perspective model, based on geometric projection and popular for SPIV camera calibration is the pinhole camera model (Tsai, 1987). It is summarised in equation (2.16).

$$\begin{bmatrix} \mathbf{x} \\ 1 \end{bmatrix} = S\mathbf{P} \begin{bmatrix} \mathbf{X} \\ 1 \end{bmatrix} \tag{2.16}$$

Here $\mathbf{x}$ is a 2D displacement vector on the image plane, $\mathbf{X}$ is a 3D displacement vector in world coordinates, S a scaling factor and $\mathbf{P}$ the camera matrix defining an arbitrary projective homography for a camera with square pixels. It is of note that the scaling factor is separated from $\mathbf{P}$, this occurs because all homographies are by definition normalised quantities, therefore they are said to be defined "up to scale". The vectors are concatenated with the number 1 to provide a representation of the vectors in homogeneous coordinates, c.f. Hartley

and Zisserman (2003a) and Hartley and Zisserman (2003b).

In equation (2.16), the camera matrix, $\mathbf{P}$ is the matrix product of intrinsic and extrinsic camera parameter matrices, $\mathbf{I_c}$ and $\mathbf{E_c}$ respectively, i.e. $\mathbf{P} = \mathbf{I_c} \cdot \mathbf{E_c}$. The intrinsic and extrinsic matrices group camera parameters into those describing the camera's positioning with respect to the object plane (extrinsic parameters) and those describing the camera's optical functionality (intrinsic parameters). These matrices are shown in equations (2.17a) and (2.17b).

$$\mathbf{I_c} = \begin{bmatrix} k_u \cdot f & s & u_0 & 0 \\ 0 & k_v \cdot f & v_0 & 0 \\ 0 & 0 & 1 & 0 \end{bmatrix} \tag{2.17a}$$

$$\mathbf{E_c} = \begin{bmatrix} \mathbf{R} & \mathbf{T} \\ \mathbf{0}^T & 1 \end{bmatrix} \tag{2.17b}$$

Here k_u and k_v are the pixel pitches for the camera in the horizontal and vertical directions respectively and s is the pixel skew factor. The location at which the optical axis intersects the imaging plane is known as the "principal point". Its position in image coordinates in the horizontal and vertical directions is given by u_0 and v_0 respectively. The camera lens' focal length is given by f, $\mathbf{R}$ is the rotation matrix, which gives the rotation of the image plane relative to the plane in which world coordinates lie. The composition of the rotation matrix is given in equations (2.18) and (2.19), for a set of Euler angles, α, β and γ. $\mathbf{T}$ is the translation vector, which gives the displacement of principal point from world coordinate origin, as a 3D vector in world units.

$$\mathbf{R} = \begin{bmatrix} r_{11} & r_{12} & r_{13} \\ r_{21} & r_{22} & r_{23} \\ r_{31} & r_{32} & r_{33} \end{bmatrix} \tag{2.18}$$

$$r_{11} = \cos(\beta)\cos(\alpha) \tag{2.19a}$$

$$r_{12} = \sin(\alpha)\sin(\beta)\cos(\gamma) - \cos(\alpha)\sin(\gamma) \tag{2.19b}$$

$$r_{13} = \cos(\alpha)\sin(\beta)\cos(\gamma) + \sin(\alpha)\sin(\gamma) \tag{2.19c}$$

$$r_{21} = \cos(\beta)\sin(\gamma) \tag{2.19d}$$

$$r_{22} = \sin(\alpha)\sin(\beta)\sin(\gamma) + \cos(\alpha)\cos(\gamma) \tag{2.19e}$$

$$r_{23} = \cos(\alpha)\sin(\beta)\sin(\gamma) - \sin(\alpha)\cos(\gamma) \tag{2.19f}$$

$$r_{31} = -\sin(\beta) \tag{2.19g}$$

$$r_{32} = \sin(\alpha)\cos(\beta) \tag{2.19h}$$

$$r_{33} = \cos(\alpha)\cos(\beta) \tag{2.19i}$$

Given a set of point correspondences between image coordinates $\mathbf{x_i}$, and world coordinates $\mathbf{X_i}$, one can estimate the calibration matrix $\mathbf{P}$. This is performed using the direct linear transformation or DLT (Tsai, 1987). From equation (2.16), we can see that $[\mathbf{x}^T \quad 1]^T \times \mathbf{P}[\mathbf{X}^T \quad 1]^T = \mathbf{0}$. One can rearrange this as in equation (2.20), where $\mathbf{P}^i$ represents the i^{th} row of the matrix $\mathbf{P}$.

$$\begin{bmatrix} \mathbf{0}^T & -w_i\mathbf{X_i}^T & y_i\mathbf{X_i}^T \\ w_i\mathbf{X_i}^T & \mathbf{0}^T & -x_i\mathbf{X_i}^T \\ -y_i\mathbf{X_i}^T & x_i\mathbf{X_i}^T & \mathbf{0}^T \end{bmatrix} \begin{pmatrix} \mathbf{P}^{1^T} \\ \mathbf{P}^{2^T} \\ \mathbf{P}^{3^T} \end{pmatrix} = \mathbf{0} \tag{2.20}$$

Since the three equations in (2.20) are linearly dependent, one of the equations

may be discarded, see equation (2.21). As $\mathbf{P}$ has 12 entries, there are 12 degrees of freedom; we have 2 linearly independent equations, therefore a minimum of 6 data points are required in order to compute a solution. In reality, it is not possible to make point correspondence measurements without significant noise, and so, we therefore require substantially more than 6 points.

$$\begin{bmatrix} \mathbf{0}^T & -w_i\mathbf{X_i}^T & y_i\mathbf{X_i}^T \\ w_i\mathbf{X_i}^T & \mathbf{0}^T & -x_i\mathbf{X_i}^T \end{bmatrix} \begin{pmatrix} \mathbf{P}^{1^T} \\ \mathbf{P}^{2^T} \\ \mathbf{P}^{3^T} \end{pmatrix} = \mathbf{Ap} = \mathbf{0} \tag{2.21}$$

It can be seen from inspection that a trivial solution exists, $\mathbf{p} = \mathbf{0}$, however we seek a non-trivial solution. This is found in the standard way, by computing the null-space of $\mathbf{A}$ (Heikkilä and Silvén, 1997).

The DLT is used to provide an initial estimate of the camera matrix, as linear solutions are efficient and robust. They do however lack the accuracy of non-linear minimisations, which are used to refine the estimate of the camera matrix. Non-linear camera matrix minimisations are generally unsuitable for use from the outset, as they can return local minima rather than the global minima sought.

When computed, $\mathbf{p}$ may be trivially rearranged to yield $\mathbf{P}$. This may then be decomposed into intrinsic and extrinsic camera matrices, $\mathbf{I_c}$ and $\mathbf{E_c}$ using the RQ-decomposition Heikkilä and Silvén (1997); Hartley and Zisserman (2003c). The pinhole model must now be modified to account for lens distortions, Scheimpflug adaptors, refractive index steps and so on. For further information on this, the reader is redirected to Maas (1995), Heikkilä and Silvén (1997) and Louhichi *et al.* (2007).

2.4.2.3 Practical calibration for SPIV

When performing a calibration for SPIV, the goal is to produce a large number of accurate point correspondences between the world and image planes. To do this, a calibration target, covered in precisely positioned marks is positioned within the measurement volume. The marks are made such that they may be easily identified using image processing algorithms and can be identified to sub-pixel accuracy. This produces several constraints, the marks must offer a high contrast to their background and must also be sufficiently large that a high accuracy measurement of their position is possible. Commonly used marks are large dots (Maas *et al.*, 1993; Heikkilä and Silvén, 1997; Scarano *et al.*, 2005), very large quantities of smaller dots (Coudert and Schon, 2001; Skeen, 2006), grids of lines (Willert, 1997) and large squares (Hartley and Sturm, 1997), although other configurations are also used.

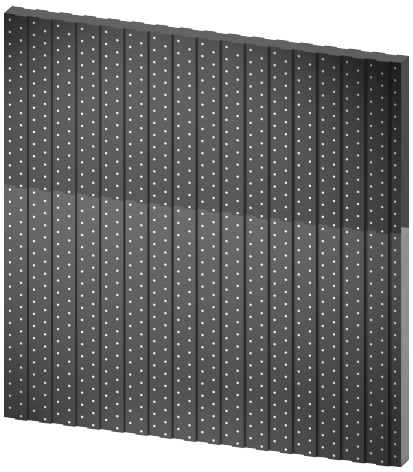

Figure 2.21: Representative dual-level calibration plate

Furthermore, as SPIV requires out of plane measurement, the calibration requires information at multiple depths in space. This is achieved either by manufacturing a target with multiple layers (Maas *et al.*, 1993), each a known separation apart, or by translating a planar target on a precision stage (Soloff

et al., 1997; Wieneke, 2005). The relative performance of these two methods for SPIV has itself been investigated (Scarano *et al.*, 2005), the results showing a slightly higher accuracy from the translation of a precision target. An example of a dual layer calibration plate is given in figure 2.21.

In an SPIV setup, two cameras are used, therefore two calibrations must be performed, one for each camera. This provides a mapping from world coordinates to each camera coordinate system and a reverse mapping from each camera coordinate system to world coordinates.

2.4.2.4 Self-calibration

Very little misalignment between calibration target and laser light sheet is needed to produce significant errors. Using an SPIV setup Willert (1997) investigated this by correlating particle images simultaneously acquired on two cameras with each other. Prior to the correlation both particle images were back-projected onto the object plane. This generates a so called "disparity vector map" and measures the spatial variation of registration error.

It was found that for the setup used, a misalignment between planes of less than 0.6° was needed to produce registration errors of $10px$ at the edges of the frames. Only in the most strictly controlled circumstances, could alignment achieve accuracy of this order, therefore most practical circumstances require a correction to account for it.

A system for correction was proposed by Coudert and Schon (2001), where the disparity vector map was used to define a spatial correction to computed vector maps, such that any registration error was removed. A modification to this was presented by Wieneke (2005), who used information from the disparity vector map to calculate the position of the light sheet relative to the currently defined object plane. Back-projecting rays through the disparity vectors should

intersect at the position of the light sheet as illustrated in figure 2.22. In reality measurement noise means these rays very rarely intersect, triangulation methods are used to find the point best representing an intersection (Hartley and Sturm, 1997).

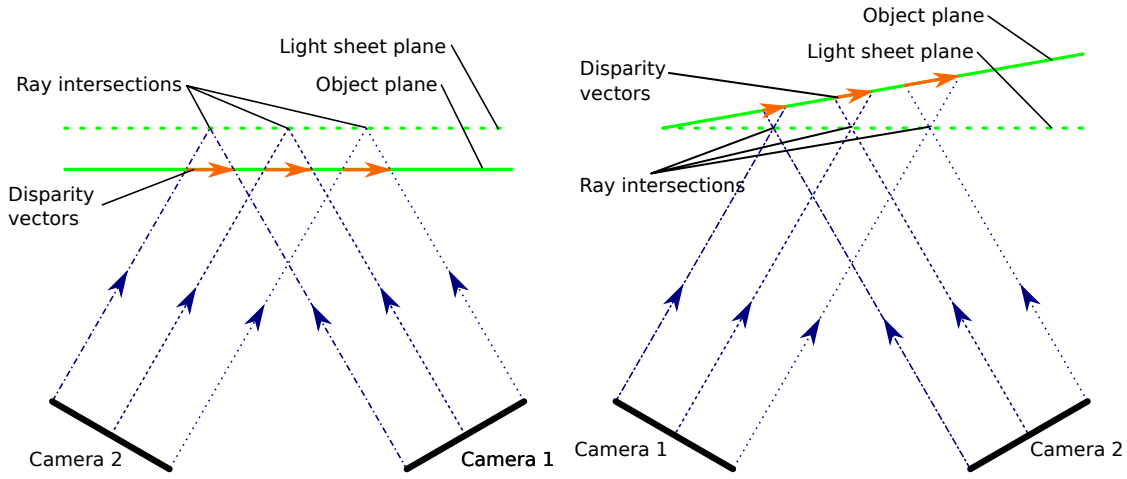

(a) Light sheet is translated with respect to the object plane

(b) Light sheet is rotated and translated with respect to the object plane

Figure 2.22: An illustration of triangulation using disparity vector maps

After the points defining the light sheet have been calculated, its position is defined through a least squares surface fit and from this, calculation of an adjustment to the extrinsic matrix, given in equation (2.17a). As the adjustment is made from the relative positions of two planes, only the angles α, β and the displacement T_z may be calculated.

Further to this Wieneke (2005) suggested that the sum of between five and fifty correlation maps be used to calculate the disparity. This is quite often required for self-calibration, as for SPIV relatively thick light sheets are required, good correlations will be made throughout the depth of the measurement volume. This produces a very low noise signal, as demonstrated in figure 2.23.

The case of single correlation map, figure 2.23a shows significant noise, al-

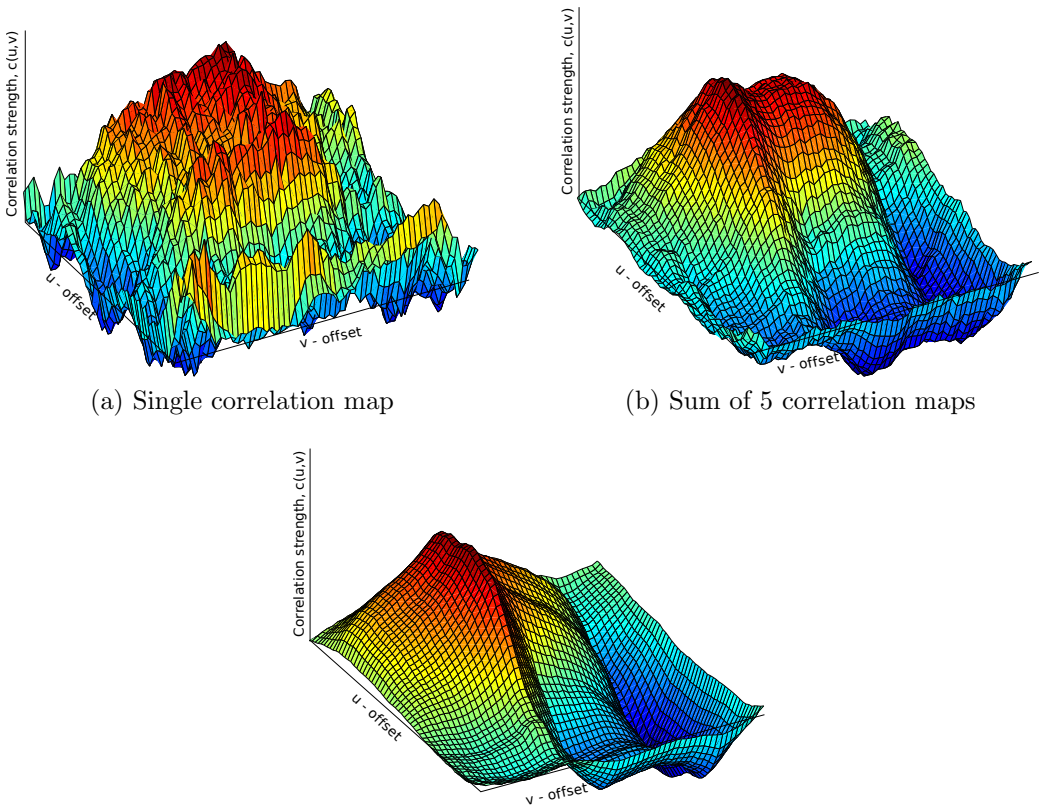

(a) Single correlation map

(b) Sum of 5 correlation maps

(c) Sum of 50 correlation maps

Figure 2.23: Correlation maps from self calibration

though a peak is defined, their are several subsidiary peaks that may actually represent the valid displacement peak. This is unsurprising, as the correlation performed integrates through the depth of the light sheet, therefore there are likely to be many valid correlation peaks, as the correlation process detects similarities at different depths within the volume. Things are much improved by summing as few as five correlation maps, figure 2.23b, however one can see there are two distinct correlation peaks in this map. Figure 2.23c illustrates the effect of summing fifty correlation maps, the signal is substantially improved, resulting in a single, easily identifiable peak. As shown by Hartley and Sturm (1997), the triangulation process is very sensitive to errors, which makes the accuracy of the correlation procedure very important, and on this basis it is advisable to sum as

many correlation maps as feasible.

Wieneke (2005) also suggested that the self calibration process be performed iteratively to further improve accuracy. The idea is that the self calibration begins with a large window size, in order to maximise signal to noise ratio. After the first disparity vector map is computed, and the calibration is refitted accordingly, the images are then back-projected with the reformed calibration and the process is iterated until there is convergence in the calibration, which normally takes around three passes (Wieneke, 2005). It is also possible that the calibration may be further improved by window size refinement and subsequent correlation passes, as this increases the number of points fitted.

Other methods for self calibration have been suggested, Hartley and Sturm (1997) put forward a method of determining two or more cameras full intrinsic and extrinsic calibration matrices, up to scale, by finding point correspondences between the two images. This last restriction is obviously imposed, as it is impossible to tell the physical dimensions of something from its image. Self-calibration has also been extended for use in volumes, primarily as an aid for tomographic PIV (Wieneke, 2008).

2.4.3 2C to 3C using the pinhole model

In order to calculate 3C vectors, it is required that vector data be projected onto the object plane, $Z = 0$, defined as the light sheet median during calibration. This projection may be performed in several ways;

1. Perform correlations on a uniform grid in image space, as per uncalibrated 2C PIV, then back-project vector fields onto the object plane. The direct back projection will result in vector measurements from camera 1 at different locations to those made by camera 2. It is therefore required that the

back-projected fields be interpolated onto a common, uniform grid.

2. Perform correlations on a non-uniform grid in image space, such that the back-projected vector field lies on a common, uniform grid. This method requires neither vector field nor image interpolation.

3. Back-project particle images onto the object plane, then perform 2C correlations in world coordinates. This requires interpolation of the particle images.

All the methods presented, have advantages and disadvantages. Method 1 is fast, however due to the interpolation pass results in erroneous vectors being spread between at least four 3C vectors. Furthermore the interpolation acts as a smoothing pass, reducing the spatial frequency of the 3C result. Method 2 is very fast and does not modify the data, however the vector maps resulting from each camera are measurements of different regions of the fluid, due to the differing projective distortions for cameras 1 and 2. Method 3 is a computationally intensive process as the full image has to be interpolated. Where fractional window offsetting or window deformation is performed in the correlation stages, image warping may be performed simultaneously, thus adding no computational overhead or additional signal degradation.

If the calibration of the cameras is accurate, the light sheet median is the plane on which there is no disparity between the back-projected particle images, on average. Consider a velocity measured on camera 1, $\mathbf{u_1}$ at the position $\mathbf{x_1}$, as in, figure 2.24. If there is any out of plane component of the real world velocity, $\mathbf{U}$, then the corresponding velocity measurement on camera 2, $\mathbf{u_2}$ at $\mathbf{x_2}$ will differ.

From this, the solution appears trivial, one simply needs to find the intersection of the rays back-projected from the position $[x_1 + u_1 \quad y_1 + v_1]^T$ and $[x_2 + u_2 \quad y_2 + v_2]^T$. Unfortunately however, due to noise in the measurement of

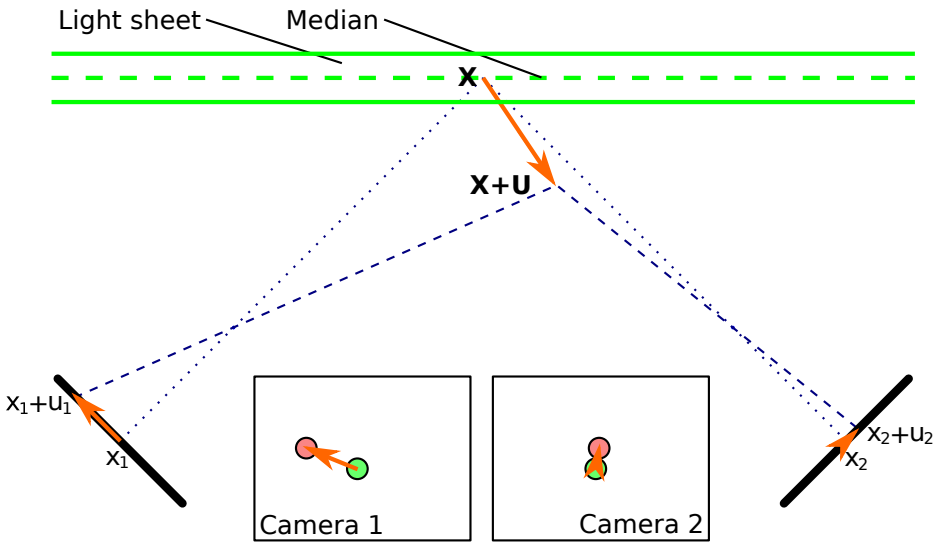

Figure 2.24: The calculation of a 3C vector from 2×2C vectors

the velocity u, these back-projected rays do not necessarily intersect. The problem, therefore becomes one of calculating the point, $\mathbf{X} + \mathbf{U}$, at which the rays come closest to intersection, this is termed triangulation (Hartley and Sturm, 1997).

Several methods are available, perhaps the most comprehensive constructs an order 6 polynomial whose minima results in the best estimate of intersection. The polynomial is derived from knowledge of the extrinsic matrix for each camera and relies heavily on epipolar geometry, which is described in full in Hartley and Zisserman (2003d). The polynomial method is shown to produce very high accuracy results, however the computational time required is significant, especially when compared with linear methods (Hartley and Sturm, 1997).

Modern SPIV comfortably produces $\mathcal{O}(10^5)$ vectors per map (Stanislas *et al.*, 2008). The sheer volume of calculations performed provide strong motivation for the use of cheaper methods. Hartley and Sturm (1997) reviews, contrasts and compares many methods and finds that a linear least squares estimation performs reasonably well in comparison to its computational time. The method

is implemented and outlined by Calluaud and David (2004).

To calculate a single 3C vector from two 2C vectors, we first consider equation (2.16), expanded to show matrix coefficients, as in equations (2.22). The expansion is limited, as it can be shown that we need only consider up to the projective transformation. As our problem is one of stereo vision, we consider equations (2.22) for the i^{th} camera.

$$\tilde{\mathbf{x}}_\mathbf{i} = \mathbf{R_i}\mathbf{X_i} + \mathbf{T_i} \tag{2.22a}$$

$$\hat{\mathbf{x}}_\mathbf{i} = \frac{f}{\tilde{z}_i}\begin{bmatrix}\tilde{x}_i \\ \tilde{y}_i\end{bmatrix} \tag{2.22b}$$

$$\tilde{\mathbf{x}}_\mathbf{i} = \mathbf{R_i}\mathbf{X_{o_i}} + \mathbf{T_i} \tag{2.22c}$$

For each vector on the i^{th} camera we define $\mathbf{X_i}$ as the sum of the particle displacement and measurement position vectors (in world coordinates). As either the images of particles or the vector field is back-projected onto the world plane at $X_z = 0$, then the vector component $Z_i = 0$. This world vector is then forward projected, such that we calculate $\hat{\mathbf{x}}_\mathbf{i}$, equations (2.22a) and (2.22b). Substituting (2.22) into (2.22b) to eliminate $\tilde{z}_i$, provides a relationship between $\mathbf{X_{o_i}}$, equation (2.23) the 3C particle displacement vector summed with its measurement position (vector $\mathbf{X} + \mathbf{u}$ in figure 2.24).

$$\begin{bmatrix}\hat{x}_i \\ \hat{y}_i\end{bmatrix} = \frac{f}{r_{31_i}X_{o_i} + r_{32_i}Y_{o_i} + r_{33_i}Z_{o_i} + T_{z_i}}\begin{bmatrix}r_{11_i}X_{o_i} + r_{12_i}Y_{o_i} + r_{13_i}Z_{o_i} + T_{x_i} \\ r_{21_i}X_{o_i} + r_{22_i}Y_{o_i} + r_{23_i}Z_{o_i} + T_{y_i}\end{bmatrix} \tag{2.23}$$

By some further rearrangement, we can the get this into the form shown in equation (2.24).

$$\begin{bmatrix} \hat{x}_i \\ \hat{y}_i \end{bmatrix} - \mathbf{K} = \mathbf{C} \begin{bmatrix} X_{o_i} \\ Y_{o_i} \\ Z_{o_i} \end{bmatrix} \tag{2.24}$$

Here $\mathbf{K}$ is a 2D vector of known coefficients and $\mathbf{C}$ a 2×3 matrix of known coefficients. For n cameras, we now have a system of $2 \times n$ equations, with which to solve for 3 unknowns. This can be done, using least squares through the computation of the pseudo-inverse of $\mathbf{C}$, sharing the error equally amongst all three velocity components (Wieneke, 2005).

CHAPTER 3

Vortex rings

3.1 Introduction

A succinct definition for vortex rings is provided by Lim and Nickels (1995): who define it as "a bounded region of vorticity in which the vortex lines form closed loops." The vortex loop formed is normally circular, and while propagating, transports significant extra fluid with it in an "atmosphere" (Tomson, 1867).

Throughout this section we shall refer to several important vortex ring properties. To aid in this, an illustration of vortex ring, showing these important properties and also the vortex ring structure is provided in figure 3.1. As the vortex ring is circular it often displays axial symmetry, therefore it is convenient to consider it in a cylindrical coordinate system $[u_\varphi \quad u_\rho \quad u_h]^T$. The closed loop has diameter D, and the region containing the bulk of the vorticity of the ring is termed the vortex core, which is of diameter δ. The vortex ring is considered to translate axially with velocity U_T.

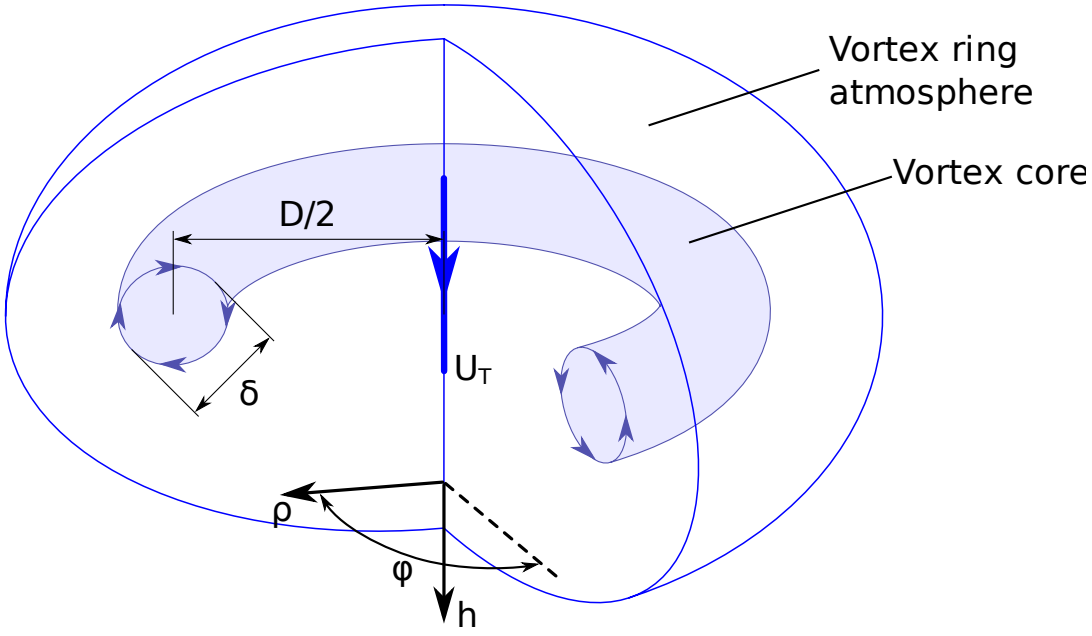

Figure 3.1: Illustration of vortex ring properties and its orientation in cylindrical coordinates

In experimental vortex ring generation, the vortices are commonly formed by expelling fluid from some orifice for a short time. This is illustrated by a generic case, figure 3.2. Here we have a piston of diameter D_p, moving with speed U_p. This ejects fluid from a narrower orifice with diameter D_o at velocity U_o, for incompressible fluid, $U_o = U_p \frac{D_o^2}{D_p^2}$. As the fluid ejection is impulsive (occurring over some short time T_o), the equivalent length of fluid ejected (L_o, equation (3.1)) by this starting jet is often considered. As U_o is time variant its time average $\overline{U_o} = L_o/T_o$ is often used as a velocity scale.

$$L_o = \int_0^{T_o} U_o(t)dt \tag{3.1}$$

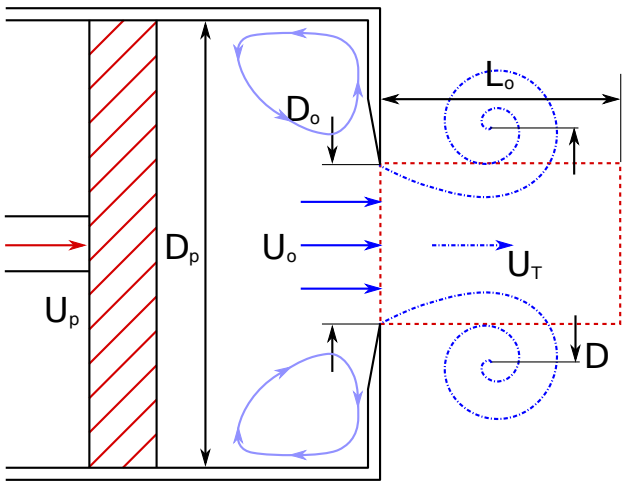

Figure 3.2: Illustration of the generic vortex formation process

3.2 Characterisation of vortex rings

Vortex rings have been characterised in numerous ways, it is currently understood that the following three non-dimensional parameters provide a reasonable characterisation of a given vortex ring: non-dimensional formation time, non-dimensional core diameter and Reynolds number. In the case of vortex rings generated under background rotation (for which few studies have been performed, c.f. section 3.4), the Rossby number is also used to quantify the effects of rotation rate.

3.2.1 Vortex ring formation time

The formation time of a vortex ring gives a measure of the time during which impulse is added to the vortex ring and Gharib *et al.* (1998) describe it as "the non-dimensional time taken for vortex ring formation." Typically it is expressed as a ratio of lengths, as in equation (3.2):

$$\frac{T_o \overline{U_o}}{D_o} = \frac{L_o}{D_o} \tag{3.2}$$

It has been shown that for $L_o/D_o \gtrsim 4$ and without extra forcing, single vortex rings are no longer formed (Tarasov and Yakushev, 1973; Gharib *et al.*, 1998), instead a jet is formed (c.f. section 3.3.2.3).

3.2.2 Slenderness ratio

The slenderness ratio provides a non-dimensional estimate of vortex ring core diameter. The core diameter is typically non-dimensionalised using, vortex ring diameter. Saffman (1978) provides a discussion on practical assessment of the vortex radius, suggesting that the true radius lies at some distance from the vortex centre a, at which the vorticity $\omega = 0$. However in practice this will not be well defined, and recommends the use of either δ or a_e, the internal and effective radii respectively. He further defines δ as being the radial extent from the vortex centre at which the tangential velocity is maximised. a_e is defined according to equation (3.3), giving an equivalent core size for a uniform vorticity vortex ring, this is illustrated and compared to δ in figure 3.3. One can see that due to the assumption of uniform vorticity, a_e is necessarily symmetric about the centre of the core. δ however is defined by the extremum in the velocity field.

$$U_T = \frac{\Gamma}{2\pi D}\left[ln\frac{4D}{a_e} - \frac{1}{4}\right] \tag{3.3}$$

3.2.3 The Reynolds number

The Reynolds number, as throughout fluid dynamics, quantifies the ratio of inertial forcing to viscous damping and further the propensity of fluid to become turbulent. Several variations on Reynolds number have been employed with the purpose of applying this ratio to vortex rings, each with its own merits.

Perhaps the simplest and most frequently used is that given by (Maxworthy,

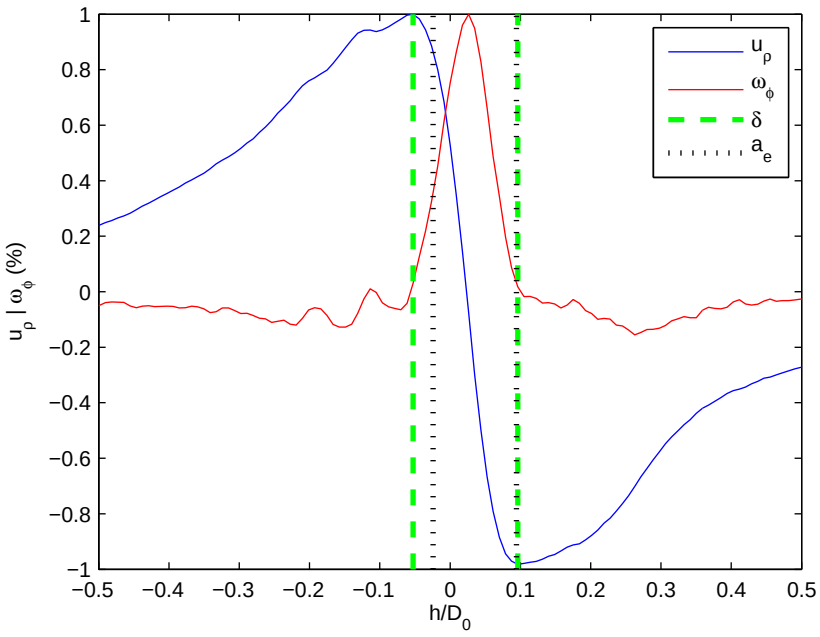

Figure 3.3: Illustration of the differences between δ and a_e

1977), equation (3.4). This formulation has the distinct advantage that for experimental generation, the parameters used to define the vortex ring are normally known and so the calculation is straightforward. The disadvantage with characterisation by Re_o is that the actual inertial forcing experienced by the fluid is further a function of the formation time, T_o, and outlet geometry. Both of these factors are of lesser importance (at least for small T_o) than U_o and D_o, however the implication is nonetheless that Re_o does not completely describe the inertial dynamics of the vortex ring.

$$Re_o = \frac{\overline{U_o} D_o}{\nu} \tag{3.4}$$

Perhaps of more relevance to the fluid dynamics however, is a definition from the vortex ring's circulation immediately subsequent to generation, Γ_0, as given in equation (3.5a) (Glezer, 1988). As this is arrived at from an actual measure of the fluid's inertia, it provides a good measure of the vortex ring dynamics, as

it encapsulates the entirety of the formation process. Circulation measurement requires a relatively complex measurement of the fluid flow field, as an integral of the vorticity field must be evaluated, this may be simplified through the use of Stoke's theorem, as in equation 3.5b (Kundu and Cohen, 2002). Here the velocity field $\mathbf{u}$ is integrated on a surface $\mathbf{S}$ bounded by the line $\mathbf{l}$.

$$Re_\Gamma = \frac{\Gamma_0}{\nu} \tag{3.5a}$$

$$\Gamma = \int_{\mathbf{S}} \nabla \times \mathbf{u}.d\mathbf{S} = \oint_l \mathbf{u}.d\mathbf{l} \tag{3.5b}$$

Similarly Stanaway *et al.* (1988) used a description arrived at from hydrodynamic impulse, equation (3.6a) for numerical simulations of vortex rings. Whilst providing the same advantages as Re_Γ, computation of Re_I from experimental data is significantly more difficult, this is because the vorticity integral in equation (3.6b) cannot be simplified through Stoke's theorem. An accurate field measurement of the vorticity field is therefore required, which poses a significant challenge.

$$Re_I = \frac{\sqrt{I_h/\rho}}{\nu\sqrt{(t)}} \tag{3.6a}$$

$$I_h = \pi\rho \int_0^\infty \int_{-\infty}^\infty \omega_\varphi r^2 dh dr \tag{3.6b}$$

For a theoretical consideration of the instabilities formed, Saffman (1978) used a strain rate formulation, Re_s, as in equation (3.7), where δ is the inner core radius (c.f. 3.2.2).

$$Re_s = \sigma\delta^2/\nu \tag{3.7}$$

Glezer (1988) showed that through application of the slug flow model (c.f. Section 3.3.2.1) one can estimate Γ_0 from simple parameters such as those used in equation (3.4). Equivalence is shown in figure 3.4. The corresponding Reynolds number is shown in equation (3.8). Note that any outlet geometry effects will be neglected from this estimate of circulation, however inertial addition due to T_o is included through L_o.

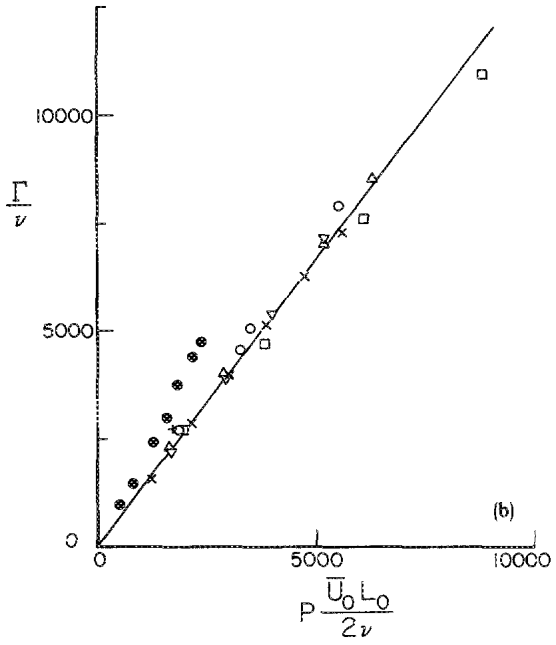

Figure 3.4: Comparison between Re_J and Re_Γ (Glezer, 1988)

$$Re_J = \frac{\overline{U_o} L_o}{2\nu} \tag{3.8}$$

3.2.4 Rossby number

The Rossby number provides a relationship between the inertial timescale of the fluid and the rotating timescale of the fluid. It is most commonly given as in equation (3.9), where Ω is the magnitude of background rotation (Johnson, 1966; Verzicco *et al.*, 1996).

$$Ro_D = \frac{\overline{U_o}}{D_o \Omega} \tag{3.9}$$

3.3 The evolution of vortex rings

3.3.1 Introduction

Vortex ring evolution has been studied extensively both analytically, numerically and experimentally. The vortex ring life cycle encompasses a number of stages of evolution: formation; laminar stage; instability; turbulence and decay. Real vortex rings, both formation and decay are required, between these regions various combinations of stages of evolution may exist.

Upon formation, the vortex ring (depending on initial conditions) may be either laminar or turbulent. Rings which are formed laminar may develop an elliptical instability, referred to as the Widnall instability (Widnall and Sullivan, 1973) and, through this, transition to turbulence (Maxworthy, 1972). As turbulent vortex rings evolve, they lose significant momentum to the surrounding fluid in the form of a wake. In typical lab measurements, sufficient inertia is lost for the vortex ring to re-laminarise and the final decay process is similar to that of the laminar ring: in the form of what is called an asymptotic drift (Maxworthy, 1972). For very high Reynolds number vortex rings, the laminar and unstable stages are completely circumvented and the vortex ring becomes turbulent at the outlet.

A transition map has been put forward to provide an indication of the state of various vortex rings, dependant upon their generation parameters (Glezer, 1988). This is presented in figure 3.5. The filled circles in the figure indicate vortex rings that were turbulent upon formation, those marked with crosses indicate initially laminar vortex rings. In both cases, the dissemination was based upon dye ob-

servations. The generation parameters are summarised by two non-dimensional numbers the formation time, L_o/D_o (c.f. Section 3.2.1) and the Reynolds number, Re_J (c.f. Section 3.2.3).

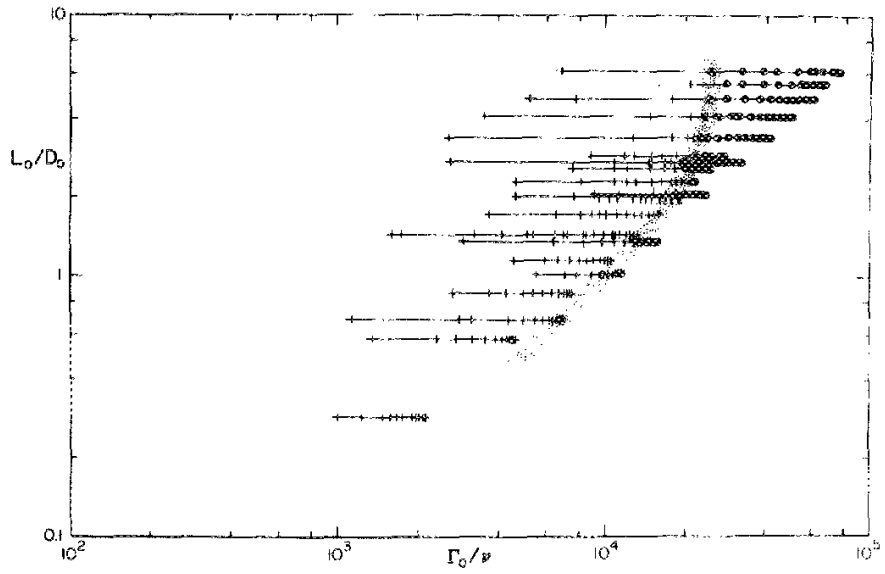

Figure 3.5: Transition map, indicating the state of a vortex ring given its generation parameters, from (Glezer, 1988)

A further investigation into the onset of turbulence in vortex rings was made by Dziedzic and Leutheusser (2004). They investigated vortex rings using hot-wire anemometry and also with smoke visualisation. Based upon the results from the hot-wire traces, the turbulent vortex rings were reclassified into two separate groups: turbulent and turbulence producing. This reclassification occurs because in the turbulence producing vortex rings, hot-wire traces through the cores indicate no presence of turbulence, the outer vortex ring atmosphere and wake however, show turbulence.

Dziedzic and Leutheusser (2004) also found a few cases displaying the traditional signs of turbulent wakes, with large scale vortex shedding to the wake, however the associated hot-wire traces indicated fully laminar vortex rings. This is of interest as it highlights the caution that should be taken in the assessment

of vortex ring properties from dye measurements, this echoes the sentiment expressed by Lim and Nickels (1995).

3.3.2 Formation

Vortex rings are formed in a variety of ways, typically fluid is ejected from a container with a circular outlet. They are usually modelled in the laboratory by pushing a column of fluid of length L_o out of an orifice of diameter D_o. In doing so, a boundary layer forms on the inside of the vortex ring generator, where the flow reaches the edge of the generator, this rolls up into a spiral. The two most common vortex ring generators, as shown in figure 3.6, commonly referred to as the piston-cylinder (figure 3.6a) and the orifice (figure 3.6b) geometries.

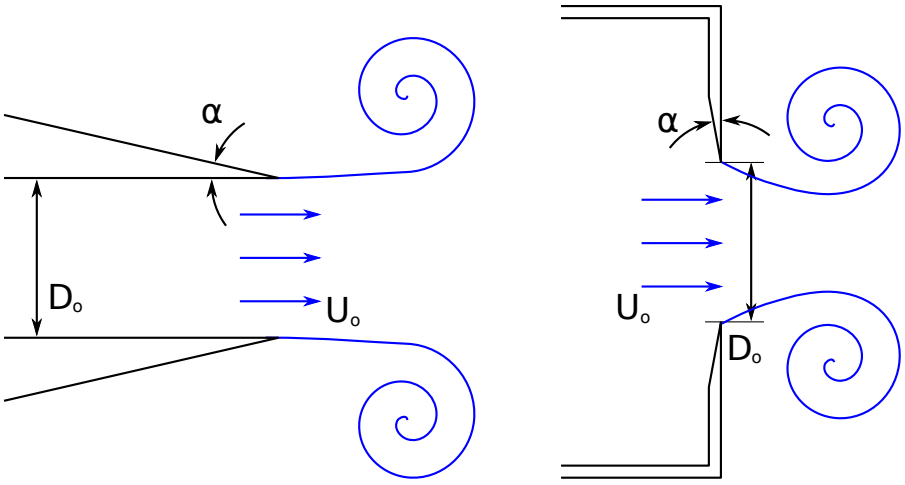

(a) Piston-cylinder (b) Orifice

Figure 3.6: Typical vortex ring generation geometries (Shariff and Leonard, 1992)

Vortex ring formation has been modelled extensively using the slug flow model. It enables simple estimation of starting flow measures, such as the circulation, Γ_0 and impulse, I_0, from experimental parameters. A more complicated and less frequently used model is that of self-similarity, which allows for estimation of vortex ring diameter, core diameter and starting circulation. Further to

this, several models have been proposed and validated concerning the formation number of vortex rings. This indicates the amount of circulation that can be added to a vortex ring prior to pinch-off (Gharib *et al.*, 1998). These models are briefly reviewed here.

3.3.2.1 The slug flow model

The slug flow model provides a means of estimating the initial circulation of the vortex ring, as a function of the generation parameters. If one makes the boundary-layer approximation, and assumes that the velocity at the edge of the boundary layer is equal to the piston velocity, one may approximate the rate of vorticity flux (Lim and Nickels, 1995), as:

$$\begin{aligned}\frac{d\Gamma_{slug}}{dt} = \int \omega_\varphi u_h dr &\simeq \frac{\partial u_h}{\partial r} u_h dr \\ &\simeq \int_0^{U_p(t)} \frac{\partial u_x^2}{2\partial r} \\ &= \frac{1}{2} U_p^2(t)\end{aligned}$$

Assuming that all of the vorticity generated then rolls up into the formed vortex ring, one may approximate the initial circulation of the vortex ring, Γ_0, as in equation 3.11 (Maxworthy, 1977).

$$\Gamma_0 = \int_0^{T_o} \frac{1}{2} U_p^2(t) dt \tag{3.11}$$

It is trivial to show that the integral in equation 3.11 may be approximated as $\overline{U_p} L_o/2$ (Glezer, 1988), where the overbar denotes the temporal mean. Upon this basis (and from the conservation of impulse), Glezer (1988) defined a velocity program factor P as in equation (3.12). The program factor is used to account

for deviations from an impulsive jet in the vortex ring generator.

$$P = \int_0^1 \left(\frac{U_p^2}{\overline{U_p^2}} \right) d\left(\frac{t}{T_o} \right) = \frac{\overline{U_p^2}}{\overline{U_p}^2} \tag{3.12}$$

3.3.2.2 Self-similarity formulation

A self-similarity approach to vortex ring formation was first discussed by Saffman (1978), who proposed a formulation from an axisymmetric model of an impulsively started jet. Upon this basis he arrived at approximations for D_0, Γ_0 and δ_0, as in equation (3.13).

$$D_0 = D_o + c_1 c_4^{\frac{2}{3}} L_o^{\frac{2}{3}} D_o^{\frac{1}{3}} \tag{3.13a}$$

$$\delta_0 = \frac{c_3^2 c_4^{\frac{2}{3}}}{c_2^2} L_o^{\frac{2}{3}} D_o^{\frac{1}{5}} \tag{3.13b}$$

$$\Gamma_o = c_3 c_4^{\frac{4}{3}} \overline{U_o} L_o^{\frac{1}{3}} D_o^{\frac{2}{3}} \tag{3.13c}$$

Where c_1, c_2, c_3 and c_4 are constants. The model was validated against experimental data for small L_o/D_o. A similar formulation was presented by Pullin (1979), who also considered the axisymmetric roll-up of a vortex sheet, from tube and orifice geometries. Furthermore this model enabled for a non-impulsive velocity profile, according to equation (3.14).

$$U_o(t) = U_p t^m \tag{3.14}$$

Here U_p and m are constants, for an impulsively started motion, $m = 0$, implying during generation $U_o = U_p$. The circulation and core radius were then defined

according to the generation time T_o, for some constant K_0, equation (3.15).

$$K_0 = K_1 A_p D^{\frac{1}{2}} \tag{3.15a}$$

$$\Gamma_0 = K_2 \left[\frac{0.75 K_0^4}{1+m}\right]^{\frac{1}{3}} T_o^{\frac{4}{3}(1+m)-1} \tag{3.15b}$$

$$\delta_0 = K_3 \left[\frac{0.75 K_0}{1+m}\right]^{\frac{2}{3}} T_o^{\frac{2}{3}(1+m)} \tag{3.15c}$$

Here K_1 is a constant related to generator geometry, K_2 and K_3 are constants obtained from similarity theory calculations. Finally the vortex ring diameter is given in terms of yet another constant, K_5, again related to generator geometry, as in equation (3.16).

$$D_0 = D_o + K_5 D_o \left(\frac{L_o}{D_o}\right)^{\frac{4}{3}} \tag{3.16}$$

3.3.2.3 The formation number

Much of the recent work concerning the formation of vortex rings has stemmed from Gharib *et al.* (1998) who attempted to ascertain the largest circulation a vortex ring can attain for a constant piston speed (generation was performed using a piston-cylinder geometry). For simple configurations, fixed piston speed allows only for variation of the stroke length L_o. It was found that circulation was maximised for $L_o/D_o \simeq 4$ with the maximum attainable value of L_o/D_o termed the formation number. Further it was found that for $L_o/D_o \gtrsim 4$ a jet would form instead a vortex ring, a result first published by Tarasov and Yakushev (1973), but commonly overlooked.

Gharib *et al.* (1998) proposed the limitation imposed upon the addition of circulation to the vortex ring arose due to the kinetic energy of the vortex ring exceeding the energy added by the generator. To this end they formulated an energy balance, where the vortex ring would continue to form whilst $E_R < E_G$, (here E_R and E_G are the energy of the ring and the energy supplied by the generator respectively). From this, the non-dimensional energy α was defined, c.f. equation 3.17. Where I is the vortex ring's hydrodynamic impulse (the hydrodynamic impulse is given in equation (3.6b)). Empirically, pinch off was found to occur at $\alpha_{lim} \simeq 0.33$, which was used to estimate the formation number for a range of theoretical generation programs. In all cases, pinch off was found to occur at $L_o/D_o \simeq 4$.

$$\alpha = \frac{E_R}{I^{1/2}\Gamma^{3/2}} \tag{3.17}$$

Numerical simulations were performed by Rosenfeld *et al.* (1998) and Mohseni *et al.* (2001) for a wide range of generation parameters. It was found that the formation number was insensitive to both Reynolds number and generator geometry. It was shown that pinch off could be delayed and hence formation number increased by increasing the piston velocity or outlet diameter during generation. In both cases, this leads to increased energy being delivered to the vortex ring over time, and forcing a fattening of the vortex core. Experiments were performed to investigate the increasing of the outlet diameter and showed that a delay in pinch off was not observed (Allen and Naitoh, 2005; Dabiri and Gharib, 2005). It was however seen that by increasing the outlet diameter, more energy was delivered to the vortex ring, and by decreasing the nozzle diameter, the vortex ring pinched off sooner, with higher normalised circulation.

Following these studies a series of models were produced to estimate formation

time: Mohseni and Gharib (1998) produced theirs from invariants of Norbury vortices (Norbury, 1973) and the slug flow model; Linden and Turner (2001) based theirs upon simple analysis of the inflow condition with the use of the Norbury family of vortices suggesting that volume constraints within the vortex ring account for the formation time. Shusser and Gharib (2000) provide another model for calculating formation time from Norbury vortices and the slug flow model, however this receives correction for the effect of a boundary layer in the cylinder (Shusser *et al.*, 2002; Dabiri and Gharib, 2004a) and an extension for time varying velocity inflow conditions (Shusser *et al.*, 2006).

3.3.3 Laminar phase

Low Reynolds number vortex rings are laminar upon creation and propagate with little loss of impulse (Maxworthy, 1972). It was shown that as they propagate, vorticity diffuses viscously from the inner core region into the outer atmosphere. Viscous diffusion of vorticity also accounts for the loss of vorticity to a weakly vortical wake, and also for the entrainment of fluid back into the vortex atmosphere. This accounts for an addition of mass to the vortex ring and hence, due to conservation of momentum, a decrease in translational velocity.

Saffman (1970) predicted that for thin cored rings, with a Gaussian core vorticity distribution, the translational velocity of the vortex ring would be given by equation 3.18. Numerical simulations (Stanaway *et al.*, 1988) showed that the error estimation of $\mathscr{O}\left(\sqrt{\frac{\nu t}{R^2}} log\left(\frac{\nu t}{R^2}\right)\right)$ to be conservative and suggested a more appropriate value of $\mathscr{O}\left(\frac{\nu t}{R^2} log\left(\frac{\nu t}{R^2}\right)\right)$.

$$U_T = \frac{\Gamma_0}{4\theta R}\left\{log\frac{8R}{\sqrt{4\nu t}} - 0.588 + \mathscr{O}\left(\sqrt{\frac{\nu t}{R^2}} log\left(\frac{\nu t}{R^2}\right)\right)\right\} \tag{3.18}$$

Base upon empirical evidence, Maxworthy (1972) proposed that for lami-

nar vortex rings (which were defined as $Re_D < 600$), the translational velocity decreased exponentially, as per proportionality (3.19a). In order for this formulation to hold, it was required that the vortex ring conserve impulse, an assumption that was revised (Maxworthy, 1974), resulting in a correction to the prediction of translational velocity c.f. equation (3.19b). Here A and B are both constants; t_0 is a virtual origin in time (the theoretical point at which the ring was of 0 diameter) R_0 is the initial radius of the vortex ring, and U_0 its initial translational velocity.

$$U_T \sim \frac{1}{t} \tag{3.19a}$$

$$U_T = At^{-\frac{1}{2}B(U_0R_0/\nu)^{-\frac{1}{2}}t_0U_0/R_0} \tag{3.19b}$$

3.3.4 Growth of the instability and turbulent transition

The wavy azimuthal instability, also known as either the elliptical or Widnal instability (Shariff and Leonard, 1992), was first visualised on vortex rings by Krutzsch (1939). Maxworthy (1972) performed dye visualisation measurements of the phenomenon, categorising wavelength and number of modes as a function of Re_D. Widnall and Sullivan (1973) performed the first detailed stability analysis, considering sinusoidal perturbations of a thin cored ring ($\delta \rightarrow 0$) in ideal fluid. Subsequently, this model was extended to include vortex rings of finite core diameter (Widnall and Tsai, 1977), and it was shown that the strain field imposed by the vortex ring causes linear growth of small amplitude perturbations to the ring at formation.

A subsequent model by Saffman (1978) used a more realistic Gaussian vortex core to model the instability. He found the number of waves to be sensitive to

the distribution of vorticity in the core and presented a prediction for the number of waves and their growth rate as a function of Reynolds number. These results were shown to agree well with those of Liess and Didden (1976), and a later PIV study (Dazin *et al.*, 2006a), found close agreement with the prediction of number of waves. Numerics and experiments have indicated that a correction to the growth rate of the instability is necessary to account for the effects of the vorticity (Shariff *et al.*, 1994) (Dazin *et al.*, 2006a). The existence of a secondary vortical structure, which grows with the same wavenumber, but which is oriented 180° out of phase to the primary instability has been shown (Shariff *et al.*, 1994). Interesting visualisations of this are inferred from the Q-criterion (Archer *et al.*, 2008). As discussed by Wray and Hunt (1988), the presence of eddies are indicated by the second invariant of Q (equation (3.20)) being negative. Here S and A are the symmetric and anti-symmetric parts of the velocity gradient tensor.

$$Q = 1/2 \left(|A|^2 - |S|^2 \right) \tag{3.20}$$

The point of transition to turbulence has received relatively little study. Dazin *et al.* (2006b) have shown through Fourier analysis of azimuthal and radial velocities (extracting from a circular profile lying through the core of the vortex ring), that subsequent to the linear instability, a phase of non-linear growth occurs. During this stage, higher order harmonics were found to grow, prior to the transition to turbulence. As this occurs, an azimuthal swirling flow is found along the vortex core, first observed by Maxworthy (1977). Naitoh *et al.* (2002) estimated the velocity of this swirl to be approximately $U_T/4$, however Dazin *et al.* (2006a) experimentally estimate this swirl to be approximately 7% of U_T. The work of Archer *et al.* (2008) also discussed this phenomenon, showing from numerical particle traces that the axial flow inside the core occurs in both direc-

tions, simultaneously.

3.3.5 Turbulent vortex rings

Weigand and Gharib (1994) present data acquired from a PIV measurement of a single vortex ring ($Re_\Gamma = 7500$). The generation was in the laminar regime, but the vortex ring subsequently transitioned through the Widnall instability phase to turbulence. The major result concerns the time evolution of the circulation, which is shown to decay in a "step-wise" fashion. This is attributed to the repeated rejection of discrete packets of vorticity from the ring into its wake. More recently numerical simulations of Bergdorf *et al.* (2007) and Archer *et al.* (2008) have also analysed similar vortex rings in the early turbulent regime, finding the same step-wise decay process.

Three models for turbulent vortex rings have been produced; Johnson (1971) and Maxworthy (1974) provide empirical models founded on the basis that vortex ring radius increases as the ring propagates. In both cases they provide a means of estimation of the vortex ring radius variation over time from initial observations, Maxworthy (1974) also allows estimation of the vortex ring's translational velocity U_T and circulation Γ. Glezer and Coles (1990) proposed a model upon the principals of self-similarity, which allows estimation of a self-similar velocity field.

3.3.5.1 Johnson's model

Johnson (1971) provides no physical interpretation of the fits presented; the model is purely empirical, based upon measurements up to $70D_o$ from the vortex generator. In this model, the vortex ring's axial position as a function of time was found to be well fitted by equation (3.21a), and the vortex ring radius R, as a function of time, by equation (3.21b). Here A and B are constants; t_0 and h_0

are virtual origins referring to the point in time and space at which the vortex ring was of $R = 0$.

$$\frac{t - t_0}{T_o} = A \left[\frac{h - h_0}{D_o} \right]^{3/2} \tag{3.21a}$$

$$\frac{2R}{D_o} = B \left[\frac{h - h_0}{D_o} \right]^{1/6} \tag{3.21b}$$

3.3.5.2 Maxworthy's model

From dye visualisations of vortex rings, Maxworthy (1974) suggested that as the vortex ring travelled, it rapidly lost impulse to its wake, thus decreasing in circulation rapidly. Upon his own observations, he suggested that the vortex ring continued to grow in size steadily, due to the entrainment of fluid from its surroundings. Based upon this he developed a semi-empirical model for the vortex ring, which was modelled as a sphere of radius equivalent to that of the vortex ring. The shape of the vortex ring's atmosphere was considered to be constant, but growing due to the entrainment of fluid. The loss of impulse to the wake was modelled as an additional drag force upon the sphere, represented by a drag coefficient C_D.

The model presented estimates for the translational velocity (3.22a), radius (3.22b) and circulation (3.22c).

$$U_T = A(t - t_0)^{(C_D+3)/(C_D+4)} \tag{3.22a}$$

$$R = B(t - t_0)^{1/(C_D+4)} \tag{3.22b}$$

$$\Gamma \sim U_T R = C\,(t - t_0)^{-(C_D+2)/(C_D+4)} \tag{3.22c}$$

3.3.5.3 Model of self similarity

The self similarity equations are derived from a non-dimensionalised axisymmetric stream function, and the hydrodynamic impulse. By taking account the vortex ring's virtual origins in time t_0, and the axial direction h_0, one may formulate this stream function into similarity coordinates ε and η, equation 3.23.

$$\varepsilon = (x - x_0)\left(\frac{\rho}{I\,(t - t_0)}\right)^{\frac{1}{4}}, \qquad \eta = r\left(\frac{\rho}{I\,(t - t_0)}\right)^{\frac{1}{4}} \tag{3.23a, b}$$

Through the stream function the velocity may then be defined in similarity coordinates (3.25) (Glezer and Coles, 1990).

$$u_h = \frac{1}{r}\frac{\partial \psi}{\partial r}, \qquad u_r = \frac{1}{r}\frac{\partial \psi}{\partial h} \tag{3.24a, b}$$

$$U_h = u_h(\frac{\rho}{I})^{\frac{1}{4}}(t - t_0)^{\frac{3}{4}}, \qquad U_r = u_r(\frac{\rho}{I})^{\frac{1}{4}}(t - t_0)^{\frac{3}{4}} \tag{3.25a, b}$$

The combination of equations (3.25) and (3.23) results in a set of rules, (1)-(3), applicable for a point fixed in similarity coordinates. Further to this, rule (4) may be arrived at through the computation of the circulation in similarity coordinates. Here Γ_T is the total circulation induced by the vortex ring (Glezer and Coles, 1990). These rules were used to test the validity of this model using LDA traces.

1. $r \sim (x - x_0)$
2. $(h - h_0) \sim (t - t_0)$
3. $u_h^{-\frac{1}{3}} \sim (t - t_0) \sim (h - h_0)$
4. $\Gamma_T \sim (t - t_0)^{-\frac{1}{2}}$

3.3.6 The evolution of vortex ring properties

The formation models discussed in section 3.3.2 are concerned only with the vortex at the point of generation. As such, measurements have only been made of vortex ring properties relatively close to the generator, in particular the initial circulation Γ_0. By contrast, relatively little work has been performed looking at the other stages of vortex ring evolution. What follows is a summary of various measures made of vortex ring properties.

Experiments have been conducted to validate the models presented in sections 3.3.3 and 3.3.5. In general, the time evolution of vortex ring radius and axial position (from which may be inferred the translational velocity) have been measured extensively.

Additionally dye measurements have been made to estimate the rate of detrainment from turbulent vortex rings (Tarasov and Yakushev, 1973). Vortex rings were generated filled with dye, and then subsequently caught in a trap. A comparison of the concentration in the trap to that injected into the vortex ring allowed for estimation of the detrained mass of fluid. The measurements were made for several vortex rings across $50D_o$, finding an asymptotic decay. Similar measurements were performed on a laminar vortex ring (Dabiri and Gharib, 2004b) and the entrainment fraction measured. This was measured by finding streamlines in a reference frame moving with the vortex ring, based upon location of the frontal and rear stagnation points, the fluid transported by the vortex ring may be found (Shadden *et al.*, 2006). The measurements were made over relatively short timescales, and demonstrated a linear entrainment fraction.

Further to this, Weigand and Gharib (1994) measured the circulation of a vortex ring, $Re_\Gamma = 7500$, over a range of $20D_o$. After the vortex ring had transitioned to turbulence, they found what was termed a "step-wise" decay in the

circulation. This was attributed to the ejection of discrete packets of vorticity from the turbulent vortex ring and supported by vorticity contours of individual frames. It should be noted that to produce measurements over this spatial range would have required the combination of PIV measurements from multiple different vortex ring runs and camera positions, or a traversing camera method. Details of which approach was used are not given. Bergdorf *et al.* (2007) performed numerical simulations on a vortex ring, also $Re_\Gamma = 7500$ and also finding the same step-wise decrease in circulation.

Dye observations have also been used to make estimations for the evolution of the vortex ring core diameter Buzukov (1971), finding that for a transitional vortex ring, this remained a constant factor of vortex ring diameter indicating a varying core diameter. Subsequently Archer *et al.* (2008) has shown the slenderness ratio increasing with time for similar vortices, albeit with low growth rates. It was found that the rate of increase was significantly faster for a thin cored vortex ring, compared with a thick cored.

3.4 Vortex rings and background rotation

Vortex rings and the effects of background rotation have received relatively little attention in the literature. Here we refer to the background rotation as the case where the fluid in which the vortex ring is generated moves in solid body rotation with the vortex ring generator.

Cases of vortex ring motion perpendicular to the axis of background rotation (figure 3.7a) have been studied Taylor (1921); Eisenga *et al.* (1998). Relatively few investigations have been conducted into the case of a vortex ring propagating parallel to the axis of rotation (figure 3.7b). There has however, been a single investigation (Verzicco *et al.*, 1996) into the effects of background rotation upon

a vortex ring propagating in this orientation, this being the case considered in this section.

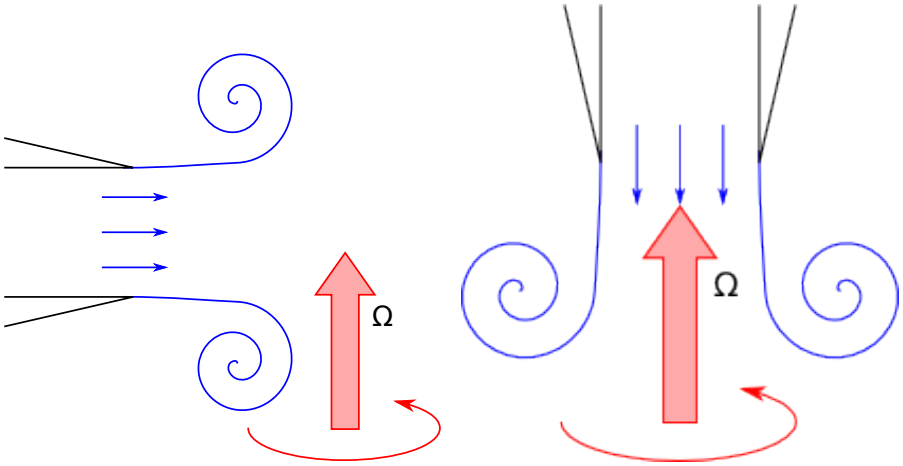

(a) Vortex ring travel perpendicular to the rotation vector

(b) Vortex ring travel parallel to the rotation vector

Figure 3.7: Vortex ring travel

The Coriolis effect leads to the apparent deflection of objects moving in a rotating reference frame, when they are observed within that reference frame. The apparent forcing arises due to the acceleration from the rotation applied to the observation point. For this reason, when equations of motion are transformed into a rotating reference frame, an acceleration term due to the Coriolis force arises, this is given in equation (3.26) (Kundu and Cohen, 2002).

$$\mathbf{a_C} = -2\boldsymbol{\Omega} \times \mathbf{v} \tag{3.26}$$

3.4.1 The effects of background rotation upon vortex rings

The most notable investigation in this area was performed both numerically and experimentally (Verzicco *et al.*, 1996), and for this reason, it shall receive special attention. Verzicco *et al.* (1996) began by showing through dye visualisation, the

structural changes that occur to the vortex ring, a sample of which is provided in figure 3.8. For the non-rotating case, figure 3.8a, we see a classic, laminar vortex ring. The dye reveals an elliptical atmosphere, containing regular, coherent streaks through the core and a small, well structured wake formed behind the vortex ring. The rotating case is however quite different, dye pattern is less coherent and significantly less well mixed. At the vortex ring's frontal stagnation point. There is a depression, and one can see a secondary vortex structure has been ejected from the rear of the vortex ring.

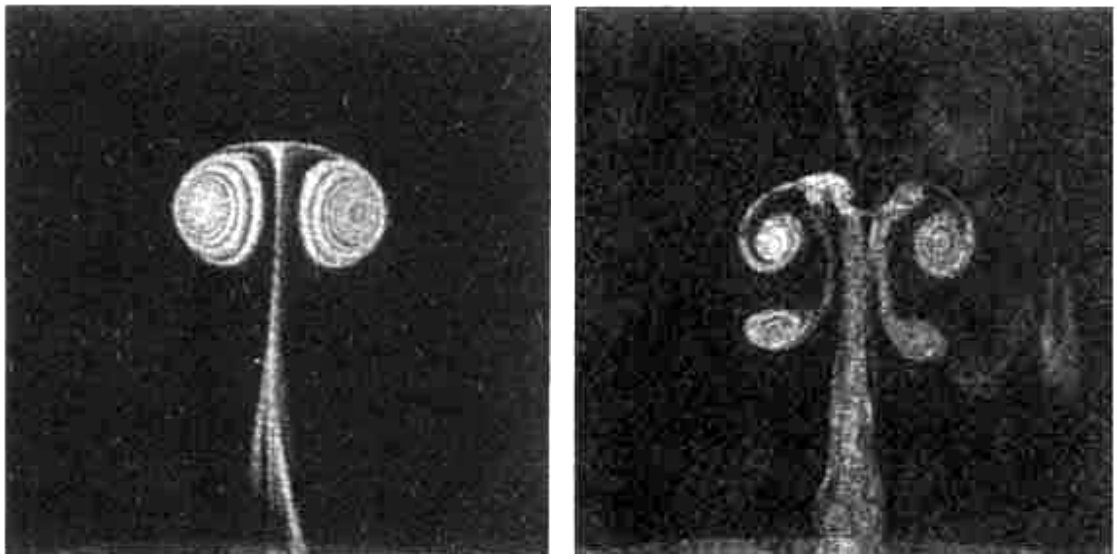

(a) Non-rotating (b) Rotating

Figure 3.8: Vortex rings, illustrated using dye visualisation, (digitally enhanced, from Verzicco *et al.* (1996))

Figure 3.9 shows plots of both numerical and experimental data from Verzicco *et al.* (1996), showing the axial position of the vortex ring as a function of time. This data highlights that for all of the conditions tested, the vortex ring initially follows the same trajectory (note that $Ro = \infty$ indicates a non-rotating condition). Under the influence of background rotation however, the vortex ring trajectory changes. After some time, the gradient of the line (and hence the

translational velocity of the vortex ring) decreases suddenly. The greater the rotation rate (and so, the lower the Rossby number), the sooner this trend is seen. After the large change in velocity the vortex rings are seen to lose velocity slowly.

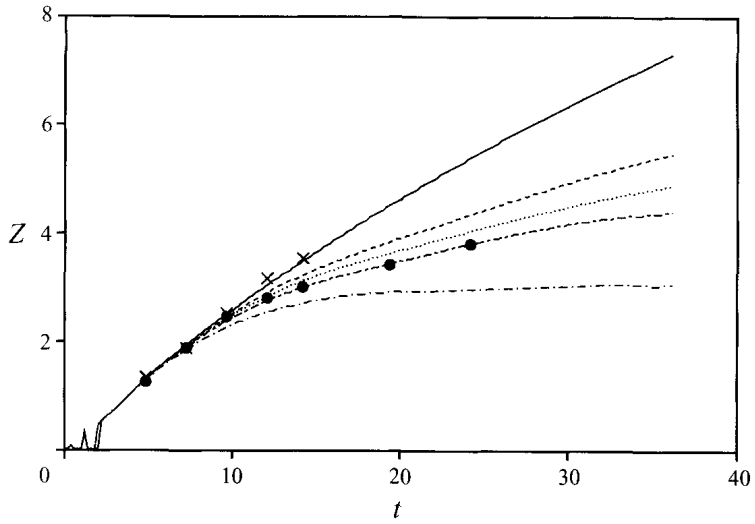

FIGURE 6. Time evolution of the axial position of the core centre of the ring (Z) for $Re = 484$ and: ——— , $Ro = \infty$; - - - - , $Ro = 10$; ····· , $Ro = 7.4$; — - — , $Ro = 5.5$; — · — , $Ro = 3$. Experimental results: × , $Ro = \infty$; • , $Ro = 5.5$.

Figure 3.9: Vortex ring trajectories (from Verzicco *et al.* (1996), including original caption)

Some contour plots from the numerical simulations used to prepare these plots are also presented. Of particular interest are the azimuthal component of vorticity ω_φ; the axial component of vorticity ω_h, and the azimuthal velocity, u_φ. These are plotted in figure 3.10 for a low Reynolds number case, $Re = 484$.

The features of interest are the areas of negative vorticity ahead of the larger positive core, figure 3.10a. It was shown that the secondary vorticity seen in figure 3.8b was actually formed ahead of the vortex ring. Verzicco *et al.* (1996) showed that this was then dragged around the core in a counter-clockwise fashion, and then ejected upstream of the vortex ring. In doing so, this leads to an increase in vortex ring diameter, which is suggested to be due to an unbalanced vortex dipole.

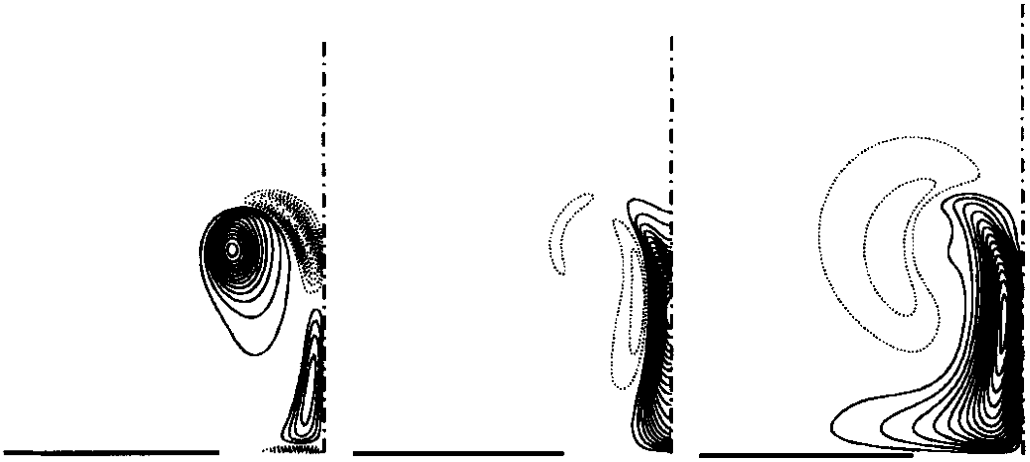

(a) Azimuthal vorticity, ω_φ (b) Axial vorticity, ω_h (c) Azimuthal velocity, u_φ

Figure 3.10: Vorticity and velocity profiles (from, Verzicco *et al.* (1996), figure 10 (a), (b) and (d))

It is well known that vortex dipoles which have circulation of opposite sign and differing magnitude will propagate with a curved trajectory. In the case of the vortex ring, with a secondary vortex of lesser circulation outside it, this tendency toward a curved trajectory will result in an increase in vortex ring diameter. This is illustrated in figure 3.11.

The ejection of this opposite signed vorticity also coincides with a decrease in peak vorticity, which is explained through viscous diffusion of the two peaks and cross-cancellation. In fact, it is shown that the decrease in vorticity magnitude precedes an increase in magnitude for the rotating conditions. This occurs in tandem with radial stretching of the vortex ring, leading to more highly concentrated vorticity (through conservation of circulation). This then diffuses at an increased rate.

We also see that there is a distinct region of positive vorticity formed behind the vortex ring, towards the axis of symmetry, it can be seen from figures 3.10b and 3.10c that this corresponds to a region of strong out of plane motion. Verzicco *et al.* (1996) state the direction of this flow as being cyclonic with the rotating

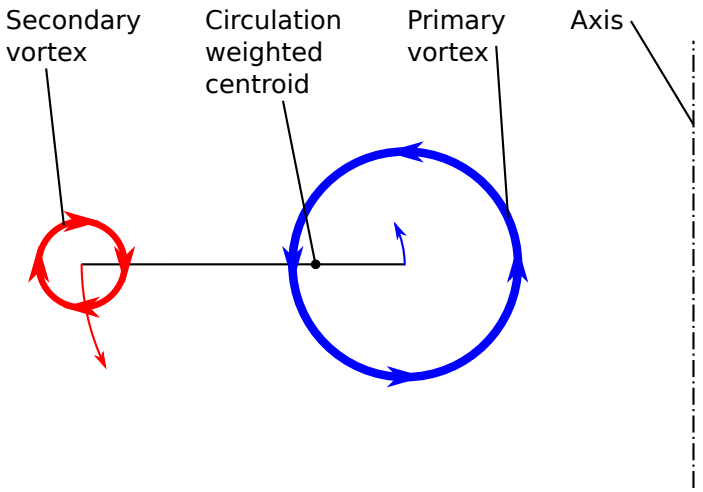

Figure 3.11: Illustration of the radial motion occurring due to an unbalanced dipole

reference frame. As this swirling flow mainly manifests itself in the wake, we have termed it "wake swirl." Further, Verzicco *et al.* (1996) show a region of opposite signed (anti-cyclonic) swirl ahead and radially displaced outward from the axis of symmetry.

The wake swirl phenomena was also seen in numerical simulations of polarised vortex rings (Virk *et al.*, 1994), where vortex rings with helical vortex lines induced swirling in the cores and in a wake region behind the vortex ring. Furthermore, Virk *et al.* (1994) went on to show, through numerical results and analytical arguments for Hill's spherical vortex ring that for all cases, U_T would be decreased by the occurrence of swirl in the vortex core. Prior to this, Shariff and Leonard (1992) had presented force balance arguments (valid only for thin cored vortex rings), suggesting that swirl would result in a reduction of translational velocity.

Both the cyclonic and anti-cyclonic swirling found under the influence of background rotation were explained by Verzicco *et al.* (1996) as originating due to the Coriolis force. Due to the rotating reference frame, Coriolis force manifests

itself as the requirement, through the conservation of angular momentum, that the value of $(ru_\varphi + r^2\Omega)$ be maintained (Verzicco *et al.*, 1996). In the case of the vortex ring we have strong radial motion both upstream and downstream of the vortex ring. At both these locations the radial motion results in the manifestation of a swirling acceleration. On the upstream side, behind the vortex ring, the motion is inward; the fluid is therefore accelerated in the same direction as that of the background rotation, i.e. cyclonically. On the downstream side of the vortex ring, the motion is outward, and so the opposite occurs, promoting a swirl in the opposite, anti-cyclonic direction.

In addition to these plots, and perhaps of equal importance are the pressure distributions, which are reproduced in figure 3.12. The most prominent difference between figure 3.12a and 3.12b is seen in the wake region, which is positive for the non-rotating case. In the rotating case however, a small region of very low pressure is found behind the vortex ring; in a position similar to that of the wake swirl. For both rotating and non-rotating vortex rings, a region of low pressure is seen ahead of the vortex ring, it is suggested that this is larger for the rotating case than the non-rotating. This certainly would be the case if the isobars plotted are of equal magnitude, but no information to this effect is presented.

The discussion presented by Verzicco *et al.* (1996) suggests that this upstream low pressure region and the upstream high pressure region arise due to the Coriolis forcing; again we use conservation of angular momentum to infer the property $(ru_\varphi + r^2\Omega)$ which must remain constant. From this, we can see that for constant angular rotation, an increase in azimuthal velocity (i.e. the occurrence of swirl) results in a forced decrease of radius (as Ω is fixed, increase of u_φ must result in a decrease of r), thus resulting in an increase in pressure.

Further simulations by Verzicco *et al.* (1996) showed that for vortex ring with a constant rotation rate but increased Reynolds number, the secondary vortex

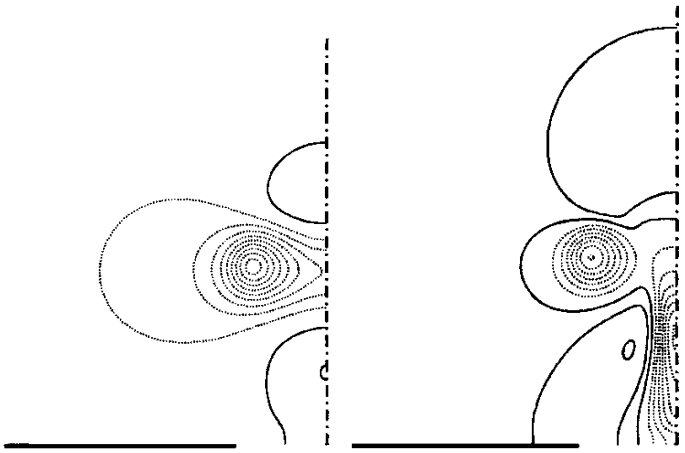

(a) Non-rotating (b) Rotating

Figure 3.12: Pressure field (from, Verzicco *et al.* (1996), figure 11 (a) and (b))

shedding had less of an effect on the primary vortex. This was attributed to the reduced timescales of motion, resulting in less time for cross-cancellation and vortex stretching. The result is that the secondary vortex structure is deposited into the wake of the primary vortex, which continues onwards; this is shown in figure 3.13. It is hypothesized that for vortex rings of sufficiently high inertia this could occur repeatedly, before their eventual destruction.

Also noticeable from the figures replicated in figure 3.13, however not commented upon by Verzicco *et al.* (1996), is the apparent separation of the vortex ring wake. The contours presented in figure 3.13a show a clear connection between the swirling wake and the vortex ring. This connection is much reduced in figure 3.13b and is clearly separated from the vortex ring in figure 3.13c.

Verzicco *et al.* (1996) state that their experimental results show that vortex rings produced under the influence of background rotation show a tendency to depart from axial symmetry, with one side of the vortex ring tending to develop before others. To evaluate this, they performed a series of targeted numerical experiments, enabling them to conclude that this arose due to misalignments of

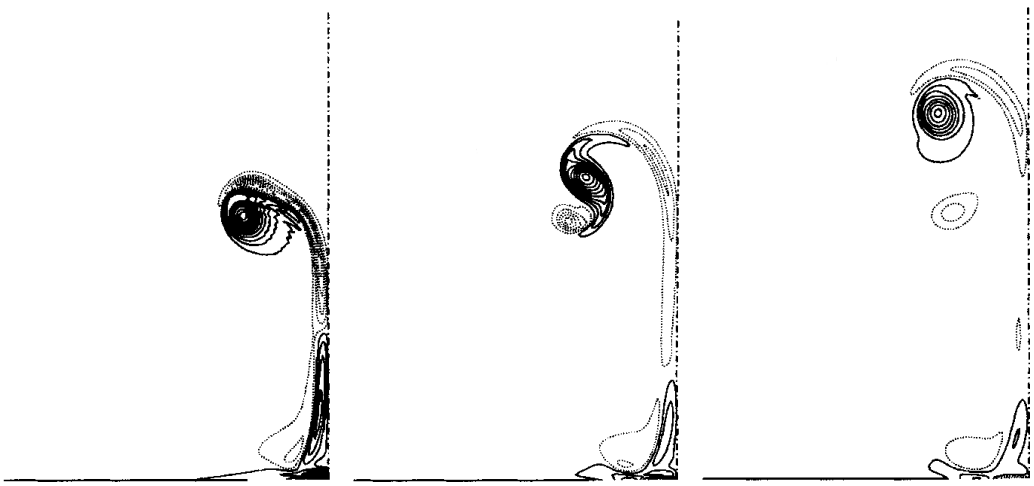

(a) $tu_o/D_o = 12.1$ (b) $tu_o/D_o = 16.9$ (c) $tu_o/D_o = 21.8$

Figure 3.13: Illustration of vortex deposition in the wake and separation of wake swirl, vorticity contour plots for vortex ring of $Re_o = 1500$, $Ro_D = 10$ (from Verzicco *et al.* (1996), figures 13(b-d))

the vortex generator with the background rotation vector $\mathbf{\Omega}$.

3.4.2 The effects of vortex rings upon a flow of uniform background rotation

The question of vortex rings propagating along the axis of a rotating flow, was first considered by Taylor (1922), where Hill's spherical vortex is used as an analogy to a sphere in terms of the type of disturbance it causes to the fluid. It was suggested that the vortex would be surrounded by spherical waves which would travel with it.

An analytical study was performed the stability of a rotating fluid under the influence of a perturbation (Johnson, 1966). In this work, a vortex ring was chosen due to the tendency of confined disturbances in unbounded fluid to form vortex rings. The vorticity equations (with Coriolis terms) were simplified on the basis that the non-linear term would be small compared with the Coriolis and

viscous terms (for high rotation rates). From this, predictions are made for the length scale L of the disturbance, and it was found that $L \sim (\Omega t)(R^2 + \nu t)^{1/2}$.

Further to this, Verzicco *et al.* (1996) also considered the high Ro_D limit, and found that the vortex ring was destroyed immediately upon generation, leaving what were termed "oblique shear layers of large axial extent". The hypothesis that these structures were inertial waves (which enabled the vortex ring to radiate energy) was tested and validated. This was done by simulating only the linear terms of the Navier-Stokes equations, as it was stated that this was all that was necessary for the formation of inertial waves.

CHAPTER 4

Experimental setup and acquisition

The study presented in this work considers the time evolution of vortex rings. The results described were achieved through experiments performed on the large vortex facility at the University of Warwick. All the measurements discussed here were made using a state of the art stereoscopic PIV system, developed through collaborations with the University of Warwick Optical Engineering Laboratory (OEL), and Etalon Research Ltd.

4.1 Overview

Each experiment consisted of a vortex ring being generated such that it travelled vertically downwards in a large $2000l$ water tank. High resolution SPIV measurements were then made in a reference frame that moved with the vortex ring, requiring the PIV equipment to traverse the side of the water tank. Measurements were made both with the water tank stationary and rotating about its centre, a unique feature for a tank of its size. This allowed the effects of

background rotation on the vortex ring dynamics to be investigated.

The rotating environment removed the possibility of access to the equipment and facility when measurements were made. To overcome problems associated with this, equipment was required to keep the facility in good working order. An example is the formation of density gradients in the water due to thermal inequalities over long periods of time. It was necessary that the water in the measurement section be mixed periodically to remove these gradients: the equipment to perform the mixing had to be mounted on the rotating turntable and controlled remotely.

Furthermore preparation of a single experimental run took a significant amount of time; acquisition time was therefore minimised and experimental repeatability maximised through full automation of the experiments. The hardware layout and control systems implemented on the tank were thus highly complex. The flow diagram shown in figure 4.1 provides an overview of the systems in place.

Initial experiments were performed in open-loop control, using a fixed velocity profile to control the movement of the PIV cameras down the side of the tank. Estimates of the vortex ring velocity profile over time were made and the moving PIV system programmed to follow this profile. Whilst these experiments were run, a unique real-time PIV system was developed and prototyped in cooperation with Etalon Research. This system adjusted the motion of the cameras in real-time based on actual measurements of the vortex ring position, thus providing real-time feedback of the vortex ring position and closing the control loop. Results from the real-time measurements are still pending data processing, and so the data presented in this work are concerned only with data from the open-loop control experiment.

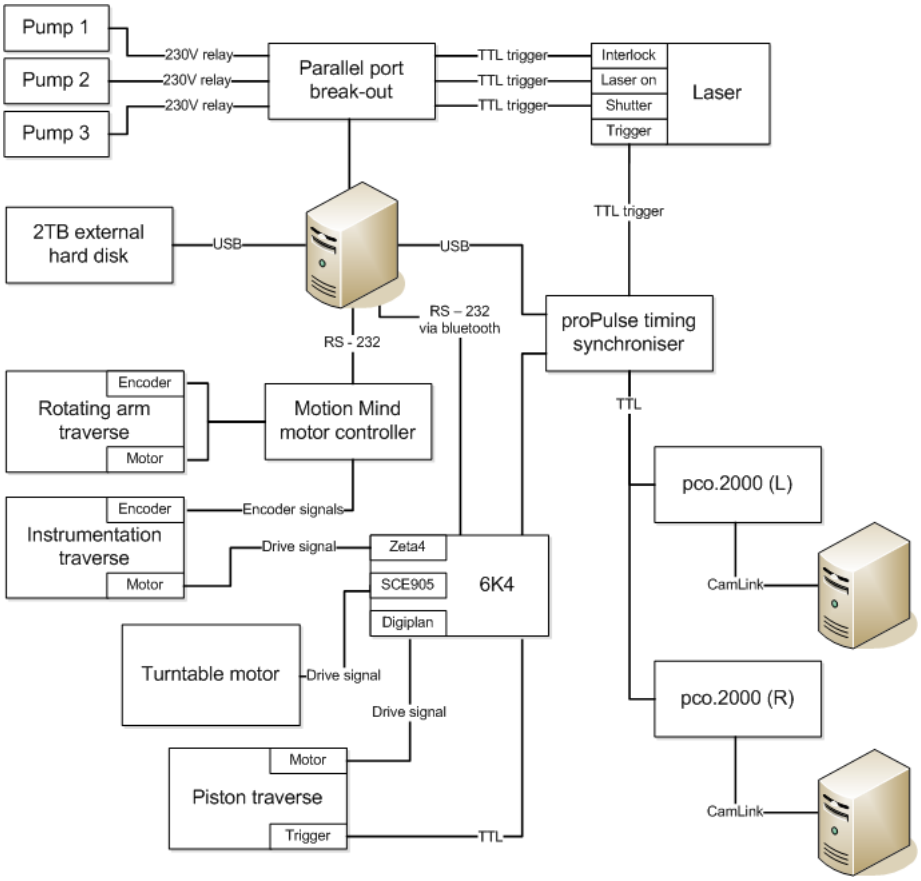

Figure 4.1: Flow diagram illustrating hardware connections

4.2 The large scale vortex ring facility

4.2.1 Rotating tank

The experiments described here were performed inside a large water tank of octagonal cross section, mounted on top of a large rotating turntable, an illustrative schematic is shown in figure 4.2 and more detailed sketches are presented in figure 4.3. The tank measures $1m$ across and $2.57m$ high, giving a filled volume of approximately $2000l$. Each wall contains a $280 \times 2200 \times 15mm$ window of float glass, enabling reduced distortion viewing and a $\varnothing 70mm$ glass porthole was built in to the centre of the base. Cylindrical rails mounted along the vertices of each wall, and a box-section gantry on top provide mounting points for equipment.

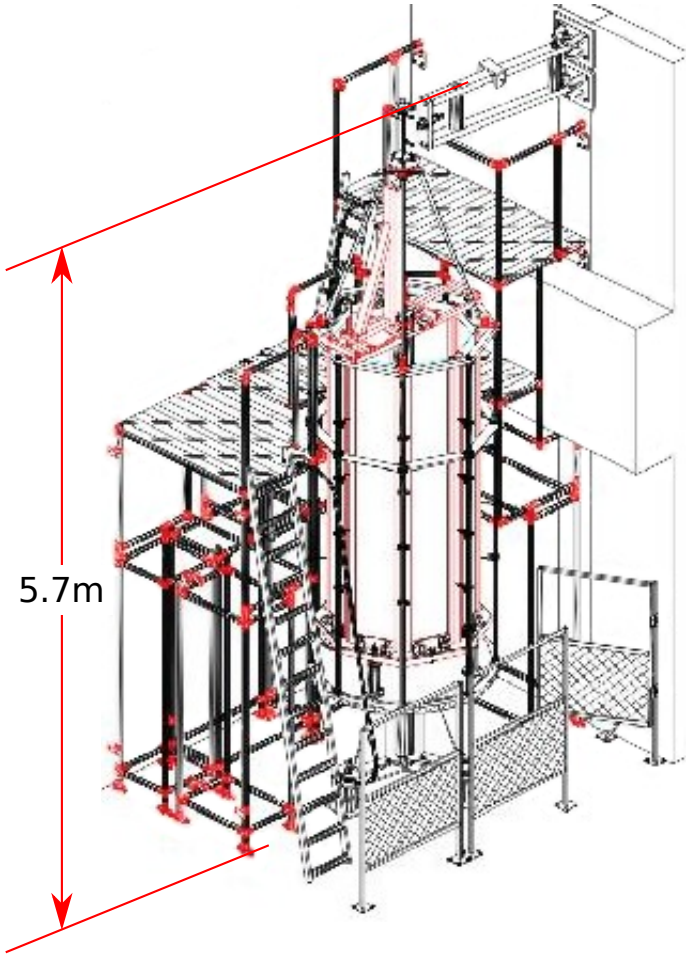

Figure 4.2: An illustrative schematic of the large vortex facility

The tank itself was mounted on top of a $1.2m$ heavy duty rotating turntable, four sturdy $\varnothing 80mm$ legs support the structure leaving a gap of approximately $0.4m$ between the top of the turntable and the bottom of the tank, giving room for equipment and instrumentation. The total height of the facility is approximately $5.7m$. To enable safe working at this height, a scaffold and gantry are positioned around the rotating facility, as seen in figure 4.2. Minimum clearance between the scaffolding and most prominent part of the rotating tank was $\sim 40mm$. Further to this, a $2.7m$ light-weight vertical traverse is mounted on the side of the water tank, to enable instrumentation to be traversed vertically, this is shown in figure 4.3.

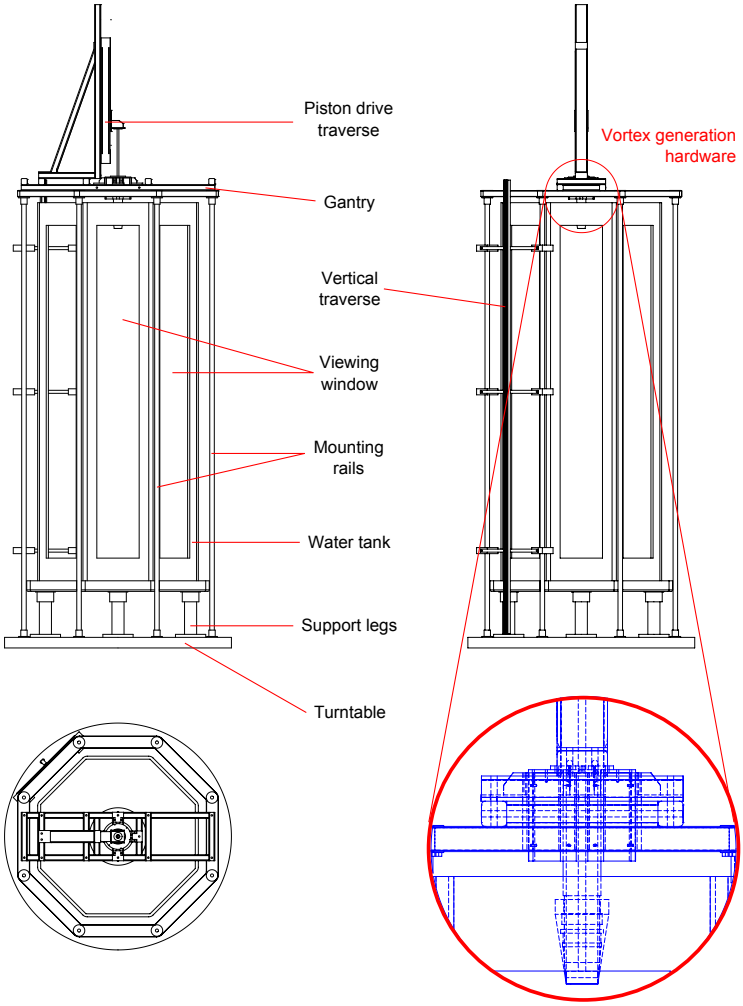

Figure 4.3: Engineering drawings of the large rotating water tank and vortex generation hardware

Upon commencement of this study, construction of the vortex ring facility had recently been completed. At that time, the hardware and software was configured such that manual operation of the facility to produce vortex rings was possible, both with and without background rotation. The vertical traverse and associated drive electronics indicated in figure 4.3 had been purchased, but not installed. Other than this equipment, details of which are outlined below for completeness, everything described in this chapter was constructed specifically for the measurements presented here.

4.3 Vortex generation

Vortex generation was provided using a standard piston-cylinder arrangement. The piston runs inside the cylinder, driven by a push-rod running through a linear bearing, and actuated using a linear traverse, 4.4. The cylinder has a thread machined onto its outer diameter, so that a nozzle may be attached to it. The nozzle has small holes machined into it, enabling a small amount of ink to be injected directly into the core of the vortex ring for visualisation. The nozzle also provides a smooth aberration free surface for vortex ring formation. The cylinder was arranged so that its centre was co-linear with the axis of rotation of the turntable. This acts to produce a vortex ring that travels along the axis of rotation. Detailed drawings of the vortex generator can be found in figure 4.4.

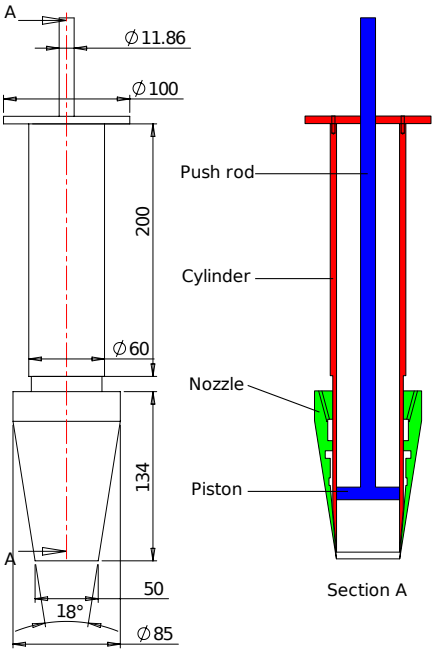

Figure 4.4: Schematics detailing vortex generation geometry

Subsequent to the reported departure from axial symmetry due to the effects of background rotation, and the conjecture that this may have arisen due to misalignment of the vortex ring trajectory, (Verzicco *et al.*, 1996), particular care

was paid to the mounting of the vortex ring generator. During construction a special laser alignment system was created, allowing alignment of the vortex ring generator with the axis of rotation to better than 1°.

4.3.1 Motors, traverses and signal lines

The large scale vortex facility contains 3 motorised elements; the drive to rotate the turntable, a linear drive to actuate piston motion and a second linear drive for traversing equipment vertically.

4.3.1.1 Turntable drive

The turntable was driven using a Bautz M714I servo motor. So that the motor operates in its optimum regime, the tank was driven through a transmission system consisting of a 30 : 1 gearbox and a 2 : 1 belt drive. The motor was controlled by a Pacific Scientific SCE905AN servo controller, which provides constant velocity through a current feedback loop.

4.3.1.2 Piston drive

The piston was actuated by a $65V$, $5.1A$ bipolar rotary stepper motor connected to a $3m$ belt driven linear traverse. The stepper motor was driven in open loop control by a Parker Digiplan motor driver. To prevent damage to the piston and cylinder, the traverse carriage's travel was limited using Hall-effect switches, as shown in figure 4.5. If the traverse passed one of these limits, it was immediately halted. Further to this, a homing limit switch was used, allowing the traverse car (and so piston) to be reset to exactly the same position for the beginning of each experiment.

Piston stroke length was limited to $130mm$ as exceeding this requires the piston to begin its travel above the water surface, causing the injection of air into the

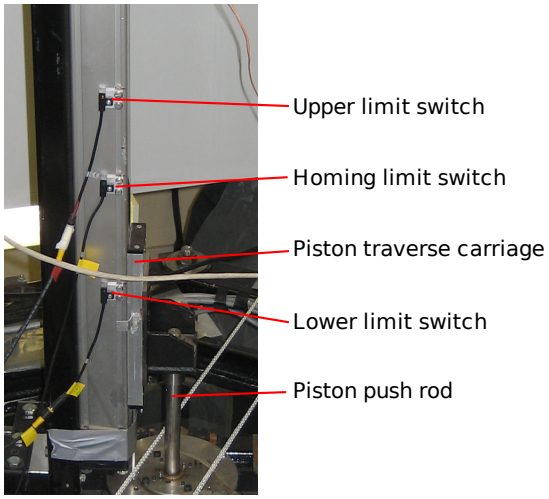

Figure 4.5: Photograph showing the limit switches mounted on the piston traverse

vortex ring. The piston acceleration/deceleration was limited to $30,000 mm/s^2$ in order to prevent the motor from missing steps. This acceleration and maximum stroke length define the upper limit for the maximum attainable piston velocity, namely $500 mm/s$.

4.3.1.3 Instrumentation drive

The instrumentation traverse was driven by a $3.4V$, $2.5A$ stepper motor, under open loop control, using a Parker Zeta4 stepper controller. The motor pulled the traverse carriage using a timing belt. The traverse was fitted with two micro-switch limit switches, to prevent the instrumentation colliding with the impediments at the ends of traverse. No homing limit switch was used, as the instrumentation drive was reset to either the top or bottom of the traverse.

The instrumentation traverse was in fact longer than the tank and due to this, maximum travel was limited to $\sim 1.7m$, as this was the displacement from the nozzle to lowest required camera position (this was defined by the position of the calibration target, c.f. section 4.4.1). Acceleration was restricted to $4m/s^2$ to prevent missed steps, and the maximum velocity possible was $1m/s$. Additionally

the traverse was incapable of carrying loads $\gtrsim 1kg$, as high loading results in extension of the belt and so a differing velocity profile of traverse motor and traverse carriage.

4.3.1.4 Drive control

All three motors described here and their associated controllers are interfaced through a 6K4 compumotor controller. The 6K4 is a fully programmable motor controller capable of interfacing with up to four motor controllers, handling encoder feedback and halting motion when limit switches are hit. Motion commands could be issued simultaneously to any combination of servo or stepper motors, with acceleration & deceleration profiles, maximum velocities and direction of travel fully configurable. The motor controller is also capable of sending and receiving hardware triggers, these triggers may then be used to initiate motor motion.

Each motor could be actuated in one of two modes, either continuous motion or discrete travel. When used in continuous motion mode, the motor accelerates up to the desired velocity and continues rotating at this velocity until the user specifies otherwise. In discrete travel, a distance and velocity are specified, the motor accelerates to this velocity, then decelerates to stop at the required position. The rotating turntable was always driven under continuous mode, the piston drive always under discrete and the instrumentation drive under both, depending upon application.

The RS-232 serial communications protocol was used to interface the control PC with the 6K4.

4.4 PIV equipment

4.4.1 Illumination

Illumination was provided by a Litron "Nano L 135-15 PIV" dual-pulse ND:YAG laser, which was capable of providing pulse pairs of $135mJ$, $9ns$ at $532nm$ wavelength and $15Hz$. Due to its weight, the laser was mounted directly onto the rotating turntable, oriented such that light emission was directed radially toward the centre of the table. A pair of broadband anti-reflective coated cylindrical lenses with focal lengths of $25mm$ and $40mm$ were used to produce a horizontal light sheet, which was then reflected through 45° by means of a $532nm$ anti-reflective coated laser mirror, illustrated in figure 4.6.

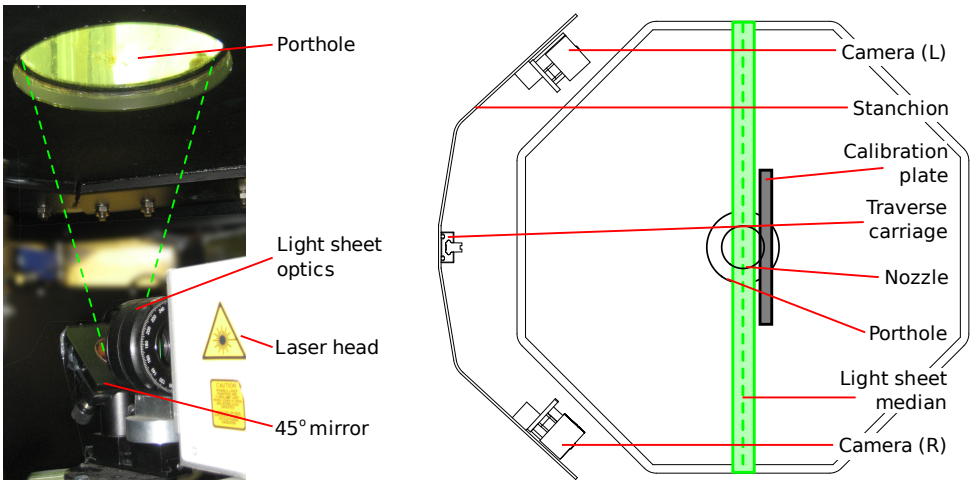

(a) Light sheet generation optics

(b) Position of light sheet

Figure 4.6: Illustration of light sheet generation and position with respect to cameras, water tank and vortex ring generation hardware.

The sheet optics were mounted onto a two axis traverse with the mirror on a kinematic mount to allow precise alignment of the light sheet with the nozzle. The light sheet was positioned such that its centre lay on the axis of the cylinder and was parallel to one of the windows. The fan angle was such that the illuminated

area was approximately $200mm$ at the base of the tank and $1m$ at the nozzle.

A LaVision type 31 dual layer calibration plate was mounted underwater, near the bottom of the tank. The calibration plate was positioned parallel to the light sheet, offset by approximately $7mm$. This is illustrated in figure 4.6b.

4.4.2 Image acquisition

Image acquisition was performed by a pair of pco.2000 cameras of $2048 \times 2048px$ resolution, 14 bit depth and capable of capturing consecutive images as little as $180ns$ apart. Each camera was fitted with a LaVision Scheimpflug mount, enabling off axis viewing, and a $50mm$ Nikon F-mount lens. As the laser provided a large illumination area at the top of the tank, but narrow at the bottom, image exposure varied greatly. Lens aperture was set to $f^\sharp = 2.8$ as it was found that this provided the best overall illumination across the tank height.

The cameras could run at a maximum acquisition rate of 7.3 image pairs per second, with the data being buffered directly to $512MB$ of on-board cam-RAM (enough for 32 image pairs). The image data was read out directly via a MicroEnable-III CameraLink capture card to the camera's host PC, and stored in RAM. At time of acquisition the cameras produce a unique identifying time-stamp in the upper left image corner. The pco.2000 control software (CamWare) provided no functionality for camera identification, for this reason each camera required its own host PC and CameraLink card.

As previously stated, to observe the development of the vortex rings over time, it was required that the cameras track down the side of the tank at the same speed as the vortex ring, the instrumentation traverse was utilised for this. Each camera was attached vertically to a mounting plate complete with a 45° mirror, this was necessary due to the cameras size, under any other orientation the cameras would have prevented the turntable from rotating. The mounting

plate is shown in figure 4.7.

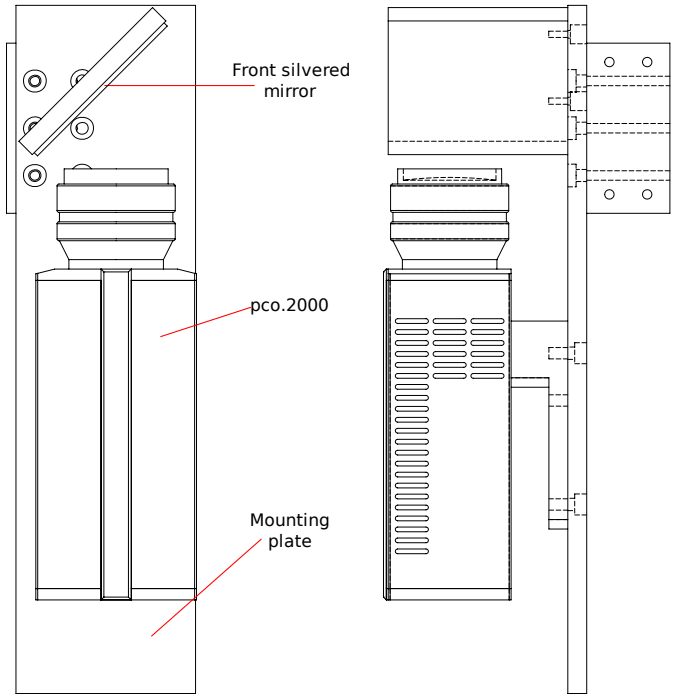

Figure 4.7: pco.2000 camera mounted with 45° mirror

These mounting plates were then connected to a horizontal stanchion containing four bend radii, see figure 4.8. This enabled the cameras to be held securely and within the tight tolerances imposed by the facility. This also provided a symmetric, rotational stereoscopic arrangement, with each camera viewing at $\sim 45°$ to light sheet normal. This orientation was convenient as it resulted in roughly symmetric loading about the traverse. In order to cost-effectively manufacture the stanchion, it was bent out of aluminium. This was beneficial as manufacturing time was low and adjustments could be made after manufacture to ensure clearance of the mounting bars on the tank and access scaffolding. To enable bending, $6mm$ sheet aluminium was used for fabrication (the maximum thickness that could be bent). Due to the cameras' mass-radii product the low aluminium thickness resulted in a less than optimum stanchion stiffness, which in turn led to camera vibration during traverse movement.

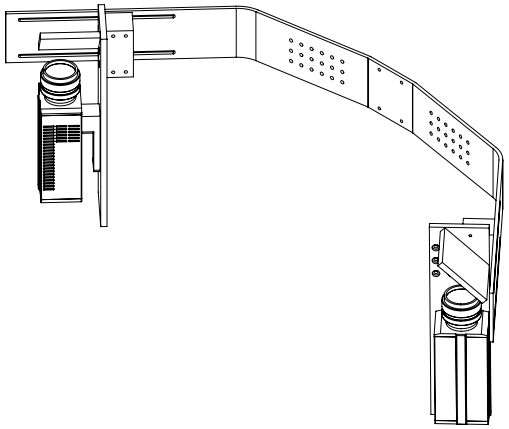

Figure 4.8: pco.2000 cameras mounted on supporting stanchion

To attempt to reduce traverse vibration and to provide extra rigidity and security, the stanchion was tensioned on each side against $2m$ guide rails made of $45 \times 45mm$ Bosch Rexroth extrusion. The tensioning was provided by spring loaded runners, as illustrated in figure 4.9.

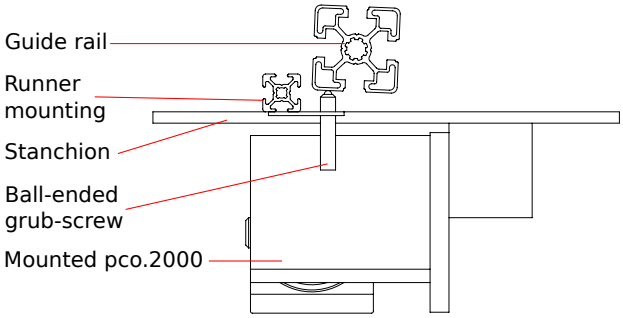

Figure 4.9: Tensioning of support stanchion

These runners were constructed to allow variable tension to be applied to the stanchion, enabling the major component of vibration to be varied, as shown in figure 4.10. High tension implies increased stiffness and a reduction of vibration in the horizontal direction. The increased tension however, causes an increase in friction between the traverse runner and guide rails, resulting in increased vibration in the vertical direction.

The guide rails were mounted to a high degree of precision, across the $1.8m$

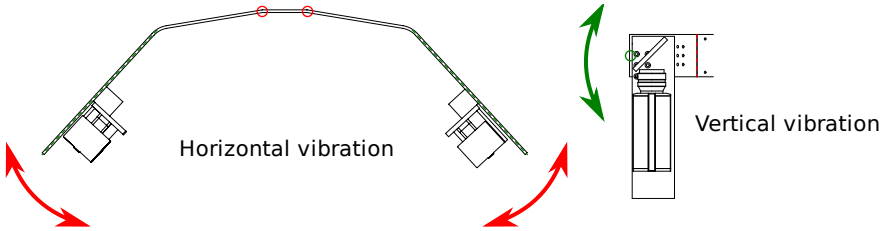

Figure 4.10: Illustration of the directions of principal vibration

drive length, the stanchion deviation due to the combination of alignments of the traverse and guide rails was $< 0.5mm$. A photograph of the complete moving assembly in position for calibration plate imaging is shown in figure 4.11.

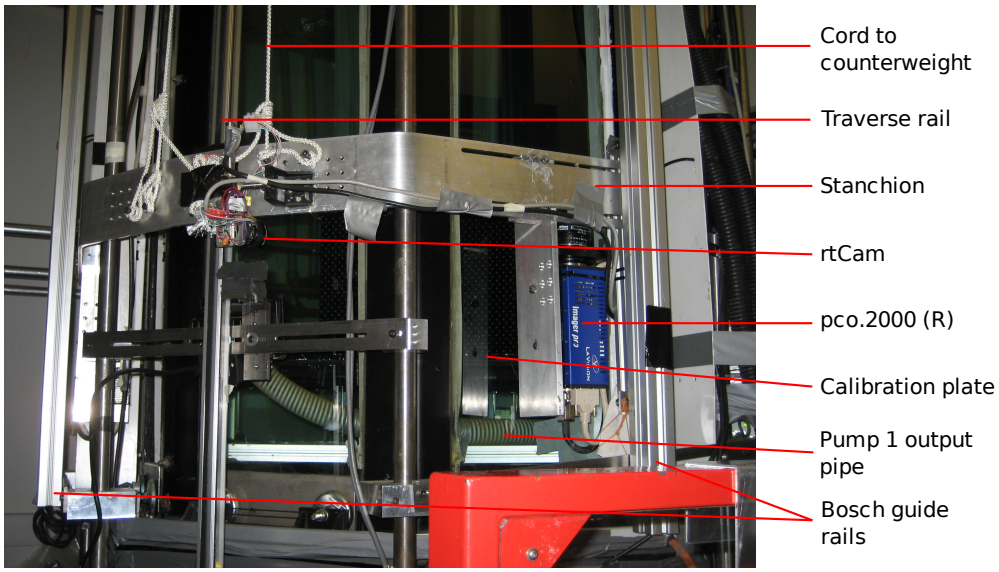

Figure 4.11: Photograph of moving assembly

As stated previously the maximum allowable load for the instrumentation traverse was $1kg$, the total weight of camera equipment, mountings and supports to be traversed was approximately $8.5kg$. To account for this difference, the stanchion was connected to a large counterweight using low extension rope and a system of pulleys, these are shown in figure 4.12a.

The counterweight ($\sim 17kg$) was mounted on the opposite side of the tank to the traverse and in such a fashion that the traverse was in a $2:1$ mechanical

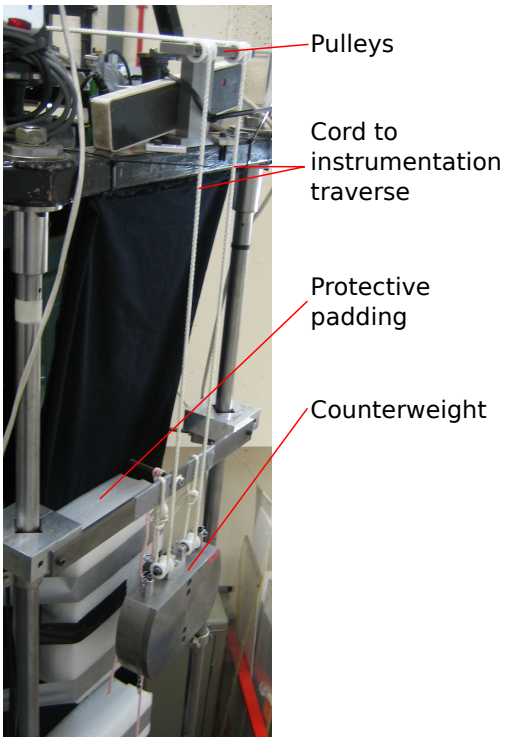

(a) Counterweight mounting

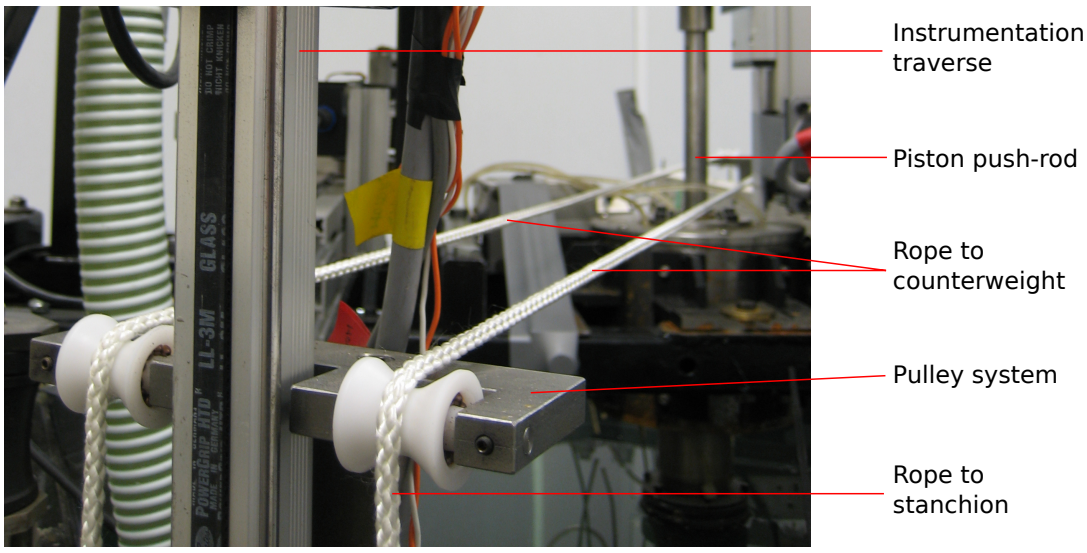

(b) Pulley system

advantage, thus the net load on the instrumentation belt was $\sim 0kg$.

4.4.3 Seeding

The seeding particles used were Potters Sphericel 110P8 hollow glass spheres (HGS), with mean diameter $11\mu m$ and density $1.1g/cm^3$ (Potters Industries data sheets). To achieve a suitable seeding density, approximately $5g$ of particles were required for $2m^3$ of water. The Sphericel particles were chosen on a trial and error basis, the primary selection criteria used was resistance to reaction with the water. Several commonly used seedings were tested, all were found to disappear after differing lengths of time, invariably leaving a cloudy opaque solution in the water. The Sphericel provided the best resistance to this dissolving process, lasting approximately 5 days. It should be noted that all the seeding tried claimed to have no chemical reaction with water.

Secondary selection criteria was the particles' performance. As the Sphericel particles are spherical they provide the optimum shape for PIV imaging. Their quoted density is of concern, however it was found that even over several days the imaged particle density appeared to not change, implying that the actual particle density was closer than expected to that of water.

The majority of vortex ring evolution is relatively steady, therefore we may assume the largest accelerations on the particle to be centripetal. This acceleration has been calculated from subsequent PIV measurements and is estimated at $\lesssim 40m/s^2$. From equation (2.3), the particle slip velocity may be calculated as $\tilde{u} \sim 3 \times 10^{-4} m/s$.

Furthermore, we may compute the maximum magnitude of Saffman lift, F_S, equation (2.4). Again from PIV measurements, we can make an estimate of maximum velocity magnitude and considering the worst case, where it would coincide with the maximum particle slip velocity already calculated, we may

compute Saffman lift as $F_s \sim 7 \times 10^{-9} N$, which is of negligible magnitude.

4.4.4 Timing

Timing synchronisation was performed by an Etalon Research proPulse; a 16 channel pulse generator capable of $5ns$ resolution with jitter of $< 0.3ns$. This was connected via USB to the control PC (so named as its purpose was to coordinate all elements of the experiment). The proPulse provided TTL level triggers to the two cameras, and four independent triggers for the laser flashlamps and Q-switchs.

4.4.5 Computer equipment

Computer control of the experiment was provided by a dedicated control PC, and each camera controlled by its own camera PC. All of the PCs used were standard desktop computers, running Microsoft Windows XP Pro. The camera PCs were fitted with Silicon Software microEnable III CameraLink frame grabber cards and 2.5GB RAM, of which 2.0GB was mounted as a RAM disk for temporary image storage (corresponding to 256 image pairs). Permanent image storage was provided through a 2TB LaCie BiggerDisk external hard disk.

4.5 Ancillary equipment

In addition to the PIV equipment detailed, a substantial amount of ancillary equipment was required in order to streamline and automate the measurements.

4.5.1 Water pumps

Three submersible water pumps were used:

1. Clarke CSE400A, flow rate: $115L/min$

2. Juwel 600, flow rate: $600L/hour$

3. Aqua-Bee UP 500, flow rate: $500L/hour$

Pump 1 was used to mix the fluid within the water tank, it was attached to the tank floor and its output directed such that it circulated the water within the tank. This provided a means of removing any stratification gradients formed due to temperature differences. Prior to beginning the experiments it was envisaged that mixing would be necessary to prevent seeding particle "dropping", this however never occurred.

Pump 2 was also mounted on the base of the tank, its output directed such that it induced water flow across the porthole. This was done to clear any debris settling on the porthole and reducing the light sheet intensity.

Pump 3 was mounted at the top of the tank, its output hose was connected to a rotating arm that could be precisely positioned to blow water across the piston surface. This was necessary to remove air bubbles that were deposited onto the piston surface during an experiment series.

4.5.2 Motor controllers

Two Solutions[3] Motion Mind (version 2) DC motor controllers were used in conjunction with Clarostat 600EN128CBL 128PPR incremental optical rotary encoders. The Motion Mind controllers are PID type, providing closed loop feedback control of DC motors for positioning or constant velocity operation. They are also capable of accurately counting steps from incremental encoders and so providing a measurement of absolute position from relative position devices. Communication to the Motion Mind controllers is performed over RS-232;

each controller may be assigned a unique identifier allowing multiple units to be connected to a single RS-232 port.

One Motion Mind with encoder was used to measure the instrumentation traverse's carriage position. This was achieved by connecting the encoder to the output shaft of the stepper motor used to drive the instrumentation traverse. The motion mind was then used to count steps from the encoder at a resolution of $8.552 steps/mm$.

The second Motion Mind was used to control a small custom built traverse, capable of positioning the output hose from pump 3 below the piston for cleaning, illustrated in figure 4.12. A $15V$ DC motor with an integrated 100:1 epicyclic gearbox (Combo Drills 942D1001) was used to power a small belt drive and thus rotate the arm. PID control was used to position the hose directly beneath the piston.

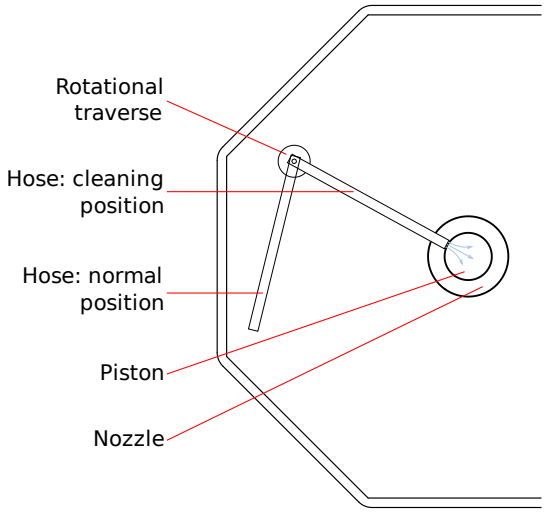

Figure 4.12: Illustration of the positioning of the output from pump 3

Slip ring	Application
1-6	Piston traverse drive control
7-12	Piston traverse limit and homing limit switches
13-18	Instrumentation traverse drive control
19-22	Instrumentation traverse limit switches
23-24	Laser interlock
25-26	Laser interlock switch
27-28	Piston trigger
29-30	Unused

Table 4.1: Slip ring allocation

4.5.3 Communications

The rotating turntable contains a set of 30 low noise slip rings, allowing data signal transmission into and off the rotating environment. Further to this, a $60A$ mains supply is provided through a secondary power slip ring mounted at the top of the facility. Signal allocation is detailed in table 4.1.

The control and camera PCs were inter-connected on the table using a Gigabit Ethernet hub and a 54G wireless bridge was used to log into and so control the PCs from off the rig. As illustrated in figure 4.1 the communications to the 6K4 were facilitated through a bluetooth RS-232 communications link. Control of all three pumps was managed by a parallel port break-out box, providing 240V mains switching capability. The same breakout box was used to switch signal relays for arming the laser interlock, switching it on and opening its shutter.

4.6 Experiment, automation and control

Each experiment consisted of two phases, the experiment was first prepared, then the automated acquisition set running. The operations associated with this are detailed below.

4.6.1 Experiment preparation

The experimental preparation procedure was largely dictated by two major problems:

1. The tank was filled directly with tap water, which was approximately $10°C$ cooler than the ambient temperature. During equilibration, a substantial amount of gas would effervesce, forming bubbles which coated the inside of the tank, in particular the piston face.

2. It was found that approximately 5 days after seeding, the particles would appear to dissolve in the water, leaving an opaque solution, chalky in colour.

The first problem of water temperature equilibration was inconvenient, however straightforward to solve. After filling, the water's temperature was monitored and no experiments were performed until the water had reached room temperature ($20.5°C$). This took approximately 4 days.

Water temperature was monitored at both the top and bottom of the tank and it was found that a temperature gradient tended to form. This was removed by periodically running the main tank pump, which improved equilibration time to around $3^1/_4$ days. After the water temperature had equilibrated, any bubbles formed on camera viewing windows or the piston surface were removed, and the tank was spun up to the required rotation rate. Typically it took around 8 hours for the water to achieve solid body rotation, however the water was always rotated for at least 24 hours to ensure complete spin-up, at which point the seeding was added.

Traverse velocity profiles were estimated prior to the start of an experiment. This was done by means of trial and error: a vortex ring was generated and the cameras followed it according to an arbitrary traverse velocity profile; a single

camera acquired particle images of the vortex ring; this data was then correlated as a series of 2C vector maps, for speed this correlation was very crude; a single pass, $64px$ interrogation window (with 50% overlap) was used; the results were local median filtered and given three smoothing passes with a 3×3 kernel; the vorticity was then computed, and the position of the vortex ring in the frame found using a Matlab script; from this an improved estimate could then be made of the traverse velocity profile and the process repeated until satisfactory tracking was achieved.

As part of this iterative testing, the traverse position and time were measured at the point at which each image pair was acquired. From this data, and the ring position in the frame, a refined estimate of traverse velocity could be made and then tested. Δt was further optimised using data from this iterative process, this was done using full resolution PIV measurements (multi-pass PIV was performed down to $12px$). The ring's out of plane velocity component was the major limitation on Δt, which was set to the maximum possible without noticeable particle loss. Upon defining a satisfactory traverse velocity profile and Δt, the cameras were moved to the bottom of the traverse and an image of the calibration plate taken. The traverse was then returned to the top of the tank and the experiment started.

Typical run-time for an experiment varied depending on the time taken for the fluid to settle between vortex generations, as this was the primary factor dictating the length of time a single vortex measurement took. Rest times were typically $10 - 15$ minutes, resulting in a total experimental run time of around $3 - 4$ days for each set of ~ 400 experiments. During this time the seeding was monitored, and if it was found to be dissolving, the experiment was halted, the turntable stopped and the water drained. Normally it would take $1-2$ hours from the onset of dissolution to the point where the water was opaque. After draining,

if the seeding had dissolved, a scummy film was left on the tank's interior, it was found that if this was not completely removed, then on subsequent refilling the seeding would dissolve after a day or two. Thus after every experiment the tank was cleaned thoroughly.

4.6.2 Control and automation

The SPIV data was acquired in a series of "runs", each run representing the generation and tracking of one vortex ring. During the experiment every aspect of the facility was controlled by Etalon Research's proControl software. proControl represented each run as a set of actions, which were grouped into three stages:

1. Setup stage: These actions are executed immediately prior to acquisition, and are used to set up and prepare the equipment for a run.

2. Acquisition stage: This was used to perform the experimental acquisition, the block of actions was repeated a number of times for each run, resulting in several measurements.

3. Reset stage: These actions are executed after the acquisition stage of a run had completed.

Images were acquired at the highest frequency possible whilst avoiding overflow of the pco.2000 on-board RAM buffer (this overflow is termed CamRAM-jam); this was determined through trial and error to be one vector map every $180ms$. At the end of each run the experiment was paused for a period of time sufficient to allow any fluid motion induced by the vortex ring to die out. This was checked with PIV measurements and a total run-time of $10 - 15min$ was found to be suitable.

4.6.2.1 Setup

The setup stage was performed at the start of every run to prepare the hardware for acquisition. It ensured that each run started from identical initial conditions and that all parameters were consistent throughout the run. The setup actions are illustrated in figure 4.13.

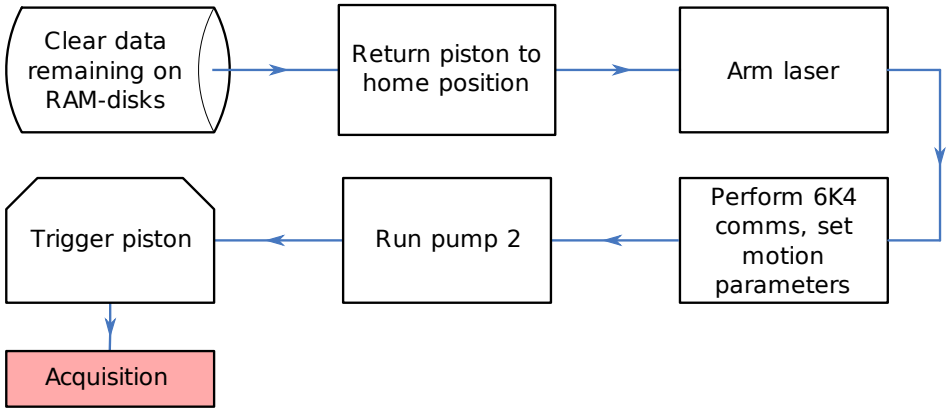

Figure 4.13: Flow-diagram illustrating proControl setup actions

4.6.2.2 Acquisition

After completion of the setup block, the acquisition block was initiated. Note that the acquisition block calls itself recursively until a user-defined number of measurements have been acquired. To avoid CamRAMjam, the acquisition of a run would not begin until some user defined time ΔT after the start of the previous acquisition, typically $\Delta T_r = 180ms$. Figure 4.14 illustrates the acquisition process.

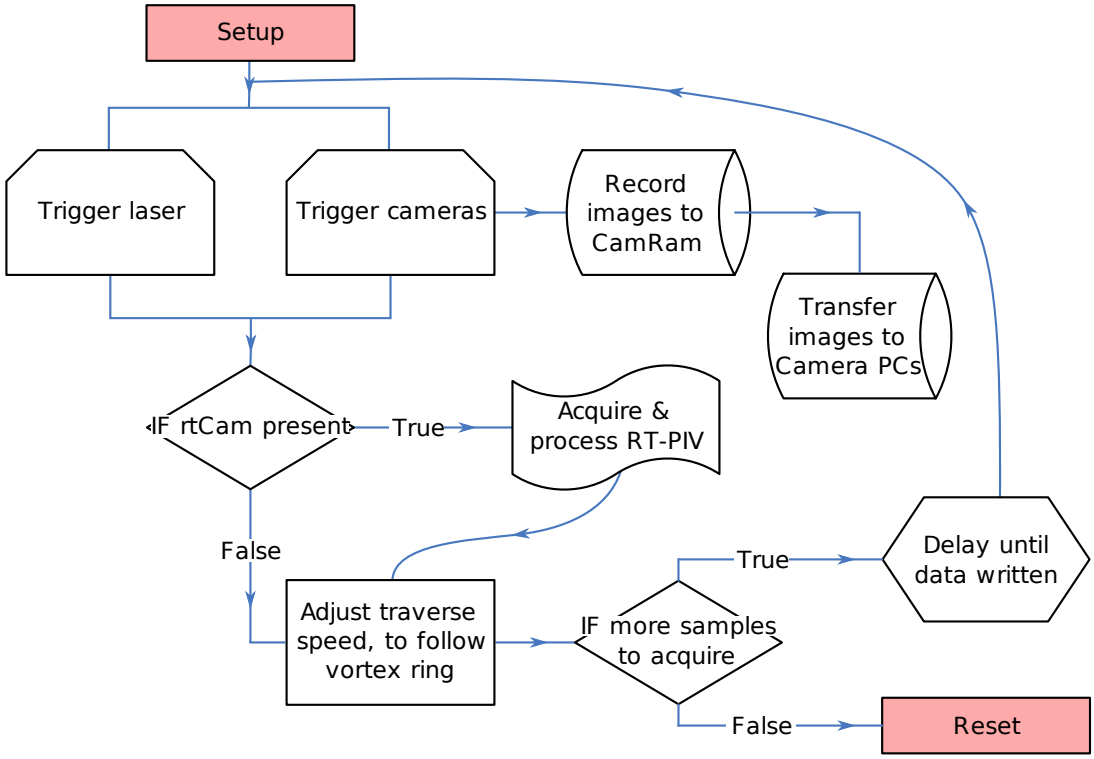

Figure 4.14: Flow-diagram illustrating proControl acquisition actions

4.6.2.3 Reset

When the required number of measurements had been recorded, the experimental equipment was reset, the acquired data was verified, some basic image processing performed and the data saved onto permanent storage, this is illustrated in figure 4.15. It was found that the laser coolant pump would intermittently trip, causing illumination to cease, so a histogram analysis was performed on the last image of each run. If the intensity dropped below some user defined limit, the experiment was paused and alert emails sent. Pumps 1 and 3 were also run periodically to prevent density gradients growing in the fluid and bubbles forming on the piston. In both cases, the action of pumping caused significant disturbance to the fluid and the next run was therefore delayed for sufficient time for the fluid to quiesce.

If all checks were passed successfully, the image data transfer completed and another run of the experiment necessary the setup block was re-run.

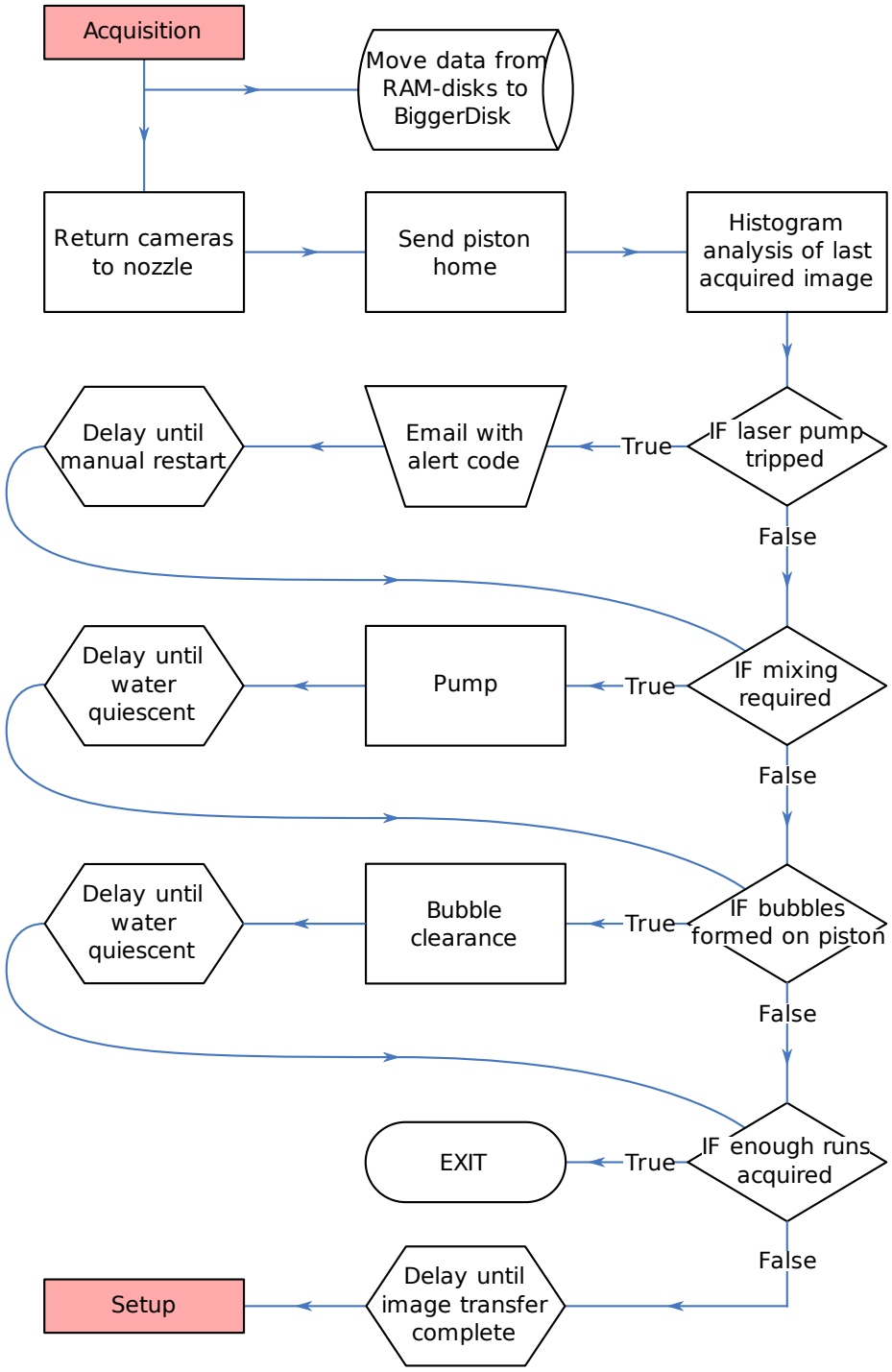

Figure 4.15: Flow-diagram illustrating proControl reset actions

4.7 Experimental acquisition plan

The experimental parameters were specified such that for each rotation rate, the same three vortex generation conditions were used. These generations were specified such that both piston stroke length and piston velocity were varied, allowing for a comparison of the relative effects of these two properties. For convenience, each condition was assigned a single letter 'A' - 'K' as a condition code, these are listed along with other parameters of interest in table 4.2. Here N_r is the number of vortex ring runs (a run corresponds to a single vortex ring generation and tracking); N_f is the number of 3C vector fields (consisting of two particle image pairs per field) acquired per run; "data" is the total amount of image data acquired for that condition. It is of note that the total quantity of data acquired amounted to slightly under $5TB$, making this, to our knowledge, one of the largest PIV investigations to date.

Code	Ω (RPM)	$\overline{U_o}$ (mm/s)	L_o (mm)	Δt (μs)	N_f	N_r	Data (GB)
A	0	500	90	1000	88	392	467
B	0	100	90	2500	150	396	807
C	0	500	30	1300	90	396	484
E	3	500	90	3000	100	400	538
F	3	100	90	3000	100	393	466
G	3	500	30	3500	100	401	580
H	-3	100	90	3000	100	285	449
I	6	500	90	1000	60	398	334
J	6	100	90	6000	60	370	332
K	6	500	30	700	60	482	348

Table 4.2: Data acquisition parameters

CHAPTER 5

Data processing and analysis methods

This chapter provides a significant proportion of the work presented in this thesis, it discusses the methods employed to turn the raw data acquired (as described in chapter 4) into data product. Standard PIV processing techniques have been employed wherever possible, using the LaVision DaVis software (on loan from Prof. Peter Bryanstan-Cross, OEL). Detailed attention was paid to ensure optimisation of all available processing options, so as to provide the highest accuracy measurements within realistic time frames.

Further to this, it was found that traversing the PIV system led to errors unaccounted for by the standard SPIV procedure, these errors are outlined in section 5.1. Procedures were developed to account for these errors and to mitigate their effects, which are outlined in sections 5.5 and 5.6 and an error analysis performed in section 5.7.

The work in this chapter is concerned with the finer details of the PIV measurement and is written with the expert in mind. Whilst the work presented here is novel and provides useful developments for PIV measurements outside of the

laboratory, readers uninterested in the inner workings of a PIV measurement are directed to chapter 7.

5.1 Introduction

As described in section 2.2.3, 3C SPIV vector fields are typically calculated in the following stages:

- Computation of a camera calibration.
- Calculation of 2C vector fields from images of particles.
- Triangulation of 3C vector fields.
- Vector post processing.

It has however been shown that acquisition of PIV image pairs with the pco.2000 cameras and the CamWare control software may result in sporadic faults (Skeen, 2006). The following errors have been described; they may occur separately or combined:

1. Fake triggers. This term is used to describe the situation where a camera performs an acquisition without a trigger signal being sent.
2. Missed frames. This is where a frame saving is skipped, this error normally occurs when the pco.2000's on board memory overflows (CamRAMjam).
3. Repeated frames. This is where a given frame is saved multiple times.
4. Frame reordering. Frames are sometimes saved out of order, i.e. the 16^{th} frame acquired is saved *after* the 17^{th} frame acquired.

These errors appear to occur randomly and so affect the stereo-cameras at different times. This is highly problematic, as the issues described cause the synchronisation between the cameras' saved data to be broken. The ramifications of this are severe for continuous SPIV acquisition as one cannot guarantee that the two calculated 2C vector fields were acquired at the same time. Furthermore loss of synchronisation is a particularly difficult error to detect from vector maps, as the errors introduced would be subtle.

Further to the image synchronisation issues, initial data analysis has shown that the computed velocity vector fields exhibited several phenomena:

1. A systematic error was found in the DaVis self-calibration process. It was found that after self-calibration a registration error remained of the order of several vector map units (VMU).

2. As the traverse travelled down the tank, the positions of the two cameras changed relative to one another. This is due to small misalignments between between the instrumentation traverse and the Bosch guide rails.

3. The traverse motion imparted vibration to the support stanchion and cameras.

4. The vortex tended not to remain in the light sheet for the course of its travel.

Figure 5.1 provides an example of data where incorrect calibration leads to incorrectly back-projected velocity fields. This leads to a registration error as discussed in section 2.4.2. Figure 5.2 shows how the relative displacement or shift between velocity fields imaged on the cameras varies with camera position.

The method used to compute the data in figure 5.2 is described in section 5.5.3; the method used is analogous to locating the core of each vortex

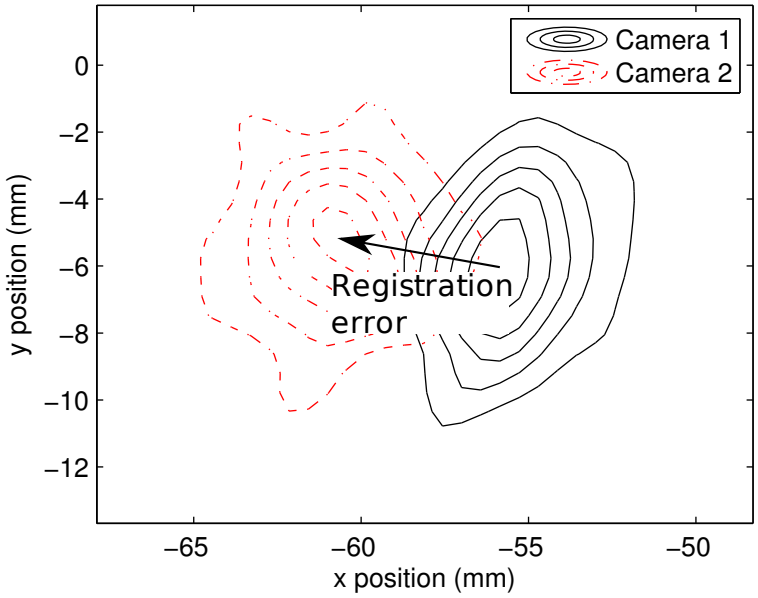

Figure 5.1: Vorticity contours indicating typical registration error

using a vortex centroid method for both camera 1 and camera 2. The shift of velocity fields measured on cameras 1 and 2 is then plotted. One can see that in this case the scatter of data points becomes quite large after $\sim 800mm$ from the nozzle, this is likely due to the vortex ring leaving the field of view, or its velocity becoming sufficiently weak that the centroiding can no longer be computed with any accuracy.

It is apparent from figure 5.2 that the registration error in the x-direction remains $\sim -4mm$, thus indicating the consistent failure of the DaVis calibration, error (c.f. point 1, p. 115). One can also see a decrease in shifts present between $0mm$ and $250mm$ from the nozzle, arising as a consequence of error (2). In addition a high frequency variation is also observable as data point scatter, this occurs due to error (3). Further to this, error (3) is of sufficiently high frequency that the PIV cameras are displaced between their two image acquisitions. Thus resulting in an additional velocity of apparently random direction and magnitude

being added to the resulting velocity vector fields.

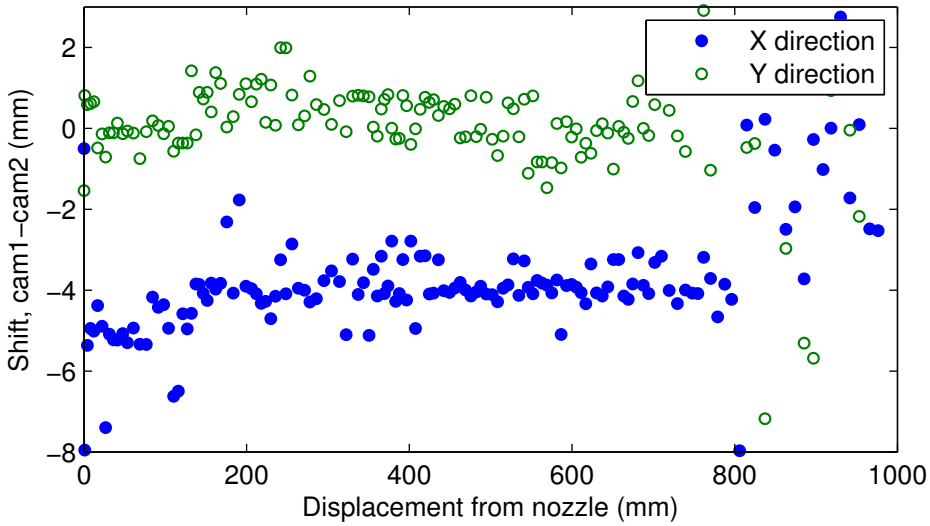

Figure 5.2: Registration error - the displacement of vector field measured on camera 2 from camera 1

When the vortex ring moves such that the light sheet no longer passes through the centre, strong out-of-plane motion is measured, as illustrated in figure 5.3. We can see large areas of oppositely signed velocity develop above and below the vortex ring.

In light of the problems described in section 5.1 significant data processing was required to achieve valid 3C vectors. The development of these data processing methods provides a major part of the work presented and are listed here:

1. Trap camera save errors.

2. Computation of a camera calibration.

3. Calculation of 2C vector fields from particle images. Multi-pass methods were used, incorporating image de-warping from the camera calibration.

4. Post processing of 2C vector field pairs.

5. Remove errors associated with camera movement.

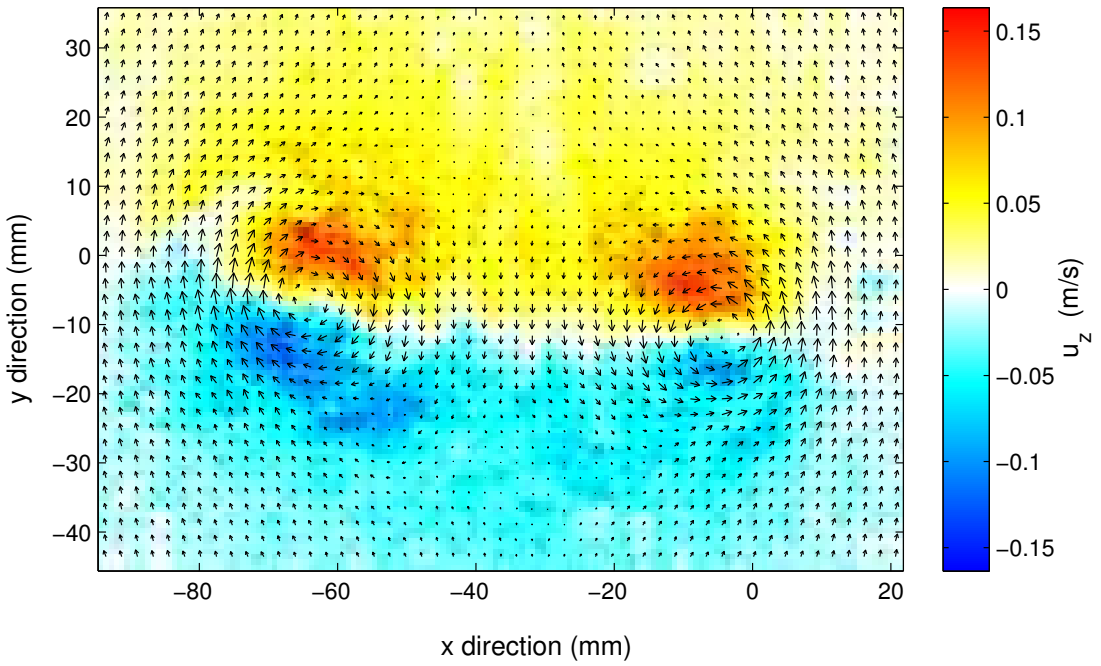

Figure 5.3: Sample 3C data for a vortex ring that has moved out of the light sheet plane

(a) Removal of additive velocity as a result of camera shaking (error 3).

(b) Recalculation of the camera calibration to account for registration errors 1 and 2. This is performed using a novel type of self-calibration where point correspondences are established from flow-field phenomena.

(c) Interpolation of 2C vector fields to implement the change in calibration described in stage (5b).

6. Triangulation of 3C vector fields from 2×2C vector fields.

7. Adjust velocity fields for vortex ring centre moving out of light sheet.

8. Calculate final 3C vectors.

Operation 1 was performed using a specialist application from Etalon Research, called MoveAndConvert. Operations 2-4 were performed using LaVision's

DaVis software (on loan from Prof. Peter Bryanston-Cross, OEL) and operations 5-8 were performed with Mathworks' Matlab. DaVis is the world leading commercial PIV package, providing highly accurate and advanced PIV processing options.

Of particular use in this study was the job distribution functionality of DaVis, which enables processing to be shared amongst remote workers. Due to the volume of data this was invaluable. Parallelization was across a cluster of 25 desktop PC's of varying specification, with total processing power of approximately $100GHz$.

This chapter details basic validation for all of the corrections applied with the aim of demonstrating that an improvement has been achieved. In each case, representative data is presented alongside corrected data to illustrate the improvements gained. A quantitative error analysis was not performed, as this project would be a major undertaking in itself.

5.2 Camera save errors

This section details the workings of the MoveAndConvert program. First the image timestamps were scanned using optical character recognition and a database built linking image name to acquisition time. By sorting the images in order of acquisition time one immediately removes the problem of frame reordering and repeated frames are easily identified. Missed frames may then be trapped by comparing the time interval between frames to the median interval. A gap larger than this median (plus some pre-defined tolerance) indicates missing frames.

If no missing frames are found, MoveAndConvert then sequentially reads in the recorded images, applies rotation and mirroring operations and saves the data in DaVis IM7 format including necessary metadata (e.g. Δt, camera number,

acquisition time). The data save, rotation and mirror are of great help, as the DaVis import process is inexplicably time consuming, furthermore the DaVis rotation and mirroring operations result in unwanted data duplication. The orientation of the saved frames is illustrated in figure 5.4, the measurement is made on a right-handed Cartesian coordinate system, with a velocity field $\mathbf{u} = [u_x \quad u_y \quad u_z]^T$ in space $\mathbf{x} = [x \quad y \quad z]^T$. .

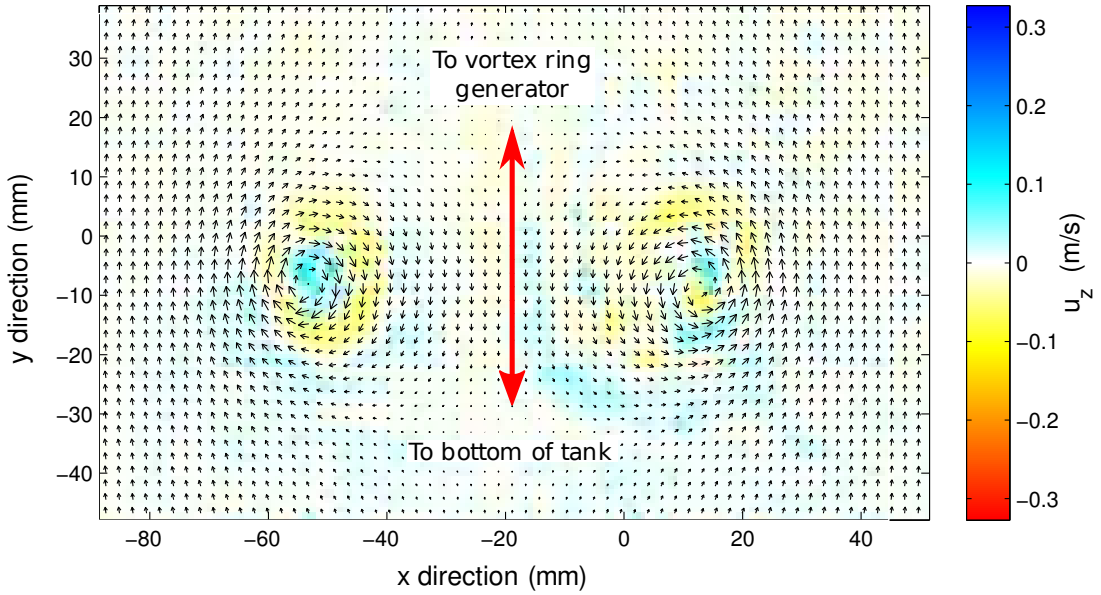

Figure 5.4: Vector map illustrating vortex ring and coordinate system orientation

5.3 Calibration

Calibration plate images were used to fit to a pinhole camera model, using the DaVis calibration function. The calibration was augmented with a second order radial distortion correction, no compensation for refractive index step was performed as the viewing angle was effectively normal to the windows, therefore would be accounted for by radial distortion. Parameters from the calibration of the real-time data are given in table 5.1, the majority of parameters being

explained in section 2.4.2.2. The radial distortion however is not discussed in detail, it is parametrised here by the factors x_p, y_p, k_1 and k_2 - see (Tsai, 1987) for more information.

Camera extrinsics			Camera intrinsics		
Field	Camera1	Camera2	Field	Camera1	Camera2
T_x	26.6994	-25.8285	f	69.8559	67.4231
T_y	-4.27898	-2.05496	k_u	0.0074	0.0074
T_z	698.126	650.971	s	1.0029	0.99553
α	1.40764	-0.132304	S	10.4117	10.4117
β	-46.6254	40.0575	x_p	1198.05	1198.05
γ	-1.82682	-0.85795	y_p	880.76	880.76
			k_1	0.21362	0.43471
			k_2	0.041971	0.020148

Table 5.1: Sample calibration parameters generated from plate calibration

Due to the uncertainty of the light sheet position relative to the calibration plate it was necessary to adjust the camera calibration using self calibration. This was performed on a selection of more than 200 images from multiple runs. The image selection was based on acquisition height so as to provide the self-calibration with suitably similar disparity vectors from each image set. The acquisition height was chosen arbitrarily at some position near the middle of the tank, this was done to remove the possibility of the self-calibration working on images of either the mounted calibration plate or the nozzle. The two image-sets nearest this chosen point were used for self-calibration. The images were first processed using a sliding minimum subtraction on a $9px$ neighbourhood, helping to improve SNR by removing any spatial intensity variations.

Point correspondences within the field of view were defined by performing normalised cross-correlation on the images, with the sum of the 200 correlation maps used to generate a disparity vector map which was used to infer point correspondences. The correlation was performed on back-projected images, the

interpolation for this was done using Whittaker's reconstruction (c.f. 2.3.2) for improved frequency response. A multi-pass method was used, starting with $256px$ windows at 50% overlap, decreasing to $64px$ at 50%. After each correlation pass, the correlation maps and disparity vector fields were checked manually, additional correlation passes where only run when the correlation map showed well formed peaks and the disparity vector map varied smoothly.

Each disparity vector map was fitted to an epipolar geometry type self calibration, refitting the camera extrinsics. At each window size, correlations were repeated until the fitted calibration converged (the computed parameters were judged to have converged when changes were $\sim 10^{-3}$). This normally took three to four passes. The calibration from a sample data set is presented after self-calibration in table 5.2.

Camera extrinsics			Camera intrinsics		
Field	Camera1	Camera2	Field	Camera1	Camera2
T_x	31.9688	-30.1232	f	69.8559	67.4231
T_y	-4.4574	-1.8539	k_u	0.0074	0.0074
T_z	692.925	646.285	s	1.0029	0.99553
α	0.25483	-1.2505	S	10.4117	10.4117
β	-46.1721	40.5278	x_p	1198.05	1198.05
γ	-1.6258	-1.0052	y_p	880.76	880.76
			k_1	0.21362	0.43471
			k_2	0.041971	0.020148

Table 5.2: Sample calibration parameters generated from self calibration

5.4 2C correlation and post processing

2C vector field computation was performed using the DaVis software. In all cases non-linear image processing was performed prior to the correlation in order to remove spatial image intensity variations. Subtraction of a local intensity minima and particle normalisation was performed. The correlation used was second order,

multi-pass phase correlation with adaptive window deformation, where the multi-pass scheme performs a localised affine transform. The image back-projection necessary for stereo calculation was combined into the interpolation necessary for each pass of the correlation process. A bilinear image interpolation scheme was chosen after Whittaker interpolation showed no apparent improvement to the vector field quality. Likewise, phase correlation was used in preference of normalised cross-correlation as there was no apparent difference in the histogram of vector component magnitude.

Vector field post-processing was applied to both the intermediate and final vector fields, using a combination of the peak quality, Q and local median filtering with replacement vectors inserted from 2^{nd}, 3^{rd} and 4^{th} correlation peak choices, where appropriate. Small groups of isolated vectors were also rejected, as these indicate regions of poor seeding, though this was a rarity. The intermediate vector fields were also smoothed with a 3×3 box kernel to remove any high frequency noise and all missing vectors replaced with interpolated data. Isolated holes in the final vector fields were removed with a single interpolation pass and the data saved.

As part of a subsequent operation, all holes in the final vector map were filled, and the data heavily smoothed. This smoothed data, and the vorticity thereof was used as part of subsequent processing stages and was not used directly for the computation of 3C vectors.

The individual correlation settings were adjusted to suit data from each of the acquisition conditions, the real-time acquisition data however was processed en-mass. Sample correlation settings are presented from the real-time data in table 5.3. Even with the workload shared across the PIV cluster, the correlation of a single condition (resulting in only 2C vectors) took approximately one week.

The velocity vector fields were computed such that the measured 2C velocity

Pre-processing		
Sliding background subtraction		4px
Offset subtraction		-50
Particle normalisation		6px
Correlation		
Pass 1	Window size	64 × 64 px
	Overlap	0%
	Number of passes	1
Pass N	Window size	12 × 12 px
	Overlap	50%
	Number of passes	2
Zero padded correlation		Off
Second order correlation		On
Correlation quality, Q		Peak 1 / Peak 2
Correlation based correction (initial passes)		On
Whittaker reconstruction (final pass)		Off
Multi-pass post-processing		
Remove when Q<		2.0
Iterative local median filtering		On
Remove when > mean + $k_1\sigma_{u_i}$, k_1 =		2.0
Replace when < mean + $k_2\sigma_{u_i}$, k_2 =		3.0
Interpolate holes		On
Interpolate all holes		On
3 × 3 smoothing passes		2
Post-processing		
Remove when Q<		1.5
Iterative local median filtering		On
Remove when > mean + $k_1\sigma_{u_i}$, k_1 =		2.0
Replace when < mean + $k_2\sigma_{u_i}$, k_2 =		3.0
Interpolate holes		On
Interpolate all holes		Off
3 × 3 smoothing passes		0
Subsequent smoothing operation		
Remove when Q<		Off
Iterative RMS filtering		Off
Interpolate holes		On
Interpolate all holes		On
3 × 3 smoothing passes		3

Table 5.3: Correlation settings for real-time data

components were aligned as shown in figure 5.4.

5.5 2C velocity field correction and computation of 3C fields

This section discusses the velocity field corrections used to account for the changes in relative camera positions. This is broken into two separate corrections, one to reduce registration error and another to remove the velocity bias imparted by camera vibration.

The magnitude of the vibrations may be estimated by considering the relative translation of the vector fields measured from the two stereo cameras, this is called registration error. Figure 5.2 shows the relative positions of the velocity fields as a function of time, details of these measurements are given in section 5.5.3. The analysis presented in this section is made significantly easier by assuming the camera motion due to shaking is purely translatory. A more likely scenario, is that the motion will be a combination of translatory and angular shaking. As the image displacements observed are small ($\sim 4mm$, figure 5.2) and the displacement of the camera from the light sheet large ($\sim 650mm$, table 5.1), it is not unreasonable to assume that the motion will be mainly due to translation, this is addressed first in section 5.5.1.

5.5.1 Translational camera model - basic validation

To investigate the validity of the assumption of purely translatory camera motion, we consider the worst possible case for our translational model; where the camera's motion is entirely rotational (as in figure 5.5b) but modelled entirely by translation (illustrated in figure 5.5a). To simplify this we use a symmetric

stereo arrangement of similar proportions to that stated in table 5.2. We consider rotation only about the y-axis (i.e. the Euler angle β), and translation only in the world x-direction (note from figure 5.5a that this corresponds to a translation in both the x and z directions in camera coordinates). Further to this, we also consider that only one camera is moving, which simplifies the modelling and increases errors compared to assuming a registration error caused by the motion of two cameras. As we only consider the rotation β it is furthermore only necessary to consider the camera sensor as 1D, only variation in the x-direction is important.

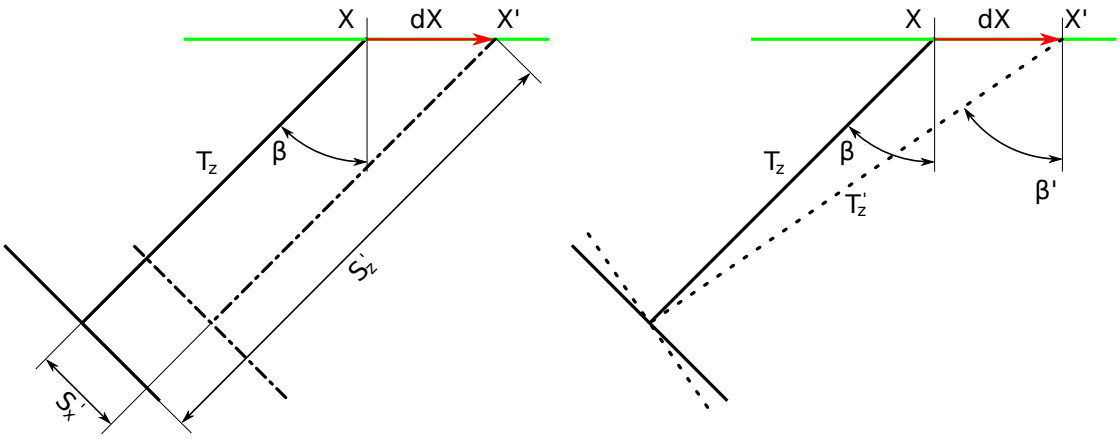

(a) Translational model (b) Rotational model

Figure 5.5: Illustration of the difference between rotational and translational models of camera motion

To evaluate the error incurred by using an inappropriate model for camera motion, we consider the impact upon the spatial misalignment of the vector fields. The estimation of this spatial misalignment is performed using triangulation, as discussed in section 2.4.3, to this end we model the camera geometry using the pinhole model. Projective distortion is inherently included in the model, accounting for Scheimpflug adaptors and lens distortions is unnecessary, as is the case when estimating 3C velocity vectors from 2×2C vector maps. To keep the

error evaluation as similar as possible to the actual measurement system, the pinhole model is parametrised with values similar to those from calibrations used to make the PIV measurements (table 5.2).

In order to perform a triangulation, we must consider a point from two cameras. To achieve this, it is necessary that a point be selected in world coordinates which is visible from both cameras. For this we choose the point $\mathbf{X}' = \mathbf{X} + \mathbf{dX}$, this point is then back-projected onto cameras one and two. As we assume all motion/vibration occurs on camera one, the back-projection for camera two is performed using the standard pinhole parameters, β and T_z. For camera one however, we must account for the registration error ($\mathbf{dX} = [dX \quad 0]$) through rotation, thus requiring definition of β' and T_z' to compute the back-projection. We provide these in terms of the standard pinhole parameters and the registration error, equations 5.1.

$$\mathbf{X}' = \mathbf{X} + \mathbf{dX} = T_z \sin(\beta) + dX \tag{5.1a}$$

$$T_z' = \sqrt{(T_z \sin(\beta) + dX)^2 + (T_z \cos(\beta))^2} \tag{5.1b}$$

$$\sin(\beta') = \frac{T_z \sin(\beta) + dX}{\sqrt{(T_z \sin(\beta) + dX)^2 + (T_z \cos(\beta))^2}} \tag{5.1c}$$

To perform the back-projection, a reduced dimensional form of the pinhole model discussed in section 2.4.2.2 is used. This is outlined for the i^{th} camera in equations 5.2, where x_i is a position in camera coordinates, $\widetilde{\mathbf{x}}_\mathbf{i}$ a position in normalised camera coordinates, $\mathbf{R_i}$ the rotation matrix, $\mathbf{X_w}$ a vector in world

coordinates and $\mathbf{T_i}$ the translation vector.

$$\widetilde{\mathbf{x_i}} = \mathbf{R_i}\mathbf{X_w} + \mathbf{T_i} \tag{5.2a}$$

$$x_i = f\frac{\widetilde{x_{x_i}}}{\widetilde{x_{z_i}}} \tag{5.2b}$$

As we are using the pinhole model to relate a 2D scene (in world coordinates) to a 1D camera, $\mathbf{R_i}$ and $\mathbf{T_i}$ are of reduced form, as shown in equations (5.3). Here we use $\theta_1 = \beta'$, $\theta_2 = \beta$, $\mathbf{T_1} = [0 \quad T_z']^T$ and $\mathbf{T_2} = [0 \quad T_z]^T$, to calculate x_1 and x_2.

$$\mathbf{R_i} = \begin{bmatrix} \cos(\theta_i) & -\sin(\theta_i) \\ \sin(\theta_i) & \cos(\theta_i) \end{bmatrix} \tag{5.3a}$$

$$\mathbf{T_i} = \begin{bmatrix} T_x \\ T_z \end{bmatrix} \tag{5.3b}$$

To proceed, one must now determine the parameters necessary for the translational model $\mathbf{S} = [S_x' \quad S_z']$ (illustrated in figure 5.5a). This translation is refitted as discussed in section 2.4.2.4 to provide an adjusted calibration. Using this modified calibration, we are then able to forward project from both cameras, triangulating a solution as discussed for 3C velocity vectors in section 2.4.3. The reduced form of the equations used are presented in rearranged form, 5.4, which may be solved by substituting in the values attained for x_1 and x_2 from the earlier

back-projections.

$$\begin{bmatrix} S'_x - S'_z x_1 \\ -T_z x_2 \end{bmatrix} = \begin{bmatrix} f_1\cos(\beta) - x_1\sin(\beta) & f_1\sin(\beta) + x_1\cos(\beta) \\ f_1\cos(\beta) - x_2\sin(\beta) & f_1\sin(\beta) + x_2\cos(\beta) \end{bmatrix} \mathbf{X_{translational}} \tag{5.4a}$$

Evaluation of these equations was performed for a range of relevant parameters. The registration error simulated was varied across the range observed in figure 5.2, $0 \leq dX \leq 8$. This was evaluated for several locations in the vector field and also for a range of values of T_z, indicated in the legend of plot 5.6. In each case, the error is evaluated by considering the magnitude of displacement between the measured position of $\mathbf{X_{translational}}$ to $\mathbf{X_{rotational}} = \mathbf{X}'$.

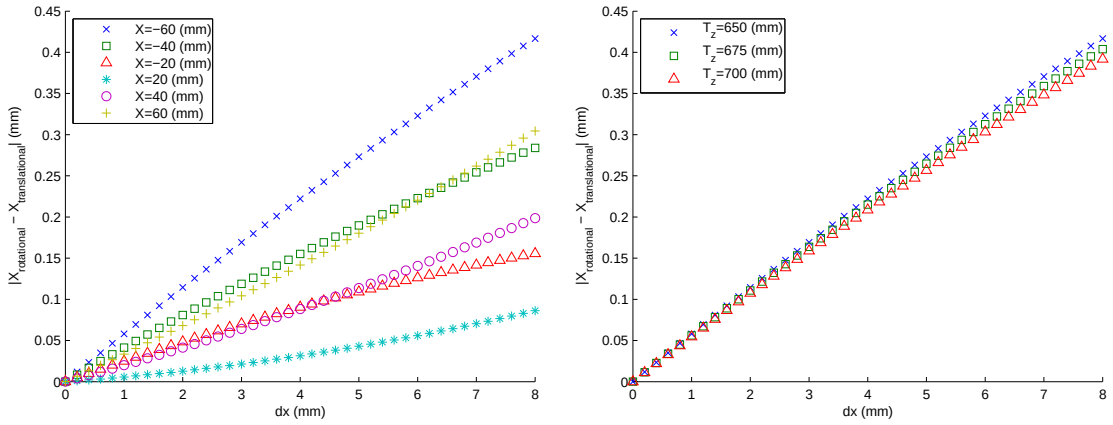

(a) $T_z = 650mm$ (b) $X = -60mm$

Figure 5.6: Error associated with modelling rotational camera motion as translational

We can see from the plots in figure 5.6 that across the ranges considered the errors are low. We can expect, at most errors of $\sim 0.4mm$, however for typical levels of registration error seen, we expect errors $\sim 0.2mm$, at the extremities,

with reduced error in the centre of the frame. It is worth note, that these errors calculated are for the worst possible case, where the motion is entirely rotational and only one camera is considered to move, which is unlikely to occur in reality. We are therefore able to assert with reasonably that translational camera motion provides a reasonable model for the camera motion observed in the PIV vector fields.

5.5.2 Removal of velocity bias

To remove the velocity bias imposed due to camera shake, the system was modelled very simply. It was assumed that the velocities within each vector field were the sum of; the vortex ring motion, the traverse motion, the background velocity of the fluid and the camera motion. The velocity camera shake was simply identified and subtracted from each measurement's vector field. This approach was based upon the assumption that the camera was moving in translation; which is a good approximation, as shown in section 5.5.1, and that the motion observed in the background is mainly due to camera motion, not fluid motion.

Each velocity component was processed independently as was each camera (although the same method was used throughout) and the shake velocity was calculated using the smoothed vector fields. First the vortex ring velocities were isolated and masked, using an inter-quartile range (IQR) based filter, as in equation (5.5), where the parameter to be filtered, x, contains n samples.

$$IQR = x_{sorted}\,[0.75\ n] - x_{sorted}\,[0.25\ n] \tag{5.5a}$$

$$x_{invalid} \geq x_{sorted}\,[0.75\ n] + 0.5\ IQR \tag{5.5b}$$

$$x_{invalid} \leq x_{sorted}\,[0.25\ n] - 0.5\ IQR \tag{5.5c}$$

In the case of vortex ring velocity fields, the IQR filter has the effect of removing the less frequently occurring velocities, as illustrated the velocity vector fields in figure 5.7. Note that in this case only u_x is displayed, though the effect is very similar for u_y.

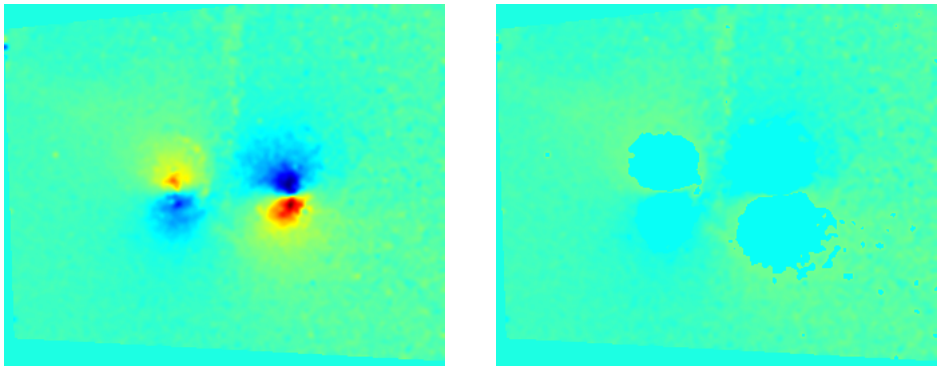

(a) Velocity field (b) IQR filter

Figure 5.7: Comparison between velocity field and IQR filtered velocity field

Figure 5.7 demonstrates that IQR filtering reliably removes areas from the field that contain velocities with magnitude significantly different to the background. As we assume that the background represents the motion of the camera, not the fluid, this filtered velocity should be representative of the camera motion. The example given also shows that the effect of the vortex ring is far reaching and that it cannot be eradicated completely in the calculation of the background velocity; this is further emphasized by figure 5.8b, which shows the variation of u_x along three profiles, whose positions are indicated in figure 5.8a.

Data was sampled from 100 sites throughout the filtered velocity field, as illustrated in figure 5.9. Here the x and y axes of the figure are presented in vector map units (VMU), a single VMU is the spacing between vectors on the PIV grid. At each site, k, a 3×3 neighbourhood of points, v_{ij_k} (v indicating either u_x or u_y) was extracted and the mean of this neighbourhood taken, v_k. In

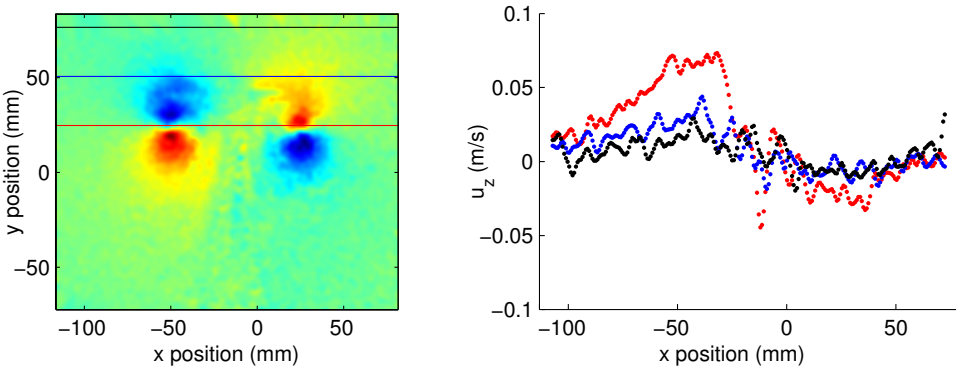

(a) Measurement position (b) Variation of u_x with position

Figure 5.8: Illustration of the variation of u_x

computing this mean, previously filtered data and rejected vectors were ignored. The 100 measurements of the background velocity v_k, are plotted for u_x, camera 1 in figure 5.10.

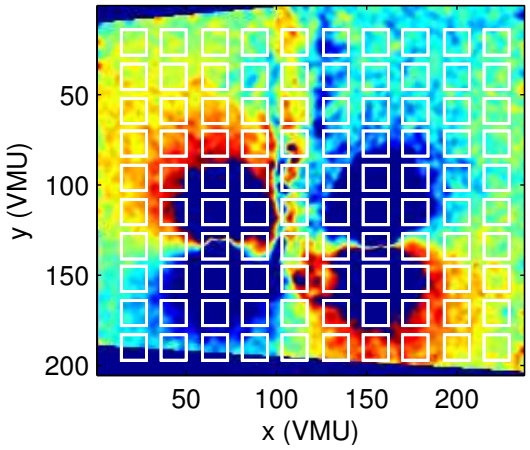

Figure 5.9: 10×10 grid of 3×3 neighbourhoods, illustrated on a u_x field from camera 1

Iterative RMS filtering using the median as an estimator was then applied to the 100 velocity samples to remove outliers, this was done to the sets of 100 points at each time step according to equation (5.6). Here $\tilde{v}_k$ indicates the median of the data and k_σ some constant defining the strictness of the filtering, in this case

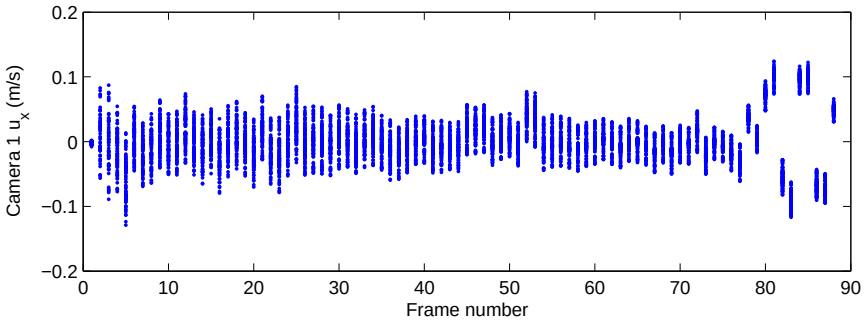

Figure 5.10: Scatter plot of u_x varying with frame number

$k_\sigma = 2$. The results of this filtering operation for u_x, camera 1 are shown in figure 5.11.

$$\tilde{v_k} - k_\sigma \sigma_{v_k} > v_{k_{invalid}} > \tilde{v_k} + k_\sigma \sigma_{v_k} \tag{5.6}$$

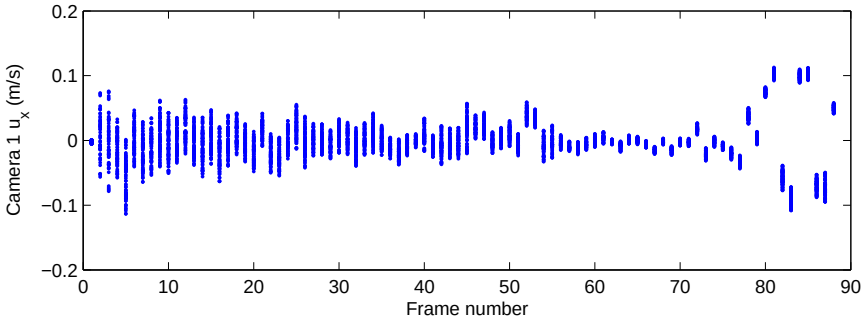

Figure 5.11: Plot of filtered u_x varying with frame number

The median of these remaining points, $\tilde{v}$, provides an estimate for the background velocity (and hence camera velocity), in each frame for each velocity component. Figure 5.12 plots them in the horizontal component of the velocity versus frame number, for both camera 1 and camera 2.

Traverse velocity, $\hat{v}$, was then computed using a 4^{th} order finite difference scheme from encoder position measurements and camera timestamps for each frame acquisition. This can then be used to find the camera shaking velocity

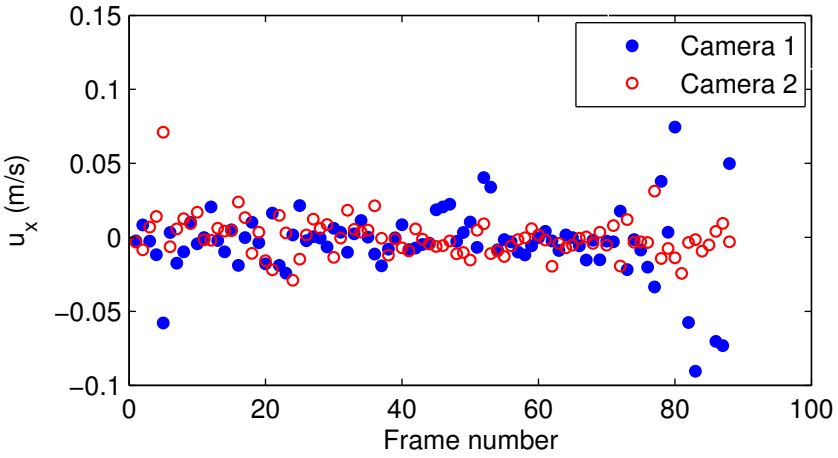

Figure 5.12: Sample plot of the estimated background velocity (u_x)

$v' = \tilde{v} - \hat{v}$, for each frame. Under the assumption of translatory motion, the velocity imparted to the measurement due to camera shaking is constant across the field, and so may be adjusted by subtraction of the shaking velocity v'.

5.5.3 Flow field self-calibration

Calculation of the relative vector field shift between camera 1 and camera 2 was performed by calculating the relative position of the vector maps, and the computed disparity used to perform a self-calibration type adjustment to the camera model which was used to then perform an associated image correction.

Two techniques were used, their relative performances compared and the method producing superior results chosen. The first technique simply estimates the relative shift of the two images using a single-pass, phase correlation of the full velocity field. The second technique is somewhat more involved and determines the disparity by accurately locating corresponding features in the 2×2C PIV vector fields.

It was found that the feature detection method was preferable where accurate 2×2C measurement of the vortex ring had been made. However in situations

where the 2C measurement was of a largely 3C or low magnitude flow, the correlation based registration tended to perform best.

As a rotational stereo setup was used and the cameras rotated about the y axis of the measurement plane, the vertical velocities computed were measurements of the same thing. The out-of-plane velocity, u_z is mainly computed from the disparity between the horizontal velocity measurements, $u_x^{\mathbf{1}}$ and $u_x^{\mathbf{2}}$ (the emboldened superscript indicating camera number) and so these two velocities often differ markedly. This is illustrated in figure 5.13 which shows the measurement of a vortex ring with a relatively high out-of-plane velocity.

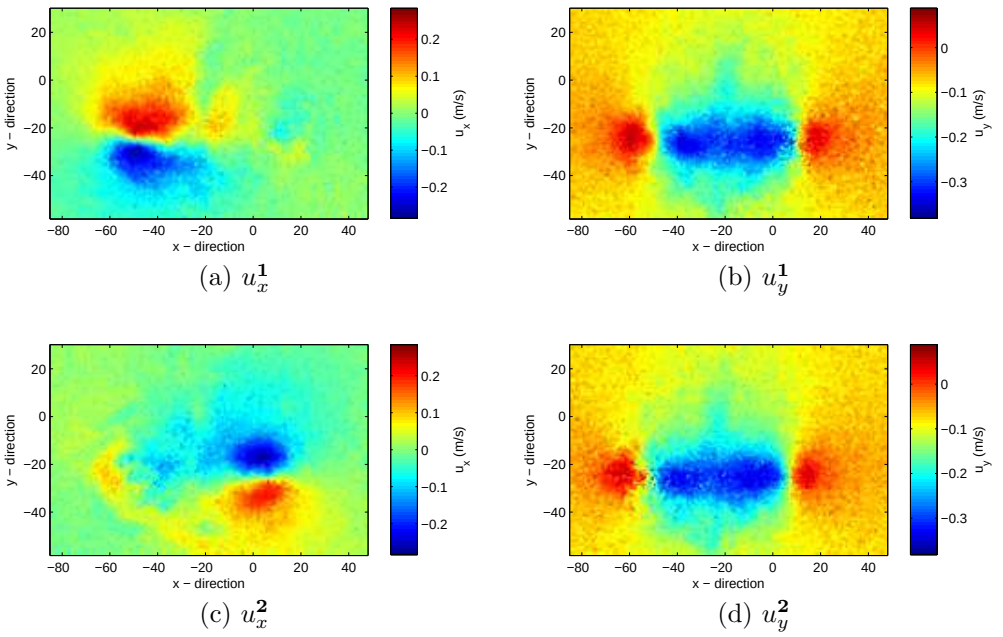

(a) $u_x^{\mathbf{1}}$ (b) $u_y^{\mathbf{1}}$

(c) $u_x^{\mathbf{2}}$ (d) $u_y^{\mathbf{2}}$

Figure 5.13: Illustration of high disparity of u_x compared to u_y in the case of flow with significant out-of-plane velocity

As can be seen, there is significant disparity between the x component of velocity, whereas the y components show strong correlation. It is for this reason that the majority of the image registration procedures were performed on the u_y velocity component.

5.5.3.1 Correlation based image registration

Phase correlation was used to generate a correlation map between the $u_y^{\mathbf{1}}$ and $u_y^{\mathbf{2}}$ fields, as in equation (2.9). This typically resulted in a very well defined, clear peak (see figure 5.14), which was interpolated to sub-VMU accuracy using a 5×5 linear least squares fit to a second order polynomial surface.

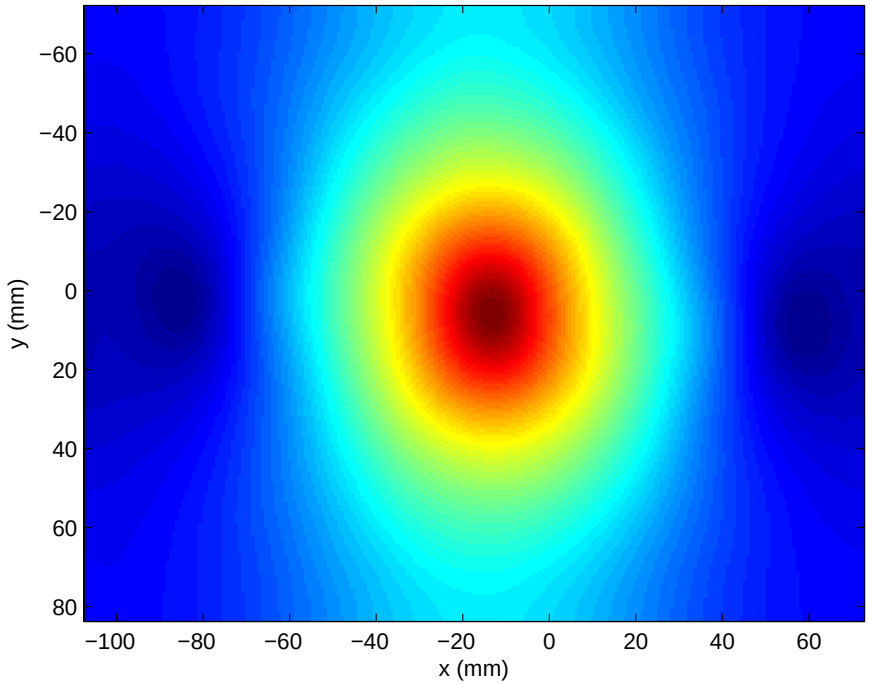

Figure 5.14: Illustration of typical correlation map resulting from $u_y^{\mathbf{1}} \star u_y^{\mathbf{2}}$

Multi-pass fractional offset methods were tested as were normalised cross correlation methods. However, in both cases, an extra time penalty was incurred with no detectable improvement in the computed registration.

5.5.3.2 Feature extraction image registration

The feature extraction image registration was split into two stages: first, the two vortex centres were located in the PIV vector field using a relatively low accuracy, but highly robust method. This was then used to restrict the search area of a

much higher accuracy velocity centroiding method. This high accuracy processing stage only considered the u_y component of velocity, as the u_x component contains disparities between camera 1 and camera 2 to account for the out of plane velocity.

The initial robust vortex centre finding method was performed not on velocity, but on vorticity swirl strength (ω_z^2). For each camera at each measurement in time, the swirl was summed horizontally. As the vortex ring almost always remained horizontal in the camera frame, this resulted in a very well defined peak; see figure 5.15b. This maxima (to VMU accuracy) was taken to be the estimate of y-axis position of the centres of both the vortices in that frame.

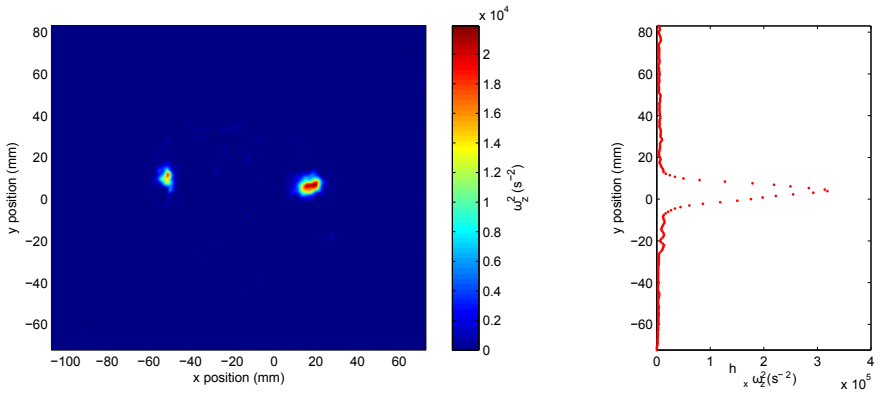

(a) Swirl strength field

(b) Horizontal sum of swirl

Figure 5.15: Illustration of the swirl strength field, ω_z^2

This y location was then used to search the vorticity field for peaks, maxima and minima were sought corresponding to each of the two vortex images in frame. To improve the reliability of the selection of the peaks, multiple peaks were chosen and the most appropriate later selected. For this the four greatest maxima and four greatest minima were used, providing estimates of the x-location of the positive and negative vorticity peaks respectively. From here on, the processes described were applied in turn to both the sets of maxima and sets of minima.

Due to the high PIV acquisition rate, the vortex ring evolution was gradual,

this was exploited in the selection of the most appropriate peaks. This selection was performed in two stages, by considering a time series of the sets of four peaks: first a very reliable starting point was found in the time series, this validated peak was then compared with the four possibilities at adjacent points in time. The peak most similar in magnitude and position was then used as the valid peak, and the process repeated. One can think of this as scanning the time series for a point which is very likely yo be a swirl maximum - i.e. lying close to the vorticity centroid. When this peak is found, we work outwards in time, following the peak with the most similarity.

To compute the starting point, only the peak with the highest magnitude was used, ω_p. The variation of the peak value and peak position σ_{ω_p} and σ_{x_p}, respectively were found for each point in time by computing the standard deviation over a sliding neighbourhood in the time domain of 5 points. These values were used to define a quality score Q, as a function of time, as in equation (5.7).

$$Q = \left| \frac{\sigma_{\omega_p} \sigma_{x_p}}{\omega_p} \right| \tag{5.7}$$

The factor Q is arranged as it is under the assumption that as the vortex ring evolves slowly with time, therefore the true swirl peak value and position should change slowly with time. We also assume that should the maximum valued peak at some time be a spurious peak, its position and value would unlikely be similar to a true peak at neighbouring times. Furthermore we assume that spurious peaks are likely to arise due to random-type noise in the correlation procedure or due to true vorticity peaks lying outside of the core region. In both cases it is highly unlikely that the peak position and value would remain similar through time.

To estimate the local temporal variation in peak location and magnitude the

standard deviation was used. For low variation, the standard deviation is low, hence Q is low. Furthermore we want to bias the peak selection toward those most likely to provide a strong signal, which occurs for higher vorticity. Due to this our quality factor is divided by the vorticity.

This point in time, t was then used to validate those peaks at previous or subsequent times. This was done by comparing the validated peak, $\omega_p[t]$ with the four peaks adjacent in time, $\omega_i[t+1]$. Note the comparison with peaks at the subsequent time, $t+1$ is discussed here, however the same operations were also performed for peaks at time $t-1$. The comparison was performed using both peak value and peak position and used to define a second quality score P_i for each of the four peaks evaluated, as given in equation (5.8).

$$P_i = \sqrt{(\omega_p[t] - \omega_i[t+1])^2 + (x_p[t] - x_i[t+1])^2} \tag{5.8}$$

The minimum of P_i therefore indicates the peak at time $t+1$ most similar to the validated peak at time t and this peak is then considered validated. The procedure was then repeated until the x-locations were found for all points in time. These estimates of vorticity centres were then filtered using the median filter described in equation (5.6), with $k_\sigma = 3$ and this data was then used as the coarse, but robust, estimate of vortex centre.

The higher accuracy method used weighted, windowed centroiding as its basis of peak estimation, this was done to sub-VMU accuracy and discrete window offset used to improve the centroid estimates. In this case the coarse estimate described previously was used to specify the windows' initial positions. The window offsetting was performed iteratively and deemed to have converged when the window was positioned with its centre on the centroid location (to VMU accuracy). As the disparity between $u_x^{\mathbf{1}}$ and $u_x^{\mathbf{2}}$ was so much higher than that

between $u_y^{\mathbf{1}}$ and $u_y^{\mathbf{2}}$, this centroiding process was restricted to the maxima and minima of the u_y data.

As the velocity profile in figure 5.16 shows, two maxima and two minima are present in the u_y field. One can further see that the peaks resulting from the corresponding vorticity field and hence the coarse estimates of vortex centre already calculated, lie between these maxima and minima. To account for this, the initial centroid search window centre was positioned at the previously calculated coarse centre $\pm$25VMU.

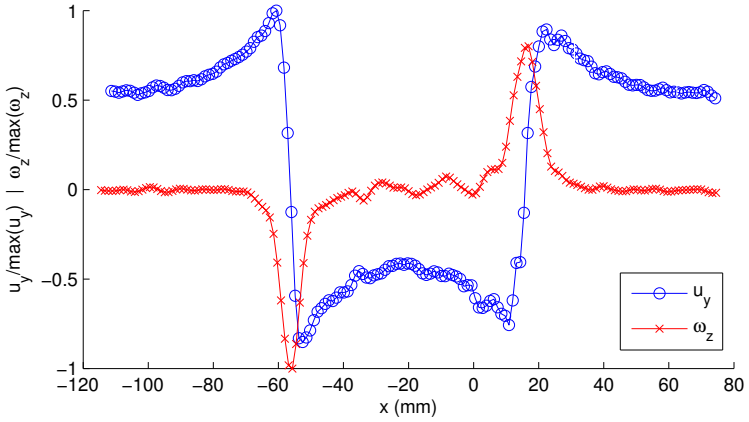

Figure 5.16: Corresponding profiles of u_y and ω_z

To perform the centroid, the data within the interrogation window was first thresholded to some arbitrarily assigned percentage - e.g. the lower 75% of data was discarded. After a centroid location had been found the window was displaced so that the centroid would lie in the centre of the interrogation window. If the interrogation window reached the edge of the frame, or if the centroid returned was the centre of the interrogation window (to integer precision) then the centroiding was determined to have converged.

As is well known, centroiding is strongly sensitive to the threshold applied; to mitigate this, upon convergence, the percentage of removed data was increased. If the centroid remained in the centre of the interrogation window (again to integer

precision) after this operation, the location was accepted as a measurement point. This measurement point used the sub-VMU precision estimate of the centroid however. If the centroid did not remain in the centre of the interrogation window, it was again shifted and the process was repeated.

These four velocity peak measurements were then used to determine four disparity vectors describing the registration error between camera 1 and camera 2. These computed field displacements were then filtered using a local median filter, with $k_\sigma = 2$. From this an estimate of the net translation may be found by taking the median of the remaining filtered field displacements. This displacement may then be used to apply a translatory shift to the vector fields in order to reduce the registration error.

5.5.3.3 Registration correction and comparison

The existence of a registration error between the back-projected vector fields implies that the calibration used to back-project the images was incorrect. This results in two errors: first and most importantly, the derived vector fields do not lie in the same place; second, even if this first error is corrected, the calibration used to compute the 3C vector field is incorrect. Therefore the estimation of the spatial distribution of disparities should not only be used to correct spatial misalignment but also modify the camera calibration such that it more accurately reflects the measurement geometry.

In the general case, there is no reason not to extend the full epipolar geometry type self-calibration, where flow-field matching defines a disparity vector field. Each extrinsic self calibration matrix contains 6 degrees of freedom, thus for a stereo setup, one would assume that the system of equations require 6 point correspondences for a solution. As shown by (Hartley and Zisserman, 2003d) complex geometry enables the problem to be reduced to the computation of a

single matrix with 10 degrees of freedom, thus requiring only 5 point correspondences (up to scale). From this matrix, and with some basic knowledge of the scene, the complete extrinsic camera calibration may be recovered.

Unfortunately in the case of the vortex ring under a rotational stereo setup, reliable features may only be attained from the u_y field, as shown in figure 5.13. In this field there are at most 4 reliable point correspondences to be found, resulting in a degenerate configuration for which a family of solutions exist. Further to this, in the u_y field the measurable point correspondences are approximately collinear, resulting in a set of equations that are not linearly independent. The upshot of this is that, at best, only an adjustment to the more critical elements of the calibration (β and $\mathbf{T}$)may be made, which requires 2 point correspondences.

Adjustment to $\mathbf{T}$ and β could made using triangulation and a surface fit as in standard self-calibration, c.f. section 2.4.2.4. Whilst this type of self-calibration presents a potentially viable correction to the calibration model, for the corrections performed, only $\mathbf{T}$ was refitted. Self-calibration is highly prone to error and to counteract this many measurement points should be used, thereby minimising the errors. It is entirely possible that with careful user supervision improvements to the calibration could be made, however with the volume of data to be processed, this was not feasible. Furthermore the sensitivity of error in the 3C measurement is much higher for β than $\mathbf{T}$, thus refitting $\mathbf{T}$ provides an improvement to the calibration with little risk of reducing accuracy. Due to this sensitivity automated refitting of β is significantly less robust.

Both the correlation and image registration type disparity calculations provide better than VMU resolution. For this reason the velocity vector fields were shifted to sub-VMU accuracy using a bilinear interpolation prior to the final 3C vector computation. Before the 3C vectors were computed, it was necessary to determine which of the correlation or image registration methods had performed

best. To check this, the u_y component of velocity was shifted by the translation determined through each of the methods, giving the shifted velocity for the i^{th} camera, $u_y^{\mathbf{i}'}$. Due to the particular stereo arrangement employed, the u_y fields from cameras 1 and 2 should be near identical.

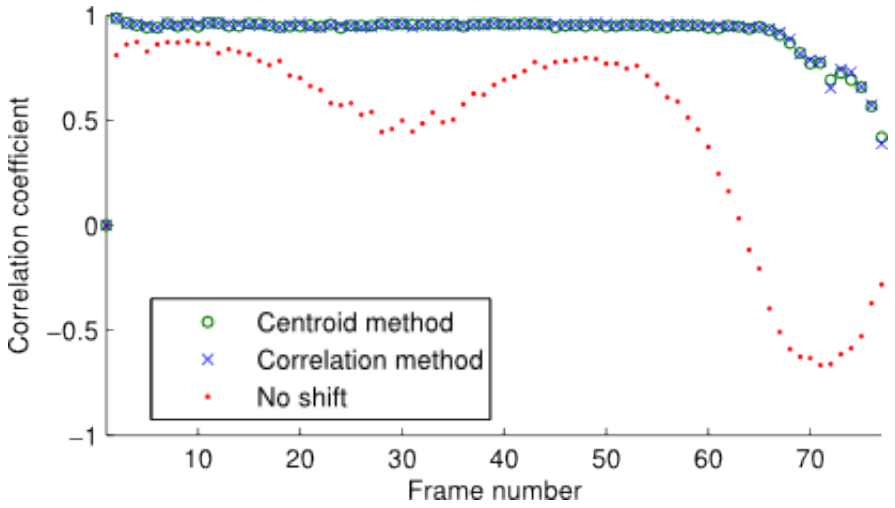

Figure 5.17: Normalised cross correlation of full u_y field

The quality of the shift may then be assessed by computing the normalised cross correlation for the full field after correction, without spatial lags, as detailed by equation (5.9). Typical values of c_{field} with frame number are shown in figure 5.17, data is shown for each of the image registration methods and also without shifting, for comparison. For each frame, the technique resulting in the maximum value of c_{field} was used to shift the u_x data and the combined shifted data used to compute the 3C vectors as described in section 2.4.3.

$$c_{field} = \frac{\sum_{x,y}(u_y^{\mathbf{1}'}(x,y) - \bar{u_y}^{\mathbf{1}'})(u_y^{\mathbf{2}'}(x,y) - \bar{u_y}^{\mathbf{2}'})}{\sqrt{\sum_{x,y}(u_y^{\mathbf{1}'}(x,y) - u_y^{\mathbf{1}'}(\bar{x},y)).^2(u_y^{\mathbf{2}'}(x,y) - u_y^{\mathbf{2}'}(\bar{x},y)).^2}} \tag{5.9}$$

5.6 Correction for vortex ring moving out of the light sheet

It was found that vortex ring travel was unpredictable, especially during the transition to turbulence and under background rotation. This is illustrated in figure 5.18, which shows the 3D position of a vortex ring over time. We see that after some point in time, the vortex ring trajectory changes greatly, with the vortex travelling away from the centre of the tank in both the x and z directions.

Motion in the z direction causes the centre of the vortex ring to move out of the light sheet, this results in the light sheet no longer lying in a plane of symmetry. Furthermore velocity that would have been measured as in-plane (had the vortex ring continued on a more ideal course) is measured as out-of-plane, as illustrated in figure 5.3. This section details the estimation of the vortex rings 3D position and the subsequent velocity field correction.

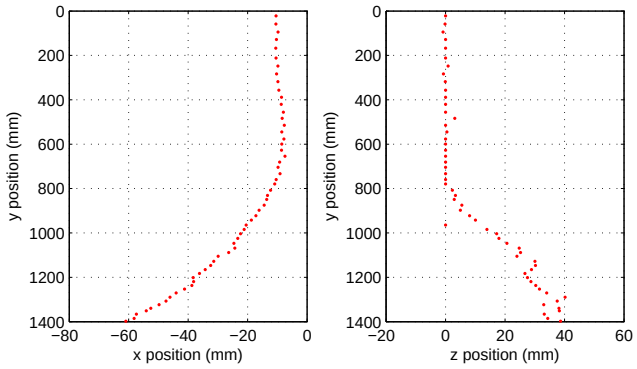

Figure 5.18: Example of 3D vortex ring trajectory

Figure 5.19 illustrates the problems associated with the vortex ring moving out of the light sheet plane. In describing these, it is convenient to consider the measurement as being made on a plane in Cartesian coordinates, however the flow as in cylindrical coordinates, of space $\mathbf{x}_\varphi = [x_\varphi \quad x_\rho \quad x_h]^T$ with the velocity

field $\mathbf{u}_\varphi = [u_\varphi \quad u_\rho \quad u_h]^T$. Therefore, when the vortex ring centre lies in the light sheet, $\Delta Z = 0$, which means that $\mathbf{x} = \mathbf{x}_\varphi$ and $\mathbf{u} = \mathbf{u}_\varphi$, however where $\Delta Z \neq 0$, $\mathbf{x} \neq \mathbf{x}_\varphi$ and crucially $\mathbf{u} \neq \mathbf{u}_\varphi$.

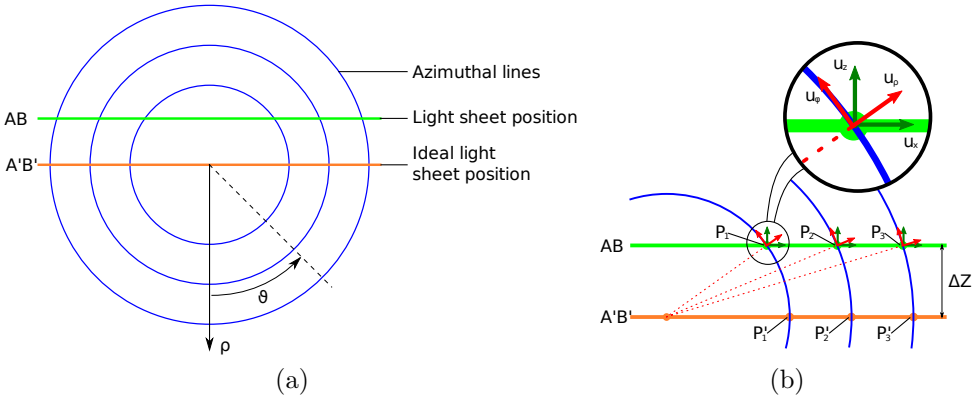

Figure 5.19: Illustration of the problems associated with vortex ring moving out of the light sheet plane

It can be seen that for the case where $\Delta Z \neq 0$, at any given point in the field, the locally measured velocity may be realigned with the actual fluid velocity, through a rotation, $\mathbf{R}_f$:

$$\mathbf{u}_i = \mathbf{R}_f \mathbf{u}_{\varphi \mathbf{i}} \tag{5.10}$$

If the velocity field of the vortex ring is axisymmetric, then a point P_i measured on the plane AB may be mapped to a corresponding point on plane $A'B'$. Under the assumption of axisymmetry, when the displacement of ring centre from the light sheet plane, ΔZ, is known, it is then possible to rotate and re-project the velocity field as if the PIV measurement had been made on a plane coinciding with the vortex ring centre.

5.6.1 Calculation of 3D vortex ring position

To compute the 3D vortex ring position, we first measure the deviation of the fluid coordinate system from that measured locally, providing an estimate of the local radial direction u_ρ across the field. We then back-project these estimates and find the point of minimum intersection. This is illustrated in figure 5.20.

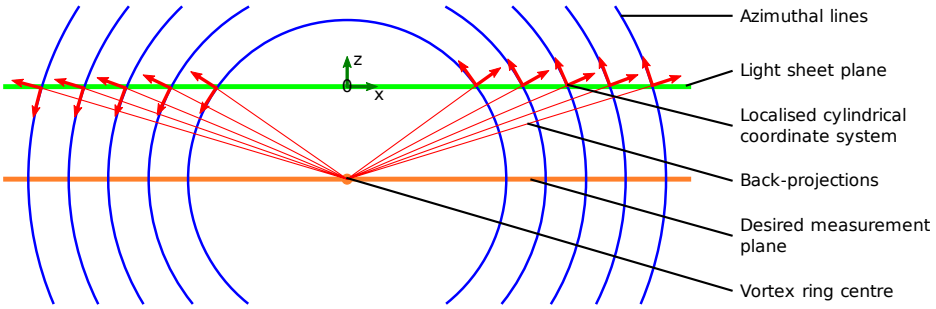

Figure 5.20: Illustration of back-projection along radial lines to find the vortex ring centre

In order to compute the 3D position of the vortex ring, we require that the velocity field be *statistically* axisymmetric. By this it is meant that the flow need not be exactly axisymmetric, however the best intersection point of the back-projected local radial lines should lie in the centre of the vortex ring, i.e. on average, the ring is axisymmetric.

We attempt only to correct for the vortex ring's translation out-of-plane; no pitching is accounted for as error from this is insignificant in comparison to that from out-of-plane motion. Because of this, and the orientation of the vortex ring, the relative rotation of the coordinate system need only be computed as a function of x. This may be seen from figure 5.20, where the rotation of the localised cylindrical coordinate system varies only with x.

To achieve this, we have two requirements, both of which should be valid for any x-location used. First, the velocity components u_φ and u_ρ must be uncorrelated. Second, for a given x-location, the range of u_ρ must be greater than

the range of u_φ. The meaning of the first requirement is that any correlation found between u_x and u_z arises from the location of the measurement plane, not the underlying motion of the measurement. The second requirement allows the fitting of any relationship occurring between u_x and u_z, as it defines the major axis of the data to be the u_ρ component.

Under these assumptions, the local coordinate system rotation at some x-location may be found by fitting u_z as a function of u_x. This is shown in figure 5.21.

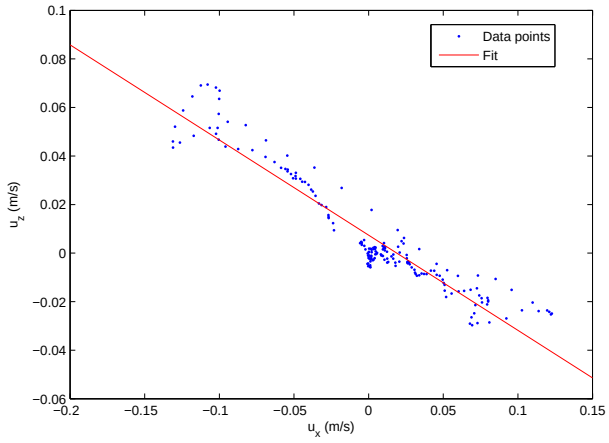

Figure 5.21: Example fit of u_z as a function of u_x

The SNR of the fits was improved by restricting fitting to areas of the vector field where it is known that $\sigma(u_x) \gg \sigma(u_w)$. On this basis the far-field of the centre of the vortex ring were excluded from the fitting. This was done by specifying a valid search range in terms of ring radius, R. The range used is shown in equation (5.11) and illustrated in figure 5.23.

$$0.2R \leq x_{valid} \leq 1.5R \tag{5.11}$$

In order to compute x_{valid} a refined estimate of vortex centroid was made. This

was done using an iterative centroiding method, as described in section 5.5.3.2, however the feature finding was performed on the preliminary 3C vectors previously computed, meaning that u_x provided a valid estimation of vortex ring position. This allowed the feature finding to be applied to both u_x and u_y.

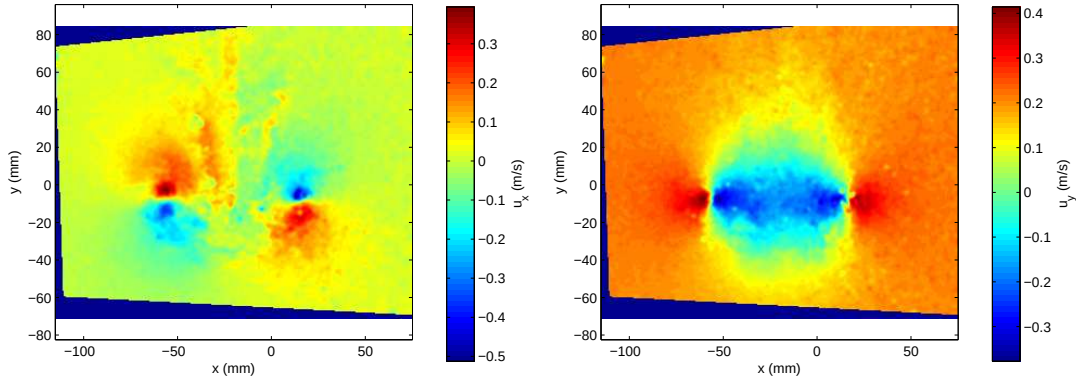

(a) u_x velocity field (b) u_y velocity field

Figure 5.22: Illustration of four peaks present in the u_x and u_y components of the vortex ring velocity field

Each component field contains four clearly identifiable peaks, this is shown in figure 5.22, giving an 8-point estimation of vortex ring position within the frame. These 8 points were then RMS filtered, and as in section 5.5.3.2, estimates of vortex centroids were made from the median of the filtered data, and from this the vortex ring radius, R could be simply calculated.

Example fits across the valid range of data are shown in figure 5.24. Each plot is labelled with the gradient calculated from the fit and the mean squared error (MSE) of the residuals from the fit.

Each fit is essentially a localised mapping function, giving an estimate to the position of the ideal measurement plane from the actual measurement plane. As the fit is linear, this mapping function is linear and so has two coefficients, an estimate of the direction, m, and an estimate of the velocity u_z at which $u_x = 0$. In this instance the latter part, the y-intercept, is useless and is only included

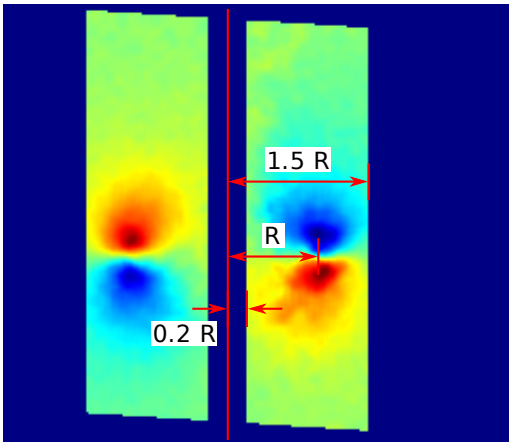

Figure 5.23: u_z field, illustrating the range of x_{valid}

in the fit to provide the degrees of freedom necessary to accurately compute the gradient. Figure 5.25a shows the intersection of the back-projected gradients and figure 5.25b indicates the triangulated point of best intersection.

The computation of the displacement of the measurement plane from the ideal measurement plane is performed as a reformulated triangulation problem 2.4.2. Considering the i^{th} estimate of gradient m_i to lie at position x_i, we may write:

$$\begin{bmatrix} m_1. - x_1 \\ m_2. - x_2 \\ \vdots \\ m_i. - x_i \end{bmatrix} = \mathbf{X}_{\Delta Z} \begin{bmatrix} m_1 & 1 \\ m_2 & 1 \\ \vdots & \vdots \\ m_i & 1 \end{bmatrix} \tag{5.12}$$

Here $\mathbf{X}_{\Delta Z}$ is the parameter to be fitted and may be solved for as a conventional least squares problem. The solution is computed in this fashion due to the notable scatter seen in the fits of u_z as a function of u_x, for example figure 5.21. The estimation of this position is shown in figure 5.25b. Here $X_{\Delta Z_1}$ is a small adjustment to the location of the ring centre in the x-direction and $X_{\Delta Z_2}$ the displacement in the z-direction.

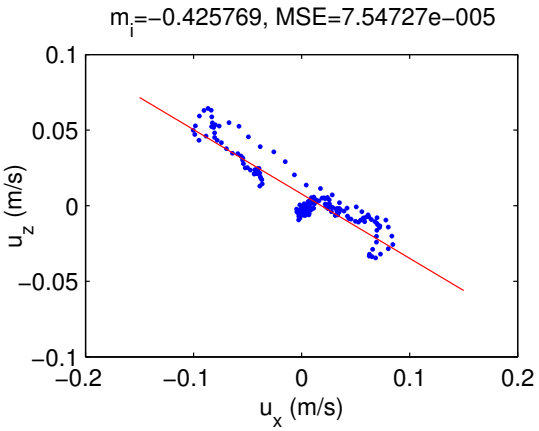

(a) Fit at x=-64

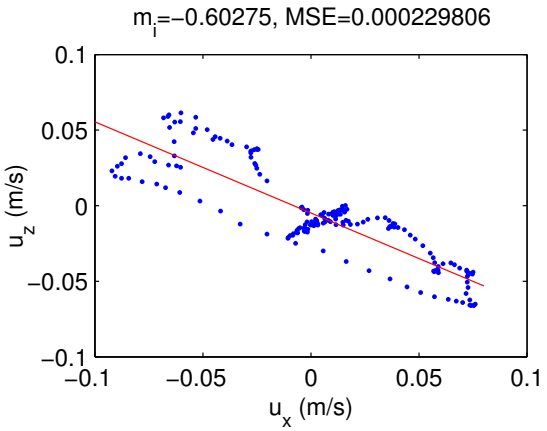

(b) Fit at x=-33

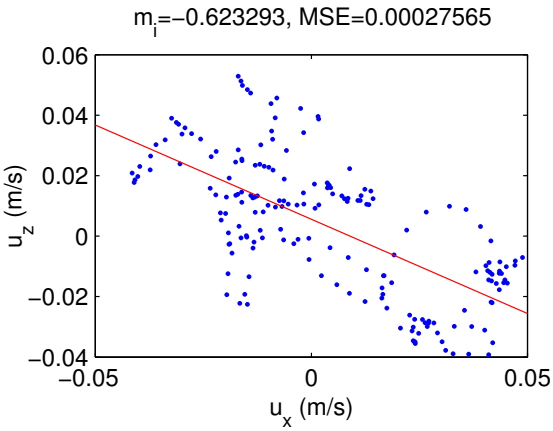

(c) Fit at x=-16

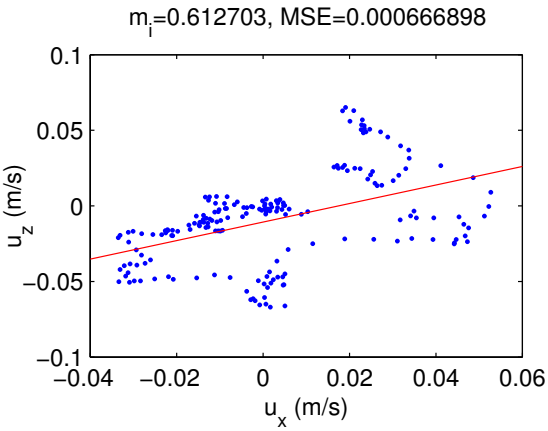

(d) Fit at x=16

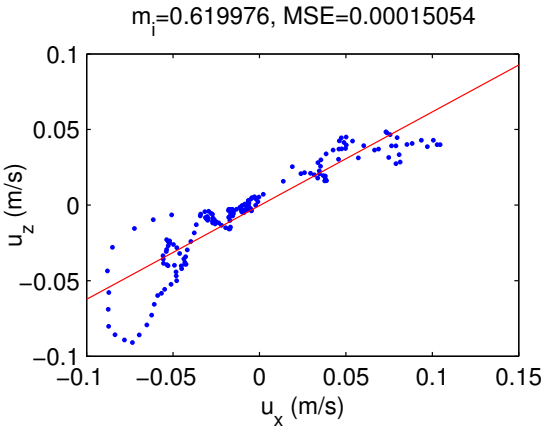

(e) Fit at x=33

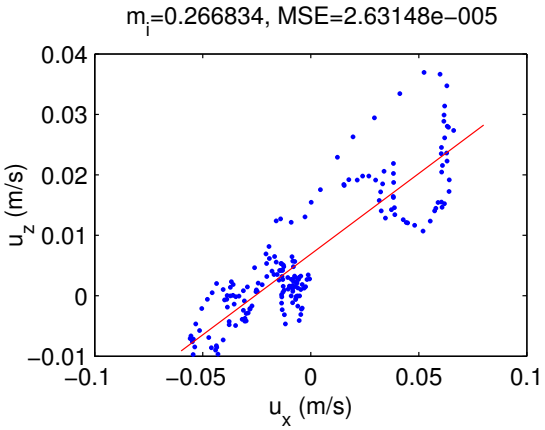

(f) Fit at x=64

Figure 5.24: Plots showing fits to compute back-projection for estimating the position of ring centre

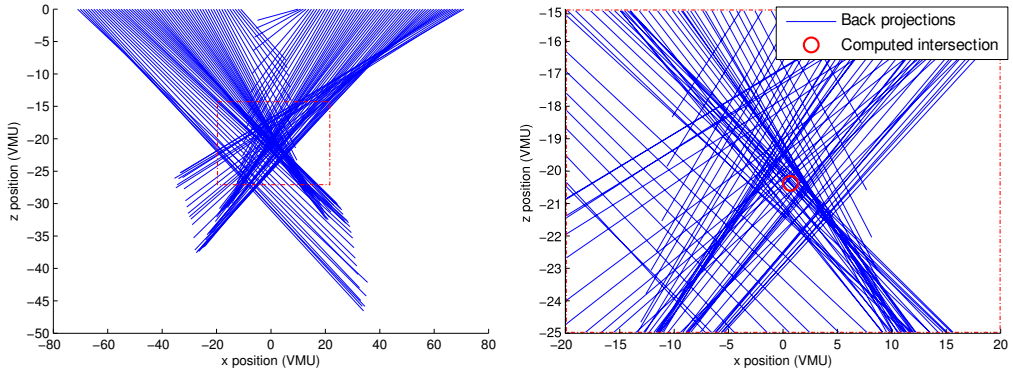

(a) (b)

Figure 5.25: Plots showing all back-projections to estimate the position of ring centre

5.6.2 Implementation: filtering and velocity field re-correction

The velocity field correction and adjustment was run on all data, as robust correction of the data was of paramount importance. It is immediately apparent that reprojection of the velocity field to account for the vortex ring moving out of the light sheet results in a non-uniform, non-linear spatial distribution of velocity. So that the data could be compared between runs and over time, the velocity field was interpolated onto a uniform grid. As the velocity field had already been subjected to one bilinear interpolation pass, this correction was applied to the raw 2C vector fields and the 3C velocities recomputed. Furthermore during this interpolation, the vector field was shifted (to sub-VMU accuracy) such that the vortex ring's centre lay in the middle of the field of view. This allowed for direct comparison between vortex rings acquired during different runs.

As the correction was to be applied autonomously, it was important that its application be restricted such that data would only be corrected in cases where it was certain that the correction would provide an improvement to the existing data. Unsurprisingly, the triangulation performed poorly when the vortex centre had moved only a very small distance from the light sheet. It was found that

in these cases the measurement of $\mathbf{X}_{\Delta Z}$ was masked by error which was most noticeable in the $X_{\Delta Z_1}$ component, which became large. As the estimation of the vortex centre position through iterative centroiding is of high accuracy, a large $X_{\Delta Z_1}$ most likely indicates error. Furthermore, should the vortex ring move *too far* out of the light sheet, there is little recoverable information. On this basis, the data was filtered according to equation (5.13). This was done, as it removed areas where the fitted velocity components were sufficiently low as to provide poor SNR. As the vortex ring's travel out of the light sheet will be steady, not jerky, an RMS filter, equation (5.6) with $k_\sigma = 2$ was used to remove measurements with high disparity relative to their neighbours.

$$X_{\Delta \mathbf{z}_{invalid}} \begin{bmatrix} < 1/4 \\ > 3/4 \end{bmatrix} R \tag{5.13}$$

Correcting the velocity fields was a two stage process; a spatially non-linear reprojection was needed to adjust the distribution of points in the x-direction, and the velocity components required adjustment with a coordinate system rotation. To compute both elements of the correction, the spatially varying angle θ_i describing the rotation between u_x and u_ρ, was needed. From this one may calculate the reprojected spatial coordinates, x' and reprojected velocity, u'_x, u'_z, equation (5.14).

$$x'_i = x_i \cos\theta \tag{5.14a}$$

$$u'_{x_i} = u_{x_i} \cos\theta - u_{z_i} \sin\theta \tag{5.14b}$$

$$u'_{z_i} = u_{x_i} \sin\theta + u_{z_i} \cos\theta \tag{5.14c}$$

To prevent unnecessary blurring of the vector fields, the interpolation required to perform the non-linear spatial transform part of the correction was performed on the 2×2C velocity fields as part of a complete vector field correction. The interpolation was performed using the Matlab spline toolbox, invalid vectors were semi-propagated; a single pass fill was incorporated into the interpolation, which is representative of the behaviour of a bilinear interpolation.

5.7 Evaluation of corrections

This chapter has described the three main corrections that were applied to the acquired PIV velocity fields. In each case an ad-hoc validation will be presented showing that the correction implemented provides a general reduction of the errors targeted. In the case of the correction for the vortex ring moving out of the light sheet, the errors are simulated synthetically using a popular model vortex and the suitability of the correction investigated in the presence of noise. A thorough error analysis of the remaining methods, although valuable, would be highly involved and beyond the scope of this work.

5.7.1 Background velocity correction

We are able to demonstrate the success of the background velocity removal process by considering the time evolution of the velocity field. This is displayed in figure 5.26 by plotting the field median for each component of velocity. It is quite apparent that the variation of this median velocity is noticeably reduced by the background velocity subtraction technique.

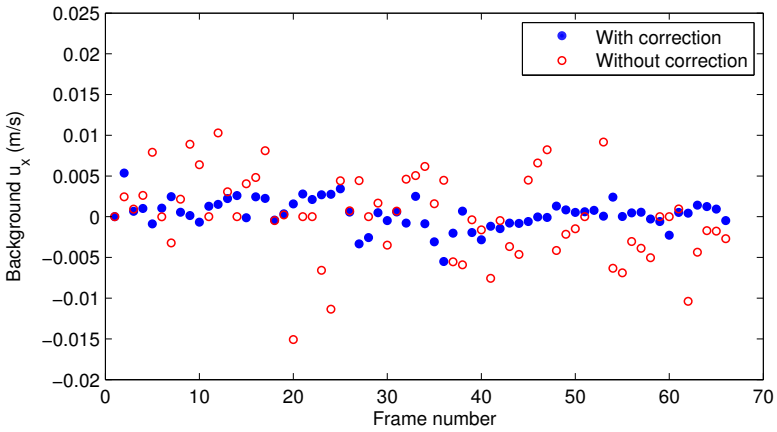

(a) u_x

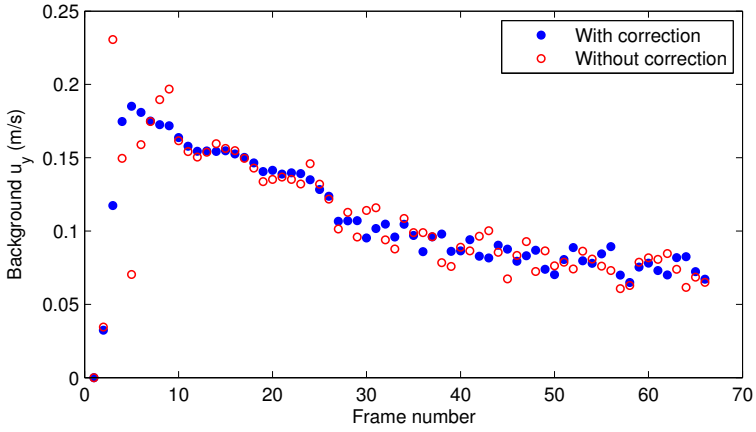

(b) u_y

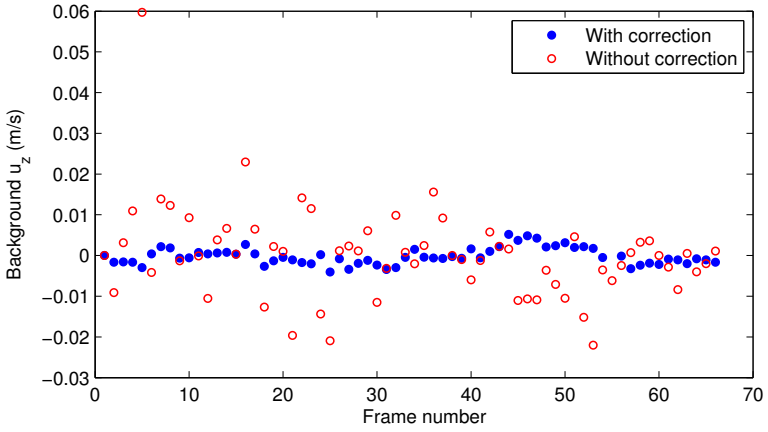

(c) u_z

Figure 5.26: Examples of velocity field background with and without background subtraction

5.7.2 Registration error removal

As demonstrated in section 2.4.2 a small registration error is most prominent in the u_z component of velocity. Figure 5.27 presents a series of vorticity contours that illustrate the relative positions of the velocity fields acquired by cameras 1 and 2 over time. It is quite apparent that without the velocity field translation there is a significant error in the image registration. Further figure 5.27 shows clearly that the registration correction employed provides significant improvement.

5.7.3 Correction for vortex ring moving out of light sheet

We investigate the effectiveness of the vortex ring correction by illustrating its success by analysing individual velocity fields and also through considerations of a theoretical model vortex ring.

As shown in figure 5.2, vortex rings moving out of the light sheet typically display large areas of oppositely signed u_z above and below the ring's centre line. Summing the u_z field horizontally provides a convenient method of determining whether or not the vortex ring has moved out of the light sheet. This is plotted against frame number in figure 5.28, which shows that although the effects of travel out of the light sheet are not removed entirety, but they are substantially reduced.

It is noticeable that there is a marked change in figure 5.28b at frame 57. At this point the vortex ring has moved sufficiently far out of the light sheet that the out-of-plane correction can no longer be implemented. This abrupt change indicates the disabling of the correction.

Further to this we investigate the error in estimating the vortex ring's out of light sheet position using a theoretical vortex model. We construct a vortex ring

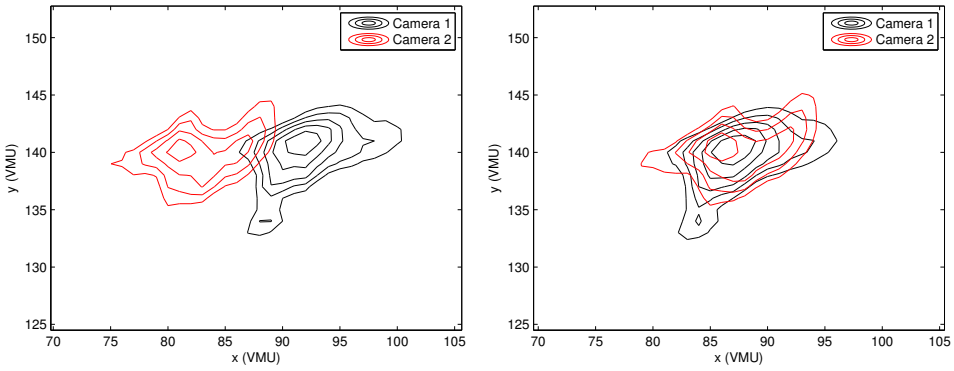

(a) $t = 0.9s$, without correction

(b) $t = 0.9s$, with correction

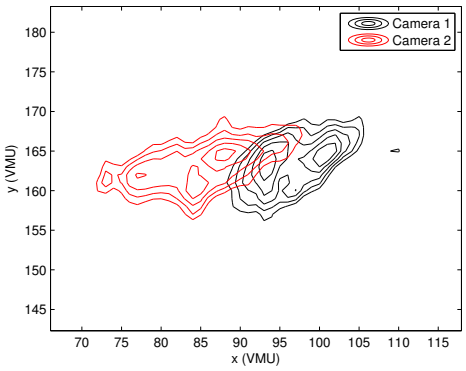

(c) $t = 1.98s$, without correction

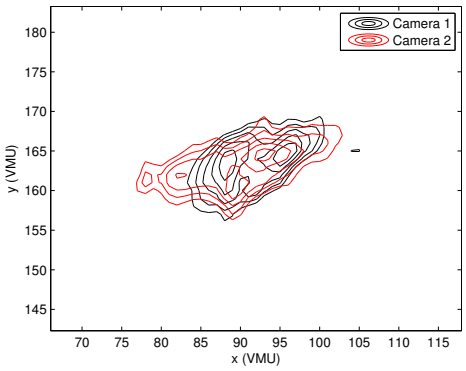

(d) $t = 1.98s$, with correction

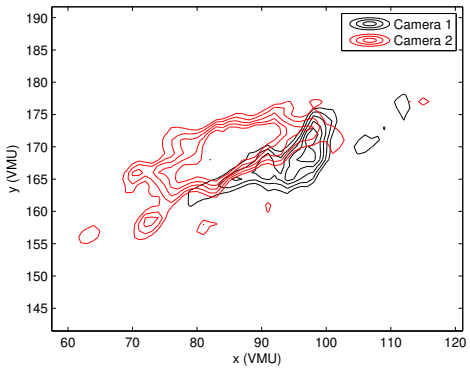

(e) $t = 2.88s$, without correction

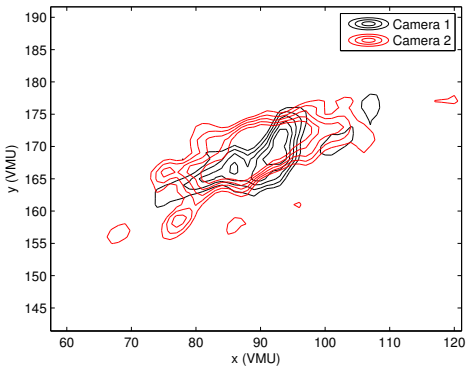

(f) $t = 2.88s$, with correction

Figure 5.27: Vorticity contours illustrating registration error removal

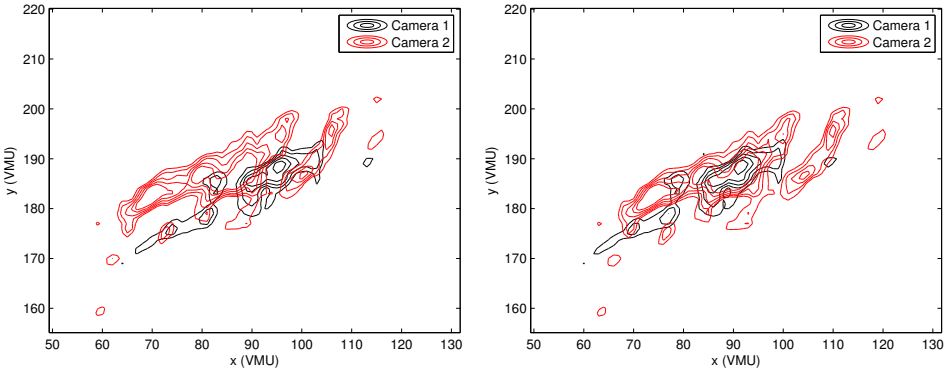

(g) $t = 4.14s$, without correction (h) $t = 4.14s$, with correction

Figure 5.27: Vorticity contours illustrating registration error removal

velocity field similar to that found in our PIV measurements using the Lamb-Oseen vortex, the formulation of which is given in figure (5.15) (Saffman, 1992).

$$v_t(r,t) = \frac{\Gamma}{2\pi\rho}\left(1 - e^{-\left(\frac{2\rho^2}{\delta}\right)}\right) \tag{5.15}$$

The velocity is specified in a polar domain, with origin coinciding with the centre of the vortex. The flow field has no radial component, only tangential (v_t), which is a function of circulation (Γ), radial position within the domain (r) and time, through the core diameter ($\delta = 8\nu t$, Saffman, 1992). We construct a vortex ring of diameter D and spatial coordinate ρ_{ring} by creating two tangential velocity profiles $v_{t_{left}}(\rho_{left})$ and $v_{t_{right}}(\rho_{right})$. We consider the vortex ring at only one point in time, thus the tangential velocity profile is a function of only localised radial position, which we define simply, equations (5.16).

$$\rho_{left} = \rho_{ring} + D/2 \tag{5.16a}$$

$$\rho_{right} = \rho_{ring} - D/2 \tag{5.16b}$$

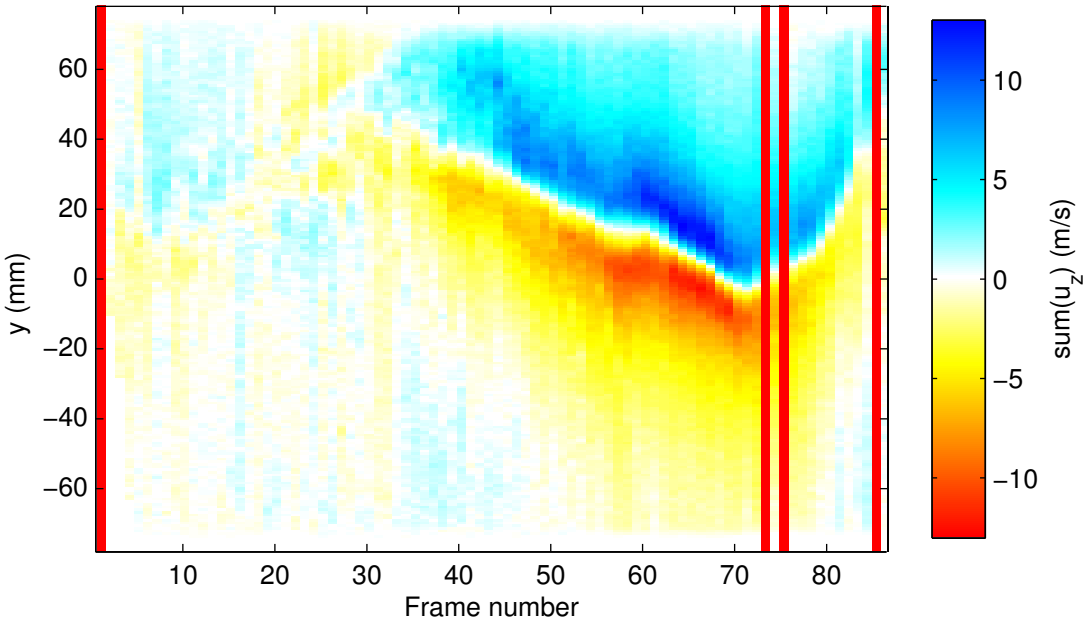

(a) Without correction

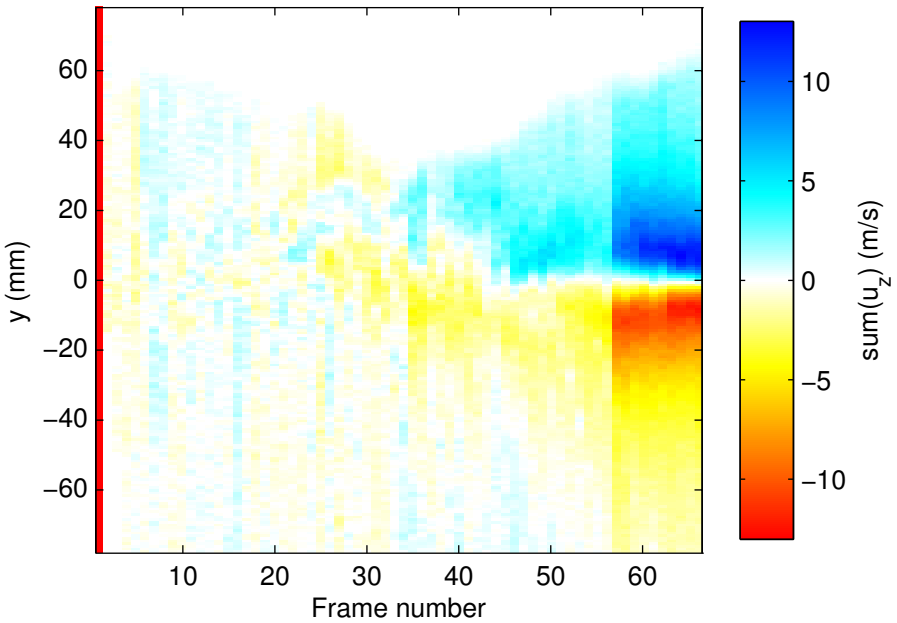

(b) With correction

Figure 5.28: Horizontal sums of velocity, indicating the effect of correction for the vortex ring moving out of the light sheet

The vortex ring velocity field is then computed through addition of the left and right tangential fields, across the domain. By choosing parameters similar to those found in the measured vortex rings $\Gamma = 0.2$, $D = 0.07$, $\delta = 0.2D$ we produce velocity fields very similar to those found in our experimental measurements. Furthermore, through the use of the methods outlined in section 5.6 we are able to establish a correspondence between a measured position x_{meas} and the corresponding location on an axisymmetric vortex ring for a given offset of the light sheet from the vortex ring centre (ΔZ). Upon this basis we are able to produce 3 component velocity fields, representative of a vortex ring with no out of plane motion, for any given ΔZ. By introducing these velocity fields, into the correction for the vortex ring leaving the light sheet (described in section 5.6.2), we are able to compare the value returned with the prescribed light sheet displacement. This is represented by the residual displacement $\Delta Z'$, this is the difference between actual the applied ΔZ and that estimated by the correction algorithm. This was performed across a wide range of ΔZ and also in the presence of Gaussian noise, which was used to simulate correlation errors. The amplitude of the noise was defined as being $N\%$ of the maximum velocity magnitude from the $\Delta Z = 0$ case. The results are given in figure 5.29, where the quantity of noise addition is listed in the legend.

In addition to the curves indicating the performance of the correction, a curve showing the line of no change is included. Data lying on this curve implies that after the correction the vortex ring centre remains the same displacement from the light sheet as before the correction. Data above this curve would indicate that the correction has moved the vortex ring further from the light sheet and data below the curve indicate that the correction has moved the vortex ring nearer the light sheet.

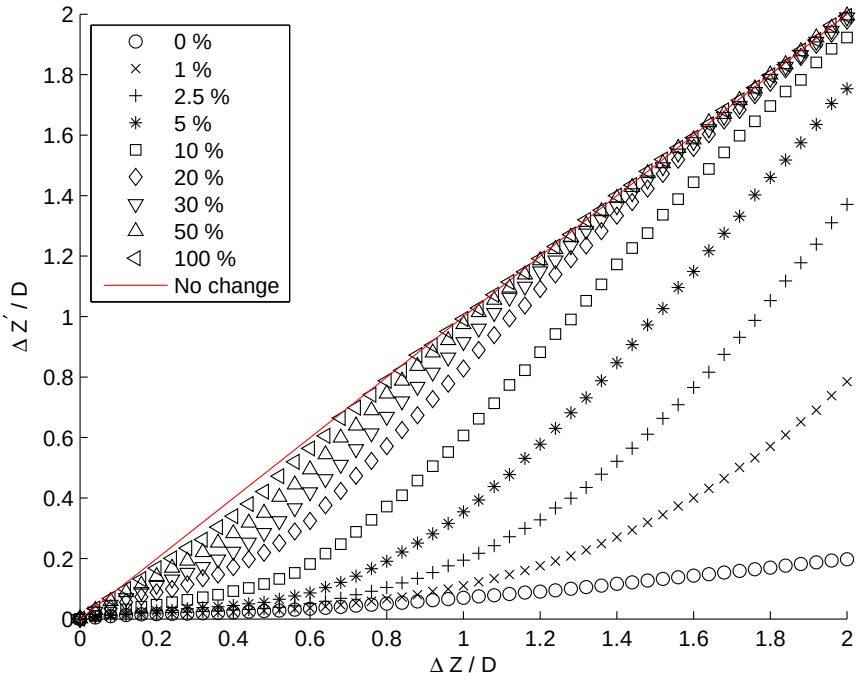

Figure 5.29: Evaluation of out of light sheet correction, using a Lamb-Oseen based vortex ring

It is apparent that in all cases, for all of the errors considered, the correction does not act to move the vortex ring further from the light sheet. It is of note that errors of the order of magnitude estimated for PIV $(1-2\%)$, the correction provides significant improvement to the data. The increase in error seen for $0.5D \lesssim \Delta Z \lesssim 1D$ occurs due to the drop off of velocity signal in these regions. Because the vortex ring is displaced so far from the measurement plane and due to the Gaussian type decay in velocity magnitude, the signal to noise ratio becomes very low at large displacements. Of course for current measurements, it is unlikely that any velocity would be measured for such large ΔZ due to the inherent restrictions upon the dynamic range of the correction.

Perhaps of more interest are the results presented in figure 5.30 where we consider the errors in typical operational regimes. The noise simulated is restricted to a few percent and the range of ΔZ tested is kept to within the approximate

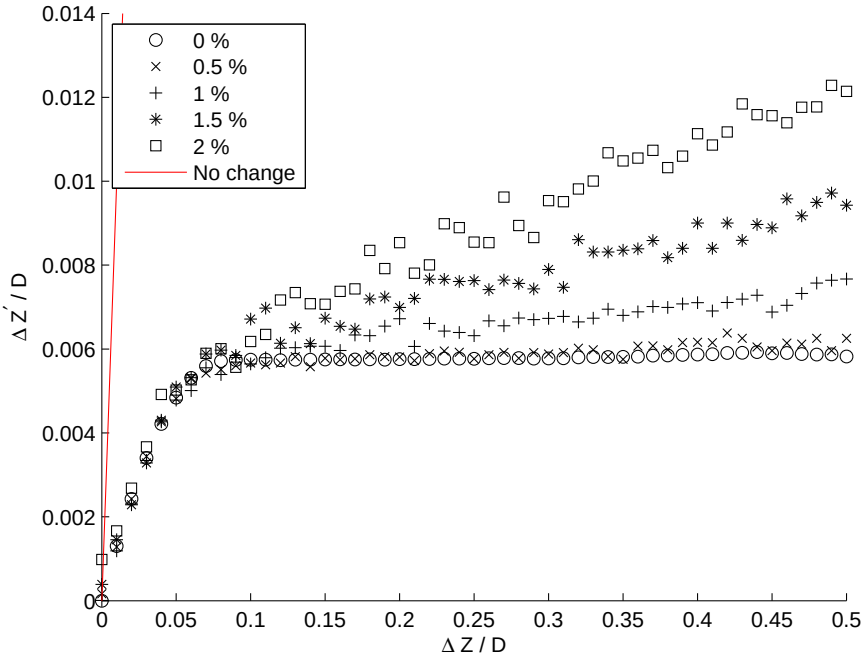

Figure 5.30: Evaluation of out of light sheet correction, typical operational parameters

limits imposed by filters described in section 5.6.2. We see that in all cases, across the whole range, the correction performs very well. The results presented in figure 5.28, showing estimates of the performance of the correction indicate that it is likely that the results presented from the analysis of the Lamb-Oseen vortex are an over-simplification. There are many reasons why this may occur, the vortex ring may not be axially symmetric, additional spatial fluctuations from turbulence may be present. In addition, many further possibilities exist, however these are not considered here and are recommended for further work.

CHAPTER 6

Initial dye visualisation measurements

The main results presented in this thesis are PIV measurements and their analysis. However, prior to the PIV study, initial measurements of the vortex rings under background rotation were made using dye visualisation techniques (Brend and Thomas, 2009) (the paper is reproduced in appendix A). This chapter presents details of the experimental setup (section 6.2), which differed slightly to the PIV experiments, some important results arising from these measurements (6.3) and provides conclusions based upon our observations (6.4). As the contents of this chapter have been published, the text of sections 6.1-6.4 closely follows Brend and Thomas (2009).

6.1 Introduction

As stated in section 3.4.1, the observation of fluid flows from a rotating inertial reference frame and hence the generation of Coriolis force gives rise to phenomena absent in non-rotating flows (Vanyo, 1993; Cushman-Roisin, 1994; Greenspan,

1968). These phenomena can appear counter intuitive to anyone not familiar with the theoretical background of rotating flows. One example is, for instance, the Taylor-Proudman theorem derived from the geostrophic approximation of the full momentum equation (Cushman-Roisin, 1994; Greenspan, 1968).

Briefly, the Taylor-Proudman theorem states that when a fluid rotates with a rotational velocity $\vec{\Omega}$ that is aligned with the $z-$axis of a Cartesian coordinate system, and if geostrophy applies, then the effect of Coriolis forces is such that the derivatives $\partial u/\partial z$ and $\partial v/\partial z$ of the velocity components u and v in the x and y coordinate directions are identically zero. Here we study vortex rings propagating with velocity $\vec{U}$ in a fluid rotating with rotational velocity $\vec{\Omega}$, as illustrated in figure 6.1. When $\vec{U}$ is parallel to $\vec{\Omega}$ and when geostrophy applies one thus anticipates on the basis of the Taylor-Proudman theorem that background rotation will tend to promote the destruction of the ring.

For the Taylor-Proudman theorem to be applicable Coriolis effects must dominate inertial effects, i.e. the Rossby number must be sufficiently low. For a general flow geometry as in figure 6.1 vortices can, in principle, be generated under conditions that violate this requirement. However, viscous effects result in losses of inertia and, thereby, the vortex rings approach the parameter regime where the Taylor-Proudman theorem holds. Therefore, it is expected that the decay of vortex rings will, ultimately, be accelerated even when a vortex ring is generated with high inertia.

One further anticipates that effects of rotation will become stronger as Coriolis effects become increasingly dominant. Hence, one expects that the average length that a vortex ring can travel before it has decayed entirely will decrease with decreasing Rossby number. The arguments leading up to the qualitative conclusion that background rotation will tend to promote the decay of vortex rings are relatively straightforward. However, obviously there exist no simple

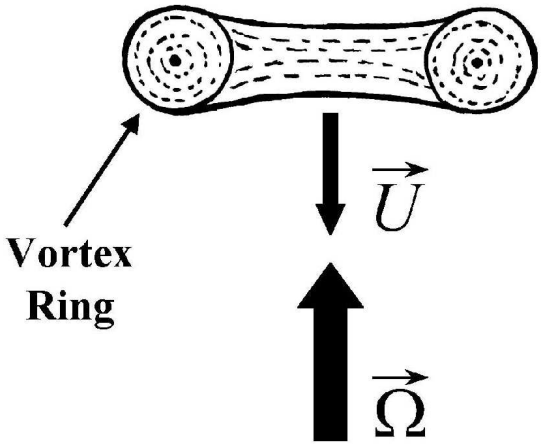

Figure 6.1: Sketch illustrating the flow geometry.

arguments to establish how the mean decay length will decrease with the Rossby number. There exist no previous studies that have investigated this fundamental question. The main motivation for the present experiments was to determine a statistical expression that relates the mean decay length of a vortex ring in a rotating fluid to its associated Rossby number.

It is no coincidence that no previous studies exist that investigated the decay of vortex rings propagating through a rotating fluid as in figure 6.1. Such experiments require a very high water-filled rotating-tank together with a suitable vortex-ring generator mounted within the rotating frame of reference. This type of large-scale facility was not available anywhere in the past. There appears to exist only one single previous study, by Verzicco *et al.* (1996), for which experiments investigating vortex rings moving through a rotating fluid in the sense of figure 6.1 were conducted. However, for this study only a comparatively small tank with a height of 1 m was available. The main focus of Verzicco *et al.* (1996) was to verify computational results primarily concerned with the velocity field and the vorticity distribution associated with the vortex ring.

6.2 Experimental set-up and techniques

We developed a new, unique large-scale experimental facility described here for the first time and the experimental results discussed are the first obtained with the new rig. Figure 6.2 displays a technical drawing of the new facility. The set up constitutes a large water-filled tank, mounted on top of a computer controlled rotating turntable. The tank is 2.5 m high and it has an octagonal horizontal cross section with a cross width of 1 m. The overall height of the facility, from the floor to the top of the support structure, is over 5.7 m. Vortex rings are generated using a standard technique Krutzsch (1939); Maxworthy (1977) where a computer-controlled piston ejects water from a circular nozzle such that a vortex ring forms at the nozzle exit.

Two alternative nozzles with diameters $D = 50$ mm and 10 mm were used. The vortex-generator nozzle is mounted rigidly at the top of the rotating tank. This means that the nozzle is stationary with respect to the water inside the rotating tank once the water has adopted a state of rigid-body rotation following an initial spin-up phase. Hence, when the piston pushes water out of the nozzle there exists no circumferential shear on the ring as would be the case if the nozzle itself was stationary and only the tank with the fluid was rotating. The vortex rings are ejected vertically downwards into the water contained inside the tank. The temperature of the water was in the range $10 - 15^{\circ}$ C such that its kinematic viscosity is $\nu \approx 1.30 \times 10^{-6}$ m^2 s^{-1}.

The results summarized here were obtained from flow visualizations. The vortex rings were visualized by means of releasing a small amount of neutrally buoyant food colouring through a narrow annular gap on the inside of the nozzle near its exit. Dye was supplied to the gap from a reservoir by a peristaltic pump through a system of thin pipes and tubes contained within the walls of the

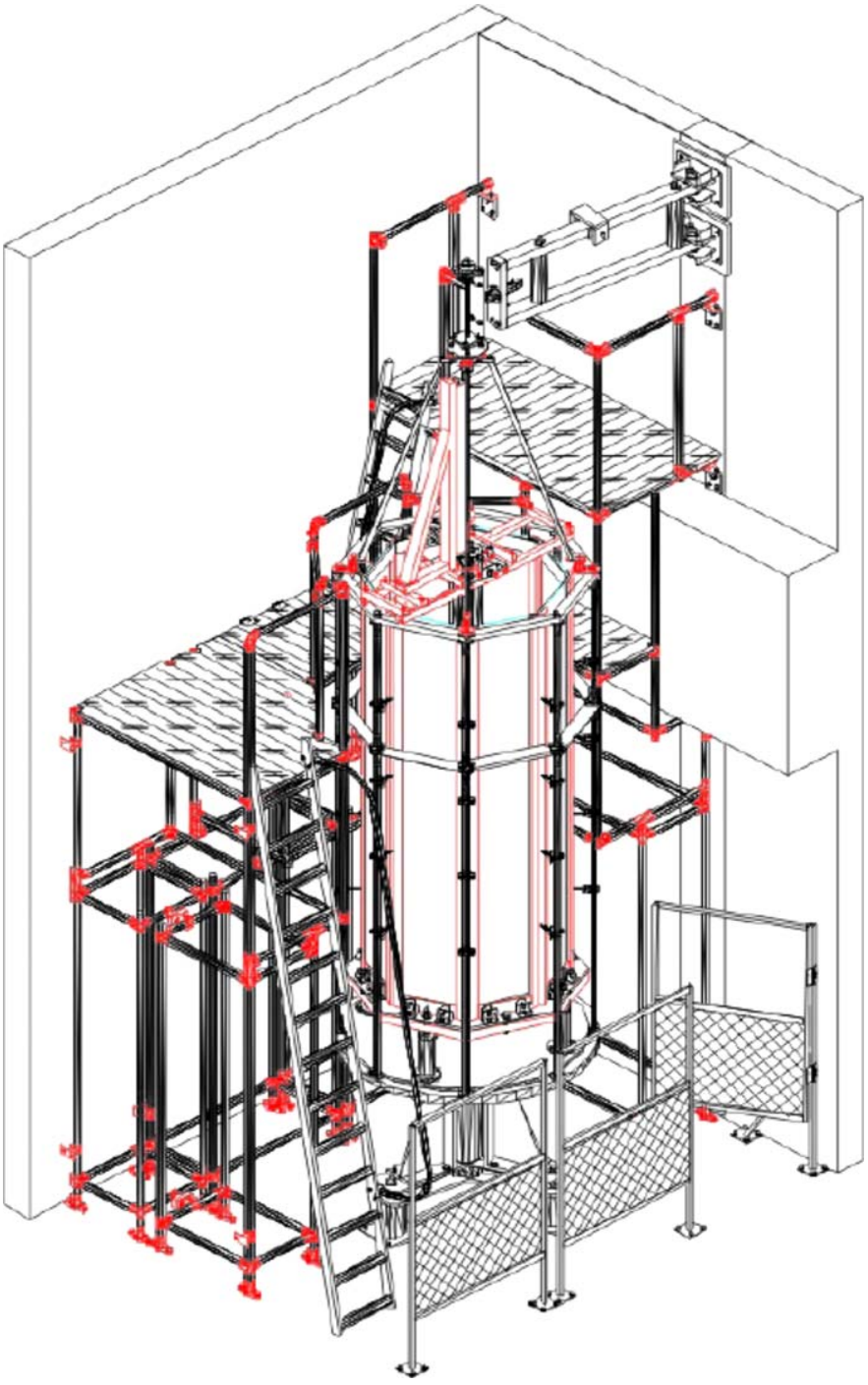

Figure 6.2: Technical drawing of the large-scale rotating tank facility. Ladder and scaffolding provide access to the top of the rig where the generator nozzle for the vortex rings is mounted.

vortex-ring generator-nozzle unit.

A Rossby number is defined as $Ro = U_M/\Omega D$. The velocity $U_M = x_d/t_d$ is the mean speed of the vortex rings where x_d represents the decay length. This length is the distance the ring travels away from the nozzle exit until it no longer represents a well-defined, coherent structure and t_d is the time interval between the formation of the ring and its decay. The definition of the decay length may appear somewhat qualitative but practice has shown that it is in fact fairly straightforward to judge when a ring has completely decayed. However, the goal is to determine an expression for the overall global trend regarding how rotation affects the vortex-ring decay. The distribution of the data to be presented below will reveal that the above definition of the decay length is sufficient for this purpose. For the experiments summarized here the Rossby number covered approximately the interval $0.1 \leq Ro \leq 25$. We further define a Reynolds number $Re = DU/\nu$. The Reynolds number covers values $40 \leq Re \leq 5300$ when U is identified with U_M or $385 \leq Re \leq 19230$ if, alternatively, based on the mean ejection speed of the fluid at the nozzle, as done by Maxworthy Maxworthy (1977).

6.3 Experimental results

Figure 6.3 displays the non-dimensional decay length, x_d/D, as a function of the Rossby number, Ro. The figure contains almost 520 data points. The results include data points for which $\vec{\Omega}$ and $\vec{U}$ were anti parallel, as sketched in figure 6.1, as well as data for which both vectors had the same orientation. Figure 6.3 reveals that the vortex rings can typically travel rather large distances of $x_d/D = 50$ at $Ro = 10$ where the effects of background rotation are comparatively weak. Note, for instance, that this value corresponds to $x_d = 2.5$ m for the nozzle with

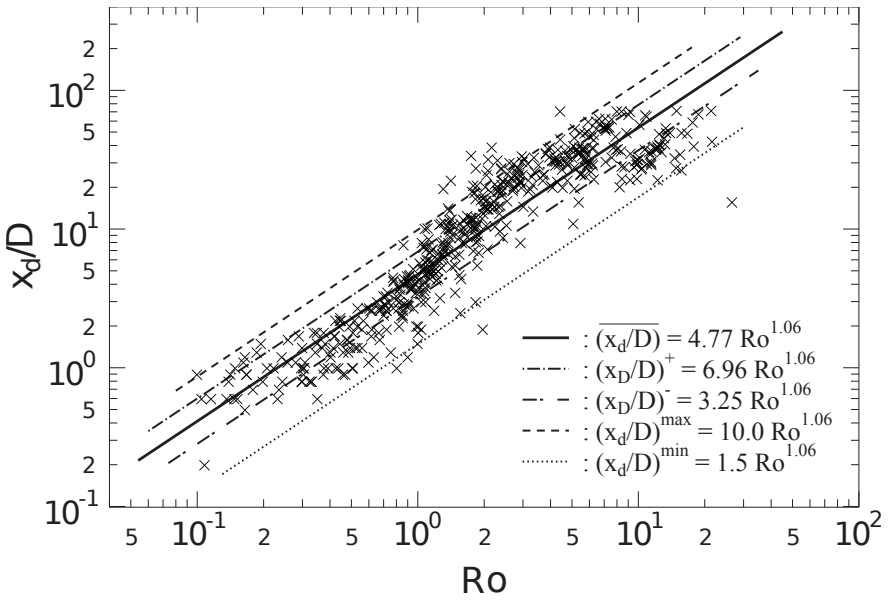

Figure 6.3: Vortex-ring decay length, x_d, as a function of the Rossby number, Ro.

diameter $D = 50$ mm. However, for $Ro = 0.1$, i.e. when effects of rotation are strong, we observed that the rings undergo a rapid and violent destruction process. Here the decay length is reduced to about $x_d/D = 0.4$, as revealed by figure 6.3. Now x_d is only 20 mm for the nozzle with $D = 50$ mm. Hence, the experimental data show that background rotation does lead to a substantially advanced decay of the vortex rings.

In order to obtain a quantitative expression approximating the overall trend of the dependence of the decay length on the Rossby number the data in figure 6.3 have been interpolated. The solid line in figure 6.3 represents a least-squares fit of type $y = kx + c$ in coordinates $y = ln(x_d/D)$ and $x = ln(Ro)$ with values of $k = 1.06$ and $c = 1.56$ implying that the mean decay length is

$$\overline{(x_d/D)} = 4.77 Ro^{1.06} \quad . \tag{6.1}$$

To quantify the errors associated with the least-squares fit we calculated

the mean deviation of the data points from Eq. (6.1). To this end the values $\Delta^i = |ln((x_d/D)_i^{exp}) - ln(\overline{(x_d/D)})|$ for all of the i experimental data points, $(x_d/D)_i^{exp}$, were determined and then averaged; this yielded $\overline{\Delta} = 0.38 \pm 0.26$. Thus, the average separation of the data points from the mean is $ln((x_d/D)^{\pm}) = ln(Ro^{1.06}) + (1.56 \pm 0.38)$. This implies that the data points with an average deviation above Eq. (6.1) are located at $(x_d/D)^+ = 6.96Ro^{1.06}$ while those with an average deviation below Eq. (6.1) are located at $(x_d/D)^- = 3.25Ro^{1.06}$ (see figure 6.3).

The increase of $\overline{(x_d/D)} \propto Ro^{1.06}$ means that the decay length increases, on average, approximately linearly with the Rossby number within the Rossby and Reynolds number regimes considered here. To obtain a convenient rule of thumb one can round the factor and the exponent in Eq. 6.1 to give $\overline{(x_d/D)}_{rd} \approx 5Ro$ Possibly of more practical interest is the maximum length a vortex ring can travel before it has entirely decayed. This maximum decay length is identified approximately by the dashed line in figure 6.3 given by $(x_d/D)^{max} = 10Ro^{1.06}$ such that, rounded, $(x_d/D)^{max} \approx 10Ro$ Similarly one can estimate a minimum decay length. This is identified approximately by the dotted line in figure 6.3 given by $(x_d/D)^{min} = 1.5Ro^{1.06}$ or, rounded, $(x_d/D)^{min} \approx 1.5Ro$

It is emphasized that the least-squares fit of Eq. (6.1) interpolating the data (solid line) in figure 6.3 is not intended to imply the existence of a genuine power-law scaling. The interpolation procedure simply averages the data to yield a statistical, quantitative expression for the overall global trend within the parameter regimes considered. It is by no means certain that the data in the figure do collapse onto a single straight line. In fact the overall data distribution in figure 6.3 suggests, as one might expect, that the data level off for $Ro \to 0$ and $Ro \to \infty$. Nevertheless, note that the data fit in figure 6.3 extends over approximately two orders of magnitude in each of the two coordinate directions.

The scatter of the data in figure 6.3 is also quite large. However, there are many reasons that can help explaining the magnitude of the data scatter. We typically waited $10 - 20$ minutes between two successive experiments to ensure that the fluid in the tank had re-adopted solid-body rotation prior to ejecting the next vortex ring. However, we cannot exclude the possibility that, in some cases, there may still have been some residual fluid motion in the tank. This would evidently be detrimental to the vortex-ring stability implying an increased likelihood for a premature decay of the vortex ring. Furthermore, due to the nature of the problem it is evidently impossible to define a quantifiable, unique criterion that characterizes when a ring has completely decayed. Judging this necessarily involves a degree of uncertainty that cannot be resolved even if sophisticated measurement techniques, such as Particle-Image Velocimetry (PIV), were used. Finally, figure 6.3 does not resolve any potentially existing Reynolds-number effects. All discussed errors are likely to tend to result in under estimates for the decay length. However, the large number of data points contained in figure 6.3 ensures that, within the Rossby and Reynolds number regimes considered, Eq. (6.1) should represent a robust statistical expressions for the overall global trend for the mean decay length with associated mean deviations and estimated maximum and minimum decay lengths as discussed above.

6.4 Discussion and conclusion

We include with a brief comment concerning the possible physical mechanism that results in the reduced decay length of vortex rings in rotating fluids. Our observations have revealed the existence of a strong secondary Coriolis-induced cyclonic swirling flow behind the rings. The existence of the wake swirl can be inferred in figure 6.4 from the helical dye streakline identified in the photo

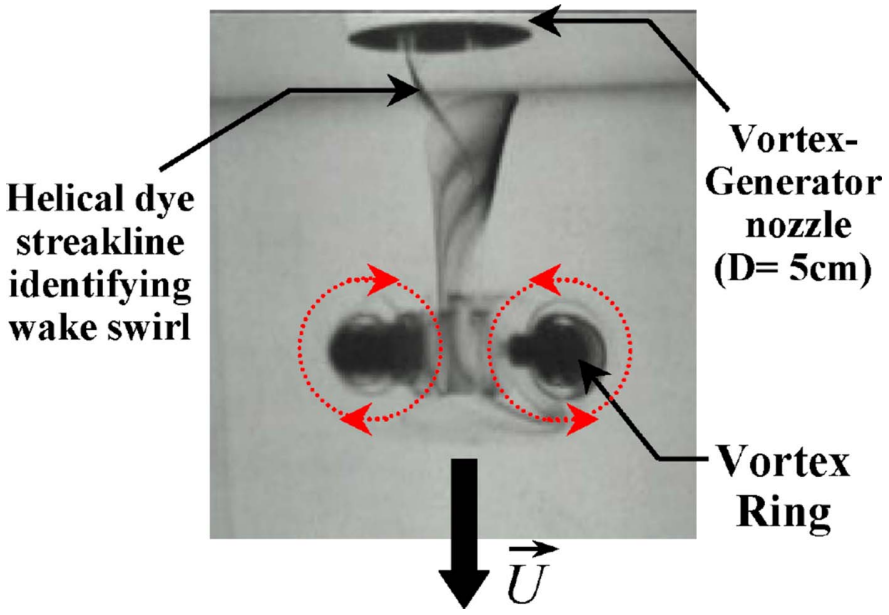

Figure 6.4: Photograph of vortex ring propagating in rotating system.

and it has previously been briefly commented on in Verzicco *et al.* (1996). The necessity for the existence of this cyclonic wake swirl follows from considering the local flow field around the core of the vortex ring as identified by the dotted lines with superposed arrow heads in figure 6.4. The ring propagates with velocity $\vec{U}$ downwards. Just upstream behind the ring the local flow velocity, $\vec{v}$, of the fluid swirling around the vortex-ring core is directed inwards, i.e. towards the axis of symmetry as indicated in figure 6.4. The vector of the rotational velocity, $\vec{\Omega}$, points upwards, i.e. it points in the opposite direction of $\vec{U}$ (compare 6.1). The Coriolis force associated with the local flow velocity, $\vec{v}$, is given by $F_C = -2\vec{\Omega}\times\vec{v}$. Hence, Coriolis forces are oriented such that $\vec{\Omega}$ and $\vec{v}$ induce a wake swirl that has the same sense of rotation as the turntable. Thus, in agreement with the observations the wake swirl is expected to be cyclonic. For reasons analogous to those establishing the cyclonic wake swirl there must exist a Coriolis-induced anticyclonic swirl ahead of the rings. The cyclonic wake swirl together with the anticyclonic swirl ahead of the rings will result in strong net torsional shear forces

acting on the vortex rings in the horizontal $x - y$ plane. It can be anticipated that this torsional shear will be detrimental to the stability of the vortex rings. The intensity of the swirling flows increases with the rotation rate $\vec{\Omega}$. Hence, the torsional shear forces increase with, $\vec{\Omega}$ and, thus, with decreasing Rossby number. It appears plausible to conclude that the torsional shear represents one of the main physical mechanism advancing the vortex-ring decay. Verzicco *et al.* (1996) remark (see p. 229 and p. 232) that the anitcyclone ahead of the ring is associated with a high-pressure region while the cyclone at its rear results in a low-pressure region. They observed that the high pressure ahead of the ring establishes a strong depression at its front. This may result in further detrimental effects as regards the stability of the vortex ring. However, in order to determine the consequences of the ring distortion and the exact effects of the torsional shear, with the ultimate goal to establish the details of the overall decay process of the rings, it is evidently required to perform detailed PIV measurements, computational studies and a theoretical stability analysis in the future.

In conclusion we emphasize once again that the interpolation of the data in figure 6.3 is not intended to suggest the existence of a genuine power-law scaling with its associated implications. The data interpolation of power-law type in the figure simply averages the data to yield a quantitative expression that roughly summarizes the overall global trend. This trend undoubtedly exists for figure 6.3 where the data extend over more than two orders of magnitude in both coordinate directions. Despite the fact that a proper power-law scaling may not exist an interpolation of the data by means of a power-law function nevertheless remains a valid averaging technique to reveal a mean statistical trend. For the data in figure 6.3 the interpolation of the data has yielded a result that can be of practical use to obtain rough estimates of the minimum, the mean and the maximum distances that nozzle-generated vortex rings can propagate

through the rotating fluid before they have completely decayed. This represents an entirely new result. However, the expressions stated should not be used to draw any further reaching inferences.

CHAPTER 7

PIV field measurements

7.1 Introduction

Here we present the results from the PIV acquisition, the parameters and number of samples for which are presented in table 4.2. Additionally some basic error quantification is presented (c.f. section 7.2). In this acquisition the traverse was driven under open-loop control (c.f. section 4.1) and so followed the same path for each run. As such, we are able to construct statistical velocity fields for the average vortex ring, at each point in time. It is these results and their derived measures that will be considered here.

Throughout this chapter the data presented provide data extracted from means of $\sim$ 400 vortex runs. This enables us to discuss trends that occur for a given generation condition, without random effects being present, data which has never before been presented experimentally for vortex rings. Furthermore, we also judiciously use the standard deviation and range of the data acquired mainly to provide estimations for the validity of our measurements, but also, occasionally to show how the set of vortex rings varies across the $\sim$ 400 generations.

As the vortex ring does not always follow the same path, it does not remain

in the same position within the frame throughout the entire run. To account for this, a sub-pixel shift to position the vortex ring in the centre of the frame was employed as part of the general data-correction procedure, c.f. chapter 5.

Table 7.1, displays the parameters pertinent to each vortex ring and some associated non-dimensional numbers. These parameters are attributed to a given vortex ring through a condition code (which shall be used to identify given conditions from here on), also listed in table 7.1. As continual reference to table 7.1 shall be made throughout this chapter, a detachable copy of this has been made available on the inside back cover of this document.

Code	Ω RPM	$\overline{U_o}$ m/s	L_o/D_o	δ_0/D_0	Re_J	Re_Γ	Ro_D	Ro_Γ
A	0	0.499	1.8	0.17406	22403	21354	∞	∞
B	0	0.1	1.8	0.24769	4483	4144	∞	∞
C	0	0.497	0.6	0.14473	7461	9638	∞	∞
E	3	0.499	1.8	0.24864	22403	14308	14	3332
F	3	0.1	1.8	0.16545	4483	2688	3	706
G	3	0.497	0.6	0.21844	7461	7627	14	2216
H	-3	0.1	1.8	0.16752	4483	2980	-3	-785
I	6	0.499	1.8	0.12953	22403	11731	7	1474
J	6	0.1	1.8	0.21858	4483	3144	1	449
K	6	0.497	0.6	0.10459	7461	7181	7	1242

Table 7.1: Table of statistical run conditions - non-dimensional numbers

In addition to the non-dimensional numbers previously used for classifying vortex rings, we introduce the Rossby number based upon eddy timescale Ro_Γ, equation (7.1). We feel this ratio of timescales better reflects the dynamics of the flow than those presented previously (Verzicco *et al.*, 1996), as it encompasses all generation parameters in the estimation of the fluid inertia, much the same as Re_Γ (c.f. section 3.2.3). The definition of Rossby number presented in section 3.2.4 was perfectly adequate for the studies in which it was used, as the vortex ring conditions were varied by changing only $\overline{U_o}$ and Ω. Hence in that case, the form

of Ro_D captures well the measure of both fluid inertia and rotation rate. In our study however, we also vary the length, L_o, which using the prior Rossby number Ro_D, would result in conditions of different inertia with the same Rossby number, as shown by conditions E and G, table 7.1. Although this formulation of Rossby number has not been used previously, the concept of the Eddy time scale has, Shariff *et al.* (1994) used a similar formulation for the characteristic timescale in their numerical simulations.

$$Ro_\Gamma = \frac{\Gamma_0}{D_0^2 \Omega} \tag{7.1}$$

To this end, the parameters we consider are non-dimensionalised by the vortex ring diameter and eddy timescale, examples of this are given in equation 7.2.

$$x^+ = x/D_0 \tag{7.2a}$$

$$t^+ = t\Gamma_0/D_0^2 \tag{7.2b}$$

$$u^+ = uD_0/\Gamma_0 \tag{7.2c}$$

$$\Gamma^+ = \Gamma/\Gamma_0 \tag{7.2d}$$

For interest, some initial parameters, measured from the PIV data are presented in table 7.2, alongside this are plotted Ro_Γ and the slug flow circulation Γ_{slug} for comparison. Upon the basis of tables 7.2 and 7.1 we can make some qualitative remarks as to the effect of varying our experimental parameters. Comparing the non-rotating data (conditions A, B and C), we see that if either the outlet velocity ($\overline{U_o}$) or the stroke length (L_o/D_o) are decreased, then the vortex ring circulation is also decreased. It may also be seen that these measured cir-

culations are reasonably well approximated by the slug flow model, Γ_{slug}. For condition C, the greatest difference between the slug flow model and the measured circulation is observed. It is believed (from high speed imaging of the piston trajectory) that this is due to belt stretch on the piston drive leading to a velocity profile different to that applied by the motor controller. This further emphasises the benefit of defining representative numbers from measurements of the fluid flow, over generation parameters, which may well be more difficult to accurately quantify.

Further to this, we find that the initial vortex ring diameter (D_0) remains constant for constant stroke length (L_o), and varying $\overline{U_o}$. This is indicated by comparison of conditions A and B. For constant $\overline{U_o}$ and decreased L_o/D_o however, it is seen that the vortex ring diameter decreases, as indicated by comparison of conditions A and C.

Concerning the initial vortex core diameter (δ_0), we see that this is a function of both $\overline{U_o}$ and L_o/D_o. Decreasing $\overline{U_o}$ for fixed L_o/D_o increases δ_0, conversely decreasing L_o/D_o, for fixed $\overline{U_o}$ results in a decreased δ_0. Table 7.1 shows the trend for initial slenderness ratio (δ_0/D_0) to follow the same trend as δ_0.

The comparisons for rotation rate are however less straightforward. Some simple trends may be observed, however to draw any meaningful conclusions, a parametric study is required across much wider ranges of stroke length, piston speed and rotation rate than have been presented here. Such data was acquired in addition to that discussed in this work, 10 vortex runs were conducted for 4 values of stroke length, 4 values of piston speed and 5 values of rotation rate (including $0RPM$), making a total of 80 vortex generation conditions. This data is still pending processing and thus is not discussed further here.

The most appreciable trend with respect to rotation rate is with regards circulation. One sees that when background rotation is added to any of the

conditions, there is a decrease in Γ_0. For conditions E, F and H, we find that the slug flow model no longer provides a good estimate for Γ_0. For condition G however, the circulation has decreased sufficiently that Γ_{slug} now approximates Γ_0, however we believe that this is coincidence and a result of the belt stretch discussed earlier. Increasing the rotation rate further appears to have less of an effect on the circulation, with Γ_0 only decreasing appreciably for condition E, in fact for condition J, Γ_0 is even seen to increase slightly.

For the lower rotation rate case (conditions E through H), we see that across all conditions the circulation decreases and the vortex ring diameter increases. For conditions E and G we find the core diameter and slenderness ratio all increase, whereas for conditions F and H, the core diameter and slenderness ratio decrease. For conditions J and K, the circulation is roughly the same as for conditions F, H and G, whereas for condition I, Γ_0 is noticeably lower than condition E. This decrease is however small compared with that observed from A to E. The initial diameters of the vortex rings produced at high rotation rate are also decreased compared to that at the lower rotation rate; they are in fact decreased to roughly the same size as in the non-rotating case. The core diameters are also reduced (this time, even below that of the comparable non-rotating cases) the same is true of the slenderness ratio.

The test conditions described by tables 7.1 and 7.2 shall be discussed in this section. We consider the effects of Reynolds number, formation time and Rossby number quantitatively upon the time evolution of the global properties of the velocity field. We shall further consider the effect of these properties quantitatively upon the velocity field, by picking out key positions in the field and comparing the time evolution of velocity at those points, and finally, use the mean velocity fields to qualitatively describe phenomena occurring in the vortex ring velocity field.

Code	Ro_Γ	Γ_0 (m^2/s)	Γ_{slug} (m^2/s)	D_0 (mm)	δ_0 (mm)
A	∞	0.0214	0.0225	65.5	11.4
B	∞	0.0042	0.0045	65.4	16.2
C	∞	0.0097	0.0075	57.4	8.3
E	3332	0.0144	0.0225	70.3	17.5
F	706	0.0027	0.0045	66.2	10.9
G	2216	0.0077	0.0075	62.9	13.7
H	-785	0.003	0.0045	66.1	11.1
I	1474	0.0118	0.0225	67.7	8.8
J	449	0.0032	0.0045	63.4	13.9
K	1242	0.0072	0.0075	57.7	6

Table 7.2: Table of statistical run conditions - dimensional properties upon generation

As the PIV measurements cannot be guaranteed to coincide with the vortex ring axis, we consider a coordinate system defined by the light sheet. For this reason, we use a right handed Cartesian coordinate system, with $\hat{\mathbf{y}}$ coinciding with the axial direction, as indicated by figure 7.1.

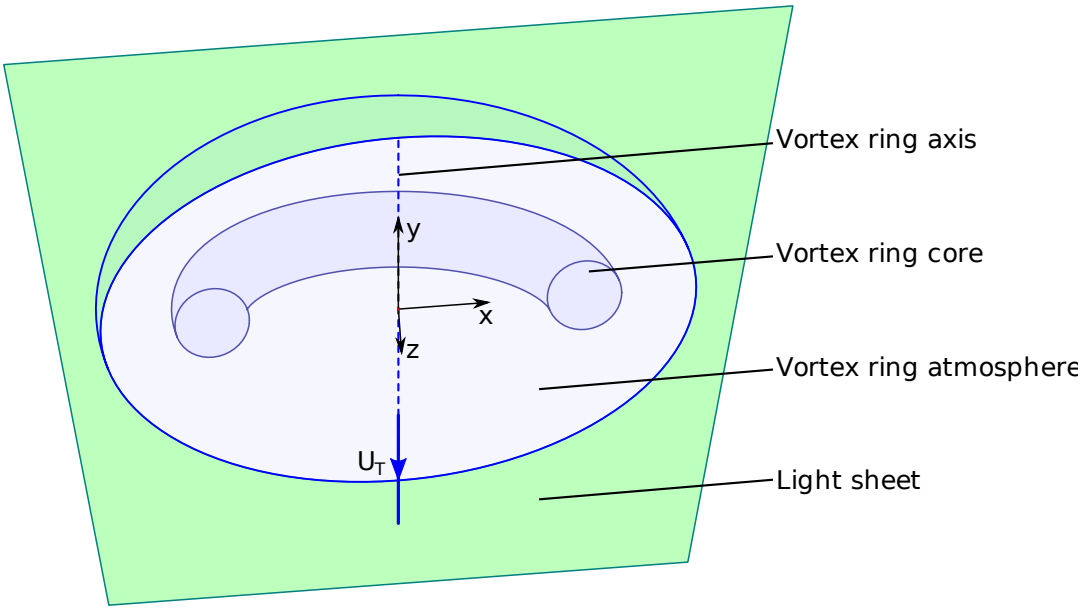

Figure 7.1: Illustration of PIV coordinate system

7.2 Basic error analysis

The following sections consider the time evolution of the velocity field and various vortex ring properties for the conditions outlined in table 7.1. The vortex ring properties considered are the 3D position of the ring-centre, the vortex ring diameter, core diameter, slenderness ratio, circulation and tilt. The final property, the tilt, provides a measure of the orientation of the vortex ring, i.e. the angle between the vortex core and the vortex generator axis.

In this section, we provide a basic estimation and quantification of the error for each condition, as only simple estimates are made, we tend to over-estimate the errors. The data discussed in this work considers the evolution of mean properties, or those extracted from mean velocity fields. The number of samples used in generating these means and so the means themselves vary with time. Because of this, the errors presented here are displayed as a function of time, t^+, in addition to this approximate errors are tabulated in table 7.3.

It must be stressed that the estimation of error here only considers random error, no account is made for any form of bias. A complete and rigorous error analysis has not been performed due to the complexity involved in estimation of the errors accrued during data processing stage. The errors arising due to adaptive multi-pass PIV processing are highly subjective to the specific processing settings chosen. Furthermore accurate estimation of the velocity field corrections imposed to account for errors arising due to the traversing of the SPIV system is not feasible, as stated in section 5.7.

The error estimation techniques used are based upon the assumption of a general long-term coherence of flow structure. As shown in the literature, the vortex ring exists across large time-scales and even at the high Reynolds numbers and intermediate Rossby numbers considered, retains a reasonable degree coherence,

c.f. sections 3.3.5, 3.3.6 and 3.4.1. It should be noted that prior measurements of circulation have shown step-wise transients in its time evolution. Although this differs to the steady state assumed, it will only act to increase the error estimated.

To this end, considering some property of the vortex ring $\zeta(t)$, we compute an estimator to this property $\hat{\zeta}(t)$ and from this estimator may then compute an estimate of the error of this property $\varepsilon_\zeta(t) = \left|\zeta - \hat{\zeta}\right|$. It may be immediately appreciated that this method is very similar to that which is used for the statistical filtering of velocity vector fields, c.f. 2.3.4.1. A slight difference exists between the computation of the estimators for vector field filtering and that for error evaluation. In the case of error estimation described here, steadiness in time is assumed, therefore the estimator $\hat{\zeta}(t)$ is computed from a neighbourhood of size 4 in time using the median. Equation (7.3) indicates the extent of this neighbourhood. The neighbourhood size was chosen as it provides a reasonable compromise between large sample size and small time and the median used due to its tolerance of outliers.

$$\hat{\zeta}(t) = f\left(\zeta(t-2), \zeta(t-1), \zeta(t+1), \zeta(t+2)\right) \tag{7.3}$$

In the case of the velocity fields, error are computed in a similar fashion, however as there are some 85,000 velocity vectors per image minor modifications are necessary. To account for this, an error estimate is computed for the full field at each point in time. The mean of this error field is then used to provide an overall estimate velocity of error at the time considered, one can see the time evolution of this error for condition A in figure 7.2a.

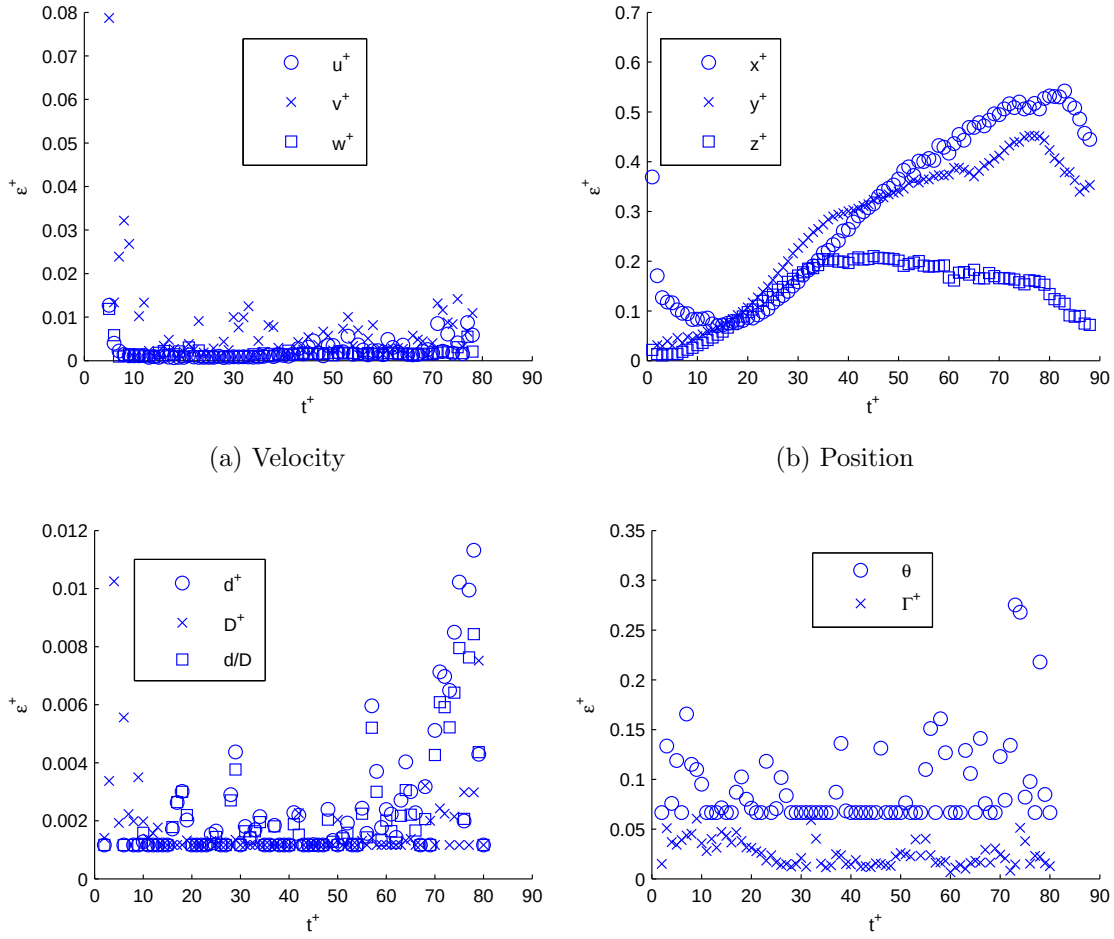

(a) Velocity

(b) Position

(c) Core/ring diameter

(d) Circulation and tilt

Figure 7.2: Condition A

The vortex ring position, tilt, core and ring diameter are all derived from the measurement of the location of the extremity of the vortex core, as described in section 5.5.3.2. As the centroiding algorithm used is weighted and iterative, $0.1VMU$ provides a conservative estimate for the minimum error expected (for the vortex ring tilt and slenderness ratio, an equivalent minimum error is computed using D_0). This minimum expected error is used as a lower threshold, which is quite apparent when considering the vortex ring/core diameter plots, figure 7.2c.

Figures 7.2b-7.2d further provide error estimates of the remaining parameters considered, groupings are made based upon magnitude of error. Similar plots are available for other conditions in Appendix C. An overview of the error time-series was also computed to provide an order of magnitude error for each property of each condition, which was done by taking the mean of the time-series of values. The results of this are tabulated in table 7.3.

	A	B	C	E	F	G	H	I	J	K
u^+	0.002	0.001	0.001	0.002	0.001	0.001	0.001	0.002	0.002	0.002
v^+	0.007	0.002	0.005	0.006	0.002	0.005	0.002	0.006	0.004	0.004
w^+	0.002	0.001	0.001	0.002	0.001	0.001	0.001	0.002	0.001	0.002
x^+	0.303	0.266	0.378	0.283	0.211	0.328	0.202	0.246	0.287	0.258
y^+	0.272	0.192	0.422	0.338	0.139	0.394	0.135	0.316	0.257	0.216
z^+	0.138	0.184	0.117	0.180	0.052	0.153	0.048	0.140	0.035	0.096
d^+	0.002	0.002	0.002	0.003	0.026	0.003	0.003	0.003	0.004	0.003
δ^+	0.002	0.005	0.002	0.002	0.007	0.002	0.009	0.005	0.010	0.004
δ/D	0.002	0.005	0.002	0.002	0.006	0.003	0.008	0.005	0.009	0.004
θ^+	0.091	0.126	0.101	0.148	0.287	0.205	0.256	0.243	0.130	0.286
Γ^+	0.025	0.058	0.095	0.055	0.052	0.126	0.066	0.073	0.051	0.060

Table 7.3: Summary of error estimates

7.3 Basic properties

Here we consider how the most basic properties of the vortex ring evolve over time. For this we consider the 3D position of the vortex ring in the tank, as well as its diameter, tilt, core size and slenderness ratio. Here the tilt refers to the orientation of the vortex ring in the frame (c.f. section 7.3.6)As the calculation of the 3D core position is necessary as part of the velocity field corrections described in section 5.6, the mean of the pre-calculated data from each run is used. For each of these parameters, we also present plots to illustrate the applicability of our use of the mean as the estimator for this data. The other parameters are derived from velocity fields and so are computed from the mean velocity field.

For each parameter discussed, we make a comparison for constant rotation rate, e.g. a given parameter for all the conditions where $\Omega = 3RPM$. Further to this we compare conditions whose generation parameters are the same, i.e. a comparison is made for $U_p = 500mm/s$ and $L_o = 90mm$ across all rotation rates. It should be noted, that in all cases we include condition H in the $3RPM$ grouping, despite the rotation rate for this condition being $-3RPM$. This is because condition H was used to highlight that the effects observed were present for both clockwise and anti-clockwise rotation.

7.3.1 Statistical relevance of vortex ring position

Here we consider the time evolution of simple vortex ring properties; 3D position, diameter, angle of tilt, core size and slenderness ratio. Knowledge of the 3D vortex ring position is necessitated by the corrections discussed in sections 5.5 and 5.6 and so estimations of this trajectory are available for all ~ 400 vortex ring runs. From this, statistics are computed, which are shown in figure 7.3 for condition A. The mean, standard deviation, σ and the range of data are plotted for time and 3D position. The trends described here are reasonably representative of the data for all conditions, which, for completeness, are presented in appendix B.

Consider first figure 7.3a, which plots the variation of acquisition time with frame number. We see in this plot that the standard deviation is effectively zero, as is the range. This is indicated by the fact that all curves effectively lie on top of one another. This implies that the timing accuracy of the PIV measurement was very high and for this reason, we will use the time t as our comparison between conditions.

Consider next figure 7.3b, the increase in x indicates that the vortex ring moves right in the frame, away from the axis of symmetry. The increasing separation of the $\bar{x} \pm \sigma$ curves from the $\bar{x}$ curve implies that the scatter of measured

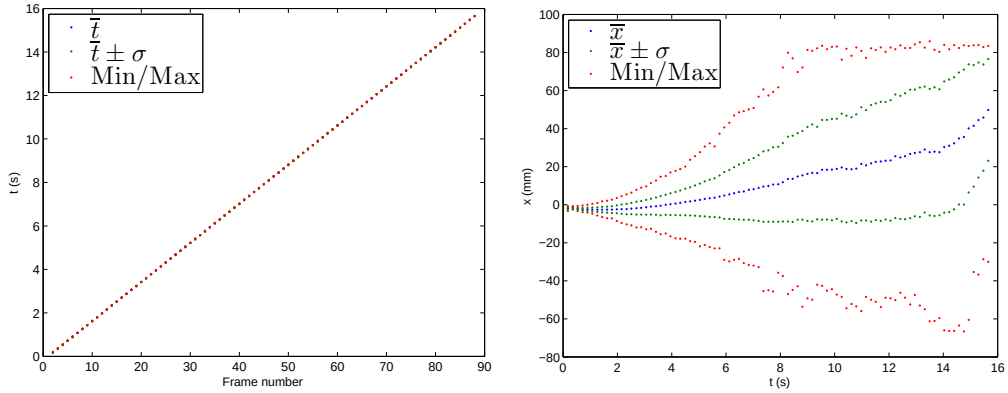

(a) t

(b) x

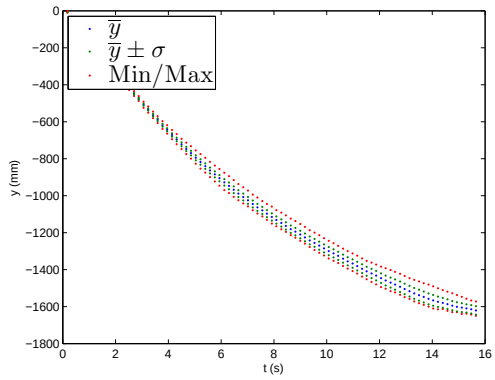

(c) y

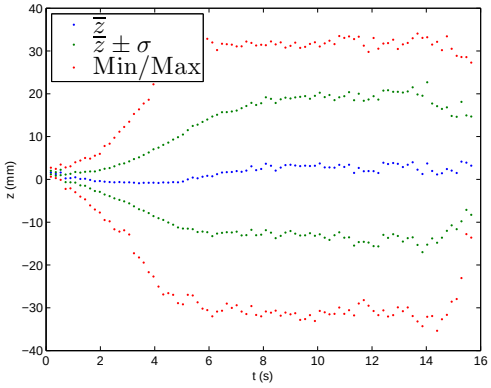

(d) z

Figure 7.3: Statistical vortex ring properties for condition A

vortex ring x positions increases with time. The actual position of these curves indicates the bounds for which the majority of the vortex rings lie within. The range of the vortex ring positions is also indicated by the min/max curves, corresponding to the minimum and maximum vortex ring position (from the ~ 400 runs) over time.

The statistical distributions for x at several points in time are also presented in figure 7.4. One can see that until relatively late in the vortex ring's evolution, the histogram of values shows a reasonable distribution, with no apparent skewness. Towards the end of the vortex ring evolution, the number of samples decreases significantly and the scatter of vortex ring position data increases significantly.

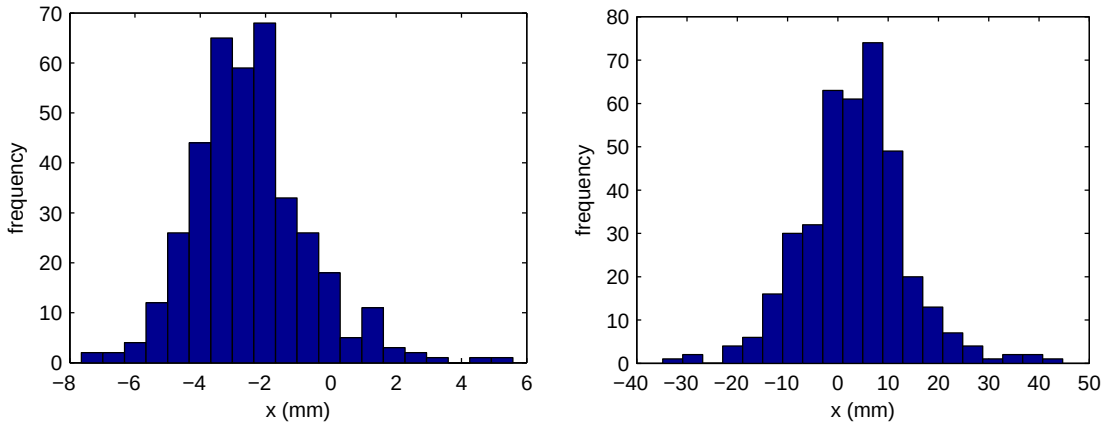

(a) $t = 1.62s$ (b) $t = 5.22s$

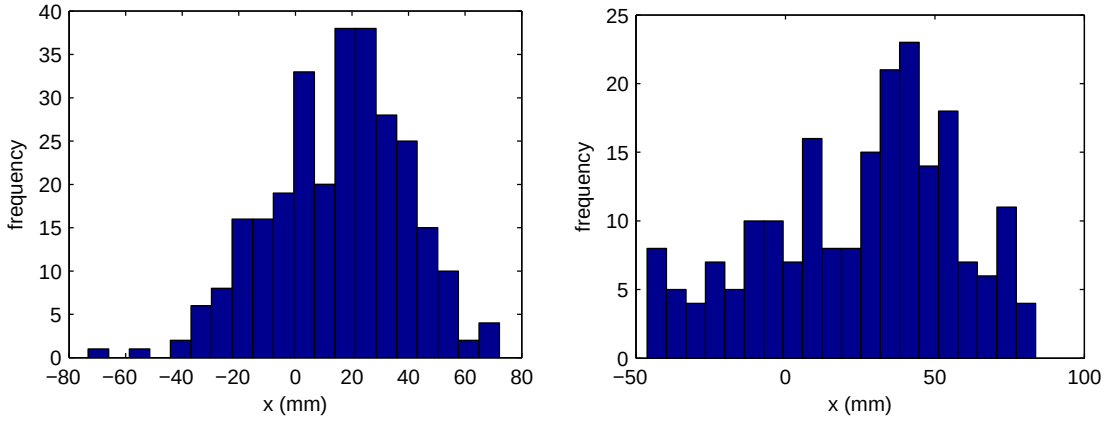

(c) $t = 8.81s$ (d) $t = 12.42s$

Figure 7.4: Statistical distribution of x for condition A

For the z position (figure 7.3d), we see that the mean remains ~ 0. The standard deviation and the range however both increase quickly with time. We see, importantly, that fairly quickly (after $t \sim 4s$) the minimum and maximum curves level off, this is also seen, although less markedly for the x direction plots, figure 7.3b, $t \sim 9s$. The point at which this levelling off occurs relates to the time at which the vortex ring moving away from the axis of symmetry (in the z direction) most quickly exceeds the maximum measurable z location, we term this, the measurement becoming "saturated."

For the case where a very small percentage of the vortex rings in the pop-

ulation leave the measurement area, this does not have a notable effect on the other statistics, as the population is sufficiently large. If however a significant proportion of the generated vortex rings do exceed the measurement limits, thus becoming saturated, then this will appear in the derived statistics. In our case, we are most concerned with the mean, as here we are really only using the standard deviation as a crude assessment for how how good an approximation to the "true" value the mean is.

It is important to note that shortly after the saturation in min/max we do find a knock-on reduction in growth of the standard deviation, indicating that the saturation has likely become statistically significant. It is worth noting that the standard deviations are much more sensitive to changes than the means and just because the standard deviation is affected, does not mean, necessarily that the mean will be. However despite this, it is apparent that a statistically representative portion of the population is no longer available for measurement and as such, caution should be used in interpreting the mean data for this property. This said, we see roughly equal growth rates of the minimum and maximum, $\bar{z} + \sigma$ and $\bar{z} - \sigma$, and the truncation of min and max occurring at approximately the same times, plus no major discontinuities are seen in the mean. All of this combined indicates that likely the mean is affected little by this truncation of the population.

The distance the vortex ring has translated from the nozzle is plotted in figure 7.3c. For this, we find that as time increases, both the standard deviation, the minimum and maximum curves increase. Throughout the measurement however, we find that both the standard deviation and the range (indicated by minimum subtracted from the maximum) are small in comparison to the measured value. Therefore, although there is obviously some variation in the y position of the vortex rings, it is noticeably small in comparison to the distances over which it

is measured.

7.3.2 Vortex ring x and z positions

Figures 7.5 and 7.6 provide comparisons across all conditions of the position of the vortex ring centre in the x and z directions respectively (where the curves plotted here are the means of $\sim$ 400 vortex generations). In these figures we produce two columns of plots, the left column shows a comparison between the differing vortex generation conditions at each rotation rate and the right column compares rotation rate for each generation condition. This arrangement shall be used throughout chapter 7.3. We find that in all cases the vortex ring is seen to move in both the x and z direction to some extent, few conclusions can be drawn about this motion however, as few consistent patterns are seen.

In both the x and z directions, we see that the vortex ring starts moving in one direction before reversing its direction of travel altogether. The curves of conditions F and H for the z direction (figure 7.6) are of particular interest, they show the same pattern as one another, however inverted. This is of interest, as conditions F and H were identical in all respects, except the direction of rotation. Upon closer inspection, one can see that in fact, condition H is the only rotating condition to begin its travel in the $-z$ direction. This is of particular interest, as it shows that the background rotation must be driving the dynamics of the trajectories seen, at least for this generation condition.

7.3.3 Vortex ring y position

The results presented in figure 7.7 present a much clearer picture than that seen for the x and z trajectories. We find reasonable collapse across the main sequence of vortex ring travel for all conditions. For the rotating conditions it is apparent

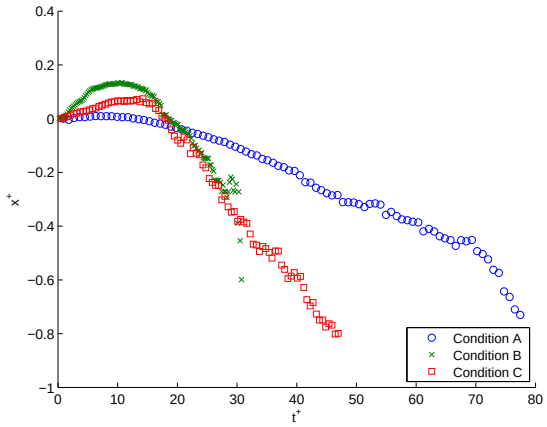

(a) $\Omega = 0RPM$

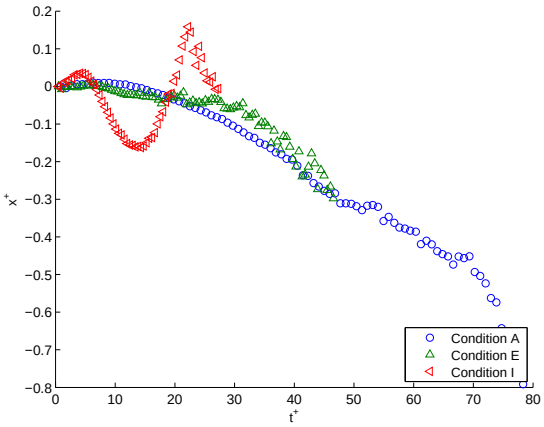

(b) $U_p = 0.5m/s, L_o = 90mm$

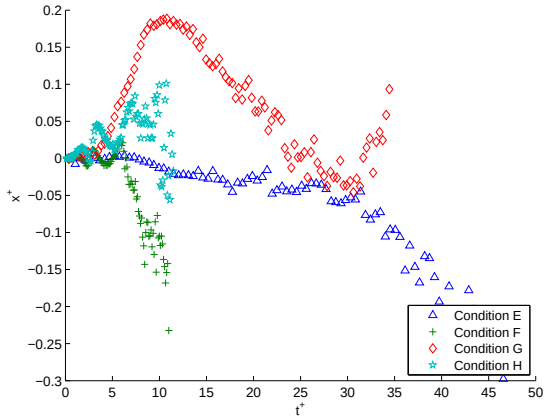

(c) $\Omega = 3RPM$

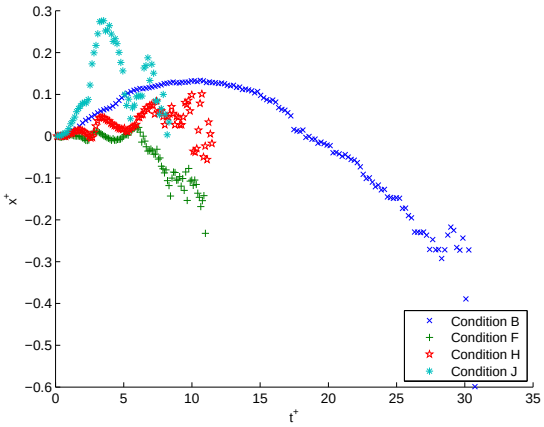

(d) $U_p = 0.1m/s, L_o = 90mm$

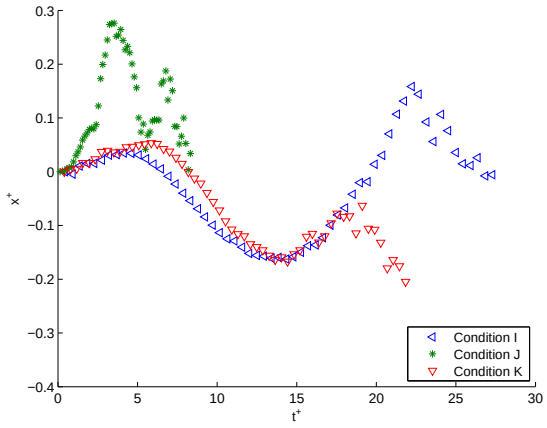

(e) $\Omega = 6RPM$

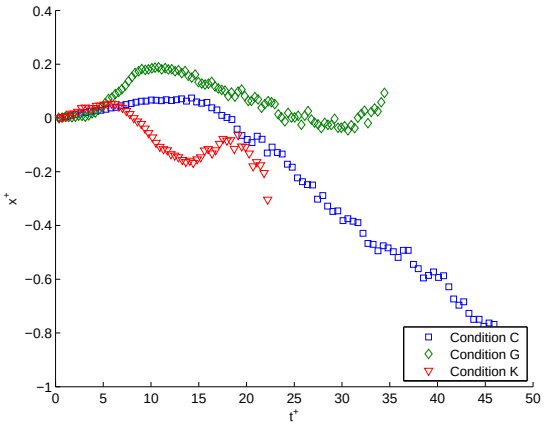

(f) $U_p = 0.5m/s, L_o = 30mm$

Figure 7.5: Comparison of vortex trajectory, x^+

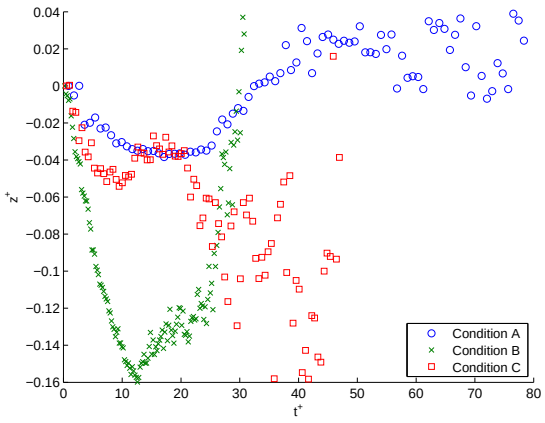

(a) $\Omega = 0RPM$

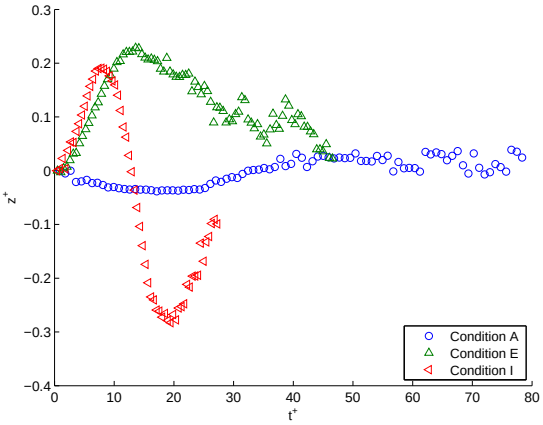

(b) $U_p = 0.5m/s, L_o = 90mm$

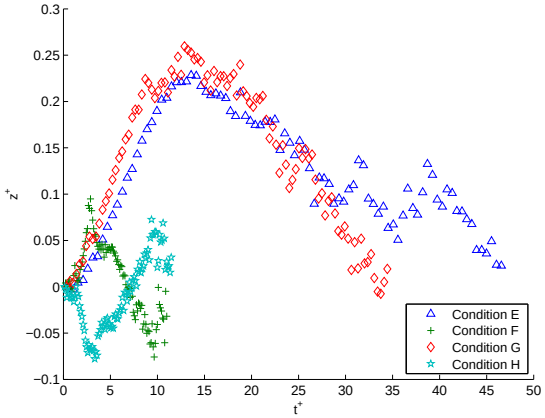

(c) $\Omega = 3RPM$

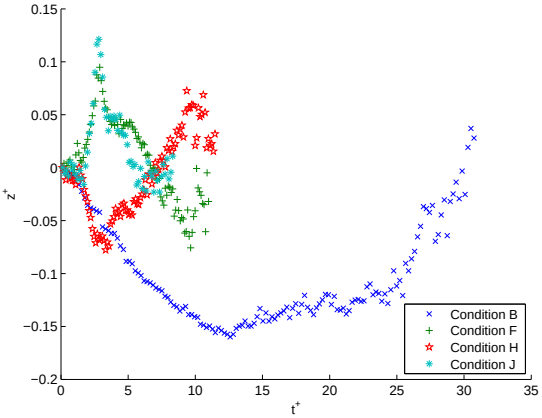

(d) $U_p = 0.1m/s, L_o = 90mm$

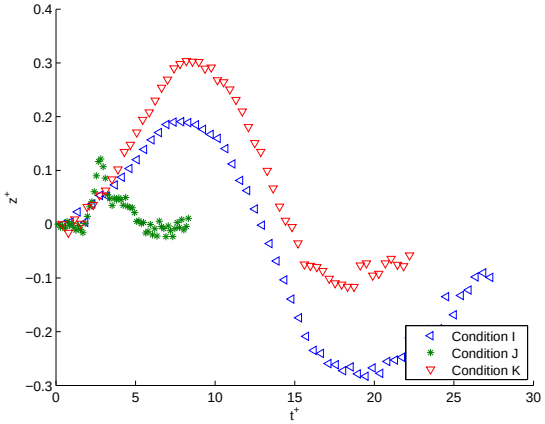

(e) $\Omega = 6RPM$

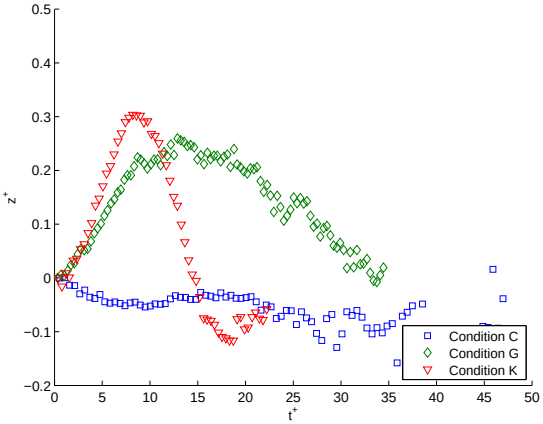

(f) $U_p = 0.5m/s, L_o = 30mm$

Figure 7.6: Comparison of vortex trajectory, z^+

that the gradient of the curves change towards the end of the vortex ring's life. The gradient change differs with rotation rate and marks a departure from the data collapse. We see that for the lower Rossby number conditions (where the effects of rotation are strongly felt) this change is quite significant, indicating a change in the dynamics of the behaviour of the vortex.

Figure 7.8 provides a comparison of the y-trajectory for raw data in world units, and that normalised by the initial ring diameter D_0, and the initial circulation Γ_0. Figure 7.8a shows that there is large variation between vortex rings generated with differing initial conditions, and further that there is significant variation between a vortex ring generated with and without background rotation. Figure 7.8b demonstrates that upon normalising the trajectory by initial ring diameter and the time by the eddy timescale, all the curves plotted collapse onto a single line. As mentioned previously, the use of the eddy timescale for non-dimensionalisation has been employed previously (Shariff *et al.*, 1994), however not for this purpose. The collapse presented in figure 7.8b is significant as it indicates a global scaling both for the rotating and non-rotating vortex rings not previously seen. Further to this, it indicates further the validity in the usage of Ro_Γ over Ro_D, as it indicates the importance of Γ_0 and D_0 in describing the dynamics.

7.3.4 Vortex ring diameter, D

The plots of vortex ring Diameter in figure 7.9 show a general trend of growth with time. The non-rotating conditions grow relatively steadily, condition B is the exception to this, showing sporadic growth and contraction.

It is quite noticeable from figures 7.9b, 7.9d and 7.9f, that the addition of background rotation causes the vortex rings to develop such that their diameter is larger than for their non-rotating counterparts. Further to this, it is seen that

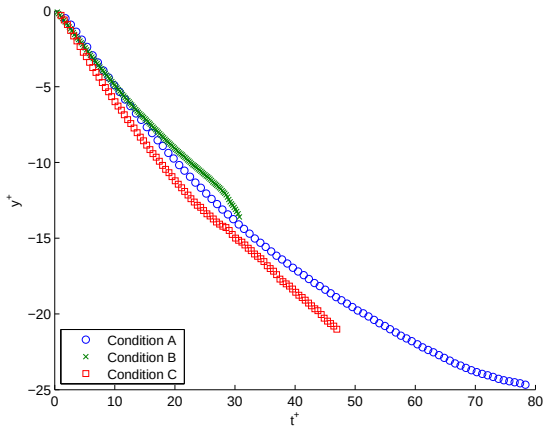

(a) $\Omega = 0RPM$

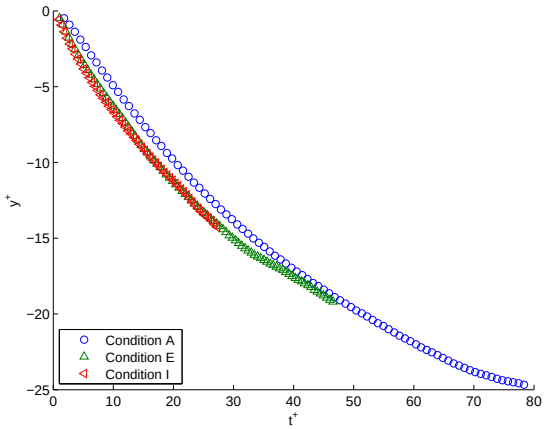

(b) $U_p = 0.5m/s, L_o = 90mm$

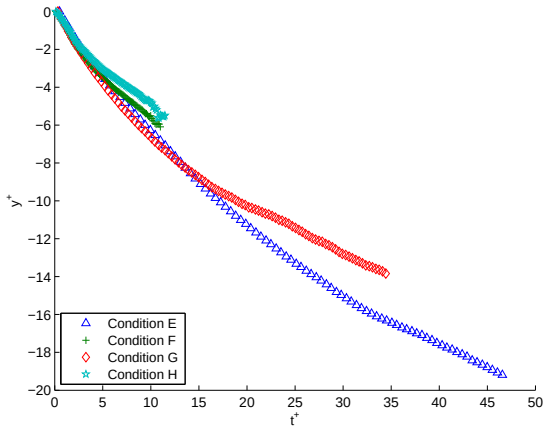

(c) $\Omega = 3RPM$

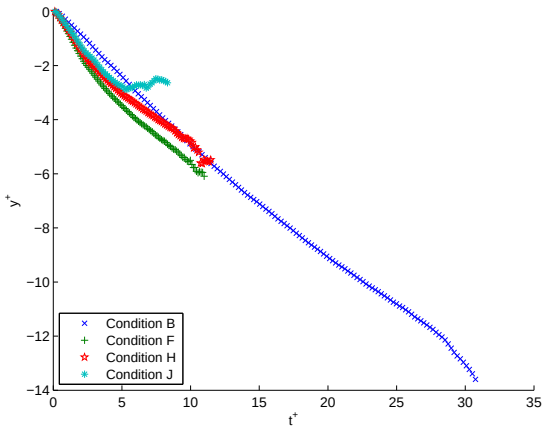

(d) $U_p = 0.1m/s, L_o = 90mm$

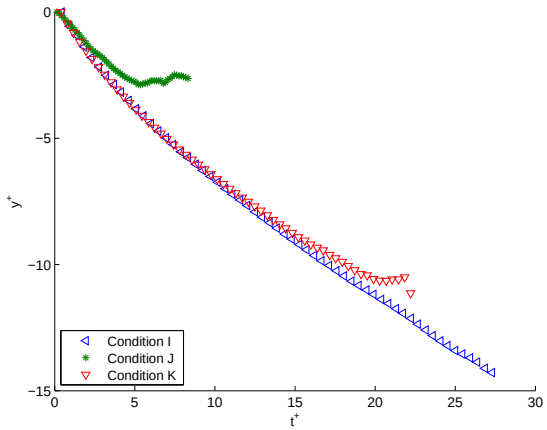

(e) $\Omega = 6RPM$

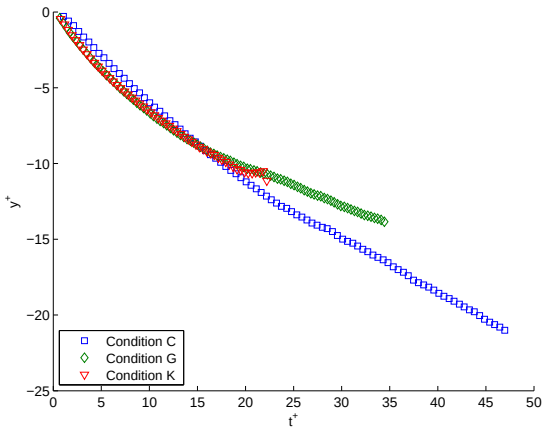

(f) $U_p = 0.5m/s, L_o = 30mm$

Figure 7.7: Comparison of vortex trajectory, y^+

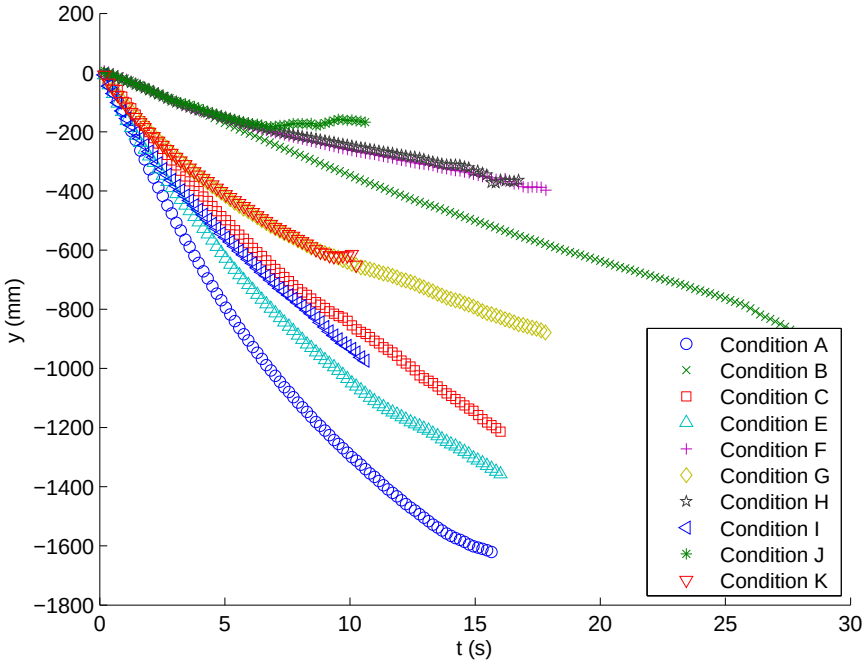

(a) Without normalisation

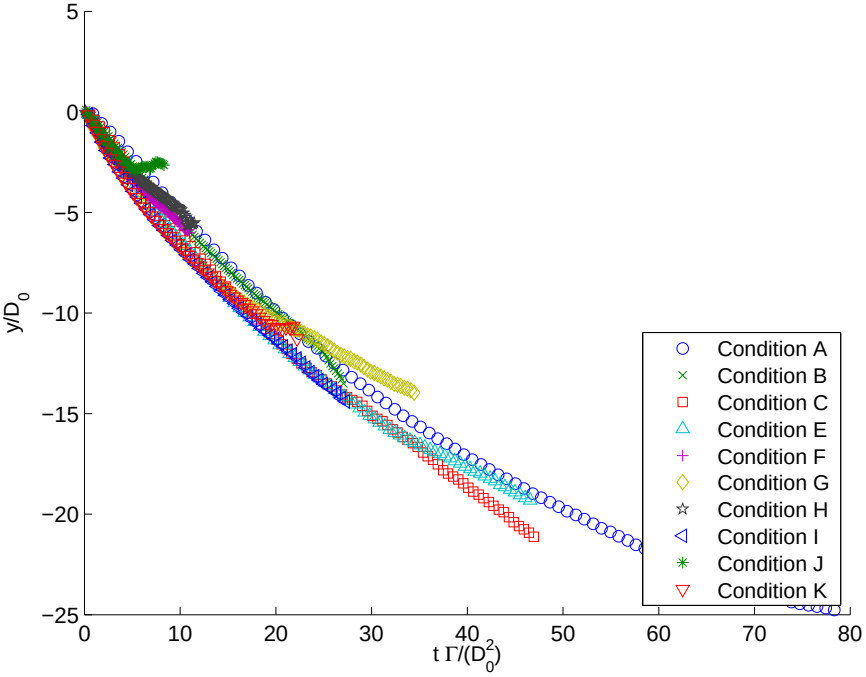

(b) With normalisation

Figure 7.8: All y data

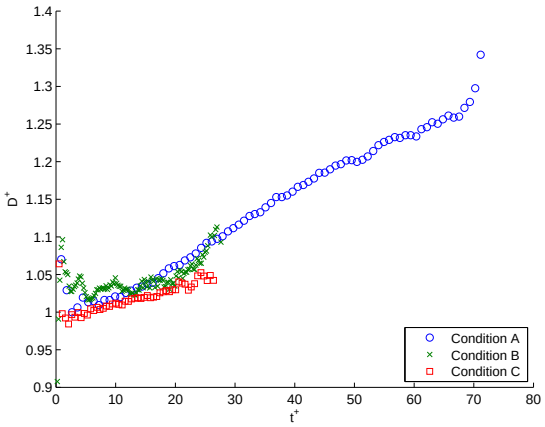

(a) $\Omega = 0RPM$

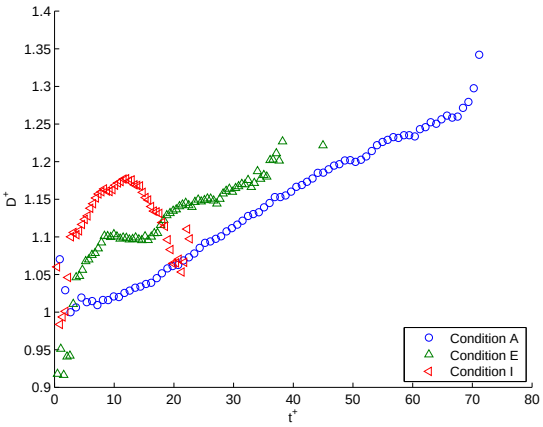

(b) $U_p = 0.5m/s, L_o = 90mm$

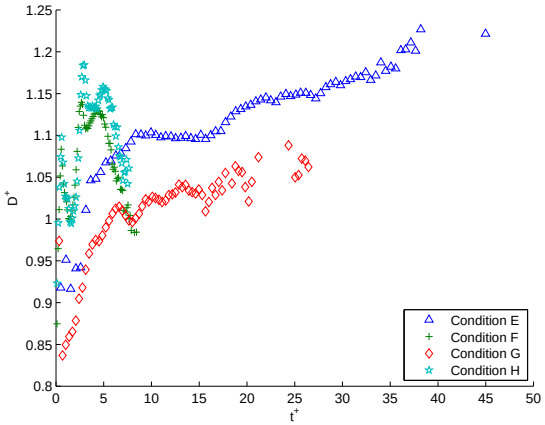

(c) $\Omega = 3RPM$

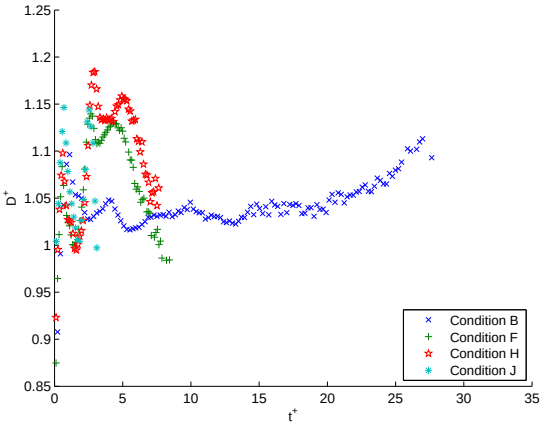

(d) $U_p = 0.1m/s, L_o = 90mm$

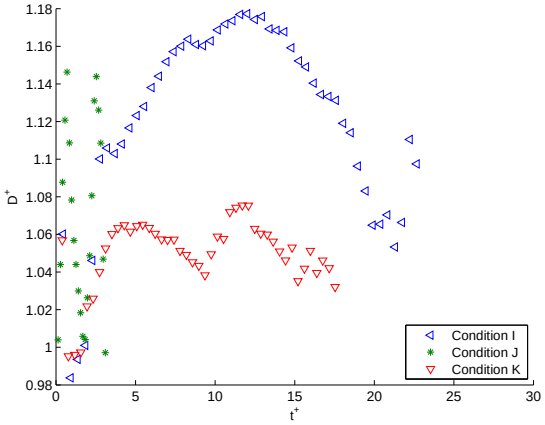

(e) $\Omega = 6RPM$

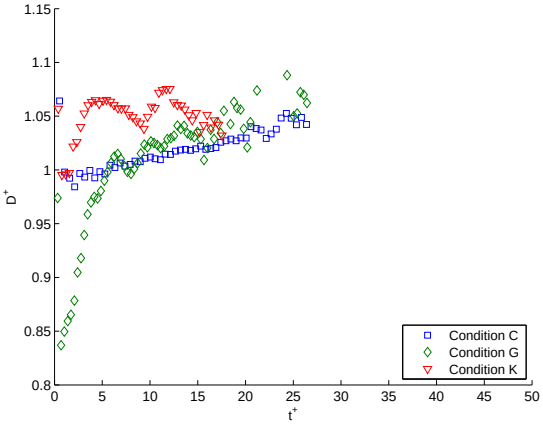

(f) $U_p = 0.5m/s, L_o = 30mm$

Figure 7.9: Comparison of vortex diameter, D^+

in their initial stages of development, the rotating vortex rings experience a rapid growth in diameter. For conditions F, H and J this is followed by a sharp decrease and subsequent increase (see figure 7.9d, $1 \lesssim t^+ \lesssim 4$).

We also see that with the exception of conditions E and G (the highest Rossby number rotating conditions, hence those feeling the effects of rotation the least), the vortex rings generated with background rotation tend to decrease in size, towards the end of their life while this is not the case for non-rotating vortex rings.

7.3.5 Vortex ring core diameter δ, and slenderness ratio δ/D

The vortex ring core diameter and its variation over time is plotted in figure 7.10. The general trend that may be seen across all conditions is for growth of the core over time. In the majority of cases, this growth is preceded by an initial contraction of the core shortly after vortex ring generation. In some cases however this data could not be reliably extracted from the rapidly changing velocity field near the nozzle, which impeded accurate extraction of the vortex ring's core size. As such, this data is not always available, for example, Condition A, $t^+ \lesssim 5$.

Conditions A, B and C show what is apparently continuous, approximately linear growth, with core growth most rapid for condition B, and slowest for condition A. This is similar to the results found found by Maxworthy (1972) who showed that increasing vortex ring Reynolds number led to turbulence and consequently reduced growth of core diameter.

Conditions F, H, I and K all show a two-stage approximately linear growth, the second stage of core growth showing increased gradient compared to the first. The initial value of δ^+ for these conditions was lower than for their non-rotating

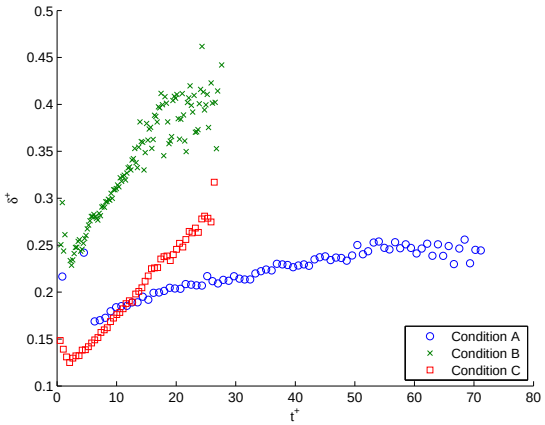

(a) $\Omega = 0RPM$

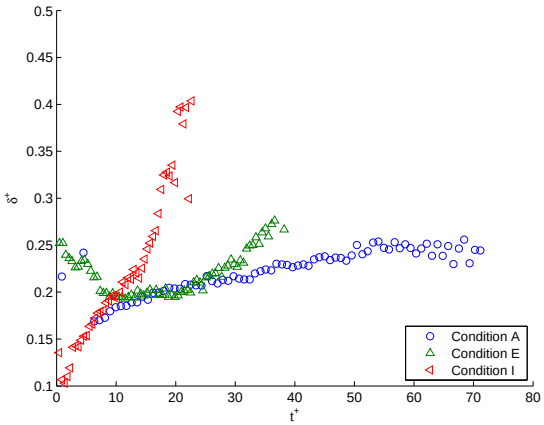

(b) $U_p = 0.5m/s, L_o = 90mm$

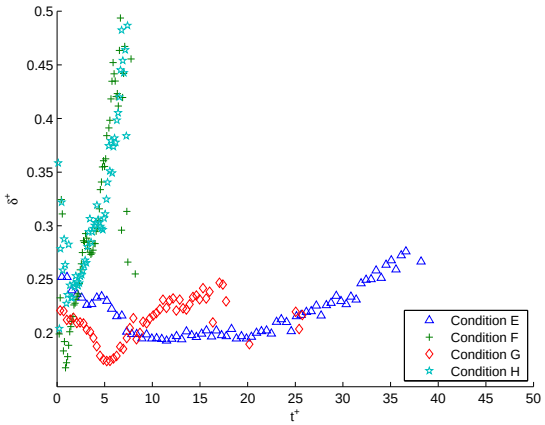

(c) $\Omega = 3RPM$

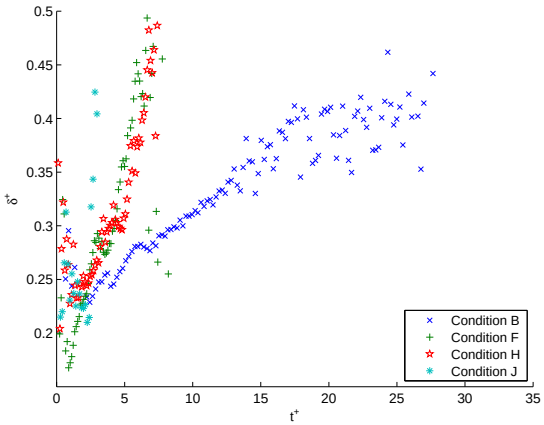

(d) $U_p = 0.1m/s, L_o = 90mm$

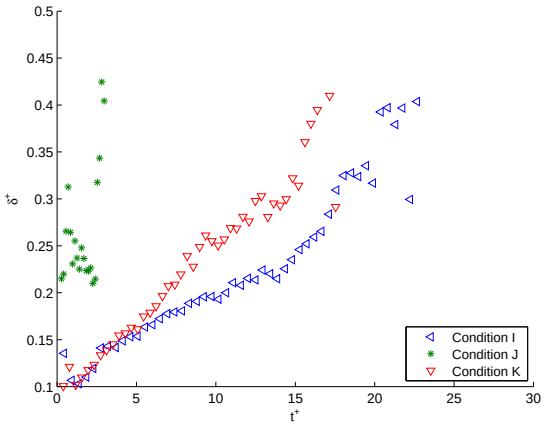

(e) $\Omega = 6RPM$

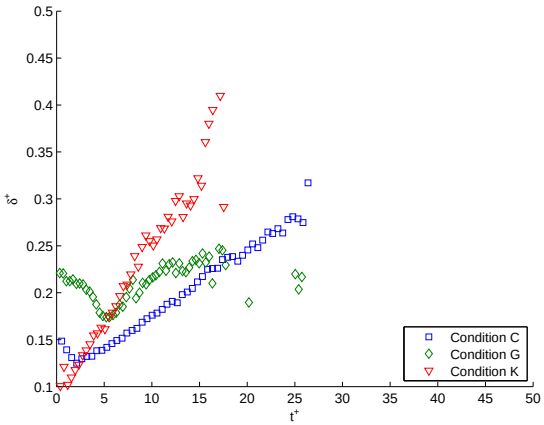

(f) $U_p = 0.5m/s, L_o = 30mm$

Figure 7.10: Comparison of vortex core diameter, δ^+

counterparts, but due to the rapid core growth, the core diameter quickly exceeds this.

For conditions E and G the initial core size is greater than for their non-rotating counterparts. Upon generation, a period of core contraction is seen until $t^+ \sim 10$ and $t^+ \sim 5$ for conditions E and G respectively. After this, the core begins to grow, later experiencing an increased growth rate. We also see, for all rotating conditions, at some point towards the late middle/early end of the vortex ring's life, there is an increase in the gradient of δ^+. It is interesting to note that this often occurs in time with a decrease in vortex ring diameter, thus is likely motivated by conservation of circulation.

Data showing the time evolution of the slenderness ratio is presented in figure 7.11. It is apparent that the variation of this derived property is driven more by the core diameter than the diameter of the vortex ring. The reason for this is that there is a much greater percentage change in the core diameter than in that of the ring diameter.

7.3.6 Vortex ring tilt, θ

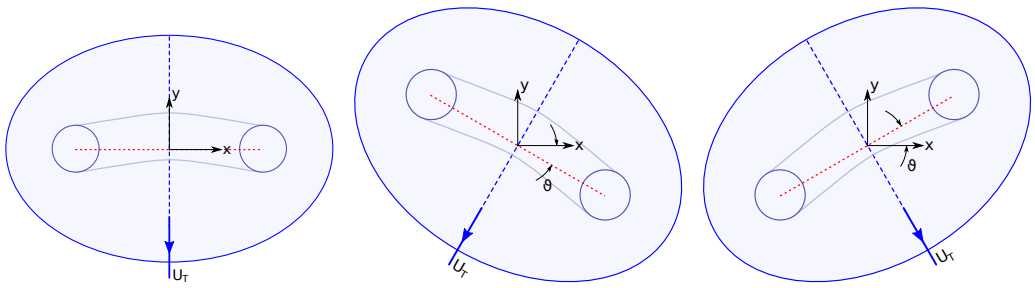

(a) $\theta = 90$ (b) $\theta < 90$ (c) $\theta > 90$

Figure 7.12: Illustration of the meaning of tilt, θ

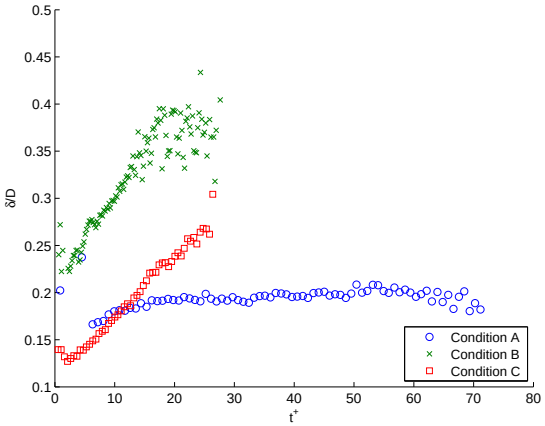

(a) $\Omega = 0RPM$

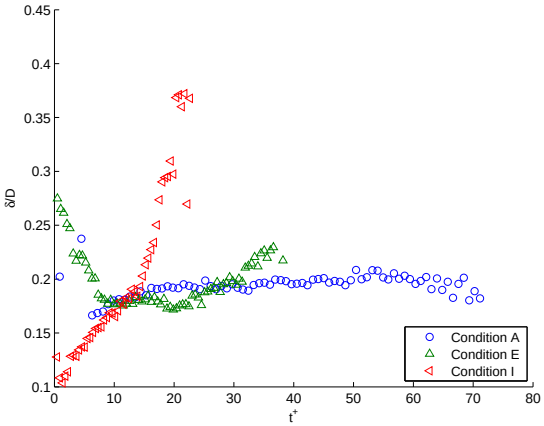

(b) $U_p = 0.5m/s, L_o = 90mm$

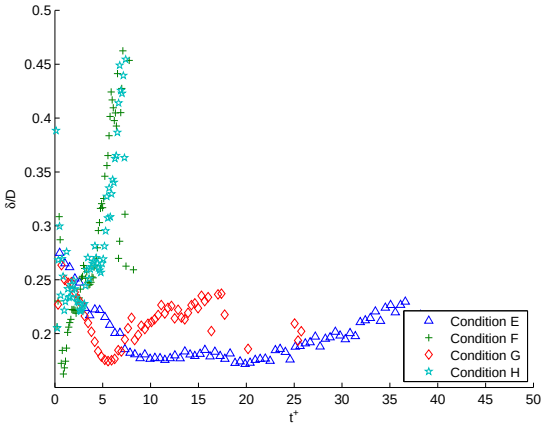

(c) $\Omega = 3RPM$

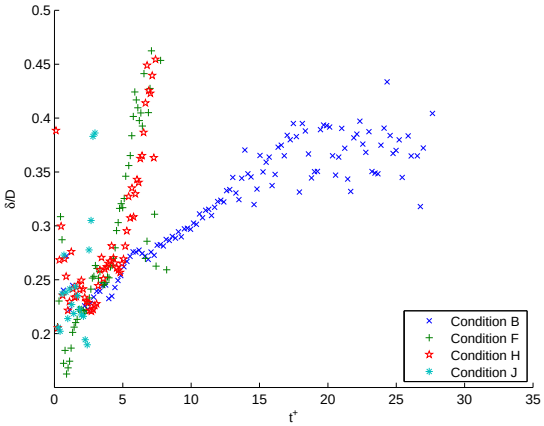

(d) $U_p = 0.1m/s, L_o = 90mm$

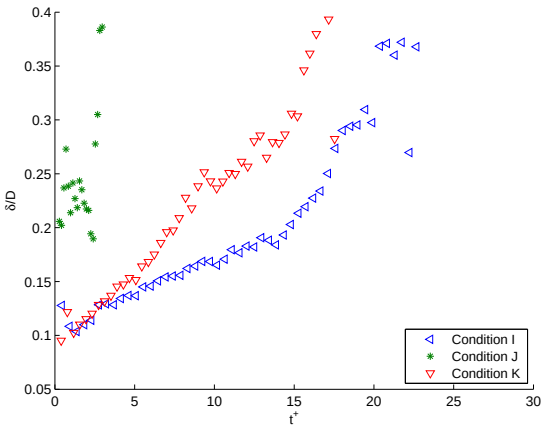

(e) $\Omega = 6RPM$

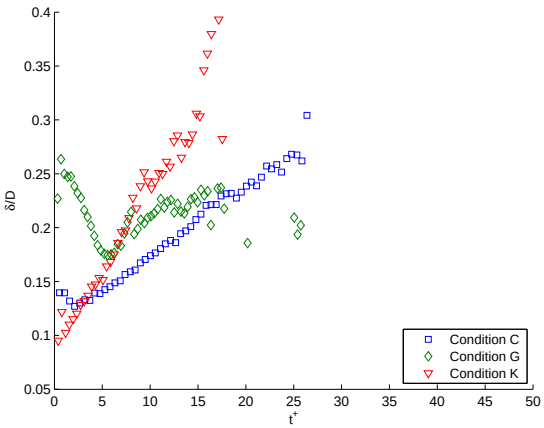

(f) $U_p = 0.5m/s, L_o = 30mm$

Figure 7.11: Comparison of vortex slenderness, δ/D

The angle made between a line drawn through the vortex ring cores, and the x-axis or tilt, θ is presented in figure 7.13 and illustrated by figure 7.12. Clockwise rotation of the vortex about the z-axis is indicated by $\theta < 90$ and corresponds to the vortex ring's direction of travel being tilted towards the negative x direction (figure 7.12b). Anti-clockwise rotation (about the z-axis) is indicated by $\theta > 90$, which conversely relates to the vortex ring's direction of travel being tilted towards the positive x direction (figure 7.12c).

Figures 7.13b, 7.13d and 7.13f show quite clearly that the both the magnitude and rate of change of this tipping is increased by increasing the rotation rate. We also see from figures 7.13a, 7.13c and 7.13e that decreasing inertia at a given rotation rate leads to an increase in the rate and magnitude of tip. Furthermore, all the figures indicate a distinct tendency toward $\theta > 90$, although some conditions rotate clockwise slightly to begin with, or rotate fully clockwise later in life, every condition does have a significant portion of time with an anti-clockwise tilt.

It is interesting to note the similarity between curves for conditions F and H in figure 7.13c, indicating the independence of tilt (about the axis considered, at least) from Ω. Also of interest is the general tendency for changes in θ to occur at the same time as changes in x^+. This is somewhat unsurprising, as the two properties are inherently linked by the definition of θ.

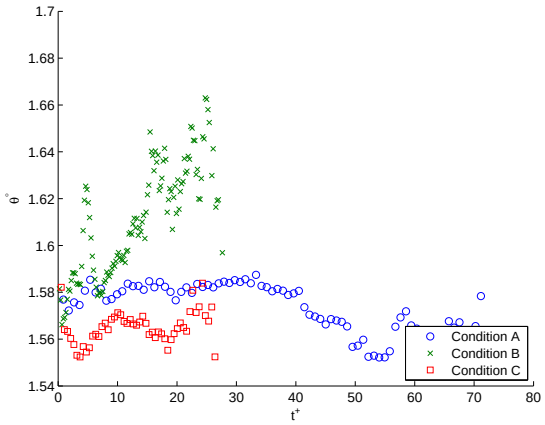

(a) $\Omega = 1RPM$

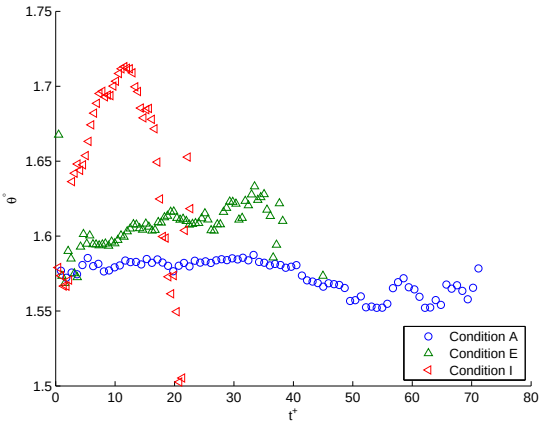

(b) $U_p = 0.5m/s, L_o = 90mm$

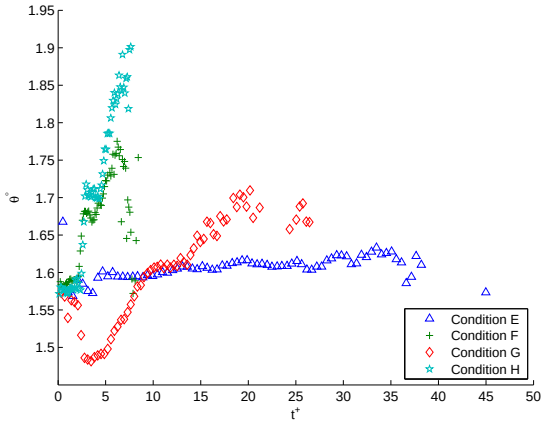

(c) $\Omega = 3RPM$

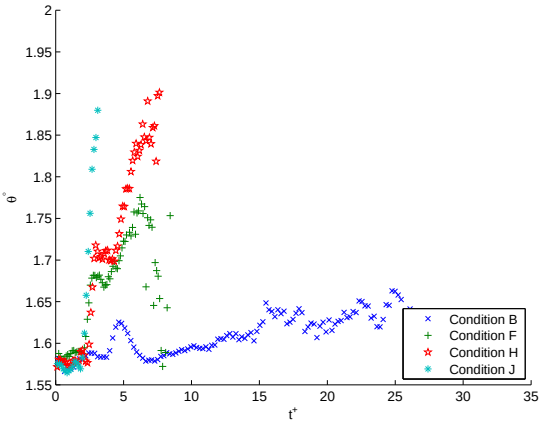

(d) $U_p = 0.1m/s, L_o = 90mm$

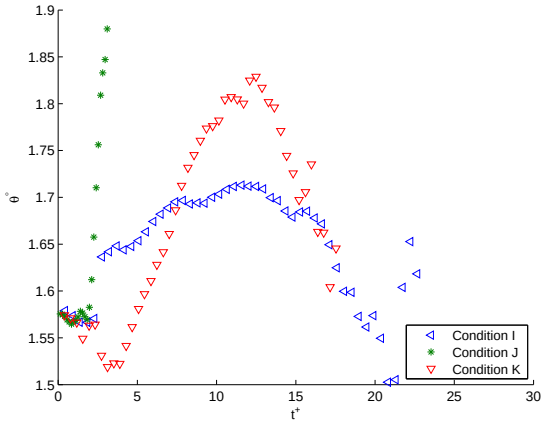

(e) $\Omega = 6RPM$

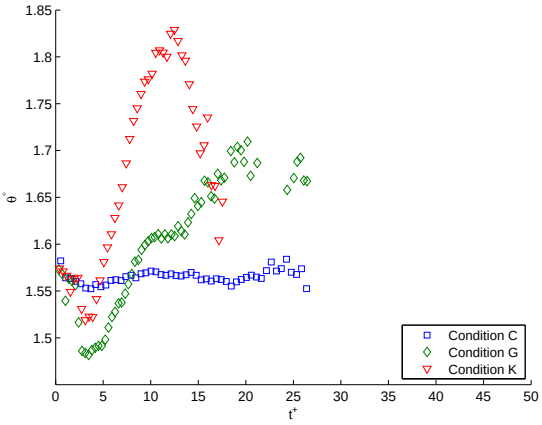

(f) $U_p = 0.5m/s, L_o = 30mm$

Figure 7.13: Comparison of vortex tilt, θ

7.3.7 Vortex ring circulation, Γ

The circulation data presented here was computed from the mean velocity fields according to equation 3.5b. Circulation was calculated for both core left and core right. For each core, the integral was evaluated along the largest rectangular path possible for the given data. For both cores, one edge of the box was set to lie in the centre of the vortex ring, see figure 7.14.

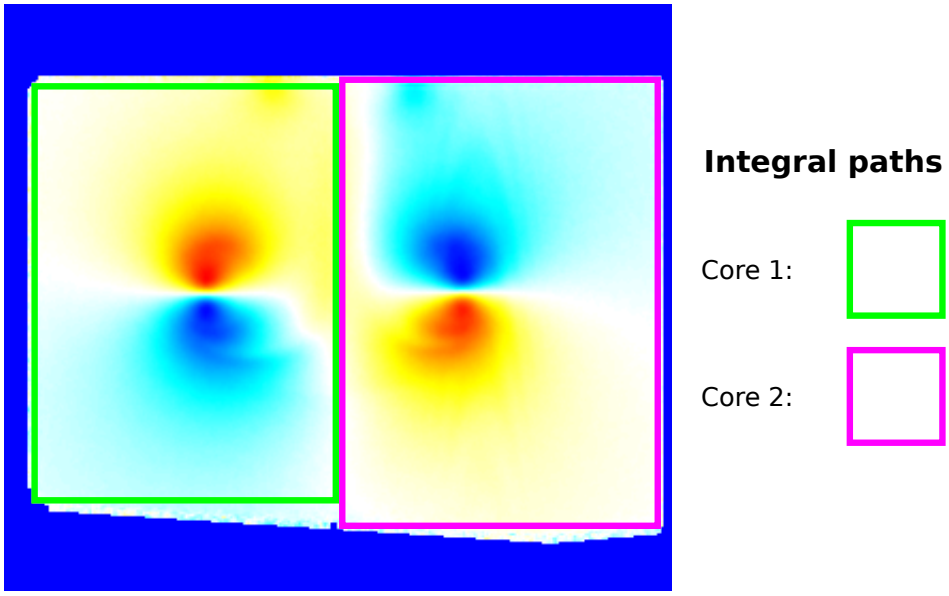

Figure 7.14: Illustration of method used to compute circulation

Figure 7.15 shows the time evolution of circulation magnitude for condition A, core left and core right. It illustrates clearly that there is little difference between the magnitude of the measured values in the two cores, which one expects for accurate circulation measurements. For this reason, the circulation data presented for comparison between conditions, figure 7.16, is given as the mean magnitude of cores left and right.

The plots in figure 7.16 show the evolution of circulation over time, compared across both rotation rate and generation condition. It is quite apparent from figure 7.16a that the rate of circulation decay is similar for the non-rotating

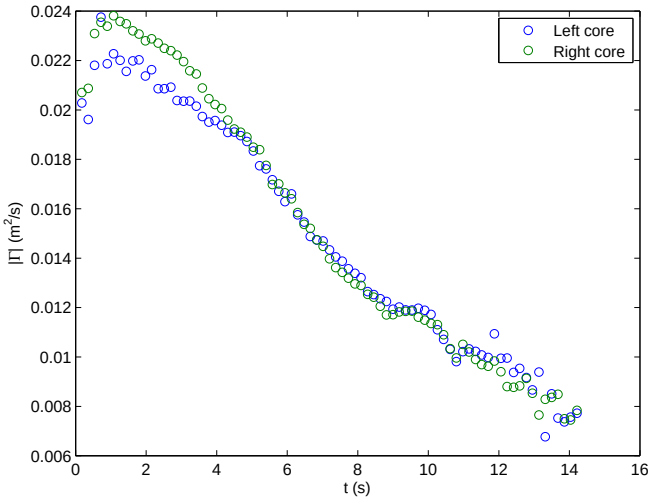

Figure 7.15: Comparison of circulation for Condition A, core left and core right

conditions. This similarity is less apparent for the rotating conditions, although conditions I and K do appear to decay at the same rate.

We further see a particularly strange phenomena manifesting in conditions F and H (indicated on figure 7.16c), the circulation appears to increase very rapidly early on, then decrease equally rapidly. Further discussion of this requires analysis of the velocity fields from which this circulation measurement is derived and will be returned to in section 8.6.2 once the necessary fields have been considered.

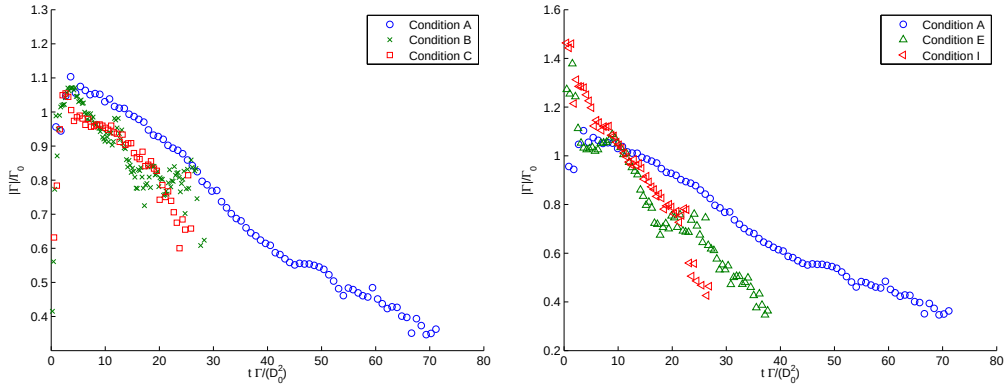

(a) $\Omega = 0RPM$

(b) $U_p = 0.5m/s, L_o = 90mm$

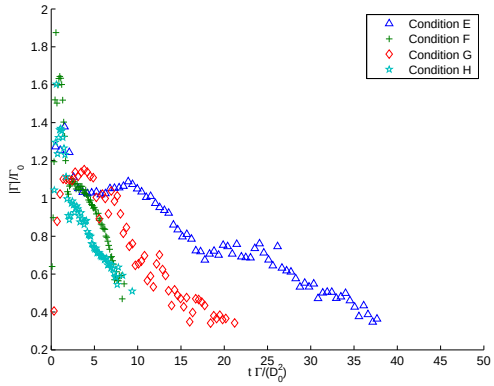

(c) $\Omega = 3RPM$

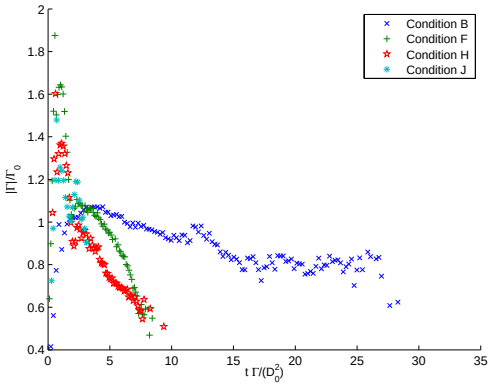

(d) $U_p = 0.1m/s, L_o = 90mm$

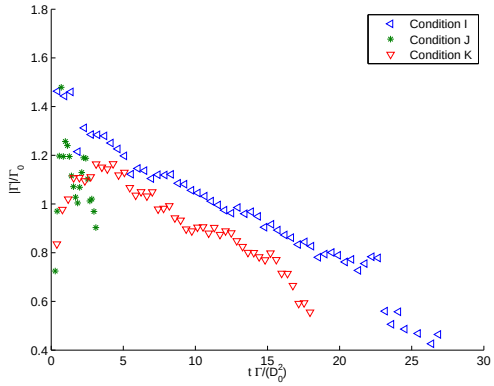

(e) $\Omega = 6RPM$

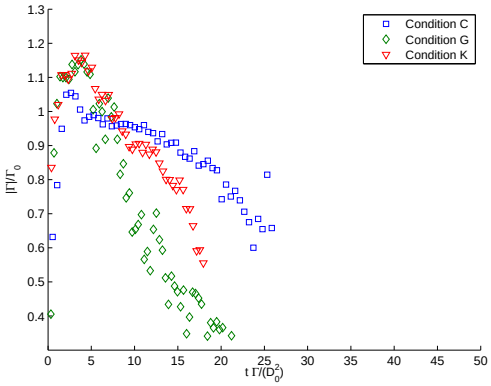

(f) $U_p = 0.5m/s, L_o = 30mm$

Figure 7.16: Comparison of vortex circulation, Γ

7.4 Time evolution of the velocity field, measurements from points and profiles

To analyse the vortex ring's time evolution, data are extracted from important points within the mean velocity fields and plotted to investigate the temporal and spatial variance of velocity. Further to this, velocity and vorticity profiles are extracted along lines through the vortex ring cores, to enable representation of the space-time variation of the vortex ring velocity fields. These are the first measurements of the velocity field in this fashion and as such the measurements presented here are new.

Figure 7.17 uses velocity vector maps overlaid on the individual velocity components to illustrate how the extraction points are chosen. The position of the peaks that occur in the vorticity and velocity fields are used to define six important areas within the vortex ring flow. Time series of data are extracted from these points, which are marked by the symbols, and the dashed red line indicates from where data profiles are extracted.

First an estimate of the centre of the vortex ring core is made by finding the centroids of the positive and negative peaks in the vorticity field. These points are referred to as "core", however they actually define the centre of the vortex core. Four more peaks are then found from the $\overline{u_x}$ and $\overline{u_y}$ fields, corresponding to the locations lying on the boundary of the vortex core (Saffman, 1978).

Two peaks are found for each core in the $\overline{u_x}$ field, these are referred to as "above" and "below", as they are found above and below the centre of the vortex core respectively. Two peaks are also found in the $\overline{u_y}$ field, these points are named "outer" and "inner". It may be considered that the outer measurement point lies radially displaced, outwards from the vortex core centre and the inner position lies radially displaced inwards from the vortex core.

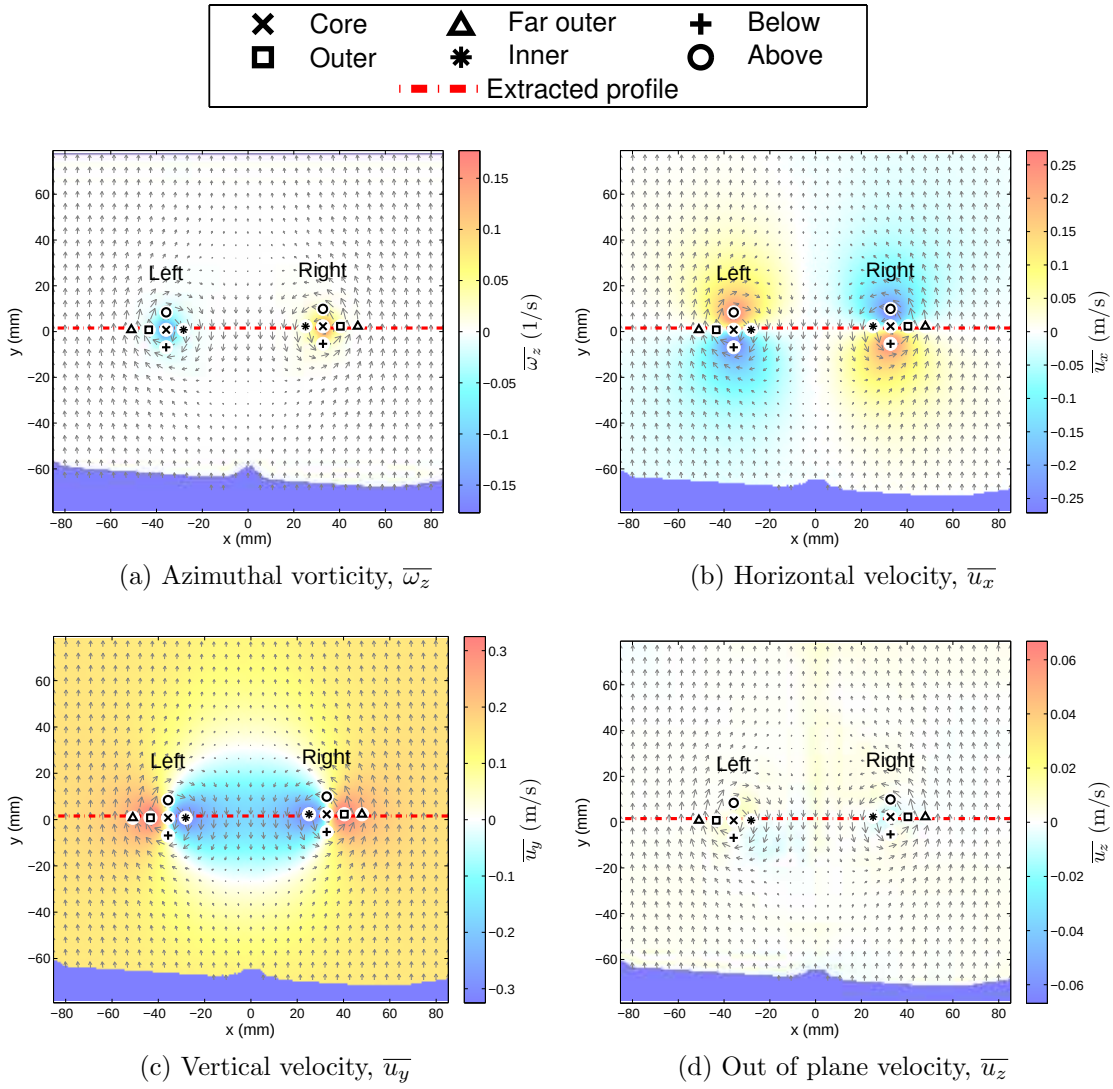

(a) Azimuthal vorticity, $\overline{\omega_z}$

(b) Horizontal velocity, $\overline{u_x}$

(c) Vertical velocity, $\overline{u_y}$

(d) Out of plane velocity, $\overline{u_z}$

Figure 7.17: Illustration highlighting points extracted from velocity field

In fact the definition of the position of points inner, outer, above and below does not necessarily coincide directly with the maxima found in the $\overline{u_x}$ and $\overline{u_y}$ fields. Instead, the points are picked to lie at locations displaced a radius $\delta/2$ from the core position. Points above and below share the same horizontal position and points outer and inner, the same vertical as their nearest core. The measurement of δ is made by finding the peaks of $\overline{u_x}$ and $\overline{u_y}$, and computing estimates for core diameter from each peak pair (i.e. above and below, outer and

inner for each core), the median of this set is used as the value for δ at each time.

Further to this, we also define a fifth measurement position, outside of the vortex ring, which we call "far outer". This point, lies on the same line as the inner and outer positions, but displaced radially outwards $\delta/2$ from measurement location outer. This value was chosen, as it positions the far outer point the same distance from outer as both outer and inner are positioned from core.

7.4.1 The symmetry of $\overline{u_z^+}$ fields

As seen in figure 7.17d, no obvious distinct maxima present in the $\overline{u_z}$ field initially, however as will be shown, the field does evolve over time. Figure 7.18a shows a plot of $\overline{u_z^+}$ for condition A at all measurement locations, the velocities presented are very low, and the scatter reasonably high, therefore, trends between measurement locations are difficult to isolate. This said, it is apparent that the out of plane velocity begins relatively high, then at $t^+ \sim 4$, drops quickly, furthermore, the velocity tends to remain positive over time for all the points plotted.

By comparing the core velocities for the left and right sides of the vortex ring, we are able to identify a distinct asymmetry which decreases with time. The general trend that is observed is positive velocity in the left core, negative velocity in the right, in both cases the velocity magnitude decreases with time. The presence of this opposite signed velocities on either side of the vortex ring provides clear indication of swirling fluid. This is the same swirling flow identified as occurring after the breaking of the wavy vortex structure which forms the Widnall instability, first described by Maxworthy (1972).

If we look first at the variation of data points extracted from the centre of the vortex cores, we can see evidence of anti-symmetry, with low magnitude velocities, indicating a very weak swirling flow inside the vortex ring core. This disparity between left and right cores, indicating swirling flow is also detectable at

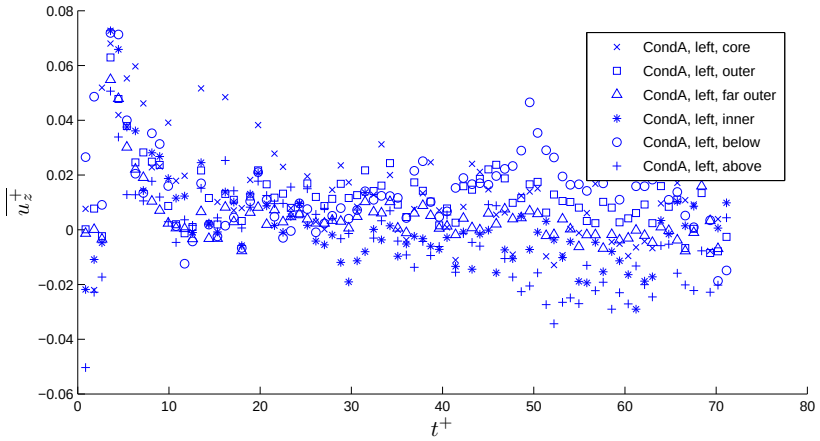

(a) Positions: All

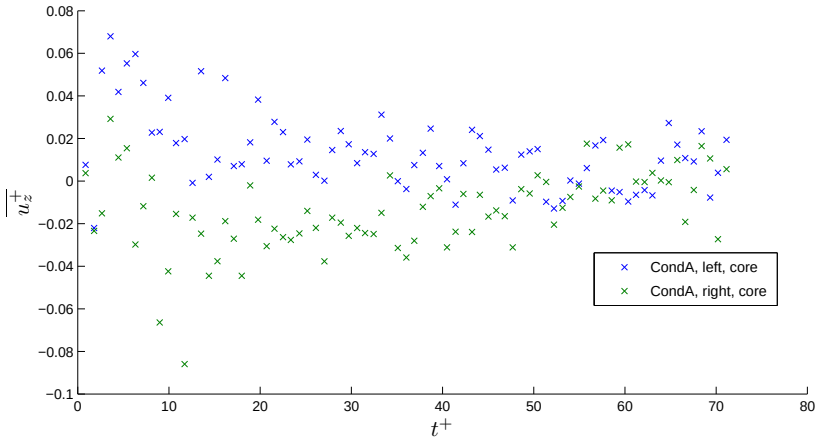

(b) Positions: vortex core

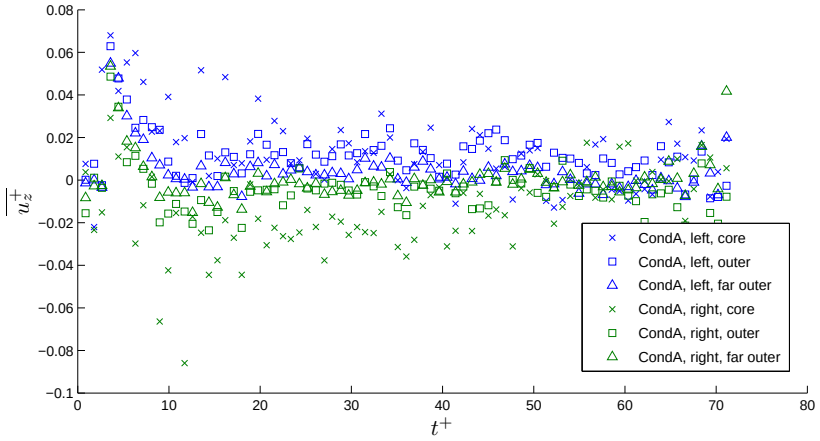

(c) Positions: vortex core, outer and far outer

Figure 7.18: Comparison of $\overline{u_z^+}$

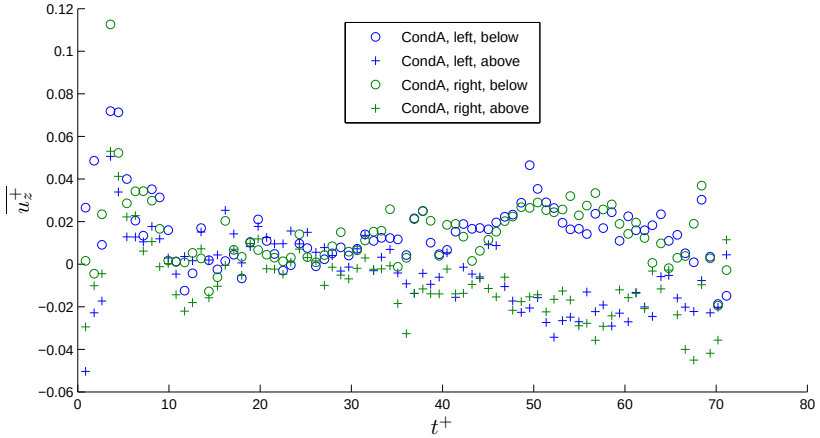

(d) Positions: above and below

Figure 7.18: Comparison of $\overline{u_z^+}$, continued

the outer and far outer positions, although with significantly reduced magnitude. Figure 7.19 further indicates the presence of a ring swirl and it is plain to see that the highest magnitude is present in the vortex cores.

In line with the results published by Naitoh *et al.* (2002) and Dazin *et al.* (2006a) we expect the presence of a swirling flow of opposite sign above and below this core swirl. Figure 7.20 shows an example frame from the $\overline{u_z^+}$ field of condition A. One can see quite clearly the presence of the core swirl flow, indicated by the disparity between velocities observed in cores left and right (recall that blue indicates velocity into the page and red, velocity out of the page). Further to this, there are signs of an opposite signed swirling flow, both above and below the vortex core, although the magnitudes of this flow are very low, hence dissemination of them from the background is difficult. This is a significant result, the prior works considered only the existence of such a flow, here we are able to show that there is some bias to its occurrence, and that on average there is a positive swirling seen.

It is also of note that on the left core, there appears to be the slight formation of a cross shape in the $\overline{u_z}$ field (this is highlighted by dotted lines). It is possible

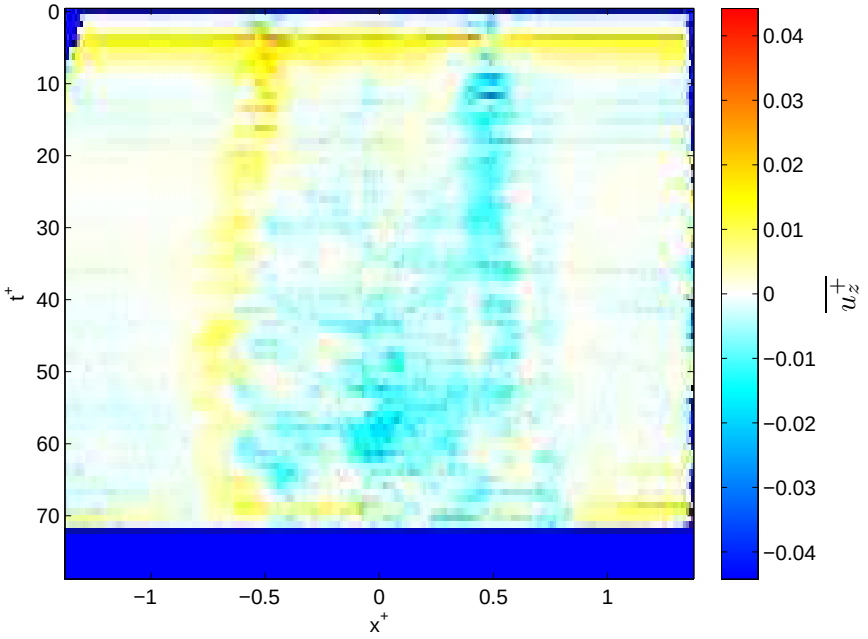

Figure 7.19: Time evolution of $\overline{u_z^+}$ profiles

that this corresponds to a slight registration error, as shown in figure 2.20 and described in section 2.4.2. Should this be the case, the registration error seen is very low (the magnitude of the effect observed around 3% of the in-plane velocities) and as the induced velocity is present for a single core only would correspond, most likely to an error not accounted for by the model used (recall from section 5.5 the camera motion was represented by plain translation).

Further to this, figure 7.21 shows horizontal sums of $\overline{u_z}$, as described in section 5.7.3. At $t \sim 8.5s$, we see that the overall the velocity on the upper side of the vortex ring differs to that on the lower side. As described in section 5.1, this means that the vortex ring is on average out of the light sheet plane and that at some point the correction for this loses full effectiveness.

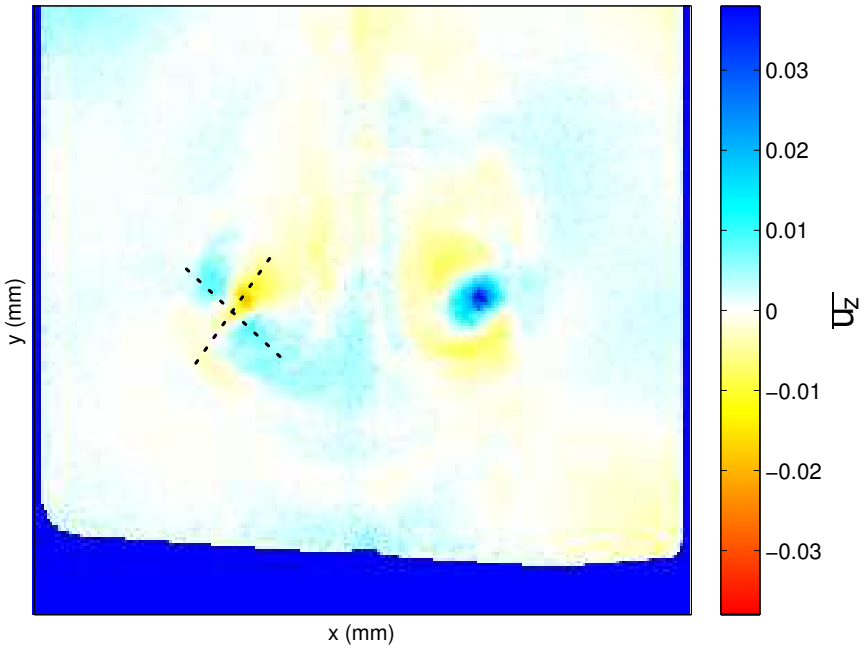

Figure 7.20: Example $\overline{u_z}$ field, showing existence of core swirl

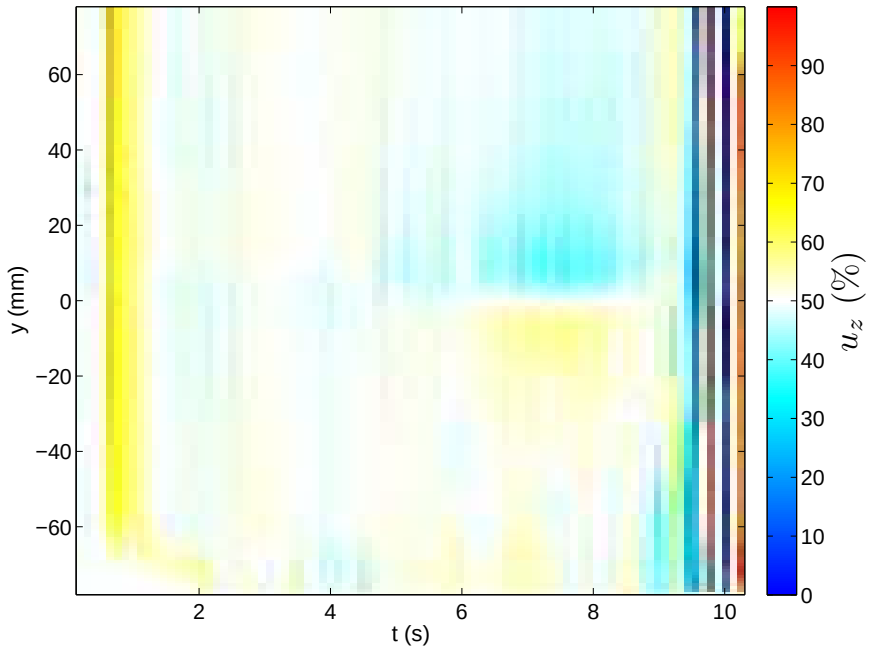

Figure 7.21: Sum of $\overline{u_z}$, variation with time

7.4.2 The effects of varying vortex ring generation parameters in non-rotating flow

In this section we present the first investigation into the behaviour of the vortex ring velocity field from a statistical stand-point. We use the mean velocity fields computed from the $\sim$ 400 vortex ring generations to compare and contrasting vortex rings with differing generation parameters. We begin by assessing the impact of varying the generation velocity U_o, and then proceed to investigate the effects of varying the generation length, L_o. Throughout this section, velocities are normalised by the generation velocity U_o, facilitating improved comparison between the different generation conditions.

7.4.2.1 The effect of varying U_o

Figure 7.22 illustrates the differences observed in $\overline{u_x^+}$ for the above and below positions. We notice that the decay of velocity is much slower for the higher Reynolds number case, condition A than for B, which likely indicates that impulse is lost at a significantly greater rate. It is interesting to note that condition B shows a rapid decrease in $\overline{u_x^+}$ at $t^+ \sim 4$, however the decrease manifests first in the velocity at the below position, $t^+ \sim 3.4$, then later in the above position, $t^+ \sim 4.2$.

Figure 7.23 shows a comparison of $\overline{u_y^+}$ for conditions A and B. One can see that for both conditions A and B, there is a smooth, steady decrease of $\overline{u_y^+}$ through time. Further to this, it is noticeable that as with $\overline{u_x^+}$, Condition A loses velocity at a lesser rate than condition B.

As stated, data displaying the time evolution of the velocity field has been presented. The trends shown here are somewhat surprising. It is expected that for condition A, the transition to turbulence would occur earlier than for condition B

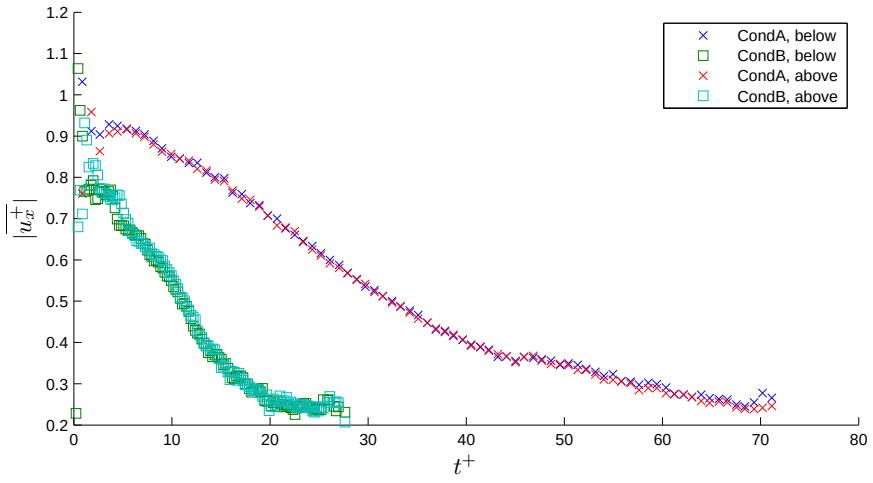

Figure 7.22: Comparison of $\overline{u_x^+}$, at positions above and below

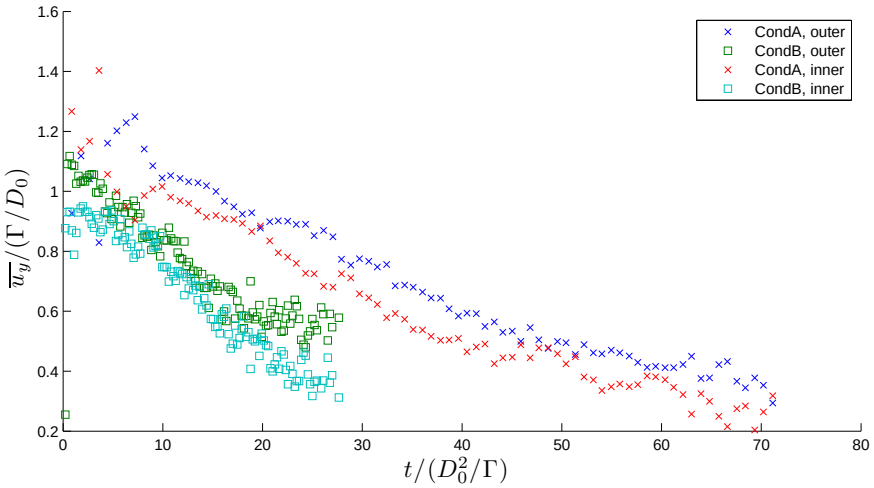

Figure 7.23: Comparison of $\overline{u_y^+}$, at positions outside and inside

(c.f. figure 3.5, page 62). It is also known that for turbulent vortex rings the vortex ring's impulse and so U_T decreases at an increased rate (c.f. section 3.3.5.2). Upon non-dimensionalisation however, we find that the converse is true, the higher Reynolds number rings decrease in velocity at an increased rate compared with that of the laminar rings. It should be noted that our results do not contradict Maxworthy's, as figure 7.24 shows, without the non-dimensionalisation, we find the velocity field decays faster for condition A than B.

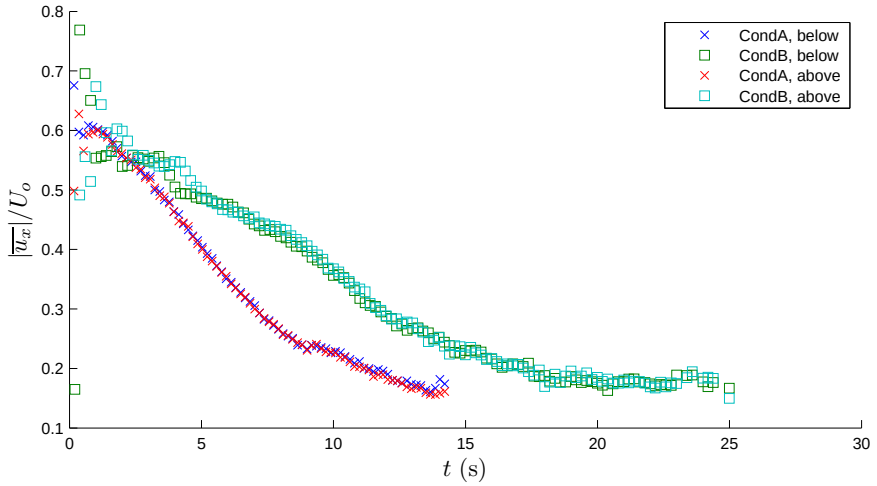

(a) $\overline{u_x}$

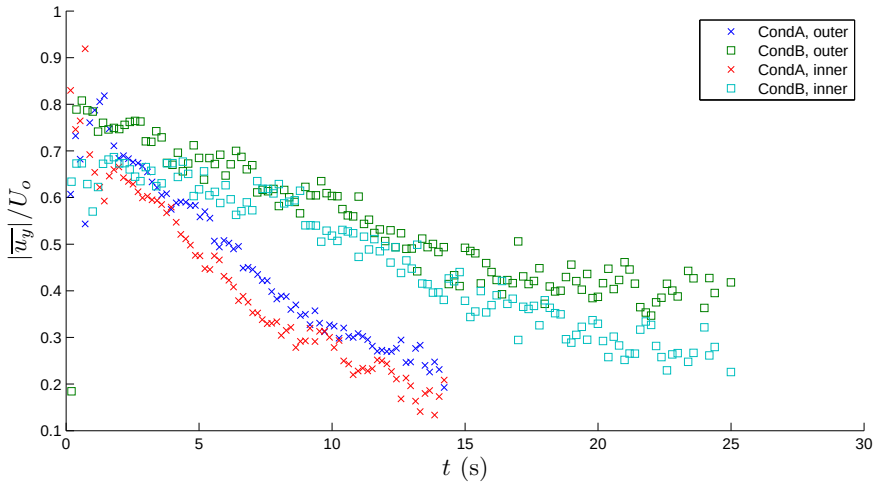

(b) $\overline{u_y}$

Figure 7.24: Comparison of $\overline{u_x}$ and $\overline{u_y}$, without non-dimensionalisation

On the basis of our observations it seems reasonable that the difference in trends observed is due to the state of the vortex ring. One could further convince oneself that the change in gradients of $\overline{u_x^+}$ and $\overline{u_y^+}$ at $t^+ \sim 45$ and $t^+ \sim 20$ for conditions A and B respectively, could be due to a relaminarisation event. No evidence is presented regarding this however.

The variation of $\overline{u_z^+}$ against time is presented in figures 7.25a and 7.25b. Figure 7.25b indicates that the correction for the vortex ring moving out of the light sheet has, as with condition A, not quite been fully successful for condition B. This is because we find the data for below to follow the same trends as for above, however inverted.

One sees that for conditions A and B respectively, the correction to account for vortex rings leaving the light sheet ceases to be effective at $t^+ \sim 20$ and $t^+ \sim 5$. However we see the opposite direction of motion, for condition B, the error in correction leaves the vortex ring the near side of the light sheet to the camera, whereas for condition A, it is the far side. Figure 7.27b highlights further the absence of any out of plane motion of interest, especially in contrast to the core swirl shown in figure 7.27a.

Figure 7.25a shows the out of plane component of velocity for the centre of the left and right vortex cores. It is apparent that condition B shows none of the asymmetry in the $\overline{u_z^+}$ field that is presented in condition A and the data for both left and right core are effectively the same, thus indicating the absence of a swirling motion. Despite this, it is interesting to consider some simple statistics related to this axial swirl.

Here we define the axial swirl velocity (S_z) as in (7.4), which provides the mean swirling flow in the vortex ring (hence the denominator). Further $\overline{u_{z_{right}}}$ is subtracted from $\overline{u_{z_{left}}}$ as for an axially symmetric vortex, we expect the left of the $\overline{u_z^+}$ field to be equal to that of the right side, but negated.

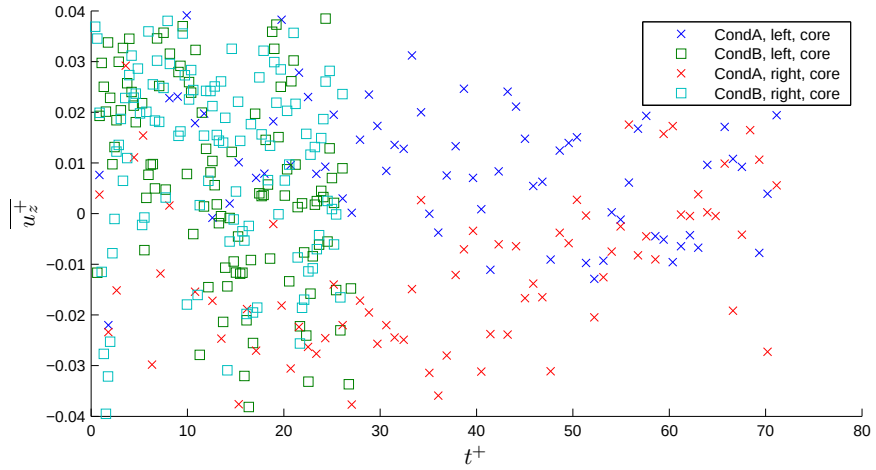

(a) Positions: vortex core

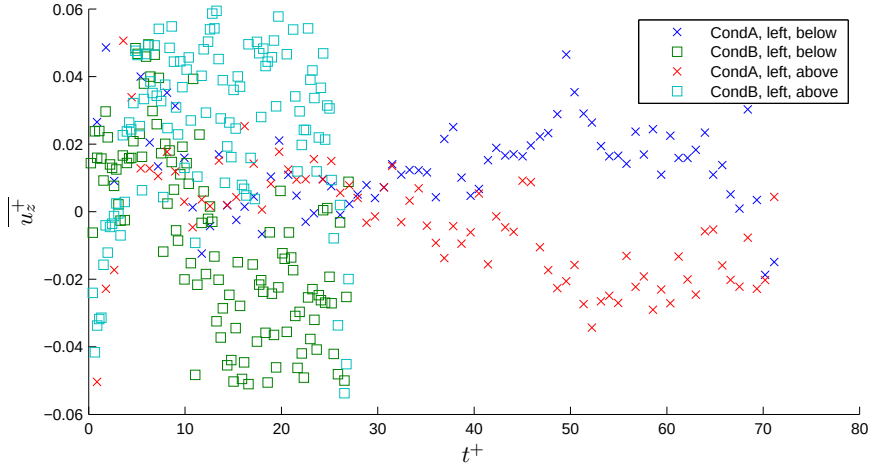

(b) Positions above and below

Figure 7.25: Comparison of $\overline{u_z^+}$

$$S_z = \frac{\overline{u_{z_{left}}} - \overline{u_{z_{right}}}}{2} \tag{7.4}$$

Presented in figure 7.26 are plots illustrating the swirling motion for conditions A and B. For consistency with Naitoh *et al.* (2002) and Dazin *et al.* (2006a) we normalise the swirl strength by vortex ring translational velocity, U_T. This is calculated from the time derivative of the y position of the vortex ring, which is computed using a smoothing spline fit. Both for conditions A and B, we plot

the mean swirling flow, the mean ± standard deviation and the minimum and maximum as a function of time. All of these statistics are computed from all available vortex ring runs for the given condition.

We see from the standard deviations, that for both condition A and B, swirling flows exist across a wide range of values, which is poorly reflected by the mean. Perhaps of most interest is the existence of both positive and negative swirls, which can be seen from the minimum and maximum curves, meaning that the swirling direction changes from run to run. In fact we find that for condition B, the distribution of the measured swirling flows is approximately symmetric about zero, giving rise to mean swirl of zero. Comparing figure 7.26a with 7.26b we see that for condition A, the variation of swirl strength varies little across the vortex ring lifetime (as indicated by standard deviation, minimum and maximum). For condition B however, we find a trend indicating a general increase of both standard deviation and range with time.

Figures 7.28a-7.28c show various plots of vorticity, ω_z, normalised by the eddy timescale, D_0^2/Γ. One can see that there is little similarity in the time evolution of $\overline{\omega_z^+}$ for conditions A and B, with the rate of vorticity decay notably greater for condition B. We find increased rate of decay at all measured points throughout the velocity field.

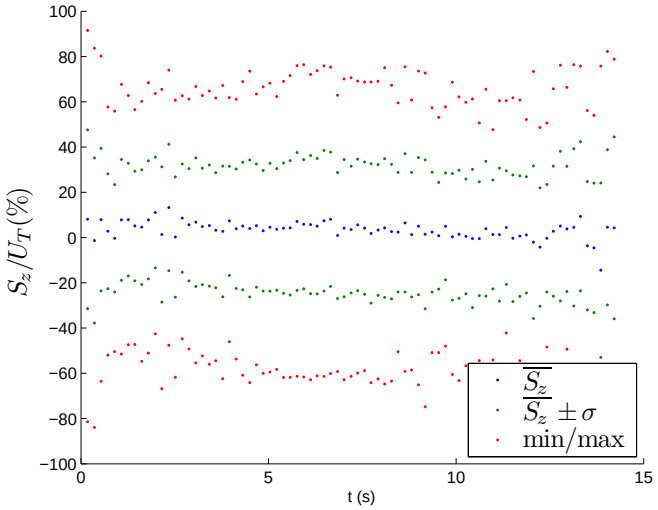

(a) Condition A

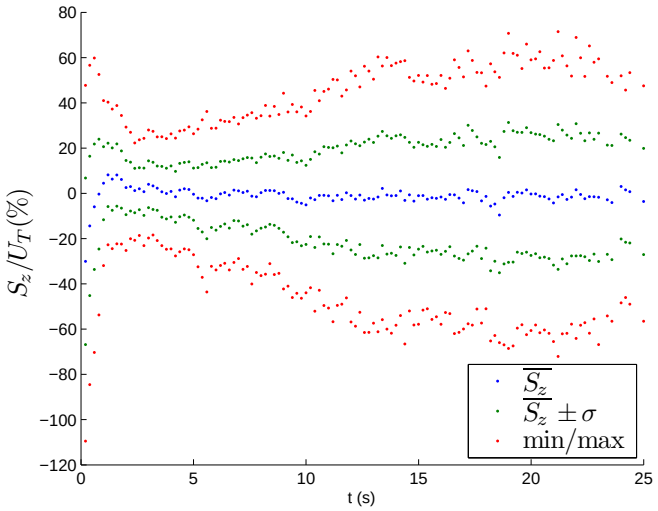

(b) Condition B

Figure 7.26: Comparison of statistics relating to swirling flow

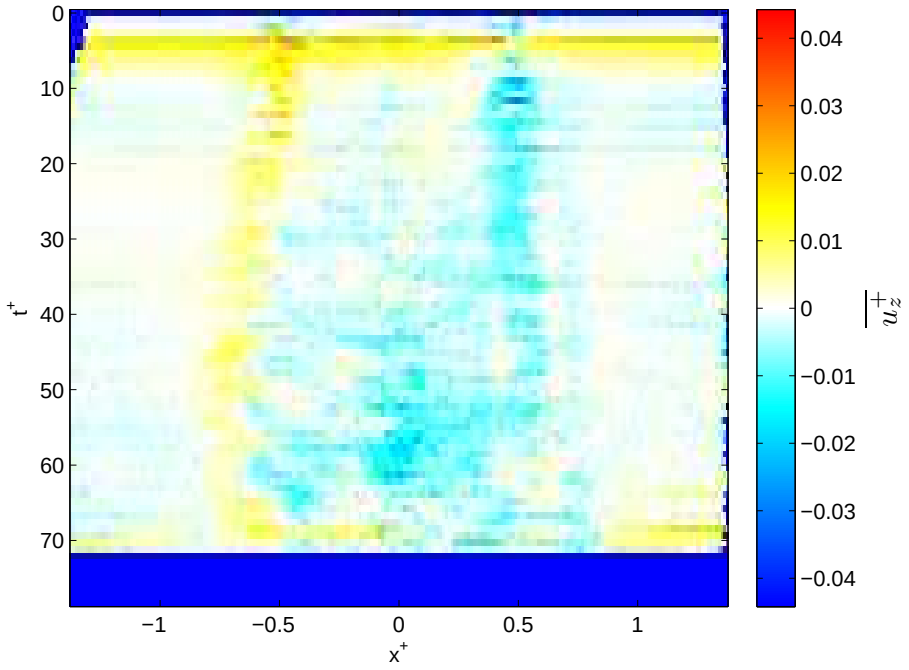

(a) Condition A

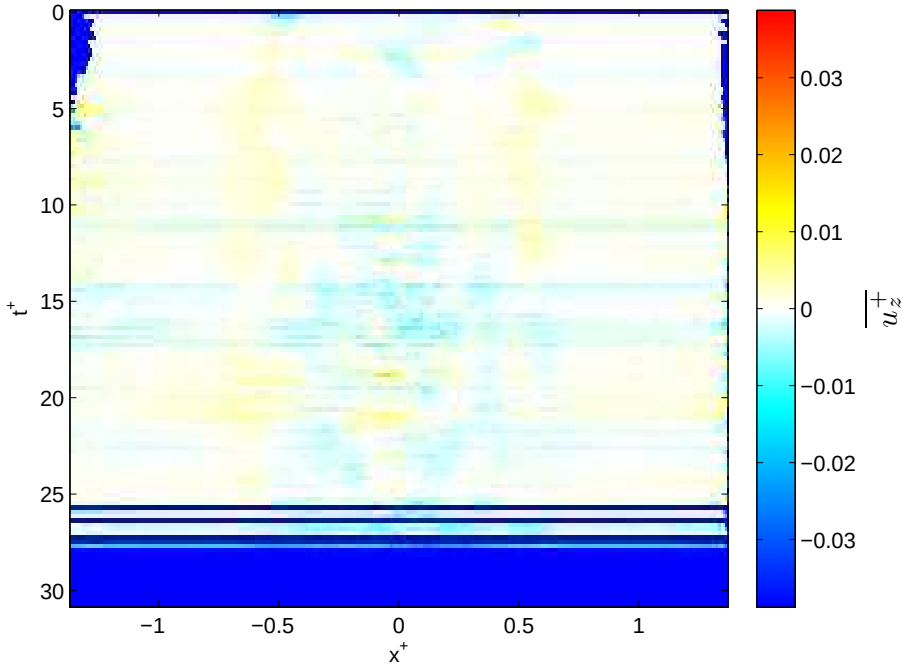

(b) Condition B

Figure 7.27: Comparison $\overline{u_z^+}$ profiles for conditions A and B

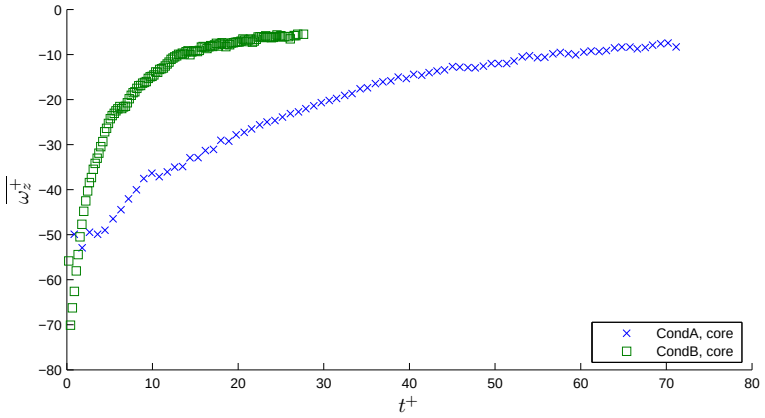

(a) Position, vortex core

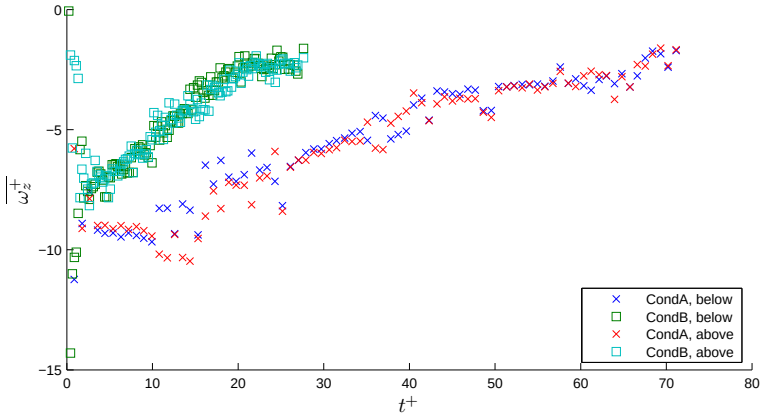

(b) Positions: above and below

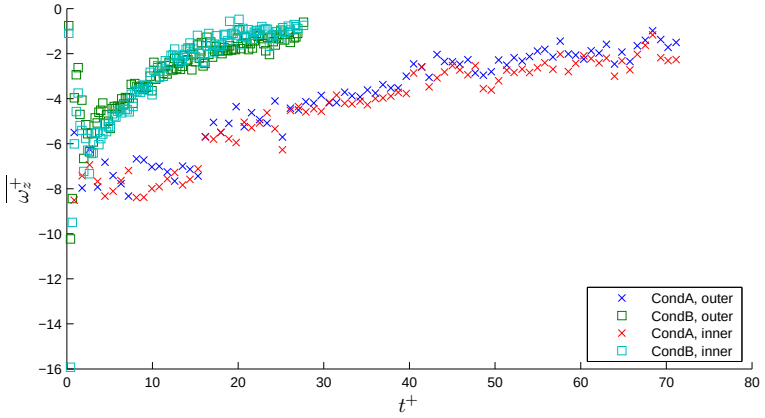

(c) Positions: outer and inner

Figure 7.28: Comparison of $\overline{\omega_z^+}$

7.4.2.2 The effect of varying L_o

Here we compare conditions A and C, both of which were produced with the same piston velocity, but differing piston stroke lengths.

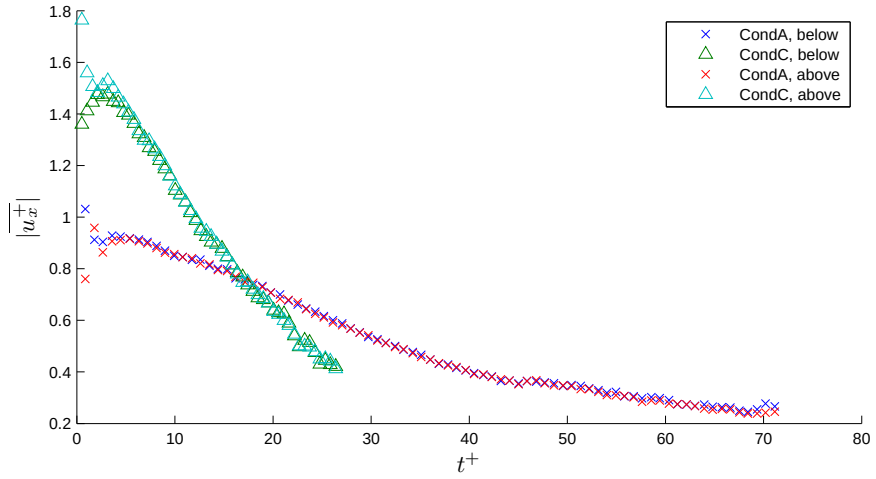

Figure 7.29: Comparison of $\overline{u_x^+}$, at positions above and below

From figure 7.29 we can see similar effects as when comparing condition A with condition B. We find that $\overline{u_x^+}$ for the lower Reynolds number vortex ring decays at a significantly increased rate, when compared with the higher Reynolds number vortex ring (condition A). The same trend is also found for $\overline{u_y^+}$ where we find greater rate of decay for condition C than for condition A.

Figure 7.31a provides a comparison between conditions A and C for the variation of $\overline{u_z^+}$ over time. One can see that for condition C, the velocity in the right core is always of higher magnitude than in the left core, although the difference is small. Furthermore the velocity in the right core tends to be of opposite sign to that in the left, the implication of this is a swirling, however for condition C, the mean swirling flow is in the opposite direction to that found in condition A.

As with condition A, we can see disparity between the points measured at locations above and below, for condition C, figure 7.31b. We see there is evidence

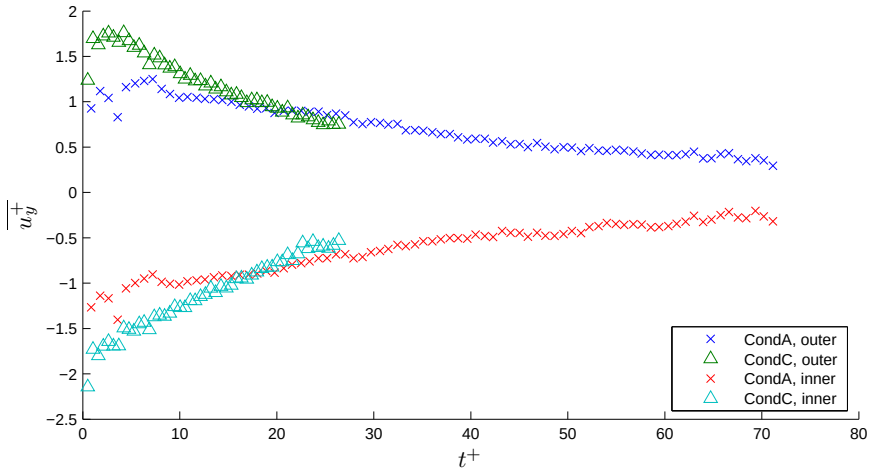

Figure 7.30: Comparison of $\overline{u_y^+}$, at positions outside and inside

that at the start of the experiment the vortex ring lies out of the measurement plane, the far side from the cameras. In both figures 7.6 and 7.32b it is seen that the vortex ring then travels toward the cameras, crossing the light sheet at $t^+ \sim 13$ and then moving out of the light sheet again toward the cameras. In figure 7.31b the ring lying the far side of the sheet to the cameras is indicated by the above data being positive, whilst the below data is negative. The opposite indicates the vortex ring centre is the near-side of the light sheet and no difference in above and below data indicates that the vortex ring is in the sheet.

The velocity profiles plotted in figure 7.32 clearly highlight this difference. One can see that for condition A, the left core remains positive throughout the experiment, and the right core negative. For condition C, one can see a similar pattern, reversed, although the magnitude is reduced and so the clarity of this trend is lower.

To better illustrate this, the time variation of the core swirl is plotted as a percentage of the vortex ring translational velocity (U_T) in figure 7.33. It is apparent from this plot that the mean swirl strength remains reasonably constant for the life of the vortex ring, $\sim 5\%U_T$ for condition A and $\sim 3\%U_T$ for condition

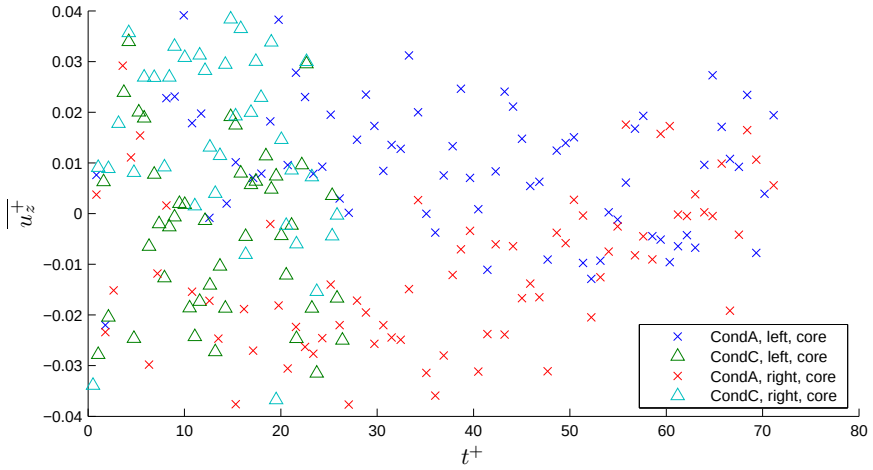

(a) Positions: vortex core

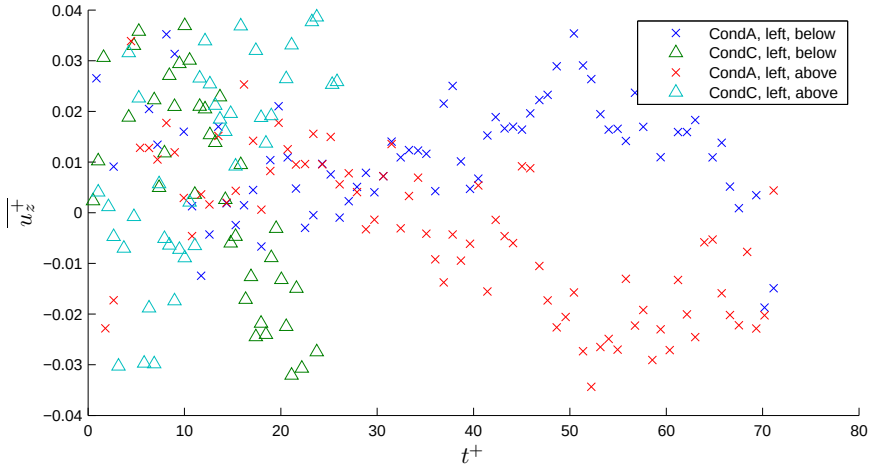

(b) Positions: above and below

Figure 7.31: Comparison of $\overline{u_z^+}$

C.

We present statistics indicating the range of the swirling motions measured across all vortex ring generations, as was done in section 7.4.2.1. The mean of the swirl, the mean ± standard deviation, the minimum and the maximum are again plotted as a function of time, for conditions A and C, figure 7.34. We see that as for condition B, both of the cases presented, positive and negative swirling flows are found, as indicated by the positive maximums and negative minimums. We also see, that for both conditions, there is a high standard deviation, implying

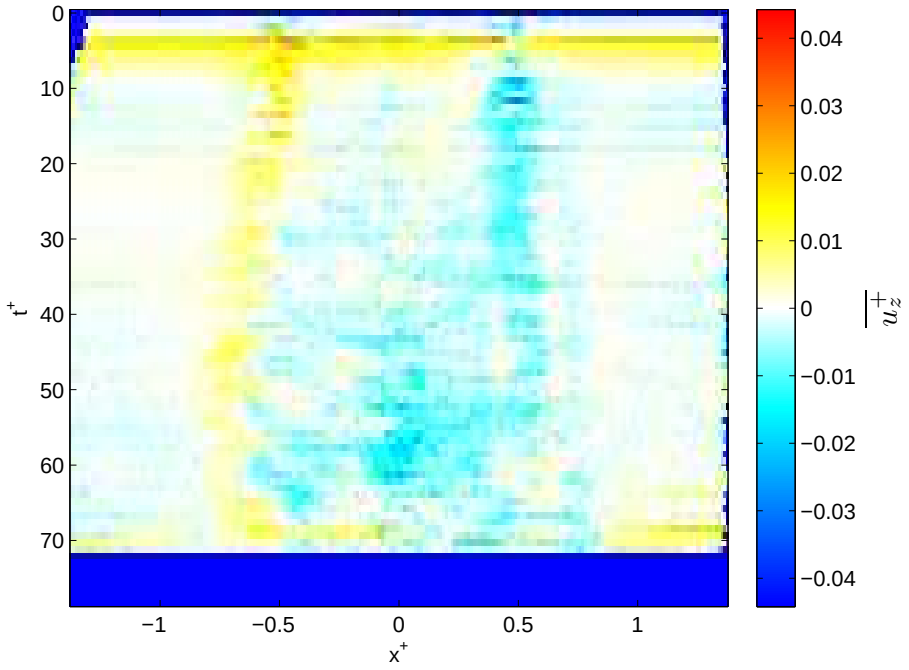

(a) Condition A

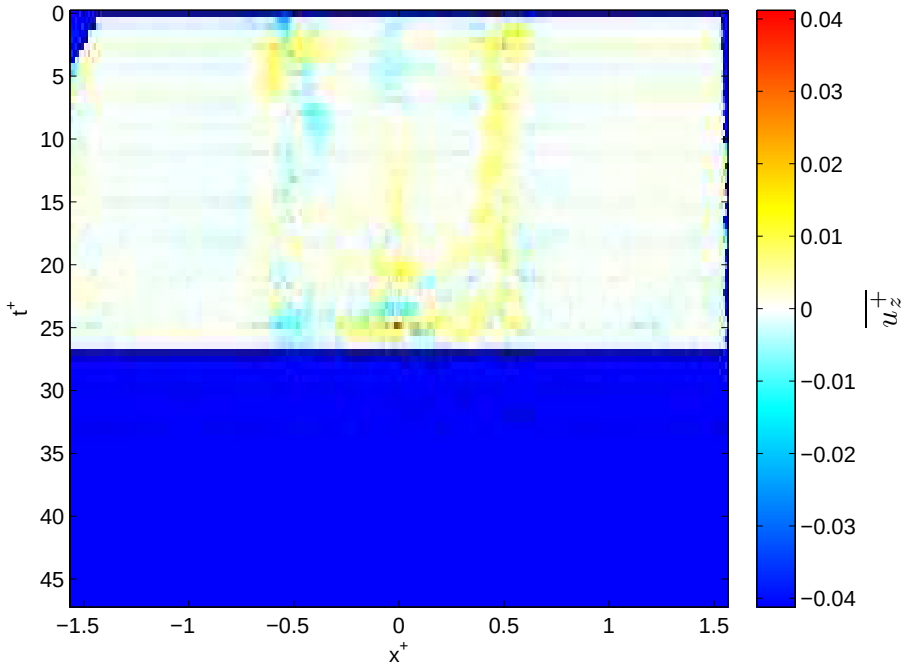

(b) Condition C

Figure 7.32: Comparison $\overline{u_z^+}$ profiles for conditions A and C

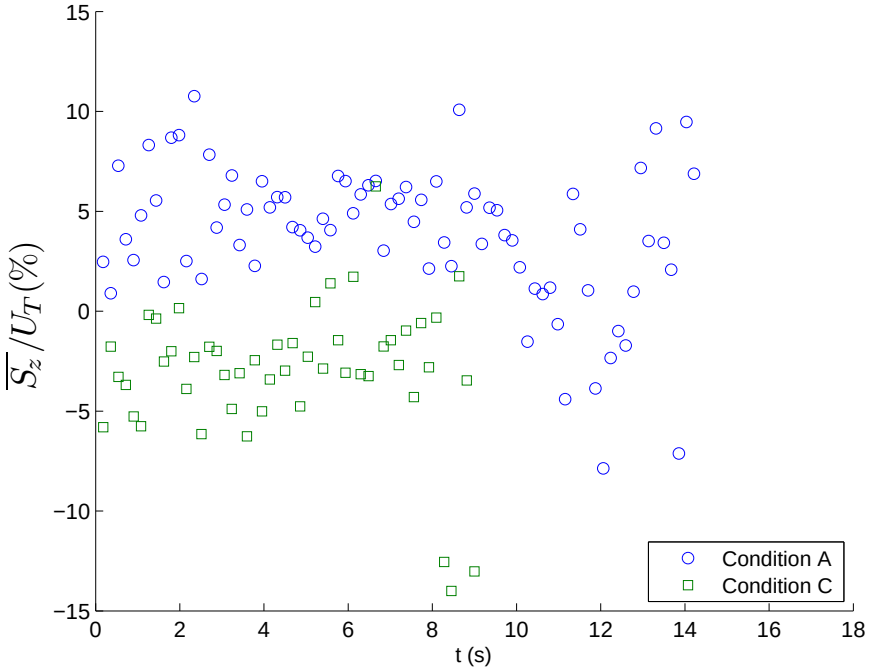

Figure 7.33: Comparison of core swirl strength

that variation in the swirl strength from run to run is high.

The vorticity variation is presented in figure 7.35. We see that a similar trend is found for all positions plotted, however, as with the other conditions, the magnitudes around the core is significantly lower than at its centre. In all cases we find that condition C has a greater normalised vorticity than for condition A. We also see that condition C decreases in vorticity at a far more rapid rate than condition A.

We also see from figures 7.35b and 7.35c that the changes found at the above and below measurement locations are similar in size to those at the inner and outer locations. We can see that at the centre of the cores, the general trend for condition C is the same as for A, after formation, there is an initial steep, almost linear decrease in $\overline{\omega_z^+}$, followed by a more gradual, steady decay of the vorticity.

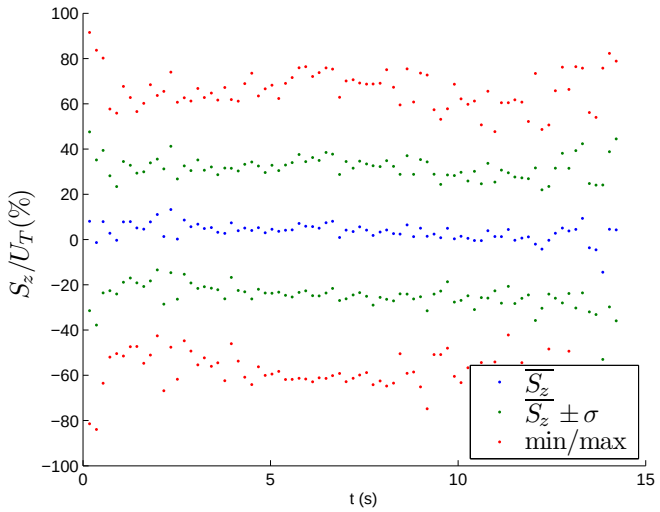

(a) Condition A

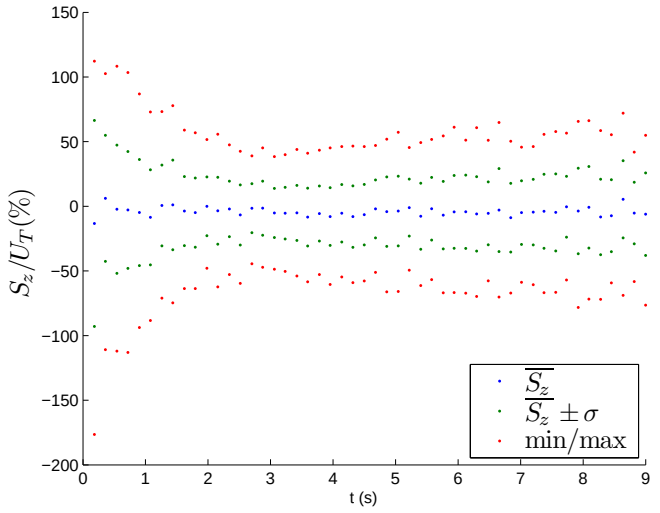

(b) Condition C

Figure 7.34: Comparison of statistics relating to swirling flow

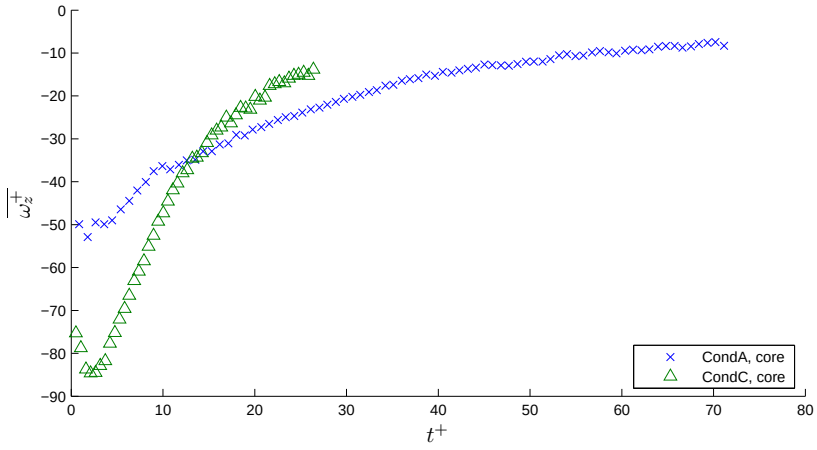

(a) Positions: vortex core

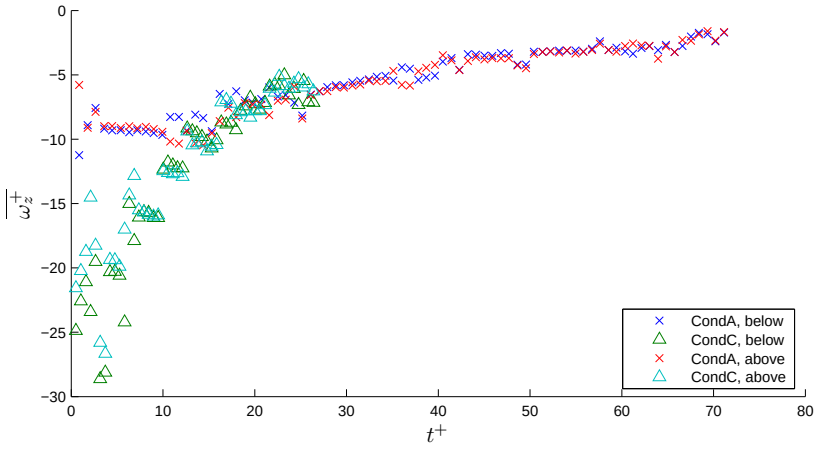

(b) Positions: above and below

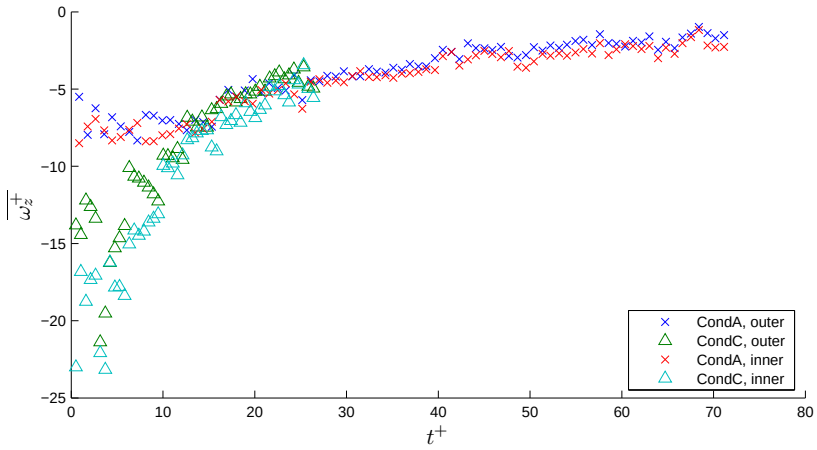

(c) Positions: outer and inner

Figure 7.35: Comparison of $\overline{\omega_z^+}$

7.4.3 The effects of background rotation upon vortex rings

To investigate the effects of background rotation upon the evolution of vortex rings, we consider plots contrasting differing rotation rates for each of the vortex rings considered in section 7.4.2. Our comparison is made across point extractions of the velocity components, and the vorticity, and in each case we compare data extracted from the six positions established in section 7.4.2. Further to this, we also utilise colour maps showing the variation of velocity along profiles through the two vortex cores.

Our results show that little variation is seen in the $\overline{u_x^+}$ field, however this data is presented for completeness. The $\overline{u_y^+}$ field however shows evidence of a previously unrecorded phenomenon, on the axis of the vortex ring, a highly localised jet of fluid is formed. It is seen that for lower Rossby numbers this jet is increasingly positive (opposite in sign to that of the flow in its locale). In the $\overline{u_z^+}$ field, we see the same axial wake swirl observed in numerical simulations by Verzicco *et al.* (1996) and also provide the first experimental measurements of the ahead wake swirl (also seen in the numerics of Verzicco *et al.* (1996)). The $\overline{u_z^+}$ field is also used to help ascertain the performance the corrections discussed in section 5.5 and 5.6. We also present analysis of the $\overline{\omega_z^+}$ field, which shows the shedding of secondary vorticity, (shown both numerically and experimentally by Verzicco *et al.* (1996)). We shall demonstrate in section 8 the importance of this shedding, previously unnoticed by Verzicco *et al.* (1996) by relating it to many of the other phenomena seen.

7.4.3.1 The time evolution of $\overline{u_x}$

Comparing the high Reynolds number conditions, A, E and I, a clear trend is seen with rotation rate, figure 7.36a. The greater the Rossby number, the lower

the initial velocity and the shallower the velocity gradient. Conditions J and G do not appear to follow this trend completely however, both having lower initial velocities than comparable conditions with lower background rotation rates.

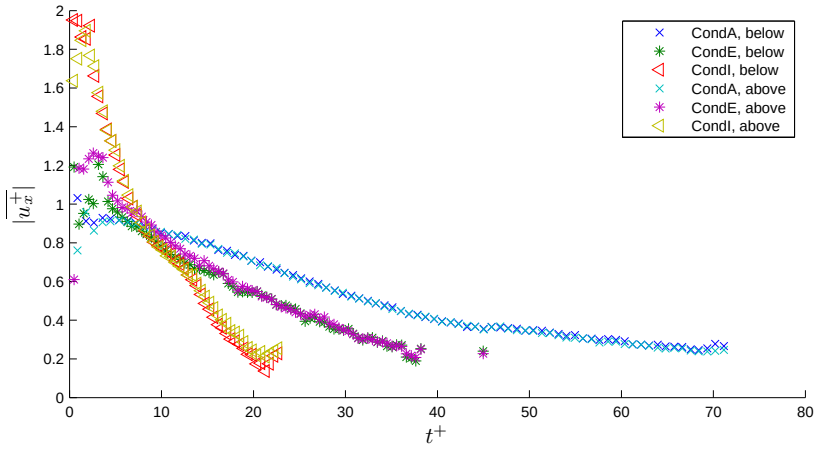

(a) Conditions A, E and I

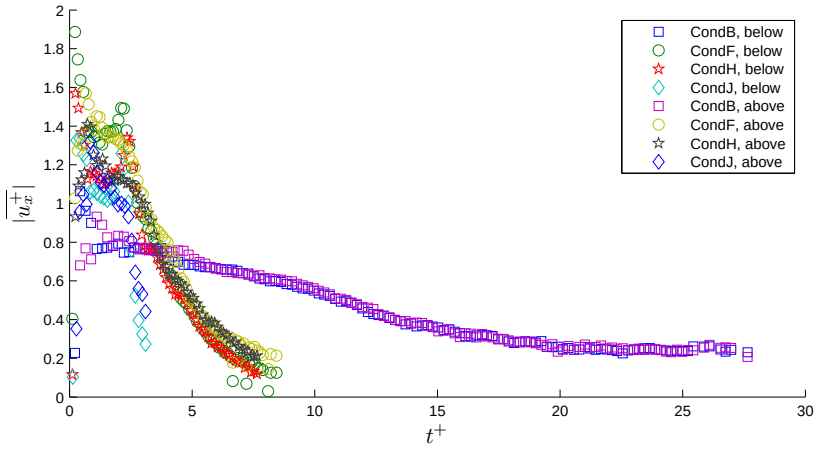

(b) Conditions B, F, H and J

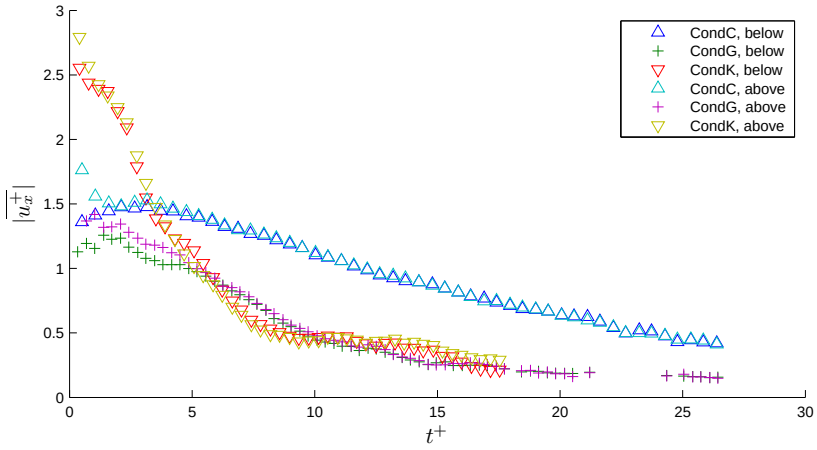

(c) Conditions C, G and K

Figure 7.36: Comparison of $\overline{u_x^+}$

7.4.3.2 The time evolution of $\overline{u_y}$

Similar trends are observed for $\overline{u_y^+}$ as in $\overline{u_x^+}$, figure 7.37a shows the variation for the high Reynolds number vortex ring. Again, initial $\overline{u_y^+}$ appears to be driven by Rossby number as does its gradient of decrease. The same departure from this trend is seen for conditions G and J as with $\overline{u_x^+}$.

Figure 7.38 provides a comparison of the time evolution of velocity. Two separate plot types are produced; the first column shows the velocity field with the colour map spanning the complete range of velocities, in the second column the data is plotted with the velocity range halved. This acts to increase the visibility of lower magnitude phenomena. In both cases the colour map is balanced, so that white indicates zero velocity which, due to the camera moving with the vortex ring, indicates that the fluid between inner and outer, i.e. in the core, is moving at exactly the same speed as the vortex ring.

In all cases we can see that the white region indicates the relative change of vortex ring diameter over time. We further see that the changes observed to the vortex ring diameter in section 7.3, are all relatively minor in percentage terms. The point of most interest is most clearly observable upon comparison between figures 7.38f and 7.38b.

We see that for condition I, at $t^+ \sim 2.5s$ (this is marked on figure 7.38f with a dashed pink circle), a small pocket of fluid with significantly differing velocity to its surroundings has formed in the centre of the vortex ring. We see the same phenomenon, but markedly reduced in magnitude for condition E and not at all for condition A.

Figure 7.39 shows again the same localised pocket of fluid with higher velocity for conditions F, H and J, but not for the non-rotating condition, B. For these conditions, this region is very obvious and does not require the range of colours

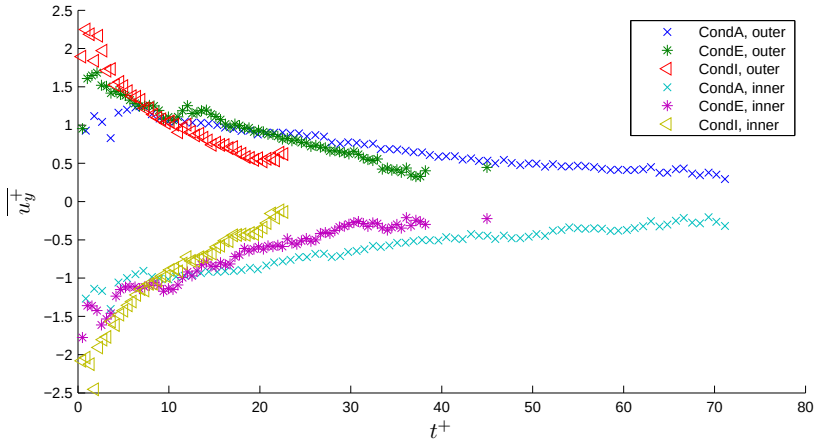

(a) Conditions A, E and I

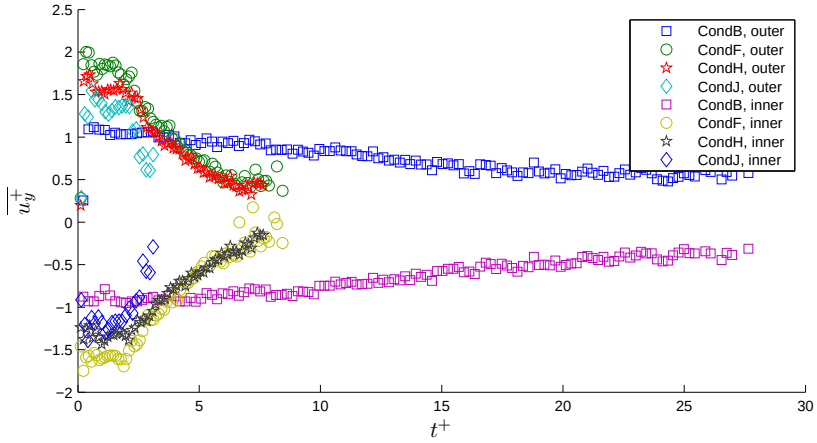

(b) Conditions B, F, H and J

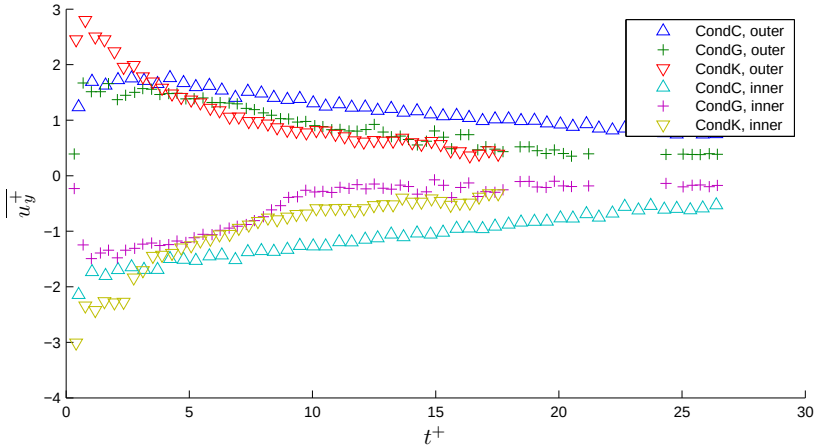

(c) Conditions C, G and K

Figure 7.37: Comparison of $\overline{u_y^+}$

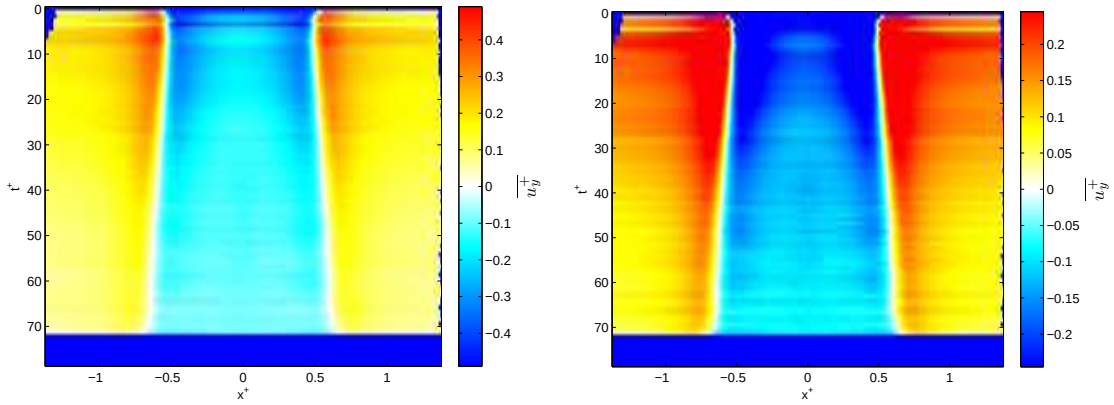

(a) Condition A

(b) Condition A, scaled

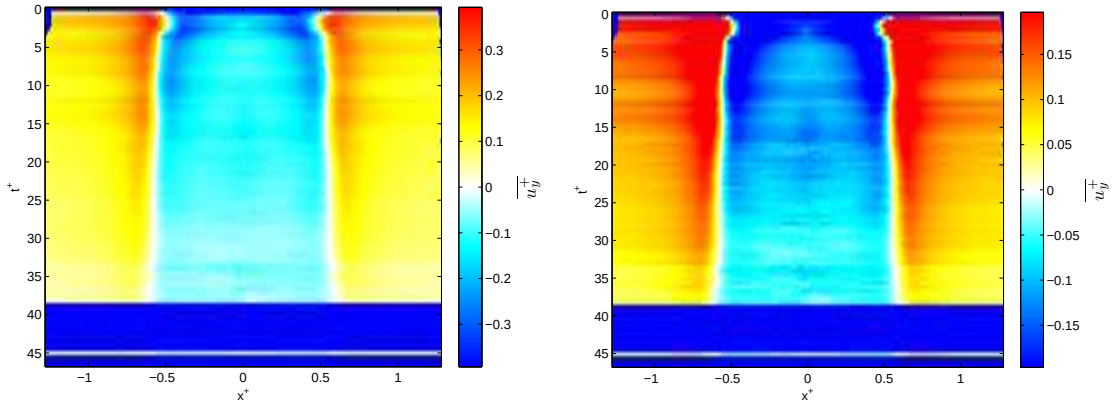

(c) Condition E

(d) Condition E, scaled

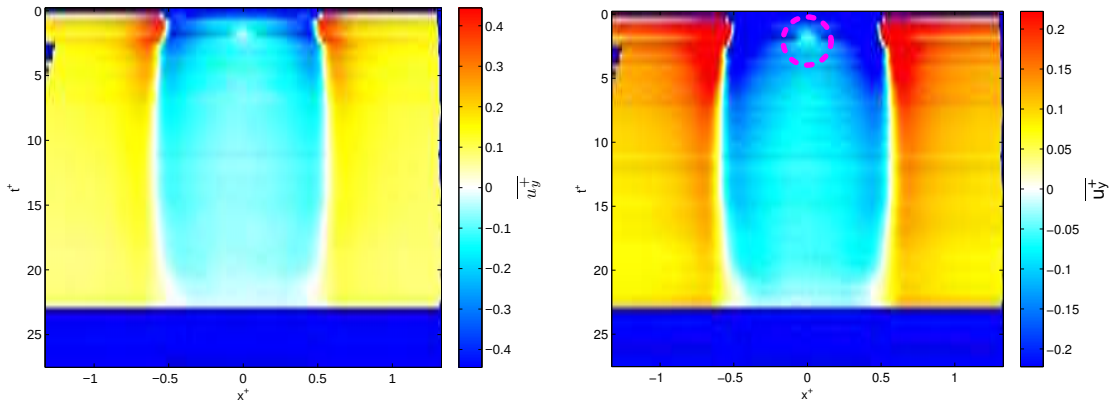

(e) Condition I

(f) Condition I, scaled

Figure 7.38: Comparison of $\overline{u_y^+}$ profiles

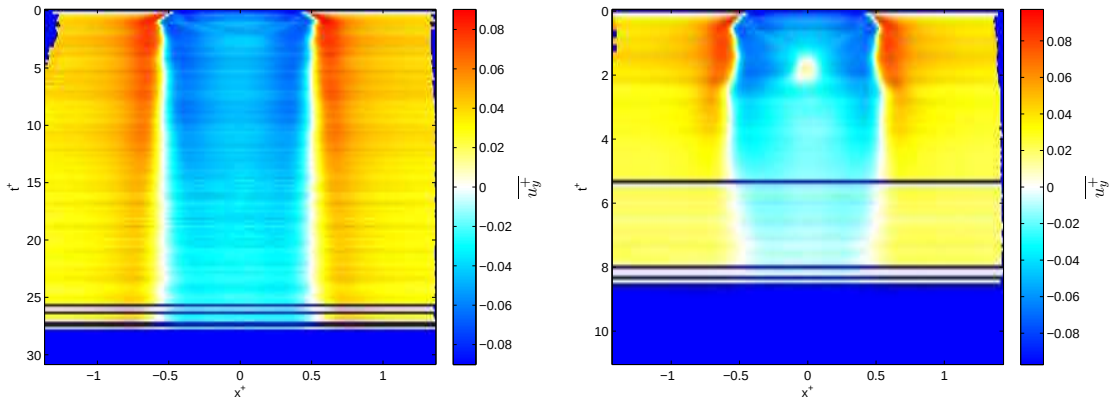

(a) Condition B

(b) Condition F

(c) Condition H

(d) Condition J

Figure 7.39: Comparison of $\overline{u_y^+}$ profiles

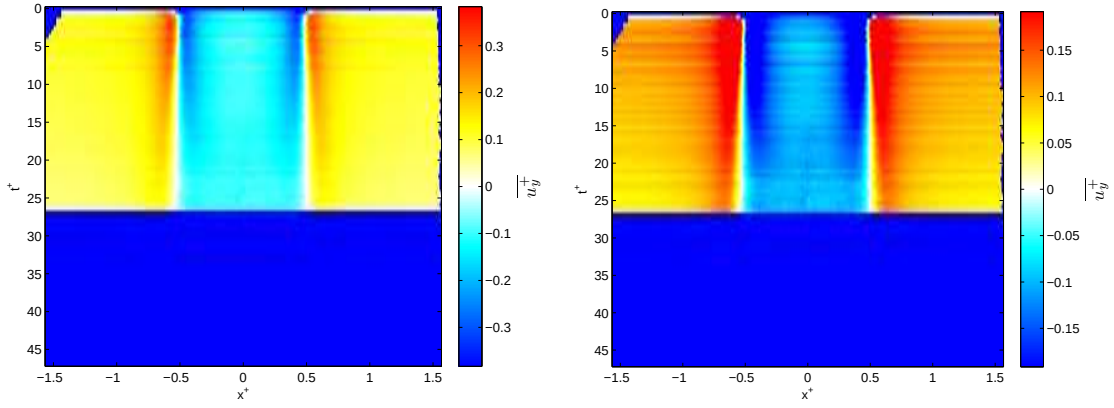

(a) Condition C

(b) Condition C, scaled

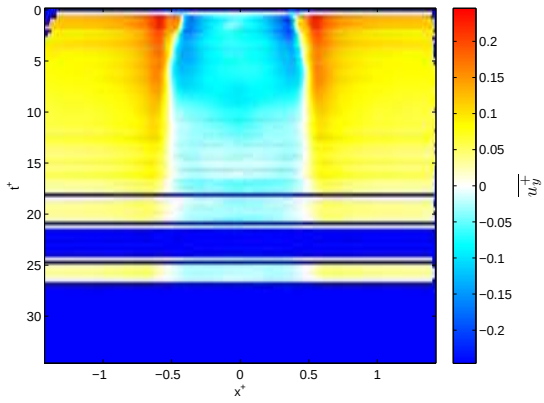

(c) Condition G

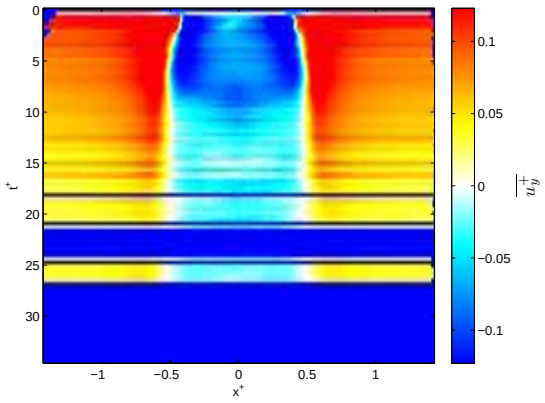

(d) Condition G, scaled

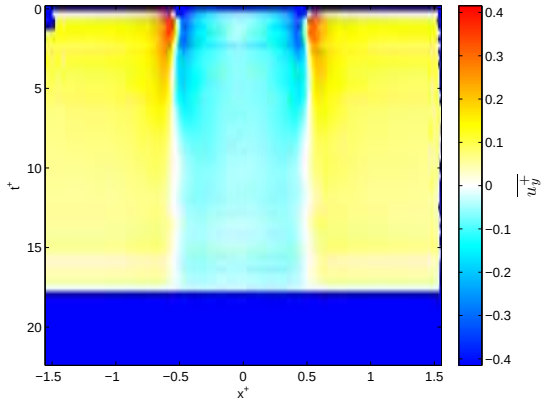

(e) Condition K

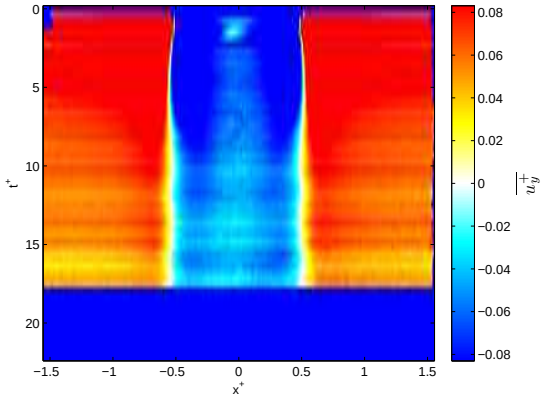

(f) Condition K, scaled

Figure 7.40: Comparison of $\overline{u_y^+}$ profiles, conditions C, G and K

to be cropped in order that it be observed. Unlike the high Reynolds number case, the reduced piston speed vortex rings, actually display the occurrence of a "jet" of fluid with positive $\overline{u_y}$, bursting through the centre of the vortex ring, upwards. Furthermore, for the reduced piston stroke conditions, the jet of fluid is actually prolonged, manifesting for ~ 1 eddy time unit. Also of interest is the apparent deformation to the vortex ring caused by this, after the event we see outwards deformation (this is indicated by the white areas in the plot, showing the core location) and a drop in maximum velocity on the profile.

Profiles of $\overline{u_y}$ for the reduced stroke length conditions are presented in figure 7.40. These figures again illustrate the presence of the bursting jet, however the magnitude and duration is similar to that observed in the high Reynolds number case. Again, for the non-rotating example, no indication of this phenomena was found.

The effect on the velocity profiles is emphasised by the line plots presented in figure 7.41, where velocity profiles displaying the jetting effect are compared against one another. These curves are extracted at points in time displaying the highest magnitude of the phenomena. For the non-rotating conditions, which do not show this, a point in time near the rotating conditions is given for reference.

This plot illustrates the departure from the standard non-rotating velocity profile, shown by solid lines, quite clearly. For conditions I, G and K, the fluid in the region described has sufficiently reduced velocity, that it is almost at rest. For conditions F, H and J the deformation to the velocity profile is very large, creating an upward jet in the centre of the vortex ring. The same phenomena is also seen to be present in condition E, but the effect is much less pronounced than for the other rotating conditions.

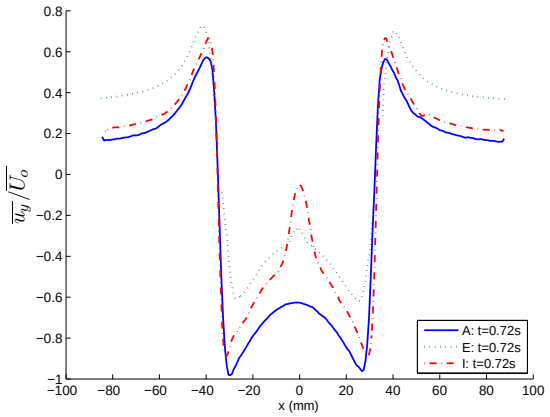

(a) Conditions A, E and I

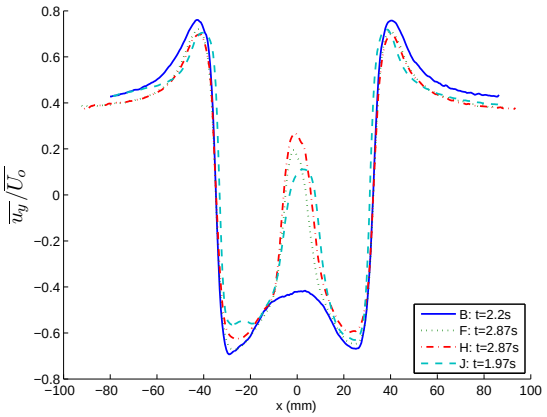

(b) Conditions B, F, H and J

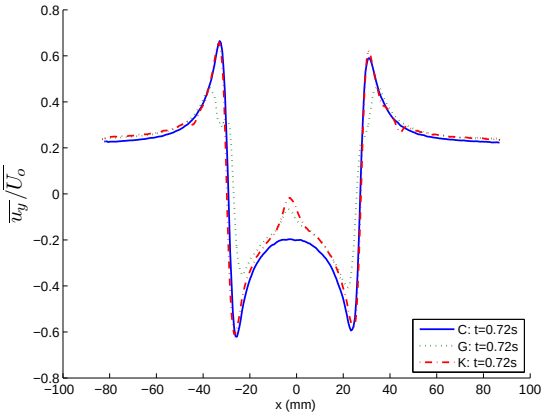

(c) Conditions C, G and K

Figure 7.41: Line plots emphasising differences in $\overline{u_y}$ under background rotation

7.4.3.3 The time evolution of $\overline{u_z}$; fluid flow phenomenon

We see from figure 7.42a that in the vortex cores, opposite signed velocities are to be found in the left and right sides for conditions A, E and I. This disparity between the left and right cores, indicates the presence of a swirling flow. For condition A, the left core has positive $\overline{u_z^+}$ and the right negative, for conditions E and I however, this is reversed, the right core has positive $\overline{u_z^+}$ and the left negative (in these cases, this means that the swirling direction is anti-cyclonic with respect to the direction of rotation).

Figure 7.42b shows data extracted from the $\overline{u_z^+}$ field of the low piston speed conditions: B, F, H and J. We can see from these plots that disparities are present between the left and right cores for conditions F, H and J, again indicating the presence of swirling flow. For condition B however, these disparities are missing, indicating a lack of swirl (this is an artefact of the statistical distribution, as discussed in section 7.4.2.1). We see that for conditions F and J, the $\overline{u_z^+}$ component of the left core is negative, and the right core is positive, indicating an anti-cyclonic swirling motion. The converse is found for condition H, with left core positive and right core negative, however because the rotation rate was reversed in condition H (table 7.1), we again find an anti-cyclonic swirl.

The same data is presented in figure 7.42c for the low stroke length conditions: C, G and K. We find that these data follow the high Reynolds number case, showing evidence of a swirling flow for all conditions.

The flow measured at the inner, outer and far outer locations, for the high Reynolds number conditions is shown in figure 7.43. These plots show very clearly that $|\overline{u_z^+}|$ increases with rotation rate, with condition I having the highest magnitude $\overline{u_x^+}$ and condition A, the lowest. We also see that of the three measurement locations displayed here, outer and far outer have noticeably higher magnitude,

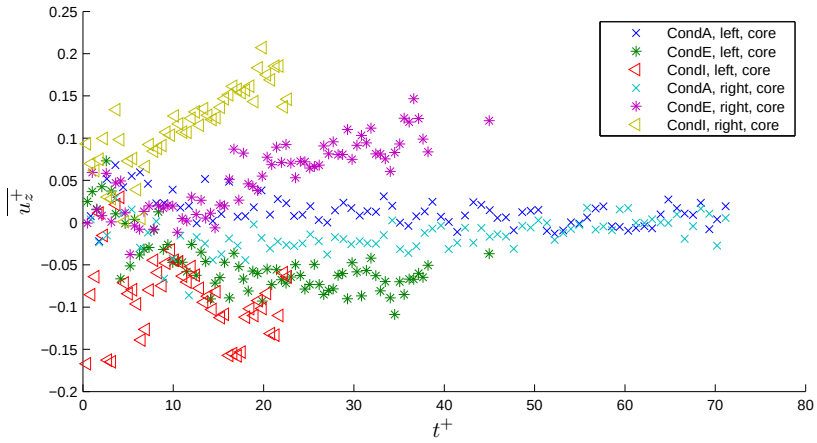

(a) Conditions A, E and I

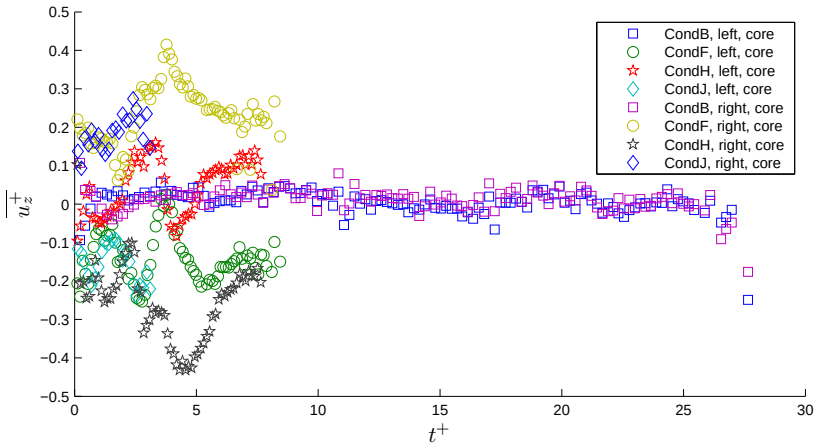

(b) Conditions B, F, H and J

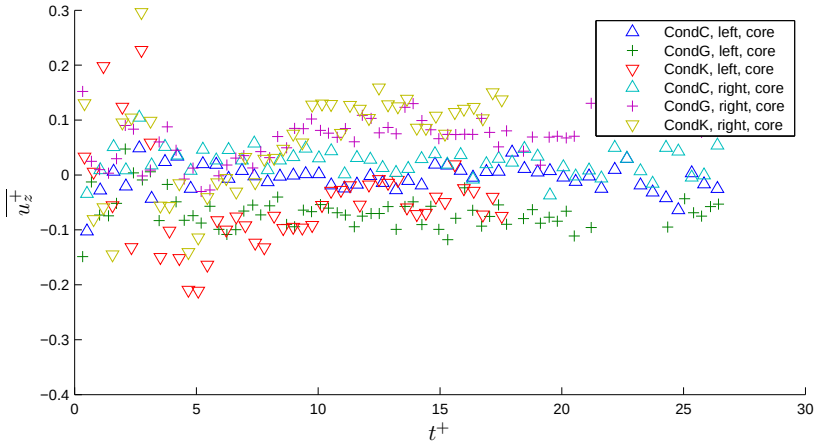

(c) Conditions C, G and K

Figure 7.42: Comparison of $\overline{u_z^+}$, vortex cores

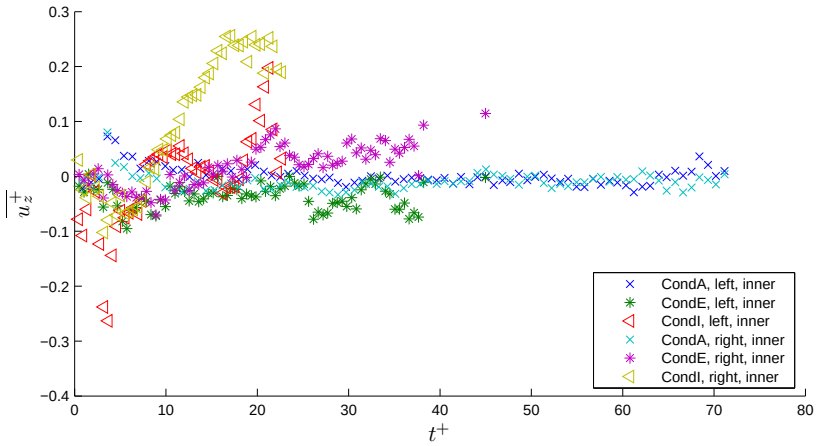

(a) Position: inner

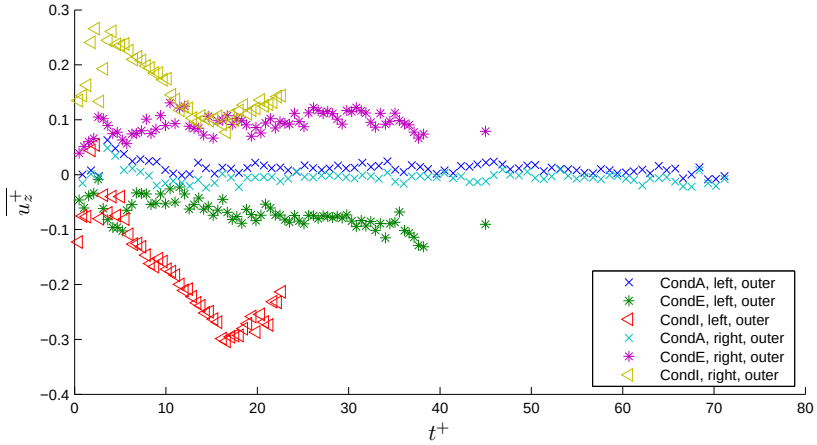

(b) Position: outer

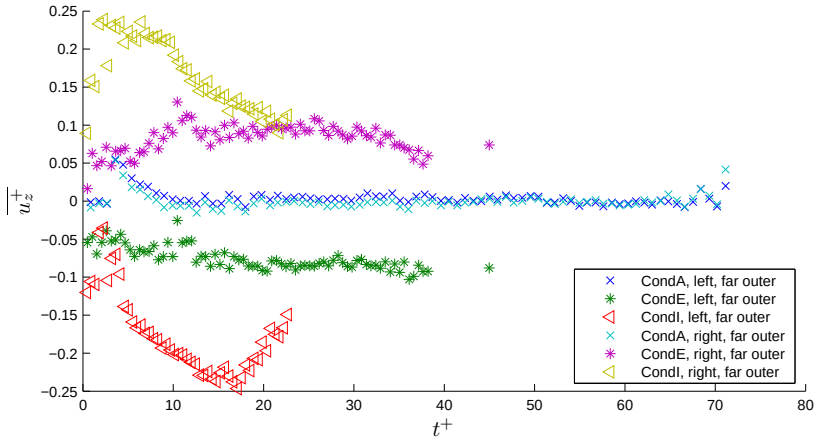

(c) Position: far outer

Figure 7.43: Comparison of $\overline{u_z^+}$, conditions A, E and I

than inner, and that the magnitude of $\overline{u_z^+}$ at outer is very slightly greater than at far outer. Through comparison with figure 7.42a we see that at the centre of the core $\overline{u_z^+}$ is greater than at inner, however less than at outer and far outer.

It can be seen from the plots in figure 7.43 that for conditions E and I, at outer and far outer, the left sides exhibit negative $\overline{u_z^+}$ and the right sides positive $\overline{u_z^+}$, opposite to that seen in condition A. The same is found for conditions E and I at the inner measurement position, although with noticeably reduced SNR, in the case of condition A, the SNR is sufficiently low that it is not possible to isolate trends from data scatter at the inner measurement location.

For condition A (after $t^+ \sim 10$) and condition E we find that the correlation between core velocity extracted around core left and core right is negative, i.e. an increase in velocity around left, results in a decrease in velocity around right. We expect to see rough axial symmetry on the vortex ring, which means that we expect for a real swirling flow, not a measurement artefact, we expect $u_{z_{left}} = -u_{z_{right}}$. This means that we have a reliable indication of swirling flow for condition E, despite the presence of trends arising due to the vortex ring moving out of the light sheet.

For condition A at $t \lesssim 10$, we see a period of decreasing $\overline{u_z^+}$ for all measurement positions. As this decrease is present in all data conditions, roughly constant, and with relatively little data scatter, it is reasonable to assume that the cause is some error in the 3C vector field generation (most likely arising from either camera motion or the calibration adjustment) which results in an erroneous out of plane velocity addition.

Condition I is another matter however, there is clearly a large $\overline{u_z^+}$ velocity at points outer and far outer with core left of opposite sign to core right. However, these values are not symmetric about zero, indicating that any swirl flow is likely to further include some extra bias. The total lack of any correlation between the

trends observed at the outer positions and inner further indicates that any trends present in the flow cannot reliably be described from these plots alone.

To aid in this discussion, we present figure 7.44 which illustrates the evolution of $\overline{u_z^+}$ profiles over time. First considering the variations shown for condition A, figures 7.44a and 7.44b, we see, as predicted, a region of high positive velocity (apparently erroneous), across the entire width of the field at $t \lesssim 10$, and a generally steady swirling motion.

We see significant similarities between the $\overline{u_z^+}$ fields of conditions E and I in figures 7.44c-7.44f.

The inner cyclonic swirl, as seen in figure 7.43a is highlighted in figure 7.44c, where we also highlight the outer, anti-cyclonic swirl. This is done simply to draw attention to the effects present, and it may also be seen in the other plots in figure 7.44 corresponding to rotating conditions. Upon formation the cyclonic wake swirl has very high magnitude, greater than that observed in the anti-cyclonic swirl flow described. This difference in magnitude is particularly noticeable from figures 7.44c and 7.44e, where the magnitude of this swirling flow masks the other velocity profiles.

For conditions E and I, we find that the inner swirl region of one sign "connects" with the outer swirling flow of the same sign, the positive side connects at $t^+ \sim 10$ for condition I and the negative at $t^+ \sim 13$ for condition E. This is highlighted, for convenience in figure 7.44e. We find that after this connection event for condition I, the $\overline{u_z^+}$ field becomes highly asymmetric, with positive velocity covering the majority of the field.

Further investigation of this requires comparison between mean velocity fields and the artefacts in figure 7.44e at corresponding points in time. These are presented in figure 7.45. We see the initial state of the $\overline{u_z^+}$ field in figure 7.45a, the cyclonic swirl shown in figure 7.44 extends from the very top of the frame, curving

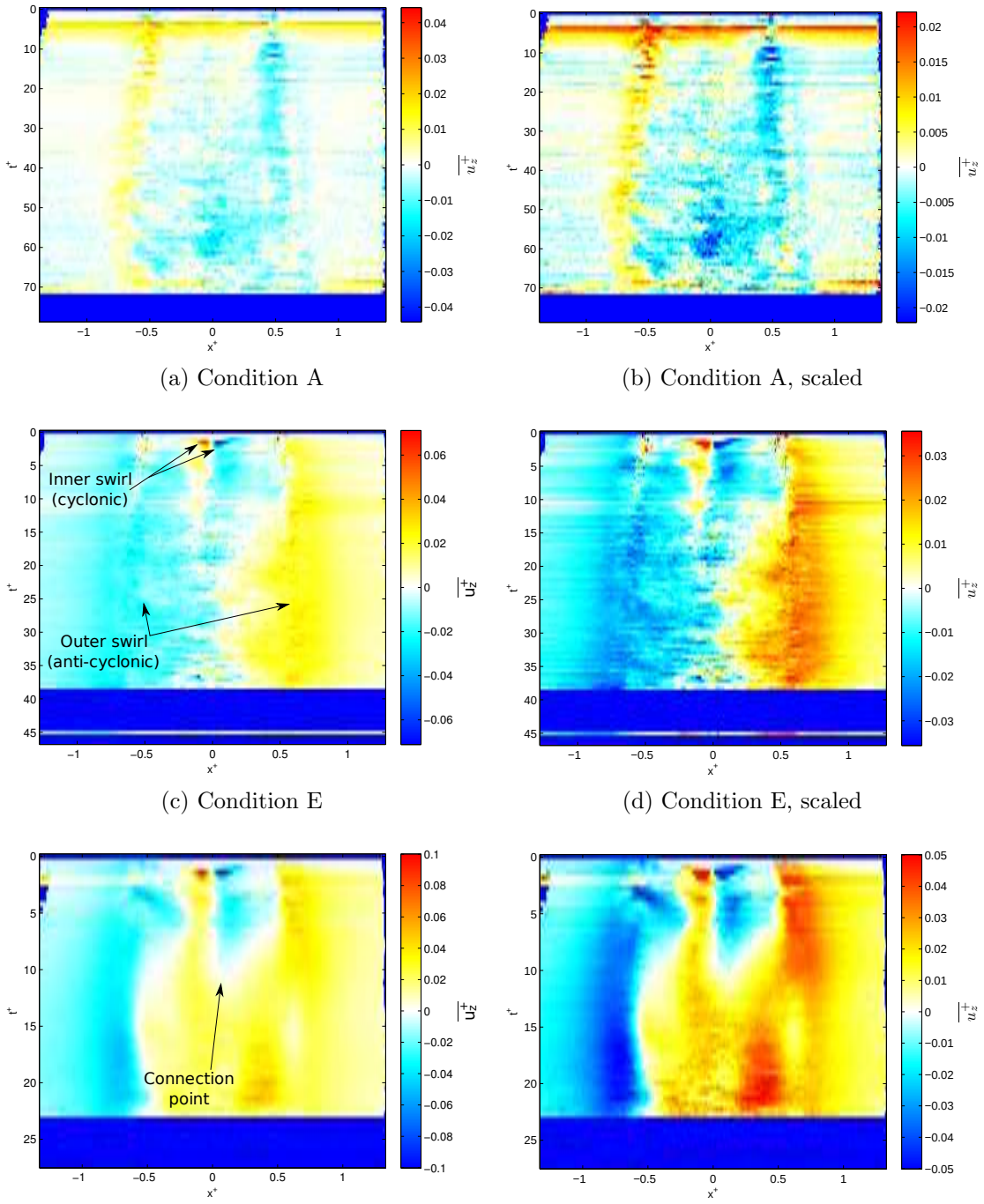

(a) Condition A

(b) Condition A, scaled

(c) Condition E

(d) Condition E, scaled

(e) Condition I

(f) Condition I, scaled

Figure 7.44: Comparison of $\overline{u_z^+}$ profiles, conditions A, E and I

around toward the core of the vortex ring. The large difference in magnitude between u_z in the wake swirl and the rest of the ring is clearly visible in this colourmap.

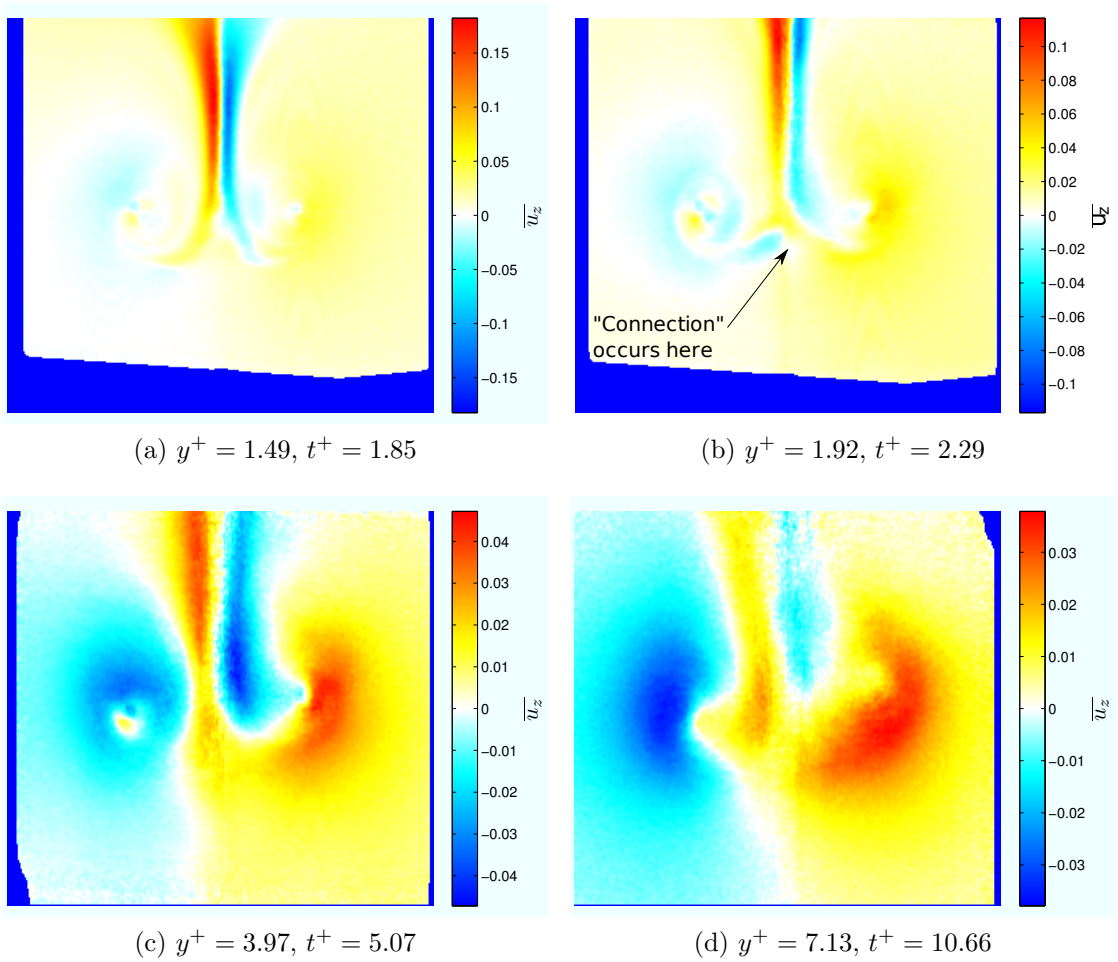

(a) $y^+ = 1.49$, $t^+ = 1.85$

(b) $y^+ = 1.92$, $t^+ = 2.29$

(c) $y^+ = 3.97$, $t^+ = 5.07$

(d) $y^+ = 7.13$, $t^+ = 10.66$

Figure 7.45: Samples from condition I, $\overline{u_z}$

Figure 7.45b shows the same field a short time later, here we see that the field has changed significantly, and a degree of axial asymmetry has formed, this is the beginnings of the asymmetry we found previously in figure 7.44e. We see that at this point in time ($t = 0.89s$), the positive wake swirl is now "connected" to the positive outer swirl, which is marked for improved clarity.

Figures 7.45c and 7.45d show the evolution of the velocity field at points

later in time, indicating how the flow shown in figure 7.45b develops. One can see clearly in figure 7.45d that the negative element of the wake swirl has been reduced sufficiently that it no longer appears in a profile extracted through the centre of the two vortex cores.

Figure 7.46 shows the variation of conditions B, F, H and J at measurement points inner, outer and far outer. As discussed in section 7.4.2.1, we see that no appreciable difference between the measurements of condition B at core left and core right, at all of the measurement points considered. As with conditions A, E and I we find that increasing the Rossby number in general acts to increase $\overline{u_z^+}$. We find that for conditions F and J, core left at positions outer and far outer $\overline{u_z^+}$ is negative and core right, positive. Condition H however displays the same variations in velocity as condition F, but with opposite sign, i.e. positive $\overline{u_z^+}$ around core left, negative around core right. We observe a similar trend for the inner measurement position, however data at this measurement position is of low magnitude and shows higher scatter. For conditions F and H, we see a sudden increase in $\overline{u_z^+}$ magnitude at $t^+ \sim 3$ for core right only. A similar phenomena is also seen for condition J, where we see a greater increase in magnitude for core right, resulting in higher $\overline{u_z^+}$ than for core left.

These phenomena and their spatial distribution can be seen from figure 7.47. Figure 7.47a shows that no major motions are present for the mean field of condition B. Conditions F, H and J are quite different however, showing a large anti-cyclonic swirling flow to be present around the outside of the vortex ring, as was displayed for the high Reynolds number cases previously. We can also observe the formation of a strong cyclonic swirling motion, between the inner measurement locations as found in the high Reynolds number cases. It can also be seen that the left hand side of this cyclonic swirling flow connects with the outer anti-cyclonic swirl at $t^+ \sim 6$ for conditions F and H.

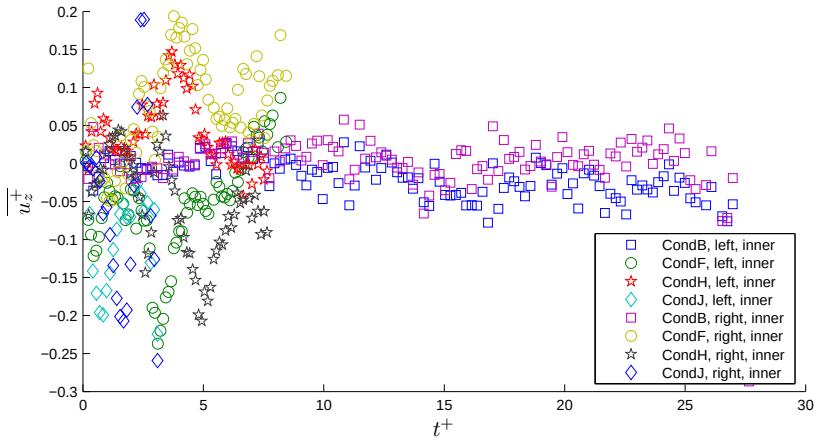

(a) Position: inner

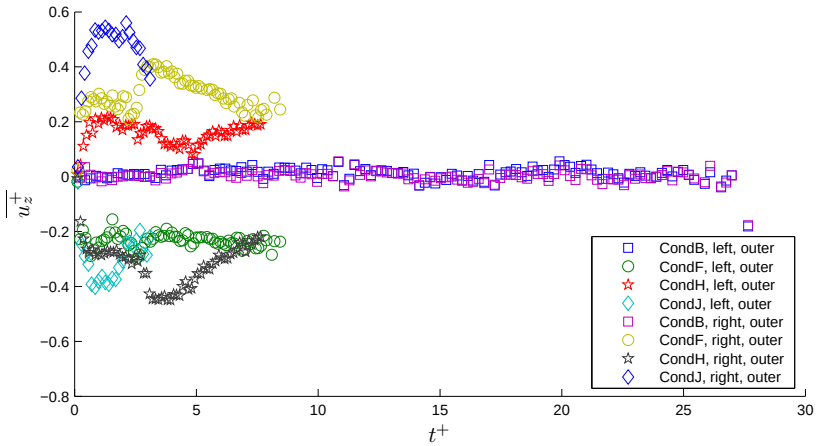

(b) Position: outer

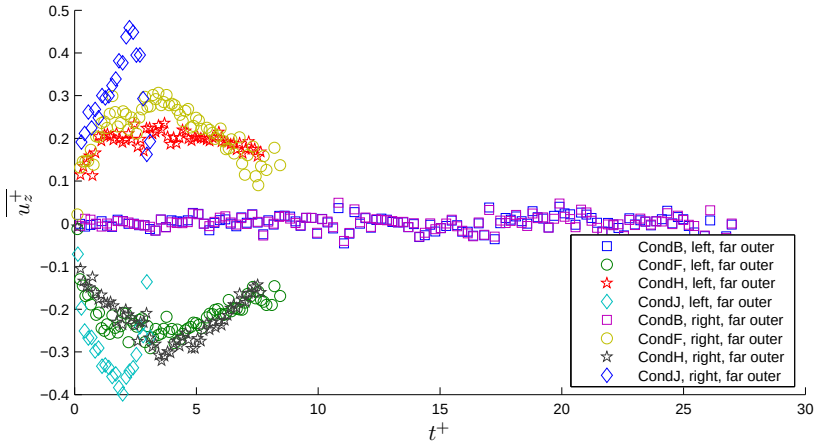

(c) Position: far outer

Figure 7.46: Comparison of $\overline{u_z^+}$, conditions B, F, H and J

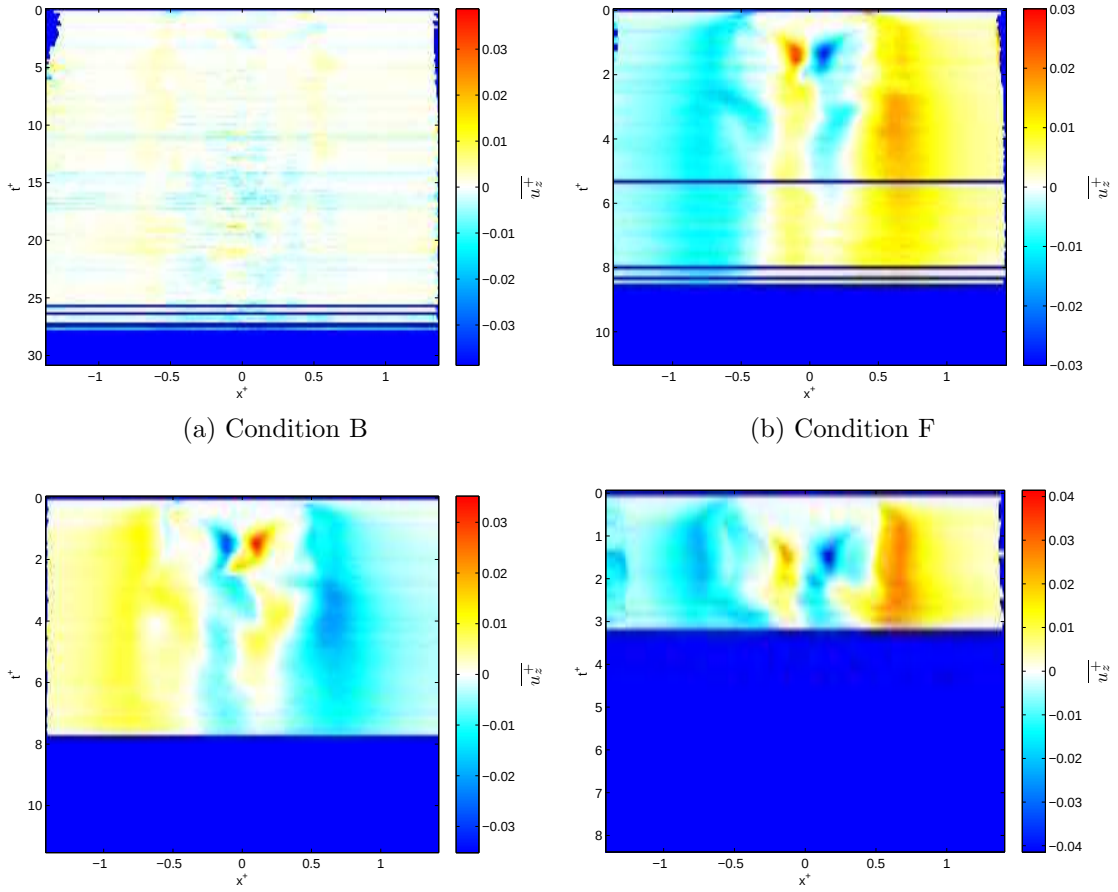

(a) Condition B

(b) Condition F

(c) Condition H

(d) Condition J

Figure 7.47: Comparison of $\overline{u_z^+}$ profiles, conditions B, F, H and J

Figure 7.48 shows an example $\overline{u_z^+}$ field for conditions F and J. We see that in both cases, the connection between the cyclonic and anti-cyclonic swirling flows forms in the same fashion as described for condition I, figure 7.45.

Figure 7.49 shows the variation of conditions C, G and K at measurement points inner, outer and far outer. The trends seen for these generation parameters are the same as for the high Reynolds number case, conditions A, E and I. We find the same general trend of an increase in the magnitude of recorded $\overline{u_z^+}$ with rotation rate, for all measurement locations. At positions outer and far outer, we see that for conditions G and K, the velocity found in the left core is negative and

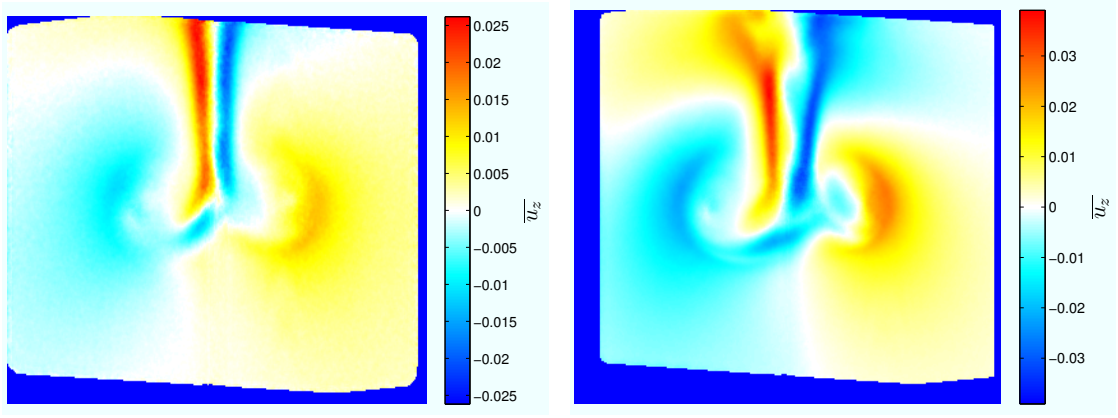

(a) Condition F, $t^+ = 1.56$, $y^+ = 1.66$ (b) Condition J, $t^+ = 2.01$, $y^+ = 1.25$

Figure 7.48: Samples from conditions F and J, $\overline{u_z}$

positive in the right core, indicating anti-cyclonic swirl, whereas for condition C the left core is positive and the right negative.

For condition G, we find good correlation between the data from core left and core right at the outer and far outer measurement locations, whereas we see strong disparity for the inner position. At outer and far outer, we find core right has slightly higher magnitude than left. At the inner measurement location, we find strong disparity between cores left and right; this same trend is observed for condition K. We also find very high scatter for condition K at $t^+ \lesssim 4$, indicating that this data is most likely unreliable. For $t^+ \gtrsim 4$ we find trends appearing both in core left and core right, however there is disparity between the magnitude of measurements from cores left and right, with core left this time tending to be larger.

Figure 7.50 shows the time evolution of horizontal velocity profiles extracted through the cores of vortex rings from conditions C, G and K. From figure 7.50a and 7.50b we again see evidence of the wake swirl for condition C. Figures 7.50c-7.50f show that the evolution for conditions G and K is similar to the other rotating conditions. We find that, again, a cyclonic central swirling is present,

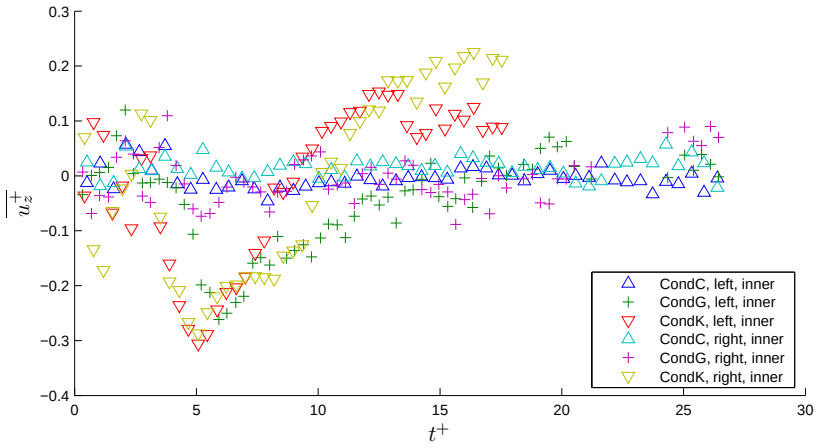

(a) Position: inner, left and right

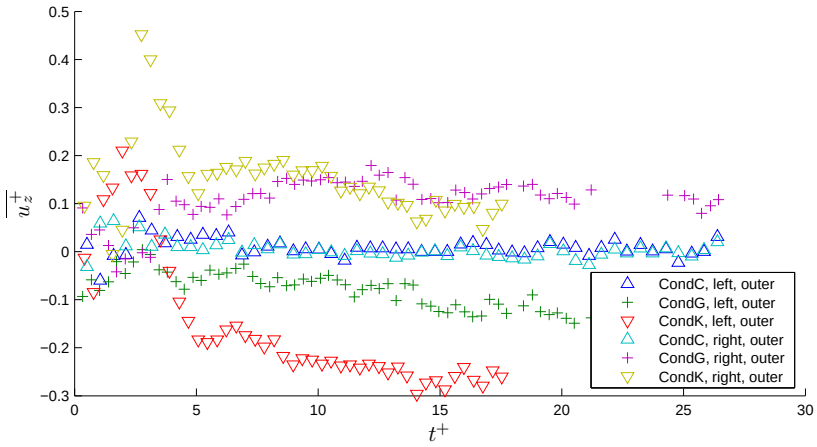

(b) Position: outer, left and right

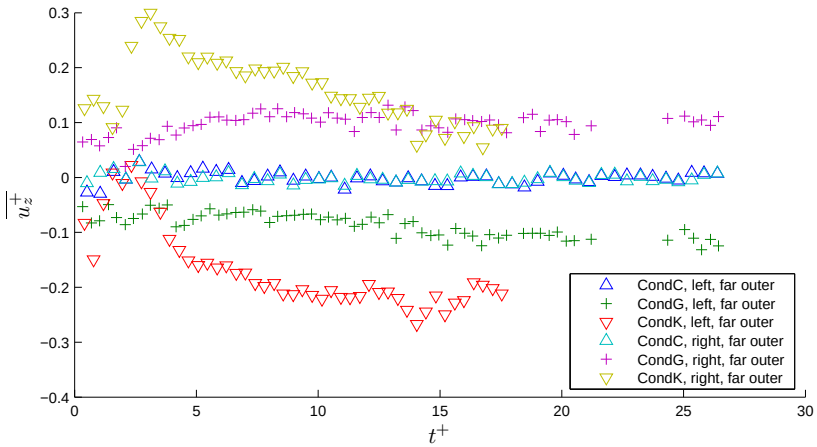

(c) Position: far outer, left and right

Figure 7.49: Comparison of $\overline{u_z^+}$, conditions C, G and K

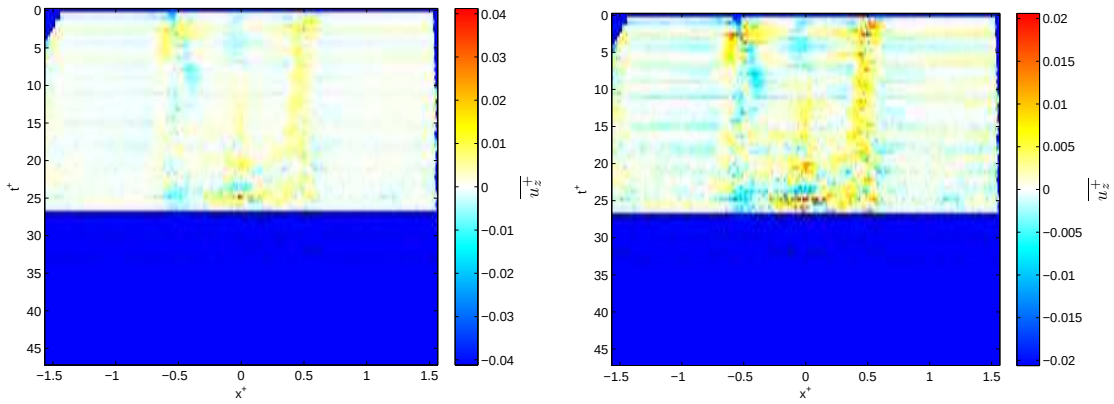

(a) Condition C

(b) Condition C, scaled

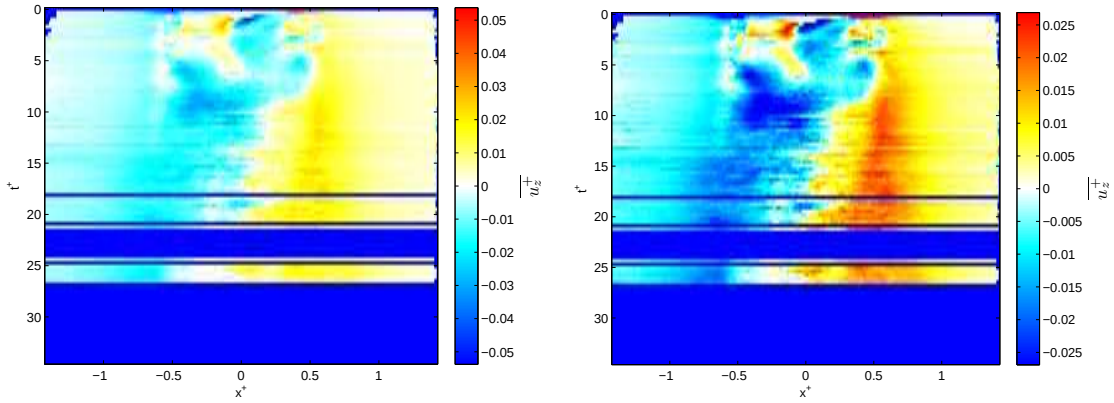

(c) Condition G

(d) Condition G, scaled

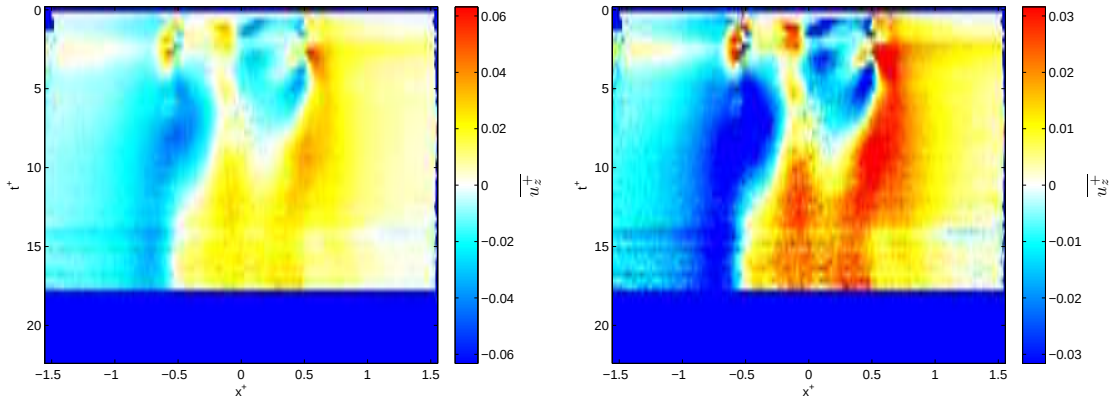

(e) Condition K

(f) Condition K, scaled

Figure 7.50: Comparison of $\overline{u_z^+}$ profiles, conditions C, G and K

which again connects with the outer anti-cyclonic swirling flow; this happens at $t^+ \sim 6s$ for condition G and $t^+ \sim 9s$ for condition K. Figure 7.51 shows the early stages of this formation, and indicates, as for conditions E and I, the presence of a complex 3D motion.

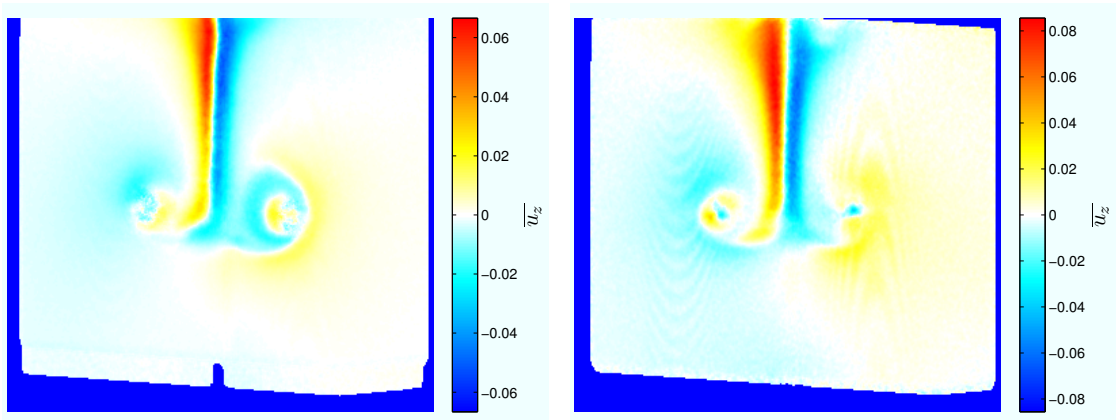

(a) Condition G, $t^+ = 1.73s$, $y^+ = 1.48$ (b) Condition K, $t^+ = 1.56$, $y^+ = 1.32$

Figure 7.51: Samples from conditions G and K, $\overline{u_z}$

7.4.3.4 The time evolution of $\overline{u_z^+}$; evaluation of velocity field corrections

Figure 7.52 illustrates the variation of $\overline{u_z^+}$ at measurement points above and below. We see that for conditions E and I, the vortex ring quickly moves out of the light sheet towards the cameras. This is indicated by the increase in the velocity measured at the above location, combined with the simultaneous decrease measured at the below location. For condition E, the ring continues upon this trajectory; for condition I however, the vortex ring then moves back through the centre of the light sheet and travels on the far side of it. The same pattern is distinguishable for both the left core, figure 7.52a and the right core, figure 7.52b. However it can be seen that for both conditions E and I, the mean of the curves for above and below, is non-zero. For left, the net $\overline{u_z^+}$ flow is negative

and for right, the net $\overline{u_z^+}$ flow positive, therefore indicating the likely presence of a cyclonic swirling flow at these positions.

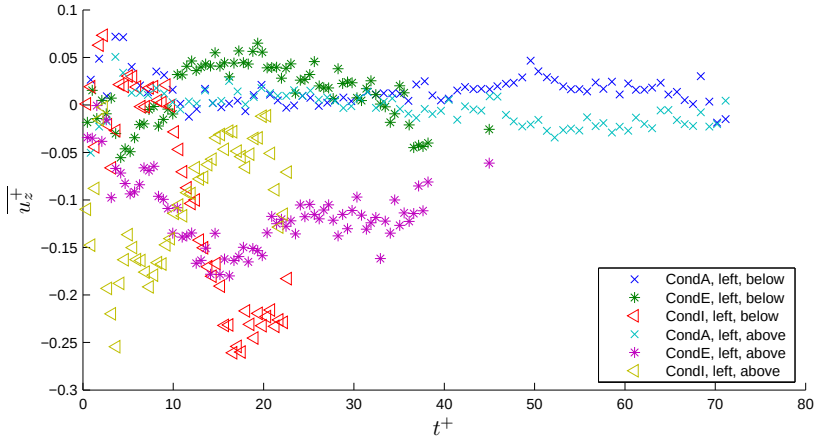

(a) Left core

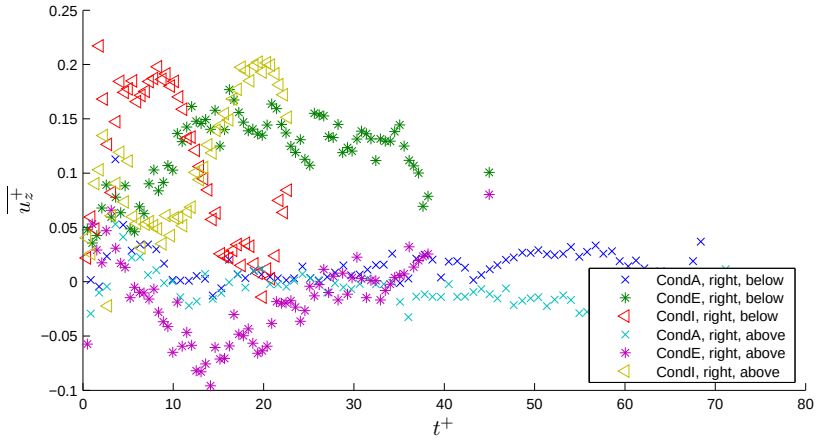

(b) Right core

Figure 7.52: Comparison of $\overline{u_z^+}$, conditions A, E and I at positions above and below

The trends presented in figure 7.53 illustrate the evolution of the measurement points above and below for conditions B, F, H and J. We can see that for condition B, over time the above measurement points become increasingly positive and the below points, increasingly negative. The same trend is observed for core left and right, thus indicating the failure of the out of light sheet correction to completely correct the data.

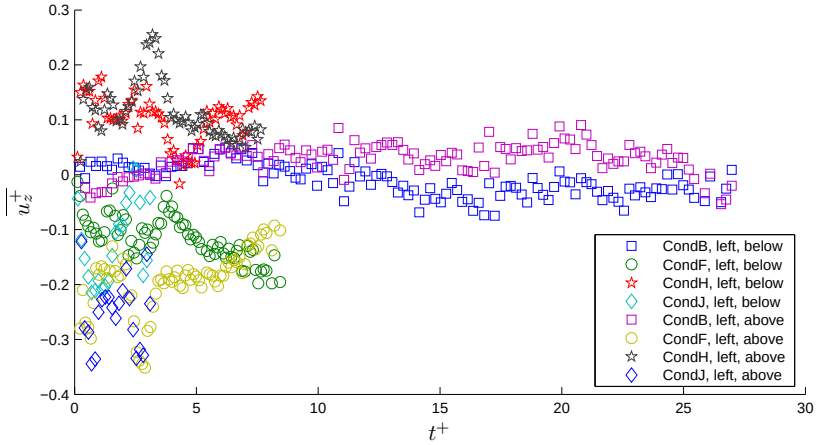

(a) Left core

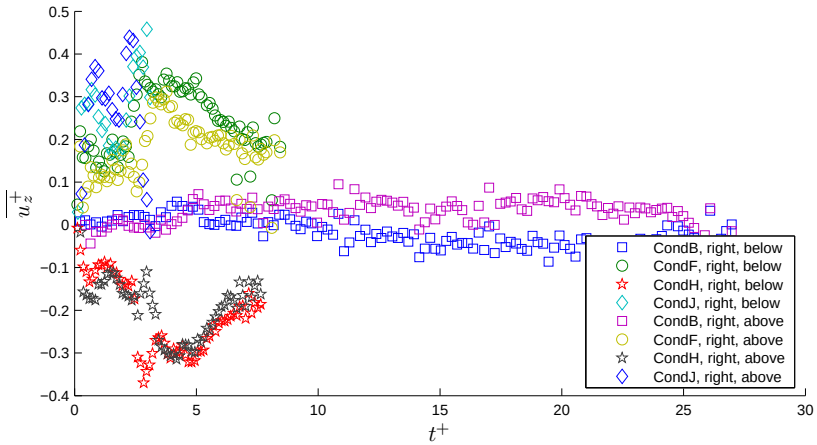

(b) Right core

Figure 7.53: Comparison of $\overline{u_z^+}$, conditions B, F, H and J at positions above and below

For conditions F, H and J, we see slightly more disparity between above and below for the left core than for the right, but on the whole, the two curves show the same trends. We also see that the data presented for the left core follows similar trends to that in the right core, but inverted, again indicating the presence of a swirling flow.

Figure 7.54 shows the variation of measurement positions above and below over time. For all conditions, we find similar trends for cores left and right. Condition C shows reasonable correlation over time, however at $t^+ \sim 15$ we see

an increase in the disparity between positions above and below, which increases with time. This indicates that some z motion has not been accounted for and the subsequent reprojection has not rendered the vortex ring such that its centre coincides with the light sheet. We find that for condition C below becomes negative and above positive, which means that the reprojected ring lies the near side of the light sheet to the cameras. For conditions G and K we find that the disparity between above and below increases quickly with below positive and above negative, thus indicating the ring no longer lies in the light sheet and is positioned the far side, away from the cameras.

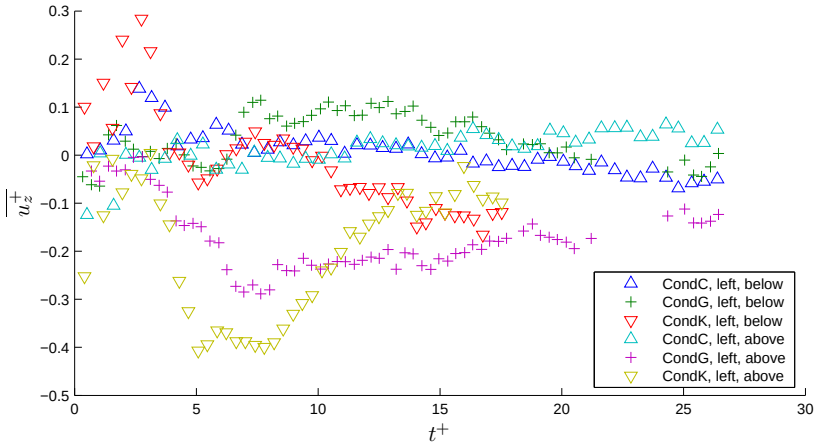

(a) Left core

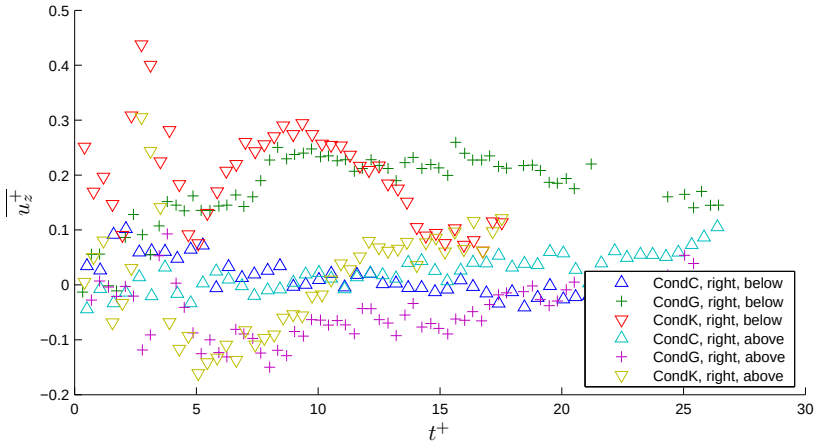

(b) Right core

Figure 7.54: Comparison of $\overline{u_z^+}$, conditions C, G and K at positions above and below

7.4.3.5 The time evolution of $\overline{\omega_z}$

Next we consider the changes imposed upon the vorticity field by the addition of background rotation. Figure 7.55 shows the variation of $\overline{\omega_z^+}$ for the conditions of the high Reynolds number case, note that the plots here are for the mean of ω_z for cores left and right. Shortly after generation however, we see that the vorticity in the centre of the vortex core in condition E is lower than in condition A (figure 7.55a). The same trend is observed for measurement point below however, at above the vorticity is found to be substantially greater than for condition A. At all these measurement locations, the decay rate for vorticity from condition E is slightly greater than for condition A. For the outer and inner measurement locations, figure 7.55c, no difference is discernible between conditions A and E.

The high rotation rate case, condition I, shows markedly increased $\overline{\omega_z^+}$ upon generation, when compared with either condition A or E, and the vorticity generated is seen to decay more rapidly than for the other conditions. This trend is found across all the measurement locations considered, however it is found that for the core vorticity, the most severe decrease in vorticity occurs in the range $2 \lesssim t^+ \lesssim 8s$.

The colour maps presented in figure 7.56 show the spatial variation of vorticity over time. We see from figure 7.56b that over time an increasing amount of vorticity appears in the region between the two vortex cores. Further we see that at $t^+ \sim 35s$ the magnitude of this vorticity increases. The vorticity deposited is of the same sign as its nearest vortex core. Figure 7.56b is annotated to aid in the visualisation of these phenomena.

For conditions E and I however, we notice that at the beginning of the run, a small quantity of low magnitude vorticity forms in the centre of the vortex ring, this is highlighted in figure 7.56b (recall that scaled means that the scale of

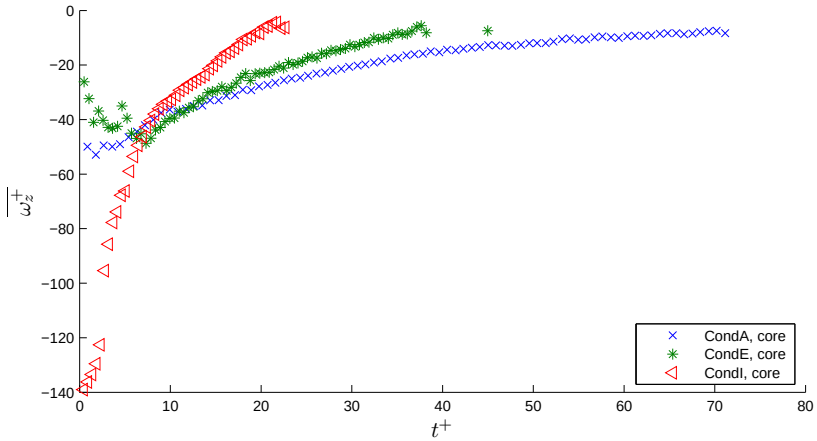

(a) Position: vortex core

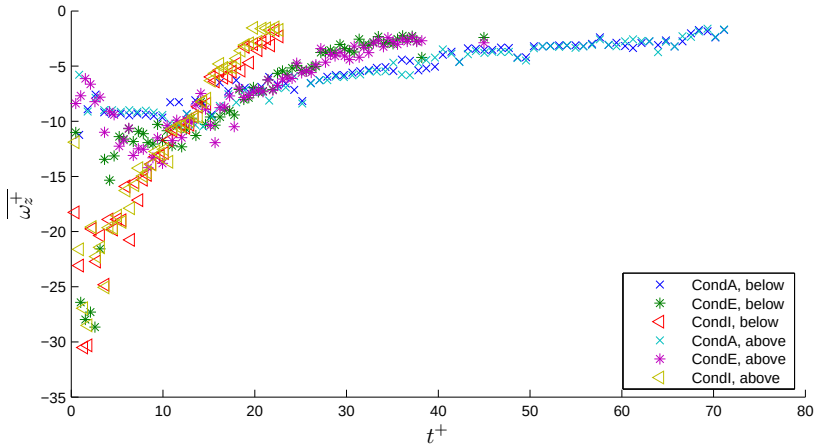

(b) Position: above and below

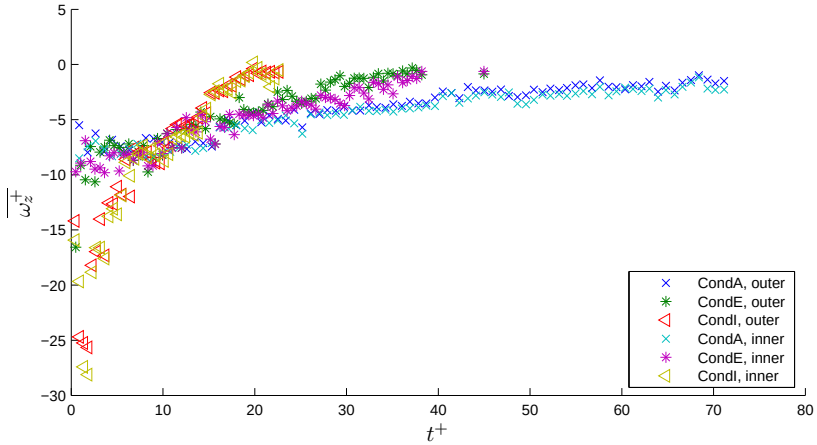

(c) Position: outer and inner

Figure 7.55: Comparison of $\overline{\omega_z^+}$, conditions A, E and I

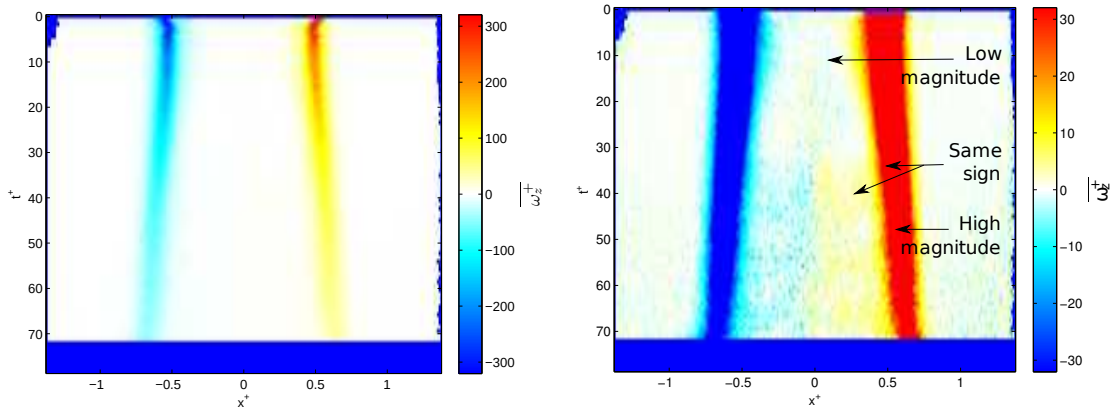

(a) Condition A

(b) Condition A, scaled

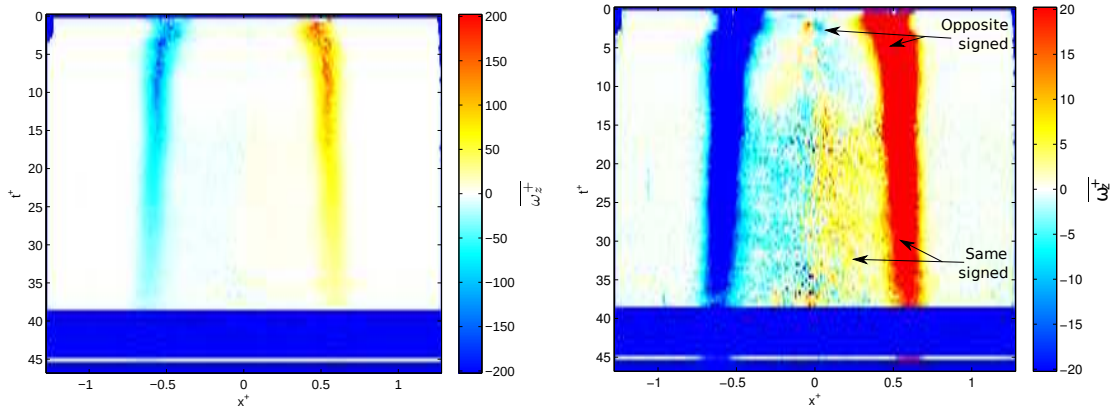

(c) Condition E

(d) Condition E, scaled

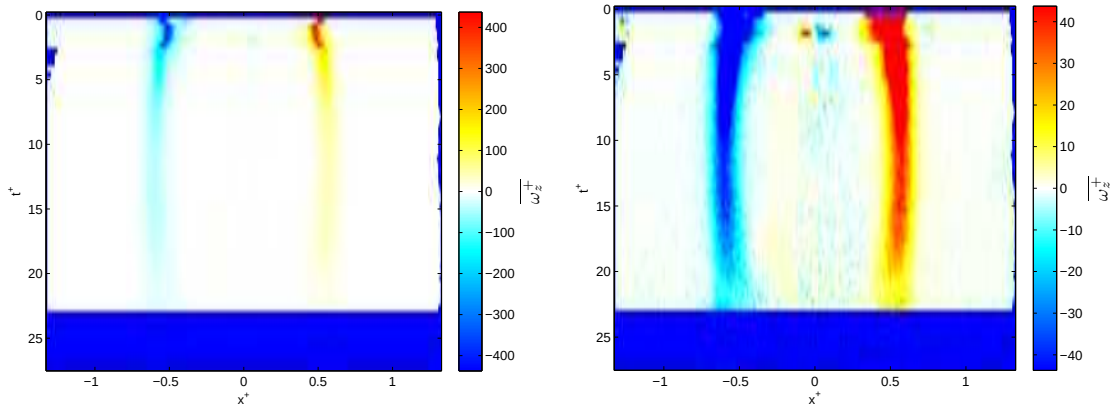

(e) Condition I

(f) Condition I, scaled

Figure 7.56: Comparison of $\overline{\omega_z^+}$ profiles, conditions A, E and I

the colourmap has been adjusted to enhance low magnitude features, otherwise less visible). This vorticity is of opposite sign to the core nearest, and shall be shown to represent the vorticity shedding described by Verzicco *et al.* (1996). In both cases the phenomena occurs at $t^+ \sim 2$, however for condition I the vorticity found near the vortex ring axis is of larger magnitude and size. We can also see from figure 7.56e that very shortly after this event ($t^+ \sim 4$) there is a noticeable and sudden decrease in the vorticity present in the cores (this corresponds to the sharp decreases noted in the point extractions).

In the case of condition E, we see that opposite signed vorticity continues to be deposited into this central region until $t^+ \sim 12$, figure 7.56d. After this point, the rate of vorticity release is increased and the sign reversed, meaning that vorticity of the same sign as the core is deposited between the vortex cores. For condition I however, opposite signed vorticity continually appears near the axis, however at a reduced rate.

We find that for the vortex rings generated with reduced piston speed, the vorticity field evolves differently to the high Reynolds number case. Considering the case of the profiles of vorticity measured from the centre of the core, figure 7.57a, upon comparison with condition B we find an increase in the magnitude of vorticity upon generation for the slower rotating conditions F and H, but a decrease for the faster rotating condition J. All three rotating conditions show similar rates of vorticity decay which are slightly faster than for condition B. For conditions H and F we find rapid, almost linear decay until $t^+ \sim 3$, where the decay rate reduces slowly, condition J similarly decays quickly and almost linearly; there is however no levelling off. Condition B shows, on the other hand, a steadily decreasing decay rate.

Trends are significantly harder to identify in figures 7.57b and 7.57c, largely due to the high data scatter at $t^+ \sim 2.5$. We do however see the same time

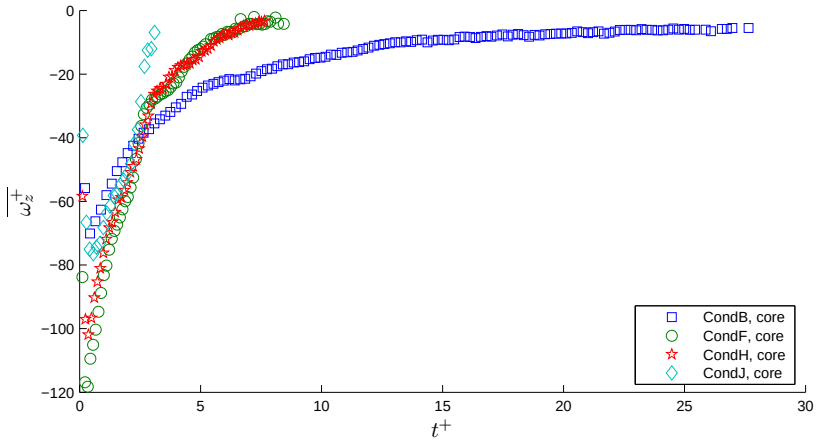

(a) Position: vortex core

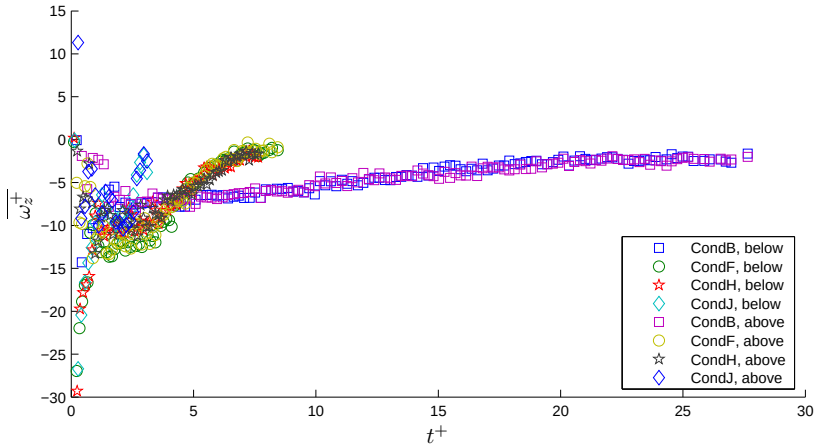

(b) Position: above and below

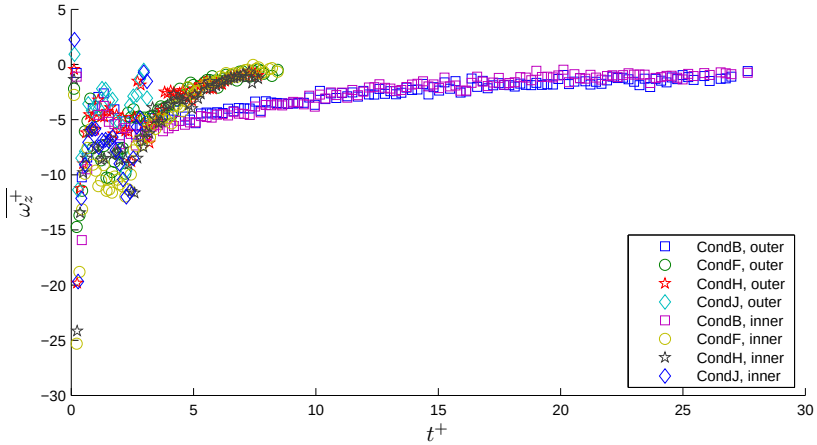

(c) Position: outer and inner

Figure 7.57: Comparison of $\overline{\omega_z^+}$, conditions B, F, H and J

evolution for above, below, outer and inner, and that profiles for conditions F and H evolve in a very similar fashion. Condition B evolves steadily, with $\overline{\omega_z^+}$ showing decreasing rate of decay, conditions F and H show a region of decay, similar in magnitude to that of condition B. This begins at $t^+ \gtrsim 3s$ and continues until $t \sim 6s$ for above and below and $t \sim 5s$ for outer and inner, where it is most noticeable in the inner profiles.

Figure 7.58 presents a set of colour maps which illustrate the time evolution of the vorticity field for conditions B, F, H and J. Figures 7.58a and 7.58b show that very little of note happens to the $\overline{\omega_z^+}$ field for the non-rotating case, especially when compared with conditions F, H and J, figures 7.58c-7.58h.

For conditions F and H, we find the appearance of high magnitude, opposite signed vorticity near the vortex ring axis, occurring at $t^+ \sim 2$. This is also accompanied by a rapid decrease in the strength of vorticity present in the field and the apparent drifting apart of the cores. We also see the occurrence of a very small parcel of weak negative vorticity, just outside of the positive vortex core, slightly before $t^+ = 3$, and a small packet of weak positive vorticity appears outside of the negative core slightly after $t^+ = 4$. These effects are annotated for condition J and all correspond to the secondary vorticity shedding discussed by Verzicco *et al.* (1996).

For condition J, we see the same phenomena as in conditions F and H, however they occur with greater magnitude and earlier in time. A major release of opposite signed vorticity occurs into the centre of the vortex ring at $t^+ \sim 1.5$ and persists until $t \sim 2.75$, when opposite signed vorticity is further deposited onto the outside of the vortex ring. This final deposition in fact initiates the collapse of the vortex ring.

For the reduced stroke length conditions, C, G and K, plots of $\overline{\omega_z^+}$ over time are given in figure 7.59 and show similar trends to that observed in conditions

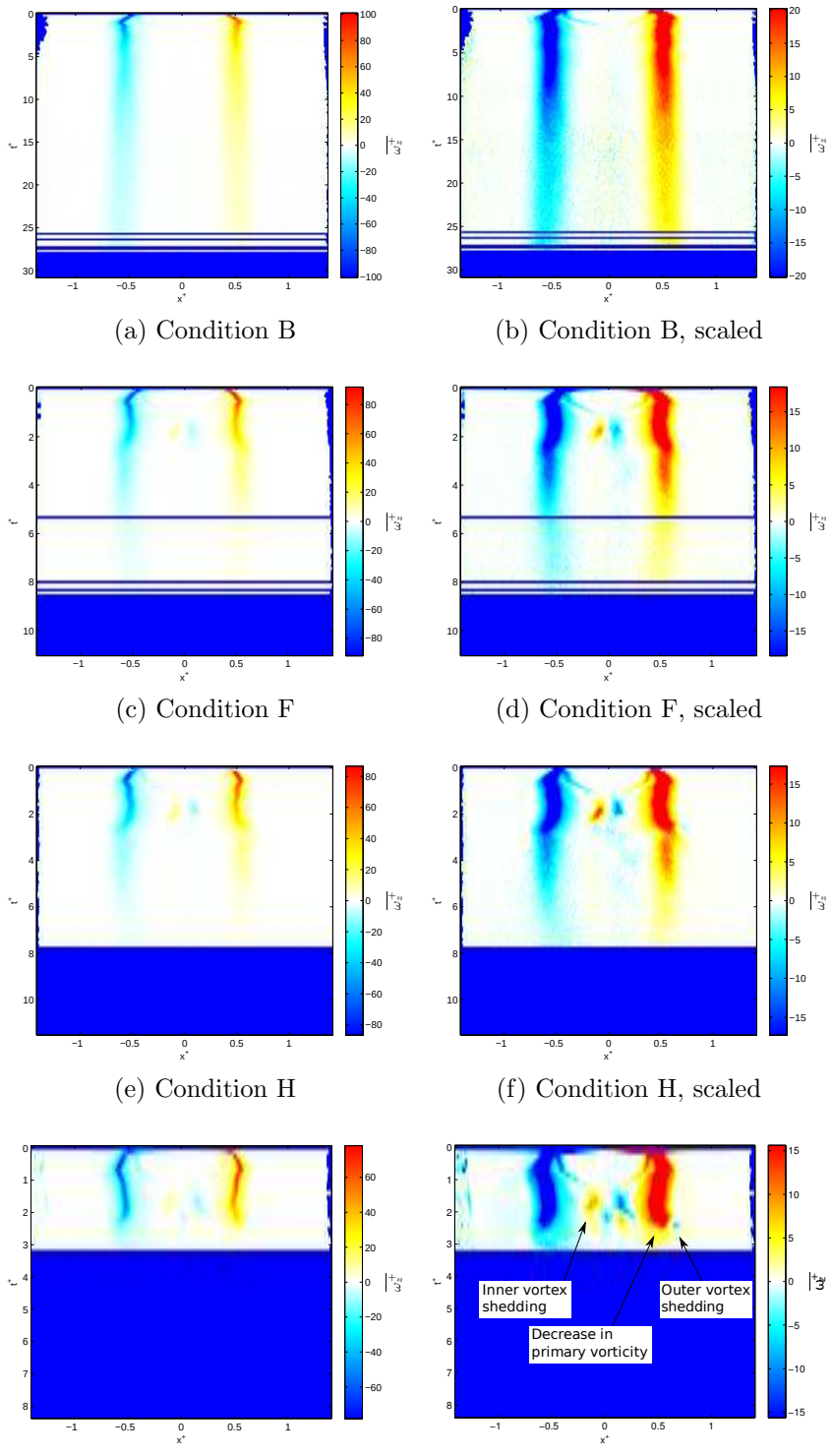

(a) Condition B

(b) Condition B, scaled

(c) Condition F

(d) Condition F, scaled

(e) Condition H

(f) Condition H, scaled

(g) Condition J

(h) Condition J, scaled

Figure 7.58: Comparison of $\overline{\omega_z^+}$ profiles, conditions B, F, H and J

A, E and I. We find the initial vorticity in the core of the low rotation rate case, G, to be lower than the initial velocity in the non-rotating case, C. The high rotating condition, K, however shows higher $\overline{\omega_z^+}$ initially, when compared with C, figure 7.59a. This is also seen, although less dramatically, in the plots for above, below outer and inner figures 7.59b and 7.59c. We also see that as with the high Reynolds number conditions, the initial rate of decay of condition K is significantly greater than for either condition G or condition C. Furthermore, we find that the rate of decay of C is slightly greater than for G, initially.

The colour maps shown in figure 7.60 show the time evolution of vorticity fields for conditions C, G and K. We find, as in the other cases, little of note for the non-rotating case, condition C. For the rotating conditions, C and K, similar patterns are seen to those found for the other vortex generation conditions, however the magnitude is notably reduced relative to conditions E, F, G, H, I and J.

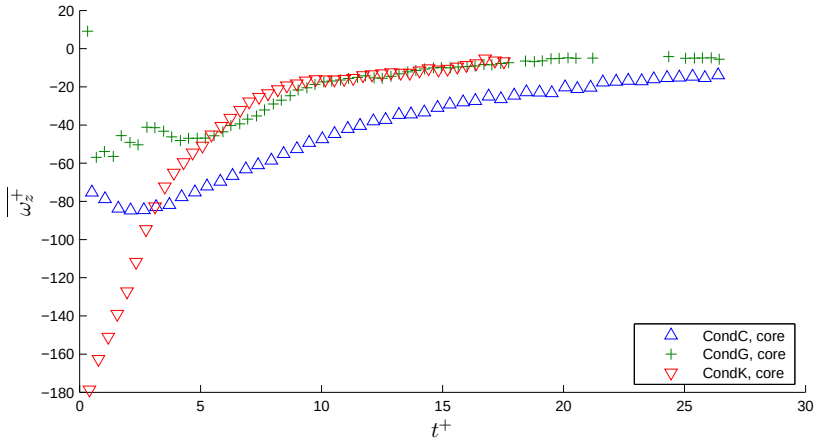

(a) Position: vortex core

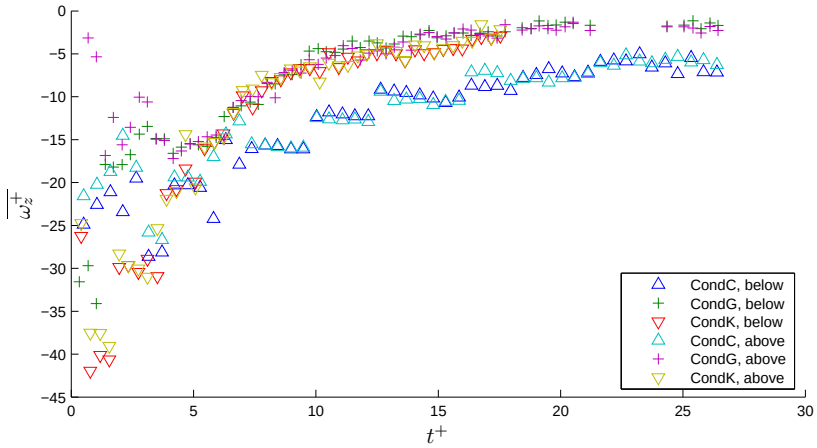

(b) Position: above and below

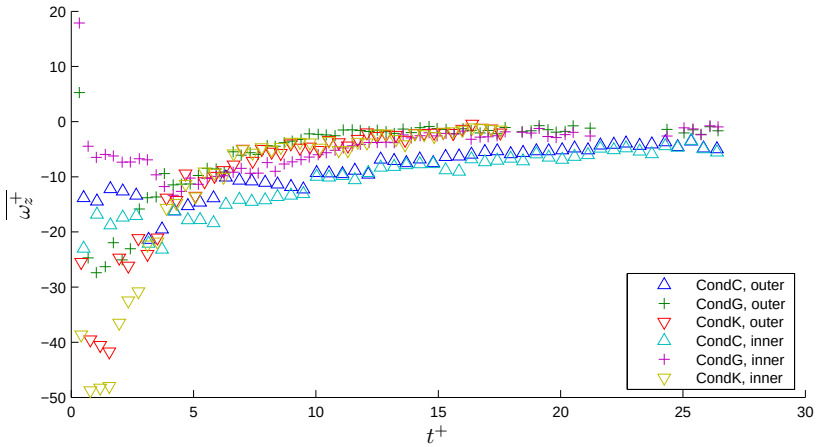

(c) Position: outer and inner

Figure 7.59: Comparison of $\overline{\omega_z^+}$, conditions C, G and K

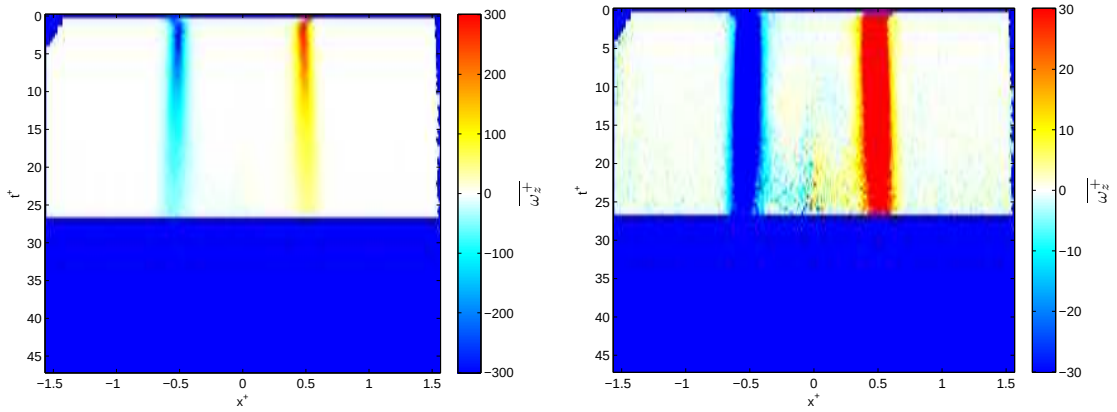

(a) Condition C

(b) Condition C, scaled

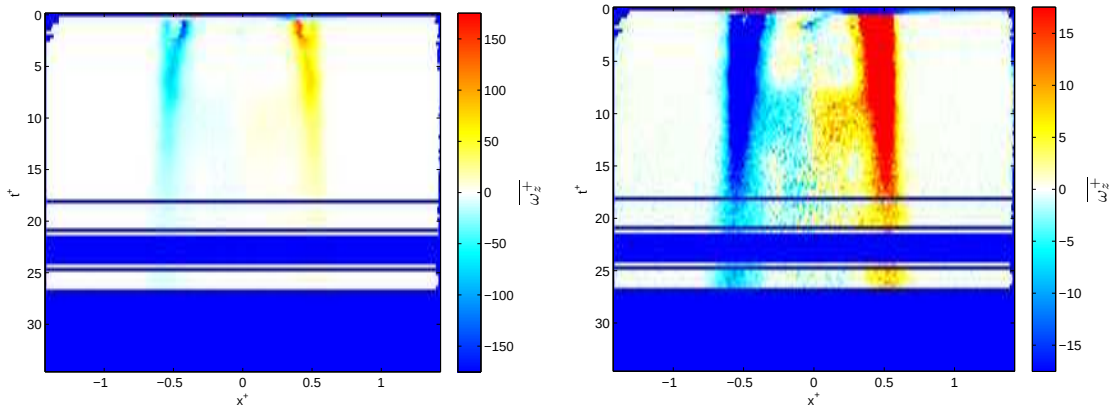

(c) Condition G

(d) Condition G, scaled

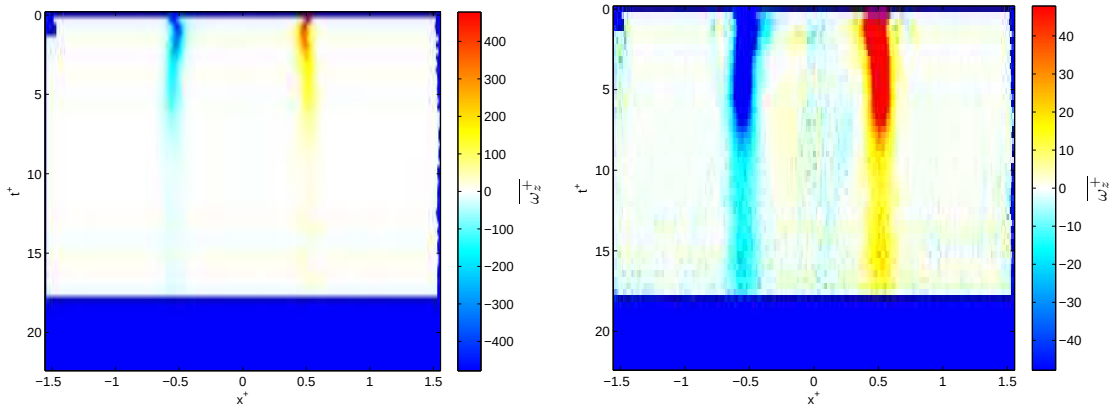

(e) Condition K

(f) Condition K, scaled

Figure 7.60: Comparison of $\overline{\omega_z^+}$ profiles, conditions C, G and K

7.5 Full field time evolution

Further to the results presented in sections 7.4, we show actual frames from components of the mean velocity and vorticity fields as well as plots of streamlines in order to qualitatively illustrate the changes imposed upon the fluid by background rotation.

For our comparison, the low inertial conditions, B and F, have been used. These conditions were selected as their timescales of evolution are relatively long, providing a good illustration of the field evolution. For interest, these plots are produced for all conditions in appendix E.

The most noticeable difference upon comparison of $\overline{u_x}$ fields of non-rotating vortex rings (figure 7.61) with those generated under background rotation (figure 7.62) is the strong deformation and loss of symmetry which occurs in the rotating case. It can be seen for example, that an asymmetry develops in the centre of the vortex ring in figure 7.62c. In the non-rotating condition B, this quickly dissipates, for the rotating condition however, we find this asymmetry persists throughout the vortex ring's evolution. Furthermore the tilt described in section 7.3.6 may be clearly seen (figure 7.62l).

The $\overline{u_y}$ field is somewhat different. Upon generation, very little change to condition B is noticeable over time, (figure 7.63). This is in strong contrast to what is observed in condition F, figure 7.64. We see in figure 7.64c the early formation of the central jetting flow described in section 7.4.3.2. The subsequent development of this phenomena can be seen in figure 7.64d, where upward moving fluid jets straight through the centre of the vortex ring, toward the vortex generator. We can see that after this event, the vortex ring develops in a similar fashion to the non-rotating case, at least in terms of $\overline{u_y}$.

The most notable changes resulting from the addition of background rotation

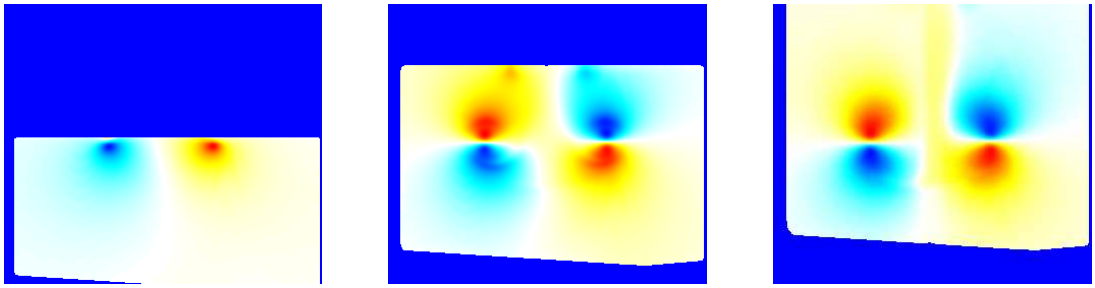

(a) $t+ = 0.22s, y^+ = -0.1$ (b) $t+ = 1.54s, y^+ = 0.52$ (c) $t+ = 2.87s, y^+ = 1.21$

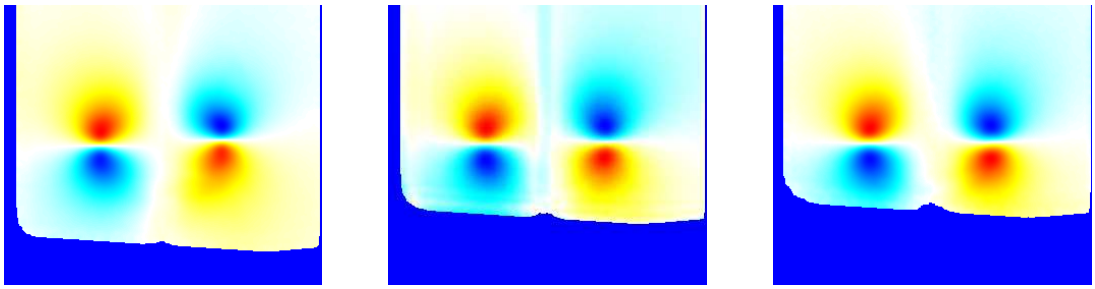

(d) $t+ = 4.42s, y^+ = 2$ (e) $t+ = 5.96s, y^+ = 2.84$ (f) $t+ = 7.52s, y^+ = 3.61$

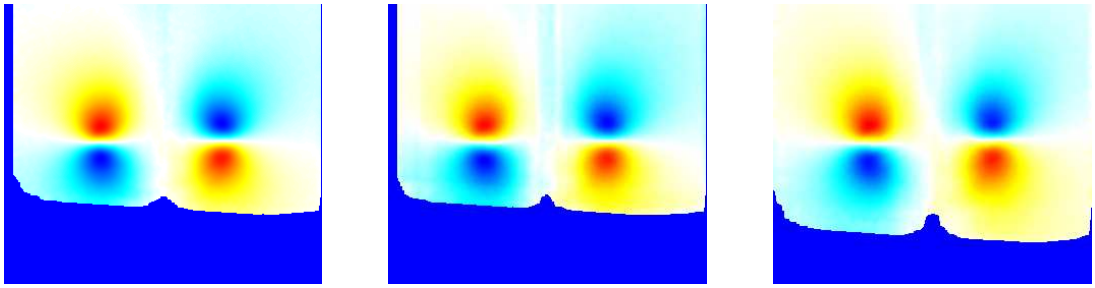

(g) $t+ = 8.85s, y^+ = 4.25$ (h) $t+ = 10.39s, y^+ = 5$ (i) $t+ = 11.94s, y^+ = 5.73$

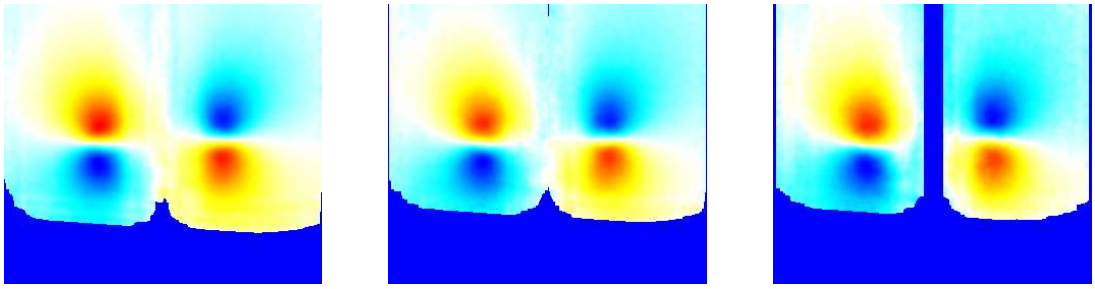

(j) $t+ = 13.5s, y^+ = 6.43$ (k) $t+ = 14.81s, y^+ = 6.97$ (l) $t+ = 16.36s, y^+ = 7.62$

Figure 7.61: Evolution of $\overline{u_x}$ field for condition B

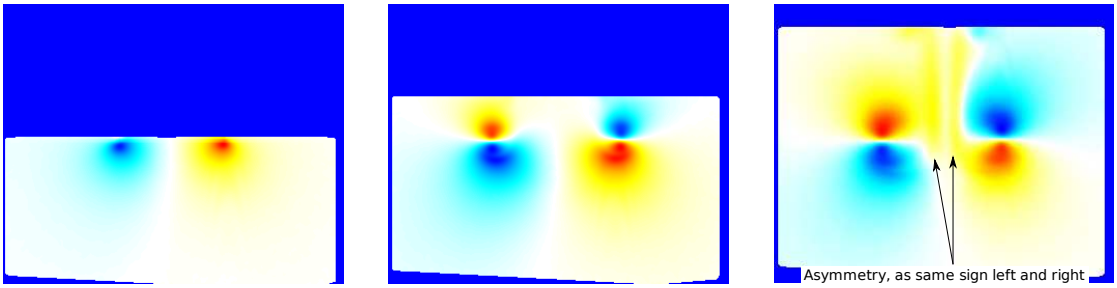

(a) $t+ = 0.12s, y^+ = -0.08$ (b) $t+ = 0.56s, y^+ = 0.26$ (c) $t+ = 1.22s, y^+ = 0.84$

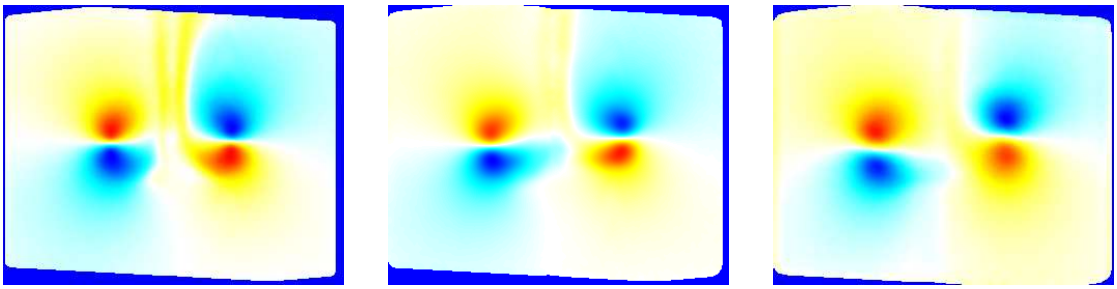

(d) $t+ = 1.77s, y^+ = 1.37$ (e) $t+ = 2.33s, y^+ = 1.84$ (f) $t+ = 2.99s, y^+ = 2.27$

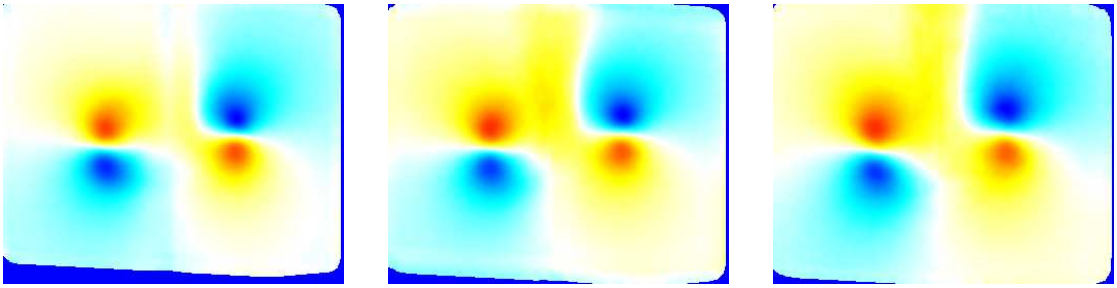

(g) $t+ = 3.55s, y^+ = 2.63$ (h) $t+ = 4.22s, y^+ = 3.01$ (i) $t+ = 4.77s, y^+ = 3.28$

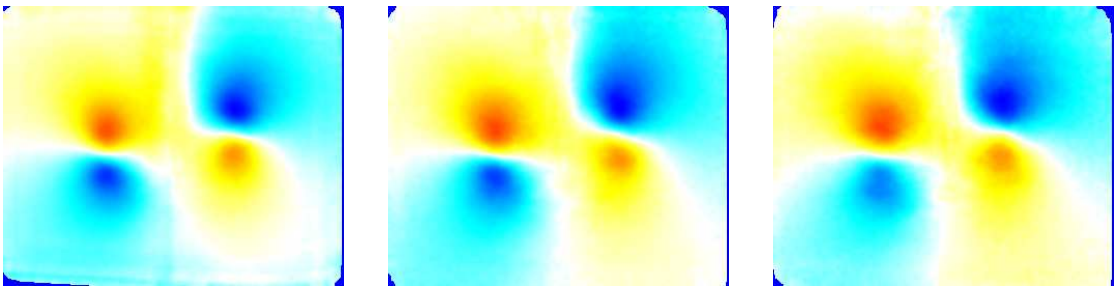

(j) $t+ = 5.21s, y^+ = 3.5$ (k) $t+ = 5.99s, y^+ = 3.87$ (l) $t+ = 6.55s, y^+ = 4.09$

Figure 7.62: Evolution of $\overline{u_x}$ field for condition F

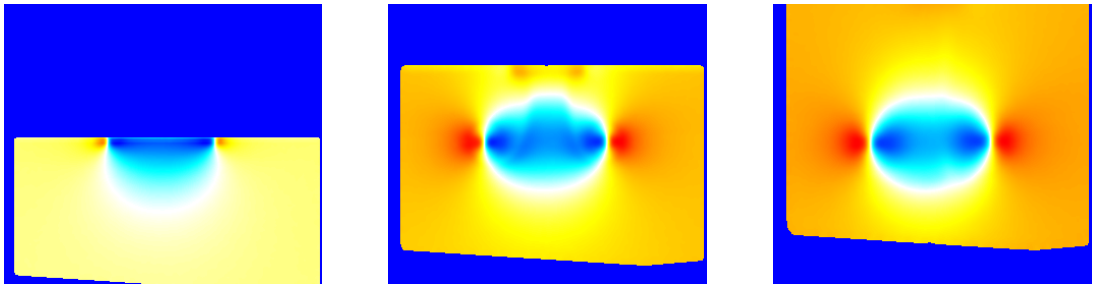

(a) $t+ = 0.22s, y^+ = -0.1$ (b) $t+ = 1.54s, y^+ = 0.52$ (c) $t+ = 2.87s, y^+ = 1.21$

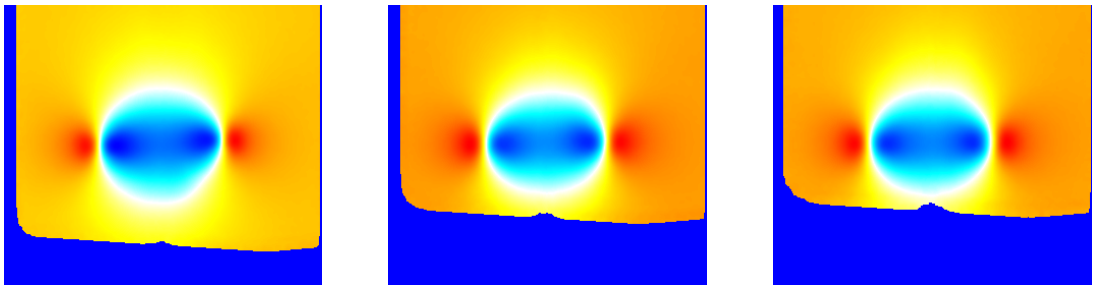

(d) $t+ = 4.42s, y^+ = 2$ (e) $t+ = 5.96s, y^+ = 2.84$ (f) $t+ = 7.52s, y^+ = 3.61$

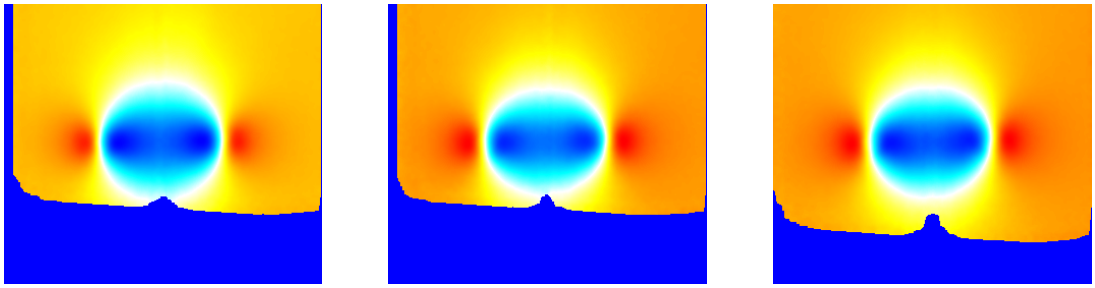

(g) $t+ = 8.85s, y^+ = 4.25$ (h) $t+ = 10.39s, y^+ = 5$ (i) $t+ = 11.94s, y^+ = 5.73$

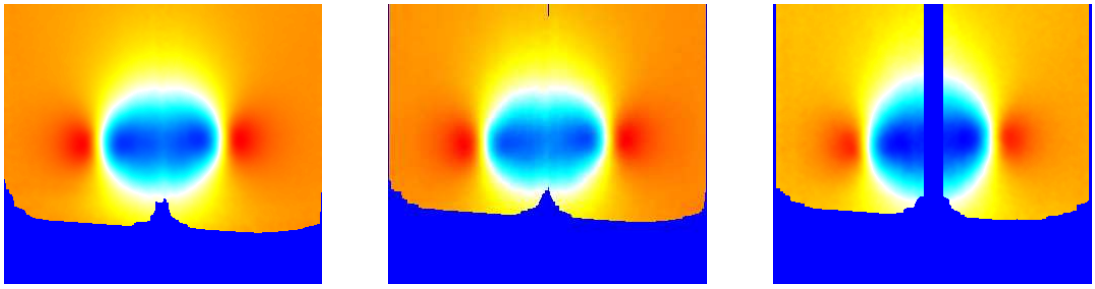

(j) $t+ = 13.5s, y^+ = 6.43$ (k) $t+ = 14.81s, y^+ = 6.97$ (l) $t+ = 16.36s, y^+ = 7.62$

Figure 7.63: Evolution of $\overline{u_y}$ field for condition B

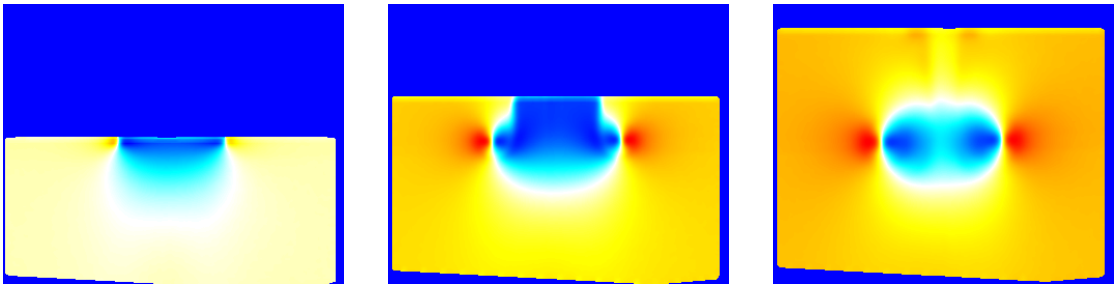

(a) $t+ = 0.12s, y^+ = -0.08$ (b) $t+ = 0.56s, y^+ = 0.26$ (c) $t+ = 1.22s, y^+ = 0.84$

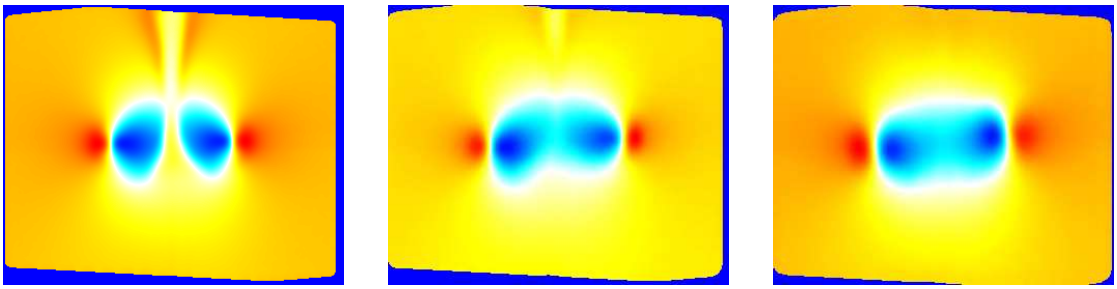

(d) $t+ = 1.77s, y^+ = 1.37$ (e) $t+ = 2.33s, y^+ = 1.84$ (f) $t+ = 2.99s, y^+ = 2.27$

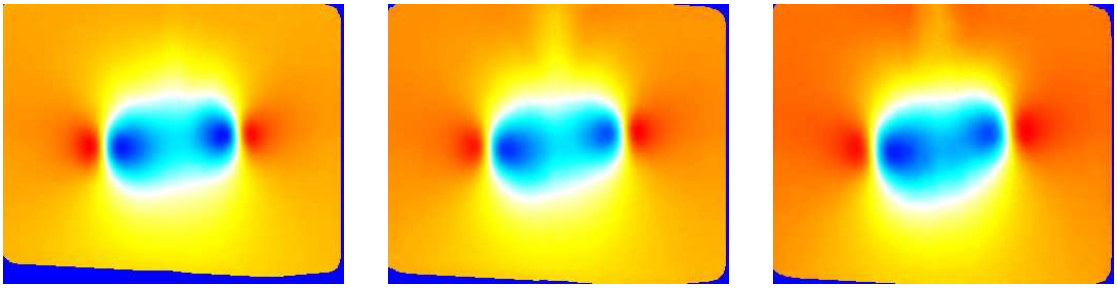

(g) $t+ = 3.55s, y^+ = 2.63$ (h) $t+ = 4.22s, y^+ = 3.01$ (i) $t+ = 4.77s, y^+ = 3.28$

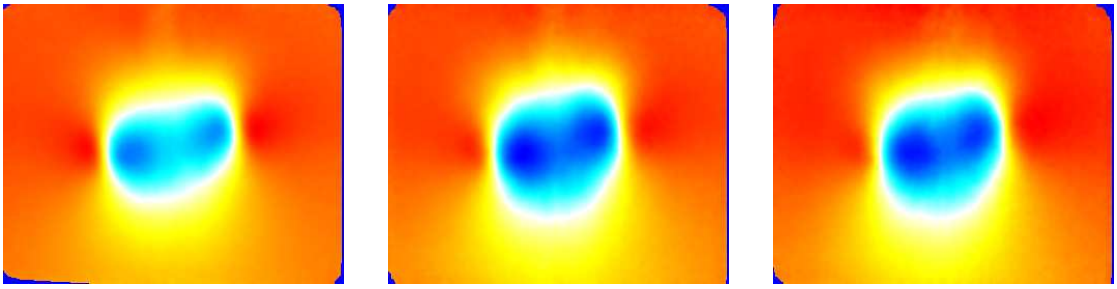

(j) $t+ = 5.21s, y^+ = 3.5$ (k) $t+ = 5.99s, y^+ = 3.87$ (l) $t+ = 6.55s, y^+ = 4.09$

Figure 7.64: Evolution of $\overline{u_y}$ field for condition F

appear in the $\overline{u_z}$ field. These are displayed for condition B in figure 7.66 and 7.67. Before commenting upon the differences introduced by background rotation, it is worth making mention of some of the PIV artefacts present in the $\overline{u_z}$ field, as this is where they show most readily. Before this discussion, it is worth noting that the velocities presented are of the orders of a few mm/s (c.f. section 7.4.3.3) and due to space constraints colour, bars have been omitted. This is in fact the reason condition B has been used for comparison, as it displays the lowest out of plane velocities and so best illustrates the type of errors observed in the velocity fields.

Of perhaps most permanence throughout the time series, is the general trend toward positive velocities on the upper side of the vortex ring, negative on the lower. This is, as discussed in section 5.6, an artefact arising from the vortex ring travelling out of the light sheet. Figures 7.66a-7.66c show a break from this, however. Again, the velocity distribution seen is due to incorrect positioning of the light sheet, and not corrected for adequately by the corrections described in section 5.6.

The final feature of note is the wavy pattern present across the vortex cores, most clearly visible in figures 7.66b. The origins of this pattern are in fact of some contention, as it only appears in the computed mean velocity fields, not in the frames which are averaged. It is known to occur as an artefact of DaVis data processing*, and has been seen in markedly differing flows. An example of this, is the velocity maps presented in figure 7.65, acquired as part of a commercial PIV test†. The appearance of such patterns is distinctly reminiscent of Moiré patterns, as appear when regular linear patterns are overlaid with angular offset.

*LaVision GMBH (private communication)
†Skeen (private communication)

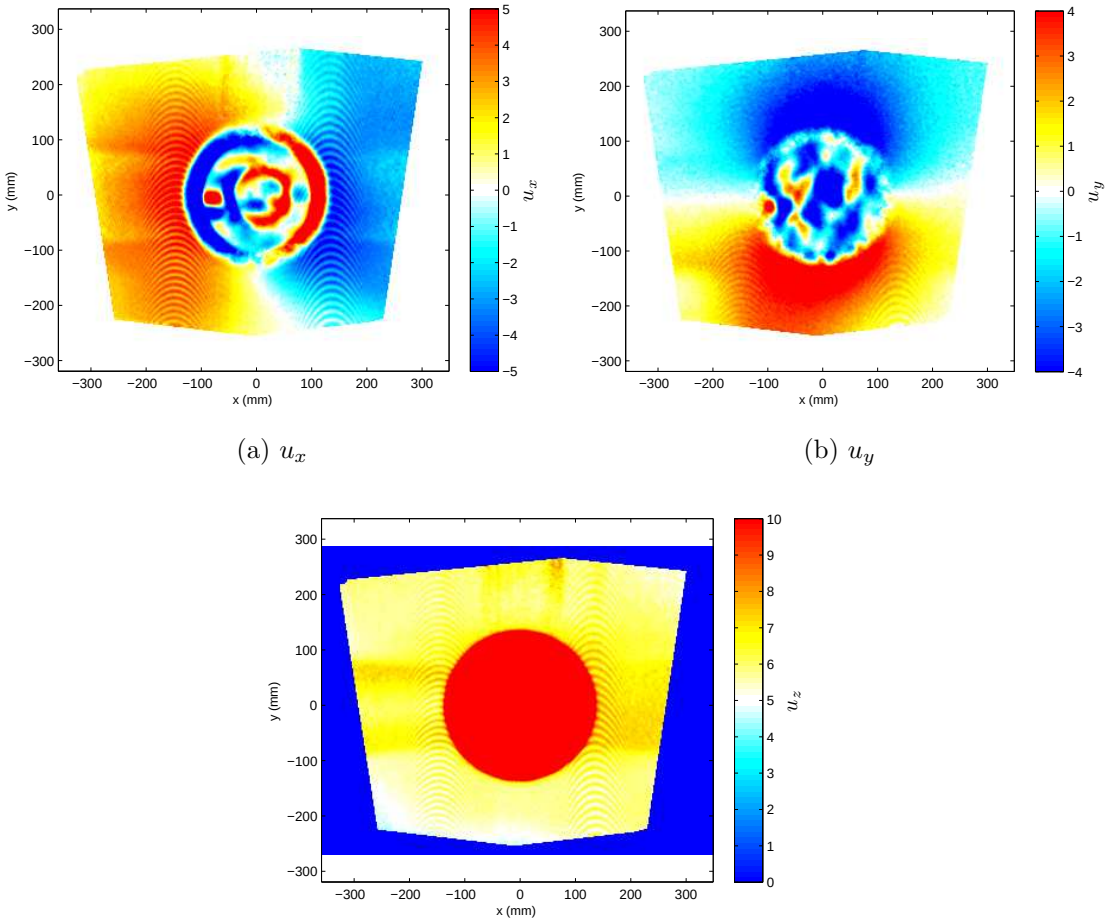

(a) u_x

(b) u_y

(c) u_z

Figure 7.65: Illustration of the occurrence of Moiré type patterns in flows of differing nature[‡]

Upon this basis, it is estimated that the appearance of these Moiré type patterns coincides somehow with operations performed during an interpolation incorporating either a rotating or projective element, likely coupled with weak peak-locking effects. The data presented so far loosely support this hypothesis, as they too used a bilinear interpolation pass to de-warp particle image data prior to computation of velocity vectors. Due to the long timescales involved, no

[‡]Skeen (private communication)

vector processing has been performed by the author in an attempt to validate this hypothesis and to our knowledge, no such studies exist in the literature. Early stereoscopic PIV measurements however used Moiré patterns arising from overlaid negatives of particle images to remove translational errors, (Prasad and Adrian, 1993). Of course this method contains many differences to what is displayed here and is only used as anecdotal evidence to support the conjectures made.

It is plain from comparison of figure 7.66 with 7.67, that under background rotation, the dynamics of the flow have changed entirely. One can see that upon formation, the velocity field is of sufficiently low magnitude that the Moiré type patterns can be seen, figures 7.67a and 7.67b, however, they are not as obvious as in the lower signal case of condition B. We see that immediately, upon generation, an anti-cyclonic swirl is generated ahead of the vortex ring.

Upon formation, we find the existence of a strong cyclonic swirling in, but not limited to, the wake of the vortex ring. This fluid motion, as seen in figure 7.67c, actually penetrates through the centre of the vortex ring, toward the frontal stagnation point. We find that as the vortex ring travels away from the nozzle, this wake is stretched, decreasing in diameter and intensified, in figure 7.67d we find that the magnitude of $\overline{u_z}$ in this swirl is sufficiently high as to mask the velocities seen in the anti-cyclonic flow.

We then see that the vortex ring undergoes a transformation, from an essentially axisymmetric form, to one with increasing asymmetry, this is seen first in figure 7.67e. At this point, we see that the magnitude of the wake swirl vortex has decreased significantly and the point at which this vortex terminates appears to move upwards. As shown in figure 7.67g, the field then develops an anti-cyclonic swirling flow inside the core of the vortex ring. We then see that the $\overline{u_z}$ field evolves to take its final form with anti-cyclonic ahead and to the sides, and cy-

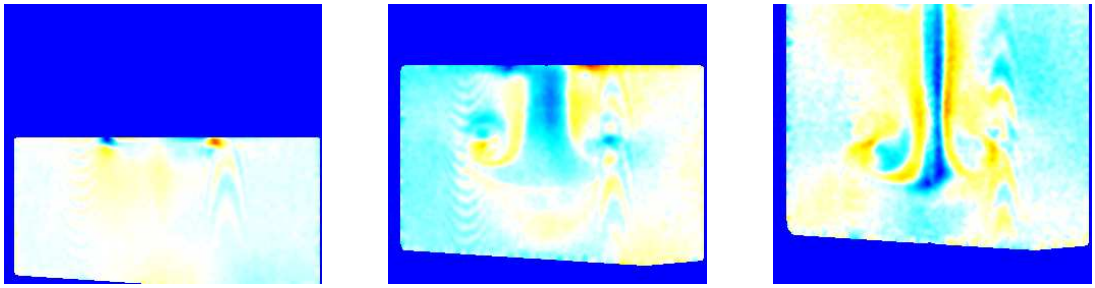

(a) $t+ = 0.22s, y^+ = -0.1$ (b) $t+ = 1.54s, y^+ = 0.52$ (c) $t+ = 2.87s, y^+ = 1.21$

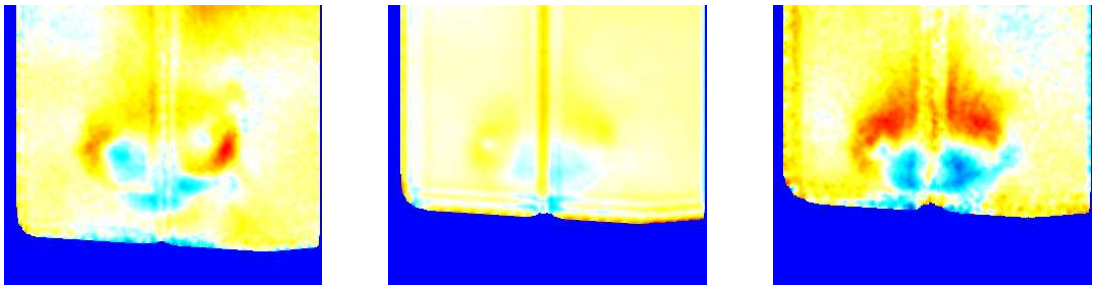

(d) $t+ = 4.42s, y^+ = 2$ (e) $t+ = 5.96s, y^+ = 2.84$ (f) $t+ = 7.52s, y^+ = 3.61$

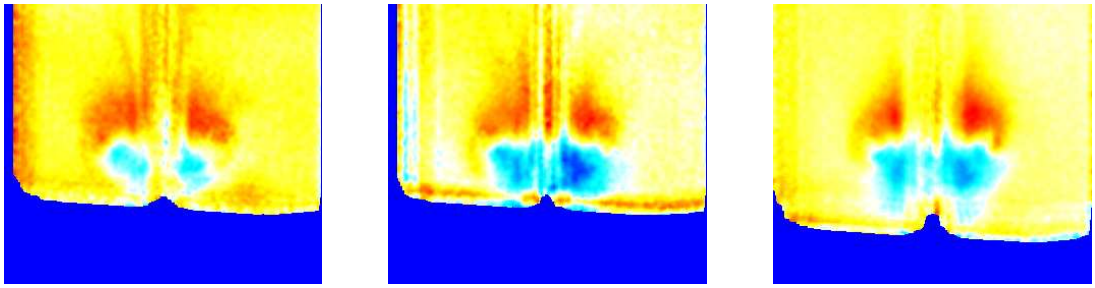

(g) $t+ = 8.85s, y^+ = 4.25$ (h) $t+ = 10.39s, y^+ = 5$ (i) $t+ = 11.94s, y^+ = 5.73$

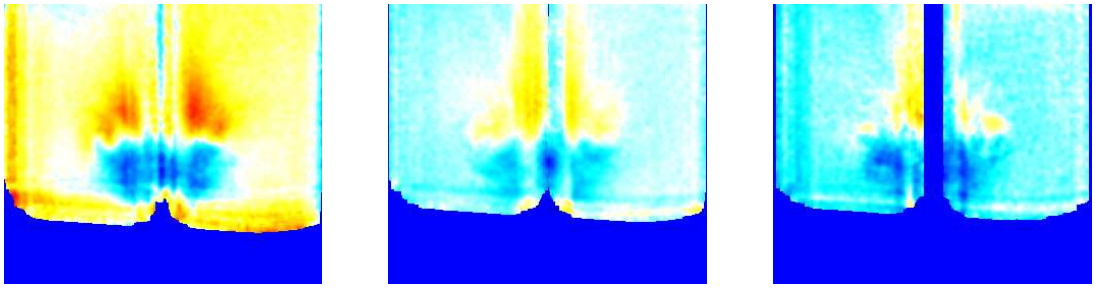

(j) $t+ = 13.5s, y^+ = 6.43$ (k) $t+ = 14.81s, y^+ = 6.97$ (l) $t+ = 16.36s, y^+ = 7.62$

Figure 7.66: Evolution of $\overline{u_z}$ field for condition B

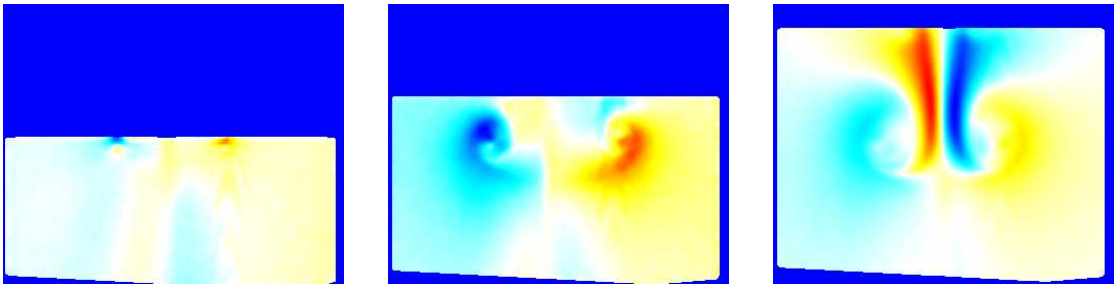

(a) $t+ = 0.12s, y^+ = -0.08$ (b) $t+ = 0.56s, y^+ = 0.26$ (c) $t+ = 1.22s, y^+ = 0.84$

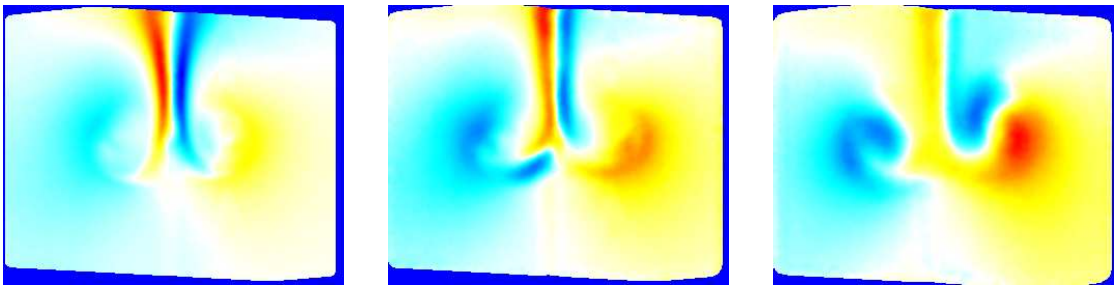

(d) $t+ = 1.77s, y^+ = 1.37$ (e) $t+ = 2.33s, y^+ = 1.84$ (f) $t+ = 2.99s, y^+ = 2.27$

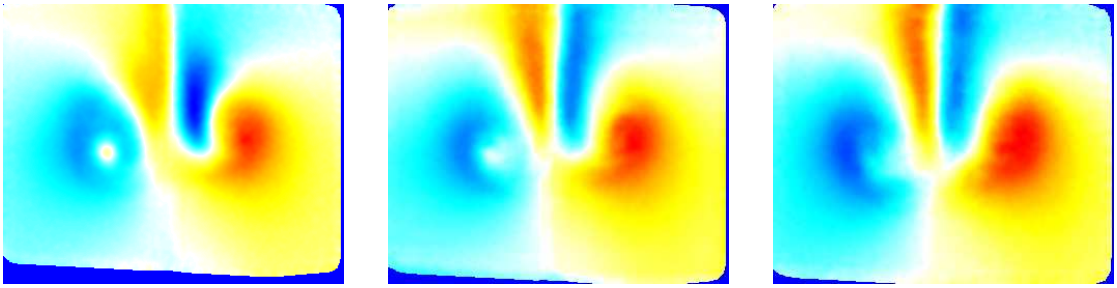

(g) $t+ = 3.55s, y^+ = 2.63$ (h) $t+ = 4.22s, y^+ = 3.01$ (i) $t+ = 4.77s, y^+ = 3.28$

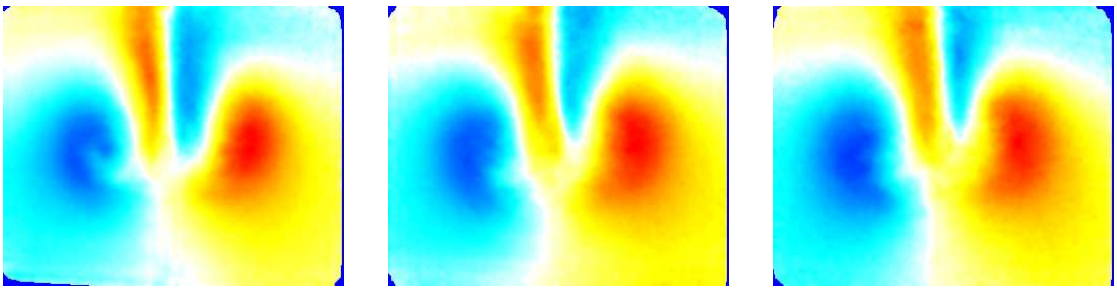

(j) $t+ = 5.21s, y^+ = 3.5$ (k) $t+ = 5.99s, y^+ = 3.87$ (l) $t+ = 6.55s, y^+ = 4.09$

Figure 7.67: Evolution of $\overline{u_z}$ field for condition F

clonic swirl emanating from the centre of the vortex ring, and being deposited into the wake. At this point the vortex ring has regained a large degree of axial symmetry.

Figures 7.68 and 7.69 show the time evolution of the vorticity field. For condition B one sees that, upon formation, the vortex ring maintains and ejects some vorticity in its wake. This may be seen in figure 7.68b and it occurs in figure 7.68c, however with sufficiently low magnitude that it cannot be observed without scaling the data. After this formation however, one can see that the vorticity field changes slowly and little. We find that through time the relative magnitude of the peaks to the surrounding flow decreases, thus the surrounding field becomes more easily observable.

For the rotating case, again, there are marked changes in comparison with the non-rotating case. We find the formation of vorticity in the centre of the vortex ring, this is then advected around the ring, into the wake. During formation, reasonably strong vorticity is ejected from the vortex generator outlet and entrained into the centre of the vortex ring, such that negative vorticity lies next to the positive vorticity. We then find this vorticity is stretched, wrapped around the vortex core and detrained into the wake flow.

As the final part of our analysis of the vortex ring fields, we consider the streamlines: figures 7.70 and 7.71. In condition B, there is little of note as the vortex ring evolves through time. Again the rotating condition is somewhat different. We see in figure 7.71d that the streamlines highlight the strong deformation that occurs to the vortex ring due to the axial jetting. It is apparent that the streamlines at the frontal stagnation point of the vortex ring undergo significant deformation, as observed by Verzicco *et al.* (1996). The axial jetting phenomenon mentioned previously was not observed however, and this deformation to the vortex bubble was attributed to pressure differentials (c.f. section 3.4.1).

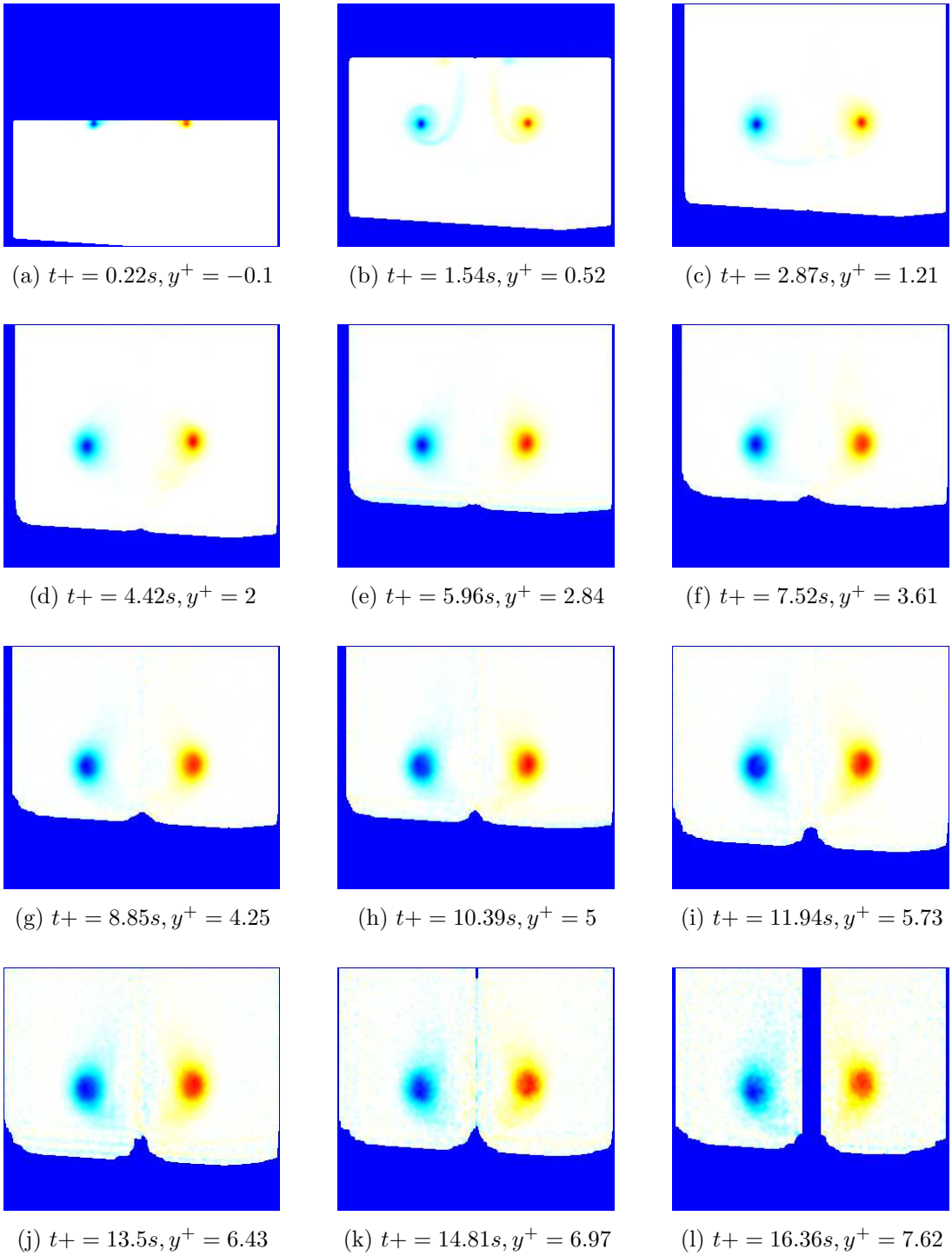

(a) $t+ = 0.22s, y^+ = -0.1$ (b) $t+ = 1.54s, y^+ = 0.52$ (c) $t+ = 2.87s, y^+ = 1.21$

(d) $t+ = 4.42s, y^+ = 2$ (e) $t+ = 5.96s, y^+ = 2.84$ (f) $t+ = 7.52s, y^+ = 3.61$

(g) $t+ = 8.85s, y^+ = 4.25$ (h) $t+ = 10.39s, y^+ = 5$ (i) $t+ = 11.94s, y^+ = 5.73$

(j) $t+ = 13.5s, y^+ = 6.43$ (k) $t+ = 14.81s, y^+ = 6.97$ (l) $t+ = 16.36s, y^+ = 7.62$

Figure 7.68: Evolution of $\overline{\omega_z}$ field for condition B

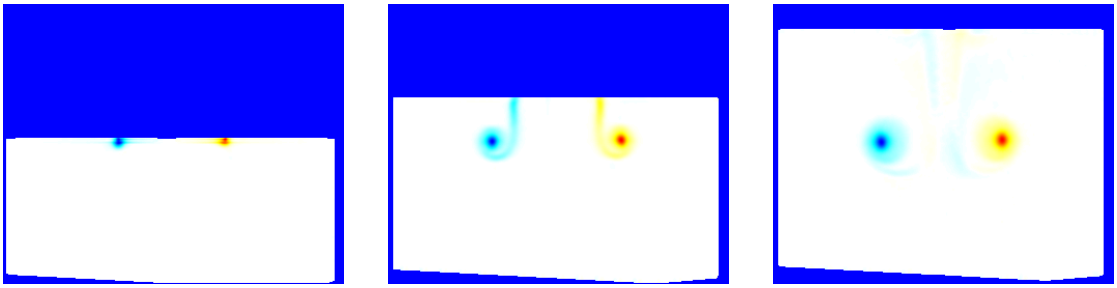

(a) $t+ = 0.12s, y^+ = -0.08$ (b) $t+ = 0.56s, y^+ = 0.26$ (c) $t+ = 1.22s, y^+ = 0.84$

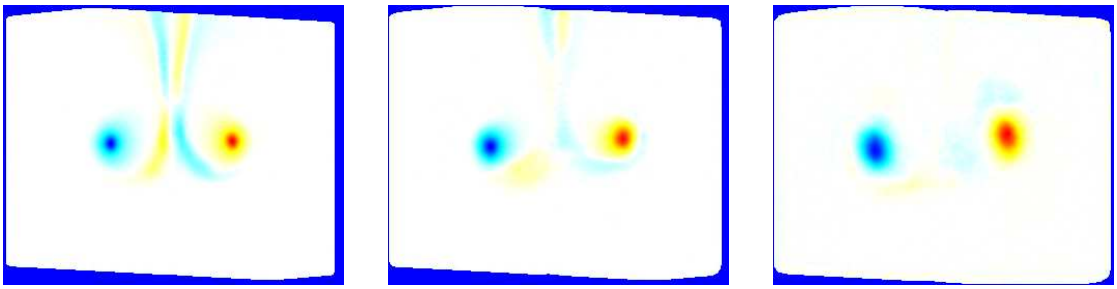

(d) $t+ = 1.77s, y^+ = 1.37$ (e) $t+ = 2.33s, y^+ = 1.84$ (f) $t+ = 2.99s, y^+ = 2.27$

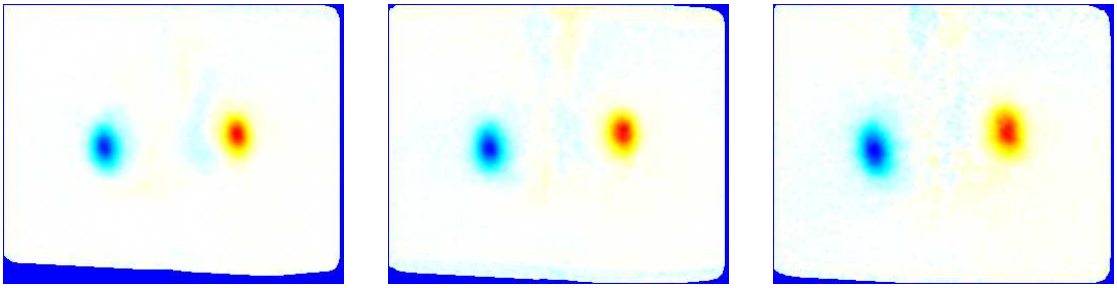

(g) $t+ = 3.55s, y^+ = 2.63$ (h) $t+ = 4.22s, y^+ = 3.01$ (i) $t+ = 4.77s, y^+ = 3.28$

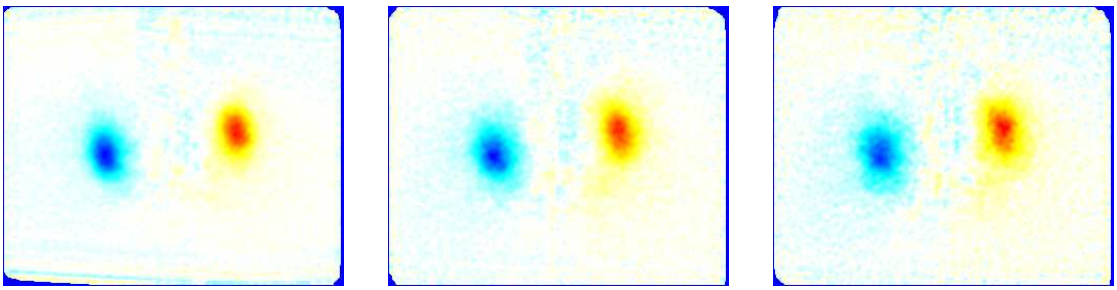

(j) $t+ = 5.21s, y^+ = 3.5$ (k) $t+ = 5.99s, y^+ = 3.87$ (l) $t+ = 6.55s, y^+ = 4.09$

Figure 7.69: Evolution of $\overline{\omega_z}$ field for condition F

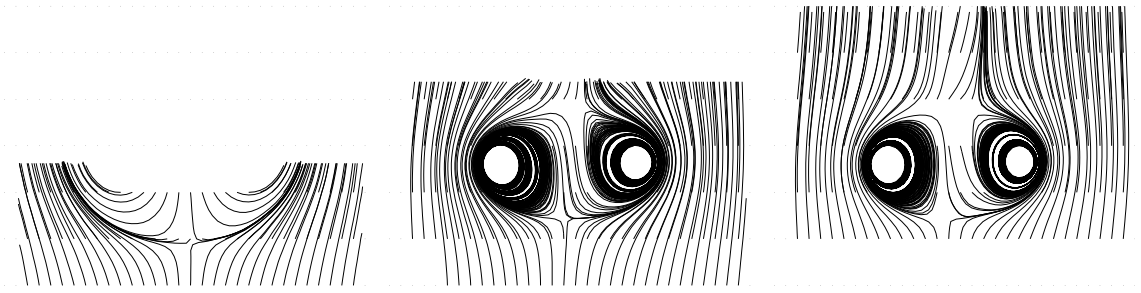

(a) $t+ = 0.22s, y^+ = -0.1$ (b) $t+ = 1.54s, y^+ = 0.52$ (c) $t+ = 2.87s, y^+ = 1.21$

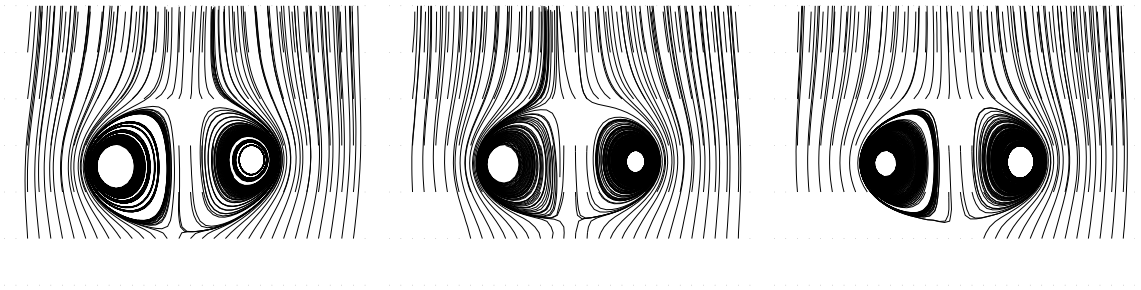

(d) $t+ = 4.42s, y^+ = 2$ (e) $t+ = 5.96s, y^+ = 2.84$ (f) $t+ = 7.52s, y^+ = 3.61$

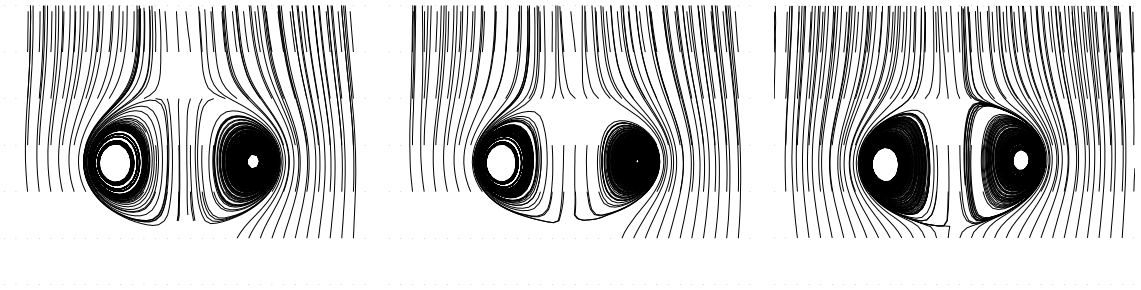

(g) $t+ = 8.85s, y^+ = 4.25$ (h) $t+ = 10.39s, y^+ = 5$ (i) $t+ = 11.94s, y^+ = 5.73$

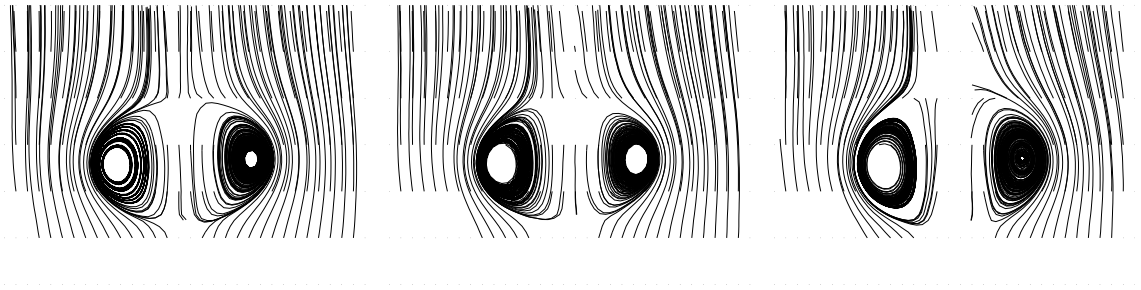

(j) $t+ = 13.5s, y^+ = 6.43$ (k) $t+ = 14.81s, y^+ = 6.97$ (l) $t+ = 16.36s, y^+ = 7.62$

Figure 7.70: Evolution of $\overline{\psi}$ field for condition B

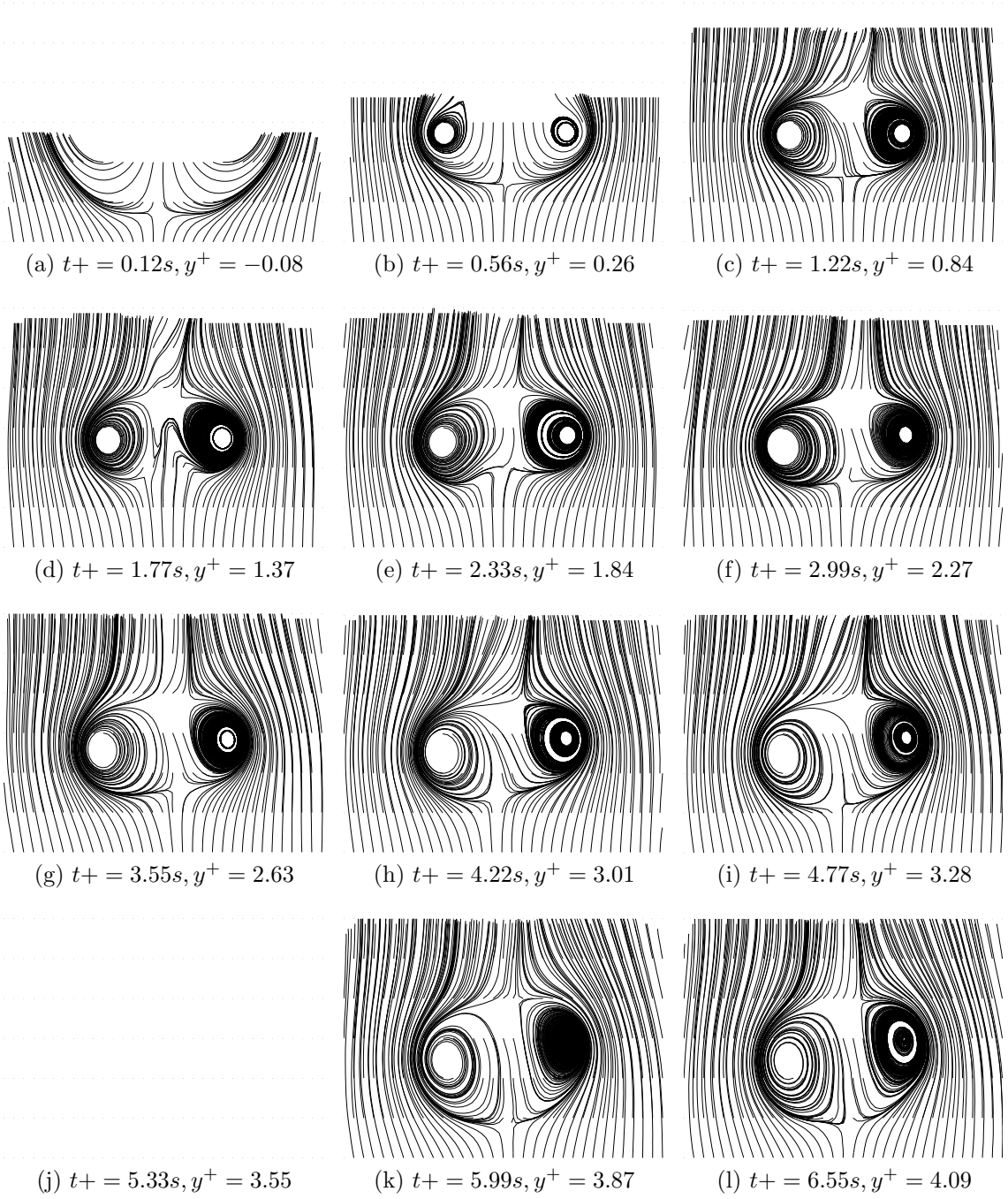

(a) $t+ = 0.12s, y^+ = -0.08$ (b) $t+ = 0.56s, y^+ = 0.26$ (c) $t+ = 1.22s, y^+ = 0.84$

(d) $t+ = 1.77s, y^+ = 1.37$ (e) $t+ = 2.33s, y^+ = 1.84$ (f) $t+ = 2.99s, y^+ = 2.27$

(g) $t+ = 3.55s, y^+ = 2.63$ (h) $t+ = 4.22s, y^+ = 3.01$ (i) $t+ = 4.77s, y^+ = 3.28$

(j) $t+ = 5.33s, y^+ = 3.55$ (k) $t+ = 5.99s, y^+ = 3.87$ (l) $t+ = 6.55s, y^+ = 4.09$

Figure 7.71: Evolution of $\overline{\psi}$ field for condition F

CHAPTER 8

Discussions and conclusions

8.1 Introduction

The work presented in this thesis has been split into several distinct groups, significant technical advances have been made to measurement systems through collaboration with Etalon Research and the University of Warwick OEL. PIV calibration and data processing techniques have been developed and advanced and furthermore, new insights into a fluid flow of fundamental interest have been achieved through the use of the advanced techniques developed on the new large scale vortex ring facility at the University of Warwick.

We have presented the first PIV measurements of vortex rings using a traversing camera system, which, to our knowledge is the first documented case of a stereoscopic PIV measurement acquiring whilst traversing. These advances in PIV have enabled new insights into the dynamics of vortex rings, and also introduced new problems concerning the accuracy of the reconstruction of the 3C velocity vector field, due to additional errors arising through acquiring data from a system in motion. The data processing techniques put forward to account for this are of interest and use to the wider academic community, in particular

enabling PIV measurements to be made outside of idealised "laboratory" conditions.

The work also includes the complete automation of the measurement process, which enabled the acquisition of large numbers of vortex ring generation runs; the first such PIV measurement of vortex rings. Due to the large number of samples which each data point presented represents, we are in an unique position to develop a deeper understanding of how vortex rings behave.

We further put forward data processing techniques specific to the PIV measurement of vortical structures. As may be expected, the vortex ring trajectories were not sufficiently repeatable to guarantee the vortex ring would travel with its axis in the light sheet. A technique has been put forward to account for this problem, and provide improvements where possible. Also, techniques enabling the statistical comparison of vortex rings with the same generation parameters were developed and implemented.

Concerning the fluid dynamics observed, we compare and contrast three separate vortex ring generation conditions; the effect of changing fluid outlet velocity, and the length of the slug ejected are compared to a reference condition. Each generation condition is tested across a range of background rotation rates. In all cases we observe almost the complete life cycle of the vortex ring, using high-resolution SPIV measurements, made possible by the novel measurement system and newly developed data processing techniques. From this, we present measurements of the time evolution of the vortex ring's 3D position, diameter, core diameter, circulation, velocity and vorticity field.

Throughout this chapter, we shall break our discussion of the results and the conclusions that may be drawn from them into sections pertaining to the novel work presented. We shall first consider the corrections applied to the PIV data, their effectiveness and validity. Our discussions then turn to the fluid dynamics,

where we consider the time evolution of vortex rings, both with and without the effects of background rotation.

8.2 Corrections applied to the PIV data

As outlined in chapter 5, three novel data corrections were developed and applied to the vortex ring velocity field data:

1. Camera calibration correction and removal of associated registration error.
2. Removal of velocity bias applied by mechanical vibrations.
3. Correction of velocity fields to account for the vortex ring travelling out of the light sheet.

A qualitative assessment of these corrections was presented in section 5.7 and throughout chapter 7 attention was drawn to results that indicated sub-optimal performance of these corrections. We saw in both cases that the corrections implemented have found differing degrees of success, which is discussed in the following sections, however in all cases it was shown that the net effect of the corrections is positive. Further to this, we also briefly address the formation of Moiré like patterns in the velocity fields, likely arising from the bilinear interpolation.

8.2.1 Camera calibration correction

The adjustment to account for incorrect camera calibration consisted of two similar parts: the calculation and elimination of the registration error in the 2×2C vector fields produced by the DaVis calibration software; the use of the values computed for these residuals to adjust the calibration to ensure that the 3C

vector calculation is performed with minimum error. This method is a form of self-calibration derived from point correspondences found in the 2×2C velocity fields and as such is termed flow-field self-calibration. Of the two errors, it has been shown that the registration error is the most important to account for.

As the camera calibration adjustment is arrived at from the removal of the registration error between the 2×2C velocity fields, it may be inferred that the absence of registration error likely implies the absence of calibration error. As actual verification of the validity of the camera calibration is not possible from direct analysis of the velocity fields computed, verification of the registration error is used instead and the most important check for this, beyond the plots presented in section 5.7.2, is from the u_z fields. For large scale vortical flows, a four quadrant pattern around the vortex core, as shown in figure 2.20, would indicate the presence of a registration error.

The type of flow patterns that indicate the presence of registration errors are only seen in condition A, as shown in figure 7.20. For this case however, it is ambiguous as to whether the pattern seen arises from a registration error or actually represents a valid flow phenomenon. Even in the worst case, i.e. a registration error, it is of very low magnitude, approximately 3% of the vortex ring translational velocity.

8.2.2 Removal of velocity bias

Analysis of this beyond what is presented in section 5.7 is difficult. As is noted in section 7.4.2, the u_z component is occasionally entirely positive (figure 7.20). This could indicate the presence of an over or under-application of the velocity bias. However, the occasions at which this manifests are rare. Also, and perhaps more importantly, at no point do we find the background velocity oscillating from high to low. This indicates that the jerking imparted from the traverse has at

least been greatly reduced. Figure 5.7.2 further supports this conclusion.

8.2.3 Correction for vortex ring leaving light sheet

Initial analysis of the corrections applied to the velocity field to account for the vortex ring moving out of the light sheet showed the correction to perform well. It was shown by example, using representative data, that the correction acted to provide an improvement to the velocity field. Further to this, it was demonstrated using a Lamb-Oseen vortex, with added spatial noise, that across a wide range of noise levels and displacements from the light sheet, the position of the vortex ring could be approximated well. As the velocity fields used in this synthetic test were generated according to the reprojection method discussed, this further suggests the actual correction procedure to be valid. Additionally, it was shown that for the orders of magnitude of noise due to PIV correlation and for a reasonable range of vortex ring - light sheet displacements the correction performed very well.

As established in section 7.3.1, the mean of z must be used tentatively as a statistical estimator to represent the general trends of vortex ring motion. The rings were found to invariably move in the z direction, and quickly travelled beyond the measurable range. From the plots of $\overline{u_z}$, at measurement locations "above" and "below" (these measurement locations are described in figure 7.17, page 205) presented throughout sections 7.4.2 and 7.4.3.3, we were able to qualitatively assess the performance of the out of plane correction from the actual PIV data.

Because of the structure of the vortex ring, we are able to determine which side of the light sheet it lies from the velocities at the "above" and "below" measurement locations. For example, if above is positive and below negative, it implies that the vortex ring is the far side of the light sheet to the cameras.

Condition	Measured z	Residual z
A	+	−
B	−	+
C	−	−
E	+	+
F	+−	0
G	+	+
H	−+	0
I	+−	−+
J	+	0
K	+−	+

Table 8.1: A qualitative comparison between measured z direction and residual z direction found

As this z position is what remains after the correction, we term it the residual z position and tabulate it (table 8.1) along with a qualitative estimate of the z position, measured as part of the correction process described in section 5.6.

For the measured and residual z entries, only the direction is tabulated and this is represented by a '+' for the positive z direction (where the vortex ring has travelled towards the cameras) and a '−' for the negative z direction (away from the cameras). Where the mean vortex ring changes side during its travel, a string of symbols (corresponding to the side of the light sheet) is used. For condition I, for example, the measured z position is listed as '+−', which means that the vortex ring started its motion on the near side of the light sheet, then moved to the far side. For conditions F, H and J, there was little evidence found of flow arising from the vortex ring lying outside of the light sheet. To indicate this, the z residual entries are marked 0.

Table 8.1 indicates that there is little correlation between the residual z position subsequent to correction and the actual correction applied. This means that in some cases, there is an under-estimation of the motion, in other cases an over-estimation. This provides indication that the errors involved are not heav-

ily biased. It is however of interest that for the low Reynolds number vortex ring, for the background rotation case, no noticeable residual was seen. This can be verified from the plots at measurement locations "above" and "below" (figure 7.53, 252) and also from the relevant plots of the horizontal sum of $\overline{u_z}$, (figures D.4, D.6 and D.9 from the appendices, pages 374, 375 and 376).

It is apparent from the results described in section 7 that in spite of any errors present, interpretation of the field data is still possible. Concerning the derived parameters however, one should take care in interpreting both the z position of the vortex ring and its diameter D. Due to the circular nature of the vortex ring, the fact that some residual z position remains after this correction implies that the diameter will necessarily be biased towards an under-estimate. As is already shown here, the z position shows little signs of bias.

8.2.4 The occurrence of Moiré type patterns

We do see the presence of Moiré patterns, which appear to result from DaVis vector processing. We suspect that the pattern arises as part of DaVis' bilinear image interpolation. Several possibilities exist for confirmation of this; performing interpolation using Whittaker's method, being perhaps the most logical. The magnitudes of the effect seen are however sufficiently small and the time taken to perform this check sufficiently long that this testing has not been carried out, and is recommended for further work.

8.2.5 Conclusions and recommendations for further work

8.2.5.1 Correction of errors due to camera motion

In chapter 5 we have presented new and novel techniques to enable analysis of PIV data in situations where camera stability cannot be guaranteed. These

include accounting for velocity biases imposed upon the field by the camera's motion between exposures, and also calibration correction, including vector field warping to account for the change in viewing angle due to the cameras motion. It is an important result that we are able to apply these corrections from analysis of the vector fields alone and still get results suitable for qualitative assessment of the fluid dynamics. In fact, it has been shown that the corrections perform remarkably well, and few artefacts arising from these corrections are ever seen.

For both corrections considered, a qualitative assessment of the performance has been assessed qualitatively, showing that the overall performance of these techniques is reasonable. Comment beyond this is difficult without significant further work, to conduct a full error analysis (which is recommended).

The analysis of this error should ideally be performed using standard error methods for PIV measurements, for the method to operate, it is required that a flow field be present, therefore this should be done through synthetic simulation. The synthetic simulation should be performed upon data acquired from a system for which it is straightforward to compute a camera calibration using established techniques. From this, a misalignment could be synthetically applied, by simply adding a known error to the calibration prior to cross correlation. From this, one can then verify that the flow-field self calibration algorithms presented in section 5.5 provide an adjustment equal to the applied misalignment. Adjustment of the magnitude of this error will provide a physically achievable error mapping. Similarly for the imposed velocity bias, a known translation could be applied to particle images from a rigidly mounted camera and an error map built from these measurements.

In this work, large data-sets were processed in a highly automated fashion. For this reason, the most basic physical models were used, to maximise robustness. Both corrections concerning the camera motion were applied through the most

simple models appropriate, by assuming camera motion to be plain translation. It was shown that due to the magnitude of the motions observed, and the geometry of the setup used, this is a valid assumption. Upon this basis we also recommend further work to extend these models to incorporate the effects of complete camera motion, thus providing applicability to generic PIV setups. In fact, for flows from which sufficiently distributed point correspondences may be extracted, this method could be extended to perform a complete camera calibration adjustment, of both intrinsic and extrinsic parameters, up to scale.

In terms of implementation, it is recommended, that the both the calibration adjustment and vibration removal be performed in-line with the cross correlation as part of a multi-pass algorithm. The time take for the flow-field self-calibration is small in comparison with both the correlation and interpolation required for every pass of an adaptive window deformation algorithm, as explained in section 2.3.3. For this reason, integration of flow field self-calibration into this process would add little overhead. Furthermore, velocity field peak finding, as performed in section 5.5.3.2 would be of improved robustness upon fitting lower resolution PIV measurements, as they tend to exhibit lower high-frequency noise. This should provide good initial guesses of the vortex positions and allow subsequent refinements, in much the same way as the adaptive gridding is performed.

8.2.5.2 Correction of errors due to out of plane vortex ring motion

The correction for errors due to the vortex ring moving out of the light sheet have had mixed success. The evaluation of the process was performed by comparing the u_z PIV field both before and after the correction had been applied and using synthetic simulation of the errors on a Lamb-Oseen based vortex ring. Subsequently the $\overline{u_z}$ field was investigated and any effects indicating failure of the out of plane correction noted.

The synthetic testing showed that for vortex rings similar to those produced in the experiments, the correction performed well in all cases; for reasonable displacements from the light sheet, reasonable errors and even unreasonable displacements and errors.

Through analysis of the mean fields we established that for conditions F, H and J, the correction appeared to work fully, however for the other seven conditions the correction failed to entirely account for the out of light sheet motion. Although the correction was shown to have a general improvement upon the data. Simple analysis showed that the remaining position, which was unaccounted for by the correction (termed residual z) showed no correlation with the correction, indicating the errors occurring are most likely random and not biassed.

8.3 Vortex ring formation

The discussion here is related to the formation of vortex rings, which as discussed in section 3.3.2 has received much attention in recent years. We show here that for the non-rotating case, our data agrees well with prior studies and also extend the discussion of vortex ring formation to the rotating case, for which no previous studies exist. We may arrive at some basic conclusions concerning the differences between rotating and non-rotating vortex rings from the properties listed in tables 7.1 and 7.2. Prior to the discussions however, a summary of the pertinent observations, from chapter 7 is provided:

- Initial circulation, Γ_0;
  - Without background rotation, increasing either stroke length or piston velocity results in an increased initial circulation.

  - The addition of background rotation results in a decrease of Γ_0.
  - For a given generation condition, as Ω increases, Γ_0 decreases.

- Initial ring diameter, D_0;
  - Without background rotation, the diameter remains the same when piston velocity is reduced, but decreases when the stroke length is decreased.
  - The addition of background rotation in general causes an increase in vortex ring diameter, when compared with a similar non-rotating condition.
  - For the low rotation rate ($3RPM$), D_0 increases compared to $0RPM$ for all conditions.
  - For the high rotation rate ($6RPM$), D_0 decreases compared to $3RPM$ for all conditions.

- Initial vortex core diameter, δ_0;
  - Without background rotation, δ_0 was reduced by decreasing stroke length, or by increasing piston velocity.
  - For the high Reynolds number conditions, we find that when compared to the non-rotating case, δ_0 increases for the low rotation rate ($3RPM$) and decreases for the high rotation rate ($6RPM$).
  - For the low Reynolds number conditions, we find that when compared to the non-rotating case, δ_0 decreases for the low rotation rate ($3RPM$) and increases for the high rotation rate ($6RPM$).

8.3.1 Without a rotating reference frame

For vortex rings without background rotation, the slug flow model accurately predicts the circulation generated for each vortex ring. There is however some slight discrepancy for condition C, it is believed (as discussed in section 7.1) that this arises due to belt stretch. With regards the vortex ring diameter, our data is in line with that of Maxworthy (1977), we find that increasing piston stroke length increases D_0, whereas increasing U_o has little appreciable effect upon D_0. With regards to the initial core diameter, it is difficult to appraise either of the self-similarity formulations which estimate δ_0, as in both cases, the computation of constants from similarity theory is required. This is an involved procedure, beyond the scope of this work and therefore has not been carried out.

8.3.2 With a rotating reference frame

The general trend observed is that circulation is decreased by rotation rate. Vortex ring diameter and core diameter is in general increased for high Rossby number (where rotational effects low compared with inertial) and in general decreased for low Rossby number (strong rotational effects).

Explanations of these observations are assisted by consideration of the effects of Coriolis force. To aid in our discussion, we consider equation (3.26) (page 76) cast into cylindrical coordinates, equation (8.1). We use spatial coordinates $\mathbf{x}_\varphi = [x_\varphi \quad x_\rho \quad x_h]^T$ and velocities $\mathbf{u}_\varphi = [u_\varphi \quad u_\rho \quad u_h]^T$.

$$\mathbf{a_c} = -2\boldsymbol{\Omega} \times \mathbf{u}_\varphi = 2\Omega \begin{bmatrix} -u_\rho \\ \rho u_\varphi \\ 0 \end{bmatrix}^T \tag{8.1}$$

Upon the basis of equation 8.1, we assess the direction of the acceleration

arising from Coriolis force, noting that $\mathbf{\Omega} = [0 \quad 0 \quad \Omega]^T$.

- Positive radial flow causes an anti-cyclonic acceleration.
  - Flow velocity: $\mathbf{u}_\varphi = [0 \quad u_\rho \quad 0]^T$
  - Coriolis acceleration: $\mathbf{a_c} = 2\Omega \begin{bmatrix} -u_\rho & 0 & 0 \end{bmatrix}^T$
- Negative radial flow causes a cyclonic acceleration.
  - Flow velocity: $\mathbf{u}_\varphi = [0 \quad -u_\rho \quad 0]^T$
  - Coriolis acceleration: $\mathbf{a_c} = 2\Omega[u_\rho \quad 0 \quad 0]^T$
- Cyclonic azimuthal flow causes a positive radial acceleration.
  - Flow velocity: $\mathbf{u}_\varphi = [u_\varphi \quad 0 \quad 0]^T$
  - Coriolis acceleration: $\mathbf{a_c} = 2\Omega[0 \quad \rho u_\varphi \quad 0]^T$
- Anti-cyclonic azimuthal flow causes a negative radial acceleration.
  - Flow velocity: $\mathbf{u}_\varphi = [-u_\varphi \quad 0 \quad 0]^T$
  - Coriolis acceleration: $\mathbf{a_c} = 2\Omega[0 \quad -\rho u_\varphi \quad 0]^T$
- In all cases, the induced acceleration scales linearly with the rotation rate.

It is important to consider the implications of the final point; to do this, we will use the example of a fluid under background rotation, with initial motion radially outwards. Where rotation is low comparable to the fluid motions, the Coriolis acceleration is relatively low and its effects are therefore only seen in very long timescales (velocity arises from the time integral of acceleration). As the motion is radially outwards the acceleration generated due to Coriolis force is in the azimuthal direction, anti-cyclonic to the rotation direction. For the case where the rotation rate is very high, this Coriolis induced velocity then experiences a

secondary Coriolis acceleration, acting in the negative radial direction, directly opposite to the initial flow direction. This counterintuitive result may be observed for motion in any given direction.

Consider now the formation of the vortex ring, in the presence background rotation. As fluid is ejected from the generator, boundary layer separation results in the roll-up of a vortex sheet, as discussed in section 3.3.2. This roll-up is initiated by fluid motion radially outwards, which implies from equation 8.1, a Coriolis force induced swirling acceleration. The effect of this acceleration is determined by the relative time-scales of the flow and rotation rate. Where the fluid-flow timescales are small compared with the rotation rate, the fluid is energetic compared with the rotational effects and this Coriolis acceleration will have little impact. For the case where fluid flow timescales are large compared with the rotation rate, $\mathbf{a_c}$ will act to spin up the fluid into an anti-cyclonic swirling flow.

To help illustrate this, we annotate the flow field, as indicated by figure 8.1, in which, for ease of viewing the vectors have been downsampled and only half of the ring is displayed. One can see that above the core, the major component of horizontal velocity is inward, generating a cyclonic acceleration. The converse is found below the core, where the major component of horizontal velocity is outward, generating an anti-cyclonic acceleration. Both for the cyclonic and anti-cyclonic generations, the maximum swirl does not occur at the same place as the maximum horizontal velocity. Instead, it occurs after the fluid has been advected beyond this point. In the case of the cyclonic swirl, the fluid is transported between the two vortex cores and in the case of the anti-cyclonic swirl, the fluid is transported outside of the two vortex cores.

The major effect of this swirl flow generation upon the flow field is that less of the energy imparted to the fluid will be retained in the vortex motion, as the

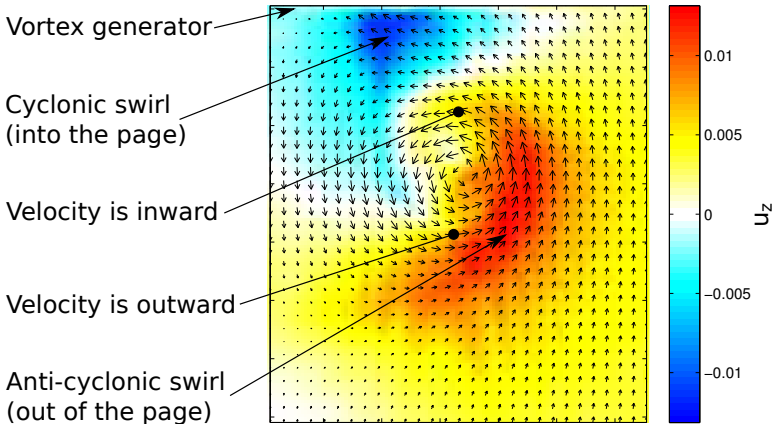

Figure 8.1: Illustration of the development of the swirling field

total kinetic energy $E = 0.5\rho\mathbf{u}^T\mathbf{u}$ cannot increase after formation. We expect that this is the reason for the reduction in circulation for rotating conditions upon formation.

For vortex ring diameter, a clear trend is seen (see bulleted list above), however an explanation of the mechanism forcing this trend is less straightforward. As stated, the addition of background rotation causes an increase in initial vortex ring diameter D_0. Increasing the rate of background rotation further however, results in a decrease in D_0. This is seen for all three vortex generation conditions.

Decreasing diameter could be expected for low Rossby numbers, as in this case rotational effects are dominant. This means, that not only would Coriolis force act to induce a swirling flow, but would further *act upon* this swirling flow. As discussed above, this secondary Coriolis forcing would be in opposition to the initial motion. From the velocity fields during formation, it is apparent that the formation of the anti-cyclonic swirl is of greater magnitude and spatial distribution, therefore we could reasonably consider the swirl flow to be anti-cyclonic. As is seen from equation 8.1, Coriolis force accelerates anti-cyclonic flow radially inwards, leading to a decrease in vortex ring diameter. No straightforward arguments concerning the increase in diameter for the low rotation rates are apparent

however.

Trends concerning the vortex ring core diameter δ_0 are also apparent. We find that for high Ro_Γ (conditions E and G) the core diameter increases and for low Ro_Γ (conditions F, H, I and K) the core diameter decreases. Condition J does not fit this trend, as it has the lowest Rossby number, but yet an increased core diameter. As was seen in section 7.3, the destruction of condition J occurs more or less immediately after its formation, as such one cannot separate the effects of destruction from those of formation. Upon this basis we suggest that the results should be considered in the absence of condition J.

As with the vortex ring diameter, the mechanism resulting in the growth of the vortex core is not apparent, however for the low Rossby number case, we can provide a feasible explanation for the trend seen. As already discussed, if the timescales of rotation are short in comparison to the inertial timescales, Coriolis force may induce motion, and through a secondary interaction a forcing is applied in direct opposition to the initial forcing. For example, outwards motion results in an anti-cyclonic swirl, which in turn results in an *inwards* forcing. As we have a cyclonic swirling flow inside the centre of the vortex ring (outwards radial secondary acceleration) and an anti-cyclonic flow around the outside (inwards radial secondary acceleration), a net compression of the vortex core exists, illustrated in figure 8.2. We believe that it is this compression in the radial direction that results in the decrease of the core diameter.

8.3.3 Conclusions and recommendations for further work

Our data shows that for non-rotating vortex rings, slug flow provides an adequate model for the estimation of the initial vortex ring circulation, Γ_0. We also see correlation between D_0 and L_o, but not $\overline{U_o}$, as did Maxworthy (1977).

The analysis performed here forms the first such assessment of the changes

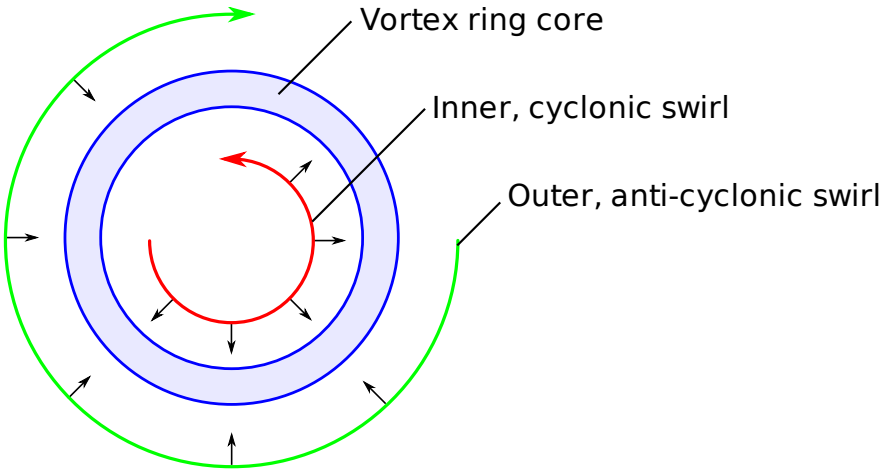

Figure 8.2: Illustration of the secondary Coriolis accelerations upon the vortex ring

to the dynamics of the vortex ring formation process under background rotation. We further show the first measurements of initial properties as a function of generation parameters and rotation rate. We find that the inclusion of background rotation results in a decrease in Γ_0 and changes in both D_0 and δ_0. We attribute the decrease in Γ_0 to the formation of a swirling flow in both the vortex ring core and the wake, thus providing a transfer of momentum from azimuthal vorticity to axial vorticity.

The relationship between vortex ring diameter and core diameter is less clear, however for both properties there appears to be some form of Rossby number dependence. The general trend is that for high Ro_Γ (the effects of rotation are small), one sees an increase in diameter and core diameter, whereas for a low Ro_Γ, we find that the vortex ring diameter decreases, as does the core diameter. In both cases we have presented possible scenarios for the behaviour at high Rossby number, further experiments are required to verify these suggestions. For the low Rossby number case however, no interpretation of the flow phenomena is immediately apparent.

8.4 Time evolution of vortex ring properties

Section 7.3 presented the first concerted statistical measurement of vortex ring properties, and the first analysis of the large scale time evolution of vortex rings under background rotation. We measured how the 3D vortex ring position evolves, as well as vortex ring properties: diameter, core diameter, tilt and circulation evolve over time. Presented below is a summary of the observations made, which are expanded upon in the subsections of section 8.4.

- x and z trajectory:
  - For all rotating conditions, the mean vortex ring shows motion in both the x and z directions.
  - In z it is noted that condition H ($-3RPM$) shows the same pattern as condition F ($3RPM$), however inverted.
- y trajectory:
  - y evolution over time was shown to collapse for all conditions, upon normalisation by D_0 and Γ_0.
  - Under rotation vortex rings show a sudden decrease in gradient of y^+ towards the end of their life
- Vortex ring diameter:
  - General trend was for vortex ring diameter to increase with time.
  - For rotating conditions, the tendency was for vortex ring diameter to increase, then decrease.
  - In all cases, diameter of rings under the influence of background rotation exceeds that of the comparative non-rotating ring.

- Vortex ring core diameter:
  - General trend was for the vortex ring core diameter to increase with time.
  - In most cases this growth was preceded by a small contraction of the core, occurring shortly after generation.
  - For the non-rotating conditions rate of core growth was seen to increase with decreasing Reynolds number.
  - It was found that subsequent to the contraction, for rotating vortex ring conditions, core growth was increased when compared with their comparative non-rotating conditions.
  - For the rotating conditions the core diameter was seen to grow relatively slowly at first, and then later on enter a period of increased core growth. The onset of this increased growth coincides with the onset of the decreasing diameter.
- Vortex ring slenderness ratio:
  - The vortex ring slenderness ratio was found to be driven by the core diameter.
- Vortex ring tilt:
  - Tilt increased as the rotation rate was increased.
  - Rate of change of tilt increases when rotation rate increases.
  - Some correlation was seen between θ and x.
- Vortex ring circulation:
  - For the non-rotating conditions, similar rates of circulation decay are seen.

– A sharp increase in Γ, followed immediately by a decrease was seen for conditions F, H and J.

– Rotating conditions decrease in circulation at an increased rate when compared with appropriate non-rotating conditions.

8.4.1 x, z trajectory

In the z direction, one finds approximately the same trend for condition F ($3RPM$) as for condition H ($-3RPM$), however negated. This result is contextualised by the observations of Verzicco *et al.* (1996), as described in section 3.4.1. It was shown that if an otherwise axisymmetric vortex ring travelled aparallel to the rotation vector, it would develop axial asymmetry. Despite the precise alignment of the vortex generator described in section 4.3, it is still feasible that some residual misalignment may occur between the vortex ring and the rotation vector. It is likely therefore, that the departure from axial symmetry during the formation of the secondary vorticity as described in section 3.4.1, provides the impetus that results in the change of z-trajectory. The fact that we show the direction of this effect is driven by the sense of the rotation rate is novel.

Further to this, our measurements show the inconsistency with which the mean vortex ring propagates, it should be noted that there is significant variance amongst the vortex rings measured, as characterised in the statistical assessment. Plots of this are shown in section 7.3.1 and appendix B. This variation clearly highlights the necessity for the development of techniques to perform corrections for misalignment between the vortex ring and light sheet.

8.4.2 y trajectory

We show that the vortex ring trajectories appear to collapse, to a reasonable approximation, when normalised by initial circulation and vortex ring diameter. This is significant as it indicates the likely presence of a global scaling for the vortex ring position, not previously seen. It is of particular interest, as it is equally applicable to both rotating and non-rotating vortex rings and as such, provides a degree of validation for using the eddy timescale in the definition of the vortex ring Rossby number Ro_Γ. It is commonplace for vortex rings to show a sudden change in y-trajectory prior to their decay, this marks the departure from the observed collapse.

8.4.3 Vortex ring diameter

For all conditions we can state some general trends concerning the vortex ring diameter. There is a general trend for the vortex rings to grow with time. This trend was also observed by Maxworthy (1977) for non-rotating vortex rings and attributed to viscous and turbulent diffusion of vorticity leading to fluid entrainment. Also in line with the measurements made by Maxworthy (1972), we find that the rate of diameter increase for all of the non-rotating conditions is roughly linear and greater for the higher Reynolds number, more turbulent conditions. This was attributed to turbulence increasing the rate of transfer of vorticity from the vortex core into the atmosphere and then subsequently into the wake of the vortex ring.

Comparing vortex rings from the same generation condition, with and without rotation, the vortex rings with background rotation tend to increase in diameter more quickly than those without. This in itself is a significant result, as measurement of vortex ring diameter has not been made previously for vortex rings

under the effects of background rotation. This result compares well with what was seen by Virk *et al.* (1994) for vortex rings with swirl induced from polarisation (c.f. section 3.4.1). For the vortex rings under the effects of background rotation, the general growth trend is also accompanied by decreases in the diameter. For all conditions under the influence of background rotation, with the exception of E and G, we find decreasing diameter at the end of the vortex ring's life, as discussed in section 7.3.4.

From the results of the errors discussed in section 8.1 it is tempting to interpret the decrease in vortex ring diameter towards the end of its life as a result of reduced accuracy in positioning the vortex centre in the light sheet. However, this is contradicted in part by the presence of the same trend for conditions F and H. These conditions show the same diameter decrease as with other rotating conditions, however none of the associated effects are seen in the profiles at above and below, as well as in the horizontal sums of $\overline{u_z}$. Upon this basis it is unlikely that error arising from inadequate correction for misalignment between the vortex ring centre and light sheet accounts for the decrease seen in D.

The implications of this are put into context by the other properties measured and not discussed yet, and will be discussed further in section 8.4.7.

8.4.4 Vortex ring core diameter and slenderness ratio

The vortex ring slenderness ratio was found to be driven strongly by the core diameter, as such all comments pertaining to the core diameter equally apply to the slenderness ratio. As with D, prior to the measurements presented here, the time evolution of δ had never been performed for rotating vortex rings. Furthermore, experimental measurement of δ over such large distances had not been performed using a quantitative technique (dye visualisation had been used, however it is notoriously unreliable measurements of this type (Lim and Nickels, 1995; Holmes

et al., 1996).

For all conditions we find a short core contraction time subsequent to generation, where we find slight decrease in δ immediately after formation. We find, for the non-rotating conditions that the evolution of the core was effectively steady and almost linear for all conditions. Condition A showed the slowest rate of growth and condition C the highest. This is in line with prior measurements, Maxworthy (1974) showed that turbulent vortex rings experience lower rates of core growth than their non-turbulent counterparts. Whilst both conditions A and B become turbulent, A is likely "more" turbulent, thus explaining the reduced growth of δ. Furthermore, Archer *et al.* (2008) shows that for a low Reynolds number thin core transitional vortex ring, core radius grows faster than for an equivalent thick cored vortex ring. Note, from table 7.2 (page 179) that condition C is a thinner cored vortex than condition A.

In all cases it was found that the rotating conditions grew faster than their corresponding non-rotating conditions. Furthermore it was seen that for all of the rotating vortex ring conditions a secondary stage of increased core growth occurred after the initial core growth period. It is interesting to note that for all rotating conditions, there is a notable increase in the gradient of δ, for the $3RPM$ conditions, this occurs towards the middle of vortex ring life and for the $6RPM$ cases, towards the end. The interesting thing about this change in gradient is that it occurs at approximately the same time as the beginnings of the decay of diameter discussed in section 8.4.3. The combination of a decrease of ring diameter combined with an increase in core diameter is unsurprising, as due to conservation of circulation, the contraction of a vortex should result in its fattening. This change however indicates that at this point, there is a large-scale reorganisation of the dynamics present in the vortex ring, we shall discuss this further in section 8.4.7.

8.4.5 Vortex ring tilt, θ

We find some strong similarities between the variation of vortex ring tilt with time and with the vortex ring x position over time. This is most noticeable for conditions B, F and H. The implication of this is that the inclination of the vortex ring is, on average, causing a change in the direction of translation. For other conditions however, little relation is found between θ and x, indicating that the translation direction is not necessarily linked to the vortex inclination, on average.

We find the general trend that upon increasing the rotation rate, the amount of tilt observed is increased. Verzicco *et al.* (1996) observed that under misalignment of the vortex ring trajectory and rotation vector, the vortex ring would undergo a non-axisymmetric transition. The vorticity contours presented by Verzicco *et al.* (1996) indicate that during this process the vortex ring undergoes a change in tilt (note that the tilt per se was not commented upon by Verzicco *et al.* (1996), only the departure from axisymmetry in the vorticity field). Our results indicate that This tilting of the vortex ring is increased with increasing rotation rate.

In addition to this, for the rotating conditions, one can also see a noticeable change in θ at approximately the same time as the observed decay in D and the change in gradient in δ. This adds further weight to the assertions that there is a significant change in the dynamics at this point.

8.4.6 Circulation, Γ

The plots of circulation presented in figure 7.16 show similar rates of decay for the non-rotating conditions. This similarity is not observed however for the rotating conditions for which it was found that the rate of decay was increased when

compared with the non-rotating. Amongst the rotating conditions, no trend was immediately obvious, i.e. no scaling with Rossby number was apparent.

Furthermore we find that for no condition does the circulation of the mean field show the step-wise decay observed by Weigand and Gharib (1994), and perhaps more interesting that for conditions F, H and J, such a large transient variation occurs early on. As mentioned when describing the plots in section 7.3.7, discussion of this will be reserved until section 8.6.2 where its relation to velocity and vorticity fields will be considered.

8.4.7 Conclusions and recommendations for further work

From the properties presented, several novel trends have be observed, the relation of these to one another and the implications this has for the fluid flow is discussed here. First, regarding the x and z motion, it is quite apparent that the vortex ring motion involves a degree of randomness as characterised by the mean values and their associated standard deviations. Aside from directionality associated with the rotation rate being seen, no trends are seen. As stated in section 8.4.1, we expect that a portion of the unpredictable motion observed in the x and z directions is driven by misalignment of the vortex ring with the rotation vector. The novel conclusion that may be arrived at from our measurements, is that the directionality of this motion is dictated by the direction of background rotation.

We present, as did Verzicco *et al.* (1996), curves of y position as a function of time. The data presented shows the same trend as that previously established, the vortex rings follow the same trajectory as their non-rotating equivalent until some point in time, where the translational velocity and hence gradient of the curve y versus t decreases suddenly. It is expected that this corresponds to a major change in the flow field, however analysis of this is reserved until information concerning the form of the velocity and vorticity fields have been presented.

A major result is the apparent collapse of the position time data upon non-dimensionalisation with initial circulation and vortex ring diameter. From this one may derive the eddy timescale with which to normalise time units, as used for time units by Shariff *et al.* (1994).

Perhaps of more significance is the collapse of both rotating and non-rotating data for varying stroke length and piston speed onto the same curve, as presented in figure 7.8b (page 193). The high level of similarity seen between the curves after this non-dimensionalisation implies that the vortex ring's dynamics may be (in terms of y trajectory at least) summarised by Γ_0 and D_0. Despite the excellent agreement presented between the means of many samples in figure 7.8b, it is recommended for further work that this relationship be tested across a wide parameter set of U_o, L_o and Ω values. Data has been acquired for this purpose, however its analysis is ongoing.

With regards the vortex ring diameter, we present the first statistical measurements of non-rotating vortex rings, which display similar trends to previous non-rotating measurements (Maxworthy, 1974). Our estimation of the time evolution of D in the rotating case, is the first such measurement presented. We find that vortex rings under background rotation have larger diameters than their non-rotating counterparts, a result which echoes that found numerically by Virk *et al.* (1994) for polarised rings. It is further seen that the vortex rings under background rotation undergo a transition and begin to decrease in size after some point in time. It is noted that this decrease is seen only for those rings whose Rossby number is below some critical value, estimated to lie somewhere in the range $1500 \lesssim Ro_\Gamma \lesssim 2200$.

It was further found that the vortex ring's core diameter was seen to increase in growth rate at the same time as this contraction set in. A possible explanation for this is in the conservation of circulation or volume associated with vortices.

In addition we find that core diameters tend to increase. The data presented show this growth rate greater amongst the low Reynolds number non-rotating conditions than the high, this supports measurements made by Maxworthy (1972) who suggested that turbulent cored rings grew at a reduced rate.

In addition to this, some general trends were noted for the vortex ring tilt. We see that as the rotation rate is increased, the magnitude of the tilt increases, indicating the occurrence of phenomena similar to that described by Verzicco *et al.* (1996) regarding the development of asymmetries under background rotation. As mentioned previously, we find correlation between the tilt direction and the x trajectory, this observation is unsurprising, as a tilted vortex ring, should travel in the x direction.

Concerning the circulation, Γ, we observed that the circulation decayed at similar rates for the non-rotating conditions A, B and C, indicating equivalent decay in impulse. Such similarity is however not observed in the curves produced for the rotating conditions. One finds that the rate of circulation loss is higher amongst the rotating conditions than their corresponding non-rotating measurements, however no link between the rate of decay and rotation rate is apparent. Furthermore the presence of a strong transient was observed for conditions F and H, it was found that this coincided with the contraction of the vortex ring core.

8.5 Evolution of velocity field; non-rotating

8.5.1 Time evolution of non-rotating velocity fields

Our comparisons between vortex rings generated with differing parameters have shown that there is a noticeable difference between conditions A and B, and also between A and C. Despite similar evolution of circulation, the time evolution of velocity for the lower Reynolds number cases shows increased rate of decay when

compared with condition A (high Reynolds number).

8.5.2 On the axial swirling flow of vortex rings

Our results provide the first statistical measurement of the azimuthal flow observed by Maxworthy (1972), Naitoh *et al.* (2002), Dazin *et al.* (2006a) and Archer *et al.* (2008). As explained in section 3.3.4, there has been some dispute as to the velocities observed in the core, Dazin *et al.* (2006a) observing lower velocities ($7\%U_T$) than Naitoh *et al.* (2002) ($25\%U_T$). Our results show somewhat conclusively that in both cases the authors observations are likely correct. We find that the mean axial swirling flow is very small for all conditions, for condition B the mean swirl is so low, that the pattern was at first not observed, only through the min/max and standard deviation curves was it appreciable.

In all cases we measure a distribution roughly centred around 0% swirl, with maximum and minimum of $\sim 70\%U_T$ and the mean plus standard deviation $\sim 20 - 40\%U_T$. Upon this basis it is not unreasonable that the percentages measured previously were so significantly different. Despite the reasonably high scatter across all conditions, it is interesting to note the differences in the means presented. We see for condition A, the net swirling direction is positive, whereas it is negative for condition C and for condition B, it is effectively 0. Perhaps more surprisingly, in all three cases the velocity remains at this level for the entire vortex run, indicating that there is perhaps some element of the dynamics of evolution producing a bias toward the swirling direction.

8.6 Evolution of velocity field; rotating

In this section we consider the development of the vortex ring flow field under the effects of background rotation, from observations of mean vortex ring velocity

and vorticity fields. To fully describe the development of the vortex rings, we use the many observations made in section 7.4.3 to build up a picture of the dynamics at work. This is done with constant reference to Verzicco *et al.* (1996), with whom we find many similarities.

To aid in the discussion, we summarise here the observations made in section 7.4.3 and link them, where possible, to observations already made in the literature:

- Upon formation, strong azimuthal flow is seen. Verzicco *et al.* (1996) show this from their numerical simulations, we provide the first experimental visualisation of this:
  - A cyclonic swirling vortex forms close to the axis of the ring, this stretches from the frontal stagnation point to the vortex generator.
  - In the core and outer vortex ring atmosphere, an anti-cyclonic swirling flow is found.
- As the vortex ring translates, we show that the wake swirl decreases in diameter and increases in magnitude. This is consistent with vortex theory, as one expects, that a vortex will conserve circulation for short timescales.
- A region of increased vertical velocity directed upwards develops upon the vortex ring axis, leading to a depression in the vortex ring streamlines, observed near the frontal stagnation point. Verzicco *et al.* (1996) noted the depression, however appreciate the relationship of this to the increased velocity, which we call an "axial jet" of fluid.
- Azimuthal vorticity was found to form in the centre of the vortex ring, close to the axis. This was found previously by Verzicco *et al.* (1996) and

attributed to the rejection of opposite signed vorticity from the vortex cores, thus forming a secondary vortex.

- No change was seen for the high piston velocity vortex rings, but for the low piston velocity vortex rings both the circulation and diameter decrease in conjunction with this secondary vortex shedding. Verzicco *et al.* (1996) noted changes in diameter for low Reynolds numbers, attributing this to the decrease in inertial timescales, when compared with viscous, no prior evaluation of circulation was performed.

- The secondary vortex which was formed in the centre of the vortex ring was then advected out of the front of the vortex and then around the sides of the primary vortex ring.

- We show that a highly three dimensional flow, without axial symmetry is seen during this period. Verzicco *et al.* (1996) showed that a break from axisymmetry during this period could occur due to misalignment between the vortex ring's direction of translation and the background rotation vector.

  - Vortex ring diameter increases for the low piston velocity vortex rings, no change is seen for the high piston velocity case. Both of these phenomena were noted by Verzicco *et al.* (1996), experimentally and numerically. Again, arguments for relative inertial and viscous timescales were made by Verzicco *et al.* (1996) as when the secondary vortex formed inside the primary vortex ring.

  - We find that the secondary vorticity is then advected around the vortex ring is deposited into the wake, again seen by Verzicco *et al.* (1996) both experimentally and numerically.

  - A corresponding circulation increase is seen for the low piston velocity

vortex rings, no change is seen for the high piston velocity case. Our results provide the first estimation of circulation of vortex rings under the effects of background rotation.

  - The flow field returns to approximate axial symmetry.
  - The origination point of the wake swirl inside the vortex ring is displaced rearwards. Our results are the first to consider in detail, the evolution of the azimuthal component of velocity (in our case, u_z is an approximation to this) and as such, we discuss the spatial origins of the wake swirl.
  - Verzicco *et al.* (1996) present data indicating the breaking of the wake swirl into two sections; one attached to the vortex ring, the other attached to the vortex generator, we repeat the plots indicating this in figure 3.13. Verzicco *et al.* (1996) did not however comment upon the development of this structure and importantly its implications upon the dynamics observed.

- We observe that for very low Rossby numbers, the vortex ring is destroyed prior to the completion of the above flow restructuring. For higher Rossby numbers, the vortex ring continues steadily, our measurements are the first of this kind.

As discussed by Verzicco *et al.* (1996) shedding of secondary vorticity shortly after vortex ring roll-up is a phenomena observed only for vortex rings under the presence of background rotation. An important observation that results from the presented data is the statistical stability and repeatability of this phenomena, which is seen clearly in the mean velocity and vorticity fields. We see, as did Verzicco *et al.* (1996), that vorticity of opposite sign to that in the core forms

Code	Vortex shedding		Axial jetting		Wake swirl transition		dy/dt change
	Start	End	Start	End	Start	End	
E	2.09	5.23	1.54	3.63	2.09	6.28	2.91
F	1.22	3.55	1.11	2.55	1.77	4.22	2.31
G	0.70	2.42	0.70	2.42	1.72	??	2.42
H	1.23	3.82	1.23	2.84	1.85	4.56	2.57
I	1.36	3.71	0.90	2.78	2.29	4.63	2.57
J	1.26	3.10	1.26	2.40	1.69	XXX	2.35
K	1.19	2.75	1.19	2.34	1.97	5.07	2.71

Table 8.2: Tabulated non-dimensional times of vortex ring transition events

near the axis of the vortex ring. This vorticity is then advected around the vortex ring and deposited into the wake.

The times at which this vorticity shedding occur are listed by condition in table 8.2. For comparison the times at which the axial jetting phenomena (described in section 7.4.3.2), the wake swirl goes through a transition and the y trajectory change are also included. For the y trajectory, data points were manually extracted by zooming in on the plots presented in figure 7.7. For the other properties, the start and end times of the various transitions were estimated through manual comparison of the velocity profiles and vorticity fields for each condition and its non-rotating counterpart.

8.6.1 The effects of axial jetting

We see from the times listed in table 8.2 that the formation of the axial jet of fluid occurs shortly before or with the onset of the secondary vorticity formation in all cases. It is therefore logical to conclude that the axial jetting phenomena described in fact causes the formation of the secondary vorticity. It should be noted that the first measurement of this jetting flow was presented without comment by Verzicco *et al.* (1996) who noticed a "depression" around the frontal

stagnation point of the vortex ring. This same phenomenon is also seen in the stream function evolution presented in figure 7.71 (page 279). From consideration of the u_y profiles presented in figure 7.41 (page 236), it is apparent that this jet of fluid provides significant vorticity generation in the centre of the vortex ring, and this vorticity is of opposite sign to the local flow.

To emphasize this point, the comparison between conditions B and F is presented in figures 8.3a and 8.3b , plotting u_y and $\partial u_y/\partial x$ through the centre of the secondary vortex. Plots of u_x and $\partial u_x/\partial y$, which are extracted through the same point, are also shown in figures 8.3c and 8.3d. These plots indicate that little contribution to this vorticity arises from the u_x component of velocity, which is found to be very similar to that of the non-rotating case (condition B). For this reason, the secondary vorticity formed is likely to arise largely from shear forces, with this shear arising from the jetting flow.

8.6.2 Analysis of $\overline{u_z}$; secondary vortex shedding

From the values listed in table 8.2 we are able to link the vortex shedding phenomena to effects seen in the other parameters and fields. Although not tabulated, we see that for conditions F and H, the onset of the vortex shedding coincides with an increase in vortex ring diameter (figure 7.9, page 194). Verzicco *et al.* (1996) attributed this effect to the forcing of the secondary vorticity upon the original vortex. They also predicted numerically that the motion of this vorticity around the ring would result in strong cross cancellation, we find evidence of this in the circulation measurements (figure 7.16) which show a significant drop in circulation subsequent to the ejection of the secondary vortex to the wake, again this is only seen for conditions F, H and J.

It is notable that a strong reduction in the circulation can be seen as the oppositely signed vorticity develops between the cores, and that after the secondary

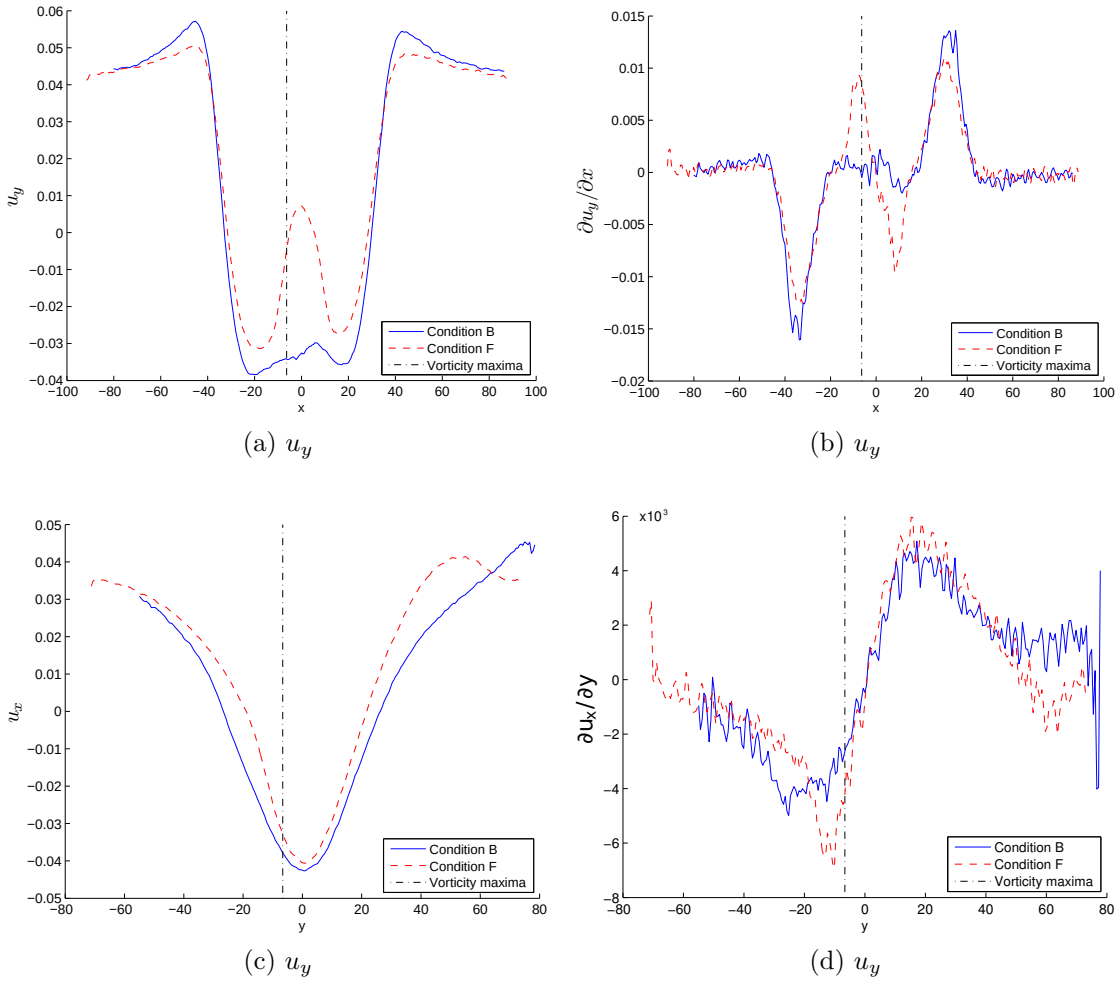

(a) u_y (b) u_y

(c) u_y (d) u_y

Figure 8.3: Comparison velocity components under the formation of secondary vorticity

vortex has been shed, a small increase in circulation is observed. This most likely occurs because the secondary vorticity rejection is of opposite sign to that in the core. Recalling the definition for circulation (equation (3.5b), page 59) it is plain that the presence of a packet of negative vorticity will result in an decrease in the surface integral of $\nabla \times \mathbf{u}$ and hence the circulation. By the same logic, the subsequent removal of this packet will in turn result in an increase in circulation (as was seen for the curves in section 7.3.7).

We see from figure 7.16c that subsequent to the increase of circulation for

conditions F and H (coinciding with the end of the secondary vorticity rejection), the value is noticeably lower than its original value. This indicates, that likely the primary core has been significantly weakened by cross cancellation as the secondary vortex is moved around the primary vortex and deposited in the wake.

The phenomena described here are not seen in the corresponding curves for conditions E, G, I and K (although we do still see the axial jetting and the subsequent secondary vortex shedding). This change in the effect of the vortex shedding is likely due to the relative timescales of the vortex motion, as suggested by Verzicco *et al.* (1996). Conditions F, H and J corresponding to low inertial (and therefore low Reynolds number) conditions, where viscosity has a greater role, and cross-cancellation between the oppositely signed vortices is prevalent. Conditions E, G, I and K however correspond to high inertial cases and as such, the timescales of evolution are much shorter. For this reason, the diameter and circulation are not noticeably effected by the vortex shedding.

8.6.3 Analysis of $\overline{u_z}$; the onset of axial jetting

Throughout section 7.4.3.3, it was found that the higher the rotation rate, the greater the magnitude of the swirl. This is an unsurprising and expected result, due to the form of the Coriolis acceleration imparted to the fluid (equation (3.26)).

We show qualitatively (figure 7.67, page 274) that upon formation, a strong wake swirl is created behind of the vortex ring. It was shown that as the vortex ring moves away from the vortex generator, this wake vortex is stretched, causing the vorticity to be concentrated into a tight, fast swirling vortex, consistent with vortex theory. We propose that it is the stretching of this vortex that results in the low pressure region seen by Verzicco *et al.* (1996).

We believe this conjecture is further supported by the velocity and pressure fields presented by Verzicco *et al.* (1996). Verzicco *et al.* (1996) figures 10(b),

10(d) and 11(b) show plots of the axial vorticity, azimuthal velocity and pressure fields respectively (reproduced in section 3.4, figures 3.10, page 79 and 3.12, page 82). They interpret these plots such that the origins of the pressure field arise from Coriolis force acting upon the wake swirl, as cyclonic flow leads to an acceleration radially outwards (c.f. equation 8.1) and reduced pressure. It appears however, that the pressure field shows strong correlation with the axial vorticity field, as would be the case were the low pressure region to be associated with a vortex tension force (arising due to vortex curvature). Furthermore, were this low pressure to arise from a Coriolis induced forcing, as proposed by Verzicco *et al.* (1996), then we should expect acceleration and so forcing radially inwards distributed with the azimuthal velocity (equation 8.1), which is not seen. Finally, as discussed in section 8.3, Coriolis force is only able to provide an appreciable effect where velocities evolution scales are slow compared to Ω. The wake vortex discussed is however one of the more energetic phenomena seen in the vortex ring velocity field, thus it is very unlikely that Coriolis force affects it and therefore unlikely that the pressures observed arise from forcing radially inwards due to Coriolis force.

From further qualitative interpretation of figure 7.67 (page 274), we see that at some point, the wake swirl vortex begins to rapidly decrease in magnitude. This marks the onset of the departure from axial symmetry inside the vortex ring and the separation of the strongly swirling wake flow from the front of the vortex ring.

In our time evolution measurements (7.67, page 274), we see that as the $\overline{u_z}$ field leaves axial symmetry, the magnitude of the velocities in the wake swirl decrease. We see from figures showing vorticity contours, presented by Verzicco *et al.* (1996) (reproduced in figure 3.13, page 83), that this actually coincides with the wake swirl breaking. When this happens, the swirling flow is separated into

two parts, that attached to the vortex ring decreases in magnitude and increases in radial extent, as seen from our results. From the simulations of Verzicco *et al.* (1996) we see that the other side, connected to the generator, propagates towards the generator and also radially outwards.

As the vortex wake enters this transitional period, so does the swirling flow inside the ring. We see that this takes on a transitional, highly 3D structure, after which, rough axial symmetry reforms. During the transitional stage, the front of the wake swirl moves significantly further back inside the vortex ring, towards its rearward stagnation point. The wake seen in the $\overline{u_z}$ field presented in figure 7.67 shows similarity to the "tail" seen by Virk *et al.* (1994) in their simulations of polarised vortex rings. This major restructuring of the vortex ring and its velocity field coincides with the points in time at which changes to the evolution of the vortex ring diameter and the core diameter occur.

It is also interesting to note that for most conditions, the return of the vortex ring to rough axial symmetry coincides with the change in gradient noted in the vortex core diameter evolution plots, figure 7.3.5. We see that for conditions E, F and H, the rate of growth of the core diameter increases at approximately the end of the transition time listed in table 8.2. Further to this, a very slight change in growth rate is noted for conditions I and K; however, the change was sufficiently slight that it could not be attributed to the transitional nature of the vortex ring with any certainty. For condition G, the out of plane correction had performed sufficiently poorly that it was not possible to determine when the vortex ring had re-stabilised subsequent to the vortex shedding.

8.6.4 Conclusions and recommendations for further work

Here we have discussed the majority of our results, concerning the evolution of the vortex rings under background rotation subsequent to formation. Throughout we

have used the prior works of Verzicco *et al.* (1996) and Virk *et al.* (1994) to provide context were appropriate. Our results show the effects of rotation discussed are felt across a wide range of both Reynolds and Rossby numbers. The main basis of our comparison is table 8.2, which provides time comparisons between several noteworthy events in the vortex rings evolution.

We suggest that upon formation the region of low pressure apparent from the numerical simulations of Verzicco *et al.* (1996) occurs due to a vortex line tension in the swirling wake vortex, not due to Coriolis force induced by this swirling motion, as previously thought. We present convincing arguments regarding this, concerning the timescales over which Coriolis force acts, the relative velocity magnitude of the inducing flow and even the velocity and vorticity distributions presented in Verzicco *et al.* (1996). Our results show that this low pressure region, causes the formation of a jet of fluid along the axis of the vortex ring, moving from the frontal stagnation point, through the ring. Whilst this was actually observed in the streamlines presented by Verzicco *et al.* (1996), who mentioned a "depression" in the vortex bubble, and claimed this to indicate high pressure fluid ahead of the vortex ring. The depression mentioned is clearly visible in our streamlines, presented as part of the full field evolution data, however the velocity fields indicate that it is a jet of fluid, passing through the vortex ring, not a high pressure region.

From analysing the horizontal derivatives of the velocity field through the core, at the point in time when the axial jet forms, we are able to show that in fact this jet causes the formation of the opposite signed secondary vortex ring. This secondary vortex is advected around the primary and this phenomena is linked with changes to the diameter, core diameter and circulation for conditions F, H and J. The circulation decreases with the onset of the axial jetting, as the secondary vortex, being oppositely signed decreases the total vorticity in the

vortex ring. The ejection of the secondary vortex thus results in an increase in circulation. The interaction between primary and secondary vortices gives rise to the observed change in diameter. When the secondary vortex forms, inside the primary vortex, the primary vortex contracts and when the secondary vortex is advected to the outside of the primary, it causes a contraction in the primary.

In the higher Rossby number cases investigated, these effects are not readily observed. However, the time at which the vortex shedding occurs is much earlier than for the lower Reynolds number and so Rossby number conditions, and so it is much more difficult to discern these effects from the transients caused by formation. In particular early circulation measurements are not reliable, as the area over which it is calculated is significantly reduced. On the other hand, it was apparent from the consideration of the circulation (c.f. section 8.4.7) that the generation of vortices both with background rotation and without differs significantly between the high and low Reynolds number cases. Thus indicating that the effects due to vortex shedding seen for the low Reynolds number generations, such as significant changes in diameter, may arise due to viscous effects, not Rossby number effects, as suggested by Verzicco *et al.* (1996). In further work we aim to clarify this matter, additional data has been acquired for vortex rings produced across a wide range of generation parameters. By comparing the vortex ring diameter and circulation as functions of both Ro_Γ and Re_Γ, we will be able to ascertain the reasons for the distinct differences seen between the high and low Reynolds number vortex rings.

8.7 Summary of discussions

8.7.1 Velocity field corrections for traversing SPIV measurement of vortex rings

In section 8.2 we discuss the success of the various corrections applied to the PIV velocity fields. Three separate corrections were applied to the velocity field data to account for motion of the cameras induced by their traversal and also the relative motion of the vortex ring to the light sheet. The correction performed on the velocity fields to remove velocities due to camera shaking appear successful in general. Some residual motion is seen to remain in the mean velocity fields only for cases when the cameras are under high acceleration. Furthermore the corrections to the camera calibration and associated removal of image misalignment through the use of flow field self-calibration are also found to be satisfactory. In both cases, little more than simple evaluations have been presented, where the net effect upon the mean fields is considered and improvements to representative individual velocity fields is shown. Concerning the corrections for the vortex ring moving away from the light sheet plane, the success of the corrections appears varied. The mean fields of conditions F, H and J appear to show no effects of the out of light-sheet motion, whereas for condition G in particular significant motion remains unaccounted for. Despite this, additional testing of the correction for vortex rings moving out of the light sheet produced results indicating that the correction would only improve the velocity field. It showed that even where significant errors were accrued for high levels of noise or large out-of-plane displacements, the correction would not act to displace the vortex ring further from the light sheet.

8.7.2 The time evolution of vortex rings

Our investigation into the time evolution of vortex rings has led to some important and interesting results. Firstly we show the significance of using the eddy timescale, D_0^2/Γ_0 as the characteristic timescale for vortex rings. Our data shows the collapse of data points after normalisation by this and the initial ring diameter D_0. It is most interesting that plots of the vortex ring y position collapse for both rotating and non-rotating conditions when this normalisation is used.

8.7.3 Vortex rings without background rotation

Our results have indicated that the slug flow model performs reasonably at predicting the vortex ring circulation. Conditions A and B were predicted very well, condition C, less so. This is likely due to some slight error in estimating the generation parameters, due to belt stretch in the piston drive.

In addition we also provide a statistical overview of the axial swirling flow commented upon. We find that the flow has a very low mean, occurring as the distribution of data is close to symmetric and centred around zero velocity. This said, the range of swirling values measured is very large, with standard deviations as high as $60\%U_T$, indicating that a wide variety of swirling motions are observable in the vortex ring. Whilst the swirling flow was observed previously, no comment regarding its statistically erratic behaviour was made.

8.7.4 The effects of background rotation upon vortex rings

Our discussion of the effects of background rotation upon vortex rings begins with consideration of the vortex rings after the formation process has completed. We compare vortex rings produced under background rotation, with equivalent conditions generated without background rotation. It is immediately apparent

from the data presented that the initial circulation decreases when background rotation is added. Through the observations made of the velocity field, we are able to state with reasonable certainty that this occurs due to conservation of energy; during roll-up, some fluid is accelerated into a swirling flow through Coriolis force, thus the net vortical flow is decreased and so is the circulation. For vortex ring diameter, we find an increase for low rotation rates, but a decrease at higher rotation rates. We present arguments centred around the Coriolis force concerning the effects on diameter at low Rossby number, where the diameter decreases, however the reasons for increase of diameter at high Rossby number are unclear. Similarly a trend is found for core diameter; at low Ro_Γ, the core diameter δ decreases, at high Ro_Γ, the core diameter increases. As with the vortex diameter, we propose physical arguments for the observed effects at low Rossby number, but are less able for the high Rossby number case.

We find evidence to suggest that the stretching of the swirling wake vortex leads to a region of low pressure directly behind the vortex ring. This region of strong low pressure, induces an axial "jetting" flow through the centre of the vortex ring. As indicated by the high shear present in this axial jet, a secondary vortex ring of opposite sign is formed in the centre of the original vortex ring, which is then advected around the primary vortex core. Whilst this is happening, the vortical wake, which initiated this process appears to separate from the vortex ring.

We further suggest that upon formation the vortex lines constituting this vortical wake merge into the vortex ring. Upon the separation of the wake, this connection to the vortex ring core is broken, leading to a complex, non-axially symmetric, transient 3D motion (this departure from axial symmetry may arise due to misalignment between the vortex ring and the axis of rotation). This 3D motion forces a restructuring of the vortex core, leading to increased growth rates

when compared to the rotating equivalent.

For cases where the effects of rotation are sufficiently low, the vortex ring is able to reform (condition J indicates that this is not necessarily possible) and it propagates with decreasing diameter and increased core growth until its decay. The form of the velocity field is unremarkable, with the most notable difference to the non-rotating equivalent being in the $\overline{u_z}$ field. Here we see a large, anti-cyclonic swirling ahead and to the sides of the vortex ring, with a large, low magnitude swirling wake flow behind the vortex ring. A noteworthy feature of this velocity field is that the wake swirl is no longer connected to the vortex generator directly and so not stretched, in turn not producing the region of intense low pressure, axial jetting or secondary vorticity. This shows that contrary to the hypothesis of Verzicco *et al.* (1996), a second occurrence of the secondary vortex shedding is not possible.

Bibliography

Adrian, R. J. (1984). Scattering particle characteristics and their effect on pulsed laser measurements of fluid flow: speckle velocimetry vs. particle image velocimetry, *Appl. Opt.* **23**: 1690–91. 6, 18

Adrian, R. J. (1986). Image shifting technique to resolve directional ambiguity in double-pulsed velocimetry, *Appl. Opt.* **25**: 3855–3858. 9, 10, 11

Adrian, R. J. (1991). Particle-imaging techniques for experimental fluid mechanics, *Ann. Rev. Fluid Mech.* **23**: 261–304. ix, 6, 8, 18, 22

Adrian, R. J. (2005). Twenty years of particle image velocimetry, *Exp. Fluids* **39**(2): 159–169. 6, 10

Adrian, R. J. and Yao, C.-Y. (1985). Pulsed laser technique application to liquid and gaseous flows and the scattering power of seeding materials, *Appl. Opt.* **24**(1): 44–52. 14, 15, 18

Allen, J. J. and Naitoh, T. (2005). Experimental study of the production of vortex rings using a variable diameter orifice, *Phys. Fluids* **17**: 061701.1–061701.4. 67

Archer, P., Thomas, T. and Coleman, G. (2008). Direct numerical simulation of vortex ring evolution from the laminar to the early transition regime, *J. Fluid Mech.* **598**: 201–226. 70, 71, 75, 302, 307

Bergdorf, M., Koumoutsakos, P. and Leonard, A. (2007). Direct numerical simulations of vortex rings at Re = 7500, *J. Fluid Mech.* **581**: 495–505. 71, 75

Bertuccioli, L., Gopalan, S. and Katz, J. (1996). Image shifting for PIV using birefringent and ferroelectric liquid crystals, *Exp. Fluids* **21**: 341–346. 9

Boillot, A., and Prasad, A. K. (1996). Optimization procedure for pulse separation in cross-correlation PIV, *Experiments in Fluids* **21**(2): 87–93. 10, 11

Brend, M. A. and Thomas, P. J. (2009). Decay of vortex rings in a rotating fluid, *Phys. Fluids* **21**(4): 044105–1 – 044105–4. 3, 162

Brücker, C. (1996). 3-D PIV via spatial correlation in a color-coded light-sheet, *Exp. Fluids* **21**: 312–314. 13

Buzukov, A. A. (1971). Properties of the formation and motion of vortex rings in water, *Zhurnal Prikladnoi Mekhaniki i Tekhnicheskoi Fiziki* **2**: 153–160. 75

Calluaud, D. and David, L. (2004). Stereoscopic particle image velocimetry measurements of the flow around a surface-mounted block, *Exp. Fluids* **36**: 53–61. 52

Cenedese, A. and Paglialunga, A. (1989). A new technique for the determination of the third velocity component with PIV, *Exp. Fluids* **8**: 228–230. 13

Coudert, S. J. M. and Schon, J.-P. (2001). Back-projection algorithm with misalignment corrections for 2D3C stereoscopic PIV, *Meas. Sci. Technol.* **12**: 1371–1381. 40, 45, 46

Cushman-Roisin (1994). *Introduction to Geophysical Fluid Dynamics*, Prentice-Hall. 162, 163

Dabiri, J. O. and Gharib, M. (2004a). A revised slug model boundary layer correction for starting jet vorticity flux, *Theoret. Comput. Fluid Dynamics* **17**: 293–295. 68

Dabiri, J. O. and Gharib, M. (2004b). Fluid entrainment by isolated vortex rings, *J. Fluid Mech.* **511**: 311–331. 74

Dabiri, J. O. and Gharib, M. (2005). Starting flow through nozzles with temporally variable exit diameter, *J. Fluid Mech.* **538**: 111–136. 67

Dazin, A., Dupont, P. and Stanislas, M. (2006a). Experimental characterization of the instability of the vortex ring. Part I: Linear phase, *Exp. Fluids* **40**: 383–399. 36, 70, 208, 215, 307

Dazin, A., Dupont, P. and Stanislas, M. (2006b). Experimental characterization of the instability of the vortex ring. Part II: Non-linear phase, *Exp. Fluids* **41**: 401–413. 70

Dziedzic, M. and Leutheusser, H. J. (2004). An experimental study of viscous vortex rings, *Exp. Fluids* **21**(5): 315–324. xxv, 62

Eisenga, A. H. M., Verzicco, R. and van Heijst, G. J. F. (1998). Dynamics of a vortex ring moving perpendicularly to the axis of a rotating fluid, *J. Fluid Mech.* **354**: 69–100. 75

Elsinga, G. E., Scarano, F., Wieneke, B. and van Oudheusden, B. W. (2006). Tomographic particle image velocimetry, *Exp. Fluids* **41**: 933–947. 14

Fessler, J. R. and Eaton, J. K. (1999). Turbulence modification by particles in a backward-facing step flow, *J. Fluid Mech.* **394**: 97–117. 17

Gharib, M., Rambod, E. and Shariff, K. (1998). A universal timescale for vortex ring formation, *J. Fluid Mech.* **360**: 121–140. 56, 57, 64, 66

Glezer, A. (1988). The formation of vortex rings, *Phys. Fluids* **31**(12): 3532–3542. x, 58, 60, 61, 62, 64

Glezer, A. and Coles, D. (1990). An experimental study of a turbulent vortex ring, *J. Fluid Mech.* **211**: 243–283. 71, 73

Gogineni, S., Goss, L., Pestian, D. and Rivir, R. (1998). Two-color digital PIV employing a single CCD camera, *Exp. Fluids* **25**: 320–328. 9

Gore, R. A. and Crowe, C. T. (1991). Modulation of turbulence by a dispersed phase, *J. Fluid Eng. T. ASME* **113**: 304–307. 17

Grant, I. (1997). Particle image velocimetry: a review, *P. I. Mech. Eng. C.-J. Mec.* **221**(1): 55–76. 6, 16

Gray, C., Greated, C. A., McCluskey, D. R. and Easson, W. J. (1991). An analysis of the scanning beam PIV illumination system, *Meas. Sci. Technol.* **2**: 717–724. 10

Greenspan, H. P. (1968). *The Theory of Rotating Fluids*, Cambridge University Press. 162, 163

Hart, D. P. (2000). PIV error correction, *Exp. Fluids* **29**: 13–22. 12

Hartley, R. I. and Sturm, P. (1997). Triangulation, *Comput. Vis. Image Und.* **68**(2): 146–157. 45, 47, 48, 49, 51

Hartley, R. and Zisserman, A. (2003a). *Multiple view geometry*, Cambridge University Press, chapter 2 - Projective geometry and transformations of 2D, pp. 25–64. 41

Hartley, R. and Zisserman, A. (2003b). *Multiple view geometry*, Cambridge

University Press, chapter 3 - Projective geometry and transformations of 3D, pp. 65–85. 42

Hartley, R. and Zisserman, A. (2003c). *Multiple view geometry*, Cambridge University Press, chapter 6 - The projective camera, pp. 153–177. 44

Hartley, R. and Zisserman, A. (2003d). *Multiple view geometry*, Cambridge University Press, chapter Part II - Two-view geometry, pp. 237–362. 51, 141

Heikkilä, J. and Silvén, O. (1997). A four-step camera calibration procedure with implicit image correction, *Proc. CVPR '97*. 40, 41, 44, 45

Hetsroni, G. (1989). Particles-turbulence interaction, *Intl. J. Multiphase Flow* **15**: 735–746. 17

Hinsch, K. D. (1995). Three-dimensional particle velocimetry, *Meas. Sci. Technol.* **6**: 742–753. 34

Holmes, P., Lumley, J. L. and Berkooz, G. (1996). *Turbulence, coherent structures, dynamical systems and symmetry*, Cambridge University Press, chapter 2, p. 39. 301

Hu, H., Saga, T., Kobayashi, T., Okamoto, K. and Taniguchi, N. (1998). Evaluation of the cross correlation Method by using PIV standard images, *J. Visual-Japan* **1**: 87–94. 21

Huang, H., Dabiri, D., and Gharib, M. (1997). On errors of digital particle image velocimetry, *Meas. Sci. Technol.* **8**: 1427–1440. 21

Huang, H. T., Fidler, H. E. and Wang, J. J. (1993). Limitation and Improvement of PIV (Part II: Particle image distortion, a novel technique), *Exp. Fluids* **15**: 168–174. 24

Ido, T., Shimizu, H., Nakajima, Y., Ishikawa, M., Murai, Y. and Yamamoto, F. (2003). Single-camera 3-D particle tracking velocimetry using liquid crystal image projector, *Proceedings of ASME-JSME FED-SM 2003*. 13

Jacquot, P. and Rastogi, P. K. (1981). Influence of out-of-plane deformation and it's elimination in white speckle photography, *Opt. Laser Eng.* **2**: 33–55. 33

Jambunathan, K., Ju, X. Y., Dobbins, B. N. and Ashforth-Frost, S. (1995). An improved cross correlation technique for particle image velocimetry, *Meas. Sci. Technol.* **6**: 507–514. 24

Jaw, S., Haik, Y., Hwang, R. R. and Chen, C. (2003). Measurements of soap bubble collapse flow using color PIV, *16th ASCE Engineering Mechanics Conference*. 13

Johnson, G. M. (1971). An empirical model of the motion of turbulent vortex rings, *AIAA J.* **9**: 763–764. 71

Johnson, J. A. (1966). The diffusion of a viscous vortex ring in a rotating fluid, *J. Fluid Mech.* **24**(4): 753–763. 60, 83

Keane, R. D. and Adrian, R. J. (1990). Optimization of particle image veIocimeters. Part I: Double pulsed systems, *Meas. Sci. Technol.* **1**: 1202–1215. 26

Keane, R. D. and Adrian, R. J. (1991). Optimization of particle image veIocimeters. Part II: Multiple pulsed systems, *Meas. Sci. Technol.* **2**: 963–974. 9

Keane, R. D. and Adrian, R. J. (1992). Theory of cross-correlation analysis of PIV images, *Appl. Scie. Res.* **49**: 191–215. 10, 12, 19

Krutzsch, C. H. (1939). Uber eine experimentell beobachtete erscheinung an wirbelringen bei ihrer translatorischen bewegung in wirklichen flussigkeiten, *Annln Phys.* **35**: 497–523. 69, 165

Kulick, J. D., Fessler, J. R. and Eaton, J. K. (1994). Particle response and turbulence modification in fully developed channel flow, *J. Fluid Mech.* **277**: 109–134. 17

Kundu, P. K. and Cohen, M. (2002). *Fluid Mechanics*, Academic press, chapter 14 - Geophysical fluid dynamics, p. 559. 59, 76

LaVision (2006). *Tools for DaVis: DaVis flowmaster software*, LaVision GmbH, chapter Fig 9.4, p. 150. ix, 35

Lawson, N. J. and Wu, J. (1997). Three-dimensional particle image veIocimetry: experimental error analysis of a digital angular stereoscopic system, *Meas. Sci. Technol.* **8**: 1455–1464. 40

Leese, J. A. and Novak, C. S. (1971). An automated technique for obtaining cloud motion from geosynchronous satellite data using cross correlation, *J. Appl. Meteorol.* **10**: 118–132. 5, 21

Levy, Y. and Lockwood, F. C. (1981). Velocity measurements in a particle laden turbulent free jet, *Combust. Flame* **40**: 333–339. 17

Liess, C. and Didden, N. (1976). Zeitschrift der angewandte, *Z. Agnew. Math. Mech.* **56**: 206. 70

Lim, T. T. and Nickels, T. B. (1995). *Vortex rings*, Kluwer academic publishers, chapter IV, pp. 95–153. 54, 63, 64, 301

Linden, P. F. and Turner, J. S. (2001). The formation of "optimal" vortex rings, *J. Fluid Mech.* **427**: 61–72. 68

Louhichi, H., Fournel, T., Lavest, J. M. and Aissia, H. B. (2007). Self-calibration of Scheimpflug cameras: an easy protocol, *Meas. Sci. Technol.* **18**: 2616–2622. 44

Lourenco, L. and Krothapalli, A. (1995). On the accuracy of velocity and vorticity measurements with PIV, *Exp. Fluids* **18**: 421–428. 22

Maas, H.-G. (1995). New developments in multimedia photogrammetry, *Optical 3-D Measurement Techniques III*. 44

Maas, H. G., Gruen, A. and Papantoniou, D. (1993). Particle tracking velocimetry in three-dimensional flows. Part 1. Photogrammetric determination of particle coordinates, *Exp. Fluids* **15**: 133–146. 13, 45

Maxworthy, T. (1972). The structure and stabilitly of vortex rings, *J. Fluid Mech.* **51**(1): 15–32. 61, 68, 69, 195, 206, 300, 306, 307

Maxworthy, T. (1974). Turbulent vortex rings, *J. Fluid Mech.* **64**: 227–239. 69, 71, 72, 302, 305

Maxworthy, T. (1977). Some experimental studies of vortex rings, *J. Fluid Mech.* **81**(3): 465–495. 57, 64, 70, 165, 167, 291, 295, 300

Melling, A. (1997). Tracer particles and seeding for particle image velocimetry, *Meas. Sci. Technol.* **8**: 1406–1416. 14, 18

Meunier, P. and Leweke, T. (2003). Analysis and treatment of errors due to high velocity gradients in particle image velocimetry, *Exp. Fluids* **35**: 408–421. 11, 23

Mohseni, K. and Gharib, M. (1998). A model for universal time scale of vortex ring formation, *Phys. Fluids* **10**: 2436–2438. 68

Mohseni, K., Ran, H. and Colonius, T. (2001). Numerical experiments on vortex ring formation, *J. Fluid Mech.* **430**: 267–282. 67

Naitoh, T., Fukuda, N., Gotoh, T., Yamada, H. and Nakajima, K. (2002). Experimental study of axial flow in a vortex ring, *Phys. Fluids* **14**(1): 143–149. xxv, 70, 208, 215, 307

Nogueira, J., Lecuona, A. and Rodriguez, P. A. (1997). Data validation, false vectors correction and derived magnitudes calculation on PIV data, *Meas. Sci. Technol.* **8**: 1493–1501. 30, 31

Nogueira, J., Lecuona, A. and Rodriguez, P. A. (1999). Local field correction PIV: on the increase of accuracy of digital PIV systems, *Exp. Fluids* **27**: 107–116. 25

Nogueira, J., Lecuona, A. and Rodriguez, P. A. (2001). Identification of a new source of peak locking, analysis and its removal in conventional and super-resolution PIV techniques, *Exp. Fluids* **30**: 309–316. 15, 21, 22, 23

Norbury, J. (1973). A family of steady vortex rings, *J. Fluid Mech.* **55**(3): 417–431. 68

Pickering, C. J. D. and Halliwell, N. A. (1984). Speckle photography in fluid flows: signal recovery with two-step processing, *Appl. Opt.* **23**: 1128–29. 6

Prasad, A. K. (2000). Stereoscopic particle image velocimetry, *Exp. Fluids* **29**(2): 103–116. ix, x, 6, 12, 14, 33, 36

Prasad, A. K. and Adrian, R. J. (1993). Stereoscopic particle image velocimetry applied to liquid flows, *Exp. Fluids* **15**: 49–60. 34, 39, 272

Prasad, A. K., Adrian, R. J., Landreth, C. C. and Offutt, P. W. (1992). Effect of resolution on the speed and accuracy of particle image velocimetry interogation, *Exp. Fluids* **13**: 105–116. 14

Prasad, A. K. and Jensen, K. (1995). Scheimpflug stereocamera for particle image velocimetry in liquid flows, *Appl. Opt.* **34**: 7092–7099. 34, 36

Pullin, D. I. (1979). Vortex ring formation at tube and orrifice openings, *Phys. Fluids* **22**(3): 401–403. 65

Raffel, M., Gharib, M., Ronneberger, O. and Kompenhans, J. (1995). Feasibility study of three-dimensional PIV by correlating images of particles within parallel light sheet planes, *Exp. Fluids* **19**: 69–77. 13

Raffel, M., Willert, C. E., Wereley, S. T. and Kompenhans, J. (1998). *Particle Image Velocimetry: A Practical Guide*, 2 edn, Springer. 6

Ronneberger, O., Raffel, J. and Kompenhans, J. (1998). Advanced evalu-ation algorithms for standard and dual plane particle image velocimetry, *Proceedings of the 9th international sympo-sium on applications of laser techniques to fluid mechanics*. 21

Rosenfeld, M., Rambod, E. and Gharib, M. (1998). Circulation and formation number of laminar vortex rings, *J. Fluid Mech.* **376**: 297–318. 67

Roth, G. I. and Katz, J. (2001). Five techniques for increasing the speed and accuracy of PIV interrogation, *Meas. Sci. Technol.* **12**: 238–245. 20

Saffman, P. G. (1965). The lift on a small sphere in a slow shear flow, *J. Fluid Mech.* **22**: 385–400. 16

Saffman, P. G. (1970). The velocity of viscous vortex rings, *Stud. Appl. Math.* **49**: 371–380. 68

Saffman, P. G. (1978). The number of waves on unstable vortex rings, *J. Fluid Mech.* **84**(4): 625–639. 57, 59, 65, 69, 204

Saffman, P. G. (1992). *Vortex dynamics*, Cambridge University Press, chapter 13 The effects of viscosity. 157

Scarano, F. (2002). Iterative image deformation methods in PIV, *Meas. Sci. Technol.* **13**: R1–R19. 10, 24

Scarano, F., David, L., Bsibsi, M. and Calluaud, D. (2005). S-PIV comparative assessment: image dewarping+misalignment correction and pinhole+geometric back projection, *Exp. Fluids* **39**: 257–266. 22, 45, 46

Scarano, F. and Riethmuller, M. L. (2000). Advances in iterative multigrid PIV image processing, *Exp. Fluids* **Suppl.**: S51–S60. 24, 25

Schröder, A. and Willert, C. E. (2008). *Particle Image Velocimetry: New Developments and Recent Applications*, Springer. 6

Shadden, S., Dabiri, J. O. and Mardesn, J. E. (2006). Lagrangian analysis of fluid transport in empirical vortex flows, *J. Fluid Mech., Phys. Fluids* **18**: 047105.1–11. 74

Shariff, K. and Leonard, A. (1992). Vortex rings, *Ann. Rev. Fluid Mech.* **24**: 235–279. x, 63, 69, 80

Shariff, K., Verzicco, R. and Orlandi, P. (1994). A numerical study of three-dimensional vortex ring instabilities: viscous corrections and early nonlinear stage, *J. Fluid Mech.* **279**: 351–375. 70, 176, 191, 305

Shusser, M., , Gharib, M., Rosenfeld, M., and Mohseni, K. (2002). The effect of pipe boundary layer growth on the formation of a laminar vortex ring generated by a piston/cylinder arrangement, *Theoret. Comput. Fluid Dynamics* **15**: 303–316. 68

Shusser, M. and Gharib, M. (2000). Energy and velocity of a forming vortex ring, *Phys. Fluids* **12**(3): 618–621. 68

Shusser, M., Rosenfeld, M., Dabiri, J. O. and Gharib, M. (2006). Effect of time-dependent piston velocity program on vortex ring formation in a piston/cylinder arrangement, *Phys. Fluids* **18**: 033601.1–033601.6. 68

Sinha, S. K. and Kuhlman, P. S. (1992). Investigating the use of stereoscopic particle streak velocimetry for estimating the three-dimensional vorticity field, *Exp. Fluids* **12**: 377–384. 8, 13, 34

Skeen, A. (2006). *The development of high-speed PIV techniques and their application to jet noise measurement*, PhD thesis, University of Warwick. 6, 11, 15, 45, 114

Soloff, S. M., Adrian, R. J. and Liu, Z.-C. (1997). Distortion compensation for generalized stereoscopic particle image velocimetr, *Meas. Sci. Technol.* **8**: 1441–1454. 33, 34, 40, 45

Stanaway, S. K., Cantwell, B. J. and Spalart, P. R. (1988). A numerical study of viscous vortex rings using a spectral Method, *Technical Report 101041*, NASA. 59, 68

Stanislas, M., Okamoto, K., Kähler, C. J., Westerweel, J. and Scarano, F. (2008). Main results of the third international PIV Challenge, *Exp. Fluids* **45**(1): 27–71. 51

Tarasov, V. F. and Yakushev, V. I. (1973). Transport in a turbulent vortex ring, *Prikladnoi Mekhaniki i Teknicheskoi Fiziki* **1**: 130–136. 57, 66, 74

Taylor, G. I. (1921). Experiments with Rotating Fluids, *Proc. R. Soc. Lond. Ser. A* **100**(703): 114–121. 75

Taylor, G. I. (1922). The Motion of a Sphere in a Rotating Liquid, *Proc. R. Soc. Lond. Ser. A* **102**(715): 180–189. 83

Tomson, W. (1867). On vortex atoms, *Phil. Mag.* **34**(4): 15–24. 54

Tsai, R. (1987). A versatile camera calibration technique for high-accuracy 3D machine vision metrology using off-the-shelf TV cameras and lenses, *IEEE T. Robotic Autom.* **RA-3**(4): 323–344. 41, 43, 121

Vanyo, J. P. (1993). *Rotating Fluids in Engineering and Science*, Dover Publications. 162

Verzicco, R., Orlandi, P., Eisenga, A. H. M., van Heijst, G. J. F. and Carnevale, G. F. (1996). Dynamics of a vortex ring in a rotating fluid, *J. Fluid Mech.* **317**: 215–239. x, xi, xxv, 2, 60, 75, 76, 77, 78, 79, 80, 81, 82, 83, 84, 90, 164, 171, 172, 175, 227, 258, 260, 275, 299, 303, 304, 306, 308, 309, 310, 311, 312, 314, 315, 316, 317, 318, 322

Virk, D., Melander, M. V. and Hussain, F. (1994). Dynamics of a polarized vortex ring, *J. Fluid Mech.* **260**: 23–55. 80, 301, 305, 316, 317

Walpot, R. J. E., Rosielle, P. C. J. N. and van der Geld, C. W. M. (2006). Design of a set-up for high-accuracy 3D PTV measurements in turbulent pipe flow, *Meas. Sci. Technol.* **17**: 3015–3026. 13

Weigand, A. and Gharib, M. (1994). On the decay of a turbulent vortex ring, *Phys. Fluids* **6**(12): 3806–3809. 71, 74, 304

Wereley, S. T. and Meinhart, C. D. (2001). Second-order accurate particle image velocimetry, *Exp. Fluids* **31**: 258–268. 11, 23

Westerweel, J. (1994). Efficient detection of spurious vectors in particle image velocimetry data sets., *Exp. Fluids* **16**: 236–247. 25, 28, 29

Westerweel, J. (1997). Fundamentals of digital particle image velocimetry, *Meas. Sci. Technol.* **8**: 1379–1392. ix, 14, 15, 21

Westerweel, J., Dabiri, D. and Gharib, M. (1997). The effect of a discrete window offset on the accuracy of cross-correlation analysis of digital PIV recordings, *Exp. Fluids* **23**: 20–28. 23

Westerweel, J. and Scarano, F. (2005). Universal outlier detection for PIV data, *Exp. Fluids* **39**: 1096–1100. 30

Widnall, S. E. and Sullivan, J. P. (1973). On the Stability of Vortex Rings, *Proc. R. Soc. Lond. Ser. A* **332**: 335–353. 61, 69

Widnall, S. E. and Tsai, C. Y. (1977). The instability of the thin vortex ring of constant vorticity, *Proc. R. Soc. Lond. Ser. A* **287**(1344): 273–305. 69

Wieneke, B. (2005). Stereo-PIV using self-calibration on particle images, *Exp. Fluids* **39**: 267–280. 41, 46, 47, 49, 53

Wieneke, B. (2008). Volume self-calibration for 3D particle image velocimetry, *Exp. Fluids* **45**(4): 549–556. 49

Willert, C. (1997). Stereoscopic digital particle image velocimetry for application in wind tunnel flows, *Meas. Sci. Technol.* **8**: 1465–1479. 38, 45, 46

Willert, C. (2006). Assessment of camera models for use in planar velocimetry calibration, *Exp. Fluids* **41**: 135–143. 41

Willert, C. and Gharib, M. (1991). Digital particle image velocimetry, *Exp. Fluids* **10**: 181–193. 10, 19

Wray, A. A. and Hunt, J. C. R. (1988). Algorithms for classification of turbulent

structures, *in* H. K. Moffatt and A. Tsinober (eds), *Topological fluid mechanics*, Cambridge University Press. 70

Zang, W. and Prasad, A. K. (1997). Performance evaluation of a Scheimpflug stereocamera for particle image velocimetry, *Appl. Opt.* **36**: 8738–8744. 33, 34

APPENDIX A

Journal publications

Decay of vortex rings in a rotating fluid

M.A. Brend and P.J. Thomas

Fluid Dynamics Research Centre, School of Engineering,

University of Warwick, Coventry CV4 7AL, United Kingdom

(Dated: March 20, 2009)

Abstract

Vortex rings propagating through a rotating fluid, along the axis of rotation, are studied experimentally. The length, x_d, travelled by the rings until they have completely decayed is measured. In agreement with theoretical arguments based on the Taylor-Proudman theorem it is observed that the value of x_d decreases with decreasing Rossby number, Ro. For the parameter range investigated here we determine an overall, global trend for the scaling of the mean decay length that can be roughly summarized by the expression $\overline{(x_d/D)} = 4.77Ro^{1.06}$, where D is the diameter of the generator nozzle used to produce the vortex rings.

Keywords: Rotating Flow, Vortex Dynamics, Vortex Rings, Vortex Stability

A. Introduction

Vortices are the basic dynamical structures governing fluid flows. Vortex rings represent one geometrically simple type of vortex that is often employed to study aspects of vortex dynamics - for review articles see Shariff and Leonard[1] or Lim and Nickels[2]. Here we investigate a new fundamental problem associated with the dynamics of vortex rings for the first time. The issue dealt with concerns how background system rotation affects the stability of a vortex ring.

Rotating flows are ubiquitous in science and technology. In rotating flow Coriolis forces give rise to phenomena absent in non-rotating flows[3–5]. These phenomena can appear counter intuitive to anyone not familiar with the theoretical background of rotating flows. One example is, for instance, the Taylor-Proudman theorem derived from the geostrophic approximation of the full momentum equation[4,5].

Briefly, the Taylor-Proudman theorem states that when a fluid rotates with a rotational velocity $\vec{\Omega}$ that is aligned with the $z-$axis of a Cartesian coordinate system, and if geostrophy applies, then the effect of Coriolis forces is such that the derivatives $\partial u/\partial z$ and $\partial v/\partial z$ of the velocity components u and v in the x and y coordinate directions are identically zero. Here we study vortex rings propagating with velocity $\vec{U}$ in a fluid rotating with rotational velocity $\vec{\Omega}$, as illustrated in Fig. 1. When $\vec{U}$ is parallel to $\vec{\Omega}$ and when geostrophy applies one thus anticipates on the basis of the Taylor-Proudman theorem that background rotation will tend to promote the destruction of the ring.

For the Taylor-Proudman theorem to be applicable Coriolis effects must dominate inertial effects, i.e. the Rossby number must be sufficiently low. For a general flow geometry as in Fig. 1 vortices can, in principle, be generated under conditions that violate this requirement. However, viscous effects result in losses of inertia and, thereby, the vortex rings approach the parameter regime where the Taylor-Proudman theorem holds. Therefore, it is expected that the decay of vortex rings will, ultimately, be accelerated even when a vortex ring is generated with high inertia.

One further anticipates that effects of rotation will become stronger as Coriolis effects become increasingly dominant. Hence, one expects that the average length that a vortex ring can travel before it has decayed entirely will decrease with decreasing Rossby number. The arguments leading up to the qualitative conclusion that background rotation will tend to promote the decay of vortex rings are relatively straightforward. However, obviously there

exist no simple arguments to establish how the mean decay length will decrease with the Rossby number. There exist no previous studies that have investigated this fundamental question. The main motivation for the present experiments was to determine a statistical expression that relates the mean decay length of a vortex ring in a rotating fluid to its associated Rossby number.

It is no coincidence that no previous studies exist that investigated the decay of vortex rings propagating through a rotating fluid as in Fig. 1. Such experiments require a very high water-filled rotating-tank together with a suitable vortex-ring generator mounted within the rotating frame of reference. This type of large-scale facility was not available anywhere in the past. There appears to exist only one single previous study, by Verzicco et al.[6], for which experiments investigating vortex rings moving through a rotating fluid in the sense of Fig. 1 were conducted. However, for this study only a comparatively small tank with a height of 1 m was available. The main focus of Verzicco et al.[6] was to verify computational results primarily concerned with the velocity field and the vorticity distribution associated with the vortex ring.

B. Experimental set-up and techniques

We developed a new, unique large-scale experimental facility described here for the first time and the experimental results discussed are the first obtained with the new rig. Figure 2 displays a technical drawing of the new facility. The set up constitutes a large water-filled tank, mounted on top of a computer controlled rotating turntable. The tank is 2.5 m high and it has an octagonal horizontal cross section with a cross width of 1 m. The overall height of the facility, from the floor to the top of the support structure, is over 5.7 m. Vortex rings are generated using a standard technique[7,8] where a computer-controlled piston ejects water from a circular nozzle such that a vortex ring forms at the nozzle exit.

Two alternative nozzles with diameters $D = 50$ mm and 10 mm were used. The vortex-generator nozzle is mounted rigidly at the top of the rotating tank. This means that the nozzle is stationary with respect to the water inside the rotating tank once the water has adopted a state of rigid-body rotation following an initial spin-up phase. Hence, when the piston pushes water out of the nozzle there exists no circumferential shear on the ring as would be the case if the nozzle itself was stationary and only the tank with the fluid was rotating. The vortex rings are ejected vertically downwards into the water contained inside

the tank. The temperature of the water was in the range $10 - 15^{\circ}$ C such that its kinematic viscosity is $\nu \approx 1.30 \times 10^{-6}$ m^2 s^{-1}.

The results summarized here were obtained from flow visualizations. The vortex rings were visualized by means of releasing a small amount of neutrally buoyant food colouring through a narrow annular gap on the inside of the nozzle near its exit. Dye was supplied to the gap from a reservoir by a peristaltic pump through a system of thin pipes and tubes contained within the walls of the vortex-ring generator-nozzle unit.

A Rossby number is defined as $Ro = U_M/\Omega D$. The velocity $U_M = x_d/t_d$ is the mean speed of the vortex rings where x_d represents the decay length. This length is the distance the ring travels away from the nozzle exit until it no longer represents a well-defined, coherent structure and t_d is the time interval between the formation of the ring and its decay. The definition of the decay length may appear somewhat qualitative but practice has shown that it is in fact fairly straightforward to judge when a ring has completely decayed. However, the goal is to determine an expression for the overall global trend regarding how rotation affects the vortex-ring decay. The distribution of the data to be presented below will reveal that the above definition of the decay length is sufficient for this purpose. For the experiments summarized here the Rossby number covered approximately the interval $0.1 \leq Ro \leq 25$. We further define a Reynolds number $Re = DU/\nu$. The Reynolds number covers values $40 \leq Re \leq 5300$ when U is identified with U_M or $385 \leq Re \leq 19230$ if, alternatively, based on the mean ejection speed of the fluid at the nozzle, as done by Maxworthy[8].

C. Experimental results

Figure 3 displays the non-dimensional decay length, x_d/D, as a function of the Rossby number, Ro. The figure contains almost 520 data points. The results include data points for which $\vec{\Omega}$ and $\vec{U}$ were anti parallel, as sketched in Fig. 1, as well as data for which both vectors had the same orientation. Figure 3 reveals that the vortex rings can typically travel rather large distances of $x_d/D = 50$ at $Ro = 10$ where the effects of background rotation are comparatively weak. Note, for instance, that this value corresponds to $x_d = 2.5$ m for the nozzle with diameter $D = 50$ mm. However, for $Ro = 0.1$, i.e. when effects of rotation are strong, we observed that the rings undergo a rapid and violent destruction process. Here the decay length is reduced to about $x_d/D = 0.4$, as revealed by Fig. 3. Now x_d is only 20 mm for the nozzle with $D = 50$ mm. Hence, the experimental data show that background

rotation does lead to a substantially advanced decay of the vortex rings.

In order to obtain a quantitative expression approximating the overall trend of the dependence of the decay length on the Rossby number the data in Fig. 3 have been interpolated. The solid line in Fig. 3 represents a least-squares fit of type $y = kx + c$ in coordinates $y = ln(x_d/D)$ and $x = ln(Ro)$ with values of $k = 1.06$ and $c = 1.56$ implying that the mean decay length is

$$\overline{(x_d/D)} = 4.77 Ro^{1.06} \quad . \tag{1}$$

To quantify the errors associated with the least-squares fit we calculated the mean deviation of the data points from Eq. (1). To this end the values $\Delta^i = |ln((x_d/D)_i^{exp}) - ln(\overline{(x_d/D)})|$ for all of the i experimental data points, $(x_d/D)_i^{exp}$, were determined and then averaged; this yielded $\overline{\Delta} = 0.38 \pm 0.26$. Thus, the average separation of the data points from the mean is $ln((x_d/D)^{\pm}) = ln(Ro^{1.06}) + (1.56 \pm 0.38)$. This implies that the data points with an average deviation above Eq. (1) are located at $(x_d/D)^+ = 6.96 Ro^{1.06}$ while those with an average deviation below Eq. (1) are located at $(x_d/D)^- = 3.25 Ro^{1.06}$ (see Fig. 3).

The increase of $\overline{(x_d/D)} \propto Ro^{1.06}$ means that the decay length increases, on average, approximately linearly with the Rossby number within the Rossby and Reynolds number regimes considered here. To obtain a convenient rule of thumb one can round the factor and the exponent in Eq. 1 to give $\overline{(x_d/D)}_{rd} \approx 5Ro$ Possibly of more practical interest is the maximum length a vortex ring can travel before it has entirely decayed. This maximum decay length is identified approximately by the dashed line in Fig. 3 given by $(x_d/D)^{max} = 10 Ro^{1.06}$ such that, rounded, $(x_d/D)^{max} \approx 10Ro$ Similarly one can estimate a minimum decay length. This is identified approximately by the dotted line in Fig. 3 given by $(x_d/D)^{min} = 1.5 Ro^{1.06}$ or, rounded, $(x_d/D)^{min} \approx 1.5Ro$

It is emphasized that the least-squares fit of Eq. (1) interpolating the data (solid line) in Fig. 3 is not intended to imply the existence of a genuine power-law scaling. The interpolation procedure simply averages the data to yield a statistical, quantitative expression for the overall global trend within the parameter regimes considered. It is by no means certain that the data in the figure do collapse onto a single straight line. In fact the overall data distribution in Fig. 3 suggests, as one might expect, that the data level off for $Ro \to 0$ and $Ro \to \infty$. Nevertheless, note that the data fit in Fig. 3 extends over approximately two

orders of magnitude in each of the two coordinate directions.

The scatter of the data in Fig. 3 is also quite large. However, there are many reasons that can help explaining the magnitude of the data scatter. We typically waited $10-20$ minutes between two successive experiments to ensure that the fluid in the tank had re-adopted solid-body rotation prior to ejecting the next vortex ring. However, we cannot exclude the possibility that, in some cases, there may still have been some residual fluid motion in the tank. This would evidently be detrimental to the vortex-ring stability implying an increased likelihood for a premature decay of the vortex ring. Furthermore, due to the nature of the problem it is evidently impossible to define a quantifiable, unique criterion that characterizes when a ring has completely decayed. Judging this necessarily involves a degree of uncertainty that cannot be resolved even if sophisticated measurement techniques, such as Particle-Image Velocimetry (PIV), were used. Finally, Fig. 3 does not resolve any potentially existing Reynolds-number effects. All discussed errors are likely to tend to result in under estimates for the decay length. However, the large number of data points contained in Fig. 3 ensures that, within the Rossby and Reynolds number regimes considered, Eq. (1) should represent a robust statistical expressions for the overall global trend for the mean decay length with associated mean deviations and estimated maximum and minimum decay lengths as discussed above.

D. Discussion and conclusion

We include with a brief comment concerning the possible physical mechanism that results in the reduced decay length of vortex rings in rotating fluids. Our observations have revealed the existence of a strong secondary Coriolis-induced cyclonic swirling flow behind the rings. The existence of the wake swirl can be inferred in Fig 4 from the helical dye streakline identified in the photo and it has previously been briefly commented on in Verzicco et al.[6]. The necessity for the existence of this cyclonic wake swirl follows from considering the local flow field around the core of the vortex ring as identified by the dotted lines with superposed arrow heads in Fig 4. The ring propagates with velocity $\vec{U}$ downwards. Just upstream behind the ring the local flow velocity, $\vec{v}$, of the fluid swirling around the vortex-ring core is directed inwards, i.e. towards the axis of symmetry as indicated in Fig. 4. The vector of the rotational velocity, $\vec{\Omega}$, points upwards, i.e. it points in the opposite direction of $\vec{U}$ (compare Fig. 1). The Coriolis force associated with the local flow velocity, $\vec{v}$, is

given by $F_C = -2\vec{\Omega} \times \vec{v}$. Hence, Coriolis forces are oriented such that $\vec{\Omega}$ and $\vec{v}$ induce a wake swirl that has the same sense of rotation as the turntable. Thus, in agreement with the observations the wake swirl is expected to be cyclonic. For reasons analogous to those establishing the cyclonic wake swirl there must exist a Coriolis-induced anticyclonic swirl ahead of the rings. The cyclonic wake swirl together with the anticyclonic swirl ahead of the rings will result in strong net torsional shear forces acting on the vortex rings in the horizontal $x - y$ plane. It can be anticipated that this torsional shear will be detrimental to the stability of the vortex rings. The intensity of the swirling flows increases with the rotation rate $\vec{\Omega}$. Hence, the torsional shear forces increase with, $\vec{\Omega}$ and, thus, with decreasing Rossby number. It appears plausible to conclude that the torsional shear represents one of the main physical mechanism advancing the vortex-ring decay. Verzicco et al.[6] remark (see p. 229 and p. 232) that the anitcyclone ahead of the ring is associated with a high-pressure region while the cyclone at its rear results in a low-pressure region. They observed that the high pressure ahead of the ring establishes a strong depression at its front. This may result in further detrimental effects as regards the stability of the vortex ring. However, in order to determine the consequences of the ring distortion and the exact effects of the torsional shear, with the ultimate goal to establish the details of the overall decay process of the rings, it is evidently required to perform detailed PIV measurements, computational studies and a theoretical stability analysis in the future.

In conclusion we emphasize once again that the interpolation of the data in Fig. 3 is not intended to suggest the existence of a genuine power-law scaling with its associated implications. The data interpolation of power-law type in the figure simply averages the data to yield a quantitative expression that roughly summarizes the overall global trend. This trend undoubtedly exists for Fig. 3 where the data extend over more than two orders of magnitude in both coordinate directions. Despite the fact that a proper power-law scaling may not exist an interpolation of the data by means of a power-law function nevertheless remains a valid averaging technique to reveal a mean statistical trend. For the data in Fig. 3 the interpolation of the data has yielded a result that can be of practical use to obtain rough estimates of the minimum, the mean and the maximum distances that nozzle-generated vortex rings can propagate through the rotating fluid before they have completely decayed. This represents an entirely new result. However, the expressions stated should not

be used to draw any further reaching inferences.

---

[1] K. Shariff and A. Leonard, "Vortex rings," *Ann. Rev. Fluid Mech.* **24**, 235 (1992).

[2] T. T. Lim and T. B. Nickels, "Vortex rings," in *Fluid Vortices*, edited by S. I. Green (Kluwer Academic Publishers, Dordrecht, The Netherlands, 1995), pp. 95–153.

[3] J. P. Vanyo, *Rotating Fluids in Engineering and Science* (Dover Publications, Mineola, New York, USA, 1993).

[4] B. Cushman-Roisin, *Introduction to Geophysical Fluid Dynamics* (Prentice-Hall, Englewood Cliffs, New Jersey, USA, 1994).

[5] H. P. Greenspan, *The Theory of Rotating Fluids* (Cambridge University Press, Cambridge, UK, 1968).

[6] R. Verzicco, P. Orlandi, A. H. M. Eisenga, G. J. F. vanHeijst, and G. F. Carnevale, "Dynamics of a vortex ring in a rotating fluid," *J. Fluid Mech.* **317**, 215 (1996).

[7] C.-H. Krutzsch, "Ueber eine experimentell beobachtete erscheinung an wirbelringen bei ihrer translatorischen bewegung in wirklichen fluessigkeiten," *Ann. Phys.* **35**, 497 (1939).

[8] T. Maxworthy, "Some experimental studies of vortex rings," *J. Fluid Mech.* **81**, 465 (1977).

Figures

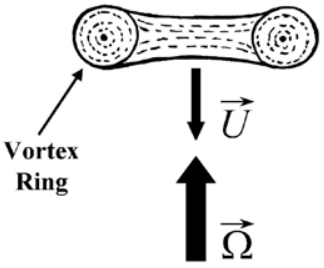

FIG. 1: Sketch illustrating the flow geometry.

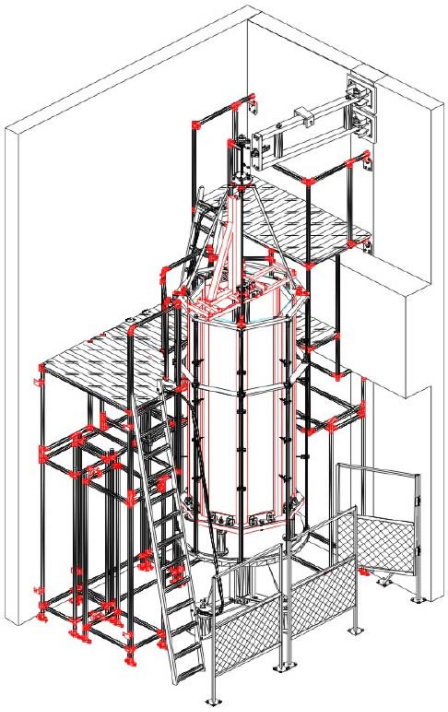

FIG. 2: Technical drawing of the large-scale rotating tank facility. Ladder and scaffolding provide access to the top of the rig where the generator nozzle for the vortex rings is mounted.

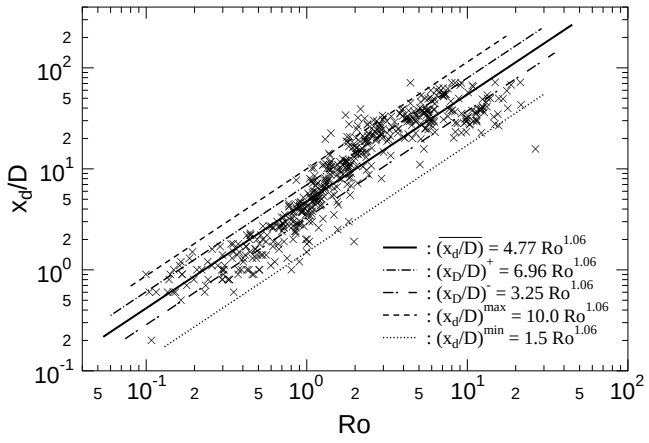

FIG. 3: Vortex-ring decay length, x_d, as a function of the Rossby number, Ro.

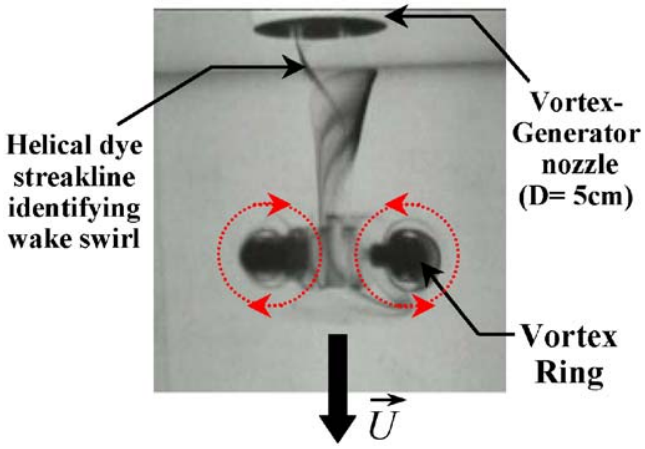

FIG. 4: Photograph of vortex ring propagating in rotating system.

APPENDIX B

Vortex ring trajectory, statistics

B.1 Condition B

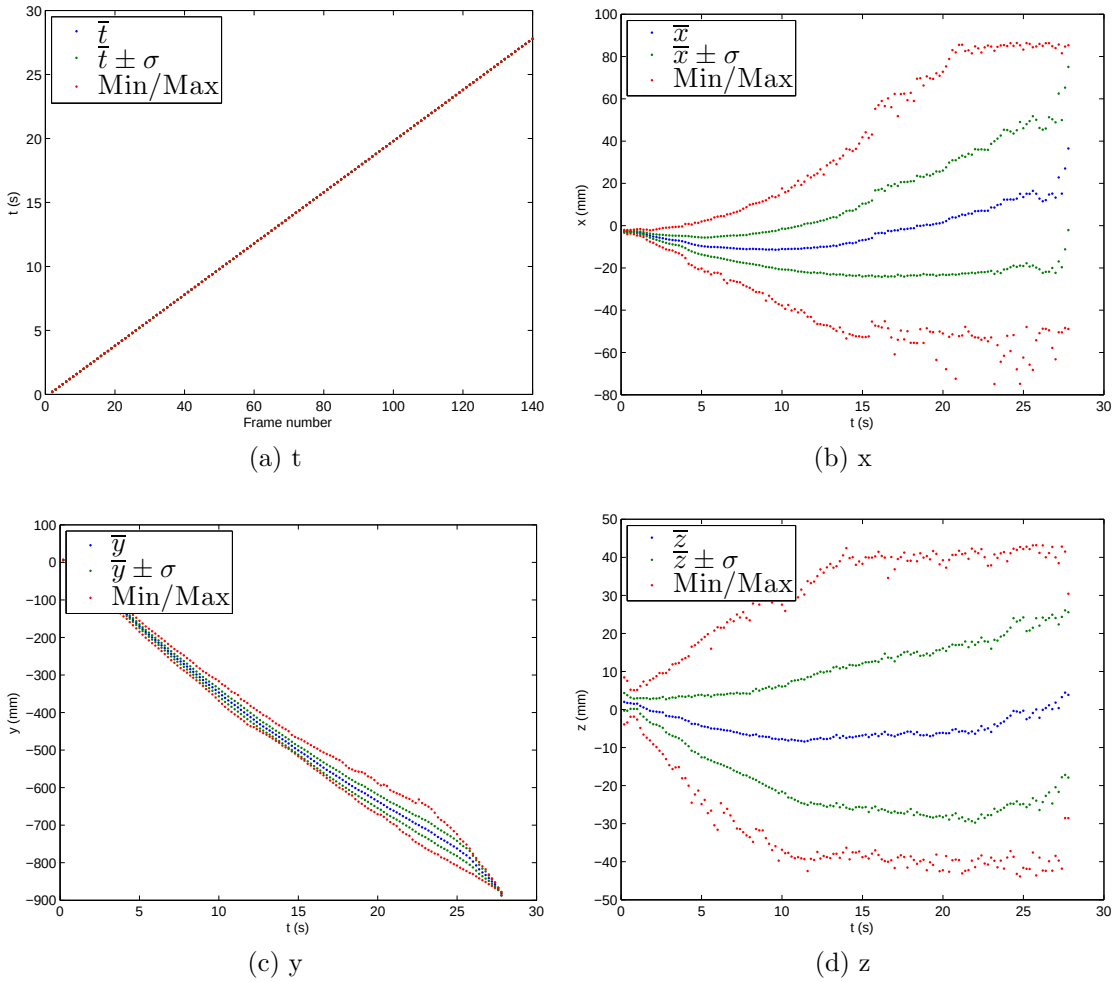

(a) t (b) x

(c) y (d) z

Figure B.1: Statistical vortex ring properties for condition B

B.2 Condition C

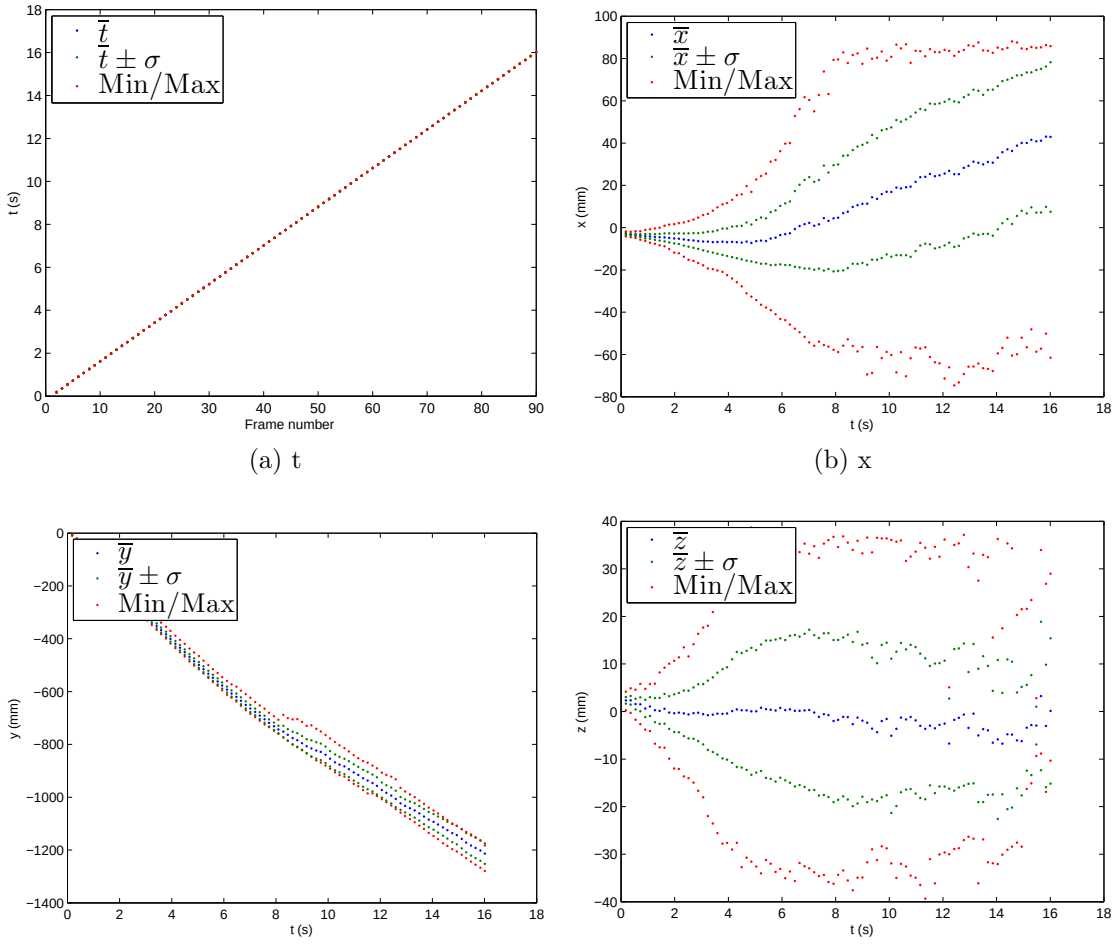

(a) t (b) x

(c) y (d) z

Figure B.2: Statistical vortex ring properties for condition C

B.3 Condition E

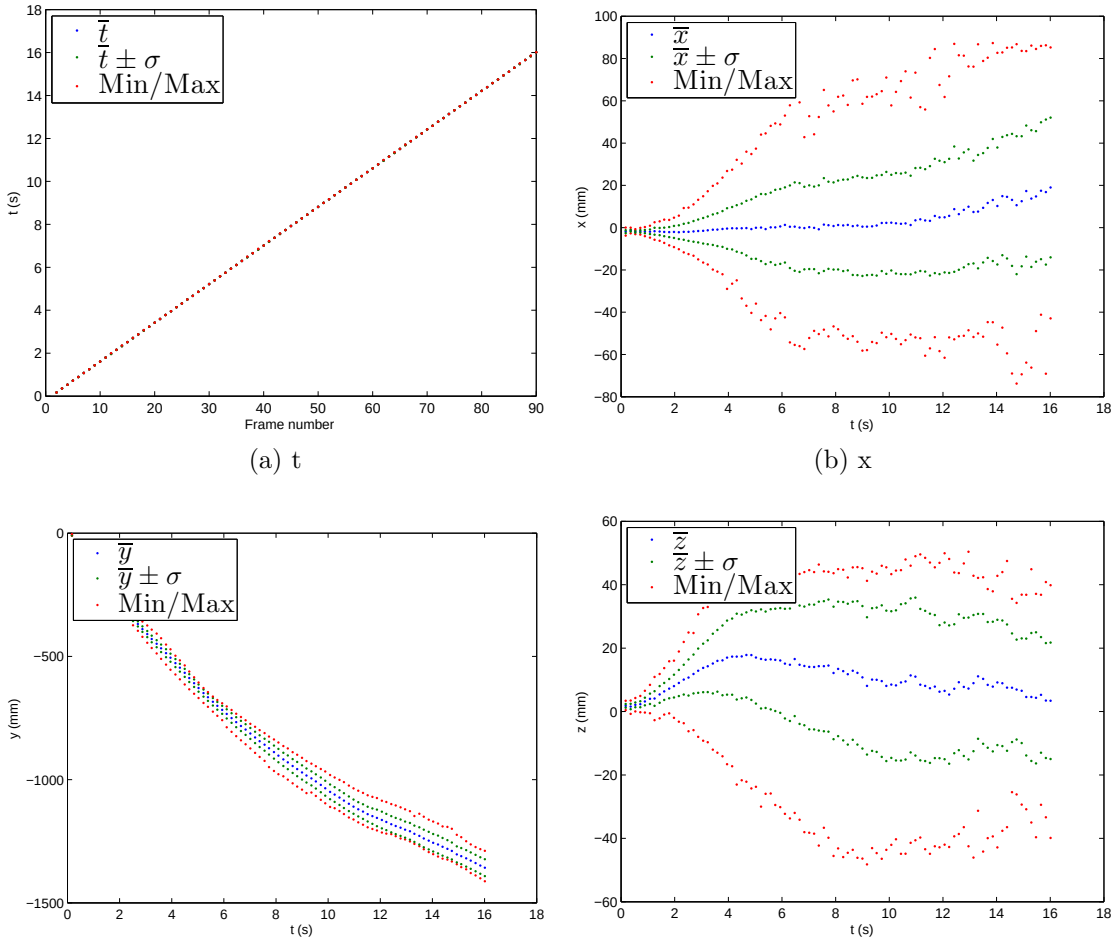

(a) t (b) x

(c) y (d) z

Figure B.3: Statistical vortex ring properties for condition E

B.4 Condition F

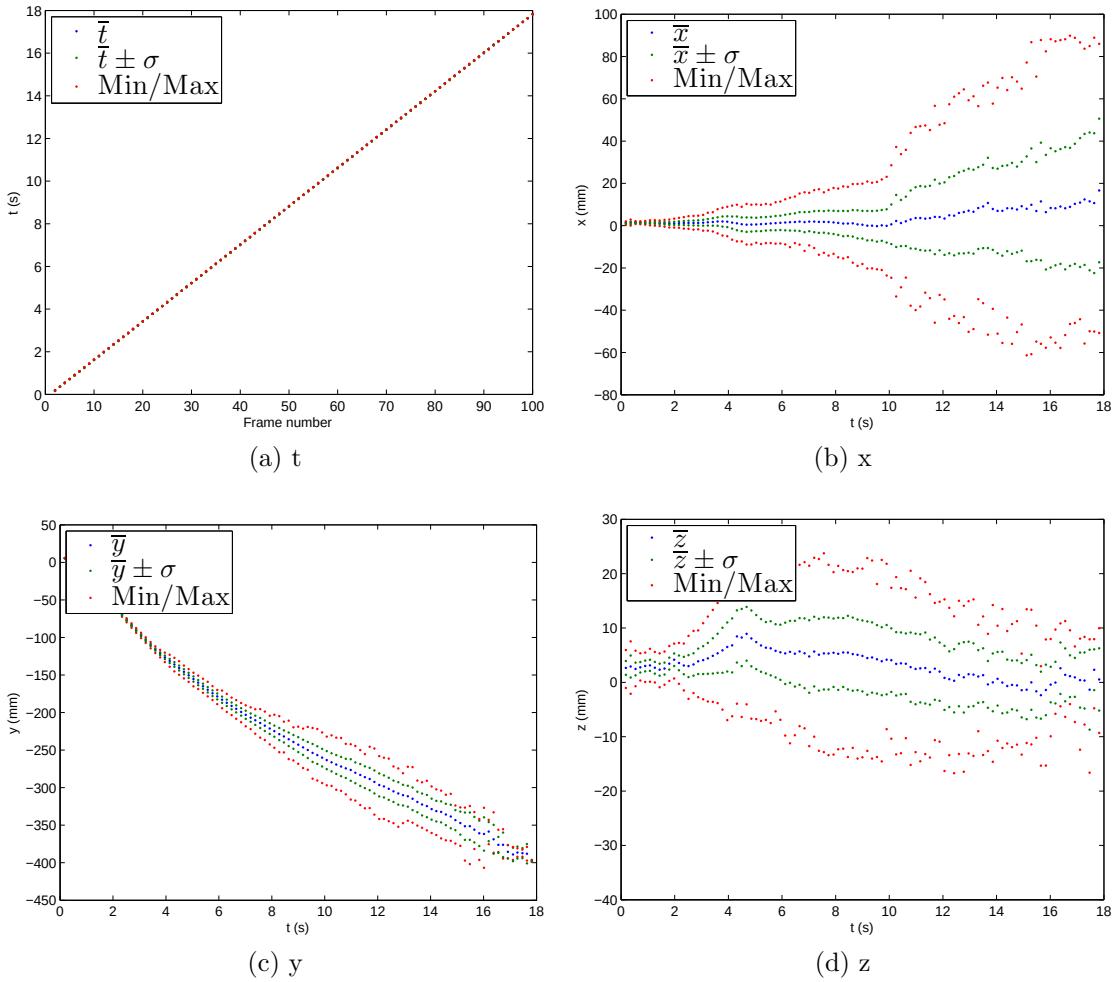

(a) t (b) x

(c) y (d) z

Figure B.4: Statistical vortex ring properties for condition F

B.5 Condition G

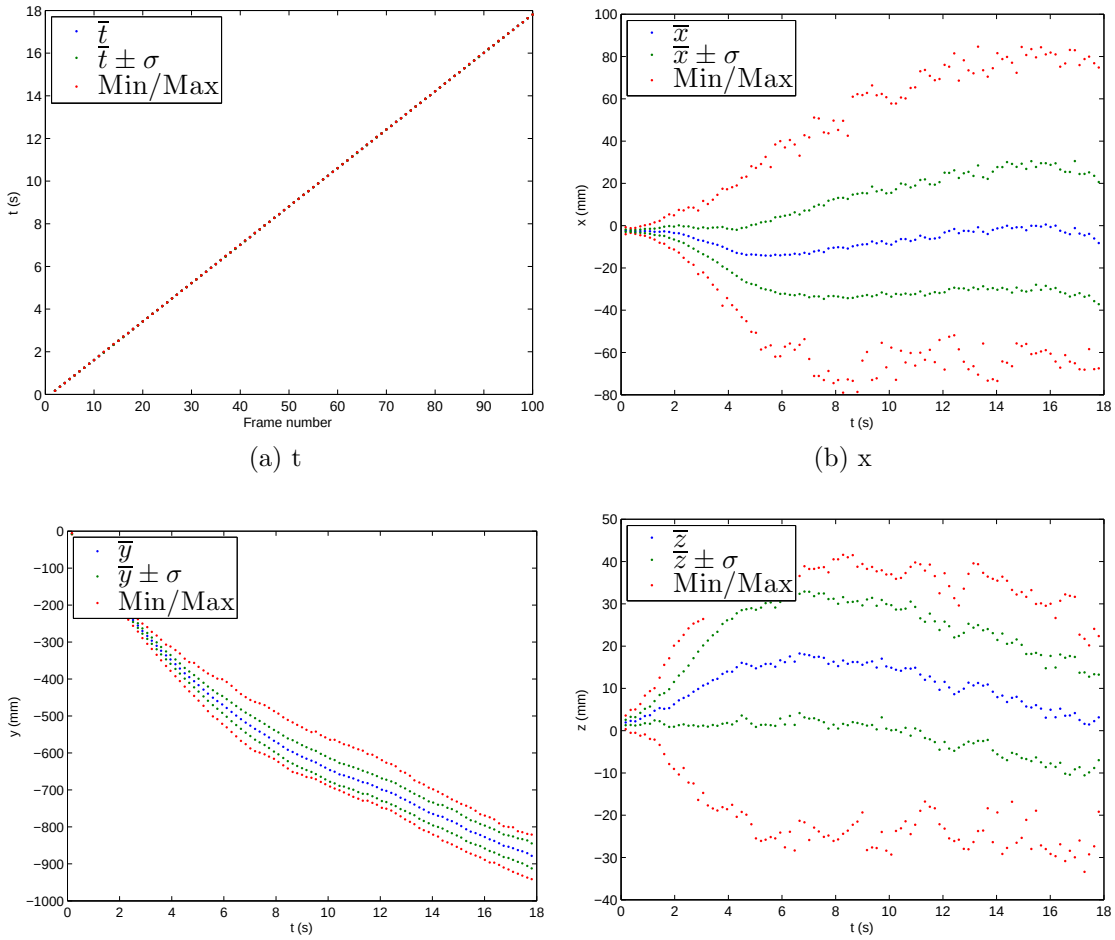

(a) t (b) x

(c) y (d) z

Figure B.5: Statistical vortex ring properties for condition G

B.6 Condition H

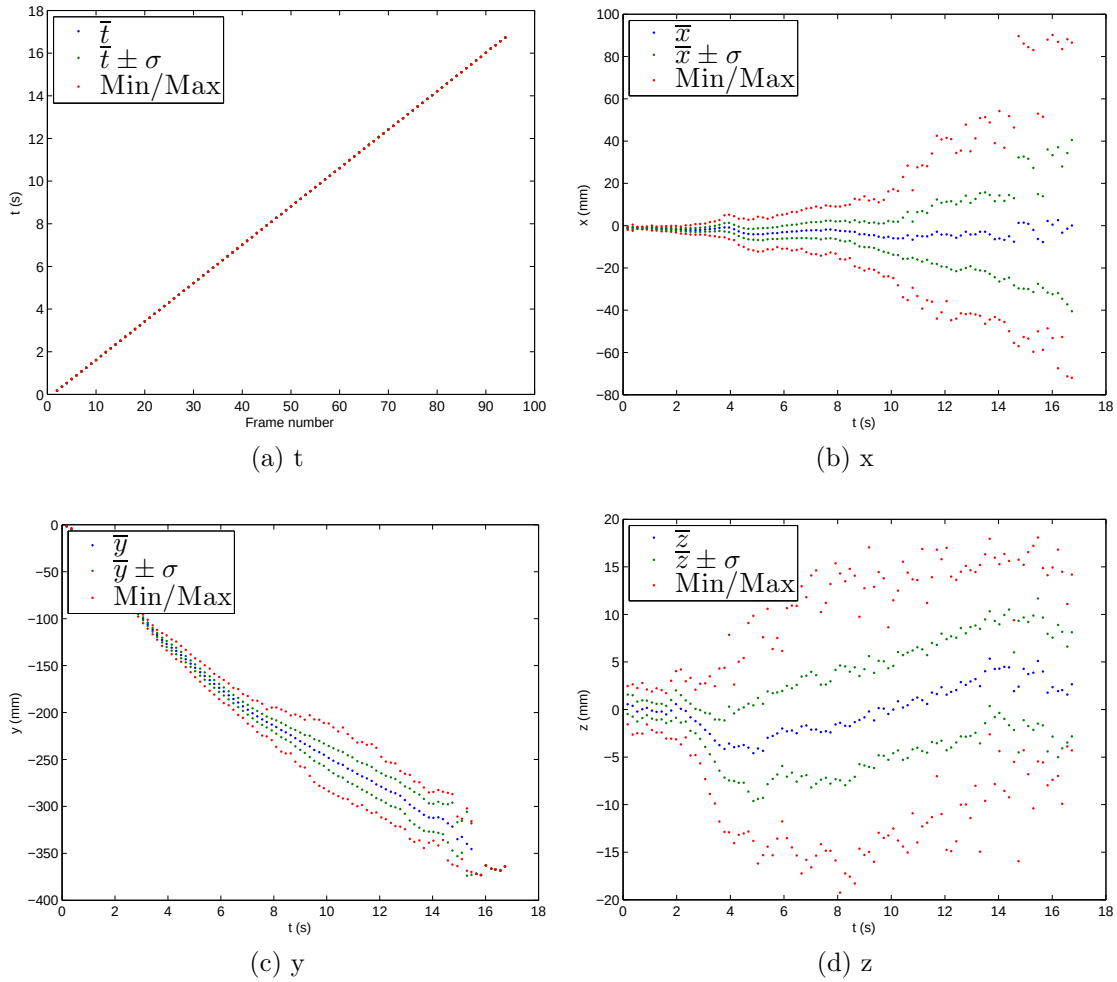

(a) t (b) x

(c) y (d) z

Figure B.6: Statistical vortex ring properties for condition H

B.7 Condition I

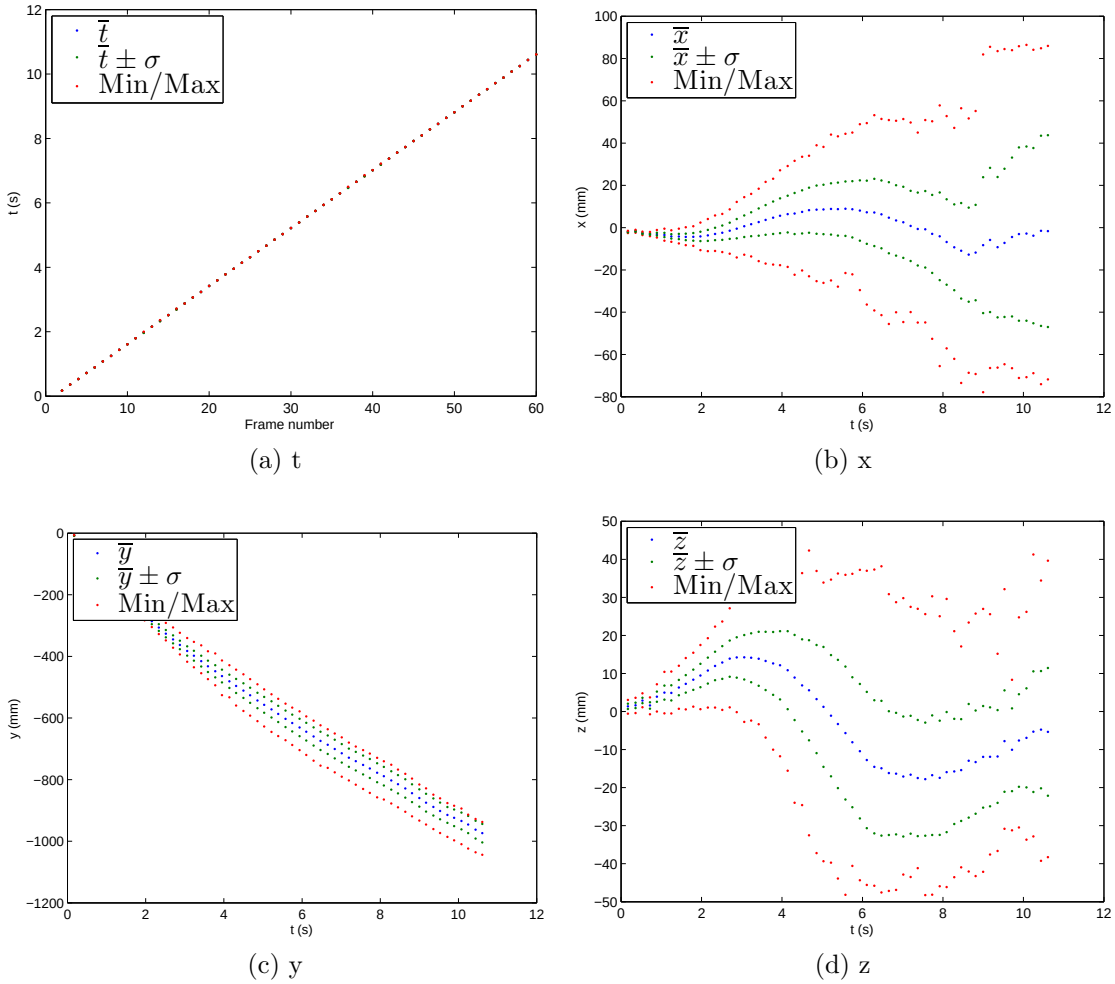

(a) t (b) x

(c) y (d) z

Figure B.7: Statistical vortex ring properties for condition I

B.8 Condition J

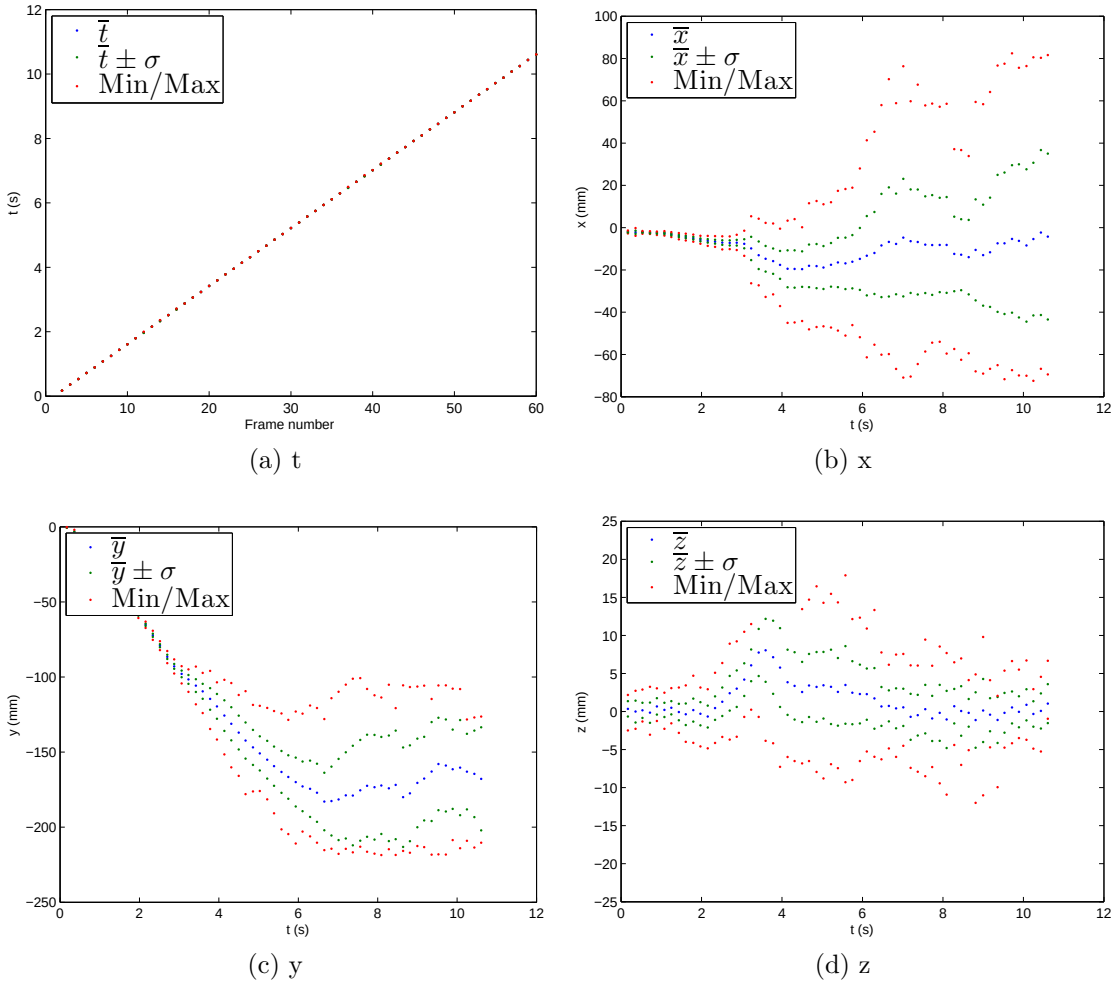

(a) t (b) x

(c) y (d) z

Figure B.8: Statistical vortex ring properties for condition J

B.9 Condition K

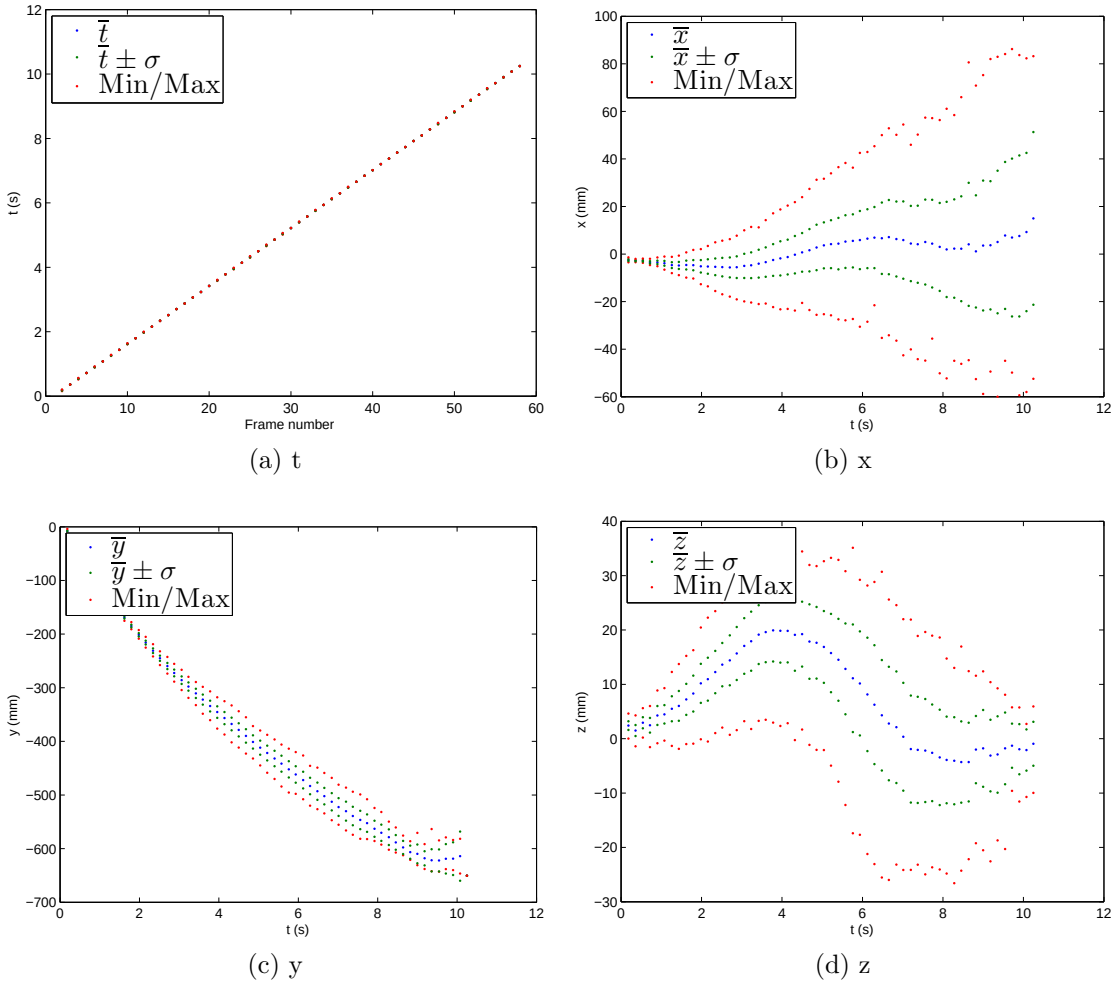

(a) t (b) x

(c) y (d) z

Figure B.9: Statistical vortex ring properties for condition K

APPENDIX C

Error plots

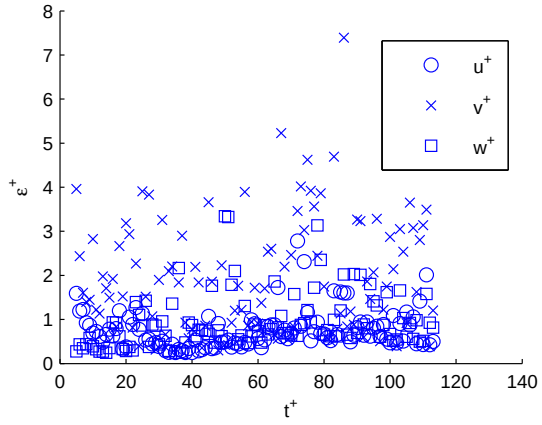

(a) Velocity

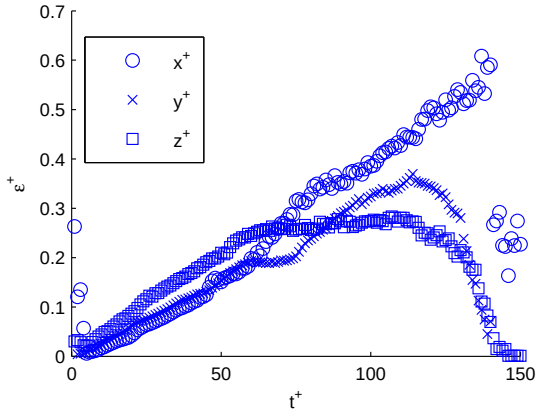

(b) Position

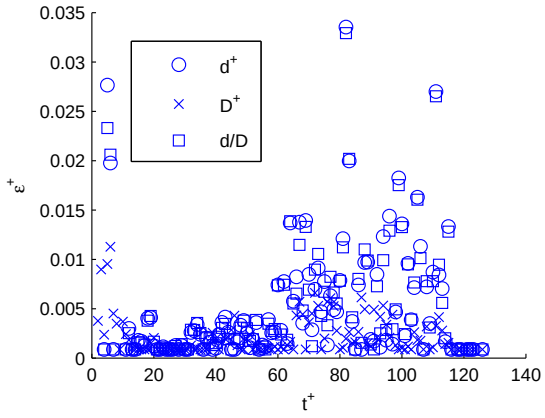

(c) Core/ring diameter

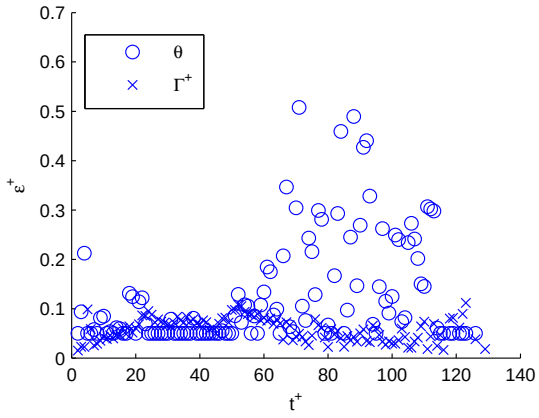

(d) Circulation and tilt

Figure C.1: Condition B

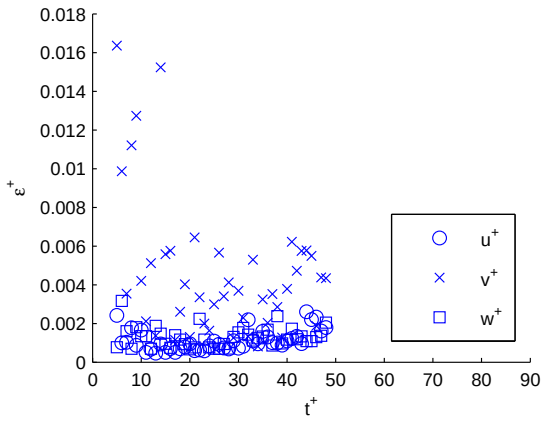

(a) Velocity

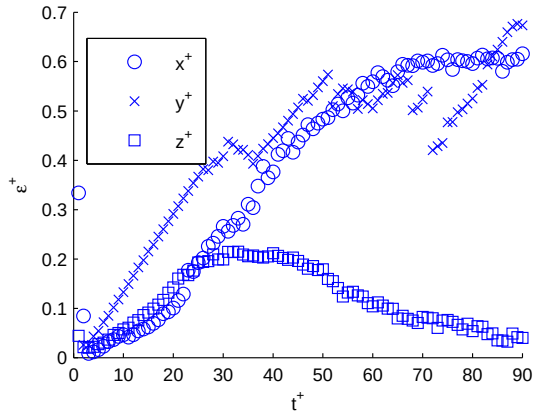

(b) Position

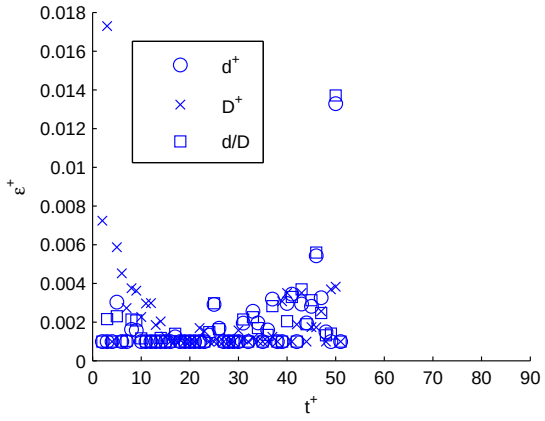

(c) Core/ring diameter

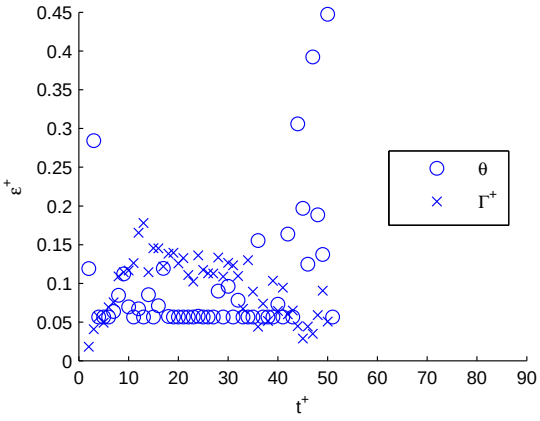

(d) Circulation and tilt

Figure C.2: Condition C

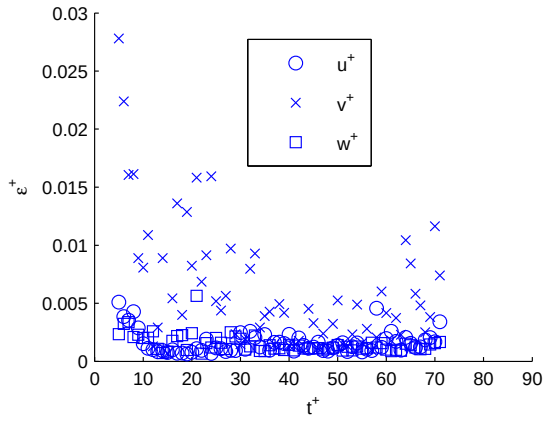

(a) Velocity

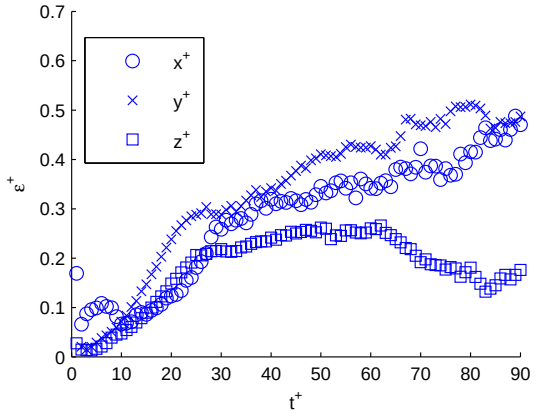

(b) Position

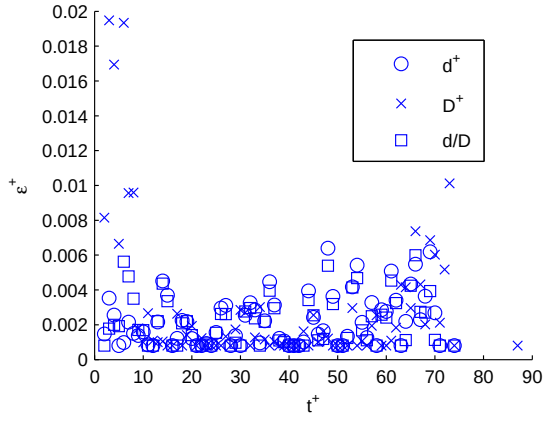

(c) Core/ring diameter

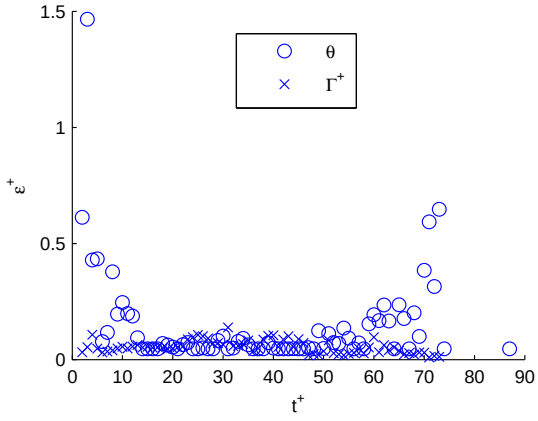

(d) Circulation and tilt

Figure C.3: Condition E

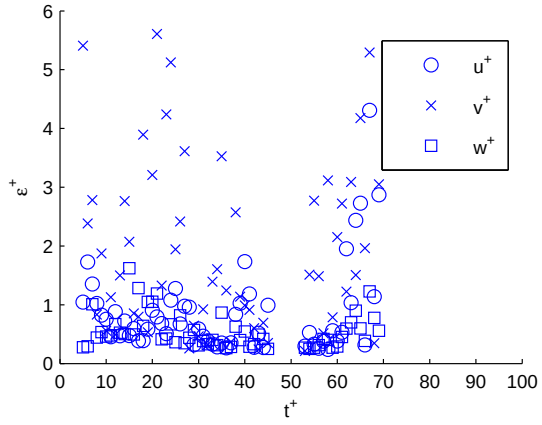

(a) Velocity

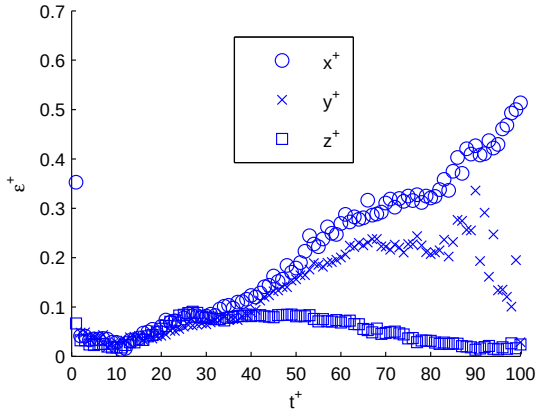

(b) Position

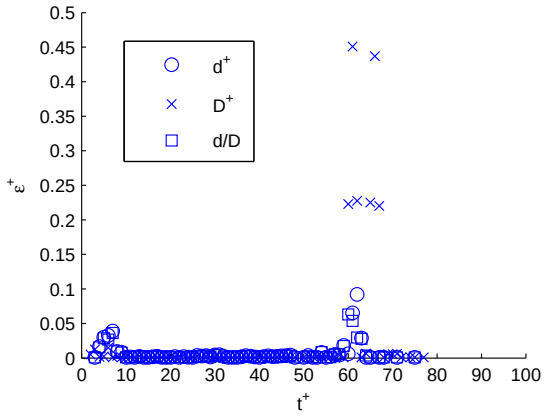

(c) Core/ring diameter

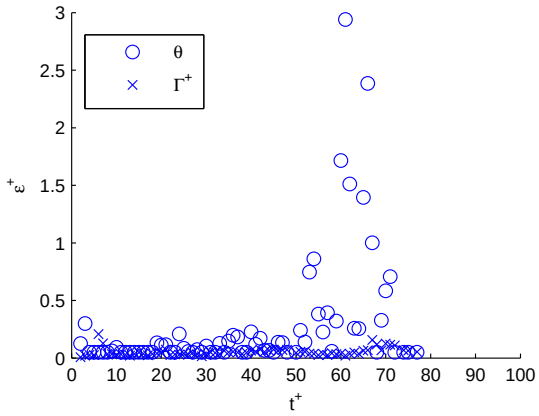

(d) Circulation and tilt

Figure C.4: Condition F

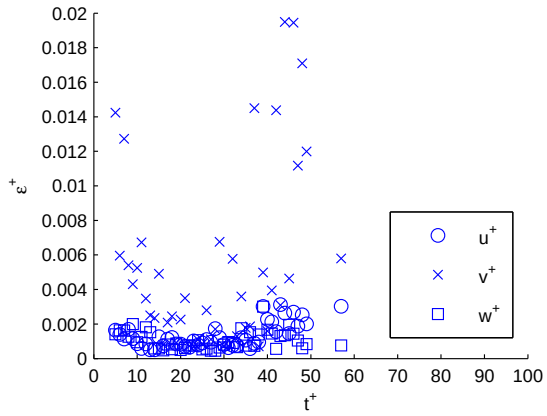

(a) Velocity

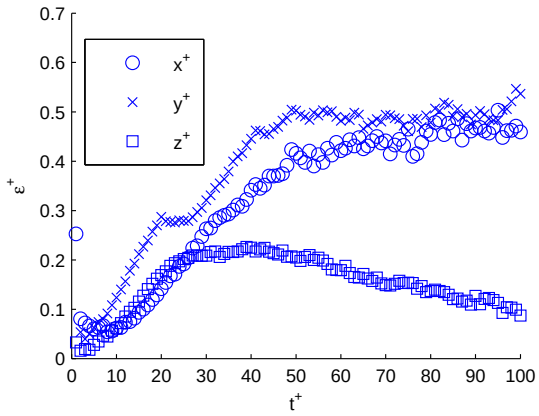

(b) Position

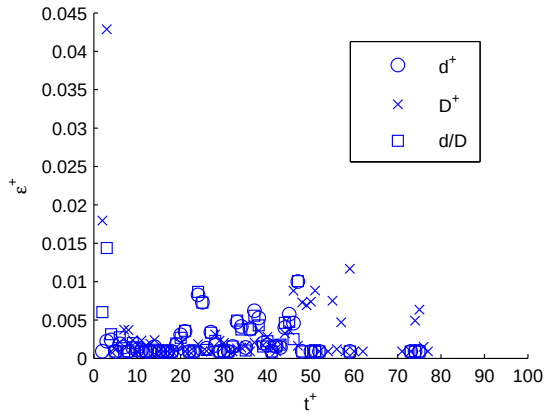

(c) Core/ring diameter

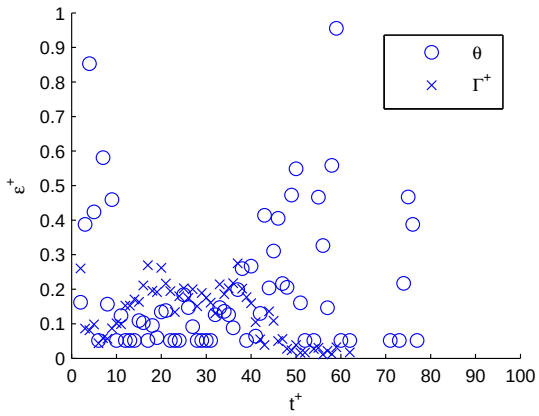

(d) Circulation and tilt

Figure C.5: Condition G

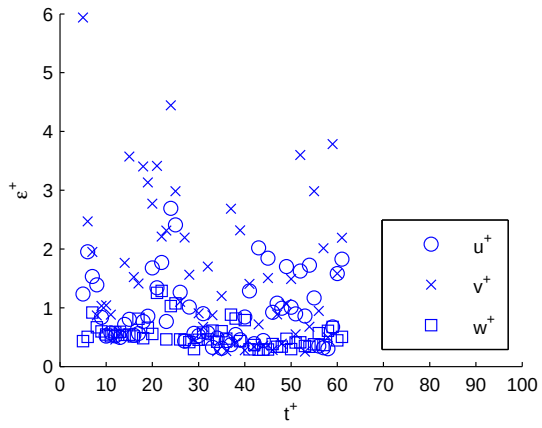

(a) Velocity

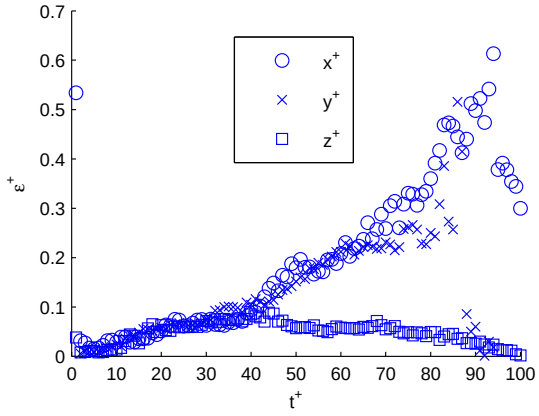

(b) Position

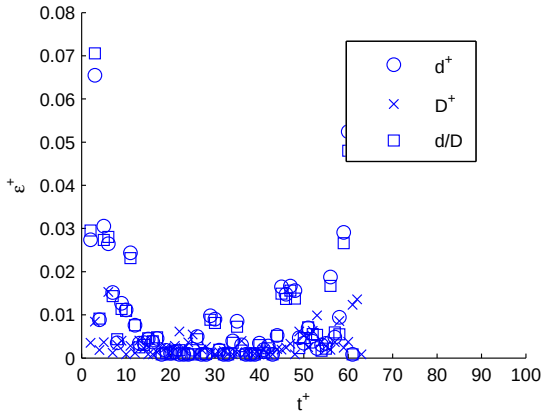

(c) Core/ring diameter

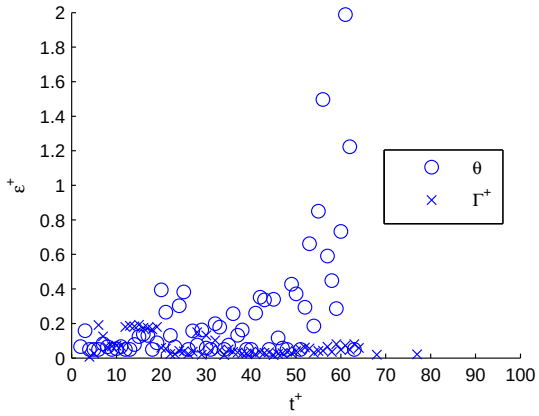

(d) Circulation and tilt

Figure C.6: Condition H

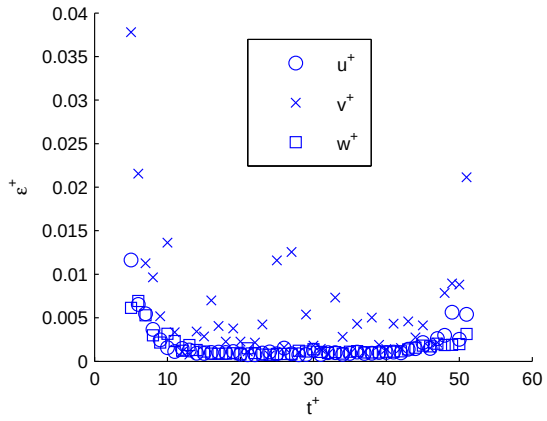

(a) Velocity

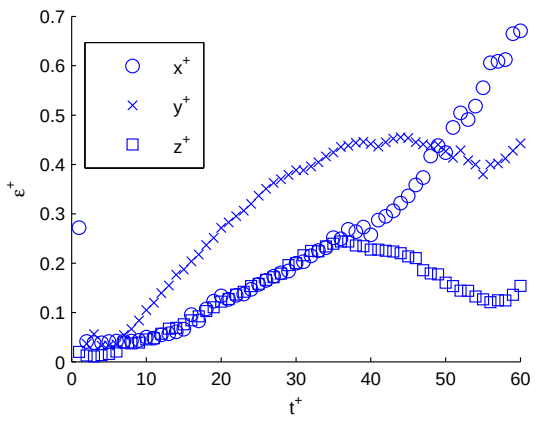

(b) Position

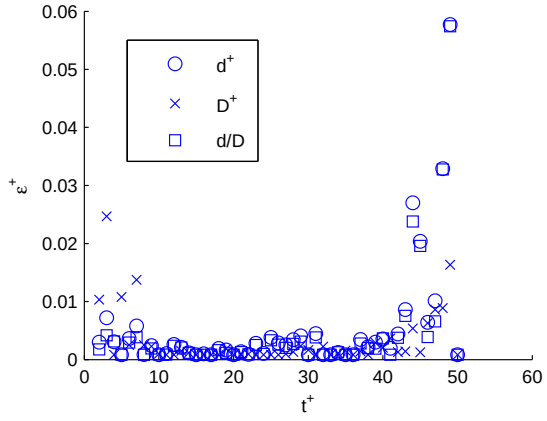

(c) Core/ring diameter

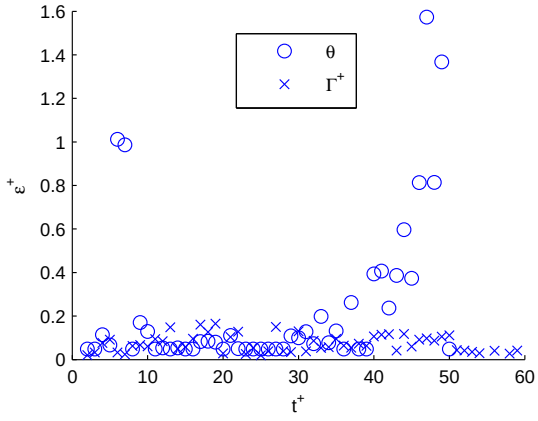

(d) Circulation and tilt

Figure C.7: Condition I

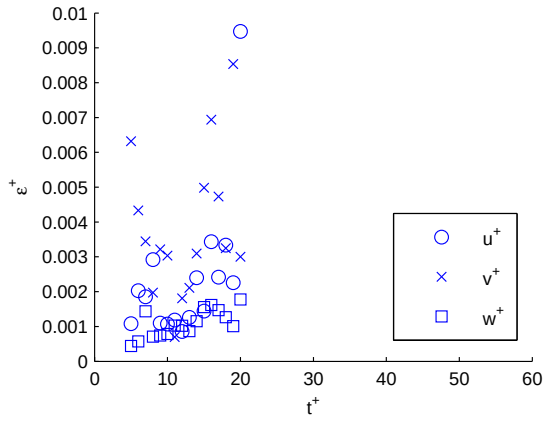

(a) Velocity

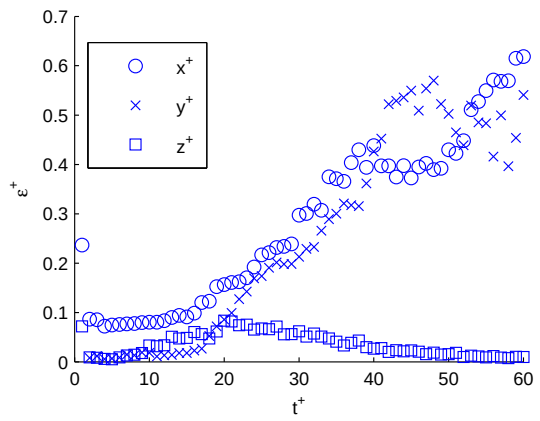

(b) Position

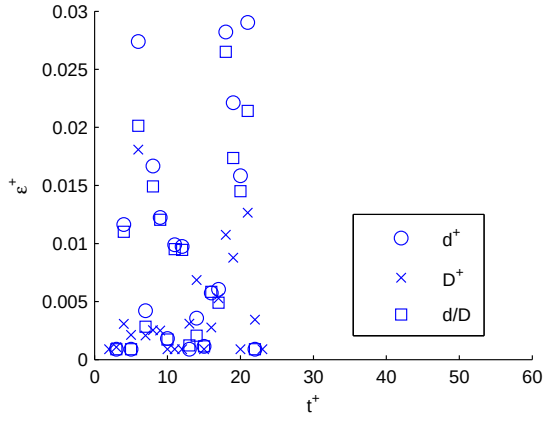

(c) Core/ring diameter

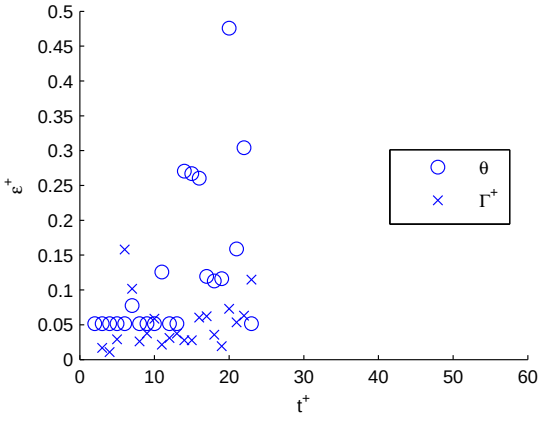

(d) Circulation and tilt

Figure C.8: Condition J

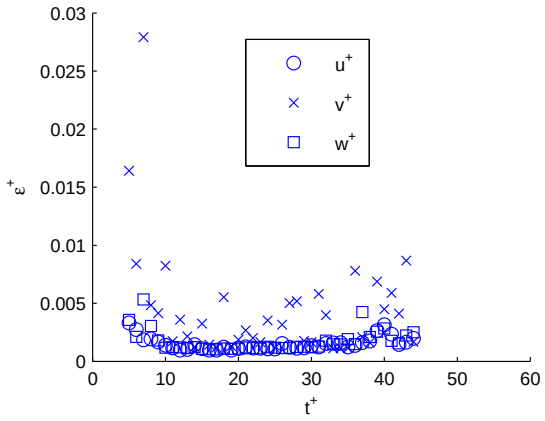

(a) Velocity

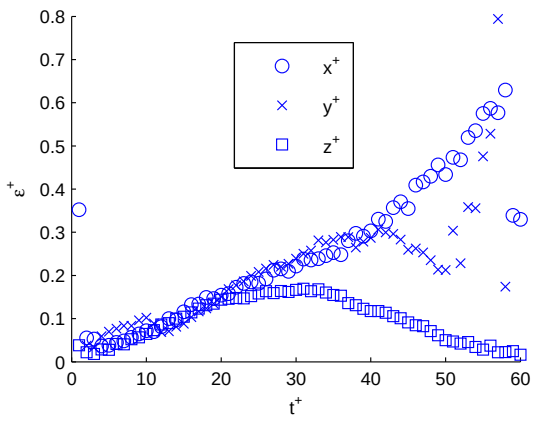

(b) Position

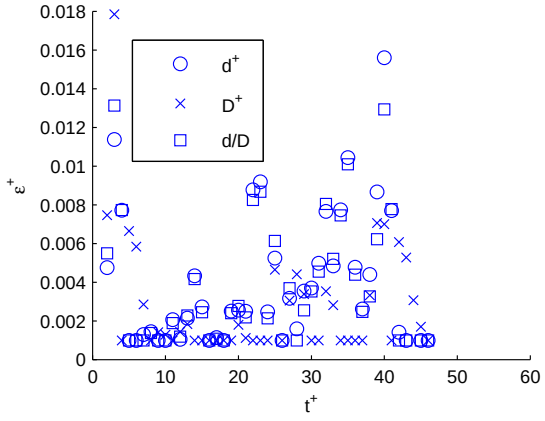

(c) Core/ring diameter

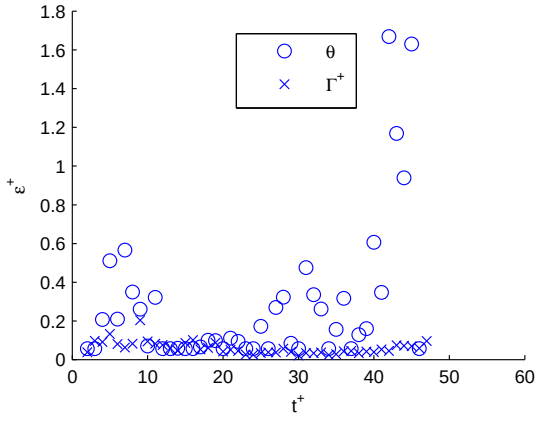

(d) Circulation and tilt

Figure C.9: Condition K

APPENDIX D

Horizontal sums of $\overline{u_z}$ as a function of time

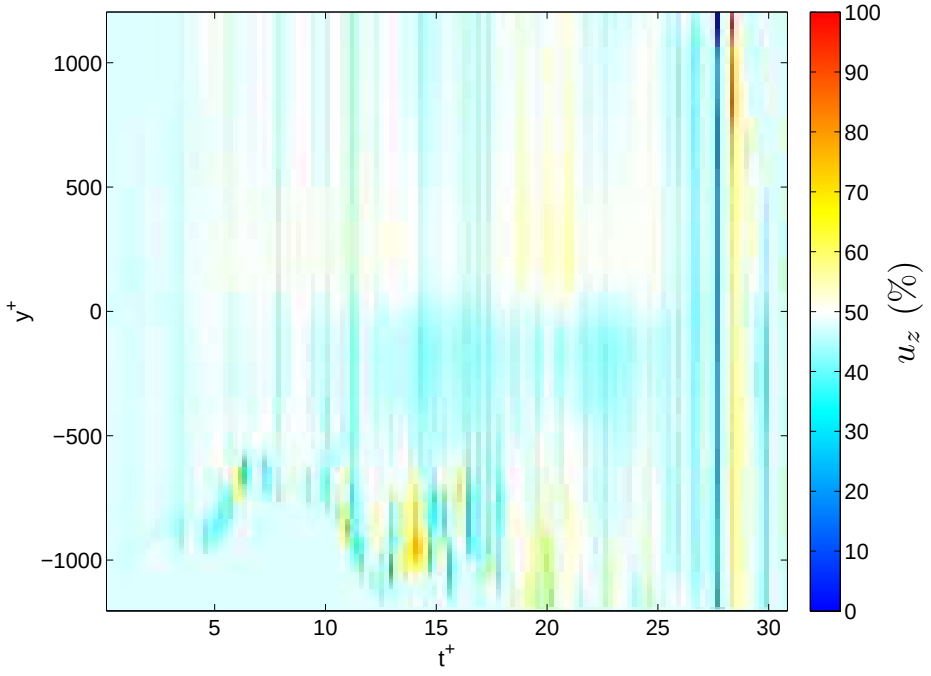

Figure D.1: Condition B, horizontal sum of $\overline{u_z}$

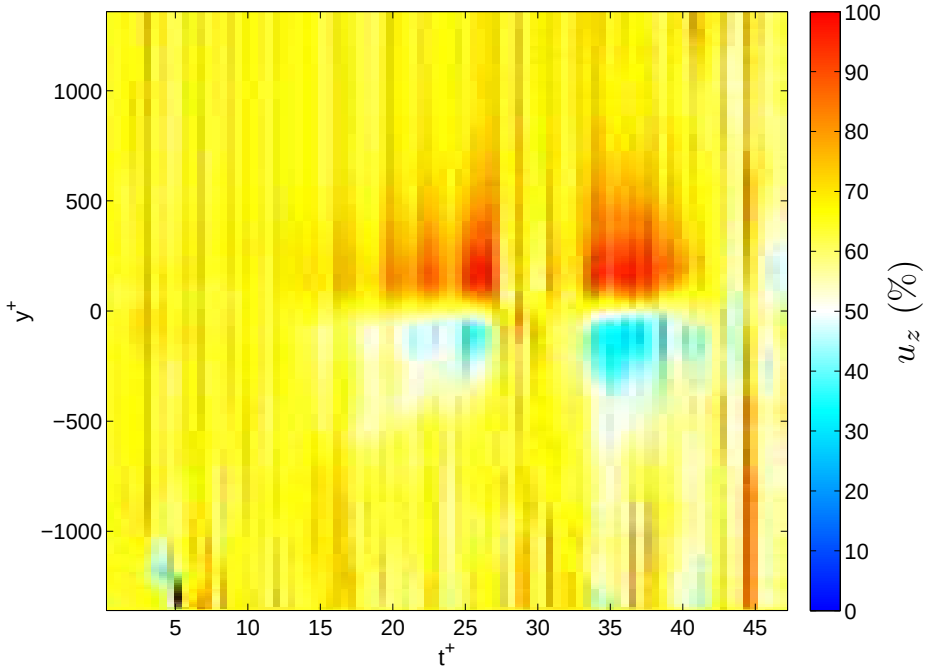

Figure D.2: Condition C, horizontal sum of $\overline{u_z}$

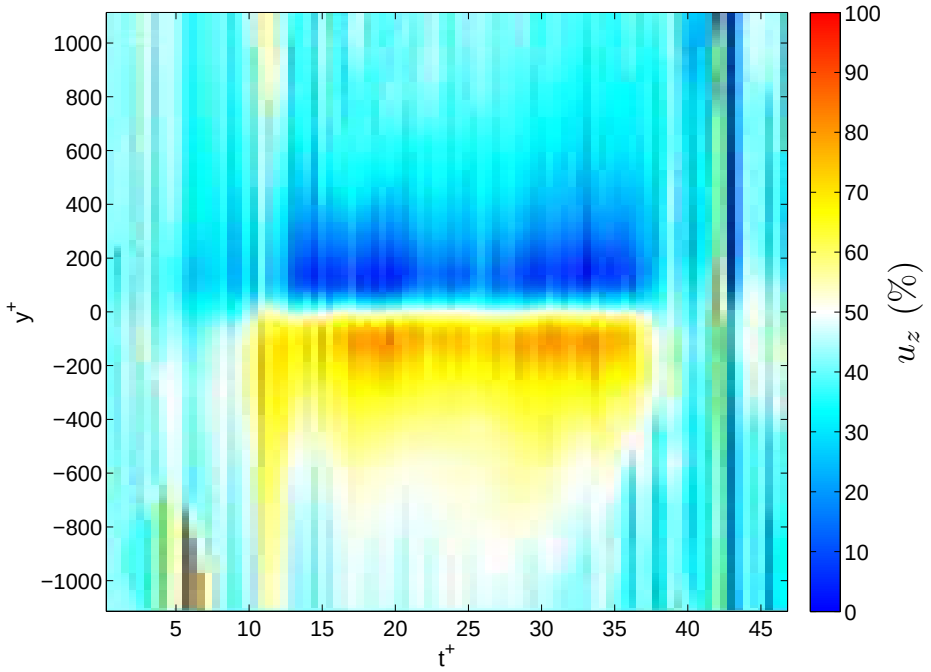

Figure D.3: Condition E, horizontal sum of $\overline{u_z}$

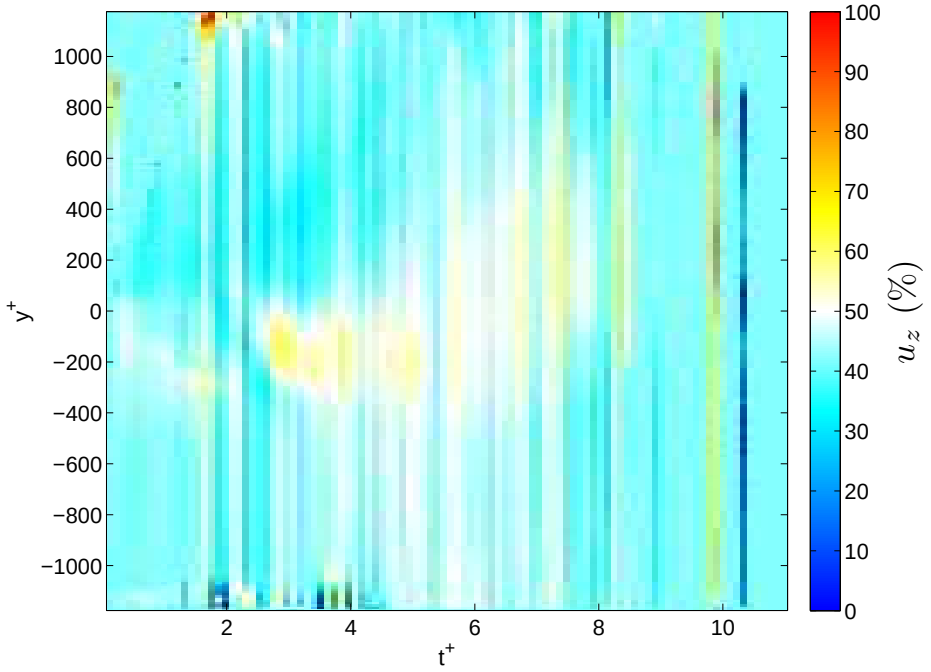

Figure D.4: Condition F, horizontal sum of $\overline{u_z}$

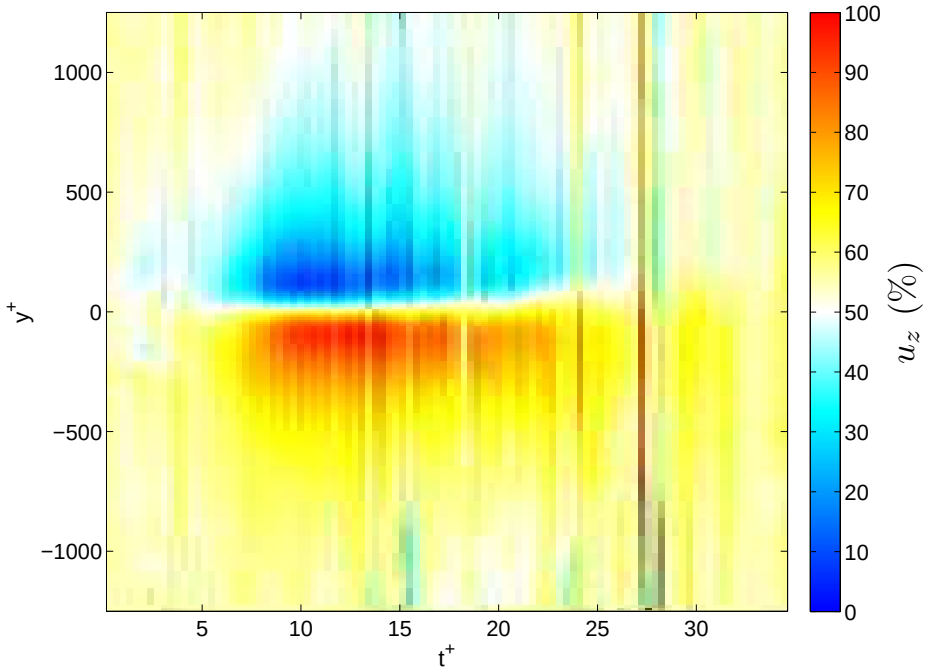

Figure D.5: Condition G, horizontal sum of $\overline{u_z}$

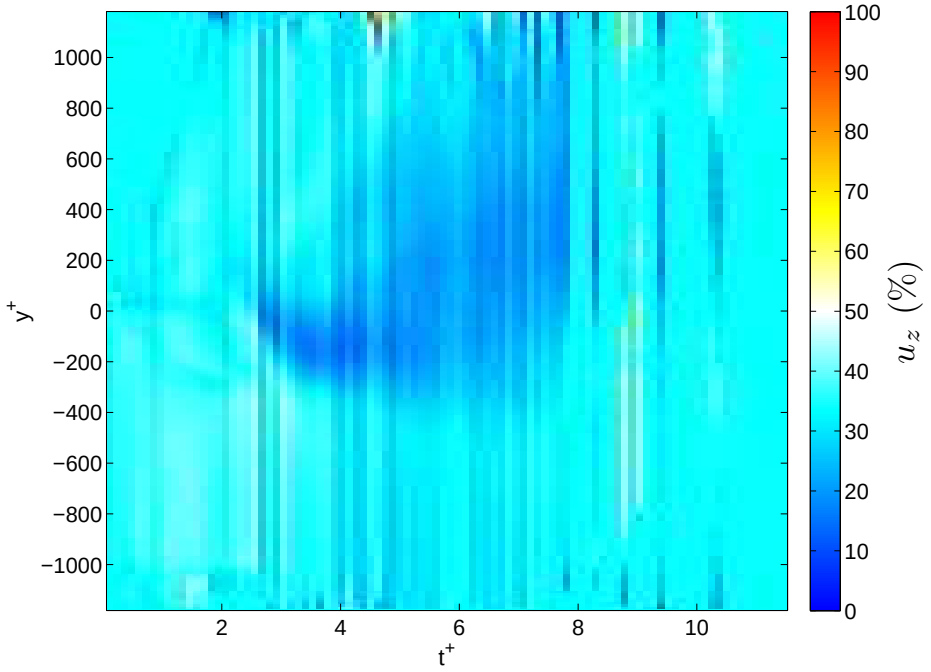

Figure D.6: Condition H, horizontal sum of $\overline{u_z}$

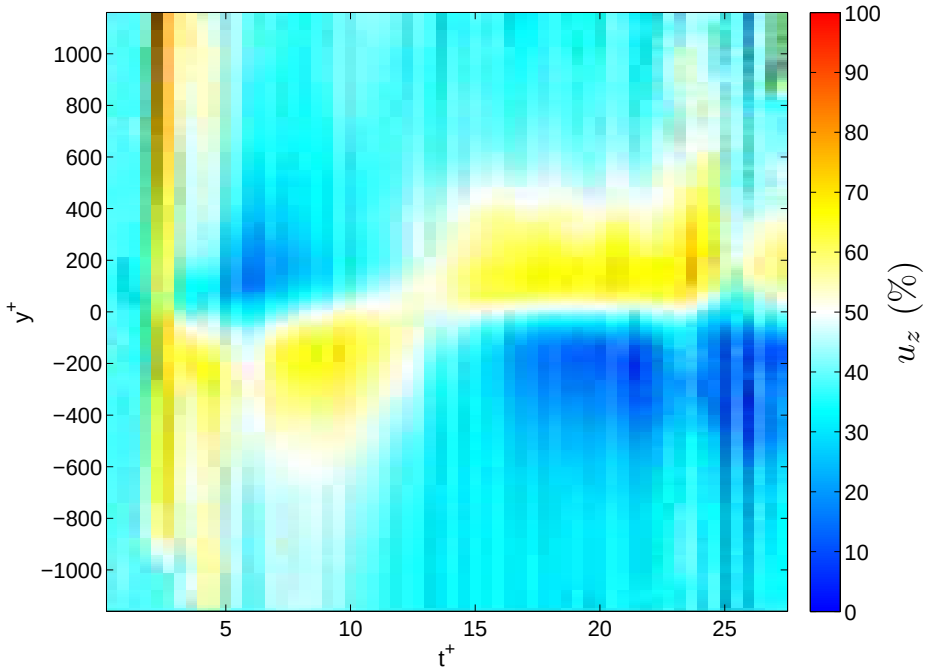

Figure D.7: Condition I, horizontal sum of $\overline{u_z}$

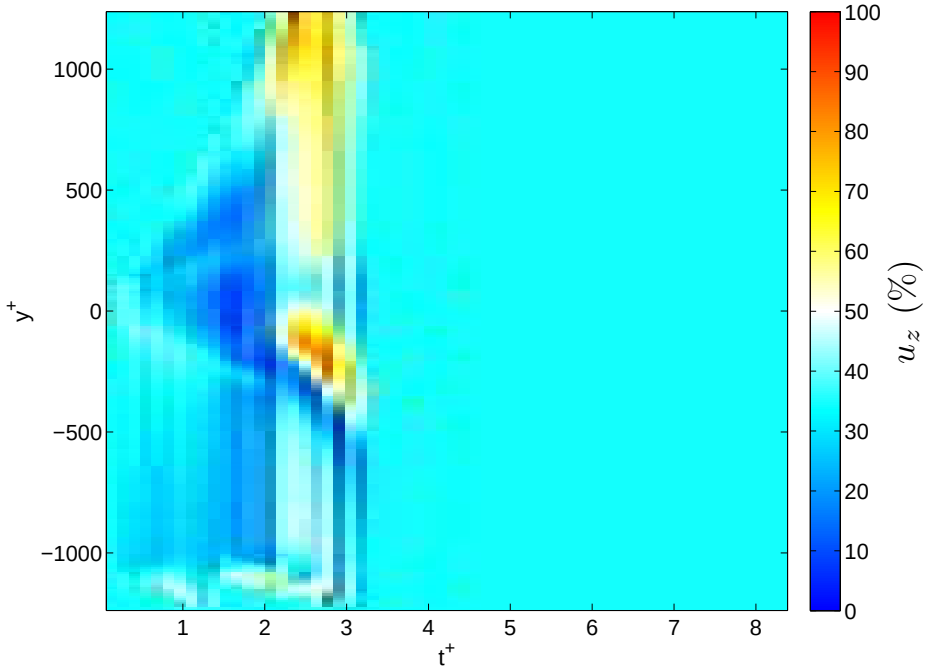

Figure D.8: Condition J, horizontal sum of $\overline{u_z}$

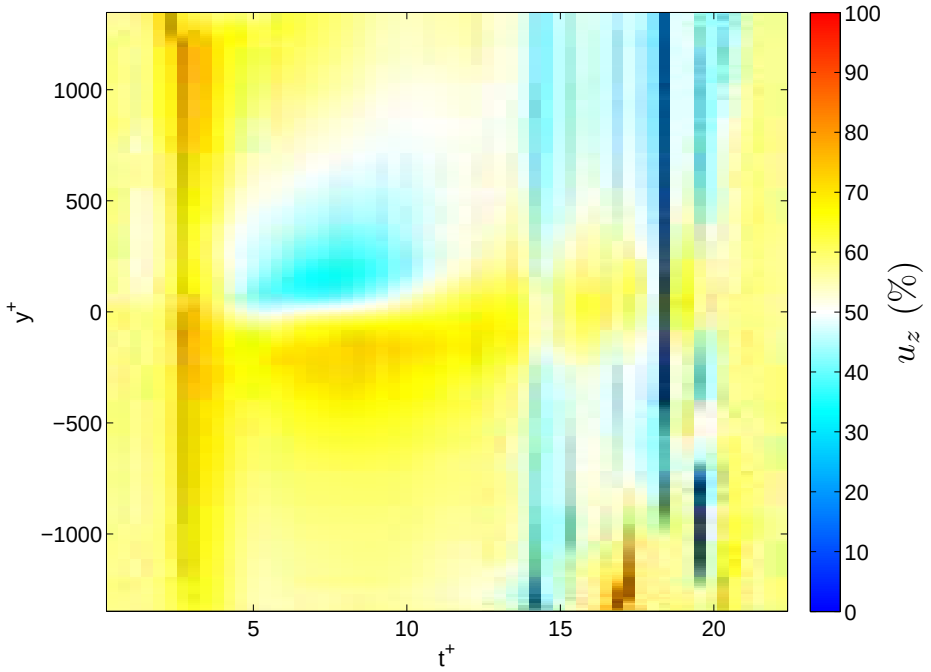

Figure D.9: Condition K, horizontal sum of $\overline{u_z}$

APPENDIX E

Full field time evolution

E.1 Condition A

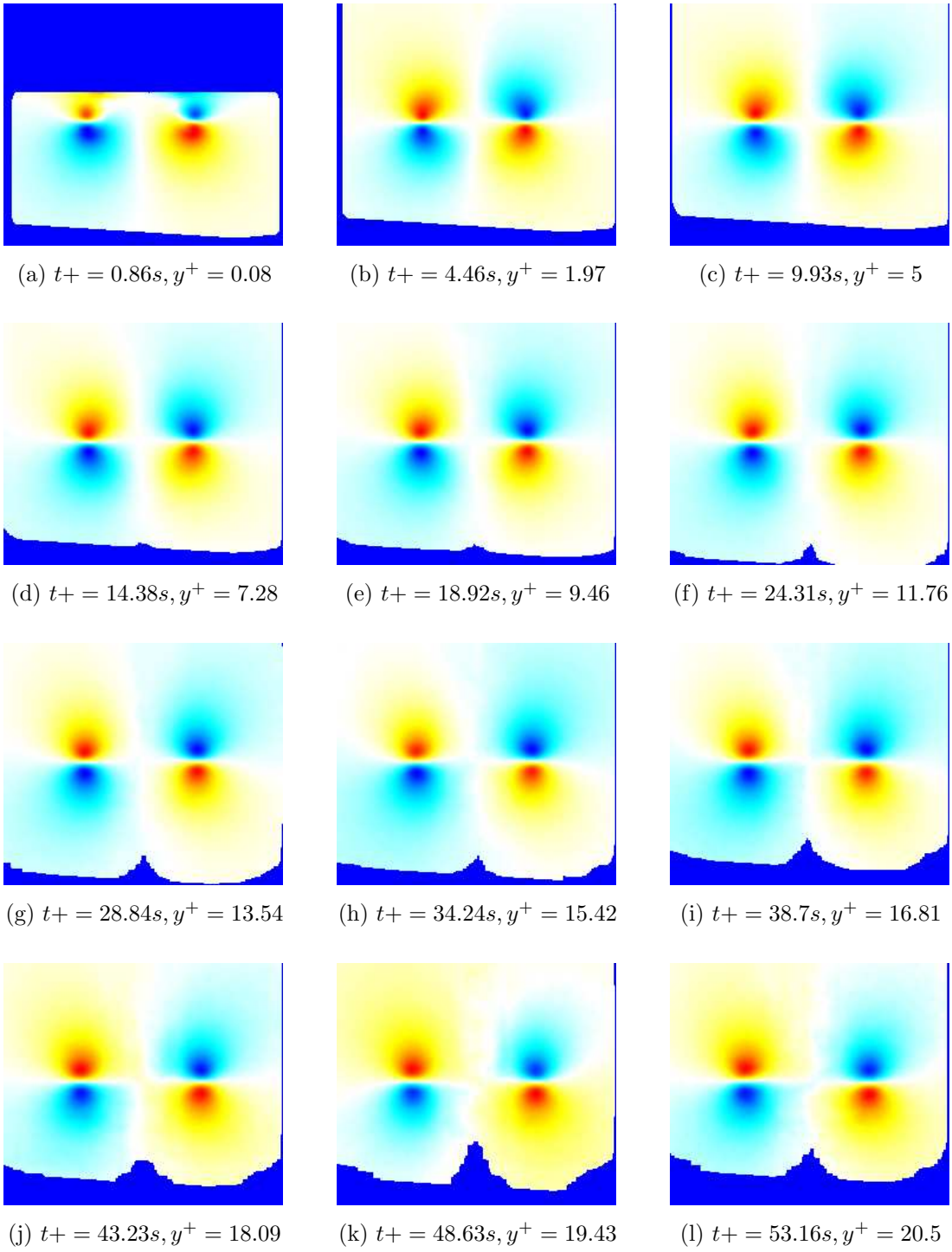

(a) $t+ = 0.86s, y^+ = 0.08$ (b) $t+ = 4.46s, y^+ = 1.97$ (c) $t+ = 9.93s, y^+ = 5$

(d) $t+ = 14.38s, y^+ = 7.28$ (e) $t+ = 18.92s, y^+ = 9.46$ (f) $t+ = 24.31s, y^+ = 11.76$

(g) $t+ = 28.84s, y^+ = 13.54$ (h) $t+ = 34.24s, y^+ = 15.42$ (i) $t+ = 38.7s, y^+ = 16.81$

(j) $t+ = 43.23s, y^+ = 18.09$ (k) $t+ = 48.63s, y^+ = 19.43$ (l) $t+ = 53.16s, y^+ = 20.5$

Figure E.1: Evolution of $\overline{u_x}$ field for condition A

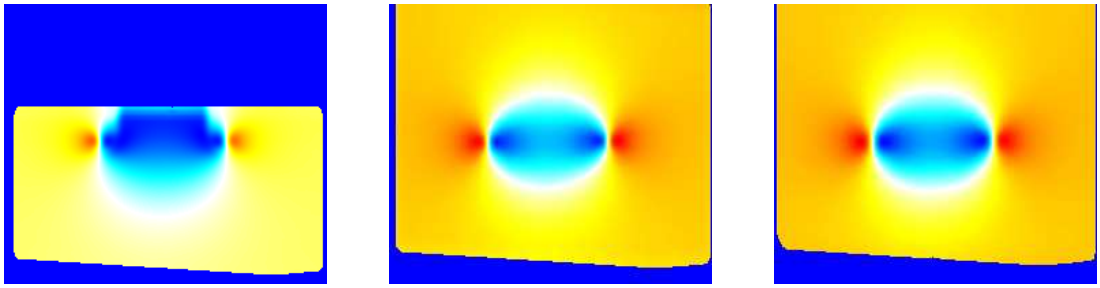

(a) $t+ = 0.86s, y^+ = 0.08$ (b) $t+ = 4.46s, y^+ = 1.97$ (c) $t+ = 9.93s, y^+ = 5$

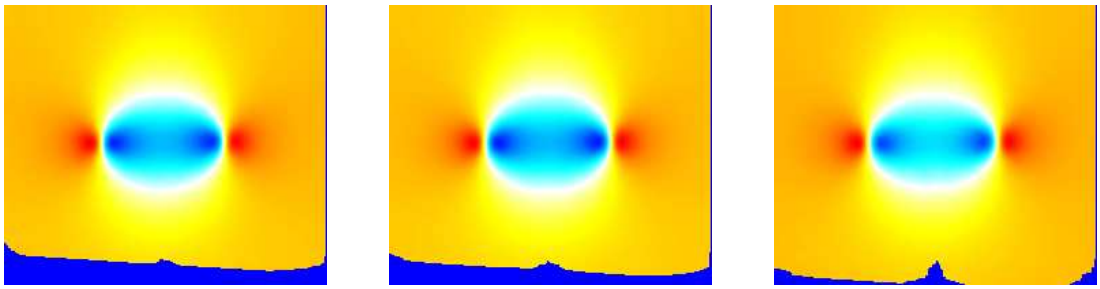

(d) $t+ = 14.38s, y^+ = 7.28$ (e) $t+ = 18.92s, y^+ = 9.46$ (f) $t+ = 24.31s, y^+ = 11.76$

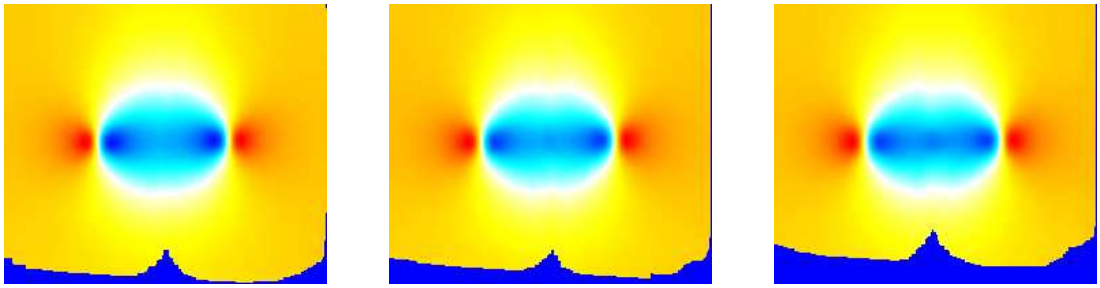

(g) $t+ = 28.84s, y^+ = 13.54$ (h) $t+ = 34.24s, y^+ = 15.42$ (i) $t+ = 38.7s, y^+ = 16.81$

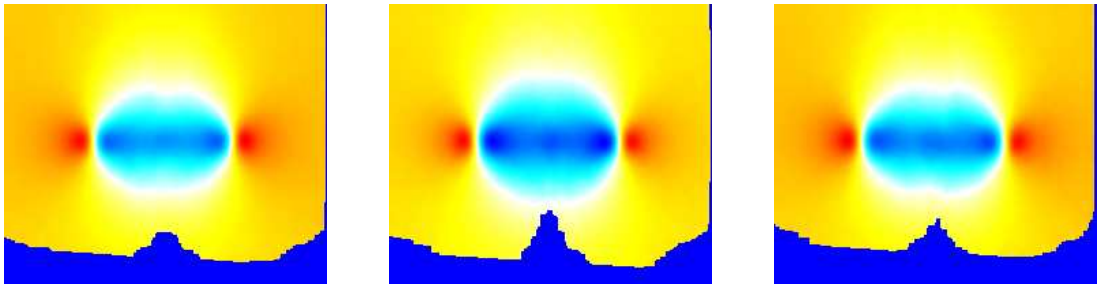

(j) $t+ = 43.23s, y^+ = 18.09$ (k) $t+ = 48.63s, y^+ = 19.43$ (l) $t+ = 53.16s, y^+ = 20.5$

Figure E.2: Evolution of $\overline{u_y}$ field for condition A

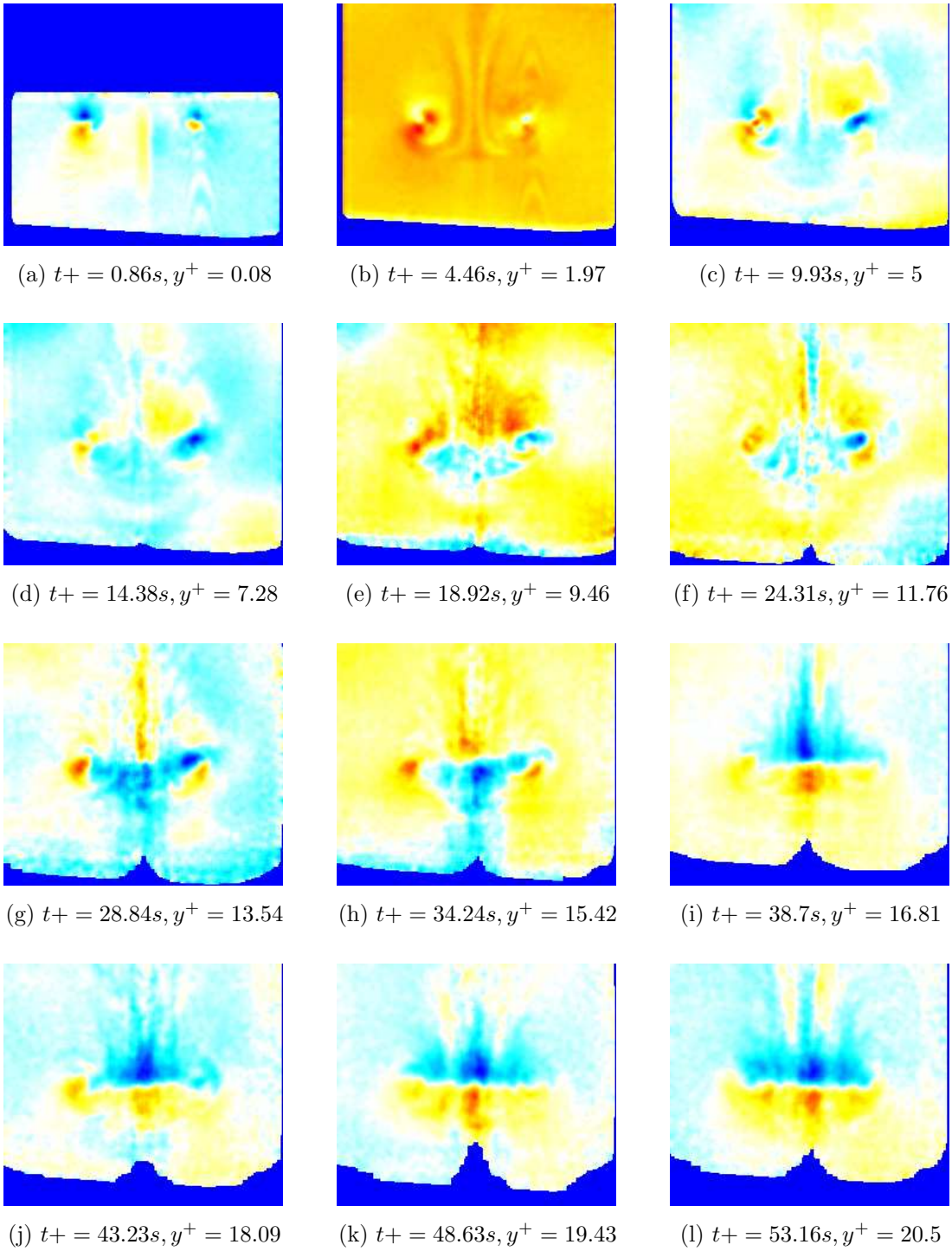

(a) $t+ = 0.86s, y^+ = 0.08$ (b) $t+ = 4.46s, y^+ = 1.97$ (c) $t+ = 9.93s, y^+ = 5$

(d) $t+ = 14.38s, y^+ = 7.28$ (e) $t+ = 18.92s, y^+ = 9.46$ (f) $t+ = 24.31s, y^+ = 11.76$

(g) $t+ = 28.84s, y^+ = 13.54$ (h) $t+ = 34.24s, y^+ = 15.42$ (i) $t+ = 38.7s, y^+ = 16.81$

(j) $t+ = 43.23s, y^+ = 18.09$ (k) $t+ = 48.63s, y^+ = 19.43$ (l) $t+ = 53.16s, y^+ = 20.5$

Figure E.3: Evolution of $\overline{u_z}$ field for condition A

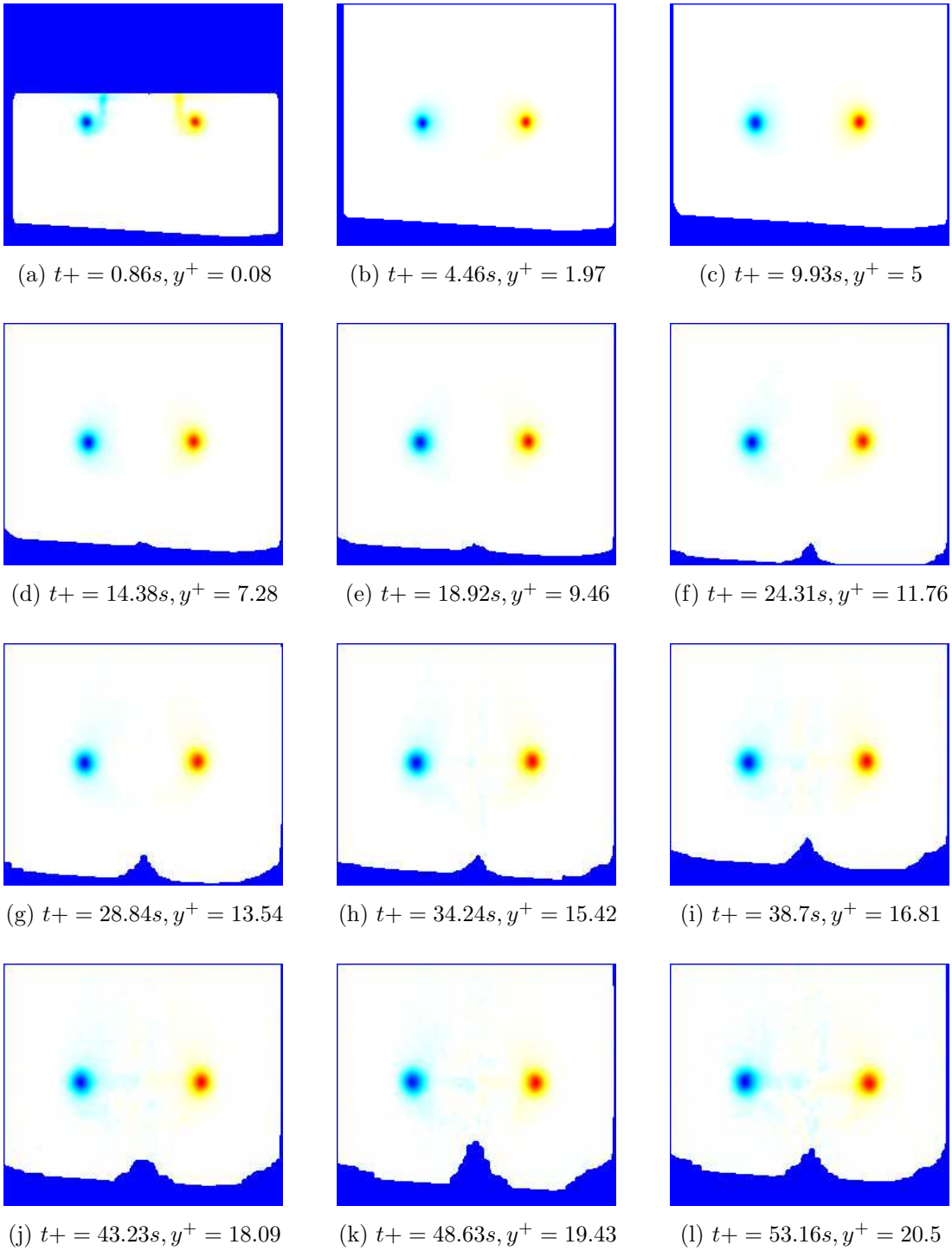

(a) $t+ = 0.86s, y^+ = 0.08$ (b) $t+ = 4.46s, y^+ = 1.97$ (c) $t+ = 9.93s, y^+ = 5$

(d) $t+ = 14.38s, y^+ = 7.28$ (e) $t+ = 18.92s, y^+ = 9.46$ (f) $t+ = 24.31s, y^+ = 11.76$

(g) $t+ = 28.84s, y^+ = 13.54$ (h) $t+ = 34.24s, y^+ = 15.42$ (i) $t+ = 38.7s, y^+ = 16.81$

(j) $t+ = 43.23s, y^+ = 18.09$ (k) $t+ = 48.63s, y^+ = 19.43$ (l) $t+ = 53.16s, y^+ = 20.5$

Figure E.4: Evolution of $\overline{\omega_z}$ field for condition A

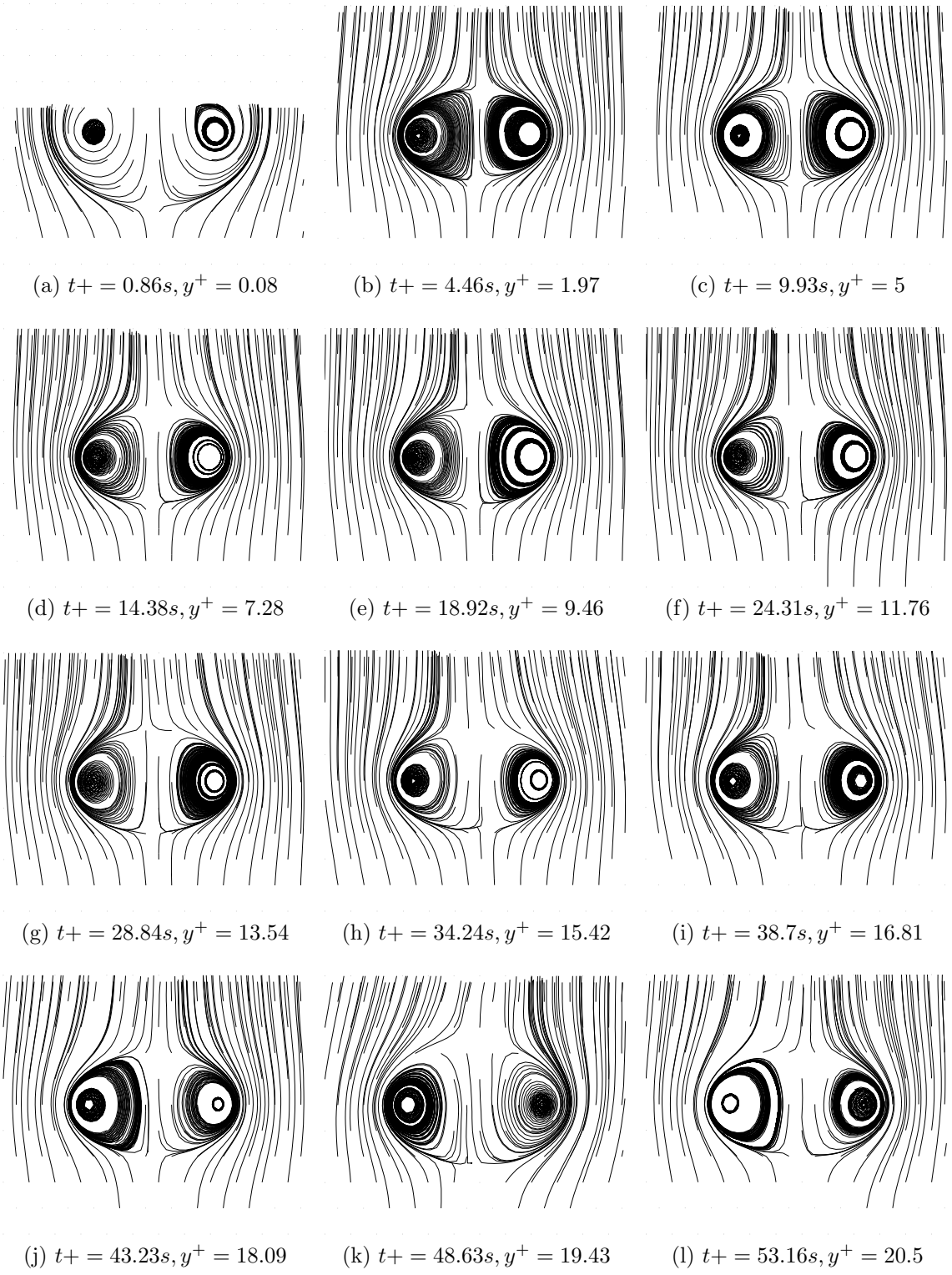

(a) $t+ = 0.86s, y^+ = 0.08$ (b) $t+ = 4.46s, y^+ = 1.97$ (c) $t+ = 9.93s, y^+ = 5$

(d) $t+ = 14.38s, y^+ = 7.28$ (e) $t+ = 18.92s, y^+ = 9.46$ (f) $t+ = 24.31s, y^+ = 11.76$

(g) $t+ = 28.84s, y^+ = 13.54$ (h) $t+ = 34.24s, y^+ = 15.42$ (i) $t+ = 38.7s, y^+ = 16.81$

(j) $t+ = 43.23s, y^+ = 18.09$ (k) $t+ = 48.63s, y^+ = 19.43$ (l) $t+ = 53.16s, y^+ = 20.5$

Figure E.5: Evolution of $\overline{\psi}$ field for condition A

E.2 Condition C

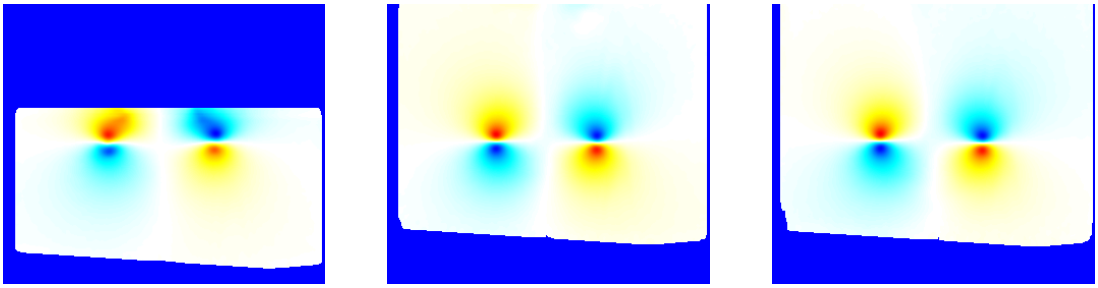

(a) $t+ = 0.51s, y^+ = 0.11$ (b) $t+ = 2.11s, y^+ = 1.02$ (c) $t+ = 3.71s, y^+ = 2.1$

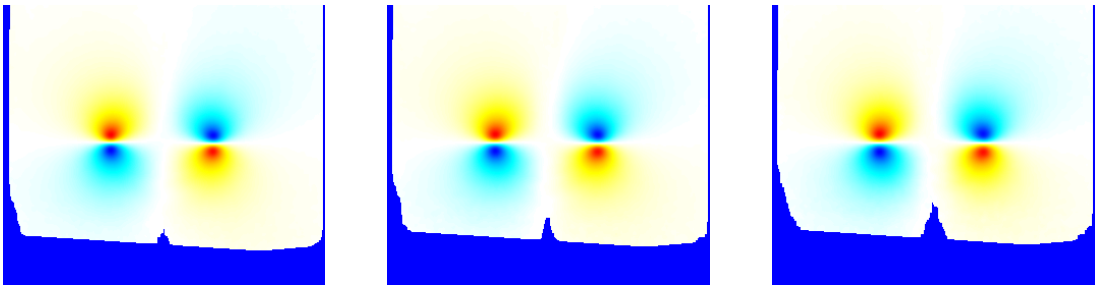

(d) $t+ = 5.82s, y^+ = 3.52$ (e) $t+ = 7.38s, y^+ = 4.49$ (f) $t+ = 9.48s, y^+ = 5.79$

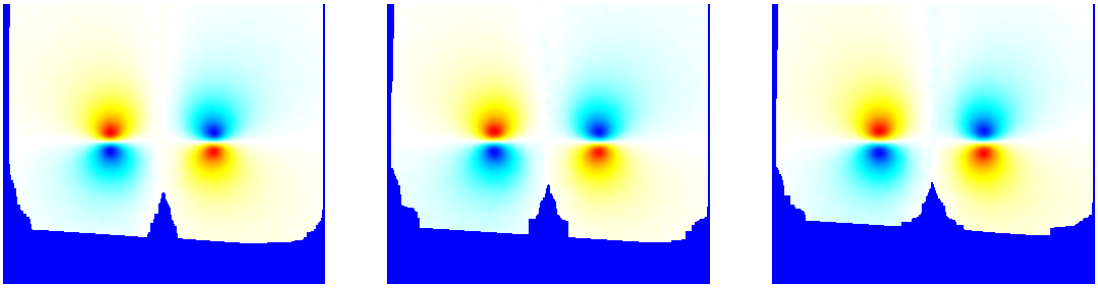

(g) $t+ = 11.09s, y^+ = 6.7$ (h) $t+ = 13.19s, y^+ = 7.87$ (i) $t+ = 14.8s, y^+ = 8.7$

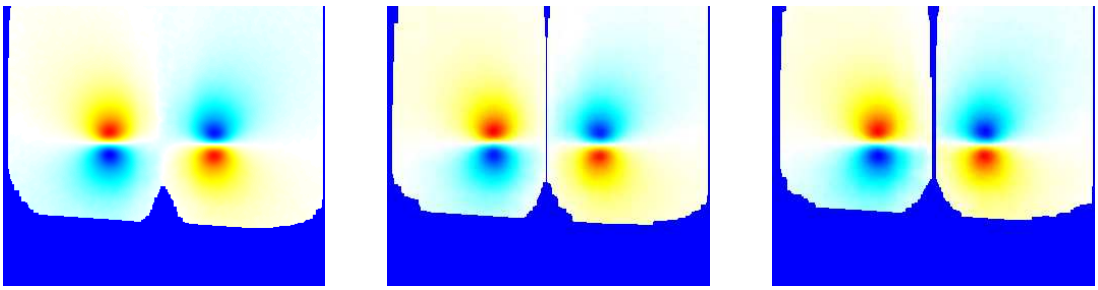

(j) $t+ = 16.91s, y^+ = 9.77$ (k) $t+ = 18.46s, y^+ = 10.57$ (l) $t+ = 20.57s, y^+ = 11.56$

Figure E.6: Evolution of $\overline{u_x}$ field for condition C

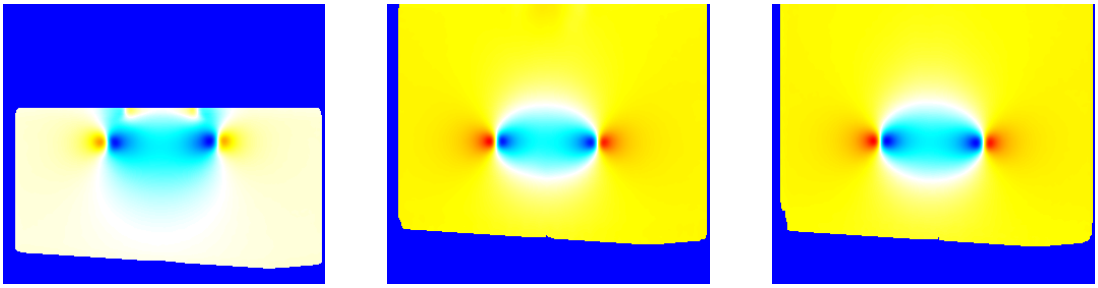

(a) $t+ = 0.51s, y^+ = 0.11$ (b) $t+ = 2.11s, y^+ = 1.02$ (c) $t+ = 3.71s, y^+ = 2.1$

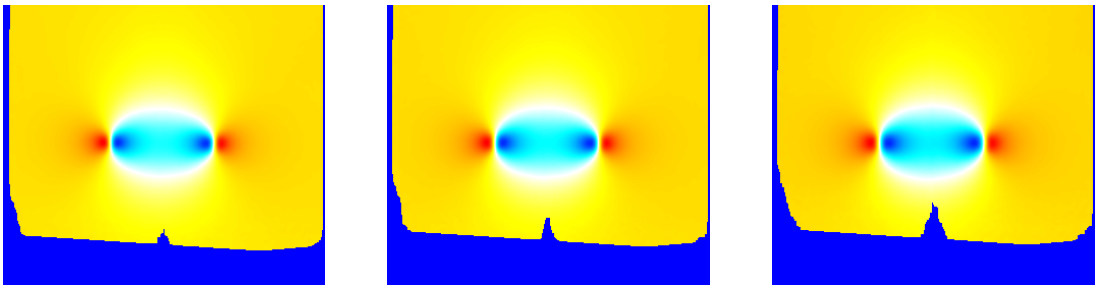

(d) $t+ = 5.82s, y^+ = 3.52$ (e) $t+ = 7.38s, y^+ = 4.49$ (f) $t+ = 9.48s, y^+ = 5.79$

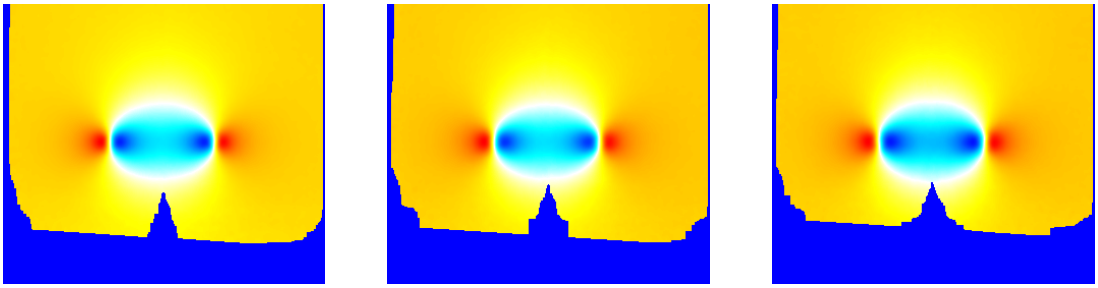

(g) $t+ = 11.09s, y^+ = 6.7$ (h) $t+ = 13.19s, y^+ = 7.87$ (i) $t+ = 14.8s, y^+ = 8.7$

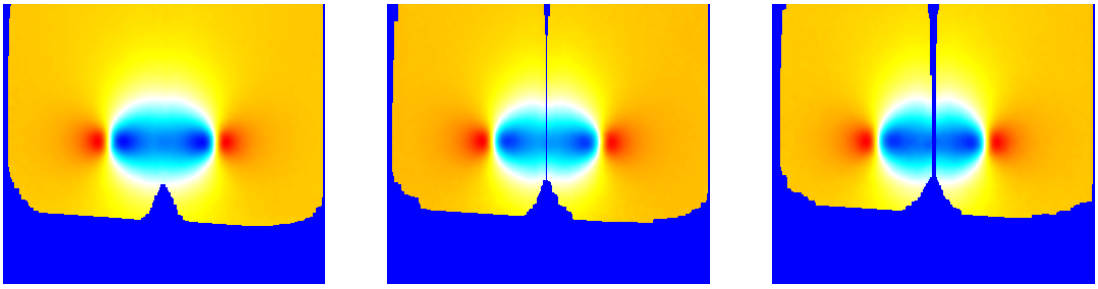

(j) $t+ = 16.91s, y^+ = 9.77$ (k) $t+ = 18.46s, y^+ = 10.57$ (l) $t+ = 20.57s, y^+ = 11.56$

Figure E.7: Evolution of $\overline{u_y}$ field for condition C

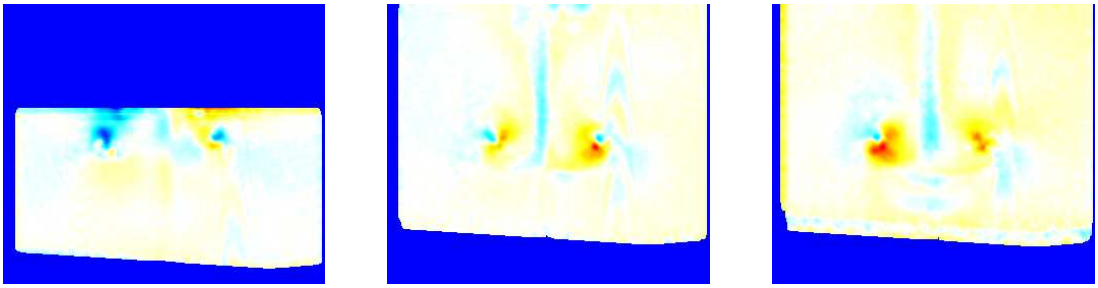

(a) $t+ = 0.51s, y^+ = 0.11$ (b) $t+ = 2.11s, y^+ = 1.02$ (c) $t+ = 3.71s, y^+ = 2.1$

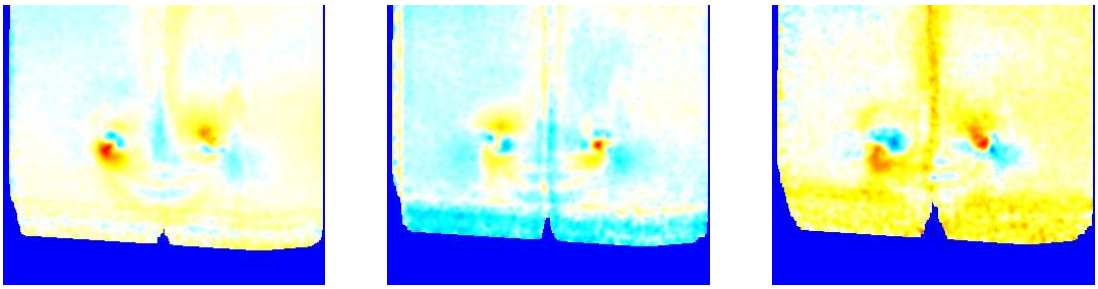

(d) $t+ = 5.82s, y^+ = 3.52$ (e) $t+ = 7.38s, y^+ = 4.49$ (f) $t+ = 9.48s, y^+ = 5.79$

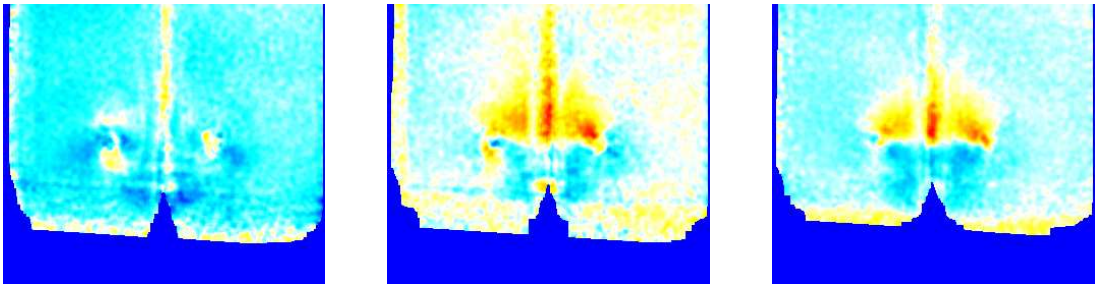

(g) $t+ = 11.09s, y^+ = 6.7$ (h) $t+ = 13.19s, y^+ = 7.87$ (i) $t+ = 14.8s, y^+ = 8.7$

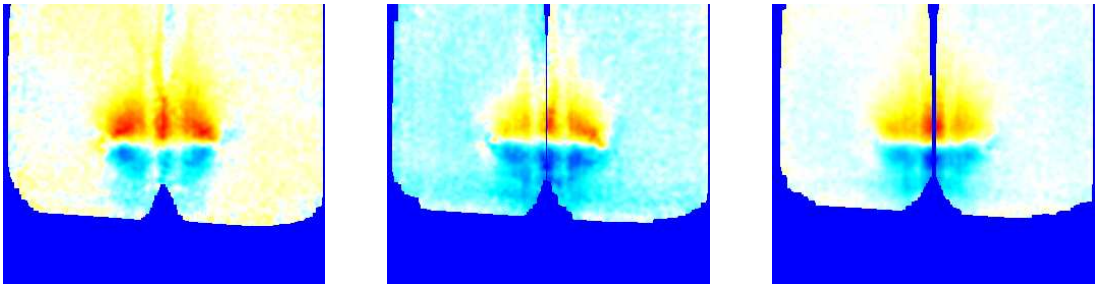

(j) $t+ = 16.91s, y^+ = 9.77$ (k) $t+ = 18.46s, y^+ = 10.57$ (l) $t+ = 20.57s, y^+ = 11.56$

Figure E.8: Evolution of $\overline{u_z}$ field for condition C

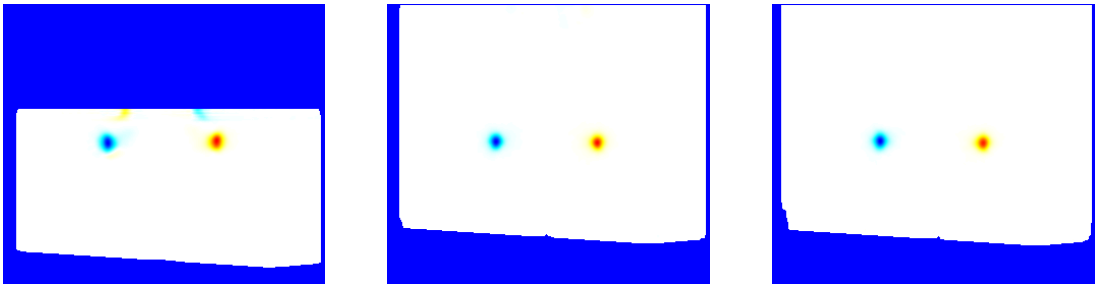

(a) $t+ = 0.51s, y^+ = 0.11$ (b) $t+ = 2.11s, y^+ = 1.02$ (c) $t+ = 3.71s, y^+ = 2.1$

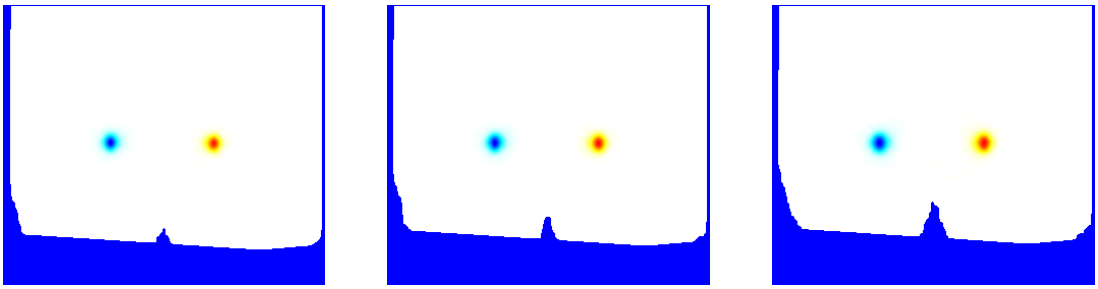

(d) $t+ = 5.82s, y^+ = 3.52$ (e) $t+ = 7.38s, y^+ = 4.49$ (f) $t+ = 9.48s, y^+ = 5.79$

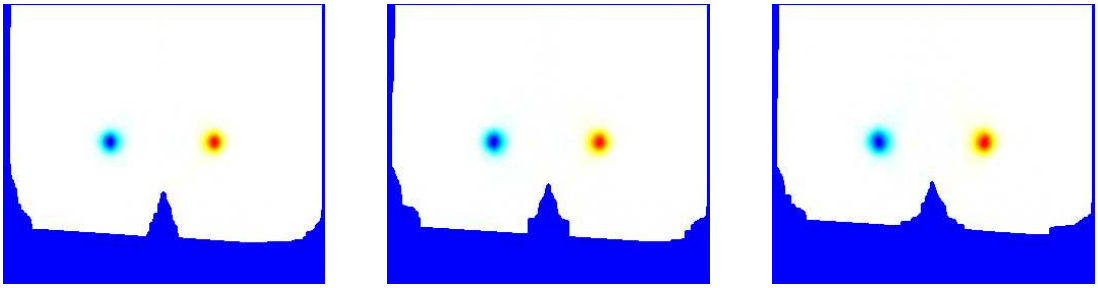

(g) $t+ = 11.09s, y^+ = 6.7$ (h) $t+ = 13.19s, y^+ = 7.87$ (i) $t+ = 14.8s, y^+ = 8.7$

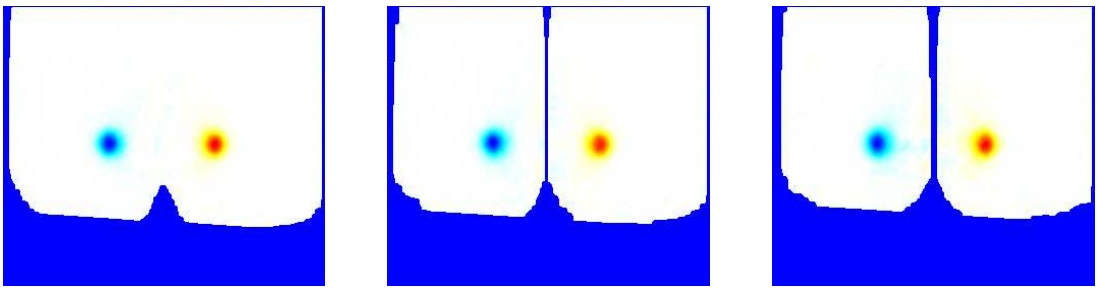

(j) $t+ = 16.91s, y^+ = 9.77$ (k) $t+ = 18.46s, y^+ = 10.57$ (l) $t+ = 20.57s, y^+ = 11.56$

Figure E.9: Evolution of $\overline{\omega_z}$ field for condition C

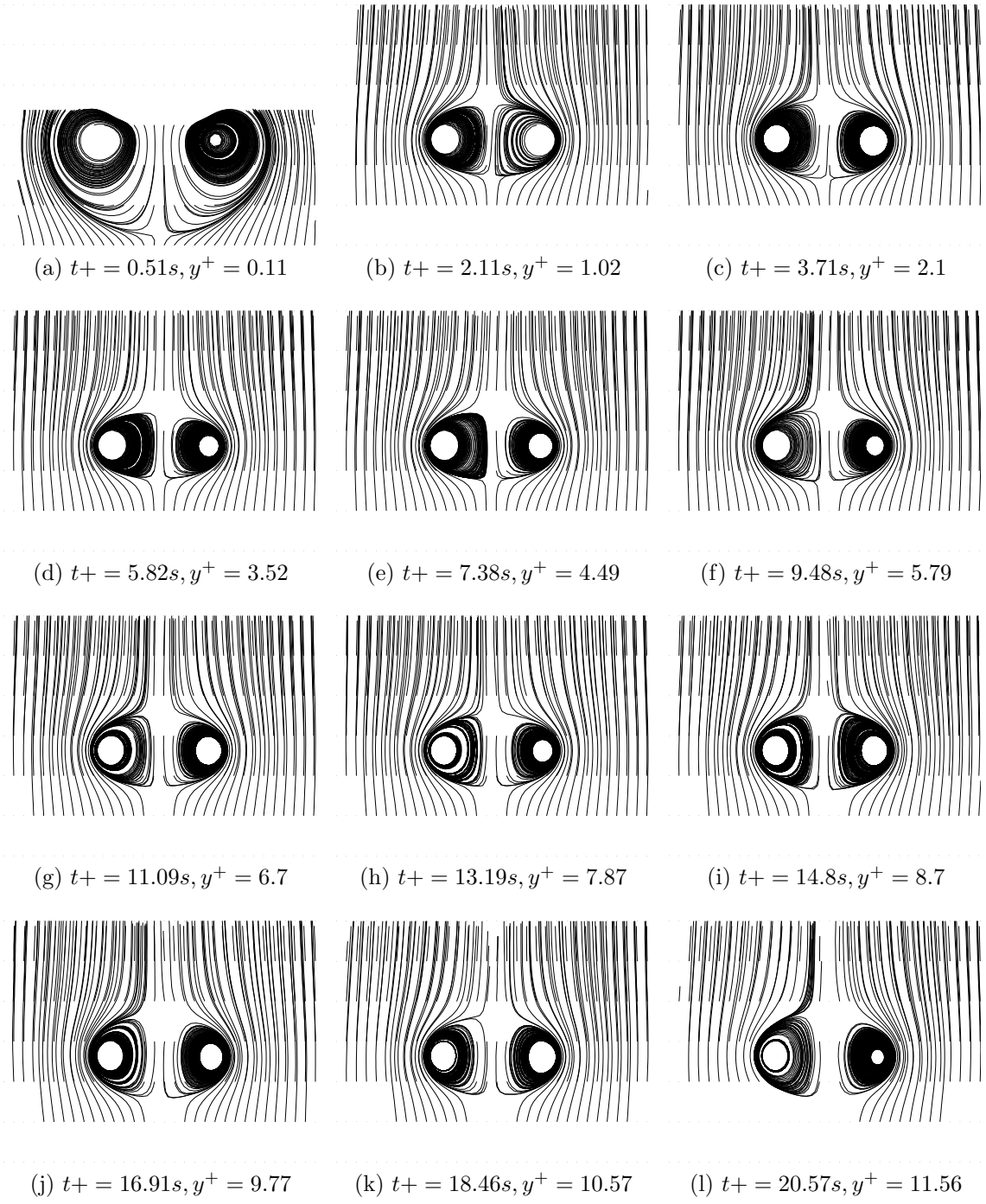

(a) $t+ = 0.51s, y^+ = 0.11$ (b) $t+ = 2.11s, y^+ = 1.02$ (c) $t+ = 3.71s, y^+ = 2.1$

(d) $t+ = 5.82s, y^+ = 3.52$ (e) $t+ = 7.38s, y^+ = 4.49$ (f) $t+ = 9.48s, y^+ = 5.79$

(g) $t+ = 11.09s, y^+ = 6.7$ (h) $t+ = 13.19s, y^+ = 7.87$ (i) $t+ = 14.8s, y^+ = 8.7$

(j) $t+ = 16.91s, y^+ = 9.77$ (k) $t+ = 18.46s, y^+ = 10.57$ (l) $t+ = 20.57s, y^+ = 11.56$

Figure E.10: Evolution of $\overline{\psi}$ field for condition C

E.3 Condition E

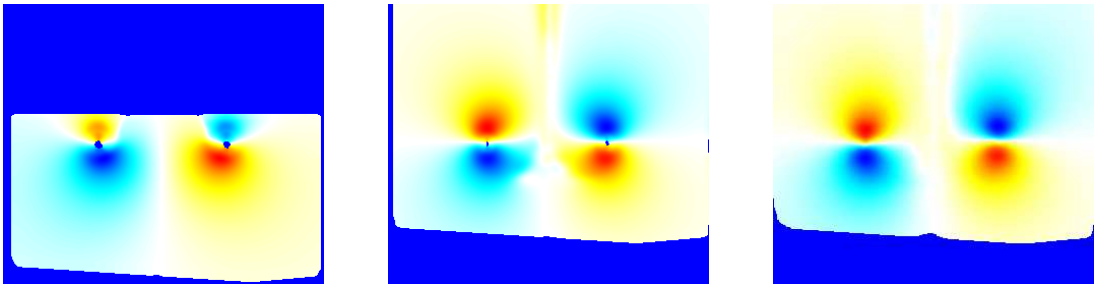

(a) $t+ = 0.5s, y^+ = 0.12$ (b) $t+ = 2.59s, y^+ = 1.88$ (c) $t+ = 5.72s, y^+ = 4.02$

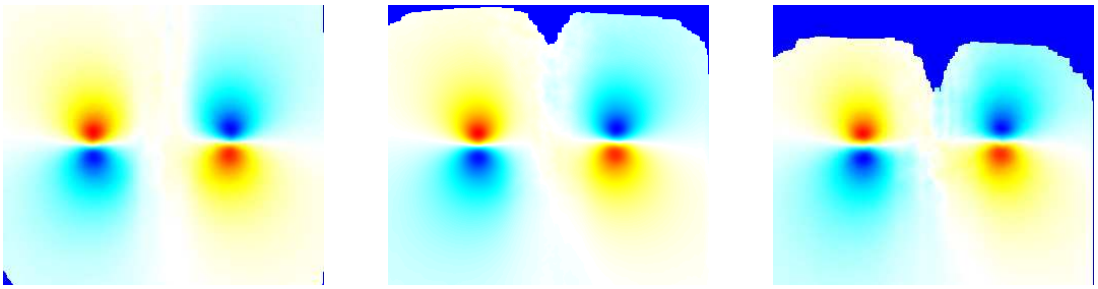

(d) $t+ = 8.36s, y^+ = 5.54$ (e) $t+ = 10.99s, y^+ = 6.92$ (f) $t+ = 14.13s, y^+ = 8.62$

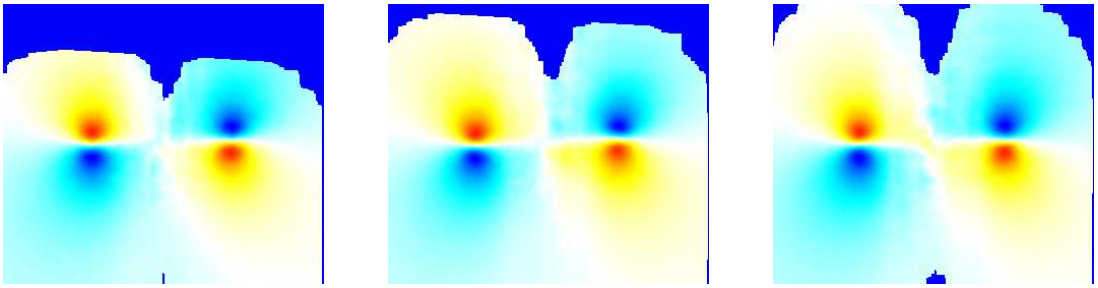

(g) $t+ = 16.72s, y^+ = 9.93$ (h) $t+ = 19.85s, y^+ = 11.31$ (i) $t+ = 22.48s, y^+ = 12.34$

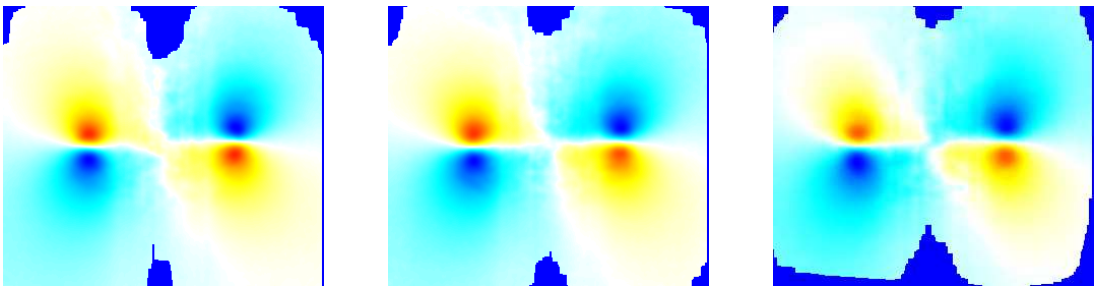

(j) $t+ = 25.12s, y^+ = 13.37$ (k) $t+ = 28.26s, y^+ = 14.5$ (l) $t+ = 30.84s, y^+ = 15.43$

Figure E.11: Evolution of $\overline{u_x}$ field for condition E

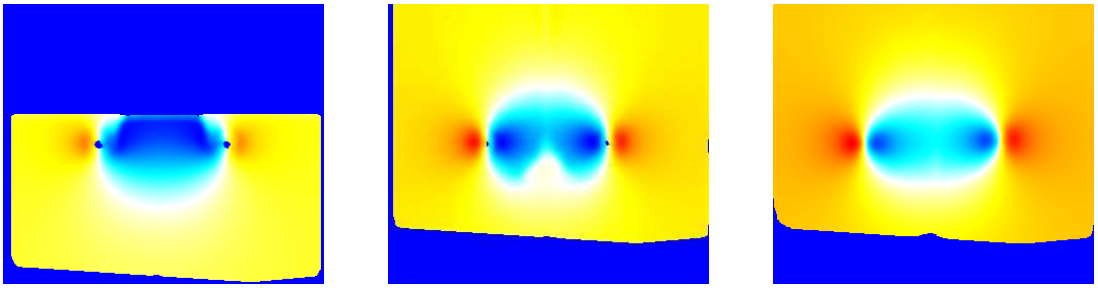

(a) $t+ = 0.5s, y^+ = 0.12$ (b) $t+ = 2.59s, y^+ = 1.88$ (c) $t+ = 5.72s, y^+ = 4.02$

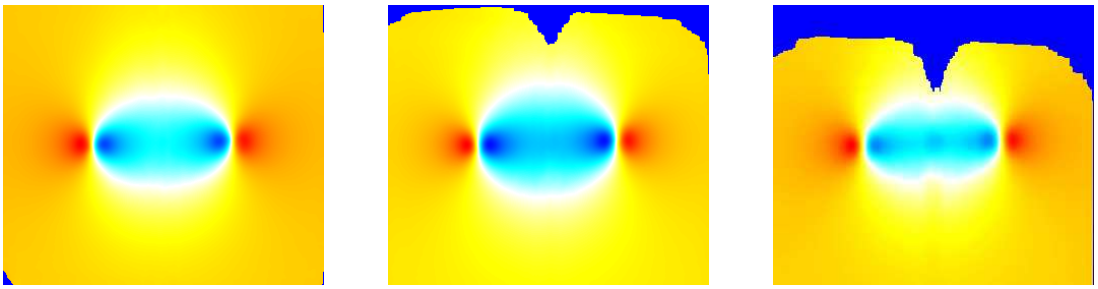

(d) $t+ = 8.36s, y^+ = 5.54$ (e) $t+ = 10.99s, y^+ = 6.92$ (f) $t+ = 14.13s, y^+ = 8.62$

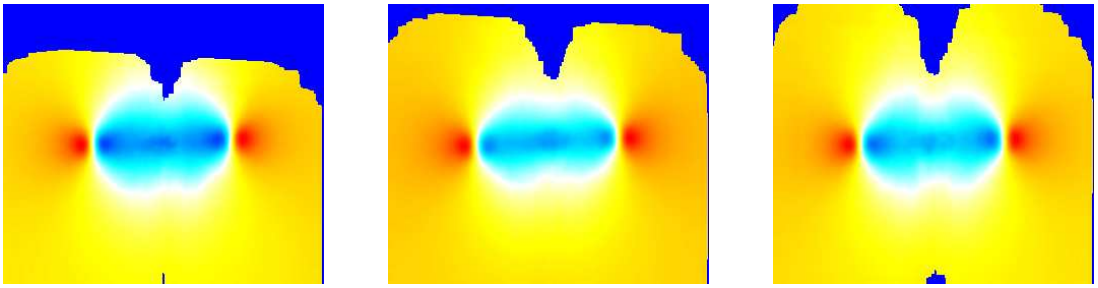

(g) $t+ = 16.72s, y^+ = 9.93$ (h) $t+ = 19.85s, y^+ = 11.31$ (i) $t+ = 22.48s, y^+ = 12.34$

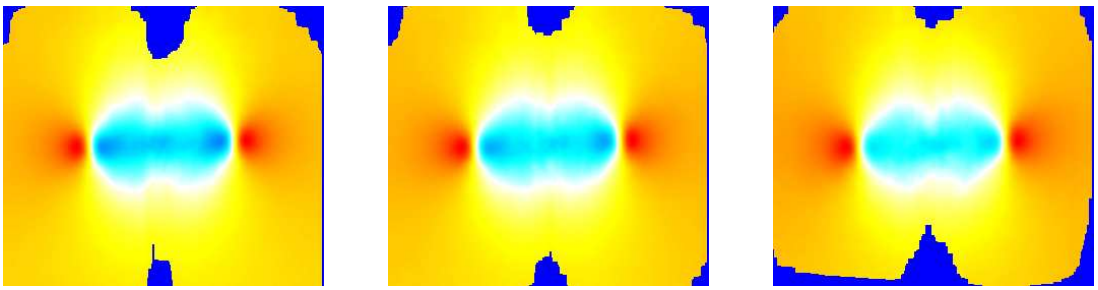

(j) $t+ = 25.12s, y^+ = 13.37$ (k) $t+ = 28.26s, y^+ = 14.5$ (l) $t+ = 30.84s, y^+ = 15.43$

Figure E.12: Evolution of $\overline{u_y}$ field for condition E

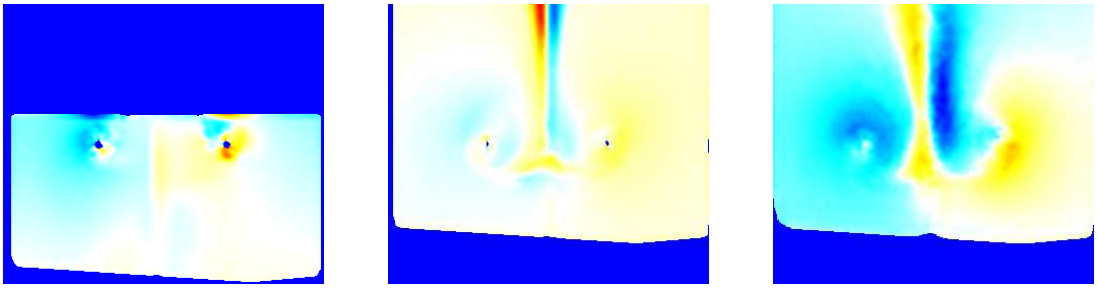

(a) $t+ = 0.5s, y^+ = 0.12$ (b) $t+ = 2.59s, y^+ = 1.88$ (c) $t+ = 5.72s, y^+ = 4.02$

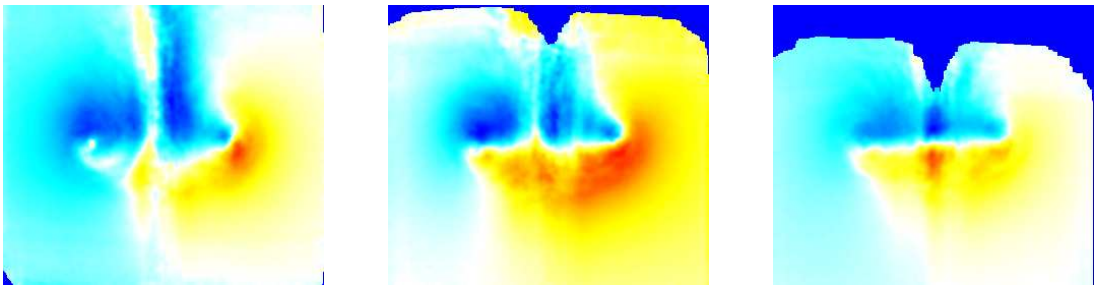

(d) $t+ = 8.36s, y^+ = 5.54$ (e) $t+ = 10.99s, y^+ = 6.92$ (f) $t+ = 14.13s, y^+ = 8.62$

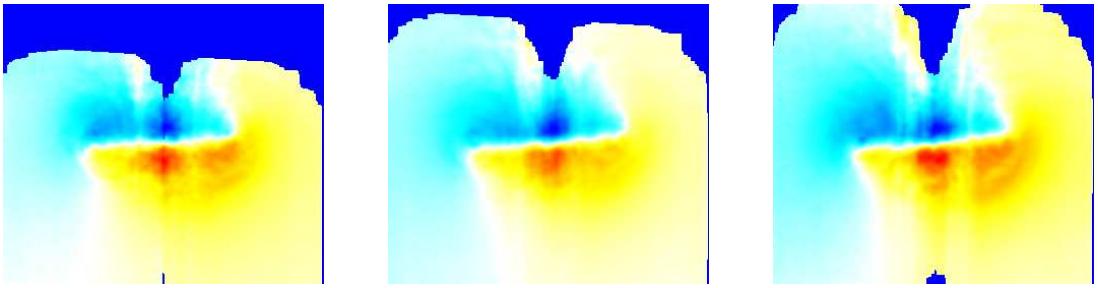

(g) $t+ = 16.72s, y^+ = 9.93$ (h) $t+ = 19.85s, y^+ = 11.31$ (i) $t+ = 22.48s, y^+ = 12.34$

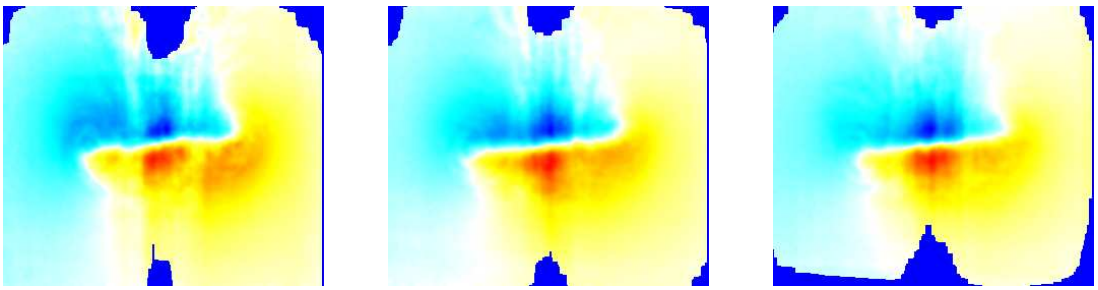

(j) $t+ = 25.12s, y^+ = 13.37$ (k) $t+ = 28.26s, y^+ = 14.5$ (l) $t+ = 30.84s, y^+ = 15.43$

Figure E.13: Evolution of $\overline{u_z}$ field for condition E

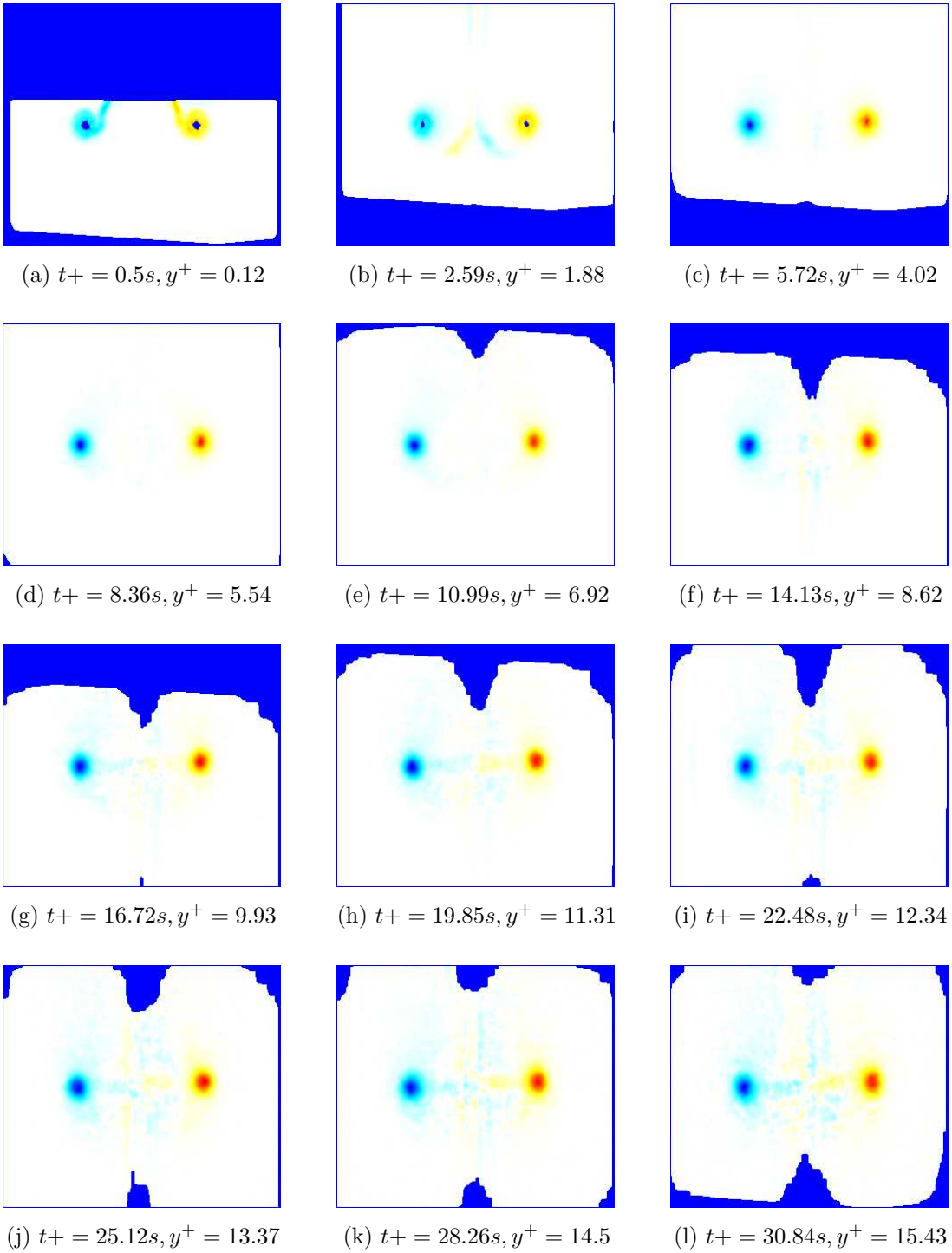

(a) $t+ = 0.5s, y^+ = 0.12$ (b) $t+ = 2.59s, y^+ = 1.88$ (c) $t+ = 5.72s, y^+ = 4.02$

(d) $t+ = 8.36s, y^+ = 5.54$ (e) $t+ = 10.99s, y^+ = 6.92$ (f) $t+ = 14.13s, y^+ = 8.62$

(g) $t+ = 16.72s, y^+ = 9.93$ (h) $t+ = 19.85s, y^+ = 11.31$ (i) $t+ = 22.48s, y^+ = 12.34$

(j) $t+ = 25.12s, y^+ = 13.37$ (k) $t+ = 28.26s, y^+ = 14.5$ (l) $t+ = 30.84s, y^+ = 15.43$

Figure E.14: Evolution of $\overline{\omega_z}$ field for condition E

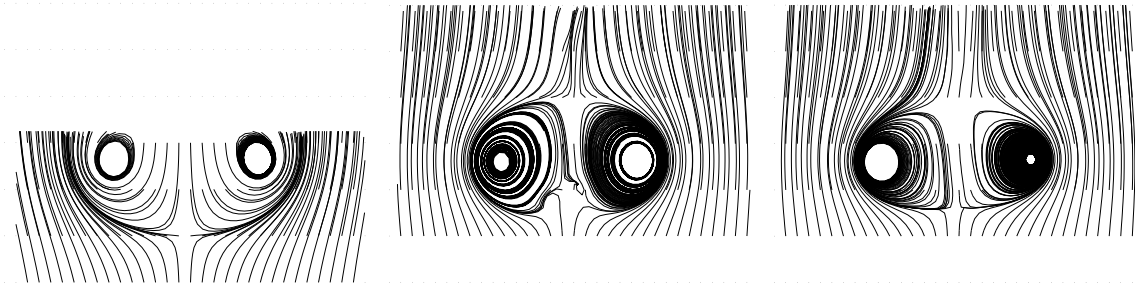

(a) $t+ = 0.5s, y^+ = 0.12$ (b) $t+ = 2.59s, y^+ = 1.88$ (c) $t+ = 5.72s, y^+ = 4.02$

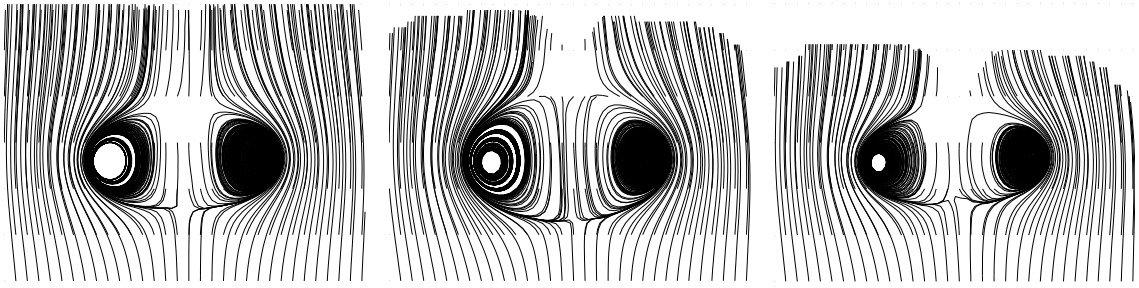

(d) $t+ = 8.36s, y^+ = 5.54$ (e) $t+ = 10.99s, y^+ = 6.92$ (f) $t+ = 14.13s, y^+ = 8.62$

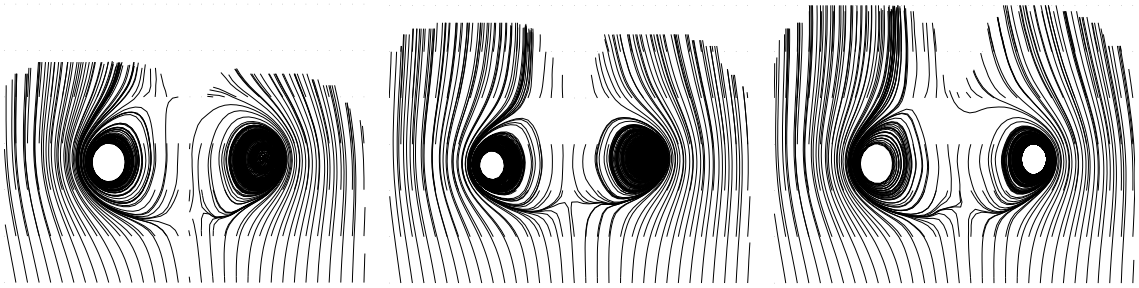

(g) $t+ = 16.72s, y^+ = 9.93$ (h) $t+ = 19.85s, y^+ = 11.31$ (i) $t+ = 22.48s, y^+ = 12.34$

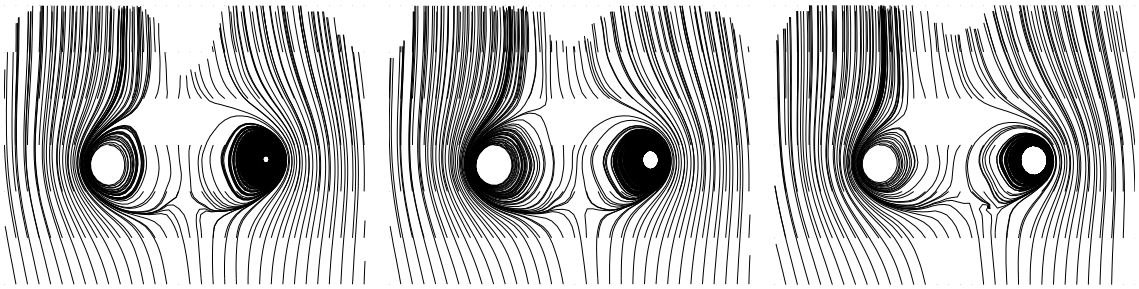

(j) $t+ = 25.12s, y^+ = 13.37$ (k) $t+ = 28.26s, y^+ = 14.5$ (l) $t+ = 30.84s, y^+ = 15.43$

Figure E.15: Evolution of $\overline{\psi}$ field for condition E

E.4 Condition G

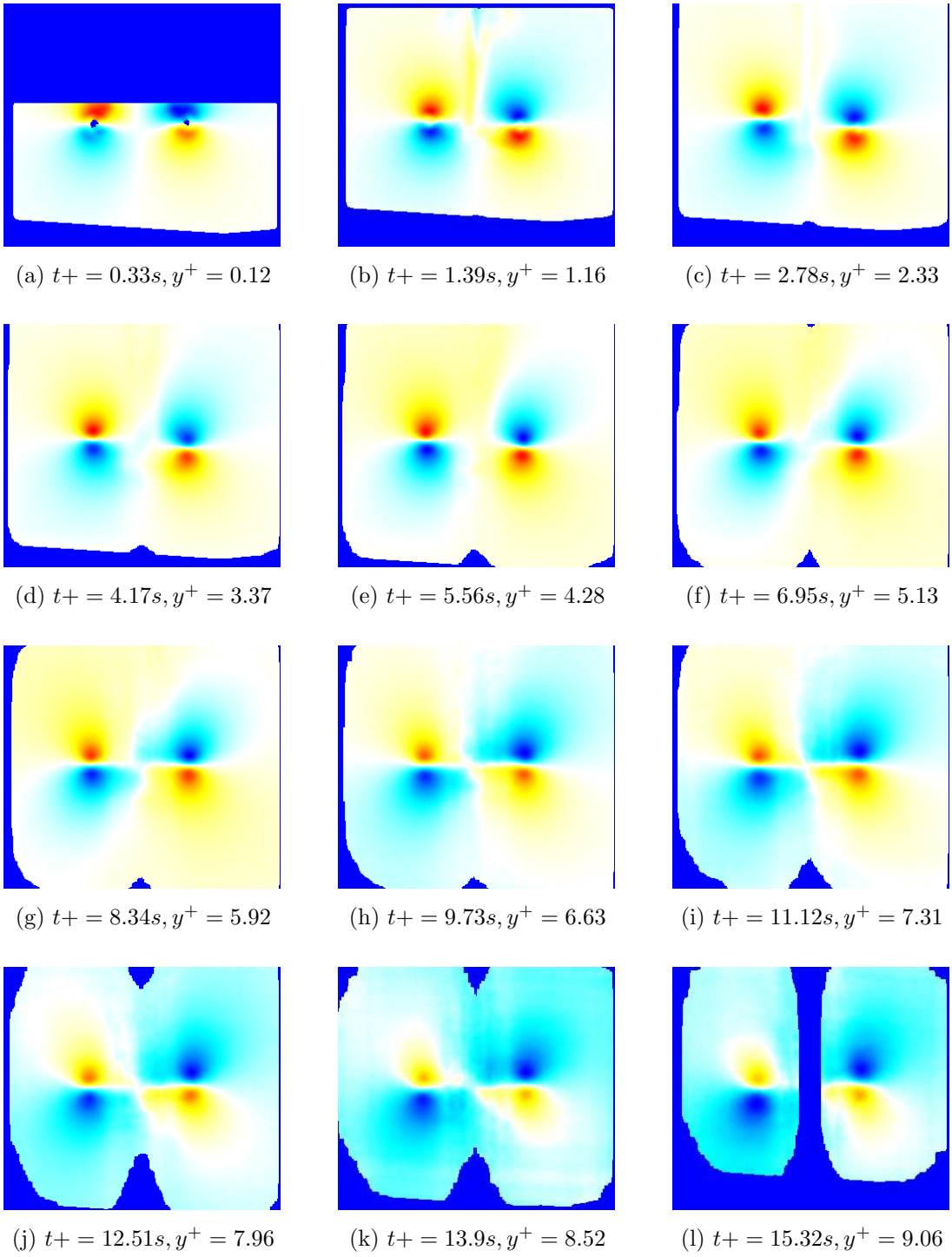

(a) $t+ = 0.33s, y^+ = 0.12$ (b) $t+ = 1.39s, y^+ = 1.16$ (c) $t+ = 2.78s, y^+ = 2.33$

(d) $t+ = 4.17s, y^+ = 3.37$ (e) $t+ = 5.56s, y^+ = 4.28$ (f) $t+ = 6.95s, y^+ = 5.13$

(g) $t+ = 8.34s, y^+ = 5.92$ (h) $t+ = 9.73s, y^+ = 6.63$ (i) $t+ = 11.12s, y^+ = 7.31$

(j) $t+ = 12.51s, y^+ = 7.96$ (k) $t+ = 13.9s, y^+ = 8.52$ (l) $t+ = 15.32s, y^+ = 9.06$

Figure E.16: Evolution of $\overline{u_x}$ field for condition G

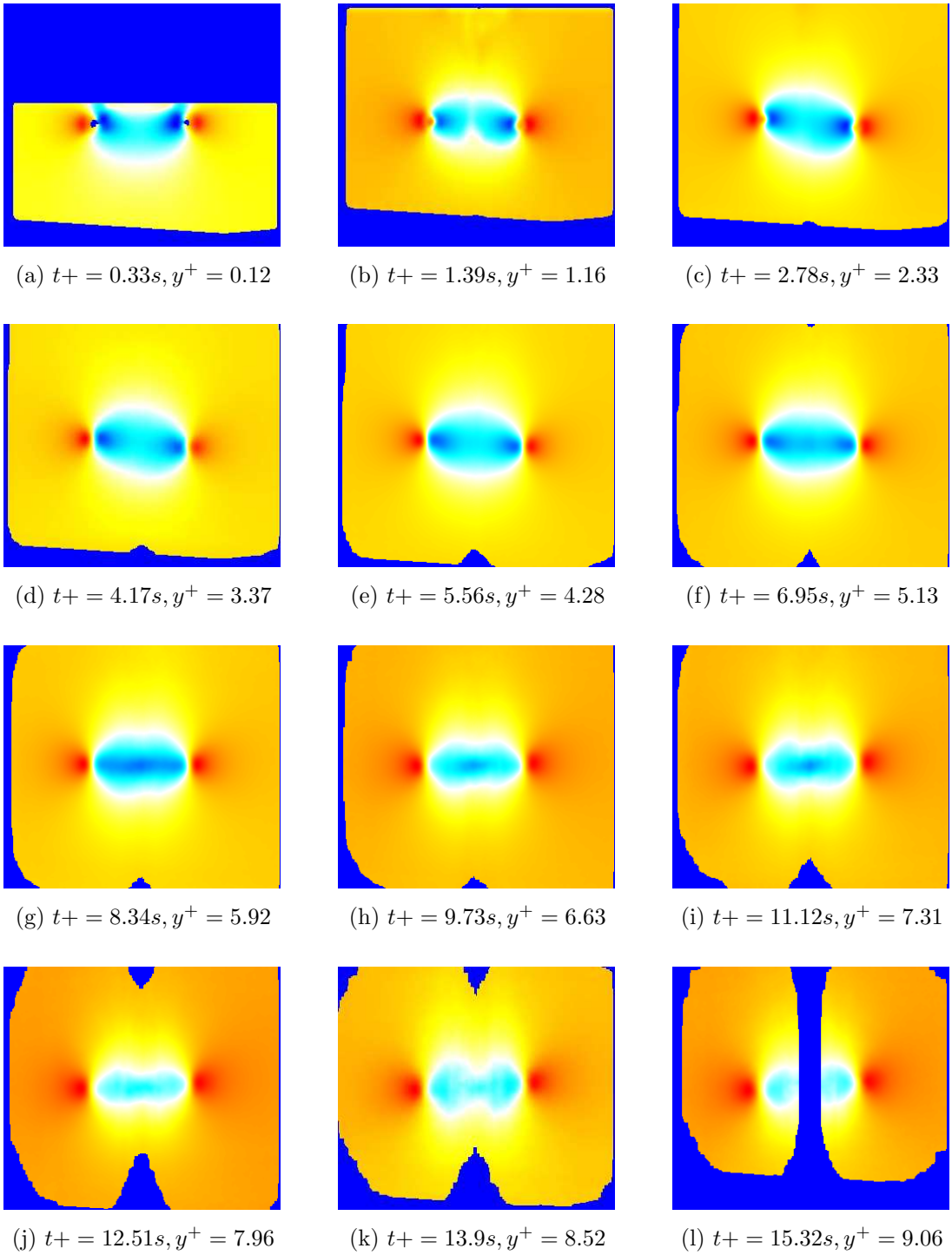

(a) $t+ = 0.33s, y^+ = 0.12$ (b) $t+ = 1.39s, y^+ = 1.16$ (c) $t+ = 2.78s, y^+ = 2.33$

(d) $t+ = 4.17s, y^+ = 3.37$ (e) $t+ = 5.56s, y^+ = 4.28$ (f) $t+ = 6.95s, y^+ = 5.13$

(g) $t+ = 8.34s, y^+ = 5.92$ (h) $t+ = 9.73s, y^+ = 6.63$ (i) $t+ = 11.12s, y^+ = 7.31$

(j) $t+ = 12.51s, y^+ = 7.96$ (k) $t+ = 13.9s, y^+ = 8.52$ (l) $t+ = 15.32s, y^+ = 9.06$

Figure E.17: Evolution of $\overline{u_y}$ field for condition G

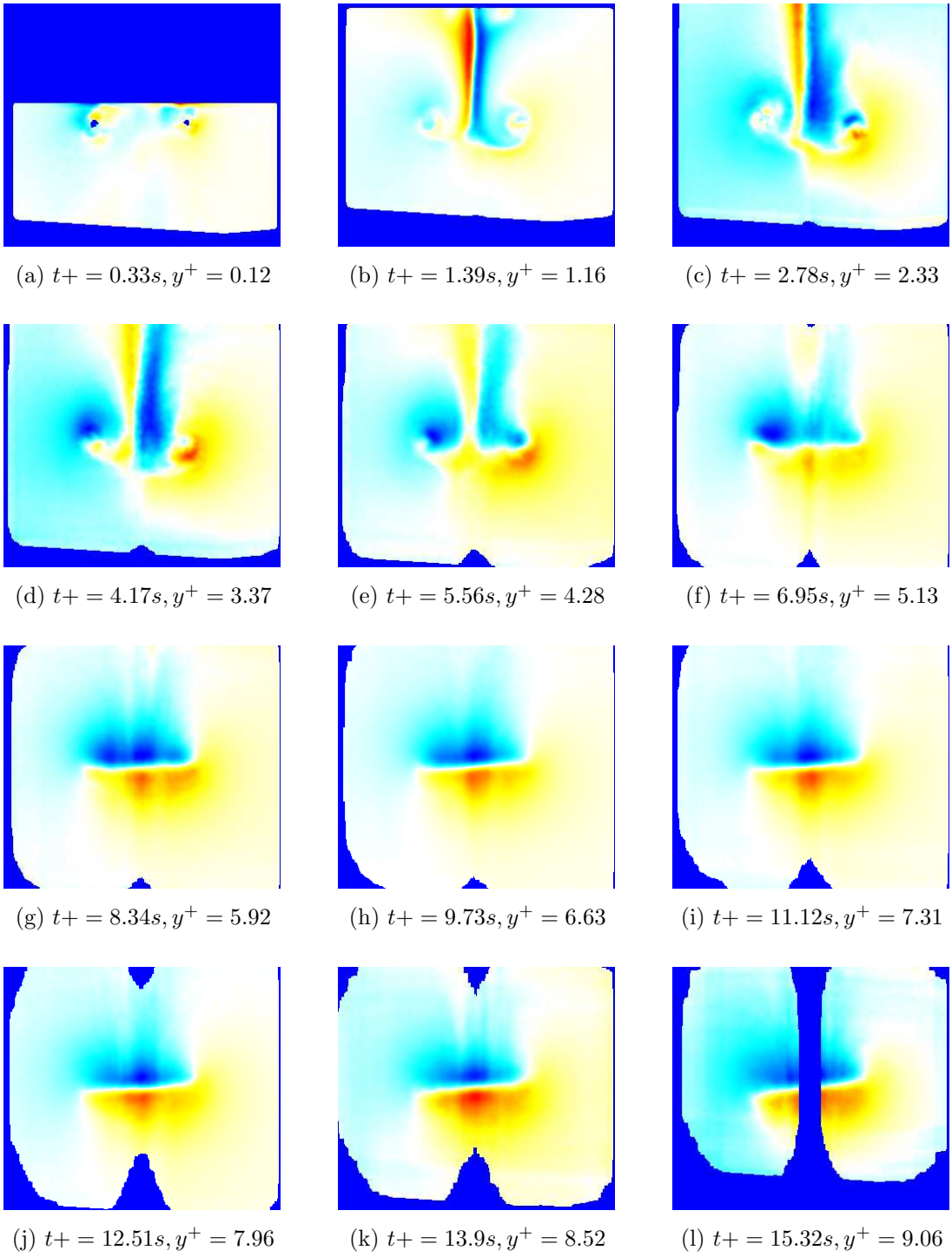

(a) $t+ = 0.33s, y^+ = 0.12$ (b) $t+ = 1.39s, y^+ = 1.16$ (c) $t+ = 2.78s, y^+ = 2.33$

(d) $t+ = 4.17s, y^+ = 3.37$ (e) $t+ = 5.56s, y^+ = 4.28$ (f) $t+ = 6.95s, y^+ = 5.13$

(g) $t+ = 8.34s, y^+ = 5.92$ (h) $t+ = 9.73s, y^+ = 6.63$ (i) $t+ = 11.12s, y^+ = 7.31$

(j) $t+ = 12.51s, y^+ = 7.96$ (k) $t+ = 13.9s, y^+ = 8.52$ (l) $t+ = 15.32s, y^+ = 9.06$

Figure E.18: Evolution of $\overline{u_z}$ field for condition G

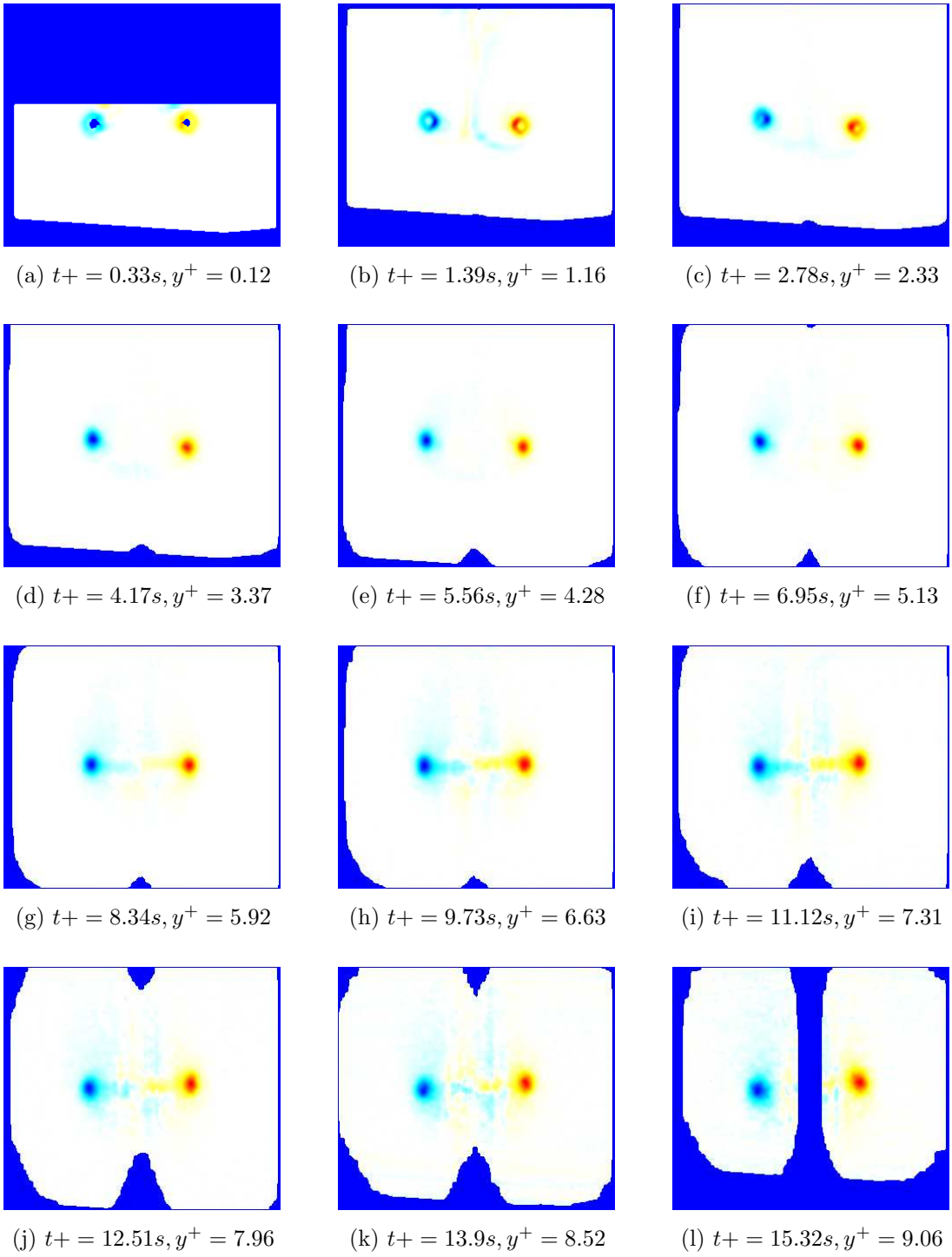

(a) $t+ = 0.33s, y^+ = 0.12$ (b) $t+ = 1.39s, y^+ = 1.16$ (c) $t+ = 2.78s, y^+ = 2.33$

(d) $t+ = 4.17s, y^+ = 3.37$ (e) $t+ = 5.56s, y^+ = 4.28$ (f) $t+ = 6.95s, y^+ = 5.13$

(g) $t+ = 8.34s, y^+ = 5.92$ (h) $t+ = 9.73s, y^+ = 6.63$ (i) $t+ = 11.12s, y^+ = 7.31$

(j) $t+ = 12.51s, y^+ = 7.96$ (k) $t+ = 13.9s, y^+ = 8.52$ (l) $t+ = 15.32s, y^+ = 9.06$

Figure E.19: Evolution of $\overline{\omega_z}$ field for condition G

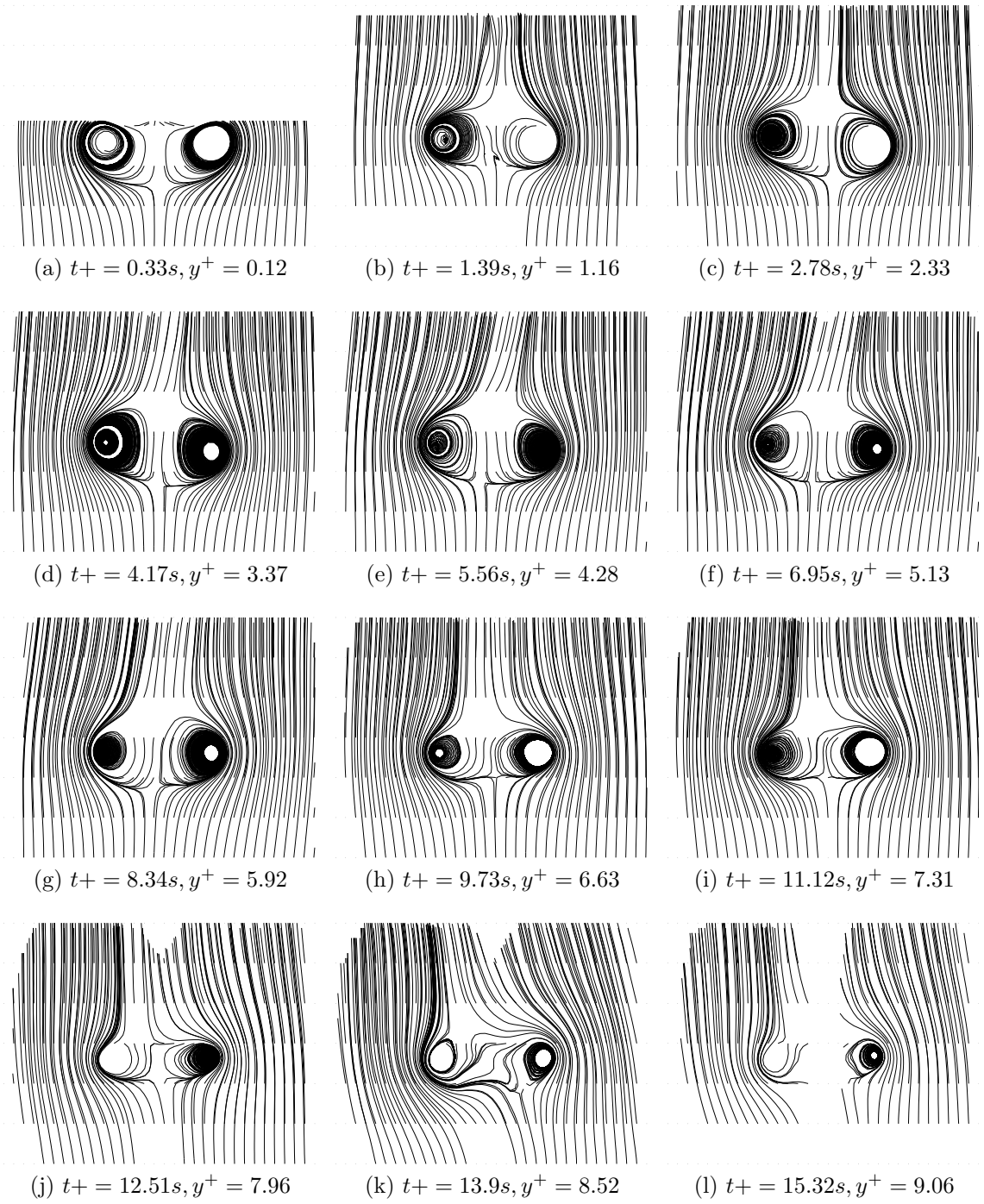

(a) $t+ = 0.33s, y^+ = 0.12$ (b) $t+ = 1.39s, y^+ = 1.16$ (c) $t+ = 2.78s, y^+ = 2.33$

(d) $t+ = 4.17s, y^+ = 3.37$ (e) $t+ = 5.56s, y^+ = 4.28$ (f) $t+ = 6.95s, y^+ = 5.13$

(g) $t+ = 8.34s, y^+ = 5.92$ (h) $t+ = 9.73s, y^+ = 6.63$ (i) $t+ = 11.12s, y^+ = 7.31$

(j) $t+ = 12.51s, y^+ = 7.96$ (k) $t+ = 13.9s, y^+ = 8.52$ (l) $t+ = 15.32s, y^+ = 9.06$

Figure E.20: Evolution of $\overline{\psi}$ field for condition G

E.5 Condition H

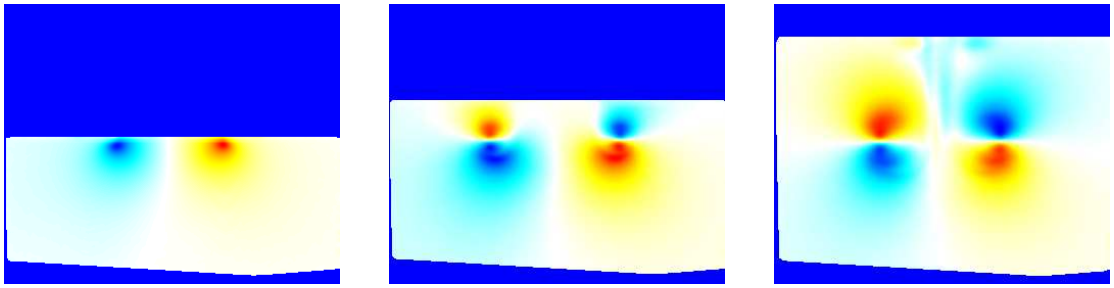

(a) $t+ = 0.12s, y^+ = 0.02$ (b) $t+ = 0.61s, y^+ = 0.34$ (c) $t+ = 1.35s, y^+ = 0.89$

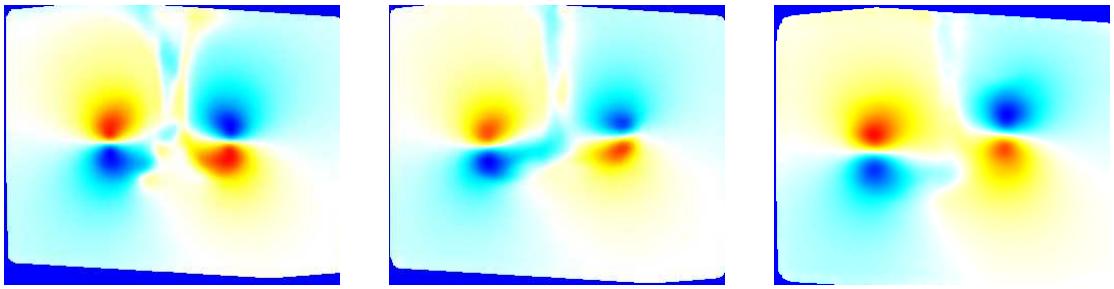

(d) $t+ = 1.97s, y^+ = 1.42$ (e) $t+ = 2.59s, y^+ = 1.86$ (f) $t+ = 3.33s, y^+ = 2.24$

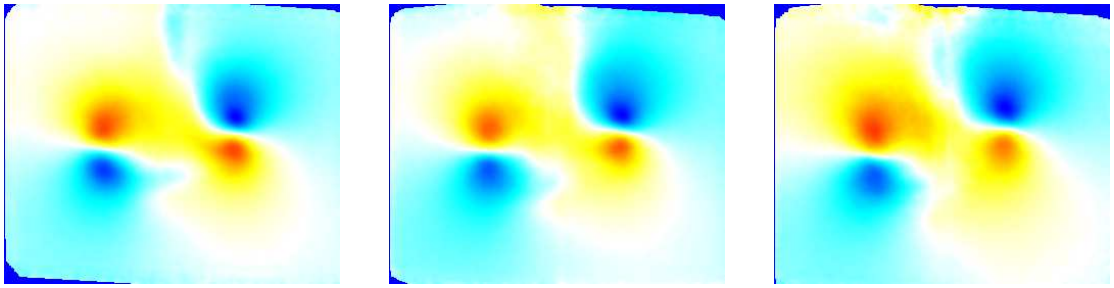

(g) $t+ = 3.94s, y^+ = 2.56$ (h) $t+ = 4.68s, y^+ = 2.92$ (i) $t+ = 5.3s, y^+ = 3.18$

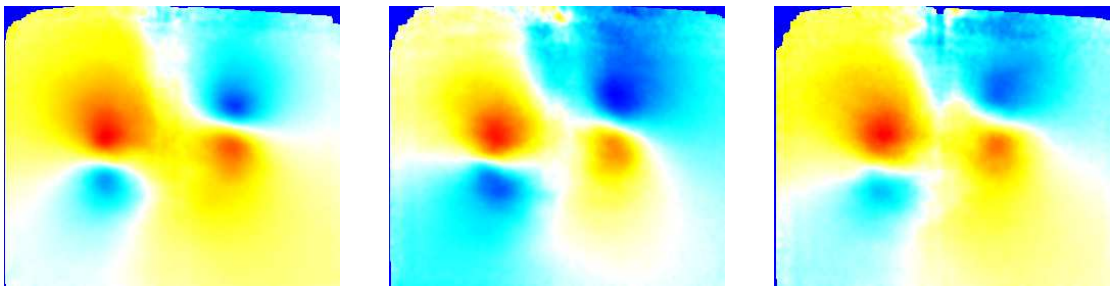

(j) $t+ = 5.92s, y^+ = 3.39$ (k) $t+ = 6.66s, y^+ = 3.67$ (l) $t+ = 7.27s, y^+ = 3.89$

Figure E.21: Evolution of $\overline{u_x}$ field for condition H

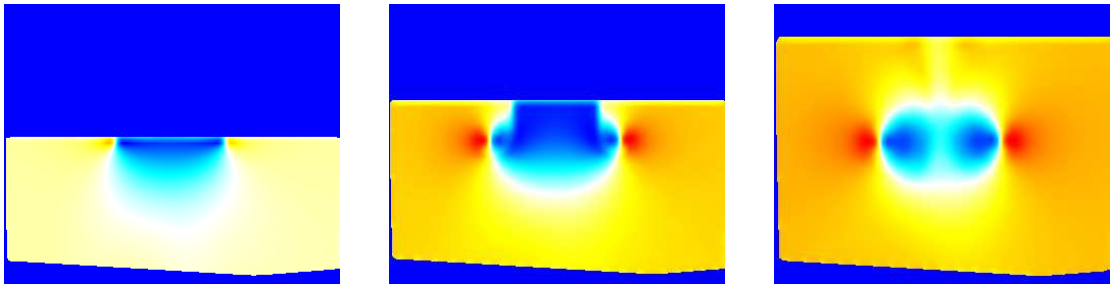

(a) $t+ = 0.12s, y^+ = 0.02$ (b) $t+ = 0.61s, y^+ = 0.34$ (c) $t+ = 1.35s, y^+ = 0.89$

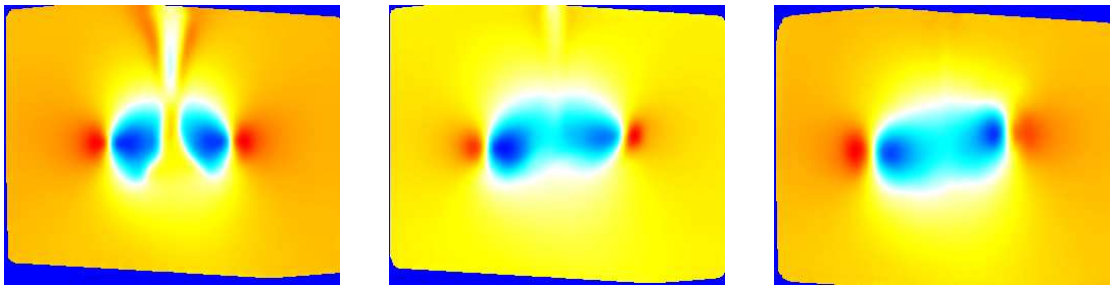

(d) $t+ = 1.97s, y^+ = 1.42$ (e) $t+ = 2.59s, y^+ = 1.86$ (f) $t+ = 3.33s, y^+ = 2.24$

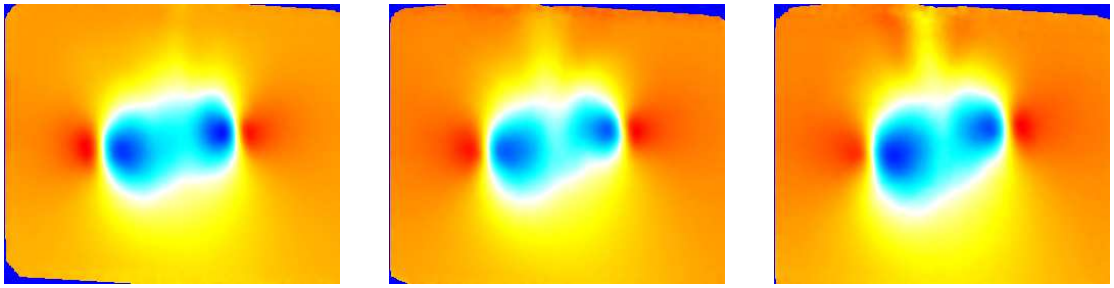

(g) $t+ = 3.94s, y^+ = 2.56$ (h) $t+ = 4.68s, y^+ = 2.92$ (i) $t+ = 5.3s, y^+ = 3.18$

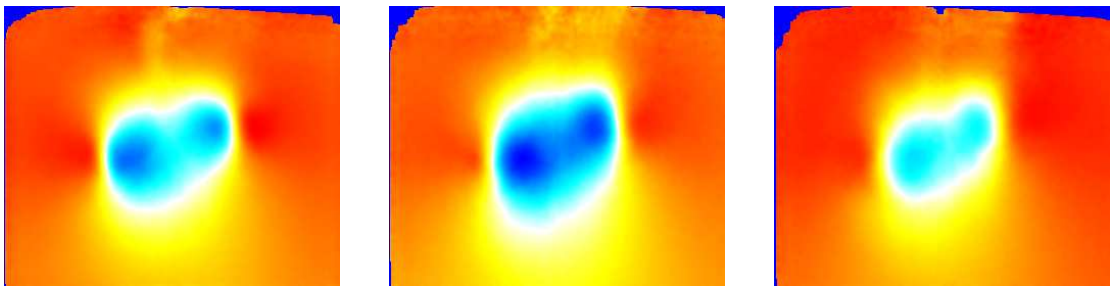

(j) $t+ = 5.92s, y^+ = 3.39$ (k) $t+ = 6.66s, y^+ = 3.67$ (l) $t+ = 7.27s, y^+ = 3.89$

Figure E.22: Evolution of $\overline{u_y}$ field for condition H

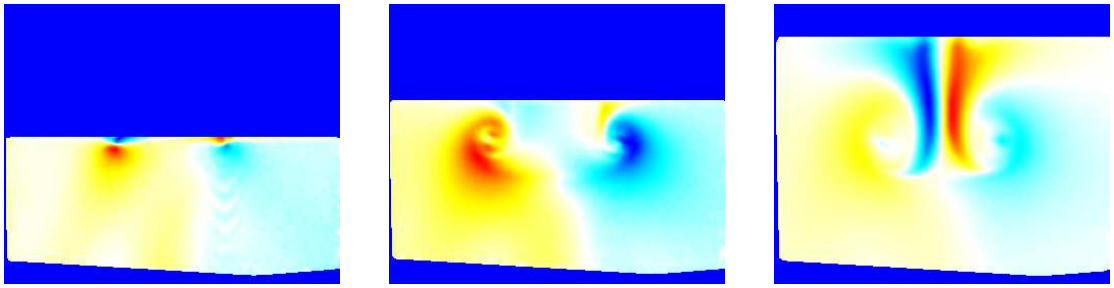

(a) $t+ = 0.12s, y^+ = 0.02$ (b) $t+ = 0.61s, y^+ = 0.34$ (c) $t+ = 1.35s, y^+ = 0.89$

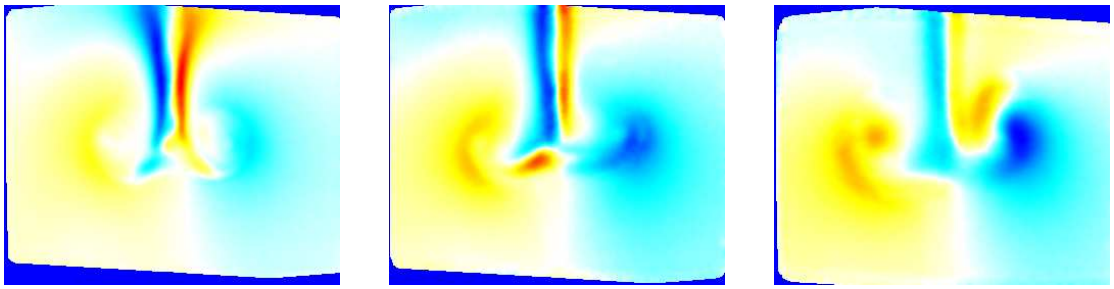

(d) $t+ = 1.97s, y^+ = 1.42$ (e) $t+ = 2.59s, y^+ = 1.86$ (f) $t+ = 3.33s, y^+ = 2.24$

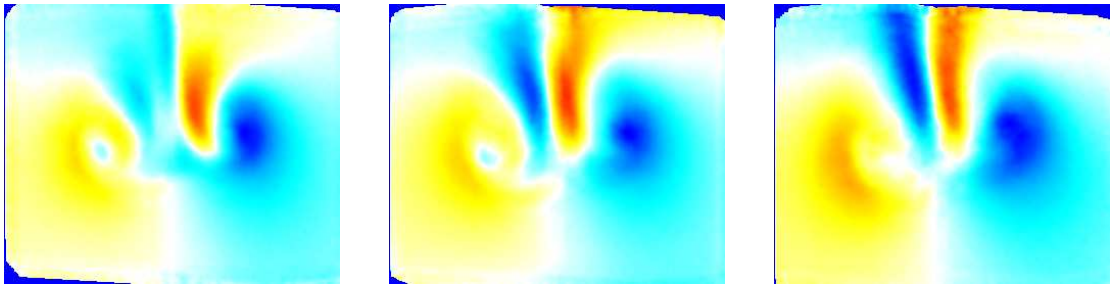

(g) $t+ = 3.94s, y^+ = 2.56$ (h) $t+ = 4.68s, y^+ = 2.92$ (i) $t+ = 5.3s, y^+ = 3.18$

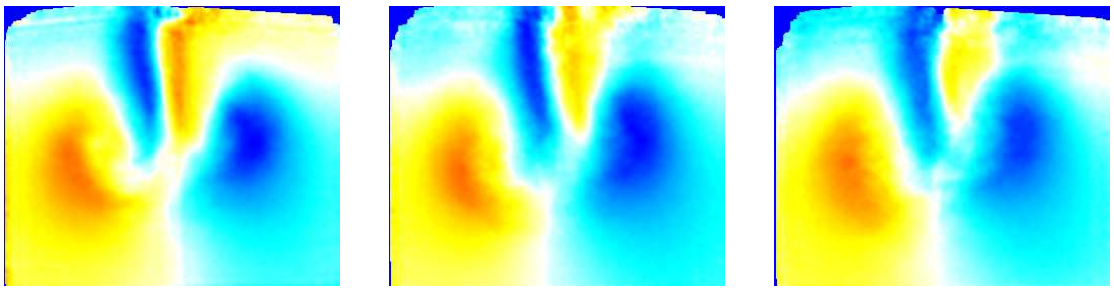

(j) $t+ = 5.92s, y^+ = 3.39$ (k) $t+ = 6.66s, y^+ = 3.67$ (l) $t+ = 7.27s, y^+ = 3.89$

Figure E.23: Evolution of $\overline{u_z}$ field for condition H

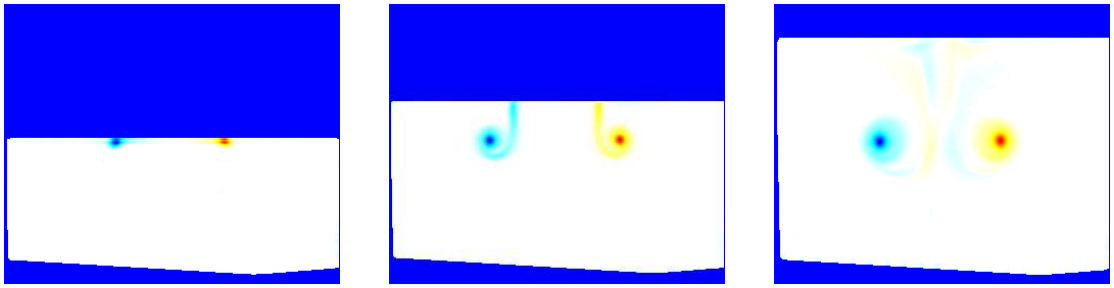

(a) $t+ = 0.12s, y^+ = 0.02$ (b) $t+ = 0.61s, y^+ = 0.34$ (c) $t+ = 1.35s, y^+ = 0.89$

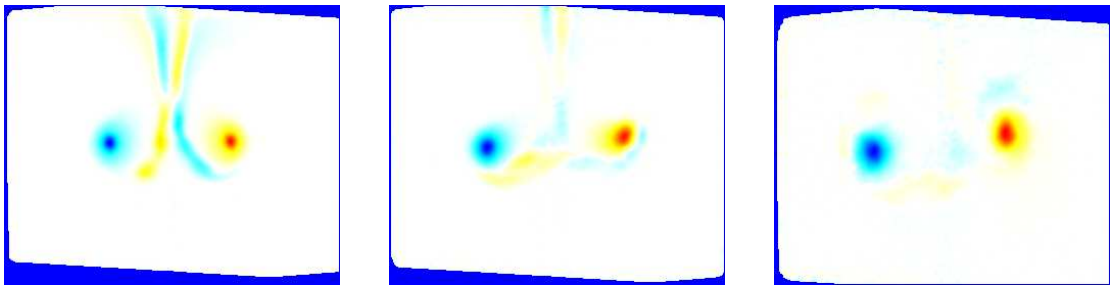

(d) $t+ = 1.97s, y^+ = 1.42$ (e) $t+ = 2.59s, y^+ = 1.86$ (f) $t+ = 3.33s, y^+ = 2.24$

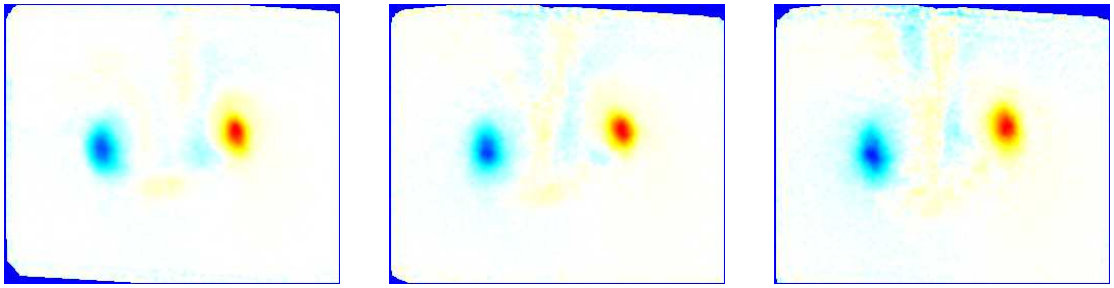

(g) $t+ = 3.94s, y^+ = 2.56$ (h) $t+ = 4.68s, y^+ = 2.92$ (i) $t+ = 5.3s, y^+ = 3.18$

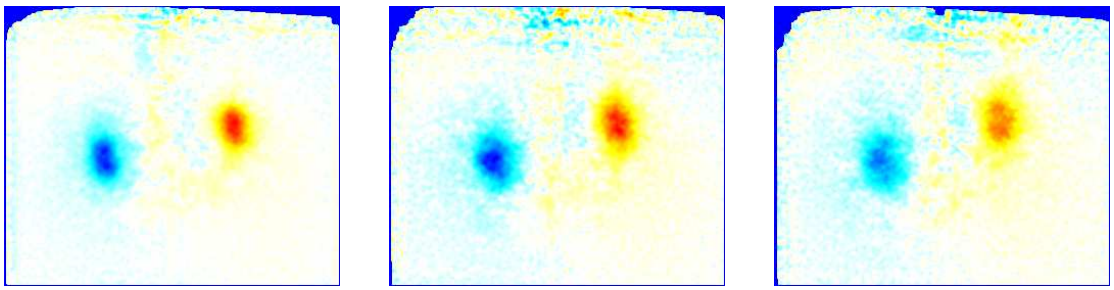

(j) $t+ = 5.92s, y^+ = 3.39$ (k) $t+ = 6.66s, y^+ = 3.67$ (l) $t+ = 7.27s, y^+ = 3.89$

Figure E.24: Evolution of $\overline{\omega_z}$ field for condition H

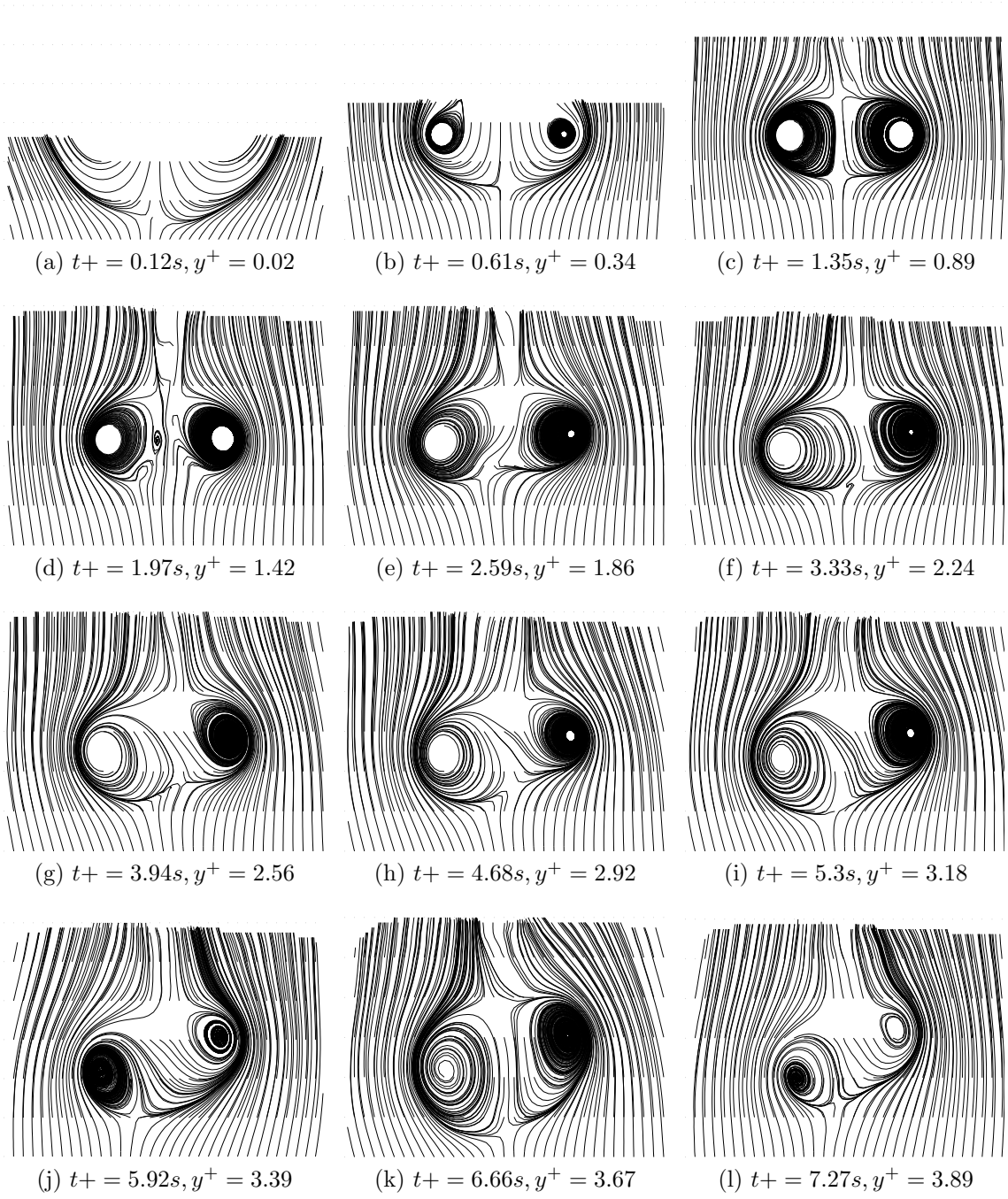

(a) $t+ = 0.12s, y^+ = 0.02$ (b) $t+ = 0.61s, y^+ = 0.34$ (c) $t+ = 1.35s, y^+ = 0.89$

(d) $t+ = 1.97s, y^+ = 1.42$ (e) $t+ = 2.59s, y^+ = 1.86$ (f) $t+ = 3.33s, y^+ = 2.24$

(g) $t+ = 3.94s, y^+ = 2.56$ (h) $t+ = 4.68s, y^+ = 2.92$ (i) $t+ = 5.3s, y^+ = 3.18$

(j) $t+ = 5.92s, y^+ = 3.39$ (k) $t+ = 6.66s, y^+ = 3.67$ (l) $t+ = 7.27s, y^+ = 3.89$

Figure E.25: Evolution of $\overline{\psi}$ field for condition H

E.6 Condition I

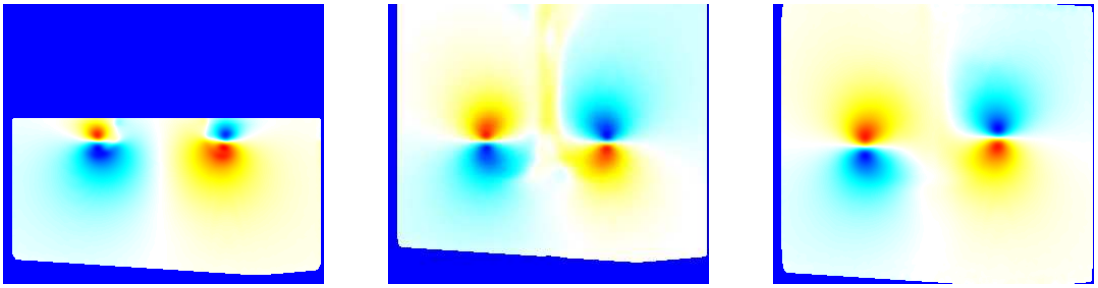

(a) $t+ = 0.44s, y^+ = 0.12$ (b) $t+ = 1.85s, y^+ = 1.5$ (c) $t+ = 3.22s, y^+ = 2.63$

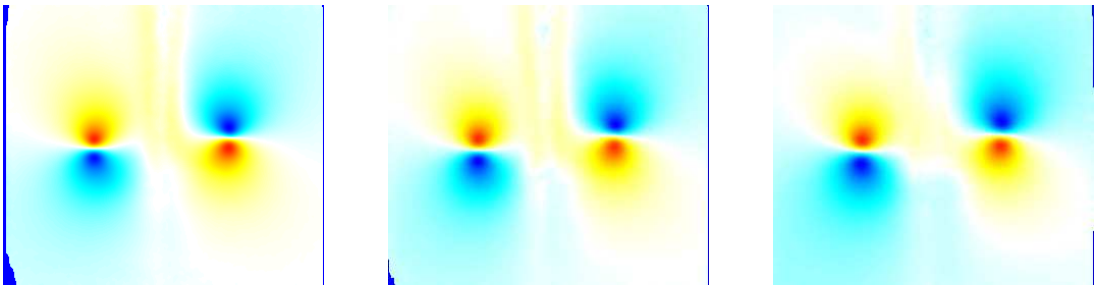

(d) $t+ = 5.07s, y^+ = 3.98$ (e) $t+ = 6.47s, y^+ = 4.86$ (f) $t+ = 8.32s, y^+ = 5.92$

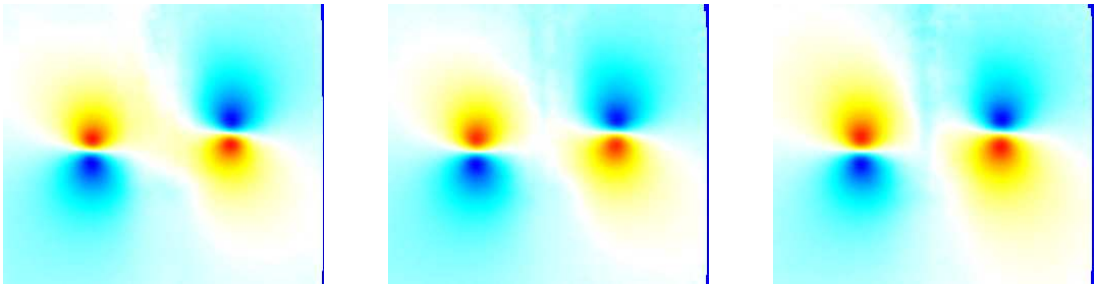

(g) $t+ = 9.73s, y^+ = 6.66$ (h) $t+ = 11.58s, y^+ = 7.57$ (i) $t+ = 12.94s, y^+ = 8.25$

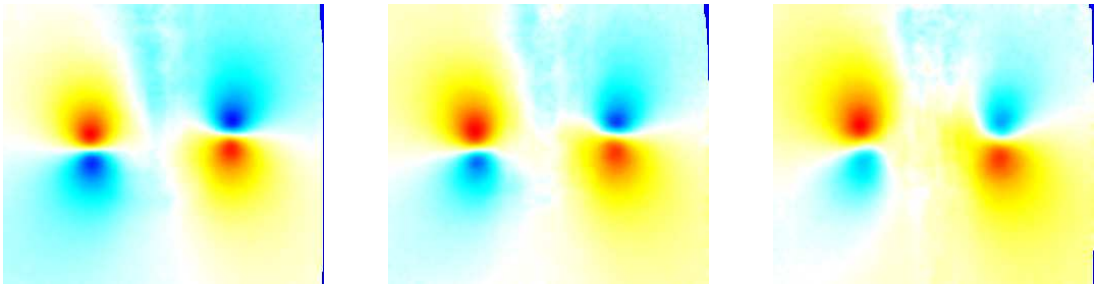

(j) $t+ = 14.79s, y^+ = 9.12$ (k) $t+ = 16.2s, y^+ = 9.75$ (l) $t+ = 18.05s, y^+ = 10.57$

Figure E.26: Evolution of $\overline{u_x}$ field for condition I

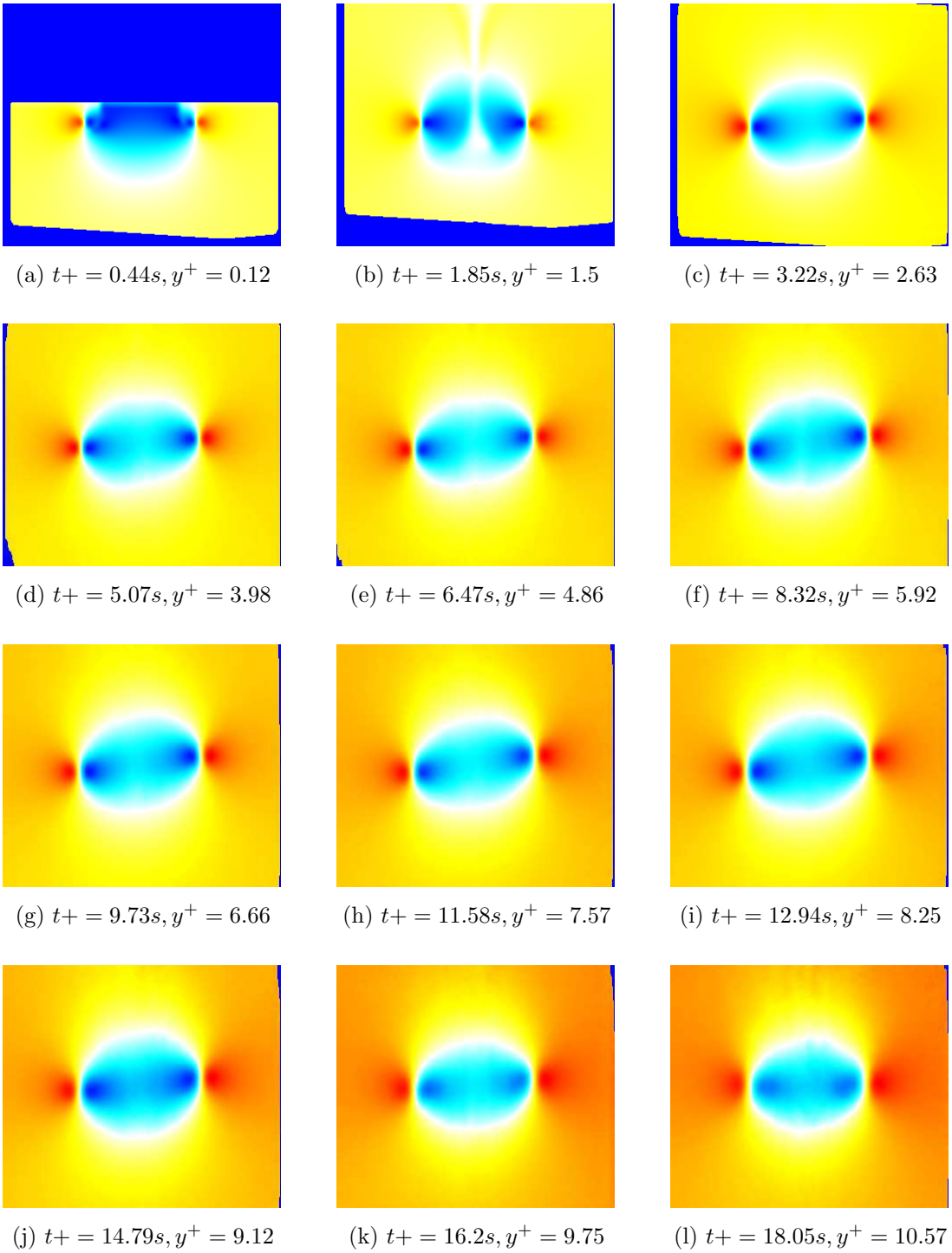

(a) $t+ = 0.44s, y^+ = 0.12$ (b) $t+ = 1.85s, y^+ = 1.5$ (c) $t+ = 3.22s, y^+ = 2.63$

(d) $t+ = 5.07s, y^+ = 3.98$ (e) $t+ = 6.47s, y^+ = 4.86$ (f) $t+ = 8.32s, y^+ = 5.92$

(g) $t+ = 9.73s, y^+ = 6.66$ (h) $t+ = 11.58s, y^+ = 7.57$ (i) $t+ = 12.94s, y^+ = 8.25$

(j) $t+ = 14.79s, y^+ = 9.12$ (k) $t+ = 16.2s, y^+ = 9.75$ (l) $t+ = 18.05s, y^+ = 10.57$

Figure E.27: Evolution of $\overline{u_y}$ field for condition I

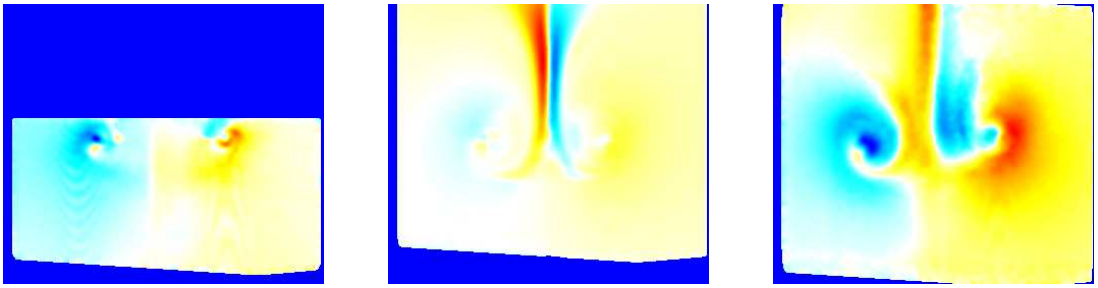

(a) $t+ = 0.44s, y^+ = 0.12$ (b) $t+ = 1.85s, y^+ = 1.5$ (c) $t+ = 3.22s, y^+ = 2.63$

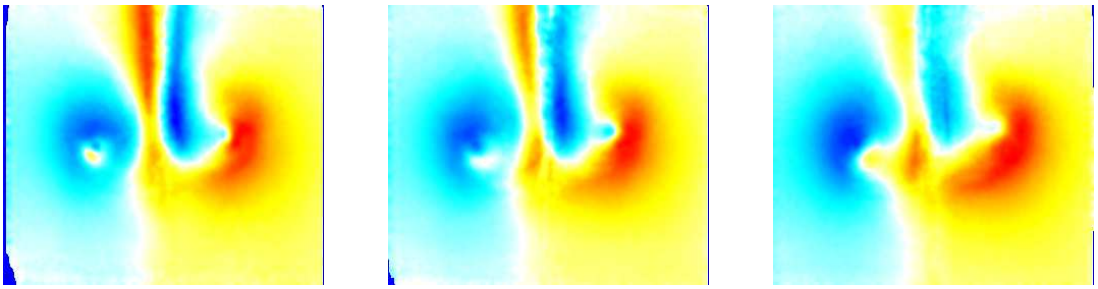

(d) $t+ = 5.07s, y^+ = 3.98$ (e) $t+ = 6.47s, y^+ = 4.86$ (f) $t+ = 8.32s, y^+ = 5.92$

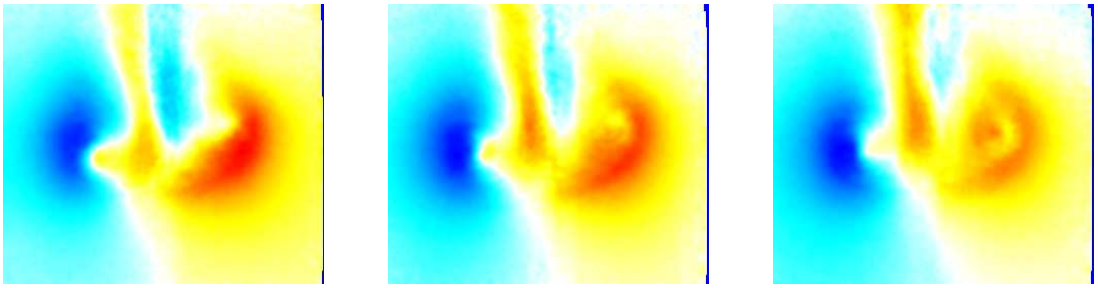

(g) $t+ = 9.73s, y^+ = 6.66$ (h) $t+ = 11.58s, y^+ = 7.57$ (i) $t+ = 12.94s, y^+ = 8.25$

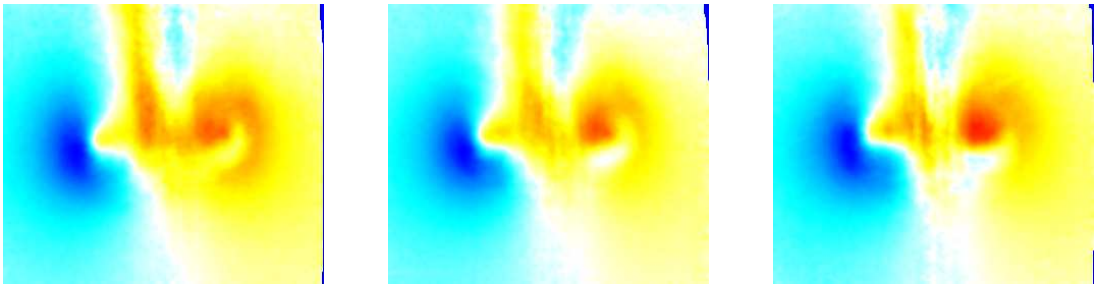

(j) $t+ = 14.79s, y^+ = 9.12$ (k) $t+ = 16.2s, y^+ = 9.75$ (l) $t+ = 18.05s, y^+ = 10.57$

Figure E.28: Evolution of $\overline{u_z}$ field for condition I

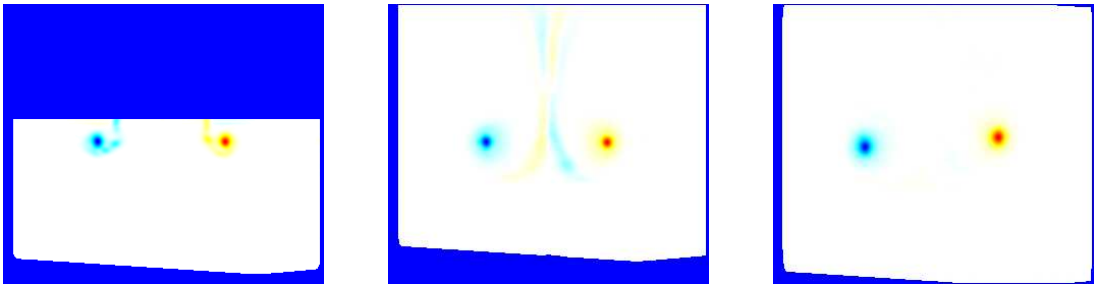

(a) $t+ = 0.44s, y^+ = 0.12$ (b) $t+ = 1.85s, y^+ = 1.5$ (c) $t+ = 3.22s, y^+ = 2.63$

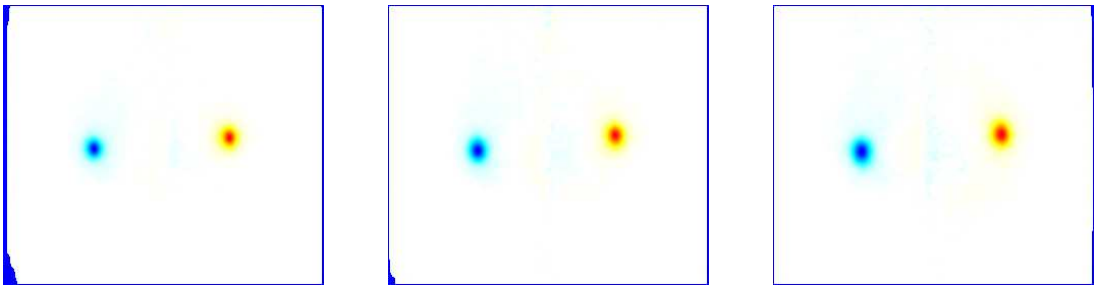

(d) $t+ = 5.07s, y^+ = 3.98$ (e) $t+ = 6.47s, y^+ = 4.86$ (f) $t+ = 8.32s, y^+ = 5.92$

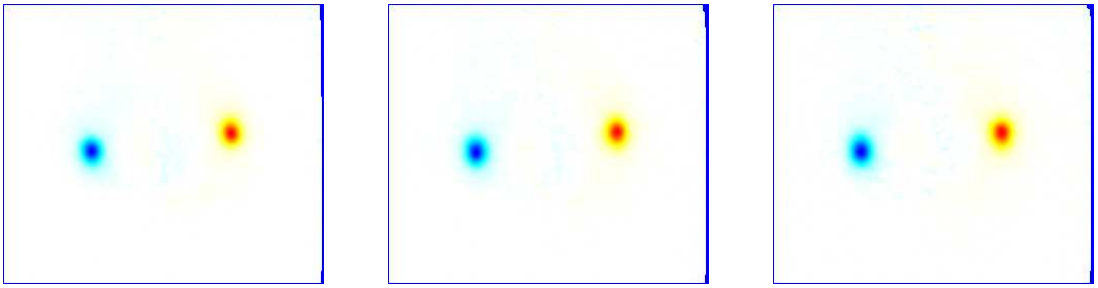

(g) $t+ = 9.73s, y^+ = 6.66$ (h) $t+ = 11.58s, y^+ = 7.57$ (i) $t+ = 12.94s, y^+ = 8.25$

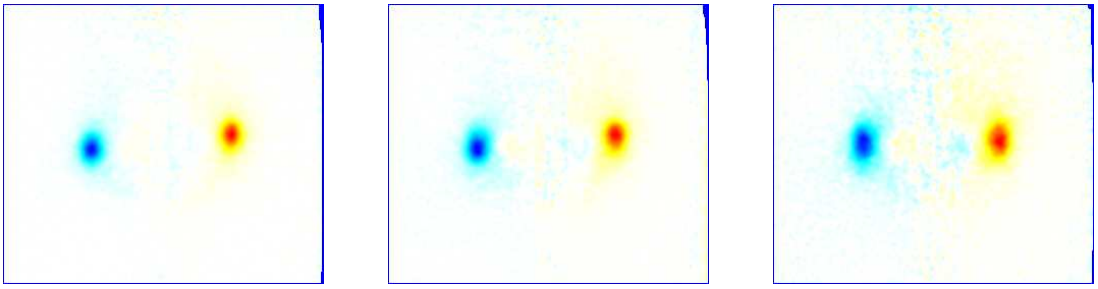

(j) $t+ = 14.79s, y^+ = 9.12$ (k) $t+ = 16.2s, y^+ = 9.75$ (l) $t+ = 18.05s, y^+ = 10.57$

Figure E.29: Evolution of $\overline{\omega_z}$ field for condition I

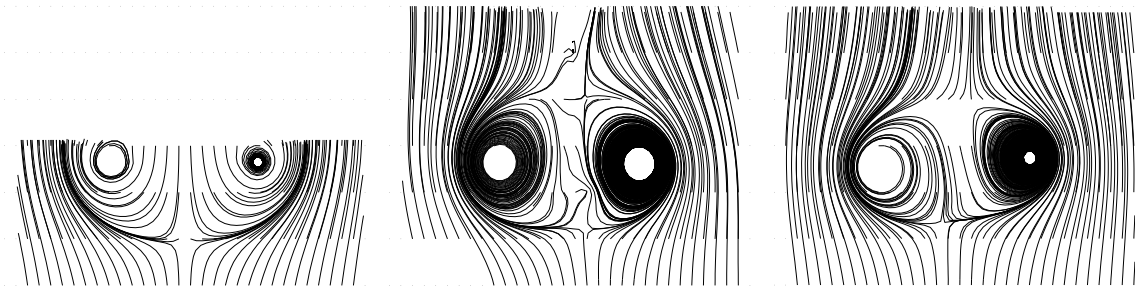

(a) $t+ = 0.44s, y^+ = 0.12$ (b) $t+ = 1.85s, y^+ = 1.5$ (c) $t+ = 3.22s, y^+ = 2.63$

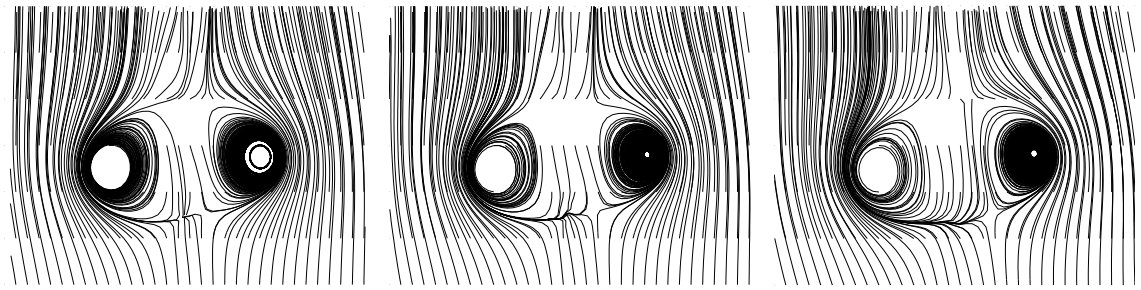

(d) $t+ = 5.07s, y^+ = 3.98$ (e) $t+ = 6.47s, y^+ = 4.86$ (f) $t+ = 8.32s, y^+ = 5.92$

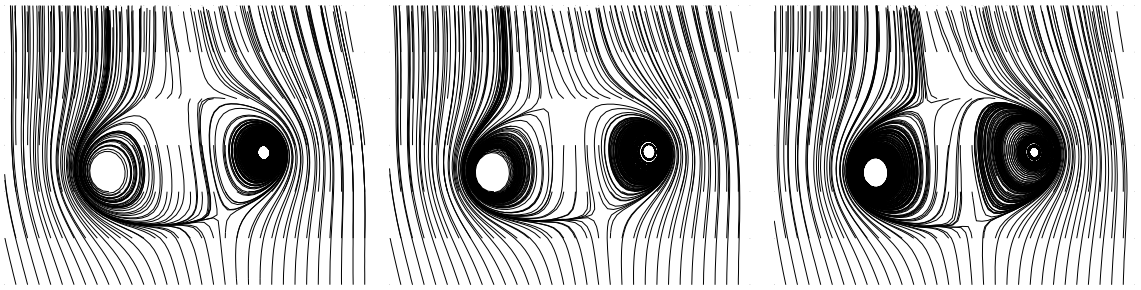

(g) $t+ = 9.73s, y^+ = 6.66$ (h) $t+ = 11.58s, y^+ = 7.57$ (i) $t+ = 12.94s, y^+ = 8.25$

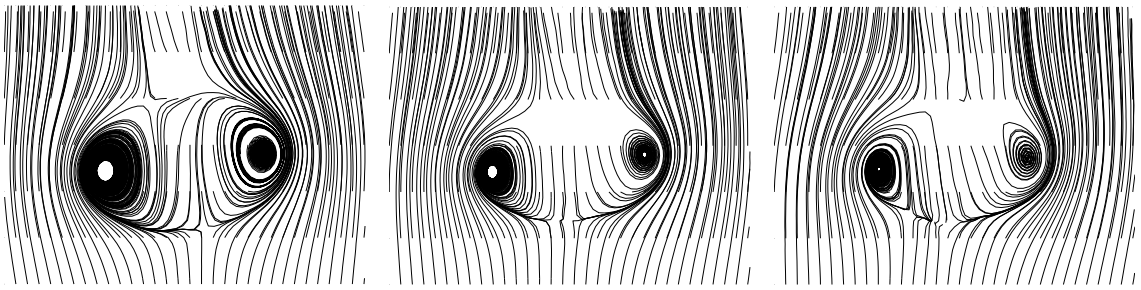

(j) $t+ = 14.79s, y^+ = 9.12$ (k) $t+ = 16.2s, y^+ = 9.75$ (l) $t+ = 18.05s, y^+ = 10.57$

Figure E.30: Evolution of $\overline{\psi}$ field for condition I

E.7 Condition J

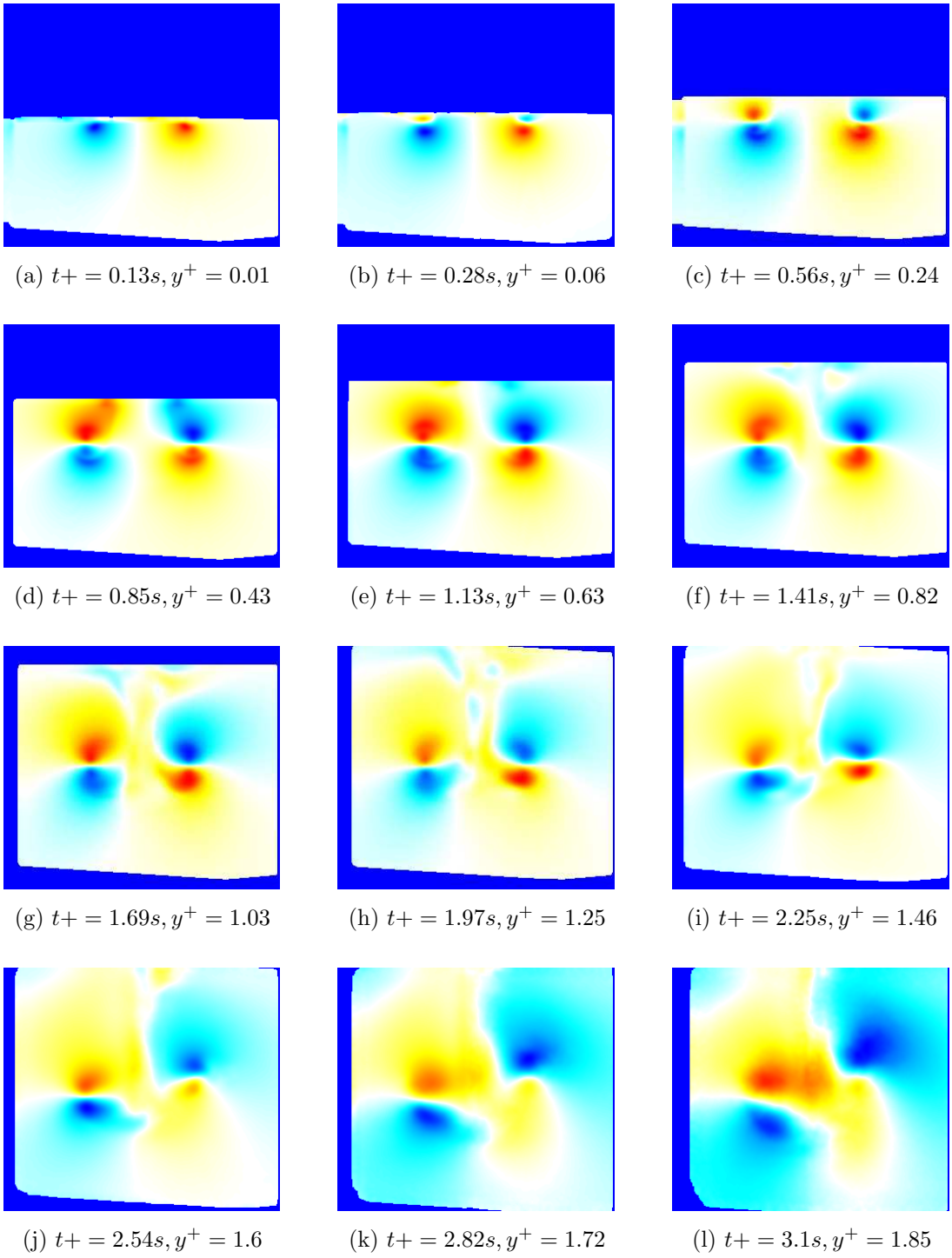

(a) $t+ = 0.13s, y^+ = 0.01$ (b) $t+ = 0.28s, y^+ = 0.06$ (c) $t+ = 0.56s, y^+ = 0.24$

(d) $t+ = 0.85s, y^+ = 0.43$ (e) $t+ = 1.13s, y^+ = 0.63$ (f) $t+ = 1.41s, y^+ = 0.82$

(g) $t+ = 1.69s, y^+ = 1.03$ (h) $t+ = 1.97s, y^+ = 1.25$ (i) $t+ = 2.25s, y^+ = 1.46$

(j) $t+ = 2.54s, y^+ = 1.6$ (k) $t+ = 2.82s, y^+ = 1.72$ (l) $t+ = 3.1s, y^+ = 1.85$

Figure E.31: Evolution of $\overline{u_x}$ field for condition J

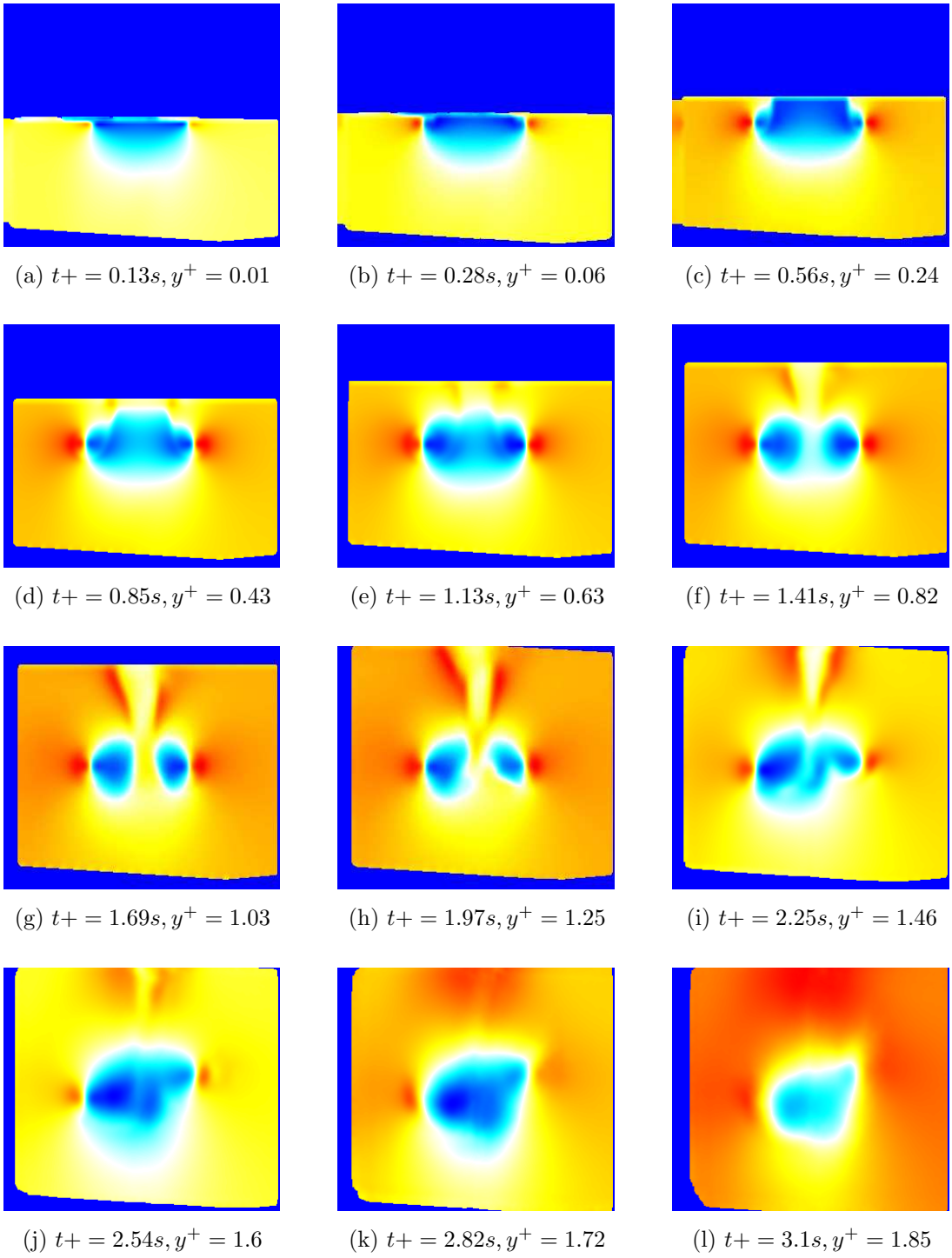

(a) $t+ = 0.13s, y^+ = 0.01$ (b) $t+ = 0.28s, y^+ = 0.06$ (c) $t+ = 0.56s, y^+ = 0.24$

(d) $t+ = 0.85s, y^+ = 0.43$ (e) $t+ = 1.13s, y^+ = 0.63$ (f) $t+ = 1.41s, y^+ = 0.82$

(g) $t+ = 1.69s, y^+ = 1.03$ (h) $t+ = 1.97s, y^+ = 1.25$ (i) $t+ = 2.25s, y^+ = 1.46$

(j) $t+ = 2.54s, y^+ = 1.6$ (k) $t+ = 2.82s, y^+ = 1.72$ (l) $t+ = 3.1s, y^+ = 1.85$

Figure E.32: Evolution of $\overline{u_y}$ field for condition J

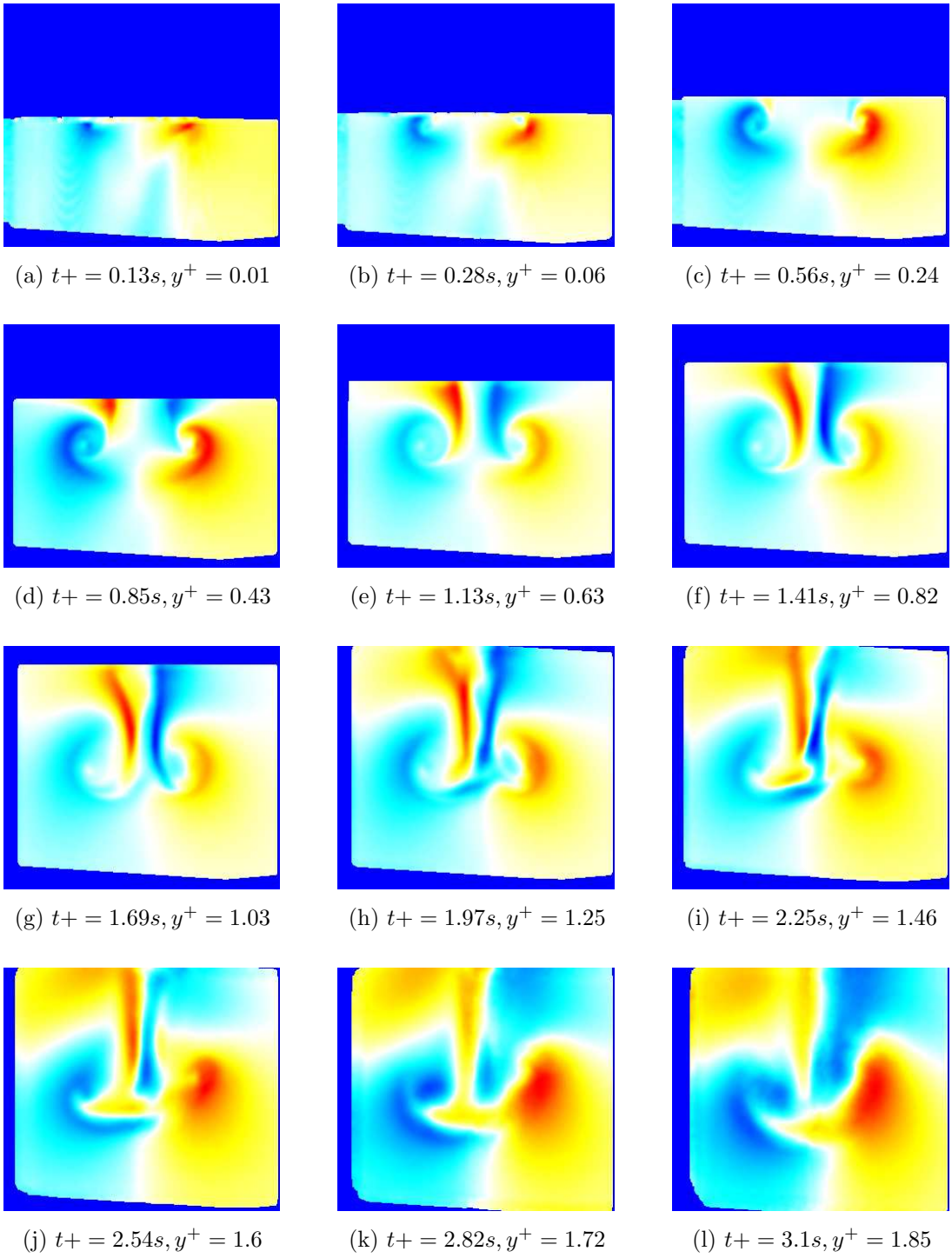

(a) $t+ = 0.13s, y^+ = 0.01$ (b) $t+ = 0.28s, y^+ = 0.06$ (c) $t+ = 0.56s, y^+ = 0.24$

(d) $t+ = 0.85s, y^+ = 0.43$ (e) $t+ = 1.13s, y^+ = 0.63$ (f) $t+ = 1.41s, y^+ = 0.82$

(g) $t+ = 1.69s, y^+ = 1.03$ (h) $t+ = 1.97s, y^+ = 1.25$ (i) $t+ = 2.25s, y^+ = 1.46$

(j) $t+ = 2.54s, y^+ = 1.6$ (k) $t+ = 2.82s, y^+ = 1.72$ (l) $t+ = 3.1s, y^+ = 1.85$

Figure E.33: Evolution of $\overline{u_z}$ field for condition J

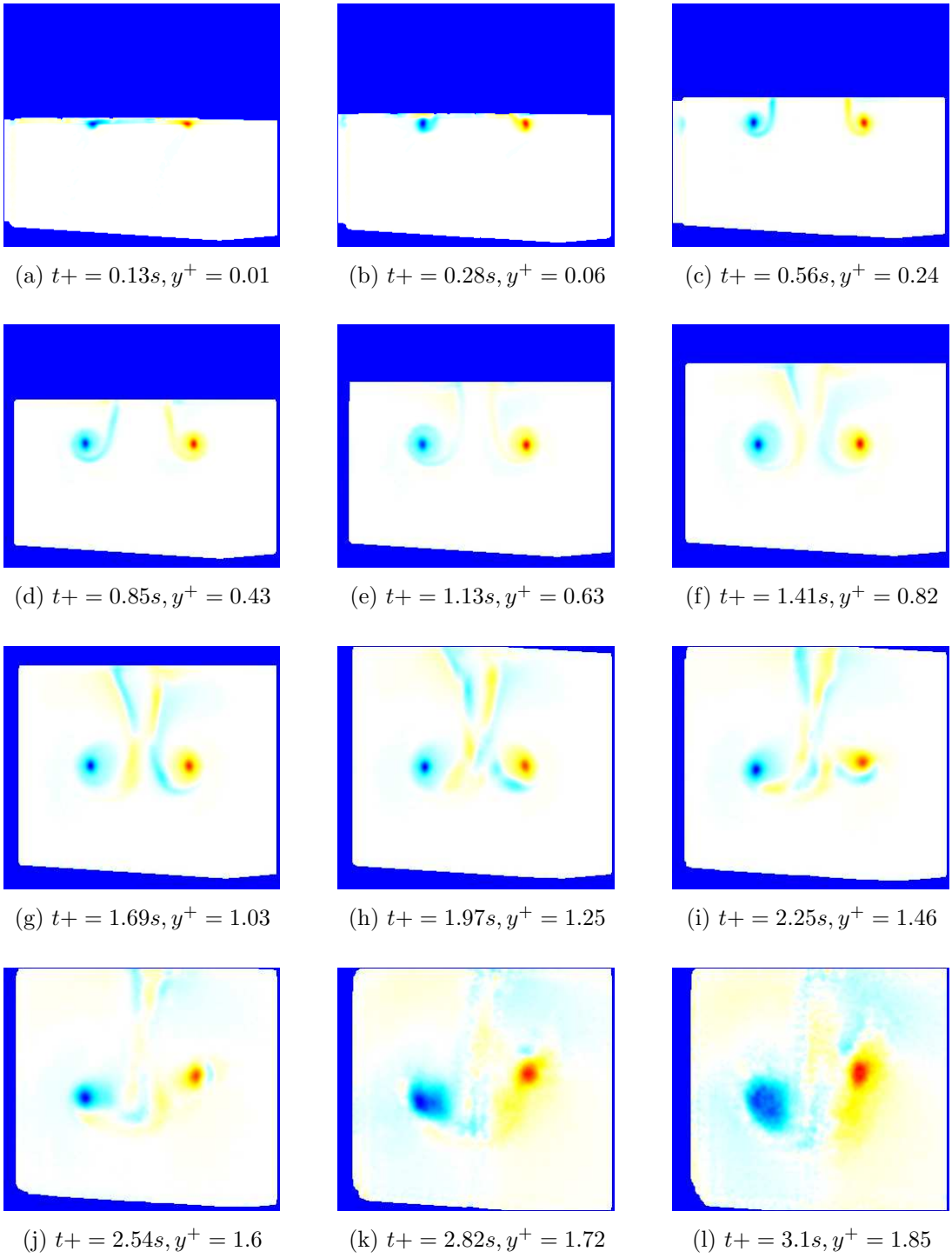

(a) $t+ = 0.13s, y^+ = 0.01$ (b) $t+ = 0.28s, y^+ = 0.06$ (c) $t+ = 0.56s, y^+ = 0.24$

(d) $t+ = 0.85s, y^+ = 0.43$ (e) $t+ = 1.13s, y^+ = 0.63$ (f) $t+ = 1.41s, y^+ = 0.82$

(g) $t+ = 1.69s, y^+ = 1.03$ (h) $t+ = 1.97s, y^+ = 1.25$ (i) $t+ = 2.25s, y^+ = 1.46$

(j) $t+ = 2.54s, y^+ = 1.6$ (k) $t+ = 2.82s, y^+ = 1.72$ (l) $t+ = 3.1s, y^+ = 1.85$

Figure E.34: Evolution of $\overline{\omega_z}$ field for condition J

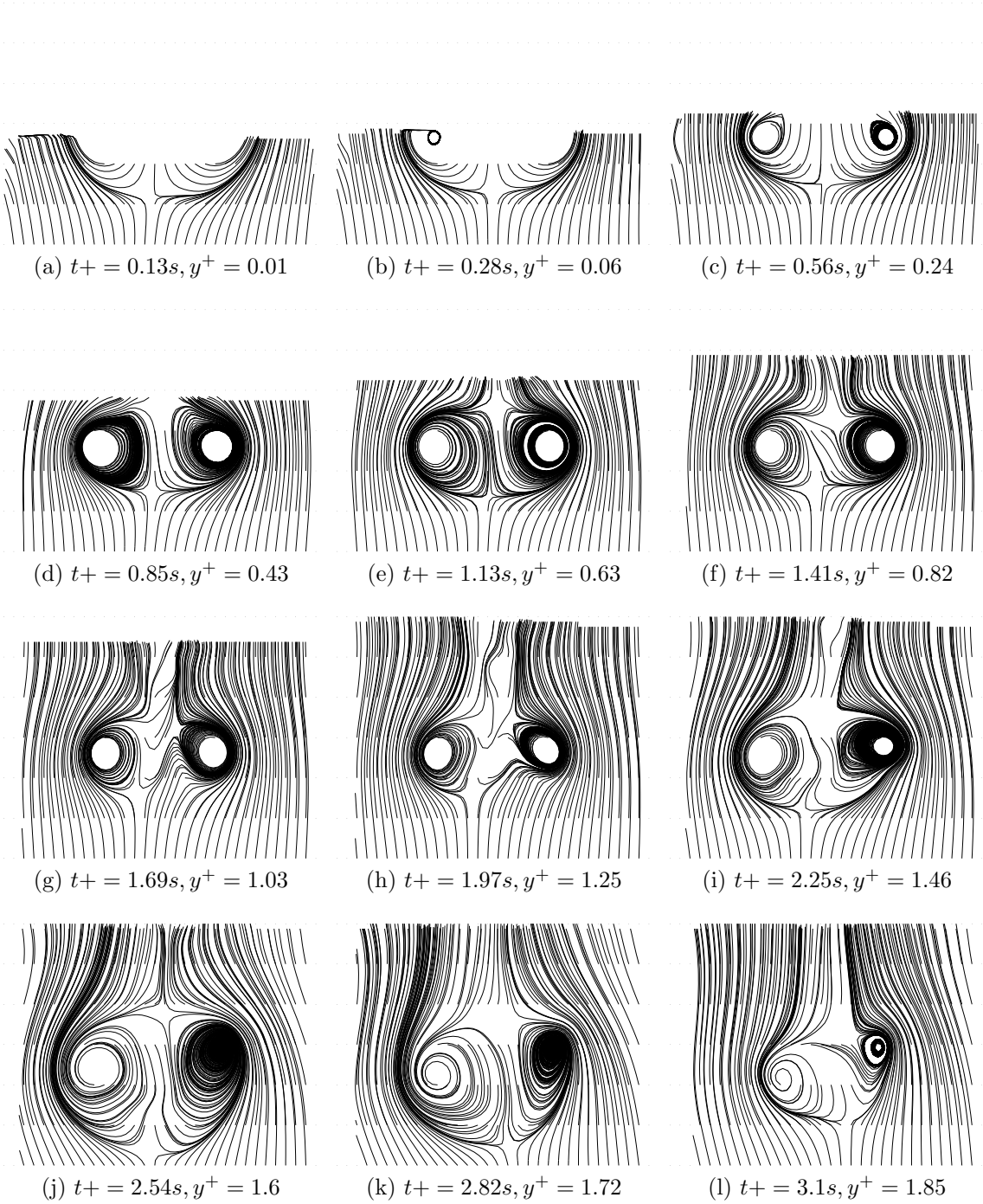

(a) $t+ = 0.13s, y^+ = 0.01$ (b) $t+ = 0.28s, y^+ = 0.06$ (c) $t+ = 0.56s, y^+ = 0.24$

(d) $t+ = 0.85s, y^+ = 0.43$ (e) $t+ = 1.13s, y^+ = 0.63$ (f) $t+ = 1.41s, y^+ = 0.82$

(g) $t+ = 1.69s, y^+ = 1.03$ (h) $t+ = 1.97s, y^+ = 1.25$ (i) $t+ = 2.25s, y^+ = 1.46$

(j) $t+ = 2.54s, y^+ = 1.6$ (k) $t+ = 2.82s, y^+ = 1.72$ (l) $t+ = 3.1s, y^+ = 1.85$

Figure E.35: Evolution of $\overline{\psi}$ field for condition J

E.8 Condition K

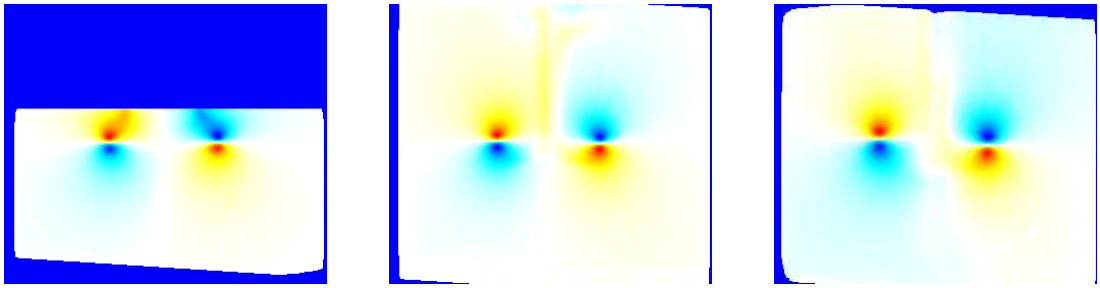

(a) $t+ = 0.41s, y^+ = 0.15$ (b) $t+ = 1.56s, y^+ = 1.32$ (c) $t+ = 3.12s, y^+ = 2.62$

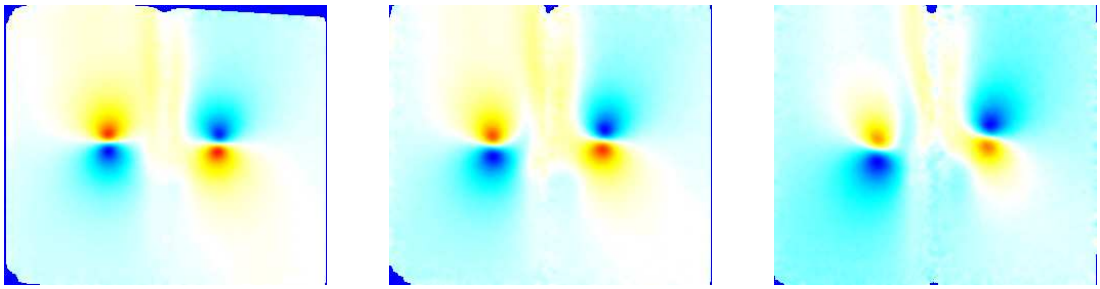

(d) $t+ = 4.67s, y^+ = 3.74$ (e) $t+ = 6.23s, y^+ = 4.72$ (f) $t+ = 7.79s, y^+ = 5.59$

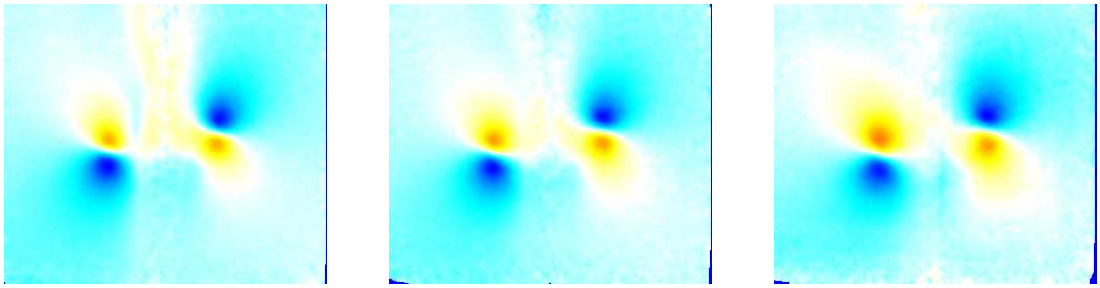

(g) $t+ = 9.35s, y^+ = 6.37$ (h) $t+ = 10.94s, y^+ = 7.13$ (i) $t+ = 12.49s, y^+ = 7.84$

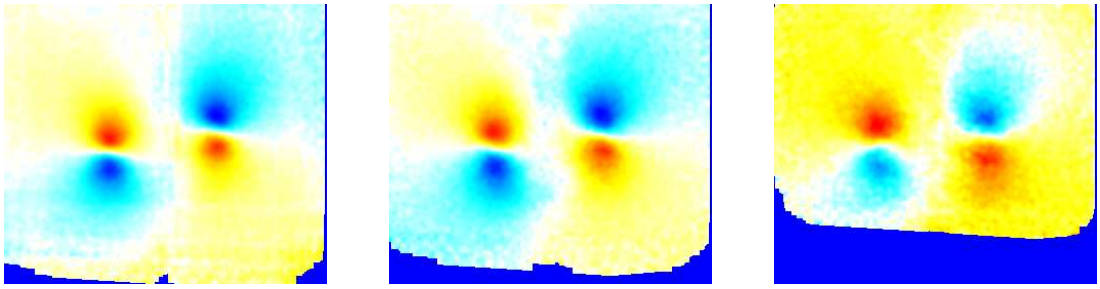

(j) $t+ = 14.05s, y^+ = 8.54$ (k) $t+ = 15.61s, y^+ = 9.21$ (l) $t+ = 17.17s, y^+ = 9.79$

Figure E.36: Evolution of $\overline{u_x}$ field for condition K

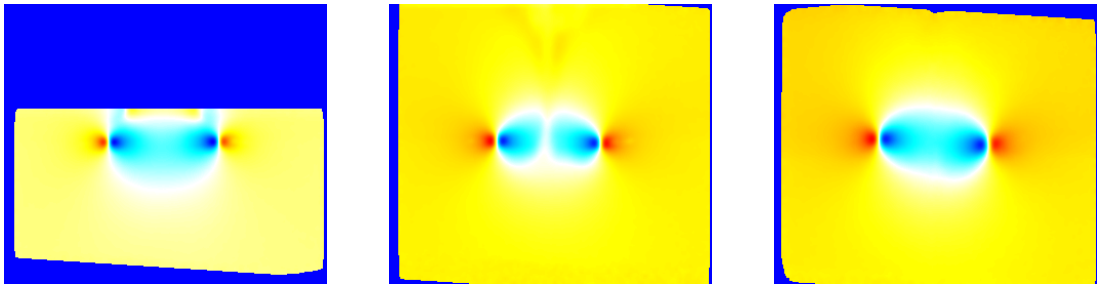

(a) $t+ = 0.41s, y^+ = 0.15$ (b) $t+ = 1.56s, y^+ = 1.32$ (c) $t+ = 3.12s, y^+ = 2.62$

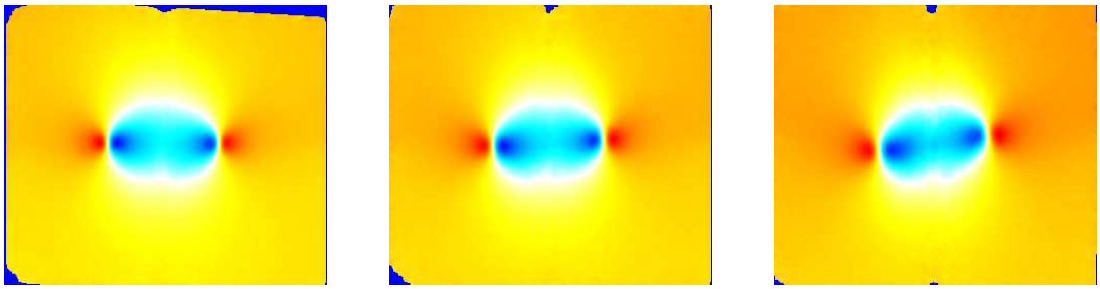

(d) $t+ = 4.67s, y^+ = 3.74$ (e) $t+ = 6.23s, y^+ = 4.72$ (f) $t+ = 7.79s, y^+ = 5.59$

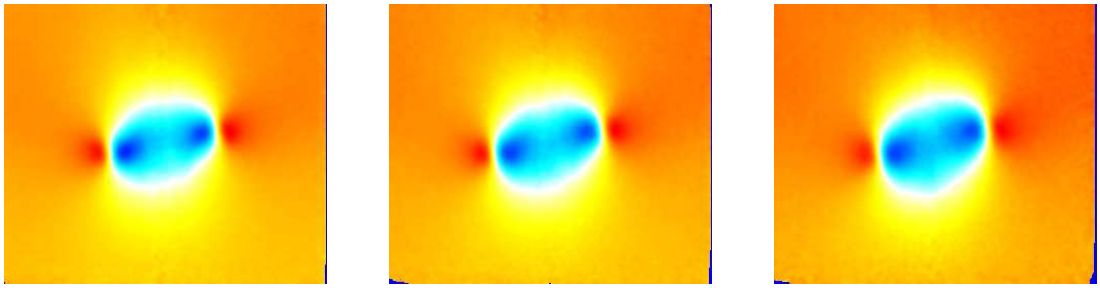

(g) $t+ = 9.35s, y^+ = 6.37$ (h) $t+ = 10.94s, y^+ = 7.13$ (i) $t+ = 12.49s, y^+ = 7.84$

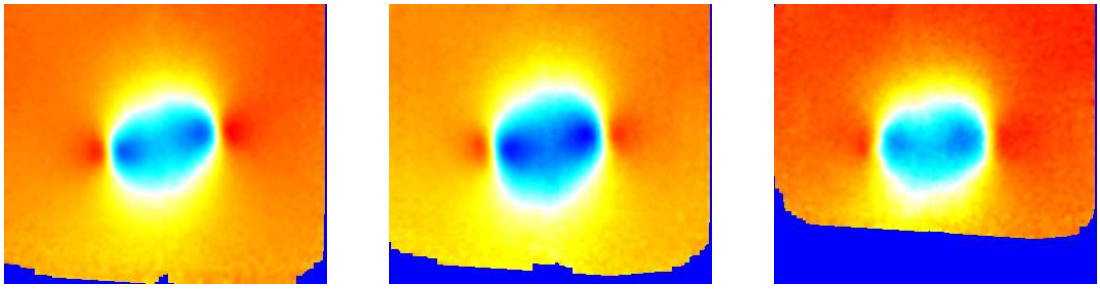

(j) $t+ = 14.05s, y^+ = 8.54$ (k) $t+ = 15.61s, y^+ = 9.21$ (l) $t+ = 17.17s, y^+ = 9.79$

Figure E.37: Evolution of $\overline{u_y}$ field for condition K

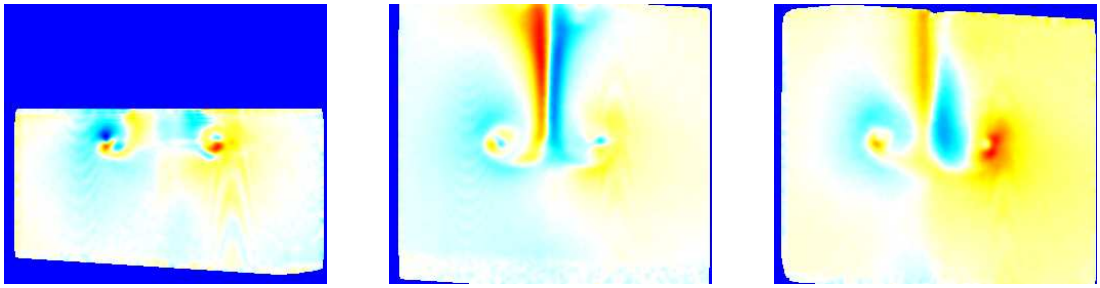

(a) $t+ = 0.41s, y^+ = 0.15$ (b) $t+ = 1.56s, y^+ = 1.32$ (c) $t+ = 3.12s, y^+ = 2.62$

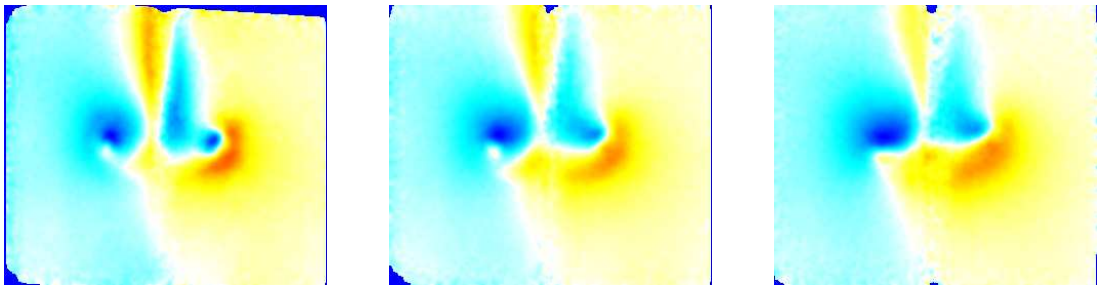

(d) $t+ = 4.67s, y^+ = 3.74$ (e) $t+ = 6.23s, y^+ = 4.72$ (f) $t+ = 7.79s, y^+ = 5.59$

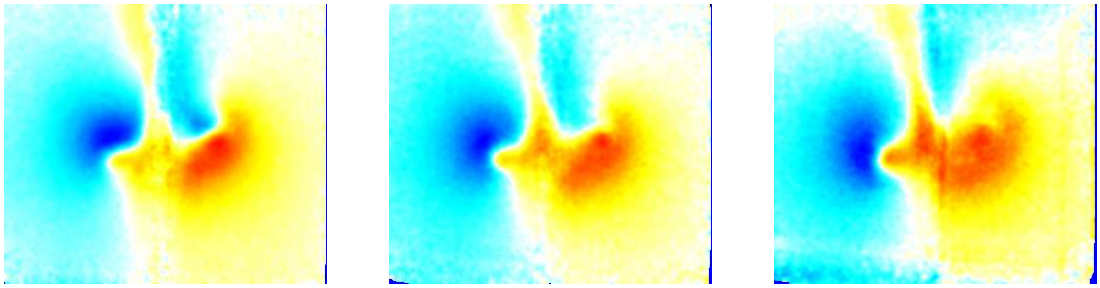

(g) $t+ = 9.35s, y^+ = 6.37$ (h) $t+ = 10.94s, y^+ = 7.13$ (i) $t+ = 12.49s, y^+ = 7.84$

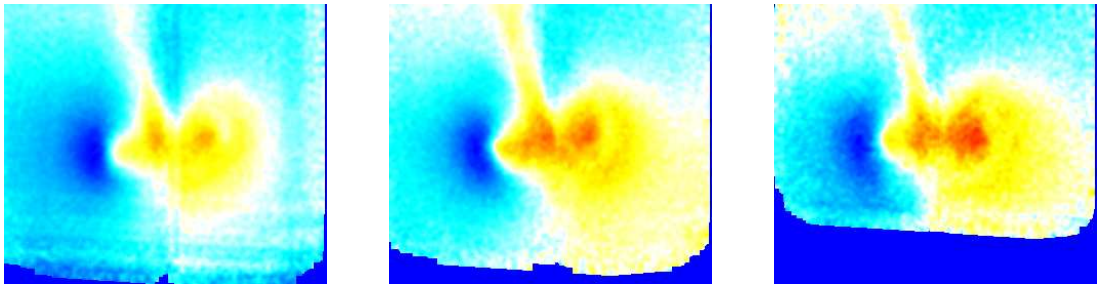

(j) $t+ = 14.05s, y^+ = 8.54$ (k) $t+ = 15.61s, y^+ = 9.21$ (l) $t+ = 17.17s, y^+ = 9.79$

Figure E.38: Evolution of $\overline{u_z}$ field for condition K

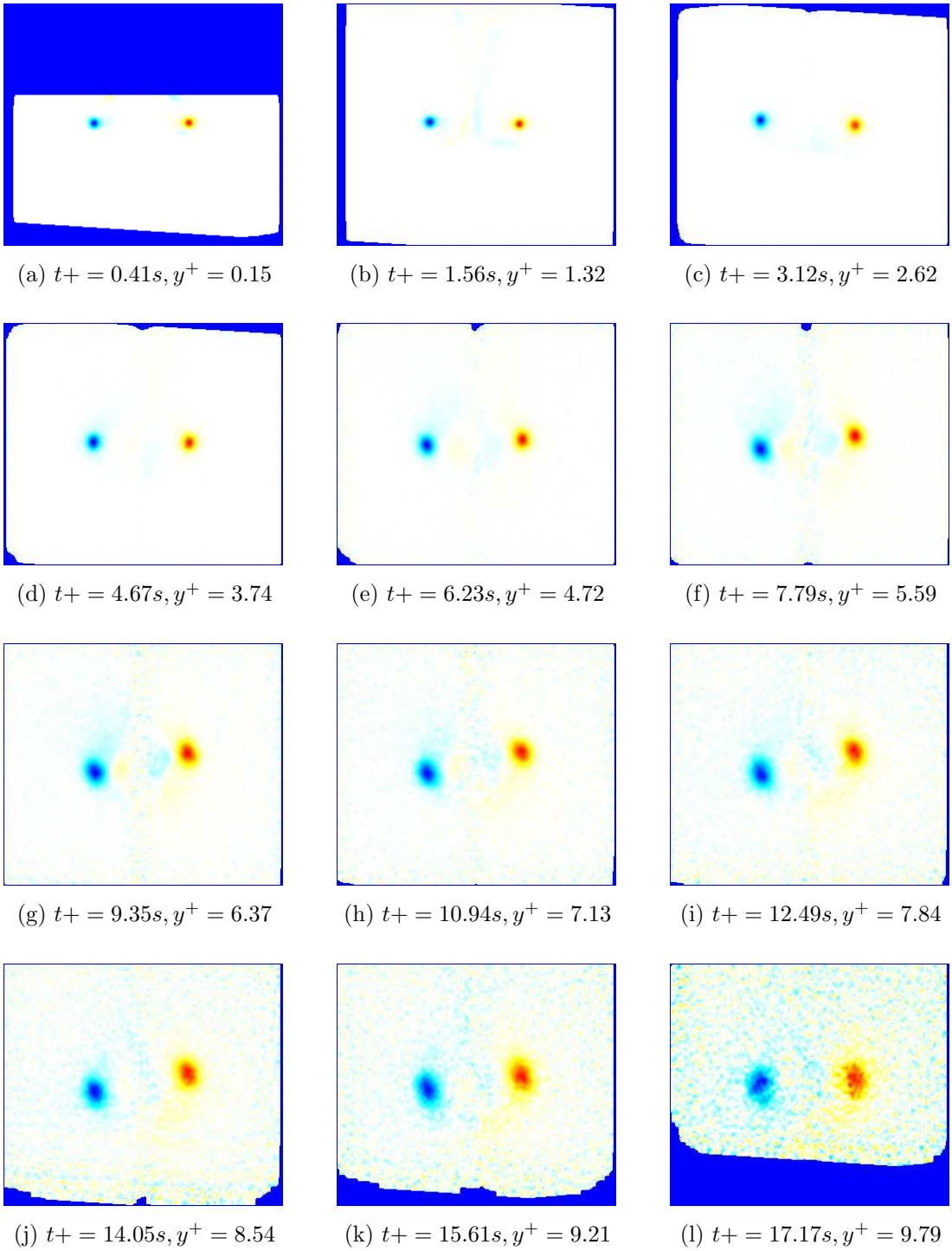

(a) $t+ = 0.41s, y^+ = 0.15$ (b) $t+ = 1.56s, y^+ = 1.32$ (c) $t+ = 3.12s, y^+ = 2.62$

(d) $t+ = 4.67s, y^+ = 3.74$ (e) $t+ = 6.23s, y^+ = 4.72$ (f) $t+ = 7.79s, y^+ = 5.59$

(g) $t+ = 9.35s, y^+ = 6.37$ (h) $t+ = 10.94s, y^+ = 7.13$ (i) $t+ = 12.49s, y^+ = 7.84$

(j) $t+ = 14.05s, y^+ = 8.54$ (k) $t+ = 15.61s, y^+ = 9.21$ (l) $t+ = 17.17s, y^+ = 9.79$

Figure E.39: Evolution of $\overline{\omega_z}$ field for condition K

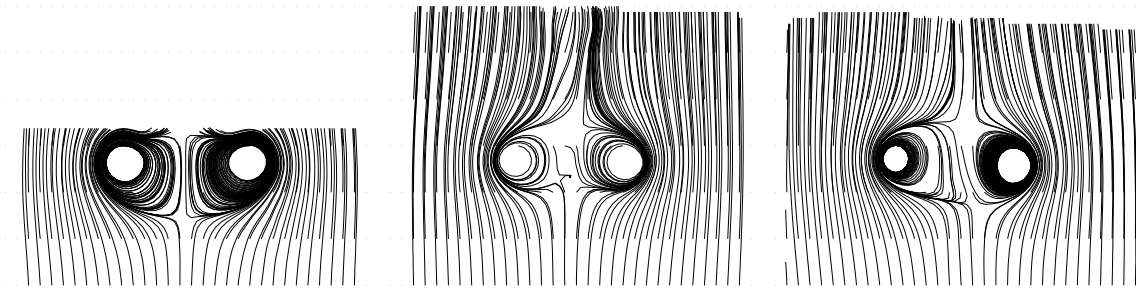

(a) $t+ = 0.41s, y^+ = 0.15$ (b) $t+ = 1.56s, y^+ = 1.32$ (c) $t+ = 3.12s, y^+ = 2.62$

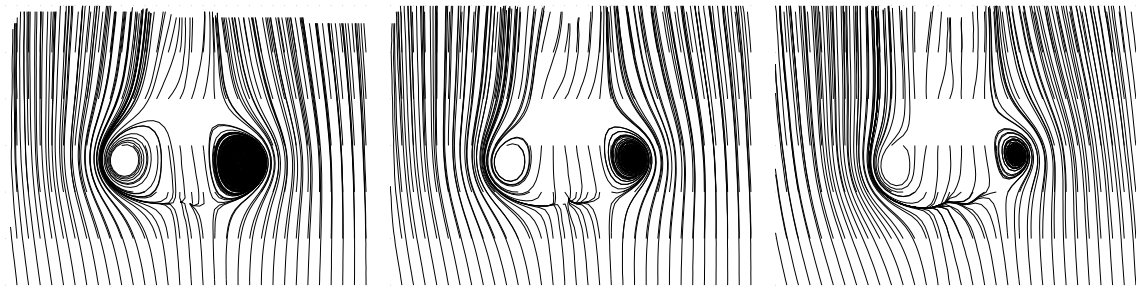

(d) $t+ = 4.67s, y^+ = 3.74$ (e) $t+ = 6.23s, y^+ = 4.72$ (f) $t+ = 7.79s, y^+ = 5.59$

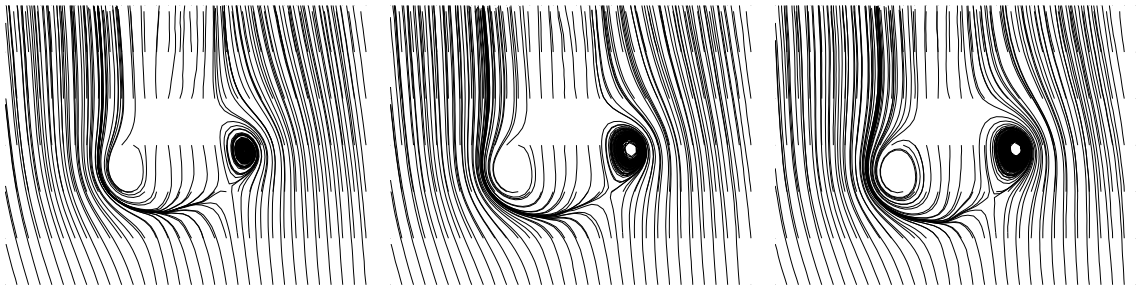

(g) $t+ = 9.35s, y^+ = 6.37$ (h) $t+ = 10.94s, y^+ = 7.13$ (i) $t+ = 12.49s, y^+ = 7.84$

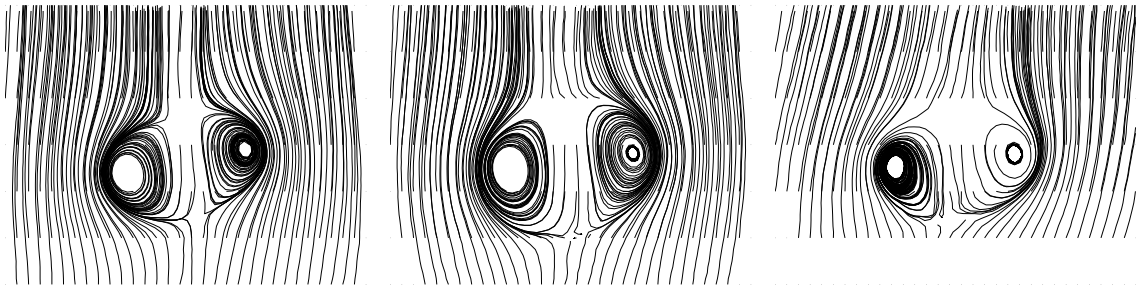

(j) $t+ = 14.05s, y^+ = 8.54$ (k) $t+ = 15.61s, y^+ = 9.21$ (l) $t+ = 17.17s, y^+ = 9.79$

Figure E.40: Evolution of $\overline{\psi}$ field for condition K